DEVELOPMENT OF SEISMIC GUIDELINES FOR DEEP-COLUMN STEEL MOMENT CONNECTIONS

by

James M. Ricles

Xiaofeng Zhang

Le-Wu Lu

John Fisher

Sponsored by the American Institute of Steel Construction (Project No. 2001 01-925 710110) and the Pennsylvania Infrastructure Technology Alliance through a grant from the Pennsylvania Department of Community and Economic Development

ATLSS Report No. 04-13

June, 2004

ATLSS is a National Center for Engineering Research on Advanced Technology for Large Structural Systems

117 ATLSS Drive
Bethlehem, PA 18015-4728

Phone: (610)758-3525
Fax: (610)758-5902

www.atlss.lehigh.edu
Email: inatl@lehigh.edu

ABSTRACT

A study was performed to investigate the effects of a floor slab on the seismic behavior of an interior moment connection between a pair of wide flange steel beams and a deep column. Emphasis was placed on a Reduced Beam Section (RBS) type of connection, because of its current popularity and the fact that recent research suggests the need for further investigations into the seismic behavior of RBS connections to a deep column.

The study involved three main tasks. These tasks included: (1) performing analytical parametric studies using nonlinear finite element models to evaluate the effect of various parameters on connection behavior; (2) conducting an experimental program with six full-scale test specimens to access the effects of selected parameters on connection performance and to examine whether RBS connections to a deep column can be qualified for seismic use in accordance with the standards in Appendix S of the 2002 AISC Seismic Provisions; and, (3) use of the results from the analytical and experimental studies to assess current design criteria and develop new design procedures for moment connections to a deep column, if required.

The finite element analysis results show that a composite floor slab provides restraint to the top flange of the beams, whereby the magnitude of beam top and bottom flange lateral movement in the RBS, as well as the column twist are reduced compared to when a slab is not present. Strength degradation due to beam instability in the RBS is also reduced by the restraint effect obtained from the floor slab. However, the floor slab increases the fracture potential of the connection, particularly at the end of the beam web-to-column flange CJP groove weld. This increase is more pronounced in RBS connections to shallower columns. The finite element studies also indicate that RBS connections have less potential for ductile fracture in the connection region than Welded Unreinforced Flange (WUF) connections. It was found that the ductile fracture potential for RBS connections to a deep column is less than that in WUF connections to a shallower W14 column section. These WUF connections were tested in prior studies and found to meet the qualification requirements for seismic use per Appendix S of the 2002

AISC Seismic Provisions. The fracture potential and column twist in an RBS connection depends on the section modulus and torsional rigidity of the column section, where larger stresses in the column flange can lead to a higher ductile fracture potential in the connection, in addition to column twist.

Six tests were conducted for the experimental program. The test results support the findings of the finite element study; all of the test specimens were found to have exceptional ductility and good performance to 4% story drift or beyond. The performance of the test specimens meet the requirements for seismic use that are stipulated in Appendix S of the 2002 AISC Seismic Provisions. Based on the test results it is concluded that an RBS connection with a floor slab or a supplemental lateral brace at the RBS will perform adequately if the column section size satisfies the weak beam-strong column criteria. Furthermore, an RBS connection to a deep column with a floor slab does not require any additional special considerations besides checking the column for torsional stresses.

Both the finite element study and experimental results indicate that at 4% story drift the out-of-plane movement of the beam bottom flange in an RBS connection with a floor slab is less than the value of 20% of the beam flange width, which is the value used in current design procedures to determine the torque applied to the column for an RBS connection. As a result, when a floor slab is present in an RBS connection the current design procedure overestimates the torsion warping stresses developed in the column. Based on the stress distribution in the beam flange from the analytical and experimental results, a new procedure is given in this report.

ACKNOWLEDGMENTS

This research project was co-funded by the American Institute of Steel Construction (AISC) and the Pennsylvania Department of Community and Economic Development through the Pennsylvania Infrastructure Technology Alliance (PITA) program. Mr. Tom Schlafly of AISC served as the project manager. The following companies donated materials for the experimental testing conducted in this research project: Arcelor International America of New York, NY (steel sections); Nucor Vulcraft Group of Chemung, NY (metal decking); and the Lincoln Electric Company of Cleveland, OH (welding wire). The Project Oversite Committee for this project consisted of the following members: Mr. Richard Drake; Mr. Lanny Flynn; Mr. Jim Malley; Mr. Hank Martin; Mr. Steven Powell; and Mr. Tom Schlafly. The funding by the project sponsors, material donations by the industry, and the helpful input from the Committee members and that provided by Dr. Chi-Ming Uang, Dr. Michael Engehardt, and Mr. Georges Axmann is greatly appreciated.

(This page left blank)

Table of Contents

(This page left blank)

List of Tables

List of Figures

CHAPTER 1 INTRODUCTION

1.1 Welded Steel Moment Resisting Connections and Deep Columns

Steel special moment resisting frame (SMF) systems are designed for earthquake loading conditions using the concept of a weak beam-strong column configuration. In the aftermath of the 1994 Northridge earthquake, damage to welded moment-resisting beam-to-column connections was discovered, where brittle fractures in or around the groove weld between the beam flanges (primarily the bottom flange) and column flange were found in over 150 welded steel moment-frame buildings (Youssef et al. 1995). The connections were found not to perform as designed, with minimal yielding occurring in the beams framing into the moment connection.

Following the Northridge earthquake, U.S. building codes have been revised to impose new requirements for moment connections in steel SMFs to ensure that they perform as designed. The 2002 AISC Seismic Provisions for Structural Steel Buildings (AISC 2002) require all moment connections be qualified for use in a seismic resisting system. Qualification typically involves testing the connection detail, where the specimen must successfully achieve at least 0.04 radians of inter-story drift during the test without fracture or significant strength degradation occurring

Since the Northridge earthquake, a wide variety of new beam-to-column moment connection details have been developed for use in steel SMFs. The new connection details include: the Reduced Beam Section connection (RBS); Welded Unreinforced Flange Welded-Web connection (WUF-W); Welded Unreinforced Flange Welded-Bolted connection (WUF-B); Free-Flange connection (FF); Welded Flange Plate connection (WFP); Bolted Flange Plate connection (BFP); and bolted fully restrained connections, which include the Bolted End Plate (BEP) connection. These connections were among those tested under Phase 2 of the SAC Steel Project (Roeder 2000). Additional studies were conducted under other research programs following the Northridge earthquake, in particular, studies on the RBS type of connection.

Figure 1.1 shows a radius cut RBS connection. This type of connection utilizes circular radius cuts in both the top and bottom flanges of the beam to reduce the flange width over a selected length of the beam near the column face. The beam flanges are welded to the column flanges with complete joint penetration (CJP) groove welds and the beam web is either welded to the column flange with a CJP groove weld or bolted to a shear tab. The shear tab is attached to the column flange by either CJP groove weld (for a bolted beam web) or fillet weld (for a welded beam web). The RBS connection is intended to force yielding and plastic hinge formation to occur within the reduced section of the beam, and thereby reduce any likelihood of fracture occurring at the beam flange groove welds and the surrounding base metal regions.

The RBS connection detail has been demonstrated to be reliable in numerous tests, and consequently has become one of the more popular connections in the design of SMF systems. Prior tests on RBS connections were performed with columns that were shallow (the columns had a maximum depth equivalent to a W14 section). The results from these tests led to design recommendations for RBS connections (Engelhardt 1999, FEMA 350 2000). These design recommendations are limited to a W14 column section.

To economically control seismic inter-story drift in an SMF, the use of deep columns has become increasingly more common. In a recent study involving the testing of an RBS connection to a deep column, a large amount of column twisting was observed (Chi and Uang, 2002). The specimen was a one-sided connection and had no floor slab. The specimen was not able to satisfy the AISC Seismic Provisions (AISC 2002) for pre-qualified use of the connection detail in the design of a SMF. Hence, there is a need to perform further studies in order to evaluate the use of RBS connections in SMFs involving deep columns.

1.2 Objectives

The above needs served as the basis for the research study reported herein. The research presented in this report was conducted under AISC Project No. 2001 01-925 710110 and is entitled *Development of Seismic Guidelines for Deep-Column Steel Moment Connections*. The main objectives of this research are:

1) To evaluate the effect of column depth on the seismic performance of moment connections and develop a more thorough understanding of the inelastic behavior of a moment connection to a deep column.
2) To evaluate the effectiveness of a composite floor slab in providing restraint to lateral-torsional buckling of the beam and twisting of the column, and enhancing cyclic strength and ductility of a moment connection to a deep column.
3) To evaluate the effectiveness of providing lateral bracing to the beam near the flexural plastic hinge to restrain the lateral-torsional buckling of the beam and twisting of the column, and promote the cyclic strength and ductility of a moment connection to a deep column.
4) To provide seismic design recommendations for the use of a moment connection to a deep column in SMFs.

The study included connections only to the strong axis of the column. Because of the current popular use of an RBS type of connection and the above concerns, the study focuses on RBS connections to a deep column. However, comparison between the expected behavior (from analysis) of an RBS connection and WUF-W connection are made.

1.3 Scope

To meet these objectives a study having three main tasks was conducted. These tasks included experimental and analytical studies, in addition to the development of design recommendations for RBS connections to deep columns. An overview of the three main tasks is given below.

1.3.1 Analytical Studies

Models of beam-to-column moment connections were developed using the general-purpose nonlinear finite element analysis program ABAQUS (HKS, 2001). The models were used to conduct a parametric study to examine the effects of the connection type, column section size, beam section size, panel zone strength, continuity plate thickness, beam web slenderness, and composite floor slab on the cyclic behavior of the connection. The connection types included an RBS and WUF-W detail. Analysis involving the application of inelastic monotonic lateral load were initially conducted to calibrate the models and to perform part of the parametric study. Analyses with inelastic cyclic lateral load were also performed to further calibrate the models and complete the parametric study. Both geometric and material nonlinearities were included in the finite element models. A sub-modeling technique was used to refine the mesh of the model in the local connection region in order to obtain a more accurate solution for the connection stress and strain states.

1.3.2 Experimental Studies

The experimental studies involve the full-scale testing of six RBS connection specimens. Each specimen represents an RBS connection to an interior column of a perimeter SMF. The details of the interior welded beam-to-column RBS connection that are shown Figure 1.1 are similar to those of the test specimens, where all of the specimens except for one had a composite floor slab. The column section sizes for the test specimens included W36x230, W27x194, W36x150, W27x146, and a W24x131. All columns were of A992 steel. The beam section sizes were a W36x150 and a W30x108. The beams for the specimens were of A572 Grade 50 steel, and A992 steel. The column and beam sizes were selected on the basis that torsional effects would have an influence on behavior accordingly to current design criteria proposed by Chi and Uang (2002). Specimens were fabricated using E70T-6 electrode for the beam flange complete joint penetration (CJP) groove welds and E71T-8 electrode for both the beam web CJP groove weld and supplemental fillet weld.

1.3.3 Development of Improved Design Procedures

In the third task the calibrated finite element models and test results were used to develop a new design procedure for an RBS and WUF connection to a deep column in an SMF. The procedure involves combining the column stresses due to flexure loading, axial loading, and torsional loading due to connection behavior, where the combined stresses are limited to the column yield stress (i.e., consistent with the current provisions in the AISC LRFD Specification (AISC 2000), Equation H2-1). The new aspects of the procedure are associated with the method for determining the torsion applied to the column due to beam flange movement. A comparison of the column stress predicted by the design procedure and the test results for the RBS connections is made to illustrate the accuracy of the design procedure.

1.4 Organization of Report

The remaining chapters of this report include Chapters 2 through 9, as well as six appendices. Chapter 2 of this report presents relevant background information on prior and concurrent research and seismic design provisions for welded beam-to-column connections in SMFs. In Chapter 3 the development and calibration of the finite element models, along with the results of the parametric study are presented. A description of the experimental study is given in Chapter 4, which includes in Chapter 4 are the test matrix, connection fabrication details, specimen dimensions, material properties, test setup, instrumentation and test procedure. The observed specimen behavior during testing is given in Chapter 5, with a comparison and analysis of the test results given in Chapter 6. Chapter 7 compares the finite element predictions of specimen behavior with specimen measured response. A new design approach for RBS moment connection with a deep column is presented in Chapter 8. A summary and set of conclusions for the analytical and experimental studies are presented in Chapter 9.

For each specimen a test summary is provided in Appendix A. The weld procedure specifications are given in Appendix B, and UT inspection reports are given in Appendix C. Stress-strain curves from tensile coupon tests for the steel material and weld metal of the specimens are provided in Appendix D. Weld metal CVN test reports are given in Appendix E. Scanning Electron Microscope pictures of the fracture surfaces for selected test specimens (SPEC-1, SPEC-2 and SPEC-6) are given in Appendix F. Appendix G introduces methods of calculating the warping normal stress for a wide flange section column subjected to torsional loading.

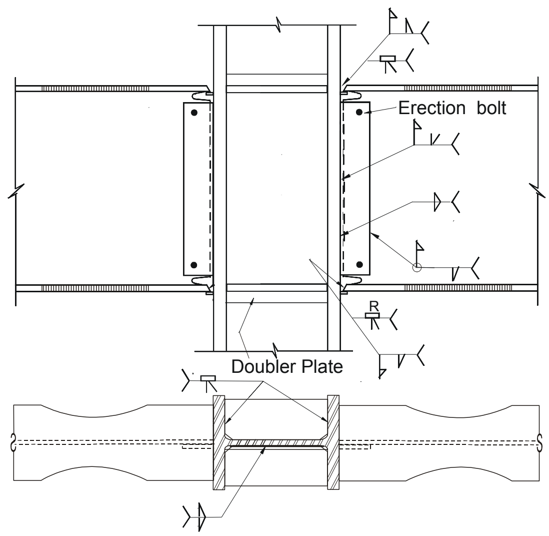

Figure 1.1 – Radius Cut RBS Moment Connection

CHAPTER 2 BACKGROUND

2.1 RBS and Relevant Prior Research

There have been numerous research studies on RBS connections, both before and after the 1994 Northridge earthquake. The SAC database (SAC 1999) reports the results of 95 RBS connection tests. The majority of the test specimens had a column depth of 14 inches (i.e., a W14 section was the most common among the columns of the test specimens). Only 12 of these 95 specimens had a column section of W24 or deeper. Figure 2.1 shows the test results for the story drift capacity of these RBS connection specimens. Drift capacity is defined as the ability of the test specimen to achieve a story drift for at least one cycle with neither fracture nor strength degradation below 80% of the specimen nominal capacity occurring. Figure 2.1 shows a trend in the data where deep columns result in a reduced story drift capacity of the RBS connection. The research by Chi and Uang (2002) showed that column twist is the cause of the reduction in story drift capacity.

This chapter presents a summary of the relevant prior research on RBS moment connections.

2.1.1 SAC Phase II RBS Connection Studies

Seventeen RBS connection specimens were tested under Phase II of the SAC Steel Project by Engelhardt et al. (2000), Yu et al. (2000), and Gilton et al. (2000). A summary of the test results is given in FEMA-355D (FEMA 2000c). Most of the specimens were tested using the SAC loading protocol (SAC 1997), which now is adopted by the AISC Seismic Provisions (AISC 2002). Eight cruciform-shaped A572, Grade 50 steel interior connection specimens were tested by Jones et al. (2002), including four specimens with a bare steel connection (i.e., no floor slab) and four with a composite floor slab. The columns in the test specimens were either a W14x398 or W14x283, while the beams were all W36x150 sections. It was found that most of the specimens developed a degradation in strength of 20% or more below their nominal capacity due to beam instability. This beam instability consisted of web and flange local buckling in the RBS.

The composite floor slab delayed the deterioration of the specimen strength and improved the load and rotation capacity of the connection. The test results suggested that the RBS segment of the beam is prone to earlier web local buckling compared to a connection with a prismatic beam. Connection specimens which had a weaker panel zone failed by fracture of the connection at a large story drift.

Finite element studies by Jones et al. (2002) and Deierlein et al. (1999) showed that a significant reduction in inelastic strain demands at the beam flange CJP groove weld occurs in an RBS connection. The studies by Deierlein et al. indicated that connections with a weaker panel zone are more susceptible to fracture than connections with a stronger panel zone. Three deep column RBS moment connection tests were conducted by Chi and Uang (2002) under Phase II of the SAC Steel Project. The column sizes for the specimens included a W27x146 and W27x194 section while the beams were W36x150 and W27x194 sections. The specimens were of an exterior connection type where only one beam was attached to the column, and no floor slab was present. The test results showed that beam web local buckling occurred in the RBS, followed by beam flange local buckling and subsequent lateral-torsional buckling. The lateral-torsional buckling led to a strength degradation of the specimens. Two of the specimens reached 3% plastic story drift while the other reached 2.8% plastic story drift. Column twisting was observed during the latter test, with an abrupt fracture occurring in the column k-area. Chi and Uang attributed this fracture to the twisting of the column. Two factors were noted as as contributing towards the fracture. The first was that the RBS lateral-torsional buckling causes torsional load and out-of-plane bending in the column. The second was that the torsional properties of deep wide flange sections tend to produce higher warping stresses in the column compared to a shallower column. Normal warping stress, when combined with bending normal stresses can cause overloading of the column. Chi and Uang correlated warping stresses to the large value for the ratio h/t_{cf}^3 for the column, where $h=d_c-t_{cf}$, with d_c and t_{cf} equal to the section depth and flange thickness, respectively. A procedure for designing an RBS connection to a deep column was developed by Chi and Uang. The procedure is discussed in Section 2.2.6.

2.1.2 Cyclic Stability Criteria for RBS Connections

Beam web stability plays a major role in the inelastic cyclic performance of an RBS connection. A statistical study was performed by Uang and Fan (2001) to evaluate web slenderness criteria of beams with an RBS connection to a column. Fifty five full-scale RBS moment connection test specimens were used in the study. In addition to web slenderness, beam flange slenderness and unbraced length were included in the study. Uang and Fan concluded from their study that the beam web slenderness ratio has the most influential effect on the plastic rotation capacity and rate of strength degradation. A concrete slab was determined to increase the plastic rotation capacity of an RBS connection under positive bending but not negative bending. Based on their study, Uang and Fan suggested that a lower beam web slenderness ratio h/t_w be considered for RBS connections than the value in the 1997 AISC Seismic Provisions (AISC 1997), which was $520/\sqrt{F_y}$, where F_y is the yield stress. Their recommendation was:

$$h/t_w \leq 418/\sqrt{F_y} \qquad , F_y \; in \, ksi \tag{2-1}$$

The new AISC Seismic Provisions (AISC 2002) requires the following criteria for h/t_w for all the members of a seismic load resisting system:

$$h/t_w \leq 2.45\sqrt{E_s/F_y} \; , \quad E_s \text{ and } F_y \text{ have the same units} \tag{2-2}$$

Equation (2-2) is identical to Equation (2-1) when a value of E_s = 29000 ksi is used for Young's modulus, E_s.

2.1.3 Use of Deep Columns In Steel Special Moment Resisting Frames

For economical reasons, design engineers tend to use deep columns in steel SMFs to meet story drift requirements. Some recent studies investigated the use of deep columns in steel SMFs (Shen et al. 2002). Two prototype moment frames were analyzed using inelastic time history analysis and the results compared. One frame utilized W14 sections as columns while the other used W27 sections for the columns. Nonlinear finite element analyses were also conducted to investigate the effect of a deep column on the performance of an RBS connection. Based on their study, Shen et al. made the following conclusions: (1) there were no considerable reasons found to suggest preventing the use of deep column sections in moment frames, including the SMFs; (2) the analyses indicated that the deep column connections should be able to provide the required strength, and especially the rotational ductility in excess of those required by FEMA-350 (FEMA 2000a) for pre-qualified connections; (3) the presence of a composite floor slab provided restraint to reduce column twist to insignificant and non-consequential levels; (4) the cyclic behavior of a RBS connection to a deep column was similar to the behavior of the same connections with W14 columns; (5) using deep columns in moment frames enable the drift limits to be satisfied with less steel tonnage compared to the use of shallower columns; and, (6) further experimental testing needs to be pursued involving specimens with RBS connections to deep columns with a composite floor slab.

2.2 Relevant Current Seismic Design Criteria for RBS Connections to a Deep Column

Current criteria contained in FEMA-350 (FEMA 2000a) and the AISC LRFD Seismic Provisions (AISC 2002) include provisions for panel zone strength, continuity plates, and the weld access hole size and geometry. These criteria are primarily for moment connections to column sections that do not exceed the depth of a W14. Below is a review of these criteria.

2.2.1 Panel Zone Strength

2.2.1.1 AISC Seismic Provisions

The current AISC Seismic Provisions (AISC 2002) requires that the panel zone strength shall be determined in accordance with the method used in proportioning the panel zone of the connection specimen for qualifying the connection by testing. As a minimum, the required shear strength R_u of the panel zone shall be determined from the summation of the moments at the column faces as determined by projecting the expected moments at the beam plastic hinge points to the column faces.

The design shear strength $\phi_v R_v$ of the panel zone shall be determined using ϕ_v=1.0, with R_v as stated below.

When $P_u \leq 0.75\ P_y$, where P_u is the column factored design load and P_y is the column axial yield force, R_v is based on the following

$$R_v = 0.6F_y d_c t_p \left[1 + \frac{3b_{cf}t_{cf}^2}{d_b d_c t_p}\right] \tag{2-3}$$

where

t_p = total thickness of panel zone including doubler plate(s),

d_c = overall column depth,

b_{cf} = width of column flange,

t_{cf} = thickness of column flange,

d_b = overall beam depth,

F_y = specified minimum yield strength of the panel zone steel.

When $P_u > 0.75\ P_y$, R_v shall be calculated using LRFD Specification Equation K1-12 (AISC 2000), which states:

$$R_v = 0.60F_y d_c t_p \left(1 + \frac{3b_{cf}t_{cf}^2}{d_b d_c t_p}\right)\left(1.9 - \frac{1.2P_u}{P_y}\right) \tag{2-4}$$

To prevent panel zone local buckling, the following must be satisfied:

$$t \geq (d_z + w_z)/90 \tag{2-5}$$

where

t = thickness of column web or doubler plate, or if plug welds are provided, the total thickness of the panel zone in inches,

d_z = panel zone depth between continuity plates in inches,

w_z = panel zone width between column flanges in inches.

2.2.1.2 FEMA-350

FEMA-350 (FEMA 2000a) suggests that moment-resisting connections be proportioned either so that shear yielding of the panel zone initiates at the same time as flexural yielding of the beam elements, or so that all yielding occurs in the beam. The required thickness of the panel zone is calculated using the following equation:

$$t = \frac{C_y M_c \frac{h - d_b}{h}}{(0.9)0.6 F_{yc} R_{yc} d_c (d_b - t_{fb})} \tag{2-6}$$

where

C_y = ratio of yield moment capacity to the plastic moment capacity of the beam, which can be calculated by:

$$C_y = \frac{1}{C_{pr} \frac{Z_{be}}{S_b}} \tag{2-7}$$

M_c = moment at column centerline based on the beam plastic moment capacity projected from beam plastic hinge; the location of expected plastic hinge formation should be identified based on the data presented in FEMA-350 for prequalified connections, or data obtained from a qualification testing program for configurations that are qualified on a project-specific basis,

h = the average story height of the stories above and below the panel zone,

R_{yc} = the ratio of the expected yield strength of the column material to the minimum specified yield strength,

C_{pr} = a factor to account for the peak connection strength, which is given by:

$$C_{pr} = \frac{F_y + F_u}{2F_y} \tag{2-8}$$

S_b = the elastic section modulus of the beam at the zone of plastic hinging,

Z_{be} = the effective plastic section modulus of the beam at the zone of plastic hinging.

The recent draft of the document entitled *Prequalified Connections for Special and Intermediate Steel Moment Frames for Seismic Applications* by AISC (AISC 2003, hereinafter referred as Draft) adopted the above criteria.

2.2.2 Continuity Plates

For the design of continuity plates in seismic regions, the AISC Seismic Provisions (AISC 2002) states that continuity plates shall be provided to match the tested connection. In the commentary of the AISC Seismic Provisions, it refers to FEMA-350 (FEMA 2000a) criteria which are based on research by Ricles et al. (2000). FEMA-350 criteria state that unless project-specific connection qualification testing is performed to demonstrate that beam flange continuity plates are not required, moment-resisting connections should be provided with beam flange continuity plates across the column web when the thickness of the column flange is less than the value given either by the following two equations:

$$t_{cf} < 0.4\sqrt{1.8 b_f t_f \frac{F_{yb} R_{yb}}{F_{yc} R_{yc}}} \tag{2-9}$$

$$t_{cf} < \frac{b_f}{6} \tag{2-10}$$

where

t_{cf} = minimum required thickness of column flange when no continuity plates are provided, in inches,

b_f = beam flange width in inches,

t_f = beam flange thickness in inches,

$F_{yb}(F_{yc})$ = minimum specified yield stress of the beam (column) flange,

$R_{yb}(R_{yc})$ = the ratio of the expected yield strength of the beam (column) material to the minimum specified yield strength.

When continuity plates are required, the thickness of the plates should be determined per FEMA-350 according to the following:

- For one-sided (exterior) connections, continuity plate thickness shall be at least one-half of the thickness of the beam flanges.
- For two-sided (interior) connections, the continuity plates should be equal in thickness to the thicker of the two beam flanges on either side of the column.

The Draft (AISC 2003) adopted the above Equations (2-9) and (2-10) for the design of continuity plates in a moment connection.

2.2.3 Weld Access Hole

A newly developed weld access hole geometry is recommended by FEMA-350 (FEMA 2000a) for most welded moment-resisting connections. And the AISC Seismic Provisions (AISC 2002) requires that it be used in fully restrained (FR) moment connections for ordinary moment frames (OMF). These recommendations are based on the research performed by Ricles et al. (2000). Figure 2.2 shows the geometry of the modified weld access hole.

2.2.4 RBS Design and Fabrication

2.2.4.1 RBS Design

The location and proportion of the beam flange cut for RBS connections need to be optimized to obtain good performance from an RBS connection. Engelhardt (1999) developed a design approach based on prior studies, which is similar to the design procedures in FEMA 350 (FEMA 2000a). Below is the FEMA 350 RBS connection design procedure. Except a few changes as noted below, the Draft (AISC 2003) adopted the same design procedure.

(1) Determine the length and location of the beam flange reduction, based on the following

$$a \cong (0.5 \text{ to } 0.75) b_f \tag{2.11}$$

$$b \cong (0.65 \text{ to } 0.85) d_b \tag{2.12}$$

where a and b are as shown in Figure 2.3, and b_f and d_b are the beam flange width and beam depth, respectively.

(2) Determine the amount of the flange reduction, c, (see Figure 2.3) according to the following

a. Assume $c = 0.20 b_f$

b. Calculate the plastic section modulus Z_{RBS} at the center of the RBS

c. Calculate the moment M_f at the column face

$$M_f = M_{pr} + V_p \left(a + \frac{b}{2}\right) \tag{2.13}$$

where M_{pr} is the expected plastic moment at the RBS:

$$M_{pr} = C_{pr} R_y Z_{RBS} F_y \tag{2.14}$$

and V_p is the shear force at the RBS, including both lateral and gravity load effects. The Draft recommends a value for C_{pr} equal to 1.15.

d. If $M_f < C_{pr} R_y Z_b F_y$, where Z_b is the beam plastic section modulus, the design is acceptable. The Draft changes this criterion to $M_f < M_{pe}$, where $M_{pe} = Z_b R_y F_y$. If M_f is greater than the limit, then increase c. The value of c should not exceed $0.25b_f$.

Note that the effect of composite action on the RBS flexural capacity is ignored in this procedure.

2.2.4.2 RBS Connection Fabrication Requirements

FEMA 353 (FEMA 2000b) has several fabrication requirements for an RBS connection. These include that no holes may be drilled or punched in either flange of the beam within the length that has received the radius cut, or between the RBS cut and the column. Shear studs and mechanical deck fasteners to the beam flange within the length of the radius cut are also prohibited.

After thermal cutting, the RBS surface shall have a surface roughness of no more than 500 micro-inches. Corners between the cut RBS surface and the top and bottom of the beam flanges shall be ground to remove sharp edges, but a minimum radius or chamfer is not required.

2.2.5 Weld Metal Toughness Requirement

2.2.5.1 AISC Seismic Provisions

In accordance with the AISC Seismic Provisions (AISC 2002) all welds used in members and connections of a seismic load resisting system shall be made with a filler metal that can produce welds that have a minimum Charpy V-Notch toughness of 20 ft-lbf at -20°F, as determined by AWS classification or manufacturer certification.

For structures in which the steel frame is normally enclosed and maintained at a temperature of 50°F or higher, the following CJP welds in Special and Intermediate Moment Frames shall be made with filler metal capable of providing a minimum Charpy

V-Notch toughness of 20 ft-lbf at -20°F by AWS classification test methods and 40 ft-lbf at 70°F, as determined by AISC Seismic Provisions Appendix X (AISC 2002) or other approved method:

(1) Welds of beam flanges to columns

(2) Groove welds of shear tabs and beam webs to columns

(3) Column splices

2.2.5.2 FEMA 353

In accordance with FEMA 353 (FEMA 2000b) all welds in members comprising the seismic force resisting system shall employ weld filler metals classified for nominal 70 ksi tensile strength, referred to as E70 electrodes, meeting the following minimum mechanical property requirements:

(1) CVN toughness of 20 ft-lbf at 0°F, using AWS A5 classification test methods

(2) CVN toughness of 40 ft-lbf at 70°F, using the test procedures prescribed in Appendix A of FEMA 353.

2.2.5.3 Draft of AISC Prequalified Connections

The Draft (AISC 2003) states "All welds shall have a toughness of 20 ft-lbf at –20-degrees F and welds designated as Demand Critical shall have a toughness of 40 ft-lbf at 70-degrees F."

2.2.6 Design Recommendations for RBS Connections to a Deep Column

As aforementioned, Chi and Uang (2002) observed severe column twisting during testing, and consequently proposed a design procedure for RBS connections to a deep column. The procedure developed is based on the beam compression flange force F being orientated at the angle θ with respect to the longitudinal axis of the beam, as shown in Figure 2.4. The angle θ develops due to the lateral movement of the beam compression flange in the RBS. The beam flange force, F, can be estimated by multiplying the reduced beam flange area by the expected yield strength at section *A-A* in the RBS. As shown in Figure 2.4, the total torque imposed to the column is $F(e_x \cos\theta + e_y \sin\theta)$, where the eccentricities e_x and e_y are defined in Figure 2.3. The stresses due to bending and torsion are subsequently calculated based on elastic theory.

Using elastic torsion theory with some simplifications, Chi and Uang arrived at the following expression for column flange warping normal stress, f_{ws}:

$$\frac{f_{ws}}{T} = \frac{1.95}{2 + C_1}\left(\frac{h}{t_{cf}^3}\right)\left(\frac{\beta}{a_c}\right) \tag{2-15}$$

where

T = applied torque

C_1 = ratio between proportion of torsion resisted by column web and flanges (according to Chi and Uang, C_1 remains relatively constant for a given column depth),

$h = d_c - t_{cf}$,

d_c = column section depth,

t_{cf} = column flange thickness,

$\beta = \theta'' \times \left(\frac{GJ}{T} \times a_c\right)$, where θ is the angle of rotation, measured in radians (see Seaburg and Carter, 1997),

$a_c = \sqrt{\frac{EC_w}{GJ}}$, with E equal to the modulus of elasticity, G the shear modulus of elasticity, C_w the warping torsional constant of the column section, and J the torsional constant of the column section.

For a given torque, the warping normal stress is considered by Chi and Uang to be proportional primarily to the ratio h/t_{cf}^3. The variation of h/t_{cf}^3 with weight for various wide flange shapes is shown in Figure 2.5. Deeper columns have a higher value for h/t_{cf}^3 than shallow columns, and in accordance with Equation (2-15) the warping normal stress in deep columns is larger.

The design procedure developed by Chi and Uang (2002) for an RBS connection is given below.

1. Assume that at 4% story drift that a lateral movement of the beam compression flange has occurred, where the eccentricity $e_x = 0.2b_f$, where b_f is the beam flange width.

This assumption is based on observations from the three RBS connection-to-deep column tests conducted by Chi and Uang (2002).

2. The inclined angle θ of the beam flange force due to the lateral movement of the beam compression flange is thus equal to

$$\theta = \tan^{-1}\left(\frac{e_x}{\frac{L}{2} - a - \frac{b}{2}}\right) \tag{2-16}$$

   where *a, b*, and *L* are defined in Figure 2.3 (*L* is the clear span length of the beam).

3. The beam flange force *F* is estimated as

$$F = b'_f t_{bf} F_{ye} \tag{2-17}$$

   where b'_f is the beam flange width at the center of the RBS and F_{ye} is the beam expected yield stress (AISC 2002). Strength degradation usually occurs at 4% story drift. Hence, no strain hardening effects are therefore considered in Equation (2-17).

4. The torsional force *T* imposed to the column by *F* for a one-sided connection, or for a two-sided connection with a floor slab, is

$$T = F(e_x \cos\theta + e_y \sin\theta) \tag{2-18}$$

5. The warping normal stress f_{ws} in the column flanges is calculated as

$$f_{ws} = \frac{EW_{n0}\beta}{GJa_c}T \tag{2-19}$$

   where W_{n0}, is equal to $\frac{hb_f}{4}$. For a two-sided connection without a floor slab the torque contributed by both beams is applied, whereby the torque T in Equation (2.19) needs to be doubled.

6. The strong-axis bending stress f_{bx} due to the in-plane bending moment of the column is

$$f_{bx} = \frac{M_{col}}{S_{xc}} \tag{2-20}$$

where M_{col} is the column moment acting about the column strong axis and S_{xc} is the column section modulus for the strong axis of bending.

7. The weak-axis bending stress f_{by} due to the out-of-plane bending of the column is calculated by applying the out-of-plane component of force F (i.e., $F\sin\theta$) to the column at the beam compression flange level, and treating the column as simply supported at two inflection points located along the column span.

8. The total stress f_{total} is then computed, and checked to ensure that it complies with the limit of ϕF_{yn}, as set forth by the permissible design stress formula (H2-1) in the AISC LRFD Specification (AISC 2000), where:

$$f_{total} = f_{ws} + f_{bx} + f_{by} \leq \phi F_{yn} \tag{2-21}$$

In Equation (2-21) ϕ=0.9 and F_{yn} is the column nominal yield stress.

2.3 WF Section Torsional Characteristics

To evaluate the impact of using deep columns in SMF systems, an investigation was conducted to establish the relationship between column section size, properties, and their ability to satisfy design criteria.

Modern building design codes require a weak beam-strong column criterion to be satisfied. Using a W36x150 section with a 50% RBS flange cut, all wide flange rolled sections in the AISC LRFD manual (AISC 2000) were studied for potential use as a column by evaluating whether they satisfied the weak beam-strong column criterion. Figures 2.6 and 2.7 show the column-to-beam strength ratio plotted against column section weight for an interior joint in an SMF. In the calculations a story height of 13 ft. and bay spacing of 29.5 ft. were assumed. In Figures 2.6 and 2.7, $\sum M^*_{pc}$ and $\sum M^*_{pb}$ are the sum of column nominal and beam expected plastic moment capacities, respectively, extrapolated to the intersection of beam and column centerline. Those sections with the column-to-beam strength ratio $\sum M^*_{pc}/\sum M^*_{pb}$ greater than 1.0 satisfy the weak beam-strong column criterion in the AISC Seismic Provisions (AISC 2002). Figure 2.8 shows the section flexural stiffness *EI* for various columns compared to a W14x398 column. For a given weight, the flexural stiffness is shown in Figure 2.8 to increase with column depth. The results in Figure 2.6 through 2.8 indicate that deeper columns are able to satisfy the weak beam-strong column criterion using a lighter section compared to a shallower column, while providing a larger flexural stiffness to control story drift. It therefore is apparent that it is more economical to utilize deeper column sections in the design of a SMF.

The effect of torsion on wide-flange sections is well known (Seaburg and Carter, 1997). Torque causes St. Venant shear stresses in addition to warping shear and warping normal stresses to develop in a wide-flange section. The section torsional characteristics for various columns sizes were therefore studied and compared. For the study, a column in a moment resisting frame was analyzed using the simplified model shown in Figure 2.9. The model consists of the column between the floor below (floor level $i-1$) and above (floor level $i+1$) the floor that is of interest (i.e., floor level i), where a torque load (T) from a beam-to-column RBS connection is applied. The ends of the column are assumed torsionally fixed (i.e., the column is restrained at floor levels $i-1$ and $i+1$ from twisting relative to floor level i), consequently, the restraint of the floors at level i and $i+1$ cause warping stresses to develop at the ends of the column. The torque diagram, as well as the components of St. Venant torque and Warping torque that resist the total applied torque T, are also shown in Figure 2.9. At the connection region (i.e., at floor level i) the column resists the torque through warping torsion. Shear and normal warping stresses will consequently develop in the cross-section of the column at floor level i, as shown in Figure 2.10.

The maximum shear and normal warping stresses were computed for various sections, and are shown normalized to the results for a W14x398 column in Figure 2.11 and 2.12, respectively. Both the shear and normal warping stresses are shown to increase as the column section becomes lighter. The shear warping stresses in Figure 2.11 show a somewhat greater sensitivity to section size (i.e., column depth) compared to the normal warping stresses plotted in Figure 2.12. The latter is shown in Figure 2.12 to be almost insensitive to column depth, and primarily influenced by the column weight. A W27x146 section would have an increase of about 6 times its normal warping stresses compared to that of a W14x398, while the increase in shear warping stress between these two sections would be about 2.

The model in Figure 2.9 was used to determine the column torsional stiffness (i.e., the amount of torque required to be applied at the connection at floor level *i* to cause a twist of one unit) for various column section sizes. These results are shown in Figure 2.13, and include the effects of St. Venant and Warping torsional resistance. For a given column weight, it is apparent in Figure 2.13 that a deeper column has a larger torsional stiffness compared to a shallower column section, particularly for sections with a weight exceeding 200 lb/ft. Lighter sections are shown to have a reduction in their torsional stiffness.

The above analyses indicate that columns with a deeper section, but lighter in weight resulting in a larger value for the ratio h/t_{cf}^3, are more susceptible to the effects of torsion. The torsional stiffness is reduced, while the warping stresses are increased. A reduced torsional stiffness will result in more twisting of the column. While the flexural stiffness and strength are enhanced by the use of a deeper column, the use of a deeper column (which results in a lighter column and larger value for the ratio h/t_{cf}^3) is likely to make the column more sensitive to the effects of torsion.

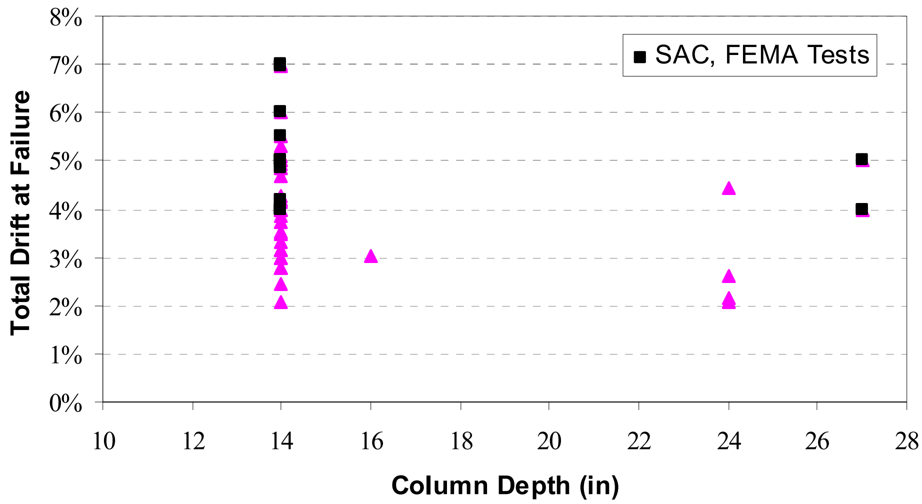

Figure 2.1 – Total story drift vs. column depth of past RBS connection tests

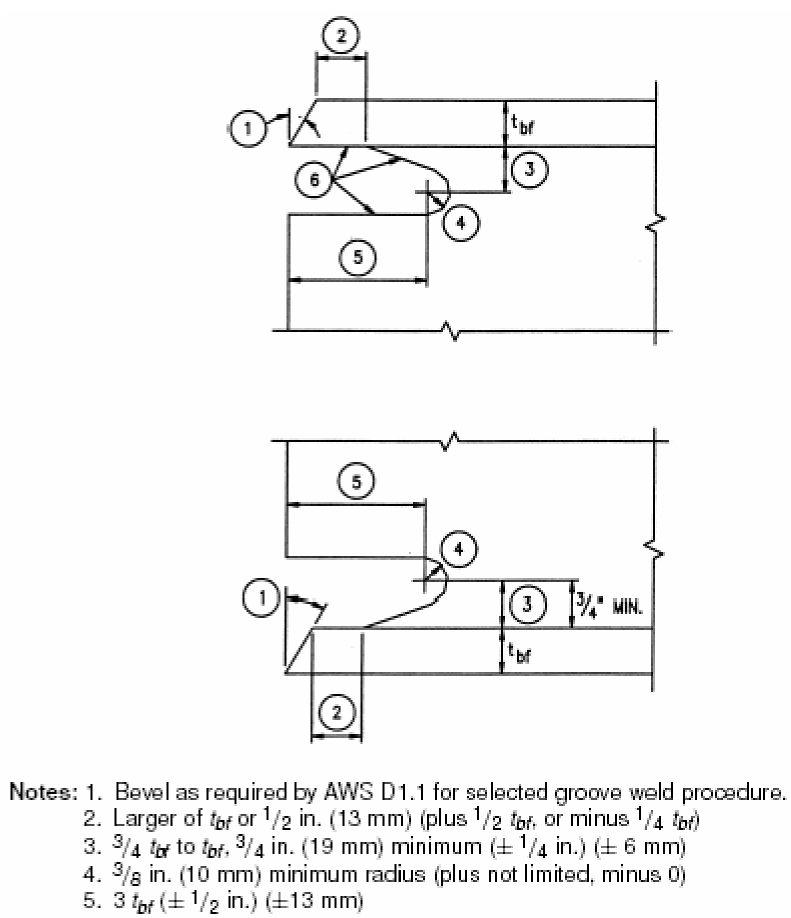

Figure 2.2 – Modified weld access hole (AISC 2002)

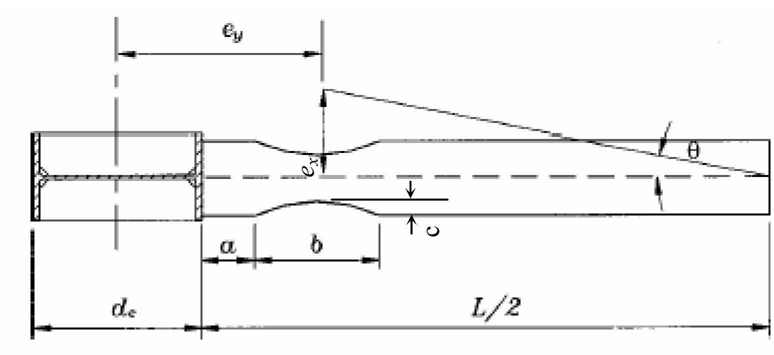

Figure 2.3 – Inclined angle of beam flange force (after Chi and Uang, 2002)

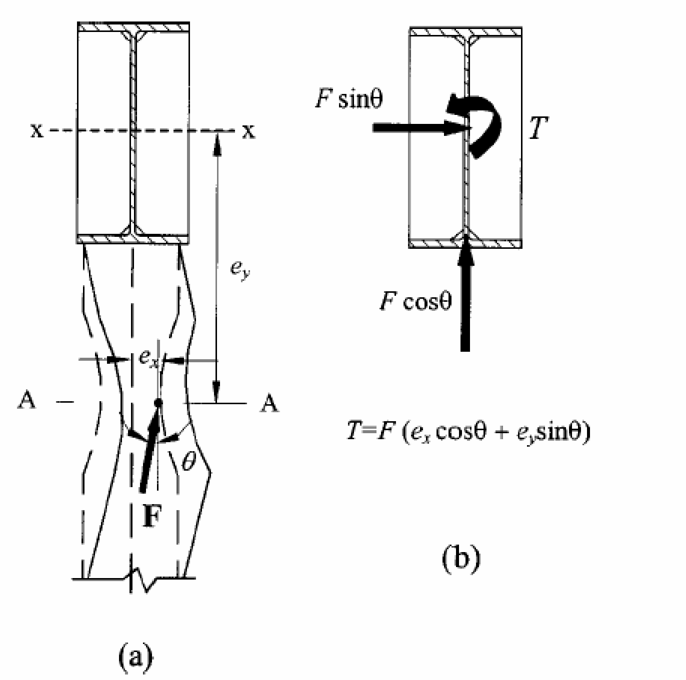

Figure 2.4 – Beam compression flange lateral movement (after Chi and Uang, 2002)

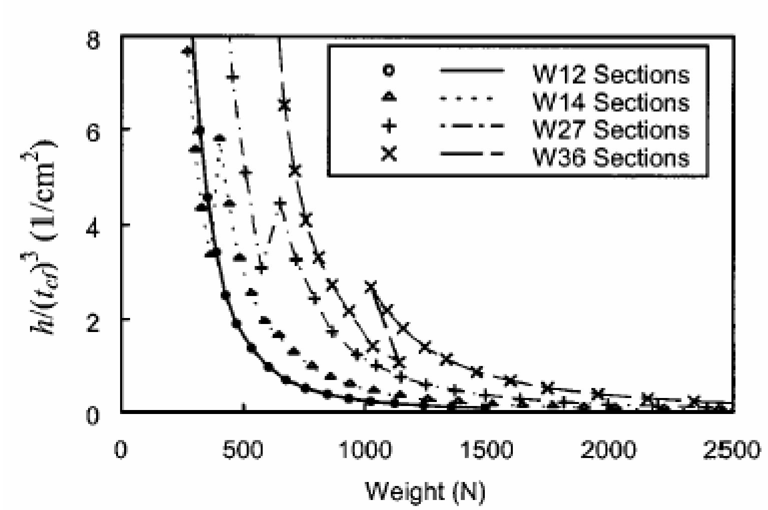

Figure 2.5 – Variation of $\dfrac{h}{t_{cf}^3}$ with section weight (after Chi and Uang, 2002)

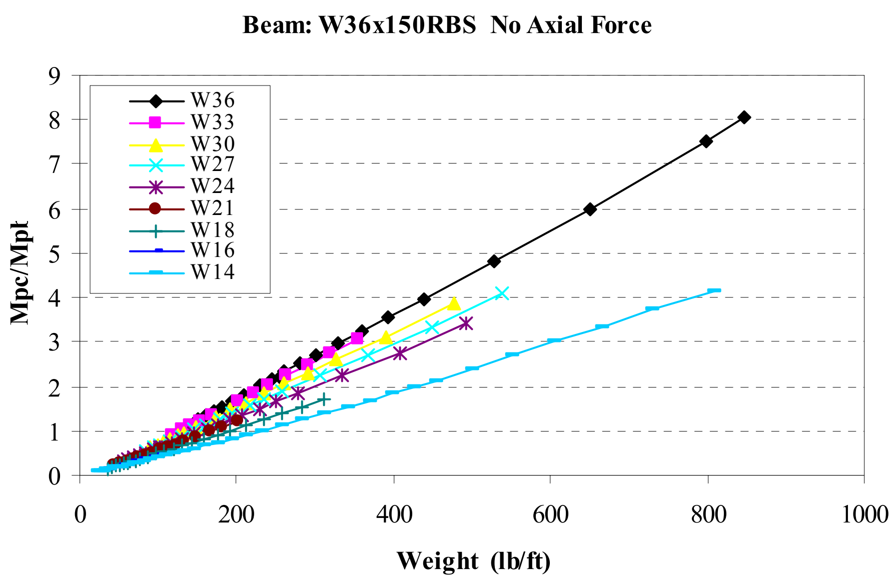

Figure 2.6 – Column-to-beam flexural strength ratio vs. column section weight, column without axial force

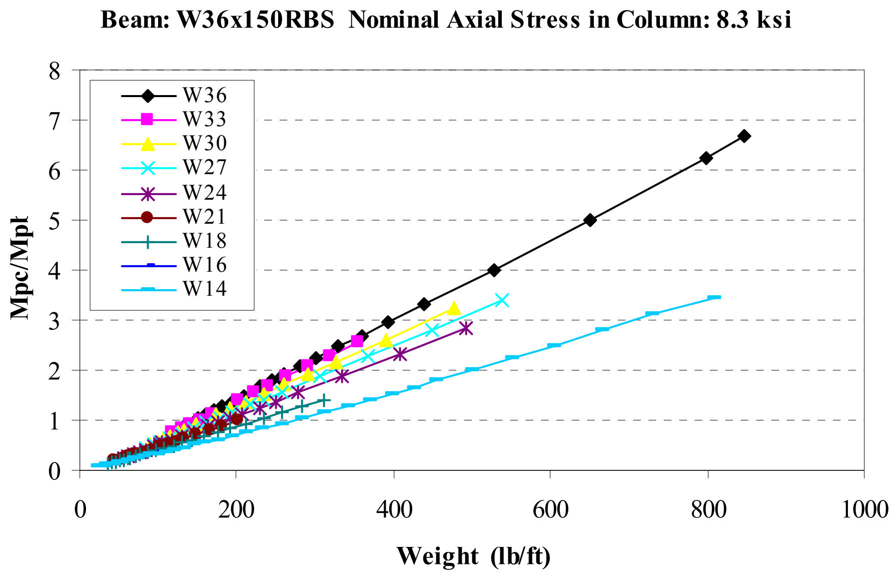

Figure 2.7 – Column-to-beam flexural strength ratio with vs. column section weight, column with axial force

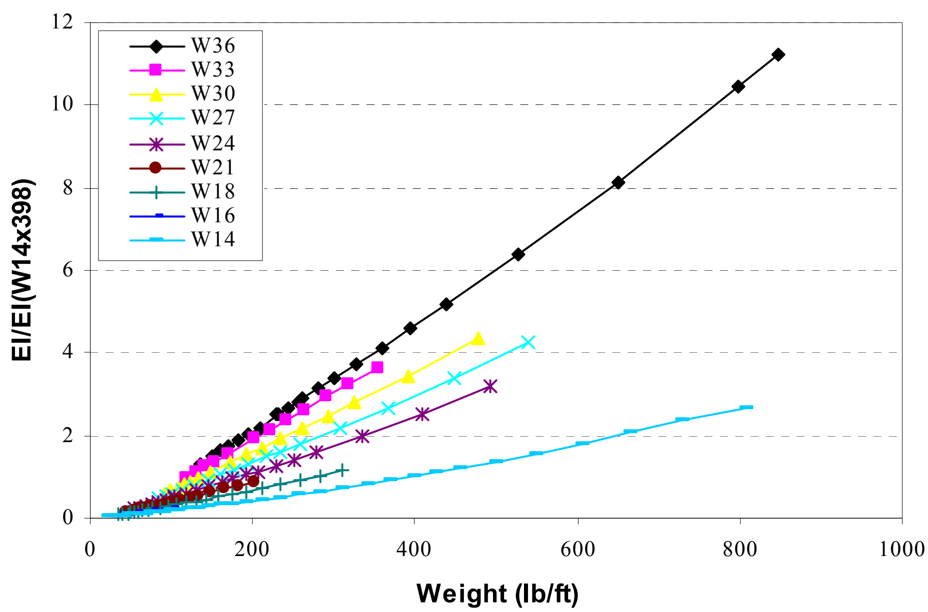

Figure 2.8 – Section flexural stiffness vs. column section weight (Section flexural stiffness normalized by *EI* of W14x398)

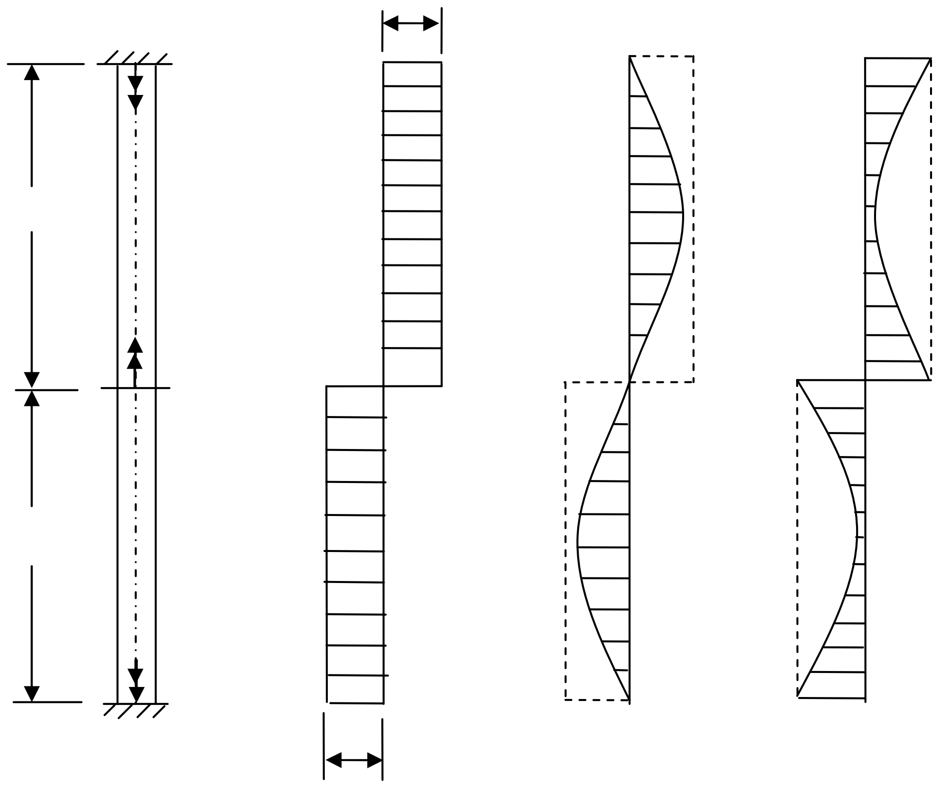

Figure 2.9 – Torsional response of WF section column

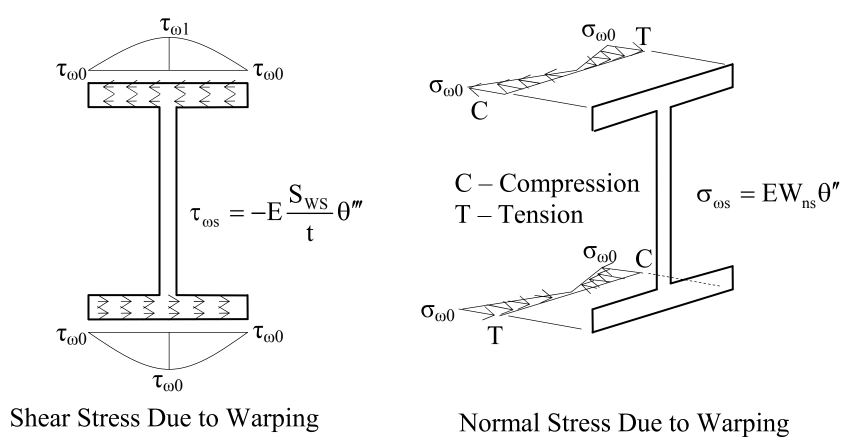

Figure 2.10 – Warping stresses developed in a WF section subjected to torsion

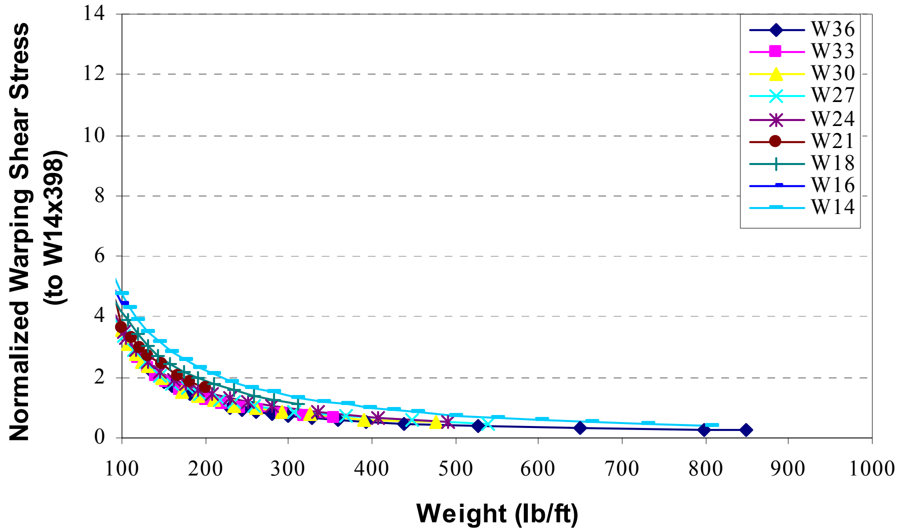

Figure 2.11 – Warping shear stresses developed in a WF section vs. section weight (Normalized by W14x398 result)

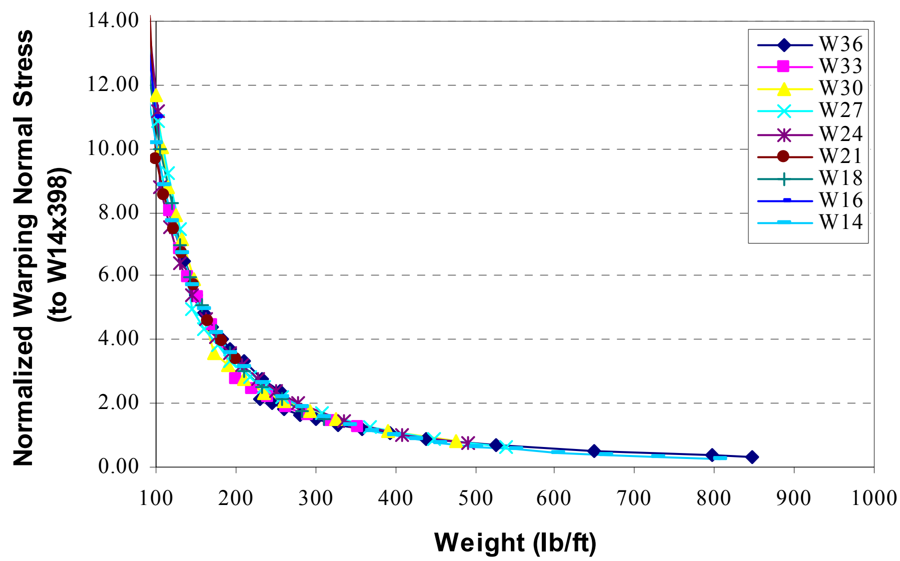

Figure 2.12 – Warping normal stresses developed in a WF section vs. section weight (Normalized by W14x398 result)

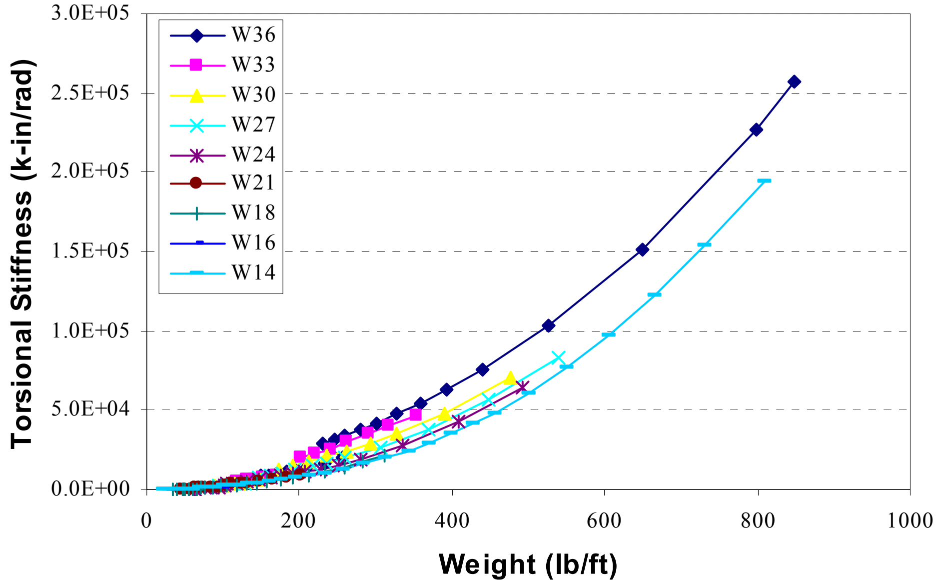

Figure 2.13 – Column torsional stiffness vs. section weight

CHAPTER 3 FINITE ELEMENT ANALYSIS

3.1 General

The finite element study involved modeling connections in order to evaluate the effect of various parameters on connection behavior. These included: (1) connection type; (2) column size; (3) beam size; (4) panel zone strength; (5) continuity plate thickness; (6) composite floor slab; and (7) axial load. The general-purpose nonlinear finite element analysis (FEA) program ABAQUS (HKS 2001) was used to develop 3-D nonlinear finite element models of connection subassemblies. The geometry (i.e., member span lengths) and boundary conditions of the connection subassemblies were based on the test setup used in the experimental study. The member section sizes for the models in the analysis matrix were based on representing the range of anticipated member section sizes for the test specimens. Furthermore, the beam section size was selected for each model to ensure a weak beam-strong column configuration, which is required by the AISC Seismic Provisions (AISC 2002). Unless otherwise noted, the continuity plates were Grade 50 steel and nearly the same thickness as the attached beam flanges. For an RBS type of connection a 50% flange radius cut was used. Unless otherwise noted, the panel zone strength of each model was based on the required strength per AISC Seismic Provisions, i.e., Equation (2.3) in Chapter 2.

The parameters were studied by varying details in a baseline model to create other finite element models. Both monotonic and cyclic loading analyses were performed.

3.2 Finite Element Models

Two types of models were developed, namely a *global model* and a *sub-model.* The global model was used to perform analysis of a connection subassembly in order to evaluate the global response, such as lateral load-story drift response and column twist-story drift response. The sub-model was utilized to perform a local analysis of the connection in the region of a beam tension flange. The mesh sizes for both the global and sub-models were based on considering computer limitations that constrained the maximum number of degrees of freedom in a model, the need for greater accuracy near the connection region, and mesh convergence. Geometric and material non-linearities were included in both models. Geometric non-linearities were accounted for using a small strain, large displacement formulation. A von Mises material with strain-hardening was used to account for material nonlinearities, and discussed more in detail below (Section 3.3.6).

3.2.1 Global Model

The test setup for the connection specimens is shown in Figure 3.1, where an interior connection exists between two beams and a column. An idealized model of the test setup for the interior connection specimen is shown in Figure 3.2. The span length from the column centerline to a beam reaction is 177 inches, and the length between the actuator at the top of column and the pin at the bottom of the column is 156 inches. Further details about the test setup will be discussed in detail in Chapter 4.

A typical three-dimensional finite element global model of a connection subassembly is shown in Figure 3.3. The entire beam and column sections were included in the global model in order to include dissymmetry due to any imperfections in the model and local buckling. In the global models, the beams and the column, as well as the connection attachments (i.e., continuity plates, doubler plates and CJP groove welds) were modeled using a four-node shell element with standard integration (element S4 in the ABAQUS element library). In some models, to reduce computational effort, a four-node shell element with reduced integration (element S4R in the ABAQUS element library) was used for the regions in the column where the results were not critical and the material remained elastic. A shell element was used to model the members in lieu of a solid element, since a shell element is more capable of properly capturing the effects of local buckling. Depending on the section sizes and connection details, the mesh for the various models had each a different number of elements, nodes, and degrees of freedom. The mesh for a typical global model (consisting of a W36x230 column and two W36x150 beams) had a total of approximately 3,600 elements and 3,820 nodes, resulting in 22,566 degrees of freedom.

The boundary conditions for a global model consisted of roller boundary conditions at the end of each beam as well as a pin boundary condition at the bottom of the column. The roller boundary condition allowed horizontal translation in the plane of the model (i.e., in the same plane as the beam and column webs) shown in Figure 3.2 and rotation about an axis that was normal to the plane of the model. At the pin boundary condition all displacements and rotation, except for the rotation about the axis normal to the plane of Figure 3.2, were restrained. Out-of-plane movement of the beam and column members was restrained at their flanges near the ends of the beams (at 177 inches from column center line), and at the top and bottom of the column to simulate the lateral-torsional bracing for the experimental setup. For models with a composite floor, slab transverse floor beams at 10 ft (for W36x150 beams) and 9 ft (for W30x108 beams) from the column centerline braced the main beams, which is similar to how the specimens were braced in the test setup. The distances of 10 ft and 9 ft were based on the AISC Seismic Provisions bracing requirements for the W36x150 and W30x108 beams, respectively, used in the models.

3.2.2 Sub-model

The area of interest in the connection analyses is primarily near the column-beam flange interface, where fracture may occur in either the weld metal or base metal near the beam flange CJP groove welds. Three-dimensional sub-models of the beam bottom flange-to-column flange connection region were therefore generated to obtain more detailed and accurate information in order to evaluate the fracture potential in the connection region. The beam bottom flange was in tension under the monotonic loading imposed to the model (to be discussed later). The areas in the connection where the ductile fracture potential were evaluated included the weld access hole region, beam flange CJP groove welds, beam flange heat affected zone (HAZ), beam web-to-column flange CJP groove weld, continuity plates, and the column k-area. These areas of a connection are deemed to be critical, and are identified in Figure 3.4.

The finite element model for a sub-model is included in Figure 3.3. The sub-model contained: (1) the beam bottom flange-to-column flange CJP groove weld; (2) weld access hole at the beam bottom flange; (3) part of beam bottom flange; (4) part of the beam web; (5) part of the column flange; (6) part of the column web; (7) part of the continuity plates; and (8) part of the beam web vertical CJP groove weld. The sub-models were composed of eight-node brick elements with standard integration (element C3D8 in the ABAQUS element library). The sub-model analysis utilized directly the results of the analysis from the global model as boundary conditions along the perimeter edges of the model. A shell element-to-solid element global to sub-model technique available in ABAQUS was used to drive the sub-model analysis. Several sub-models were developed in order to accommodate the geometry of the beam and column section sizes and parameters in the model. The mesh for each model varied slightly in the number of elements, nodes, and degrees of freedom and was established through mesh convergence studies (to be discussed later). The mesh for a typical sub-model (W36x230 column and W36x150 beam) consisted of approximately 3,800 brick elements, 5,000 nodes, and 15,000 degrees of freedom. This sub-model had 18 elements and 6 elements through the width and thickness of the beam flange, respectively. Six elements were used through the thickness of the beam web and four elements through the thickness of the column flange.

3.2.3 Sub-Model Mesh Convergence Study

It is well known that finite element analysis results are sensitive to the type of elements as well as the mesh size and element orientation used in the model. Accurate results from the sub-model are required for evaluation of the connection performance. A mesh refinement inelastic convergence study was therefore performed to determine an adequate mesh density for the sub-models. Based on the research done by Ricles et al. (2000), the solid element C3D8 in the ABAQUS element library was shown to have good convergence properties and accuracy. Element C3D8 was therefore selected for the sub-models and used in the convergence study. The convergence study included variations in the number of elements across the beam flange width as well as through the beam flange thickness.

The sub-model for the inelastic convergence study was composed of a welded connection for a W36x150 beam and W36x230 column. The continuity plates in the model are one-inch thick. The displacements imposed at the boundaries of the sub-model are from the results of a global model monotonic nonlinear analysis, where the connection subassembly was monotonically loaded to a story drift of 4%.

A number of cases with different mesh densities used in the convergence study are shown in Figure 3.5. The mesh in the models in Figures 3.5(a) through (c) differed from each other by the number of elements through the beam flange thickness, while the mesh in the models in Figure 3.5(d) through (f) differed from each other by the number of elements across the beam flange width.

Convergence was studied through an examination of stress and strain distributions along the beam flange width. The von Mises stress, the equivalent plastic strain (PEEQ), and hydrostatic stress (pressure) across the outer surface of beam flange HAZ adjacent to the groove weld are compared to each other for various cases in Figures 3.6 and 3.7 (these quantities are defined later). The results in Figure 3.6 included models with four, six, and eight elements through the beam flange thickness with 18 elements cross the beam flange, while the results in Figure 3.7 included models with fourteen, eighteen, and twenty two elements across the beam flange width and 6 elements through the beam flange thickness. An examination of the results in Figures 3.6 and 3.7 shows that the stresses and strain are not symmetric about the beam centerline. This phenomenon is due to the occurrence of local buckling of the beam web and flanges and subsequent beam lateral buckling (in the global model).

Figures 3.6 and 3.7 indicate that the mesh density used in the convergence study led to similar results. For computational efficiency the C3D8 element was therefore used in conjunction with the mesh size of eighteen elements across the beam flange width and six elements through the beam flange thickness for the sub-model in the parametric study.

3.2.4 Column Bracing

In the test setup bracing is required to stabilize the subassembly that is used to perform the experimental testing. This includes braces at both ends of the column. The effect of the stiffness of column lateral bracing, which also provided torsional restraint to the ends of the column in the subassembly, was investigated in order to ensure that it did not influence the analysis results of the parametric study in such a way that they would not be representative of actual behavior.

The column torsional bracing in the test setup is located near the ends of the column where the inflection points are assumed to be located at mid-height in the prototype column under lateral loading *H*, as illustrated in Figure 3.8. In the prototype building the portion of the column beyond the inflection point provides torsional restraint to the part within the distance of the inflection points of the column. To examine the effect of column torsional restraint, monotonic loading analyses were performed with a torsional spring placed at both ends of the column, where the spring stiffness was varied in the model among the analyses.

The torsional spring can be represented by four linear springs of stiffness *K*, each attached to a column flange as shown in Figure 3.9. This representation is similar to the actual bracing provided in the test setup (to be discussed in Chapter 4). The spring stiffness *K* is determined from the torsional stiffness K'_T of a section over half the story height:

$$K = \frac{K_T^{'}}{\left(d_c - t_f\right)^2} \tag{3.1}$$

In Equation (3.1) d_c and t_f is the column section depth and flange thickness, respectively.

Four cases were run, each involving a model of an interior connection with a W36x230 column and W36x150 beams. The four cases had the following spring stiffness values: (1) *K*=0, representing no column bracing at all; (2) *K*=42 k/in., representing a case with the bracing stiffness based on simulating the torsional and lateral stiffness from a W36x230 column for the portion of the column removed on the test setup; (3) *K*=300 k/in., the torsional restraint for this case corresponds to a W14x398; and (4) infinitely large torsional bracing stiffness (i.e., rigid bracing).

The results of all four cases are compared in Figure 3.10. Figure 3.10(a) shows the lateral load vs. story drift response of the connection subassembly; and Figure 3.10(b) shows the response for column twist at the beam-to-column connection plotted against story drift. The results indicate that the column bracing is very important, where columns with a lack of torsional bracing have a reduction in strength and ductility of the subassembly due to excessive twist that results in yielding of the column. On the contrary, torsional bracing with stiffness comparable to the portion of the column removed in the subassembly leads to better performance. Considering the results with the stiffness in the practical range (i.e., K = 42 k/in. to K=300 k/in.), similar results were obtained compared to the case with rigid bracing (where the springs are replaced with rollers). Hence, excessively stiff torsional bracing does not significantly affect the results. Therefore the use of rollers to laterally and torsionally brace the ends of the column in the finite element models as well as in the test setup appears to be reasonable.

3.2.5 Modeling of Floor Slab

The composite floor slab is an important parameter in this study. To investigate the effects of a composite floor slab, Specimen UTA-DBBWC tested by Jones et al. (2002) with a floor slab was modeled. Specimen UTA-DBBWC was tested under Phase II of the SAC Steel Project. The connection details and a plan view of Specimen UTA-DBBWC are shown in Figure 3.11. The connection is an RBS type, and the composite floor slab has shear studs to affix it to the main beam as well as transverse floor beams (W14x22). Shell element type S4 in the ABAQUS element library was used to model the slab while beam element type B33 (a two-node three-dimensional cubic formulation beam element) was used to model the transverse floor beams. The model consisted of a total of 3,365 nodes, 3,112 elements and 19,476 degrees of freedom. Several cases were run, which are summarized in Table 3.1, to study the concrete material model, the shear stud model, slab reinforcement, and lateral bracing of the beam.

When shear stud modeling was included in the model, spring element type SPRING2 in the ABAQUS element library was used to model the shear studs. The spring elements were put in both horizontal directions (i.e., longitudinal and transverse directions with respect to the beam axis), as shown in Figure 3.12, and displacement constraints were used in the vertical direction (3-3 in Figure 3.12) to avoid vertical separation between the beam and the floor slab. The shear stud model was based on that recommended by Lee and Lu (1989). Shear studs were placed at 12 inches on center, with no shear studs located in the plastic hinge or RBS region of the beam. The first shear stud was thus located at one beam depth (i.e., 36 inches) from the column face.

All the cases in Table 3.1 were analyzed under monotonic loading. A comparison of the analysis results is given in Figure 3.13, which shows the applied lateral load-story drift response of the connection subassembly with the various slab models. The modeling of the composite floor slab had effects on both the strength and deformation capacity. Models using the ABAQUS concrete material model (Cases 8 and 9) had difficulty to converge at larger deformations, for concrete cracking in tension caused a convergence problem. It can be seen in Figure 3.13 that with the reinforcement introduced in the concrete, Case 9 had better convergence than Case 8, yet not to as large a story drift as the other models with a floor slab. Because of this convergence problem, and the fact that the ABAQUS concrete material model is not applicable for cyclic loading analysis, an elastic-perfectly plastic model with a reduced stiffness and strength was used to model the floor slab in the parametric studies. Case 6, involving a floor slab with a reduced concrete stiffness and strength (to account for limited concrete tensile strength), and shear studs (with a 50% reduction in their shear stiffness) was judged to be the most accurate and feasible model. The verification of the slab model is presented later in Section 3.3.2.

3.2.6 Material Properties

Grade 50 steel was assumed for the beams, column, doubler plates and continuity plates. Figure 3.14 shows a stress-strain curve for nominal Gr.50 steel (Salmon et al. 1996) that was used for the monotonic load analysis. The stress-strain curve for cyclic analyses is shown in Figure 3.15, which was obtained from Grade 50 material cyclic coupon tests conducted by Kaufmann et al. (1999). The monotonic stress-strain relationship for the E70T-6 filler metal used in the models is shown in Figure 3.16 and was obtained from tensile coupon material tests performed for this study.

The stress-strain relationship was used in conjunction with the assumption that the material was a von Mises material and followed the associated flow rule. The hardening model used in the analysis included combined nonlinear isotropic and kinematic strain hardening. The stress-strain curve for the cyclic analysis was based on the Grade 50 steel cyclic relationship, where the initial loading response and fully saturated condition was based on the properties displayed in Figure 3.15. The engineering stress-strain curves (Figures 3.14 through 3.16) were adjusted to establish the true stress-true plastic strain relationships, where:

$$\sigma_{true} = \sigma_{eng}(1 + \varepsilon_{eng}) \tag{3.2}$$

$$\varepsilon_{true}^{pl} = \ln(1 + \varepsilon_{eng}) - \frac{\sigma_{true}}{E} \tag{3.3}$$

In Equations (3.2) and (3.3), σ_{true} and ε_{true}^{pl} are the true stress (Cauchy stress) and true (logarithmic) plastic strain, respectively, and σ_{eng} and ε_{eng} are the engineering stress and strain (referred to as the nominal stress and strain in the ABAQUS manuals), respectively, and E is Young's modulus.

3.2.7 Loading Protocol

The analyses are conducted by applying either monotonic increasing static displacement or cyclic variable amplitude displacement at the top of the column. The cyclic displacement amplitude followed the loading protocol in the AISC Seismic Provisions (AISC 2002), which is the same as the SAC loading protocol (1997). The loading protocol is shown in Figure 4.26.

3.2.8 Stress and Strain Indices

A number of different stress, strain, and combined stress-strain indices were computed using the finite element results in order to compare the behavior of the different connection configurations, and to access the effect of the parameters discussed in Section 3.1 on behavior. Some of the stress and strain indices used by El-Tawil et al. (1998) and Ricles et al., (2000) were used in the present study, and are described below.

Hydrostatic (Pressure) Stress - the hydrostatic (or pressure) stress p is defined as:

$$p = -\frac{1}{3} trace(\sigma_{ij}) = -\frac{1}{3}\sigma_{ii} \tag{3.4}$$

where σ_{ij} are the Cauchy stress tensor components, and i, j represent the global directions, i = 1, 2, 3, and j = 1, 2, 3. The hydrostatic stress has a negative value for tensile hydrostatic stress. A high tensile hydrostatic stress is usually accompanied by large principal stresses. When a crack or some other type of flaw exists, high principal stresses can result in large stress intensity factors at the crack tips, which increase the potential for brittle fracture.

Von Mises Stress - the von Mises (or equivalent) stress q is defined as:

$$q = \sqrt{\frac{3}{2} S_{ij} S_{ij}} \tag{3.5}$$

where S_{ij} are the deviatoric stress tensor components, with $S_{ij} = \sigma_{ij} + p\delta_{ij}$, p equal to the hydrostatic stress, and δ_{ij} equal to the Kronecker delta.

PEEQ Index - the PEEQ index is defined as the ratio of equivalent plastic strain *PEEQ* to the yield strain ε_y:

$$PEEQ \text{ Index } = PEEQ / \varepsilon_y \tag{3.6}$$

The equivalent plastic strain PEEQ that appears in the numerator of Equation (3.6) is defined as:

$$PEEQ = \sqrt{\frac{2}{3} \varepsilon_{ij}^{pl} \varepsilon_{ij}^{pl}} \tag{3.7}$$

where ε_{ij}^{p} are the plastic strain components in directions i and j. The PEEQ index is a measure of local ductility.

Rupture Index - defined as the ratio of the PEEQ index to the ductile fracture strain ε_f multiplied by the material constant α, where:

$$Rupture\ Index\ (RI) = \alpha \frac{PEEQ/\varepsilon_y}{\varepsilon_f} = \frac{PEEQ/\varepsilon_y}{\exp(1.5\frac{p}{q})} \tag{3.8}$$

The quautities *p* and *q* were defined previously as the hydrostatic and von Mises stresses, respectively. The ratio of hydrostatic stress-to-von Mises stress (*p/q)* that appears in the denominator of Equation (3.8) is known as the triaxiality ratio, *TR*.

Equation (3.8) can be used to compare values of the Rupture Index in order to evaluate the potential for ductile fracture of two locations in a finite element model or between two different models at the same location. Research by Hancock and Makenzie (1976) has shown that this criterion is accurate for the types of steels that they tested. The failure strain depends on the direction of rolling, initial imperfections, pre-straining, and accumulated strain at the potential failure point.

3.3 Model Verification

In order to verify the selected element type and mesh density for the global models, as well as the slab modeling technique discussed previously, finite element models were generated of specimens tested in prior researches and the analysis results compared to the test results.

3.3.1 WUF-W Connection Specimen T5

Specimen T5, which was an exterior welded unreinforced flange-welded beam web (WUF-W) to column connection tested by Ricles et al. (2002), was modeled using the techniques described previously. Specimen T5 was a specimen without a floor slab and consists of a W14x311 column and a W36x150 beam. The specimen details are given in Figure 3.17. The model consisted of 1154 elements, 1282 nodes and 7542 degrees of freedom. Initial imperfections were included in the analysis, and were based on a proportion of the amplitude of a lower buckling mode of the model. The buckling mode was determined by a linear eigenvalue buckling analysis.

Figure 3.18 shows the comparison of the test and analysis results, where the lateral load-story drift response is plotted. The model properly predicted panel zone yielding, beam yielding, cyclic beam web and flange local buckling, and strength deterioration that occurred in the test specimen. The test results are considered to be in good agreement with the experimental results. The degradation in specimen strength seen in Figure 3.18 is associated with the effects of local buckling in the web and flanges of the beam.

3.3.2 RBS Connection Specimen DBBWC

The calibrated slab model was verified by comparing the predicted cyclic behavior of Specimen UTA-DBBWC (Jones et al. 2002) with the test results. Specimen UTA-DBBWC was discussed previously, where the specimen details were given in Figure 3.11. The specimen was modeled using similar modeling methods as described previously. The model consisted of 3365 nodes, 3112 elements, and 19476 degrees of freedom. Figure 3.19 shows the model and the first buckling mode from an eigenvalue buckling analysis, where a proportion of the amplitude was used as the initial imperfection.

The result of the nonlinear cyclic analysis is shown in Figure 3.20, where the lateral load-story drift response is plotted and compared with the test results. The model properly predicted panel zone yielding, beam yielding, cyclic beam web and flange local buckling in the RBS, and strength deterioration that occurred in the test specimen. The predicted response by the model is in good agreement with the experimental results.

The comparison between the experimental results and finite element analysis indicates that the finite element modeling procedures produce an accurate model, which should lead to accurate response prediction in the parametric study. The finite element model is able to capture the effects of cyclic local buckling and predict the cyclic behavior of the specimens very well.

3.4 Parameter Studies

The results of the parametric study are presented below. The potential for ductile fracture is presented first, which is based on the maximum values of the Rupture Index in critical regions of the connection. The Rupture Index is computed using the stress and strain state determined from the sub-models subjected to monotonic loading. Although a connection is expected to be cyclically loaded during an earthquake, the Rupture Index under monotonic loading gives a good indication of expected inelastic cyclic performance (Ricles et al 2000, El Tawil et al. 1998). The global behavior (from the global finite element models) under cyclic loading is then presented, where the effects of the parameters in the study on the lateral load-story drift response and column twist response are evaluated.

3.4.1 Potential for Ductile Fracture

3.4.1.1 Effect of Connection Type

To examine the effect of connection type on ductile fracture potential, two types of connections were investigated. These included a WUF-W connection and RBS connection. The analysis matrix is given in Table 3.2, and included three column depths and one beam section size, resulting in a total of five cases. None of the cases include a floor slab. The values of the ratio of panel zone shear strength-to-panel zone shear (R_v/V_{pz}) are summarized in Table 3.2, where R_v is based on Equation (2.3) and V_{pz} on the expected plastic moment M_{pr} (Equation (2.14)) developing at the RBS. Except for Case 2, the panel zones for each case were based on a balanced design, where the current AISC seismic design procedure for panel zones discussed in Chapter 2 (using Equation (2.3)) was used. Case 2 had a stronger panel zone. Consequently, Case 3, 4 and 5 had a value of R_v/V_{pz} = 1.05 to 1.09, and Case 2 a value of 1.36. Case 1 had R_v/V_{pz} = 1.22 due to the fact that the column web alone was more than adequately thick enough. Panel zone strength effects will be discussed in Section 3.4.1.2. Cases 1 and 2 in Table 3.2 both include a W14x398 section for the column. Case 1 is an RBS connection while Case 2 is a WUF-W connection. Cases 3 and 4 in Table 3.2 are an RBS and WUF-W connection type, respectively, where both cases have a deeper column section (W36x230). Case 5 is a deep column, but of smaller depth and weight (W27x194), with an RBS connection. Case 5 is included in the analysis matrix because torsion was determined by Chi and Uang (2002) (see Chapter 2) to have a greater effect on a W27x194 section as a column in conjunction with an RBS connection. In addition, the W27x194 section matched the column section size in Specimen D3 tested by Chi and Uang that failed due to torsional effects. All cases in Table 3.2 had a W36x150 section for the beam, with no floor slab.

Cases 1 and 2 modeled specimen C2 and specimen UTA-DBBW tested by Ricles et al (2002) and Jones et al. (2002), respectively. During testing, both Specimen C2 and Specimen UTA-DBBW developed a total story drift that exceeded 4% and met the AISC Seismic Provisions (AISC 2002) for connection qualification. Case 5 had similar section sizes as Specimen D3 tested by Chi and Uang (2002) except that their specimen was a one-sided connection.

The maximum values for the Rupture Index for Cases 1 and 2 are shown in Figure 3.21 at 4% and 6% imposed story drift. Figure 3.21 indicates that the RBS connection to a W14x398 column has a lower Rupture Index, and thus fracture potential, than a WUF-W connection to a similar column section. The cause for the higher value of the Rupture Index in the WUF connection is due to the larger plastic strains, and thus PEEQ Index, that develop in the connection region near the column face. The RBS connection concentrates the plastic deformations in the reduced beam sections, where the plastic hinges form. The maximum moment in the beam at the column face is smaller in the RBS connection than the WUF connection, where the latter has a considerable amount of strain hardening (Ricles et al, 2000). The maximum moment in the RBS connection typically develops at 2% to 4% story drift, with a subsequent deterioration in capacity occurring. As a result, no additional plastic deformations developed. Consequently, Figure 3.21 shows that there is a minimal increase in the maximum values for the Rupture Index in the RBS connection beyond 4% story drift. At 4% story drift the largest fracture potential is at the end of the beam web-to-column flange CJP groove weld in both connection types, where the WUF connection has a 27% greater value for the Rupture Index compared to the RBS connection.

The maximum values for Rupture Index for Cases 3 through 5 are shown in Figure 3.22 at 4% and 6% imposed story drift. These cases involve a deeper column (W36x230 and W27x194 section). The results in Figure 3.22 also show a larger value for the Rupture Index for the WUF connection type (Case 4) throughout most regions of the connection compared to the RBS connection cases (Cases 3 and 5), and thus a greater fracture potential. As noted above, the cause of this is due to the larger plastic strains that develop in the connection near the column face in the WUF connection. However, the reduced strength of the W27x194 section compared to the W36x230 resulted in an increase in the Rupture Index throughout the RBS connection in Case 5 (W27x194) compared to Case 3 (W36x230), as well as in the most critical connection regions of Case 1 (see Figure 3.21) involving a W14x398 column section. Similar to the above Cases 1 and 2, for the deeper column cases (i.e., Cases 3, 4, and 5) the largest fracture potential is at the end of the beam web-to-column flange CJP groove weld. The value of the Rupture Index at this location is almost doubled in the RBS connection for the lighter W27x194 column section (Case 5) compared to the W36x230 column section (Case 3). In addition, there is a noticeably increase in the Rupture Index in the beam flange CJP groove welds in Case 5. The larger value for the Rupture Index for Case 5 at the end of the beam web-to-column flange CJP groove weld and the beam flange CJP groove weld is associated with a larger plastic strain that develops locally at these locations compared to the other cases.

At the end of the beam web-to-column flange CJP groove weld of the WUF connection (Case 4, W36x230 column) the Rupture Index value is 221% greater compared to the RBS connection (Case 3) with the same column and beam section sizes as Case 4, and 63% greater compared to the RBS connection with a W27x194 column (Case 5). Similar to Cases 1 and 2, the results in Figure 3.22 for the RBS connections (Cases 3 and 5) show no appreciable increase in the Rupture Index beyond 4% story drift.

The thinner flanges in the deeper columns resulted in a greater Rupture Index at the continuity plates, as evident by comparing the results in Figures 3.21 with 3.22 at this location. However, the values are not considered to be large.

Shown in Figures 3.23 and 3.24 are the contour plots of the von Mises stresses, equivalent plastic strain (PEEQ), and hydrostatic stress for the connection region and beam tension flange region, respectively, for Cases 3 (W36x230 column) and 5 (W27x194 column). These results are for 4% story drift. The column flange in the sub-models of Cases 3 and 5 are seen in Figure 3.23(a) to have a von Mises stress larger than the yield stress of 50 ksi (due to yielding and strain hardening). However, it is more extensive and localized in the W27x194 column (i.e., Case 5) than in the W36x230 column for Case 3, where in the former the yielding extends through the column flange thickness into the region adjacent to the beam web. The more extensive local yielding in the column of Case 5 is due to the reduced section modulus and torsional resistance of the W27x194 section, resulting in larger column flange normal stresses. The plastic section modulus for the W36x230 section is 49% larger, and the warping normal stresses based on elastic theory (see Chapter 2) are about 50% less in magnitude compared to the W27x194 section.

Figure 3.23(b) shows that the equivalent plastic strain is larger in Case 5 (W27x194 column) than in Case 3 (W36x230 column), and concentrated at the toe of the beam web-to-column flange CJP groove weld, with the plastic strain extending into the column flange of the W27x194 section. The effective plastic strain is seen in Figure 3.24(b) to be more extensive in the center of the beam tension flange for Case 5 (at the bevel and near the bottom surface of the flange), and is also caused by the column flange localized yielding near the column web.

The results above indicate the RBS connections do not appear to have any greater potential for fracture than a WUF connection for various column depths. However, deeper columns with a smaller section modulus and torsional resistance result in the development of higher local plastic strains and an increase in the potential for ductile fracture of the connection compared to a connection to a deep column with a larger section modulus and torsional resistance.

3.4.1.2 Effect of Panel Zone Strength

A deep column RBS connection was modeled and analyzed to investigate the effects of panel zone strength on its behavior. The analysis matrix is given in Table 3.3, and included two column sizes and three different panel zone strength design conditions, resulting in a total of four cases. The section for the column was either a W36x230 (Cases 1, 2, and 3) or a W27x194 (Case 4). All cases had a W36x150 section for the beam. None of the cases included a floor slab.

The panel zone strength is expressed in the second-to-last column of Table 3.3, where values for the ratio of R_v/V_{pz} are tabulated. As indicated in Table 3.3, the panel zone strengths correspond to values of R_v/V_{pz} equal to 0.83 (Case 1), 1.09 (Case 2), 1.34

(Case 3), which are classified as a weak, balanced, and strong panel zone condition, respectively. Case 4 is also considered to be a balanced panel zone design, with R_v/V_{pz} = 1.05.

The lateral load-story drift response for Cases 1, 2, and 3 is given in Figure 3.25 for a story drift imposed to 6%. As noted above, these three cases had the same corresponding member sizes. The balanced and strong panel zone designs (Cases 2 and 3) develop beam local web and flange buckling in the RBS, causing a deterioration in strength beginning at a story drift of 2% to 3%. On the contrary, the weak panel zone design has yielding and plastic deformations concentrated in the panel zone, and as a result local web and flange buckling does not develop in the RBS and cause a deterioration in strength. For this latter case the maximum moment developed in the beam at the RBS was less than the nominal strength $M_{p,n}$.

A summary of the maximum values of the Rupture Index at locations throughout the connection is given in Figure 3.26 at 4% and 6% story drift. Considering the results for Cases 1, 2, and 3 in Figure 3.26, it is apparent that reduced panel zone strengths result in an increase in the Rupture Index. The panel zone design (Case 2) based on current AISC Seismic Provisions (AISC 2002), i.e., when R_v/V_{pz} is about equal to 1.0, shows a reduction in the Rupture Index by a factor of almost 2.0 throughout the connection compared to the weak panel zone (Case 1) at 4% story drift, with an even further reduction occurring at 6% story drift. The strong panel zone design (Case 3) results in a further reduction in the Rupture Index at the end of the beam web CJP groove weld by as much as a factor of 6.0 compared to the weak panel zone case. The reason for this is because in the weak panel zone case, the panel zone underwent excessive plastic deformation and developed a large concentration of local plastic strain at the beam-to-column interface, particularly at the end of the beam web-to-column flange CJP groove weld, which results in a large PEEQ Index, and thus Rupture Index value. In the balanced panel zone case, the panel zone deformation was reduced, while in the strong panel zone case most of the plastic deformation develops in the RBS of the beam. The phenomenon of developing a large local plastic strain at the end of the beam web CJP groove weld in weaker panel zones was also found in the studies by Ricles et al. (2000) on WUF connections to W14 column sections.

Comparing Cases 2 and 4 in Figure 3.26, which both involve a balanced panel zone design, it is seen that the use of a W27x194 section for a column (i.e., Case 4) increases the Rupture Index throughout the connection, except in the continuity plates, compared to the use of the W36x230 section (Case 2). The reason for the larger value of Rupture Index is due to the higher local plastic strain that develops in the flanges of the W27x194 column, as noted previously.

In summary, a weaker panel zone in a deep column results in a significant increase in the potential for ductile fracture of the connection. The use of the current AISC Seismic Design Provisions (AISC 2002) results in an appreciable reduction in the fracture potential of the connection compared to cases where no doubler plates were used and the panel zone strength is such that the R_v/V_{pz} ratio is less than 1.0. The use of a deeper column section that results in larger total stresses due to flexure and torsion, and a higher local plastic strain, leads to an increase in the fracture potential of the connection with a balanced panel zone strength.

3.4.1.3 Effect of Column Section Size

To evaluate the effect of column section size on the performance of an RBS connection, the five analysis cases summarized in Table 3.4 were performed. For each case, the beam size was selected to ensure a weak beam strong column configuration, and the panel zone was designed in accordance with ASIC Seismic Provisions (AISC 2002), resulting in a balanced strength condition. Cases 1, 2, and 3 all were interior RBS connections with W36x150 beams, with the column sizes equal to a W14x398, W36x230, and W27x194, respectively. Case 4 consisted of an interior RBS connection with a W27x146 column and W30x108 beams. Case 5 was an exterior RBS connection (i.e., one-sided connection) with a W27x194 column and one W36x150 beam. The continuity plates were A36 steel for Case 5 (Gr. 50 was used for all the other cases). Case 5 is identical to Specimen D3 that was tested by Chi and Uang **(**2002**)**, where as noted previously the performance of the RBS connection was found to be poor, and affected by the column twist that occurred.

The elastic torsion analysis presented in Chapter 2 indicates that Case 1 is not as sensitive to torsional loading, for the W14x398 section is the heaviest column section in the analysis matrix. The W14x398 column has lower elastic warping stresses and a larger elastic torsional stiffness than the lighter W27x194 and W27x146 columns of Case 2 and 3, respectively. According to the elastic torsion analysis in Chapter 2, the elastic warping normal stresses developed in the W27x146 section are about 2 times more compared to the W27x194 section, 3 times more compared to the W36x230 section, and 6 times more than a W14x398 column.

The Rupture Index at the critical locations in the connection region for the various cases is summarized in Figure 3.27 at 4% and 6% story drift. It appears that the maximum Rupture Index value in each case again occurs at the end of the beam web-to-column flange CJP groove weld. The Rupture Index in the column k-area and continuity plates is small for all cases. Case 3 (W27x194) has the largest value for the Rupture Index among all the cases. The increase in the value of the Rupture Index at the end of the beam web-to-column flange CJP groove weld and beam flange CJP groove welds in Case 3 compared to the other cases is due to the larger local plastic strain that develops in the column flange, as explained previously. Although the W27x146 column (Case 4) has a smaller section modulus and torsional resistance than the W27x194, the RBS connection to the W27x146 involves a smaller beam section (W30x108). As a result, in Case 4 the total stresses in the column are smaller than Case 3, as are the local plastic strains in the column flange and at the beam-column interface. Consequently, the Rupture Index is smaller in Case 4 than in Case 3.

The RBS connection with a W36x230 column (Case 2) has lower values for the Rupture Index throughout the connection compared to the RBS connection to the shallower W14x398 column (Case 1). The reason for this is due to the smaller local plastic strains that develop at the interface between the beam and the W36x230 column. An exception is at the continuity plates. However, at this location the Rupture Index values are small for both cases. Case 5 (one-sided RBS connection to a W27x194 column) has a noticeable larger value for the Rupture Index value in the continuity plates than the other cases. Because the continuity plates in the model for Case 5 are A36 steel, they yielded earlier and developed larger plastic strain compared to the other cases, leading to a larger PEEQ Index.

In summary, it was found that the fracture potential does not necessarily increase in an RBS connection to a deeper column. Rather, the fracture potential of an RBS connection is highly dependent on the plastic strain that develops at the beam-column interface. For a given beam section size, a deeper column with a larger section modulus will have a lower fracture potential than one with a smaller section modulus, since in the latter case the flexural and torsional warping normal stresses are smaller, leading to smaller local plastic deformations at the beam-column interface. Smaller beams can reduce the fracture potential of the connection by imposing smaller forces on the connection and column, leading to reduced plastic deformations in the connection.

Judging the performance based on the elastic total stress for an RBS connection with a slab, where the warping stresses are computed as recommended by Chi and Uang (2002) does not appear to be consistent with the trend in the values for the Rupture Index. As shown in Figure 3.28, the RBS connections with a W30x108 beam and W27x146 column and a W36x150 beam and W36x230 column would have the second and third largest column total normal stress, respectively. The Rupture Index at the most critical location in the RBS connection with a W27x146 column (at the beam web-to-column flange CJP groove weld) was found to be the lowest among the two-sided connections in Figure 3.27, while the RBS connection to a W36x230 column had the second lowest maximum value for the Rupture Index in Figure 3.27. Thus, evaluating the performance of an RBS connection to a deep column based on total normal column elastic stress appears to need refinement. The values for the normal warping stress appear to be the cause for the discrepancy between the trend in total stress and the Rupture Index values.

3.4.1.4 Effect of Continuity Plate Thickness

The effect of continuity plate thickness on the fracture potential of an RBS connection to a deep column was investigated by performing the two analysis cases identified in Table 3.5 as Cases 1 and 2, which had a balanced panel zone design. Both cases consisted of a W27x194 section for the column, which as reported above was found to result in the largest fracture potential for an RBS connection (see Figure 3.27). The beam for both cases was a W36x150 section. For Case 1, a one-inch thick set of continuity plates was included in the model (referred to as *Full Thickness*), where the continuity plates were as thick as the beam flanges. For Case 2, the continuity plates were reduced to half of this thickness (i.e., 0.5 inches), and referred to as *Half Thickness*.

The results for the Rupture Index are given in Figure 3.29 at 4% and 6% story drift. The results in Figure 3.29 show an increase in the ductile fracture potential of the connection when the continuity plate thickness is reduced. The largest values for the Rupture Index are at the beam web-to-column flange CJP groove weld and the beam flange CJP groove weld. At a story drift of 4% the Rupture Index at these locations increases by 15% and 32% when the continuity plate thickness is reduced. These values are however less than that in the WUF connection to a W36x230 column section (see Case 4 in Figure 3.22), and therefore have a lower fracture potential than this WUF connection had with full thickness (one-inch) continuity plates.

3.4.1.5 Effect of Floor Slab

The effect of a floor slab on the ductile fracture potential of an RBS interior connection was investigated by performing the six analysis cases identified in Table 3.6. The two parameters varied in the analysis matrix included the column section size and the presence of the floor slab. All cases have a W36x150 beam. Cases 1 and 2 have a W14x398 column without and with a floor slab, respectively, while Cases 3 and 4 have a W36x230 column without and with a floor slab, respectively. Cases 5 and 6 have a W27x194 column without and with a floor slab, respectively. All cases had a balanced panel zone design.

The results for the values of the Rupture Index at the connection are shown in Figures 3.30 through 3.32 for the various cases at 4% and 6% story drift. The floor slab is shown to increase the Rupture Index in all cases, where the maximum value for all cases occurs at the beam web-to-column-flange CJP groove weld. The increase in the Rupture

Index at this location when adding a floor slab to the RBS connection having a W14x398 column (Case 2) is due to an increase in both the local plastic strain (by a factor of two) and the triaxiality ratio (by 25%). For the deeper columns the increase in the Rupture Index when adding the slab is less, and equal to 47% for the W36x230 column (Case 3 vs. Case 4) and about 9% for the W27x194 column (Case 5 vs. Case 6). This modest increase in the Rupture Index for the RBS connections with a deeper column is due to the increase in the local plastic strain at the column-beam interface, with the triaxiality ratio not being affected as much by the presence of the floor slab.

Thus, the floor slab appears to increase the fracture potential of an RBS connection, where the RBS connection to the shallower W14x398 RBS column with a floor slab has a greater potential for ductile fracture than the RBS connections to a deeper column.

3.4.1.6 Effect of Axial Load

To investigate the effect of axial load, analyses were done with the axial load imposed to the finite element models before applying the cyclic lateral loading. Three cases were analyzed as shown in Table 3.7. All three cases had a W27x194 column, W36x150 beams and a composite floor slab. The only varying parameter was the axial load. Case 1 had no axial load applied to the column, Case 2 had 285 kips of axial load applied to the column (resulting in a column stress of 5 ksi due to axial load), and Case 3 had 570 kips of axial load applied to the column (resulting in a column stress of 10 ksi due to axial load). The stresses due to axial load in Cases 2 and 3 correspond to 10% and 20% of the nominal yield strength of the column material, respectively.

The results for the Rupture Index at the connection are given in Figure 3.33 for the various cases at 4% and 6% story drift. It can be seen from the figure that the axial load doesn't increase the value of the Rupture Index in the connection at story drift of 4%. In fact, at most locations the value of the Rupture Index remained basically unchanged with the presence of an axial load, regardless of the magnitude of the axial load; and at some locations, the value of the Rupture Index was even slightly reduced with the presence of axial load. However, at 6% story drift, the value of the Rupture

Index increased at most locations in a presence of the axial load. The maximum increase of the value of the Rupture Index caused by the axial load is less than 20%.

It appears that the axial load does not have a significant effect on fracture potential at the connection region at 4% story drift. The axial load slightly increases the fracture potential at 6% large story drift level.

3.4.2 Cyclic Global Behavior

3.4.2.1 Effect of Panel Zone Strength

The effect of panel zone strength on the cyclic behavior of an RBS connection was investigated by performing the analysis cases summarized in Table 3.8. The analysis included one column size (W27x194) and three different panel zone strengths (*weak, balanced, and strong*), resulting in a total of three cases (Cases 1, 2, and 3). The thickness of the doubler plate to achieve the different panel zone strengths is noted in Table 3.8. The section size for the beams in all cases was a W36x150. None of the cases included a floor slab. The panel zone strength is expressed in the second-to-last column of Table 3.8, where values for the ratio of R_v/V_{pz} are tabulated. Cases 1, 2, and 3 correspond to a weak panel zone (R_v/V_{pz} = 0.65), a balanced panel zone (R_v/V_{pz} = 1.05) and a strong panel zone (R_v/V_{pz} = 1.25), respectively. The W27x194 section was selected for this study on global behavior, in lieu of the W36x320 section used in the study of the effect of panel zone strength on ductile fracture potential, because it was found that the W27x194 is more effected by panel zone strength (see Figure 3.26).

The lateral load-story drift hysteretic response for all three cases is shown plotted in Figure 3.34. Similar to the monotonic analysis results shown in Figure 3.25, the hysteretic response has the weak panel zone (Case 1) developing the lowest strength, but not degrade in capacity, while the balanced and strong panel zone cases (Cases 2 and 3, respectively) have a deterioration in capacity due to beam local web and flange buckling, as well as lateral flange movement in the RBS. The deterioration in capacity commenced between 2% to 3% story drift. The balanced and strong panel zone cases in Figure 3.34 show an almost identical lateral load-story drift hysteretic response. The weak panel zone design had yielding and plastic deformations concentrated in the panel zone, leading to local buckling in the panel zone as shown in Figure 3.35.

The column twist for all three cases at selected story drifts is given in Figure 3.36. The case with a weak panel zone (Case 1) is shown to have minimal column twist, with significantly more twist developing in the models with a balanced and strong panel zone (Cases 2 and 3, respectively). The reason for this is because in the weak panel zone case the RBS did not develop significant yielding that would cause local buckling in the RBS. In the other two cases significant inelastic deformations developed in the RBS, leading to local buckling in the RBS and lateral beam flange movement. This local buckling and lateral flange movement lead to torsional loading and twisting of the column.

In summary, the RBS connection with a weak panel zone had minimal column twist, while the balanced and strong panel zone cases had an increase, and similar amount of column twist. While beam instability, strength deterioration, and column twist are avoided in an RBS connection with a weaker panel zone, the overall strength of the connection is jeopardized. Furthermore, as noted in Section 3.4.1.2 the larger amount of plastic deformation that develops in weaker panel zones increases their potential for ductile fracture of the connection.

3.4.2.2 Effect of Floor Slab

To investigate the effects of a composite floor slab on the global performance of an RBS connection, models with a bare steel connection and with a composite floor slab were both analyzed and their results compared. The analysis matrix to investigate the effects of a floor slab consisted of the four cases given in Table 3.9. All cases had the same W36x150 beam size. Cases 1 and 2 both had a W14x398 column, with the former having no floor slab and the latter a floor slab. Cases 3 and 4 both had a W27x294 column without and with a floor slab, respectively.

The lateral load- story drift hysteretic response for all four cases is given in Figure 3.37. Cases with the same column section size are superimposed in Figures 3.37(a) and (b), respectively. It is apparent in Figure 3.37(a) and (b) that the floor slab enhances the performance of an RBS connection to both a shallow and deep column, by stabilizing the beam in the RBS region. The floor slab appears to increase the strength of the connection, delay the onset of strength degradation, and reduce the amount of strength degradation. The floor slab appears a somewhat greater effect on a shallower column section (Case 2 – W14x398) than a deeper W27x194 column section (Case 4), where in the former there is a greater increase in the strength and a reduction in the amount of strength degradation of an RBS connection. The increase in the maximum strength provided by the floor slab in Case 2 and 4 is 4% and 2%, respectively. The increase in strength at 4% story drift for Case 2 compared to the bare steel connection with a similar W14x298 column (Case 1) is 18%, and 16% for Case 4 at 4% story drift compared to the bare steel connection with a similar W27x194 column (Case 3). The enhancement of the connection performance (i.e., reduction in the amount of strength degradation) is consistent with the finding in the study by Jones et al. (2002) on RBS connections to W14 column sections, who observed that the slab appears to have a stabilizing effect on the RBS moment connection, increasing the load and rotation capacity of the specimen.

Figure 3.38 shows the column twist angle at selected story drift levels for the four analysis cases. The results show a greater column twist for a deeper column (i.e., Cases 3 and 4), and a significant reduction in the column twist with the addition of the floor slab, particularly with a story drift up to 4%.

The column twist for these four cases is plotted in Figure 3.39 against the elastic torsional stiffness from Chapter 2. Included in Figure 3.39 are the analysis results for an RBS connection to a W36x230 column, with and without a floor slab. The appreciable reduction in column twist when adding a slab to the model is apparent in Figure 3.39. The trend in the relationship between column twist and column elastic torsional stiffness is a straight line for cases with a floor slab, implying that the column is behaving in a global sense elastically. The localized flange yielding in the W27x194 column section without a floor slab led to an increase, not only in the Rupture Index but also in the column twist, where Figure 3.39 shows a deviation from a linear response. The column twist appears to be functionally related to neither the torsional constant J by itself (see Figure 3.40) nor the value for the ratio h/t_{cf}^3 (see Figure 3.41), where in these figures there is a scatter in the data. Consequently, the section property J and the ratio h/t_{cf}^3 cannot be used as a good indicator of column twist. Instead, the column elastic torsional stiffness is best used.

3.4.2.3 Effect of Beam Web Slenderness

The effect of beam web slenderness on the behavior of an RBS connection to a deep column was investigated by considering the 32 analyses summarized in Table 3.10. The parameters in the analysis matrix consisted of beam web slenderness (W36 sections ranging in weight from 135 lbs/ft to 256 lbs/ft), column section size (W36x230 and W27x194), and the floor slab. The proportioning of the beam and column sizes in all of the analysis cases in Table 3.10 satisfied the weak beam-strong column criteria in the AISC Seismic Provisions (AISC 2002).

The out-of-plane (i.e., lateral) movement of the beam bottom flange at the center of RBS is plotted as a function of the beam web slenderness in Figure 3.42, where the results for the W36x230 column and W27x194 column are shown in Figure 3.42(a) and (b), respectively, at 4% story drift. The results from the analysis show that the movement of the beam flange increases with a reduction in beam web slenderness for the cases without a floor slab. Furthermore, cases with a W27x194 column develop more beam flange movement in the RBS than those with a W36x230 column. The reason for this is associated with the column torsional flexibility and yielding phenomena discussed previously. The addition of the floor slab is shown to significantly decrease the transverse movement of the beam flange at the RBS, where the transverse movement is less than the value of $0.2b_f$, (b_f is the beam flange width), suggested by Chi and Uang (2002) in their design procedure.

The increase in the beam flange transverse movement with a less slender beam web is due to the increase in beam flange force. The area of the beam flange increases in wide flange sections as the beam web slenderness is decreased. A larger beam flange area results in a larger flange compressive force, leading to a grater applied torque to the column by the RBS connection.

The column twist developed in the models at 4% story drift is plotted against beam web slenderness in Figure 3.43, where the results without and with a floor slab are shown in Figure 3.43(a) and (b), respectively. For the cases without a slab (Figure 3.43(a)) it is seen that the increase in beam flange area offsets the reduction in beam web slenderness, leading to an increase in column twist. Because the W27x194 is more flexible in torsion compared to the W36x230 section, for the same beam section the RBS connection to the lighter column results in a greater amount of column twist, (see Figure 3.43(a)). The results for analyses with a floor slab are shown in Figure 3.43(b) to have a significant reduction in column twist, with an almost constant value compared to the results plotted in Figure 3.43(a). Similar to the results in Figure 3.39, Figure 3.43 shows that the column twist for cases involving the W27x194 section is slightly more than that involving a W36x230 section when the floor slab is present.

In summary, the restraint provided to the beam top flange in the RBS results in the column twist not being sensitive to the beam web slenderness, and significantly reduces the beam bottom flange movement and column twist compared to results from models without the floor slab. The column torsional rigidity appears to be the main variable in column twist when a floor slab is present.

3.4.2.4 Effect of Axial Load

The effect of axial load on the connection cyclic behavior was investigated by analyzing and comparing cases with different axial load levels. Table 3.11 summarizes the three cases that were studied. All three cases had a W27x194 column, W36x150 beams and a composite floor slab. The only varying parameter is the axial load in these cases. Case 1 had no axial load on the connection, Case 2 had 285 kips of axial load on the column, resulting in a stress of 5 ksi due to axial load, and Case 3 had 570 kips of axial load on the column, resulting in a stress of 10 ksi due to axial load. Case 2 and 3 correspond to an axial stress of 10% and 20%, respectively, of the column nominal yield stress.

The comparison of the lateral load-story drift hysteretic response for the three cases is shown in Figure 3.44. The axial load has only a slight effect on the connection cyclic behavior, particularly after 3% story drift. This is associated with the P-Δ effect

The axial load is shown to slightly reduce the maximum capacity and result in a slightly greater amount of deterioration in capacity following the peak load. Cases 2 and 3 have a **2.2**% and **3.9**% reduction in maximum load capacity compared to Case 1. At 5% story drift, Cases 2 and 3 developed **9.8**% and **21.8**% greater strength deterioration than Case1.

3.5 Summary and Conclusions

A parametric study was performed to investigate the ductile fractional potential and cyclic behavior of moment connections. The parameters in the study included: (1) connection type; (2) column size; (3) beam size; (4) panel zone strength; (5) continuity plate thickness; (6) composite floor slab; and (7) axial load. The major conclusions and recommendations based on the parametric study involving the finite element analysis are noted below.

(1) The finite element studies indicate that RBS connections have less potential for ductile fracture at the connection region than WUF connections.

(2) The fracture potential and column twist in an RBS connection depends on the section modulus and torsional rigidity of the column section, where larger stresses in the column flange can lead to a higher ductile fracture potential in the connection as well as column twist. An RBS connection with a deeper column can have a smaller ductile fracture potential than an RBS connection to a shallower column, if the deeper column has lower stresses in the column flanges.

(3) Panel zone strength plays an important role in RBS connections to deep columns. Weaker panel zones have an increase in the ductile fracture potential in the connection. Stronger panel zones result in an increase in the column twist and degradation in connection capacity under cyclic loading due to beam local and lateral buckling in the RBS. A balanced panel zone strength design is recommended, using the current AISC Seismic Provisions (AISC 2002).

(4) The finite element analysis results show that a composite floor slab provides restraint to the top flange of the beams whereby the magnitude of beam top and bottom flange lateral movement in the RBS, as well as the column twist are reduced. Strength

degradation due to beam instability in the RBS is also reduced by the restraint effect obtained from the floor slab. However, the floor slab increases the fracture potential of the connection, particularly at the end of the beam web-to-column flange CJP groove weld. This increase is more pronounced in shallower columns.

(5) With the presence of a floor slab, out-of-plane movement of the RBS bottom flange and column twist are not sensitive to the beam section size and beam web slenderness. Without the floor slab, the RBS lateral movement and column twist tend to increase with an increase in beam section size. Heavier beam sections have a smaller web slenderness, which can improve the beam stability; but at the same time the driving force for the column twist gets larger since the beam flange area increases. The lateral movement of the beam bottom flange in the presence of a floor slab is less than the value of 20% of the beam flange width proposed by Chi and Uang (2002**)**.

(6) Reducing the thickness of the continuity plates increases the ductile fracture potential of an RBS connection to a deep column. The critical location with the largest Rupture Index remains at the end of the beam web-to-column flange CJP groove weld; however, there is an increase in the Rupture Index in the beam flange-to-column flange CJP groove welds when the continuity plate thickness is reduced.

(7) The axial load has a slight effect on connection behavior, including both local fracture potential and global behavior. Applying practical values of the axial load on a perimeter moment frame column, the axial load will not significantly degrade the connection performance when the stress due to axial load is less than 20% of the column material yield strength. The axial load of 20% of the column nominal yield stress is well within the range of axial load applied to the columns in a perimeter SMF.

(8) The total column normal elastic stresses based on the procedure proposed by Chi and Uang (2002) does not show consistent trends with the performance based on the Rupture Index for the RBS connections. The value of the elastic warping normal stress appears to be high based on the procedure proposed by Chi and Uang.

(9) The best indicator for column twist is the column elastic torsional stiffness, considering both the effects of St. Venant and Warping Torsion. No clear trend was

found to exist between the column twist from the finite element analyses and the ratio of h / t_{cf}^{3} for the column.

Table 3.1 – Analysis matrix for calibration of composite floor slab model

Case	Comments
1	Bare steel connection subassembly without a floor slab; laterally braced to prevent lateral-torsional buckling of the beams.
2	Connection subassembly with an elastic-perfectly plastic material model for the concrete floor slab, using 60% of the original concrete Young's modulus and 2 ksi for concrete yield stress.
3	Connection subassembly with an elastic-perfectly plastic material model for the concrete floor slab, using 30% of the original concrete Young's modulus and 1 ksi for concrete yield stress.
4	Connection subassembly with an elastic-perfectly plastic material model for the concrete floor slab, using 3% of the original concrete Young's modulus and 0.1 ksi for concrete yield stress.
5	Bare steel connection subassembly without a floor slab; laterally braced to prevent lateral-torsional buckling of the beams; beam local buckling restrained by excluding geometric nonlinearities.
6	Same as Case 3, with elastic-perfectly plastic spring elements added to model flexibility of the shear studs; shear studs were also assigned a 50% reduction in their elastic stiffness.
7	Same as Case 3, with elastic-perfectly plastic spring elements added to model flexibility of the shear studs; the full elastic stiffness of the shear studs were used.
8	Connection subassembly with a floor slab; the concrete constitutive model in ABAQUS was used as the material model for the floor slab.
9	Same as Case 8, with reinforcement added to the concrete floor slab.

Table 3.2 – Analysis matrix to evaluate effect of connection type on ductile fracture potential

Case	Column	Beam	Doubler Plate Thickness (in.)	Continuity Plate Thickness (in.)	Connection Type	R_v / V_{pz}
1	W14x398	W36x150	0	1	RBS	1.22
2	W14x398	W36x150	2@¾	1	WUF	1.36
3	W36x230	W36x150	1@¼	1	RBS	1.09
4	W36x230	W36x150	1@⅝	1	WUF	1.09
5	W27x194	W36x150	1@½	1	RBS	1.05

Note:, R_v = Panel zone shear strength, Equation (2.3);
V_{pz} = Panel shear force, based on beam moment from Equation (2.14).

Table 3.3 – Analysis matrix to evaluate effect of panel zone strength on ductile fracture potential of an RBS connection to a deep column

Case	Column	Beam	Doubler Plate Thickness (in.)	Continuity Plate Thickness (in.)	R_v / V_{pz}	Comments
1	W36x230	W36x150	0	1	0.83	Weak panel zone
2	W36x230	W36x150	1@¼	1	1.09	Balanced panel zone
3	W36x230	W36x150	1@½	1	1.34	Strong panel zone
4	W27x194	W36x150	1@½	1	1.05	Balanced panel zone

Note:, R_v = Panel zone shear strength, Equation (2.3);
V_{pz} = Panel shear force, based on the beam moment from Equation (2.14).

Table 3.4 – Analysis matrix to evaluate effect of column depth on ductile fracture potential of an RBS connection

Case	Column	Beam	Doubler Plate Thickness (in.)	Continuity Plate Thickness (in.)	R_v / V_{pz}
1	W14x398	W36x150	0	1	1.22
2	W36x230	W36x150	1@¼	1	1.09
3	W27x194	W36x150	1@½	1	1.05
4	W27x146	W30x108	1@⅜	¾	1.05
5	W27x194	W36x150 (1)	0	1 (2)	1.31

Note: 1. All cases are interior connections, except Case 5, which is a connection to an exterior column;
2. All cases have Gr. 50 steel continuity plates, except Case 5 which has A36 steel continuity plates;
3. R_v = Panel zone shear strength, Equation (2.3);
V_{pz} = Panel shear force, based on the beam moment from Equation (2.14).

Table 3.5 – Analysis matrix to evaluate effect of continuity plate thickness on ductile fracture potential of an RBS connection to a deep column

Case	Column	Beam	Doubler Plate Thickness (in.)	Continuity Plate Thickness (in.)	R_v / V_{pz}
1	W27x194	W36x150	1@½	1	1.05
2	W27x194	W36x150	1@½	½	1.05

Note:, R_v = Panel zone shear strength, Equation (2.3);
V_{pz} = Panel shear force, based on the beam moment from Equation (2.14).

Table 3.6 – Analysis matrix to evaluate effect of floor slab on ductile fracture potential of an RBS connection to a deep column

Case	Column	Beam	Doubler Plate Thickness (in.)	Continuity Plate Thickness (in.)	Floor Slab	R_v / V_{pz}
1	W14x398	W36x150	0	1	No	1.22
2	W14x398	W36x150	0	1	Yes	1.22
3	W36x230	W36x150	1@¼	1	No	1.09
4	W36x230	W36x150	1@¼	1	Yes	1.09
5	W27x194	W36x150	1@½	1	No	1.05
6	W27x194	W36x150	1@½	1	Yes	1.05

Note:, R_v = Panel zone shear strength, Equation (2.3);
V_{pz} = Panel shear force, based on the beam moment from Equation (2.14).

Table 3.7 – Analysis matrix to evaluate effect of axial load on ductile fracture potential of an RBS connection to a deep column

Case	Column	Beam	Doubler Plate Thickness (in.)	Continuity Plate Thickness (in.)	R_v/V_{pz}	Stress due to Axial Load (ksi)
1	W27x194	W36x150	1@½	1	1.05	0
2	W27x194	W36x150	1@½	1	1.05	5
3	W27x194	W36x150	1@½	1	1.05	10

Note: R_v = Panel zone shear strength, Equation (2.3);
V_{pz} = Panel shear force, based on beam moment from Equation (2.14).

Table 3.8 – Analysis matrix to evaluate effect of panel zone strength on cyclic global performance of an RBS connection to a deep column

Case	Column	Beam	Doubler Plate Thickness (in.)	Continuity Plate Thickness (in.)	R_v/V_{pz}	Comments
1	W27x194	W36x150	0	1	0.65	Weak panel zone
2	W27x194	W36x150	1@½	1	1.05	Balanced panel zone
3	W27x194	W36x150	1@¾	1	1.25	Strong panel zone

Note: R_v = Panel zone shear strength, Equation (2.3);
V_{pz} = Panel shear force, based on beam moment from Equation (2.14).

Table 3.9 – Analysis matrix to evaluate effect of composite floor slab on cyclic global performance of an RBS connection

Case	Column	Beam	Doubler Plate Thickness (in.)	Continuity Plate Thickness (in.)	Slab	R_v/V_{pz}
1	W14x398	W36x150	0	1	No	1.22
2	W14x398	W36x150	0	1	Yes	1.22
3	W27x194	W36x150	1@½	1	No	1.05
4	W27x194	W36x150	1@½	1	Yes	1.05

Note: R_v = Panel zone shear strength, Equation (2.3);
V_{pz} = Panel shear force, based on beam moment from Equation (2.14).

Table 3.10 – Analysis matrix to evaluate effect of beam web slenderness on cyclic global performance of an RBS connection to a deep column

Column	Beam	Beam Web Slenderness h/t_w	Doubler Plate (in.)	$\frac{\Sigma M^*_{pc}}{\Sigma M^*_{pb}}$	$\frac{R_v}{V_{pz}}$	Composite Floor Slab
W36x230	W36x135	54.1	1/8	2.28	1.08	No
	W36x150	51.9	1/4	2.03	1.09	
	W36x160	49.9	1/4	1.91	1.01	
	W36x170	47.7	3/8	1.79	1.06	
	W36x182	44.8	1/2	1.66	1.08	
	W36x194	42.4	1/2	1.55	1.01	
	W36x210	39.1	5/8	1.42	1.01	
	W36x232	37.3	7/8	1.28	1.05	
	W36x256	33.8	1	1.14	1.01	
	W36x135	54.1	1/8	2.28	1.08	Yes
	W36x150	51.9	1/4	2.03	1.09	
	W36x160	49.9	1/4	1.91	1.01	
	W36x170	47.7	3/8	1.79	1.06	
	W36x182	44.8	1/2	1.66	1.08	
	W36x194	42.4	1/2	1.55	1.01	
	W36x210	39.1	5/8	1.42	1.01	
	W36x232	37.3	7/8	1.28	1.05	
	W36x256	33.8	1	1.14	1.01	
W27x194	W36x135	54.1	1/2	1.58	1.16	No
	W36x150	51.9	1/2	1.39	1.05	
	W36x160	49.9	5/8	1.32	1.07	
	W36x170	47.7	5/8	1.23	1.01	
	W36x182	44.8	3/4	1.15	1.01	
	W36x194	42.4	7/8	1.07	1.02	
	W36x210	39.1	1	0.98	1.00	
	W36x135	54.1	1/2	1.58	1.16	Yes
	W36x150	51.9	1/2	1.39	1.05	
	W36x160	49.9	5/8	1.32	1.07	
	W36x170	47.7	5/8	1.23	1.01	
	W36x182	44.8	3/4	1.15	1.01	
	W36x194	42.4	7/8	1.07	1.02	
	W36x210	39.1	1	0.98	1.00	

Note: 1. ΣM^*_{pc} = sum of the column nominal plastic moment capacity extrapolated to the intersection of the beam and column centerlines;

ΣM^*_{pb} = sum of the beam expected plastic moment capacity extrapolated to the intersection of the beam and column centerlines.

2. R_v = Panel zone strength, Equation (2.3);

V_{pz} = Panel zone shear force, based on beam moment from Equation (2.14).

Table 3.11 – Analysis matrix to evaluate effect of axial load on cyclic global performance an RBS connection to a deep column

Case	Column	Beam	Doubler Plate Thickness (in.)	Continuity Plate Thickness (in.)	R_v / V_{pz}	Stress due to Axial Load (ksi)
1	W27x194	W36x150	1@½	1	1.05	0
2	W27x194	W36x150	1@½	1	1.05	5
3	W27x194	W36x150	1@½	1	1.05	10

Note: R_v = Panel zone shear strength, Equation (2.3);
V_{pz} = Panel shear force, based on beam moment from Equation (2.14).

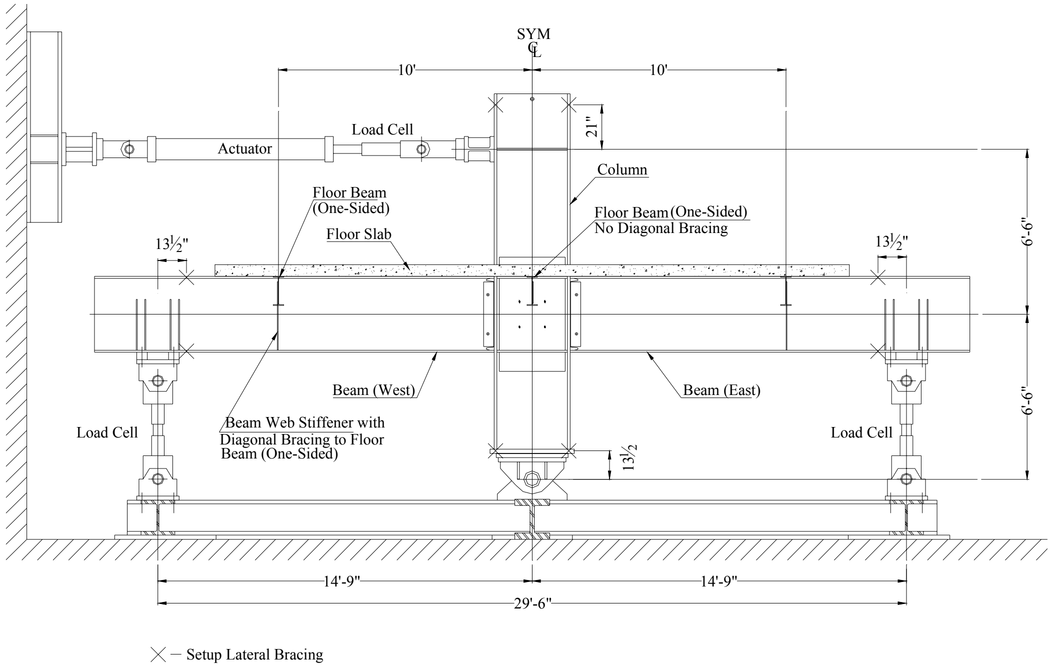

Figure 3.1 – Test set-up

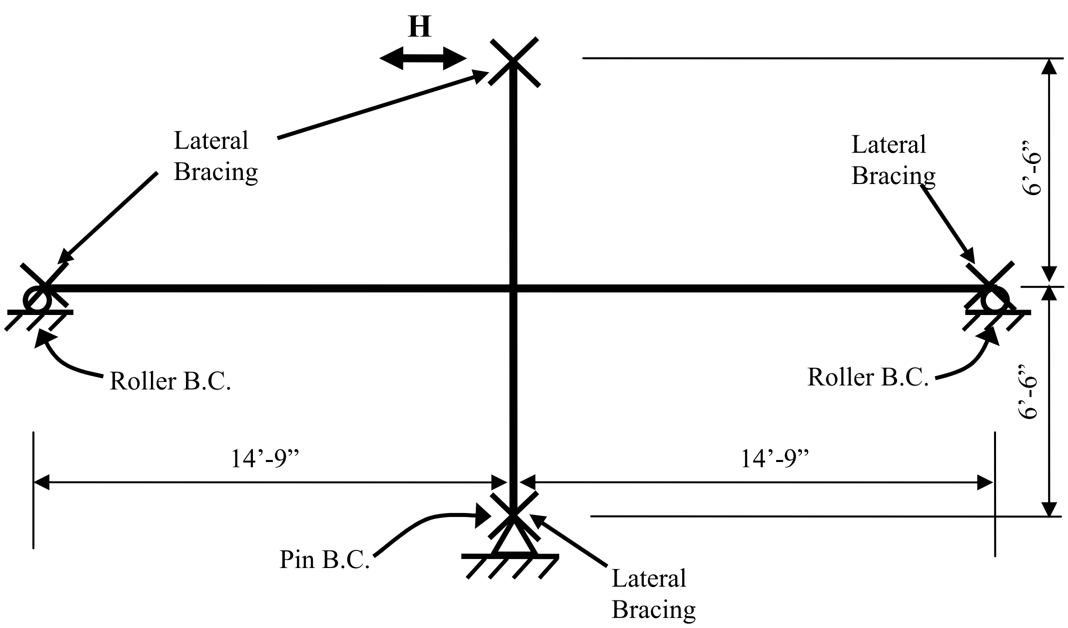

Figure 3.2 – Global model span length and boundary conditions

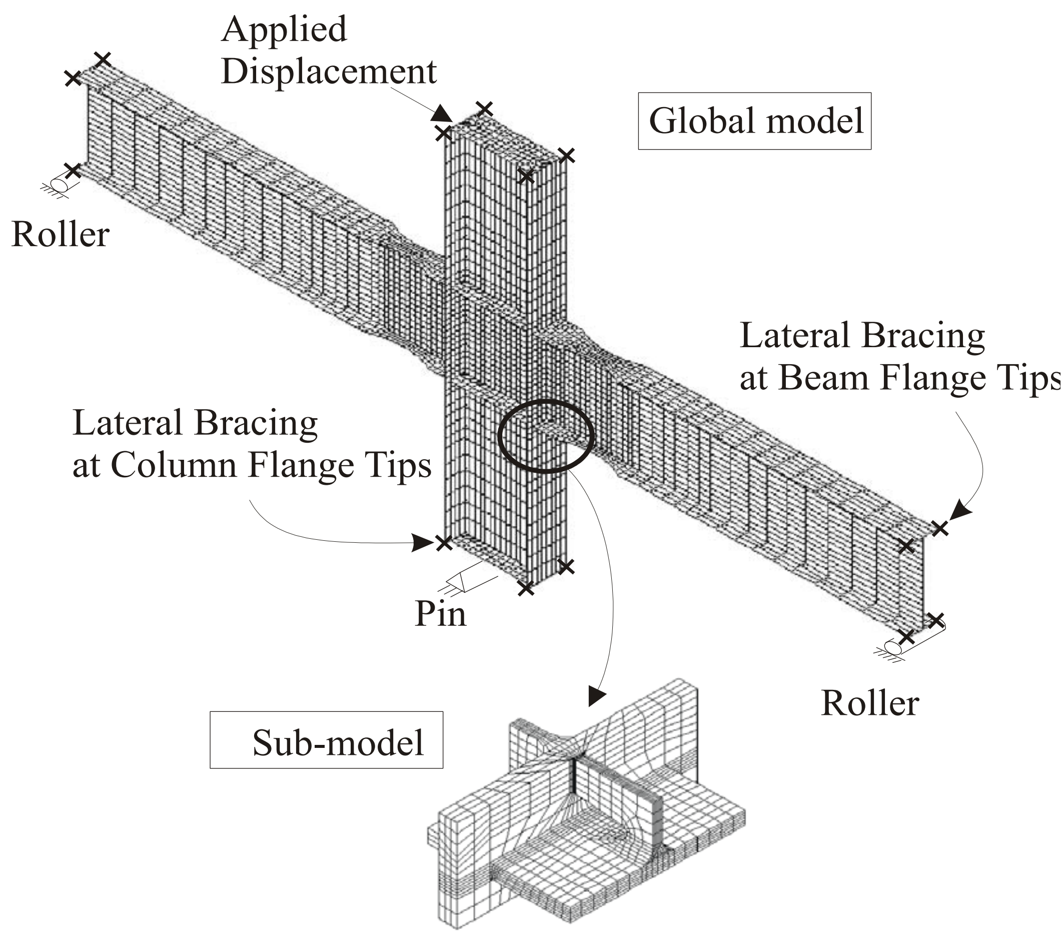

Figure 3.3 – Three-dimensional connection finite element model

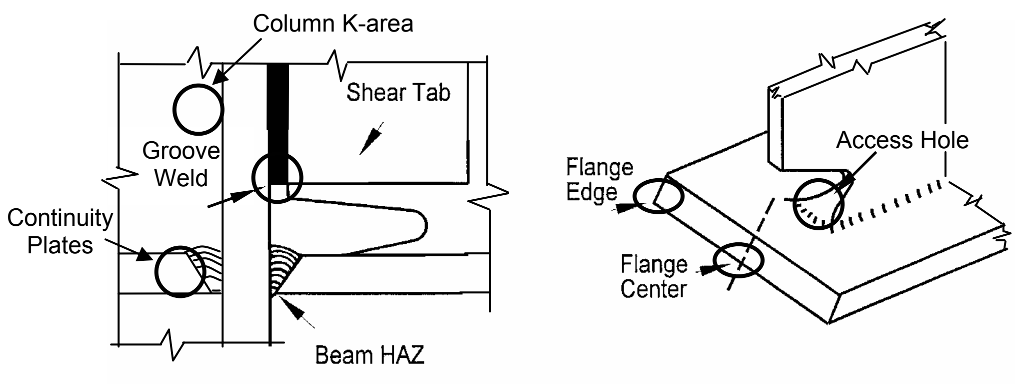

Figure 3.4 – Critical locations in connection where rupture index values were determined in sub-model

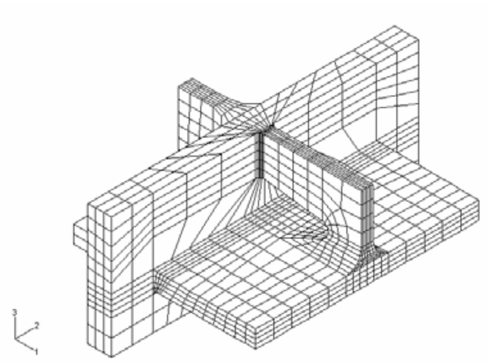

(a) 4 elements through beam flange thickness, 16 elements across beam flange width

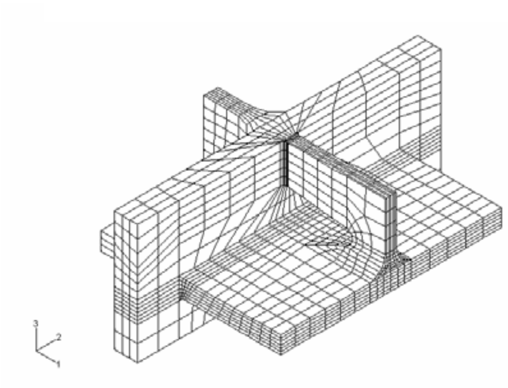

(b) 6 elements through beam flange thickness, 17 elements across beam flange width

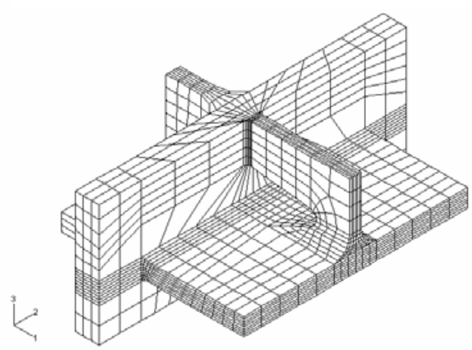

(c) 8 elements through beam flange thickness, 16 elements across beam flange width

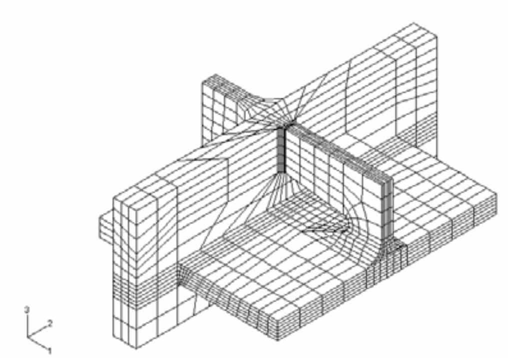

(d) 6 elements through beam flange thickness, 14 elements across beam flange width

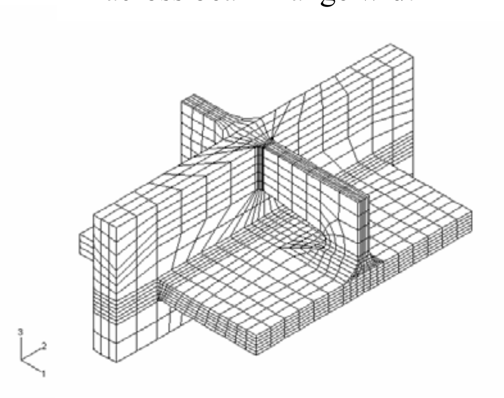

(e) 6 elements through beam flange thickness, 18 elements across beam flange width

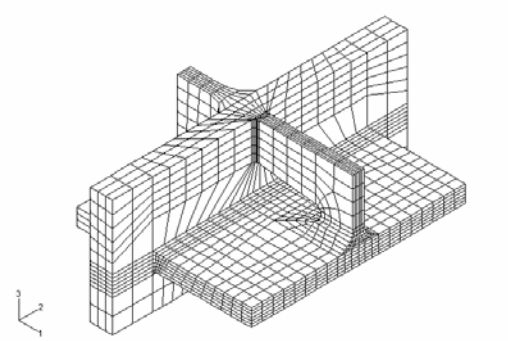

(f) 6 elements through beam flange thickness, 22 elements across beam flange width

Figure 3.5 – Mesh for convergence study of sub-model

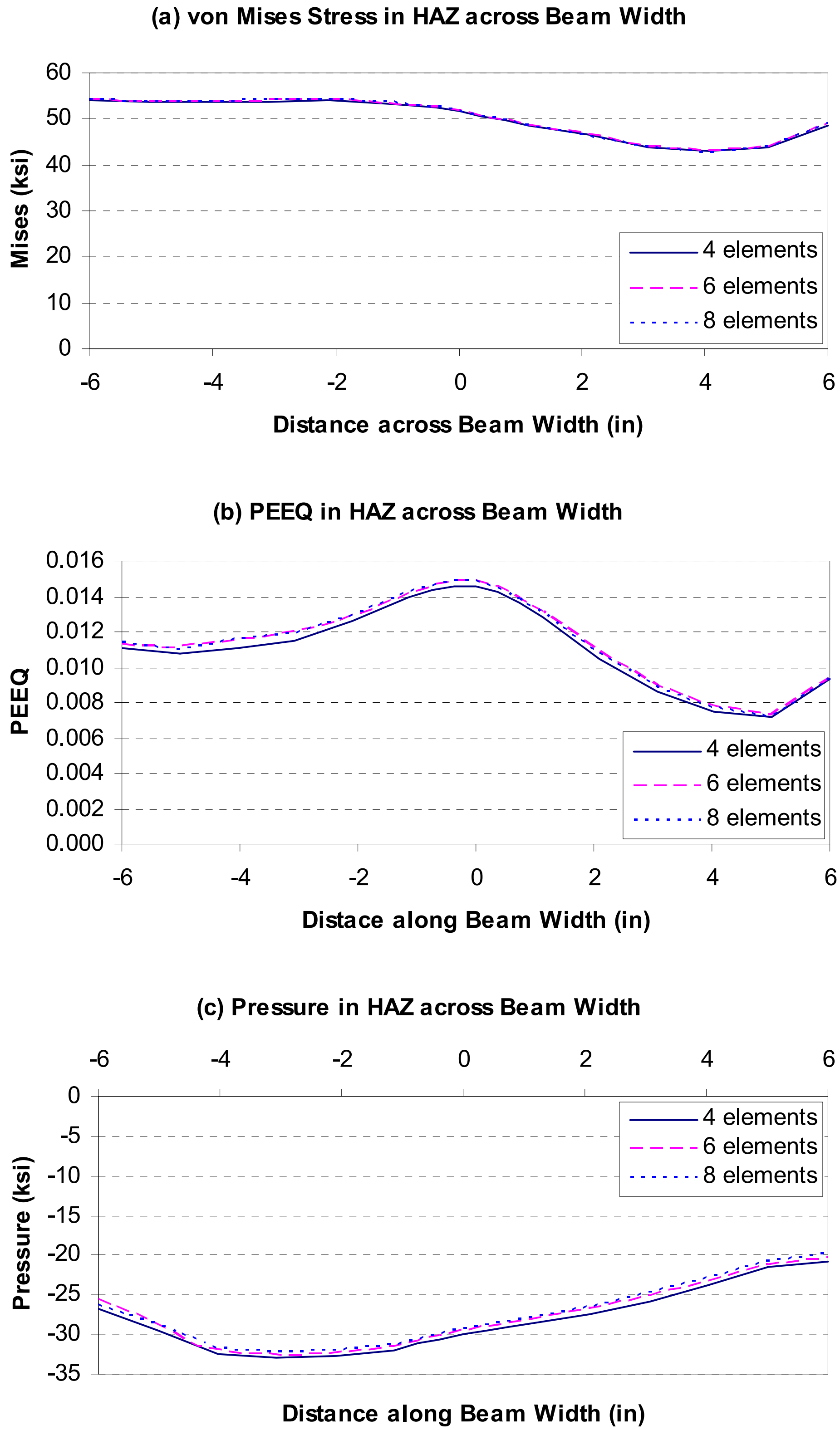

Figure 3.6 – Comparison of results for meshes with different number of elements through the beam flange thickness

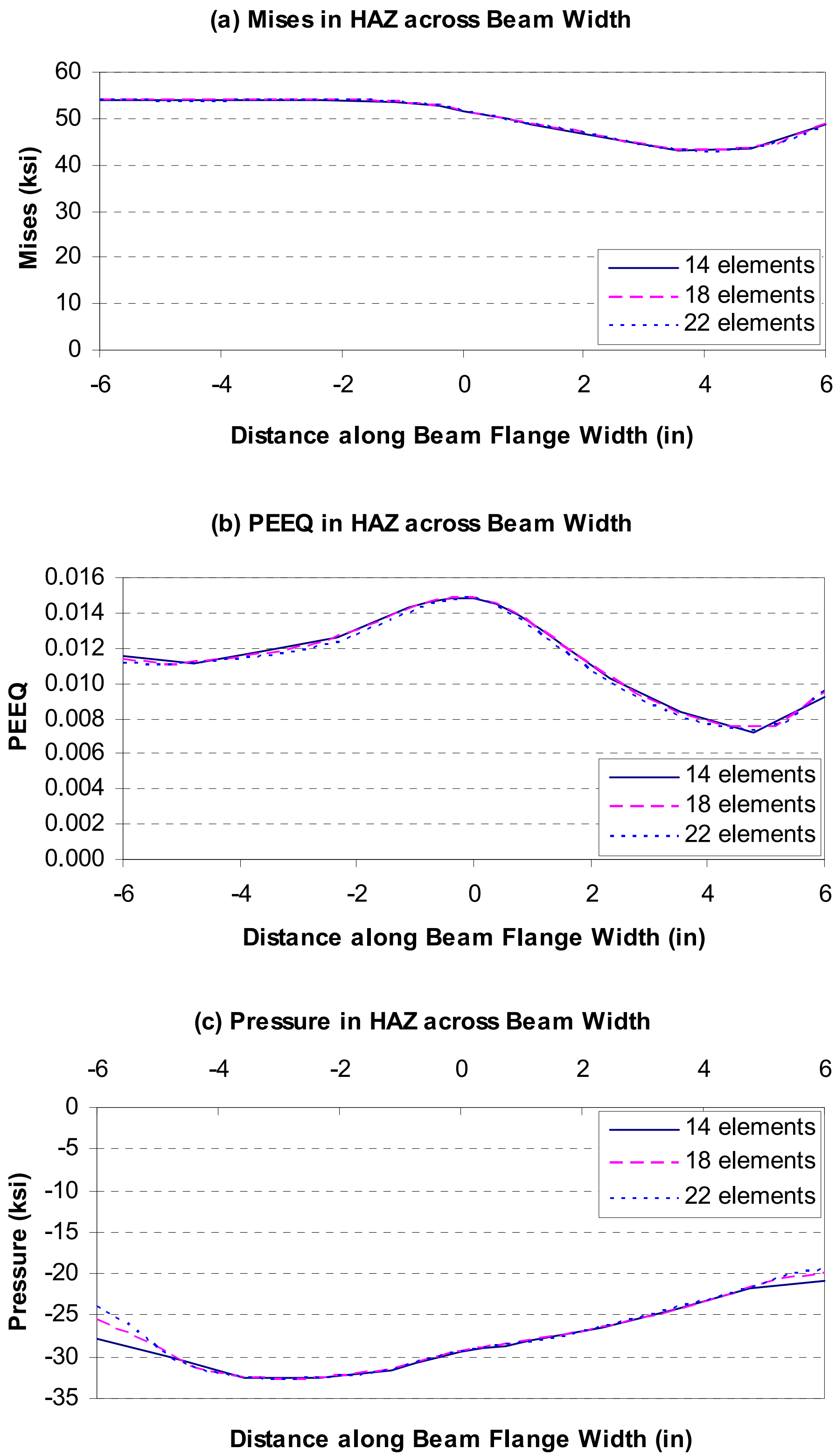

Figure 3.7 – Comparison of results for meshes with different number of elements across the beam flange width

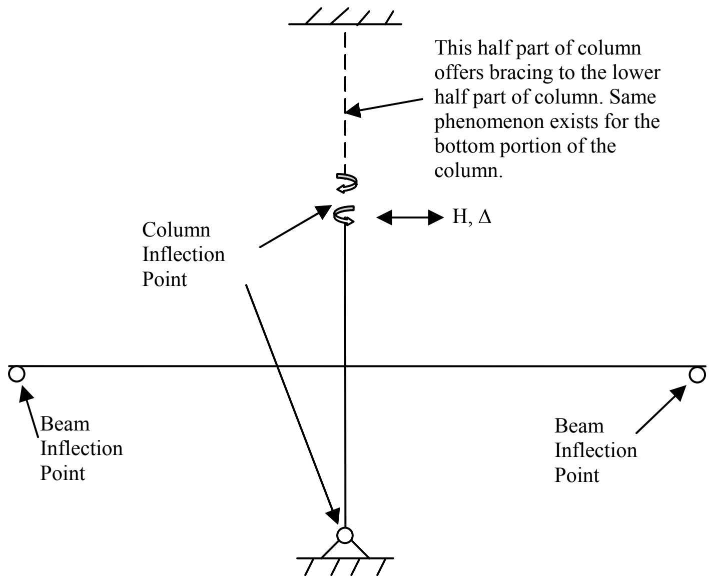

Figure 3.8 – Column torsional bracing in test setup

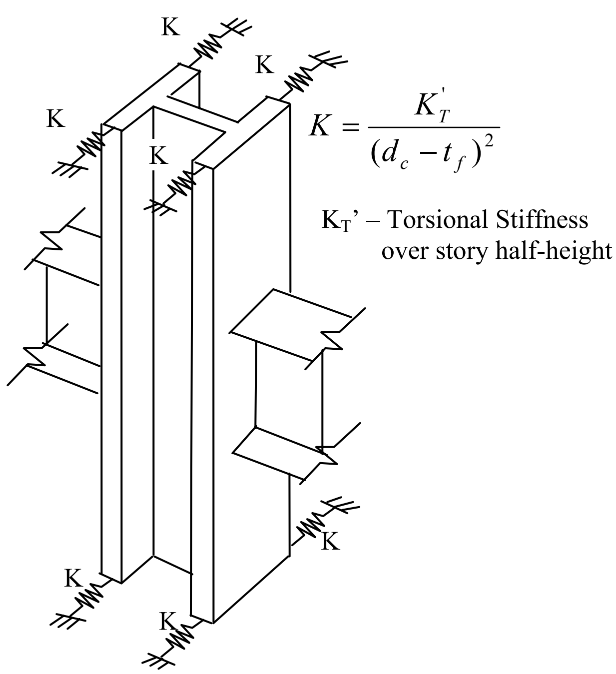

Figure 3.9 – Column bracing modeling in analysis

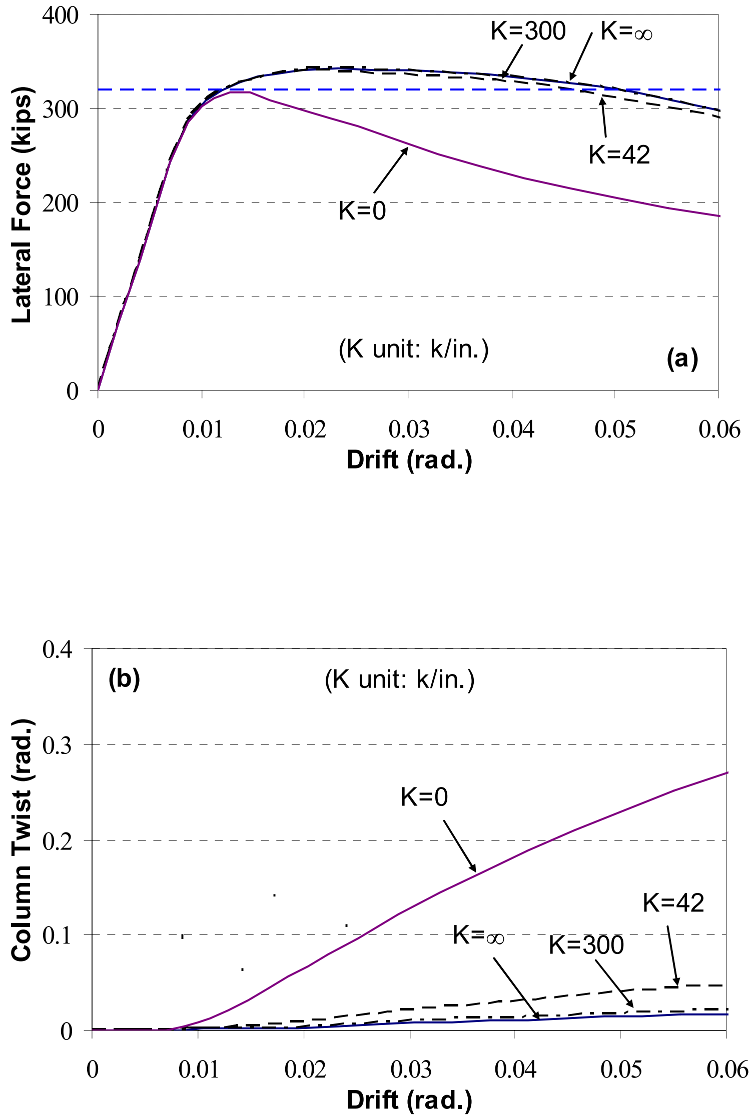

Figure 3.10 – Effect of column torsional bracing stiffness

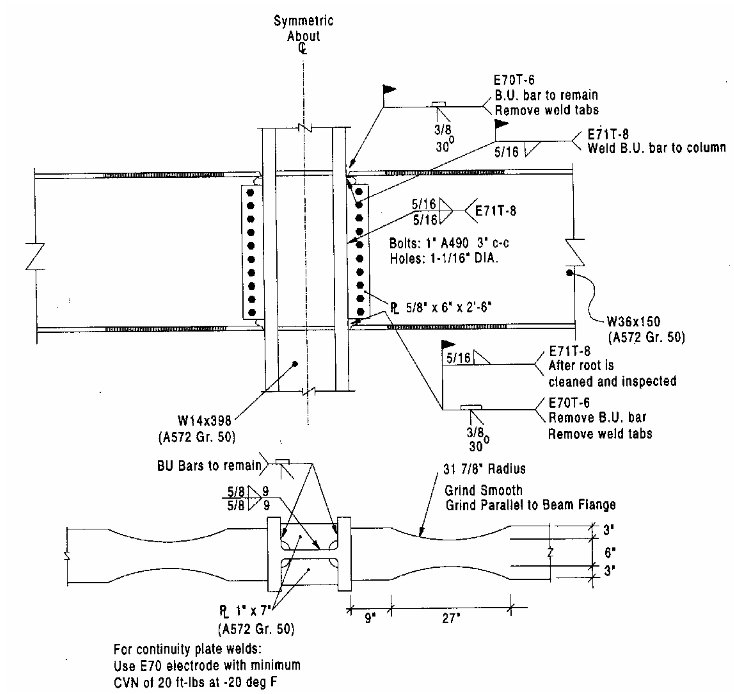

(a) Connection details

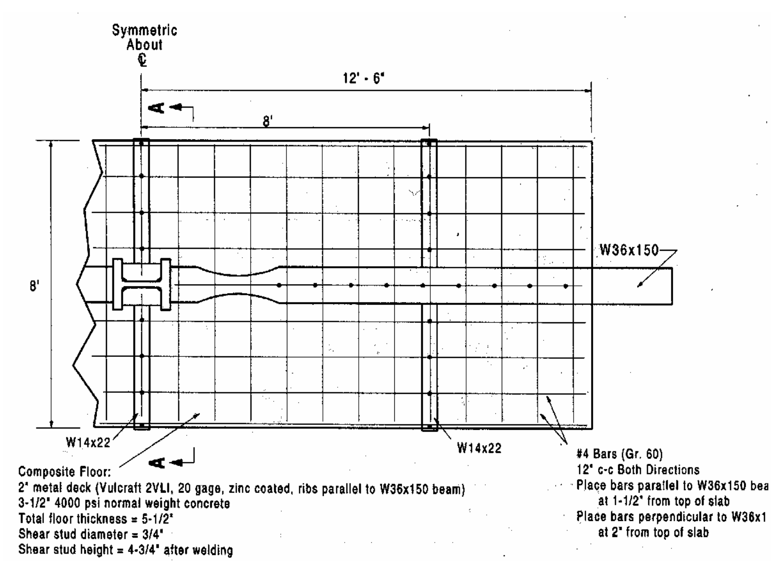

(b) Slab details

Figure 3.11 – Connection details of Specimen UTA-DBBWC
(after Jones et al. 2002)

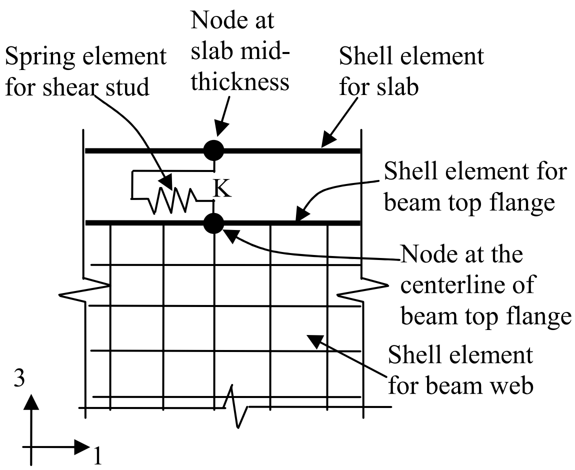

(a) Spring model for shear studs in axis-1 (longitudinal) direction

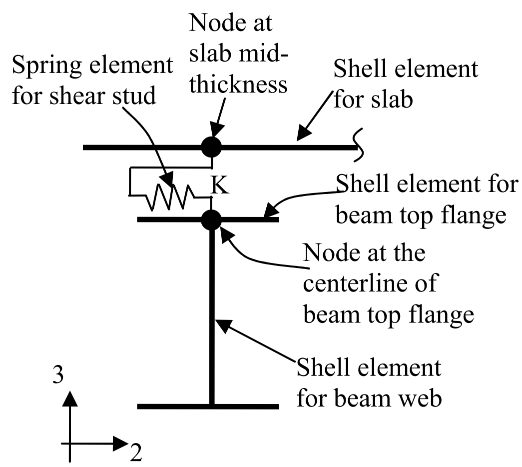

(b) Spring model for shear studs in axis-2 (transverse) direction

Figure 3.12 – Spring models for shear studs

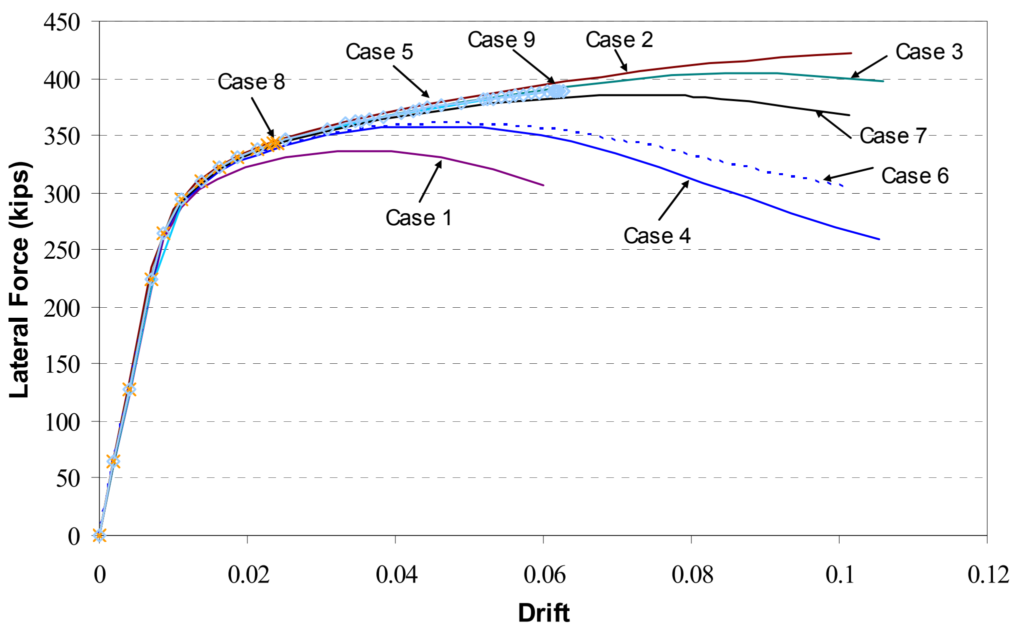

Figure 3.13 – Comparison of analysis results for different modeling cases (from Table 3.1) to develop the floor slab model

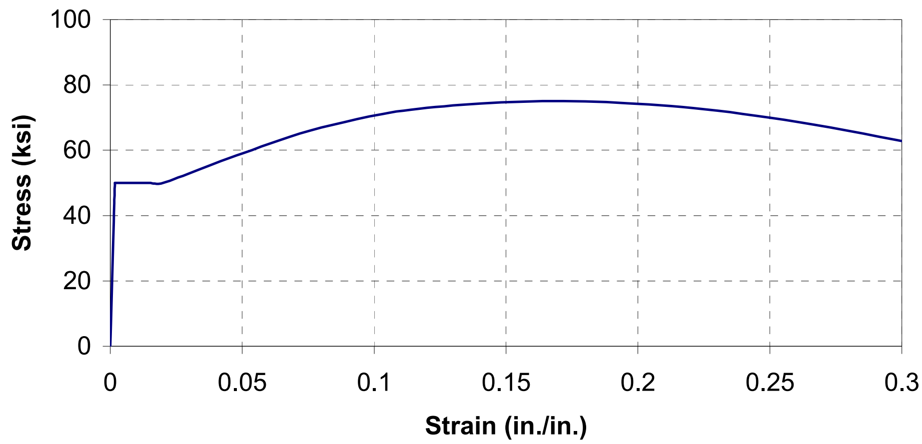

Figure 3.14 – Nominal Gr. 50 steel stress-strain curve (Salmon et al. 1996)

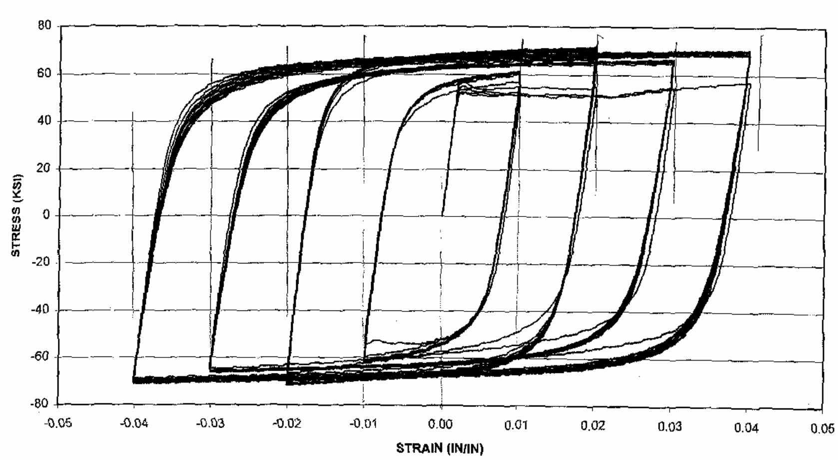

Figure 3.15 – Nominal Gr. 50 steel cyclic stress-strain curve (Kaufmann et al. 1999)

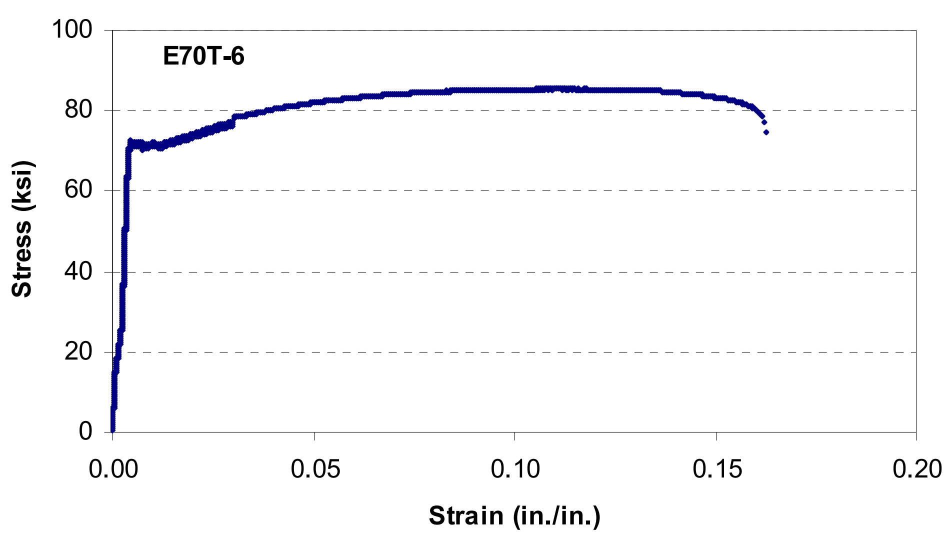

Figure 3.16 – E70T-6 electrode stress-strain curve

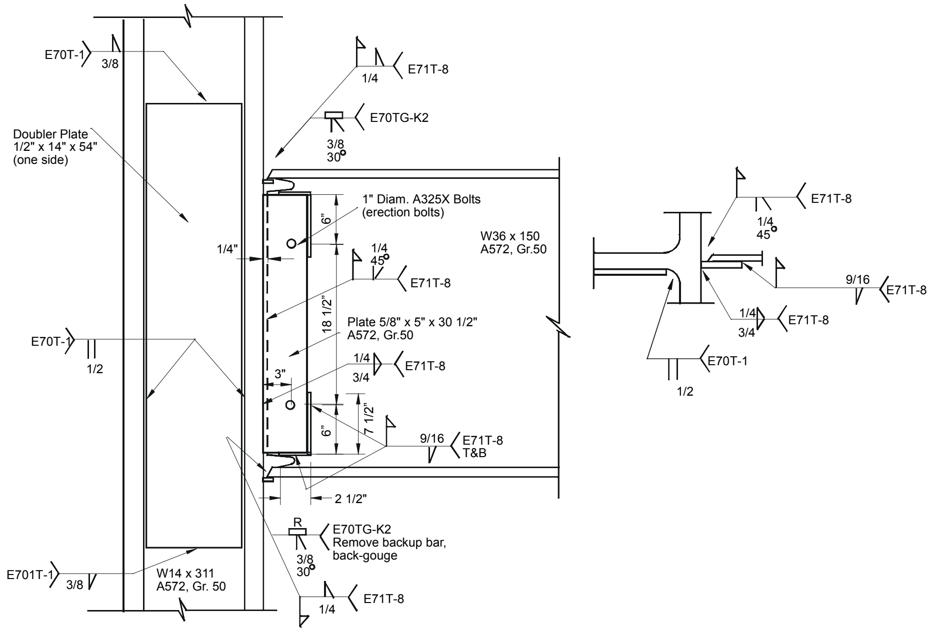

(a) Connection details

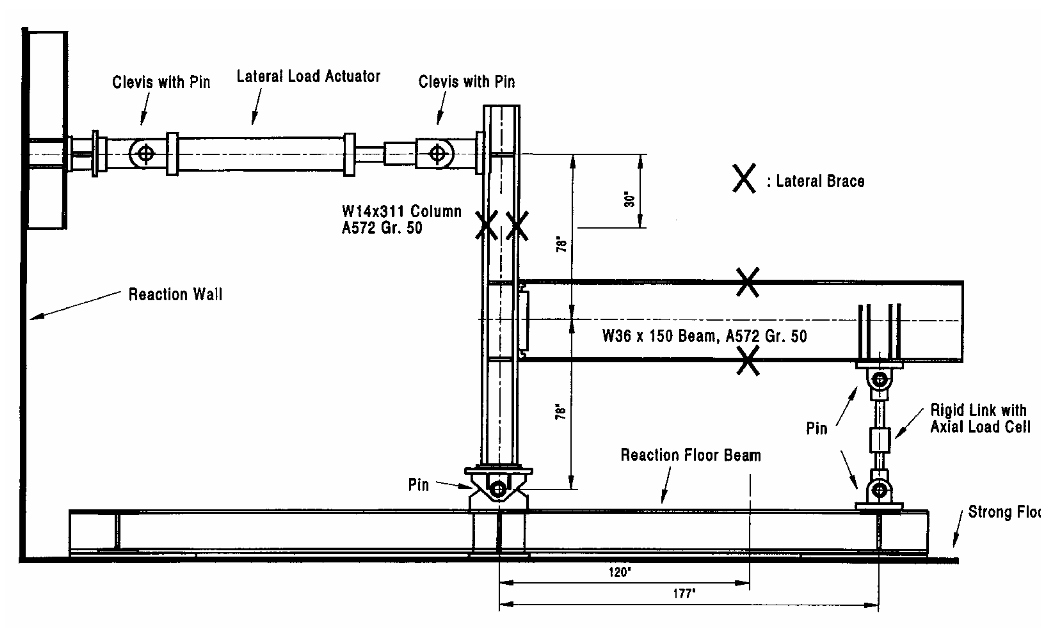

(b) Test set-up

Figure 3.17 – Connection details and test set-up of SAC Specimen T5
tested by Ricles et al. (2002)

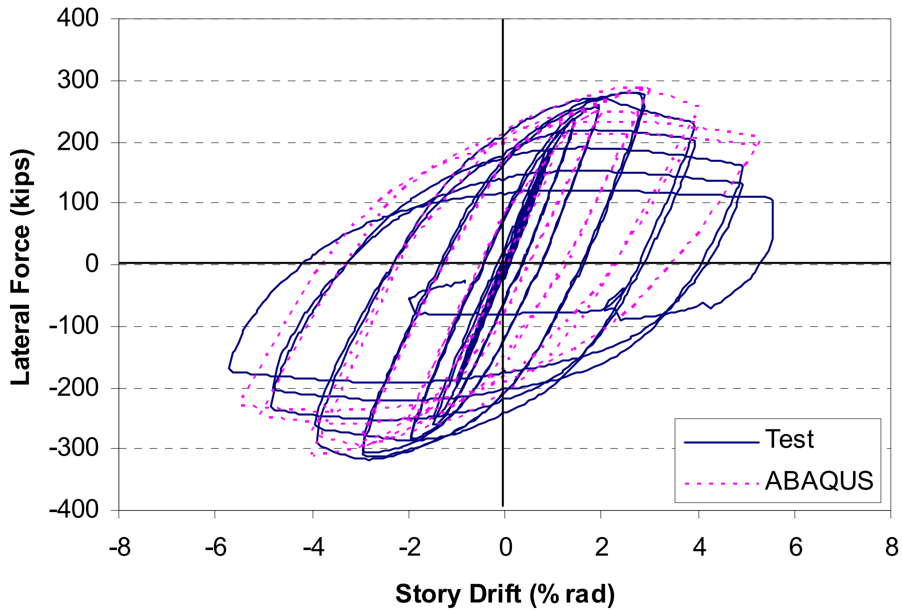

Figure 3.18 – Comparison of experimental and analytical (ABAQUS) results for lateral force vs. story drift of Specimen T5

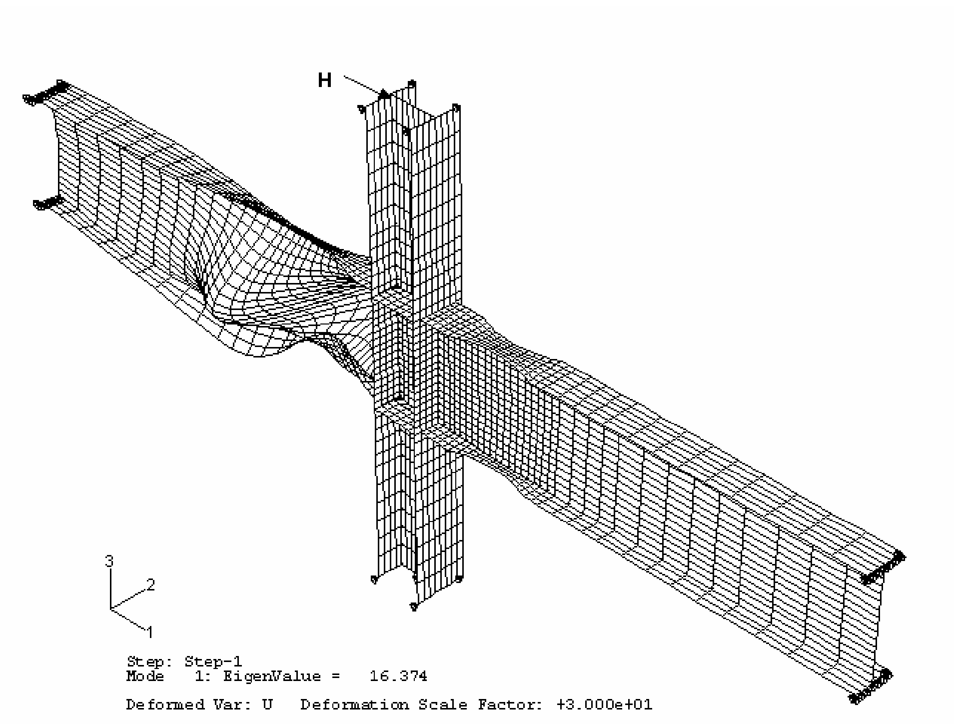

Figure 3.19 – First buckling mode of Specimen DBBWC (slab not shown for clarity)

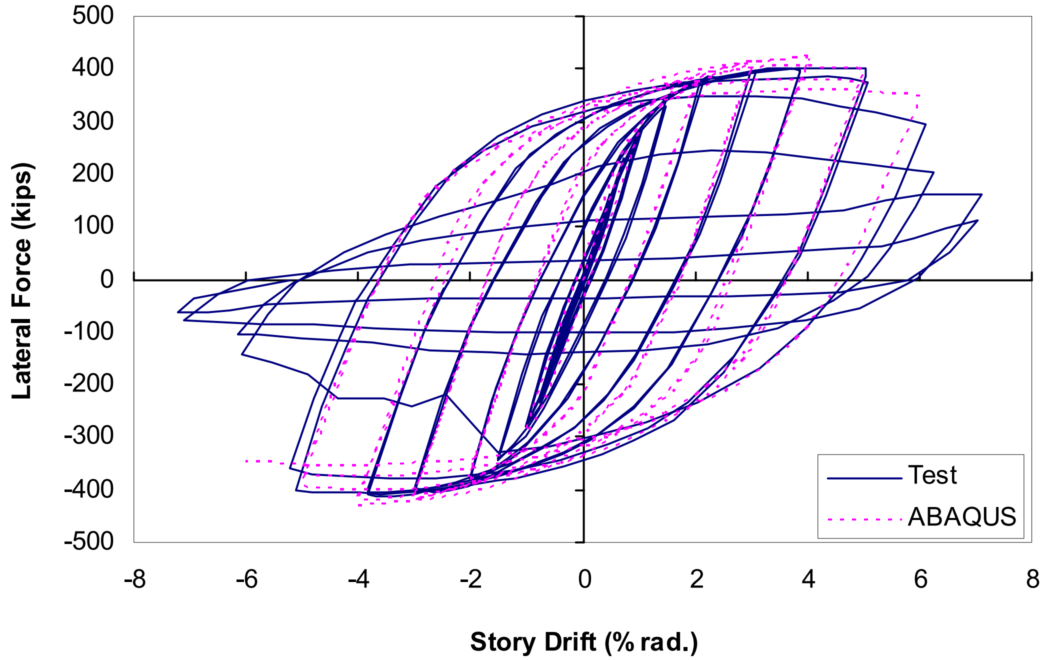

Figure 3.20 – Comparison of experimental and analytical (ABAQUS) results for lateral force vs. story drift of Specimen UTA-DBBWC
(Courtesy of Dr. Engelhardt for the experimental data)

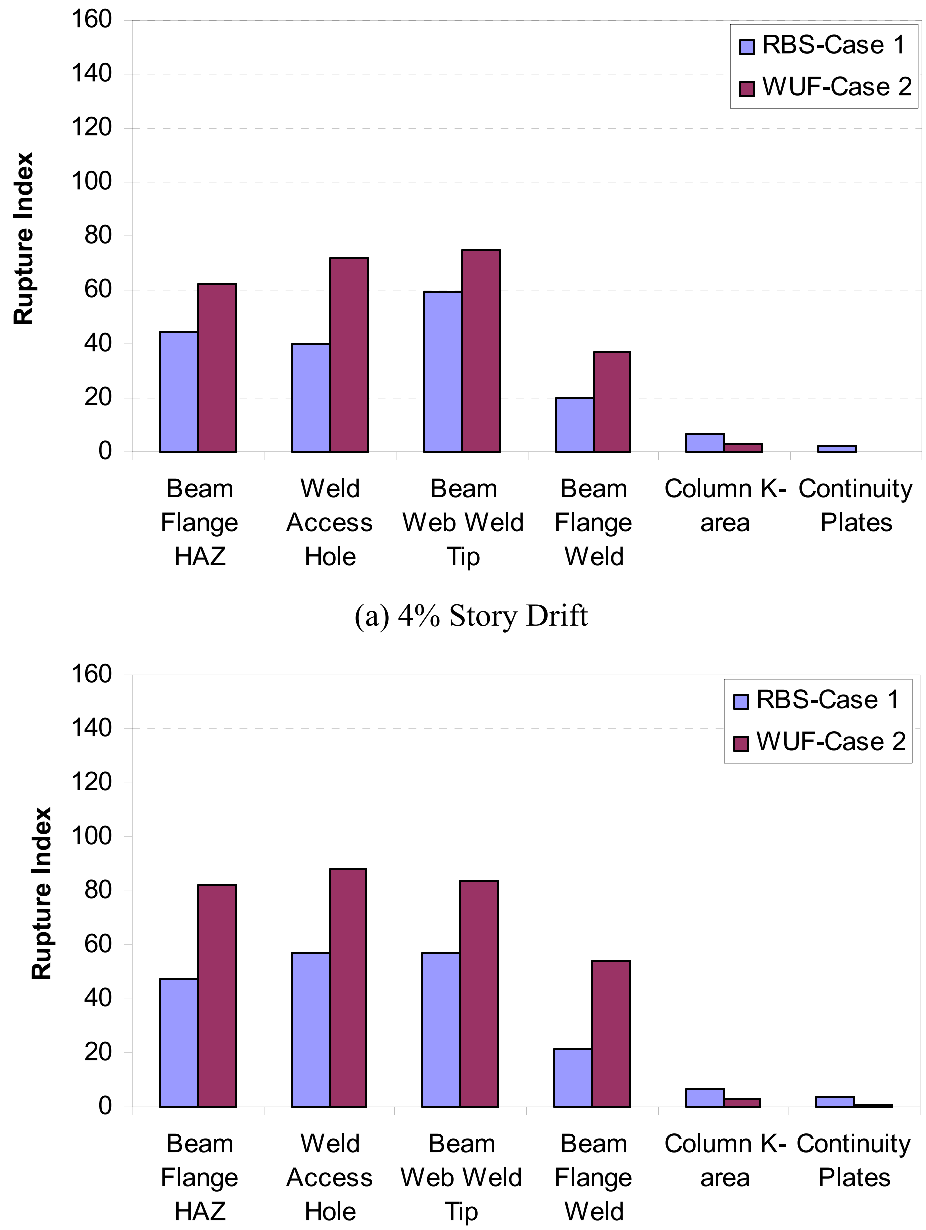

(a) 4% Story Drift

(b) 6% Story Drift

Figure 3.21 – Comparison of Rupture Index for RBS and WUF interior connections with a shallow column (W14x398 column; W36x150 beams; refer to Table 3.2 for case details)

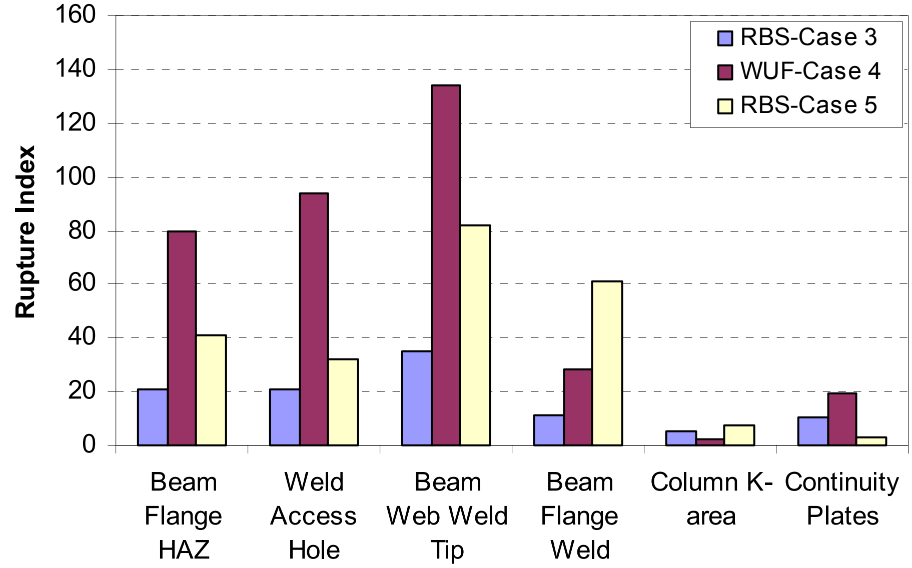

(a) 4% Story Drift

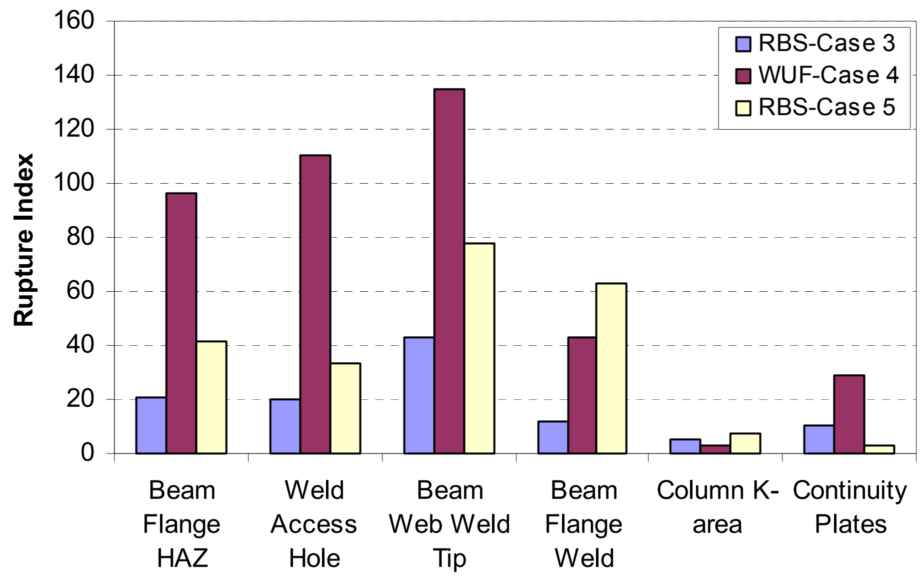

(b) 6% Story Drift

Figure 3.22 – Comparison of Rupture Index for RBS and WUF interior connections to a deep column (W36x150 beams; refer to Table 3.2 for case details)

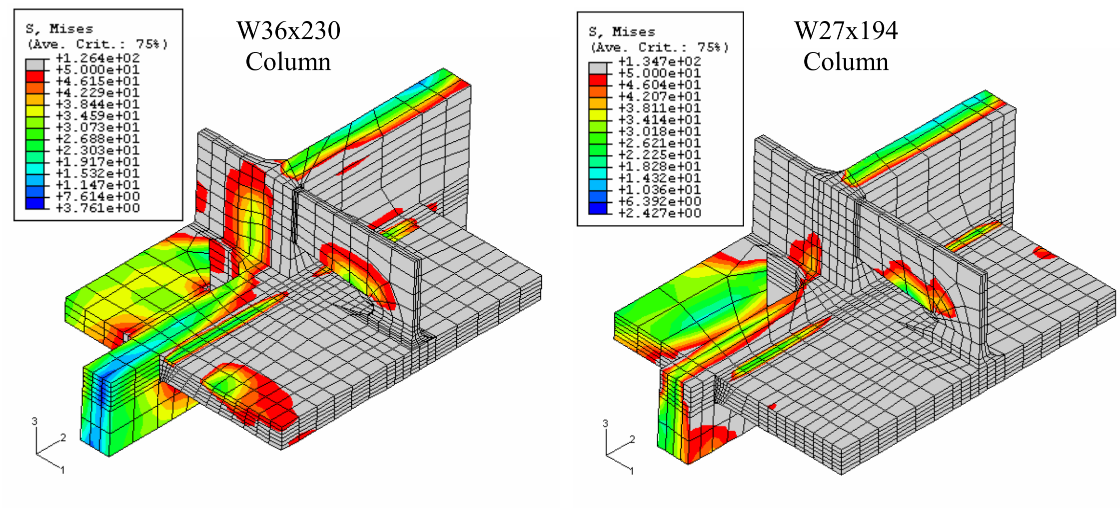

(a) von Mises Stress

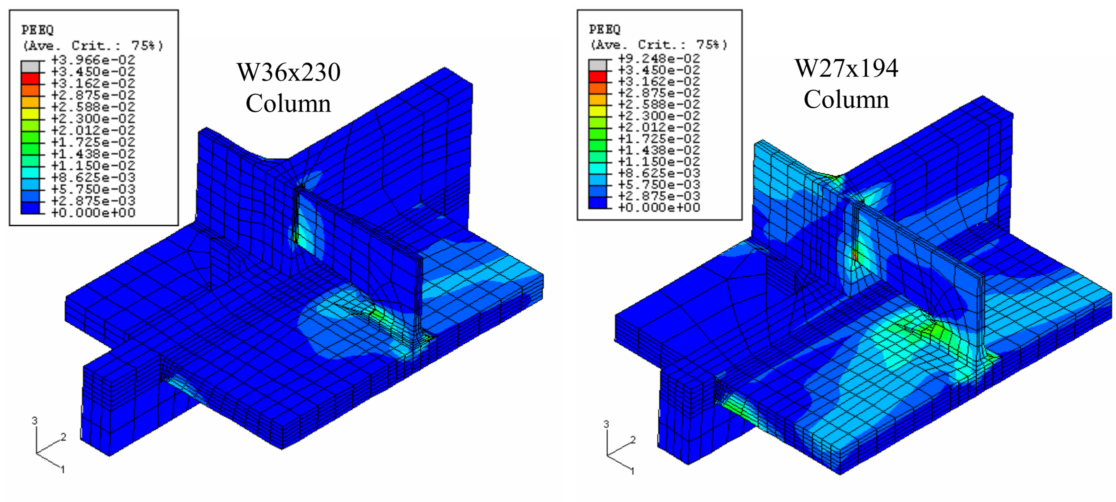

(b) PEEQ

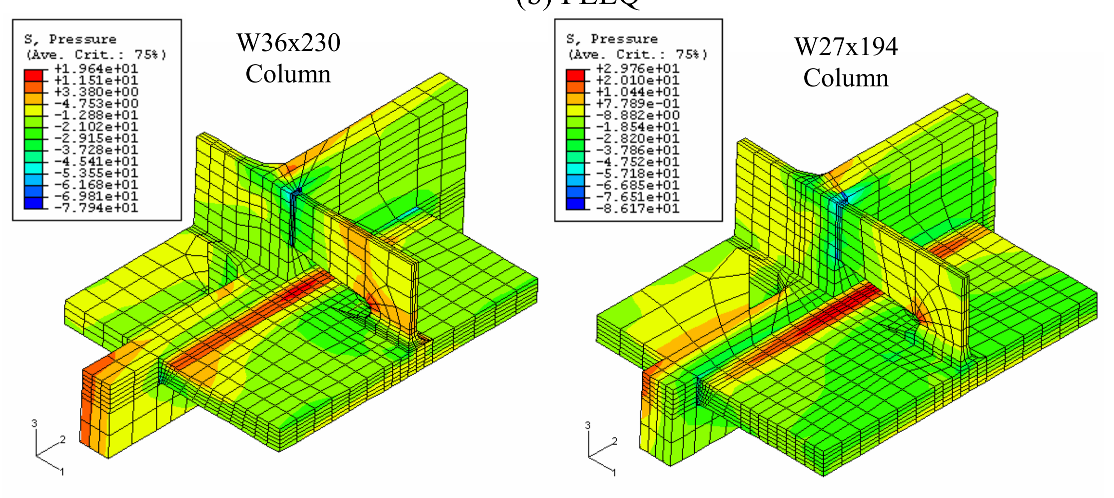

(c) Pressure

Figure 3.23 – Contour plots of sub-model at 4% story drift, with exposed cuts through the left-hand column flange

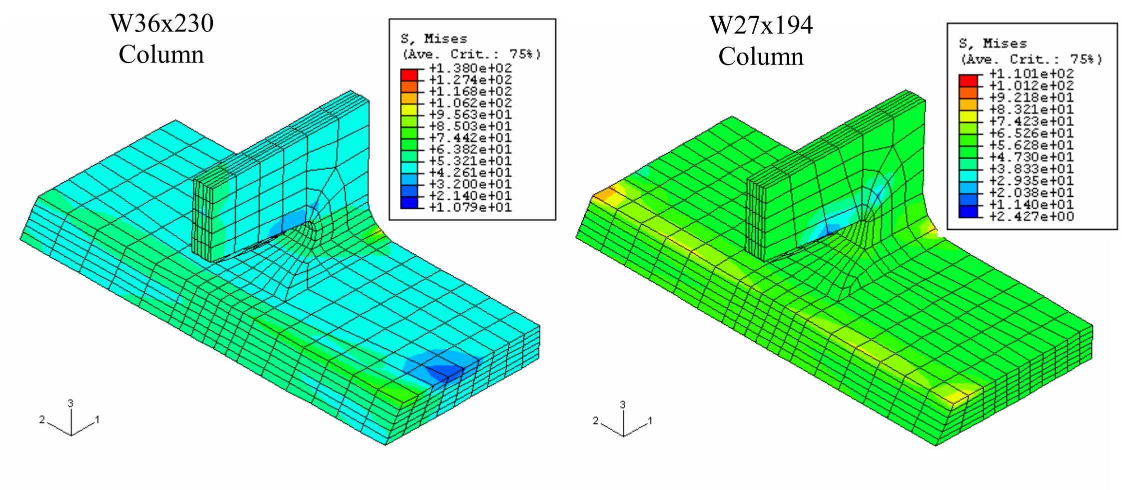

(a) von Mises Stress

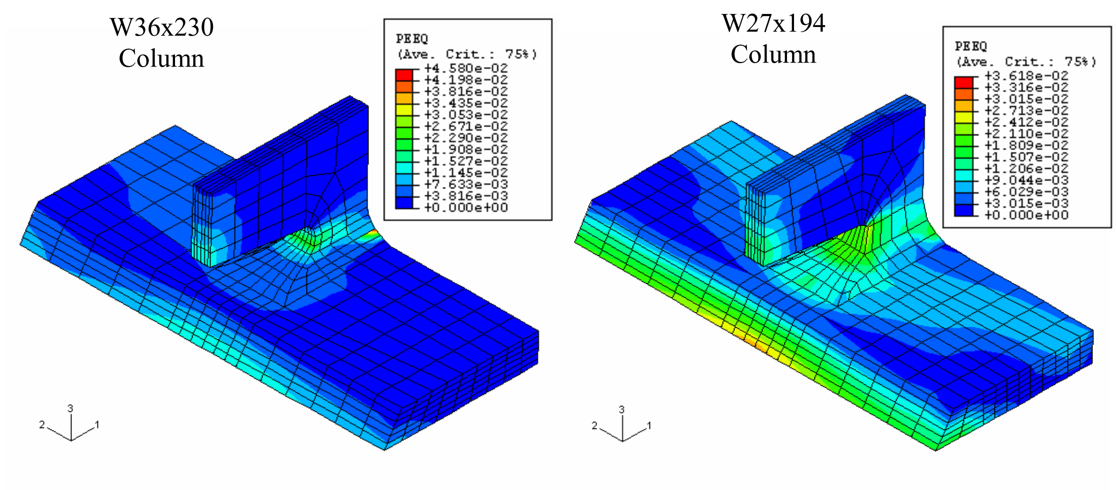

(b) PEEQ

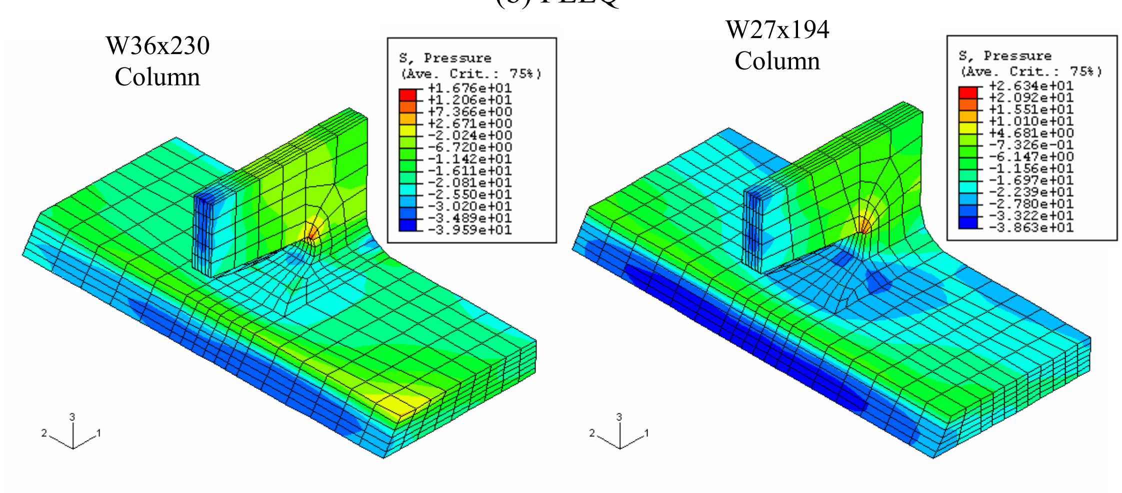

(c) Pressure

Figure 3.24 – Contour plots of beam flange and weld access hole region of sub-model at 4% story drift

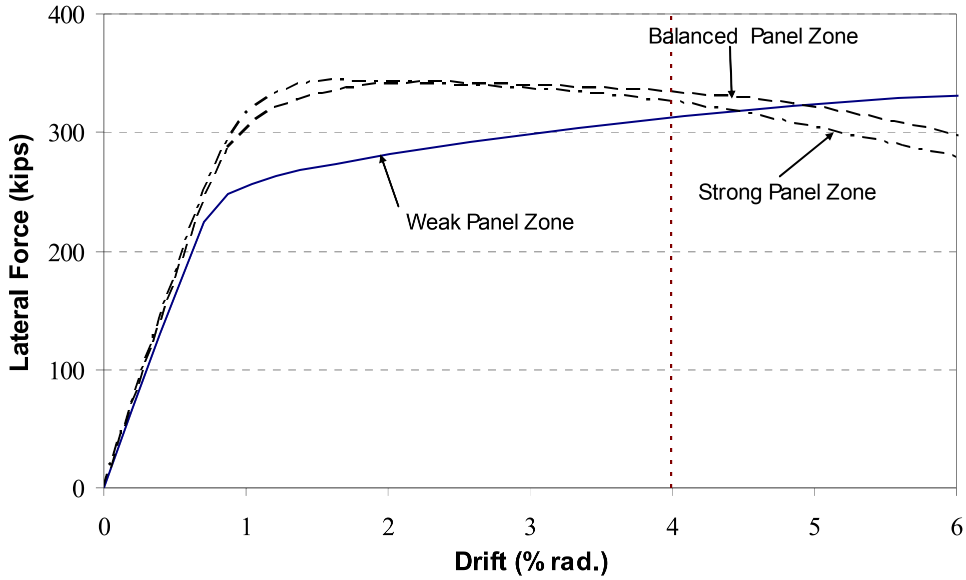

Figure 3.25 – Effect of panel zone strength on lateral load-story drift behavior of RBS-to-deep column connection

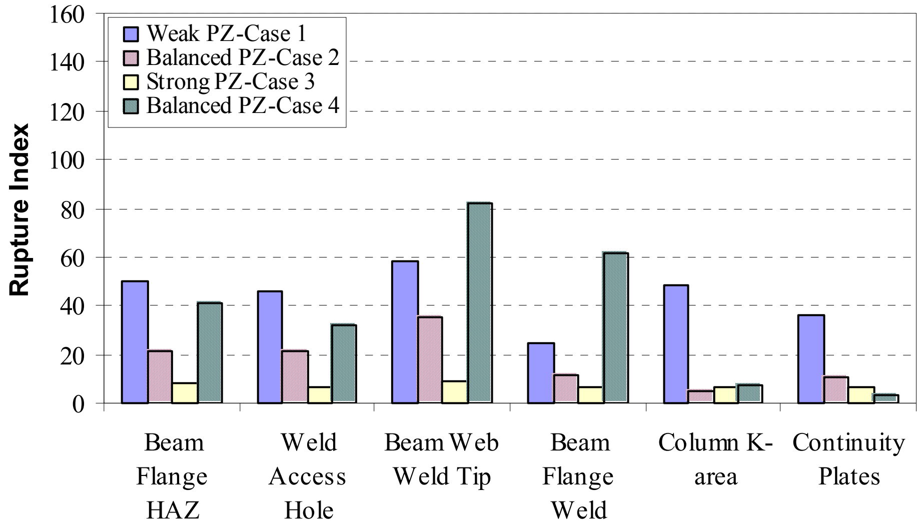

(a) 4% Story Drift

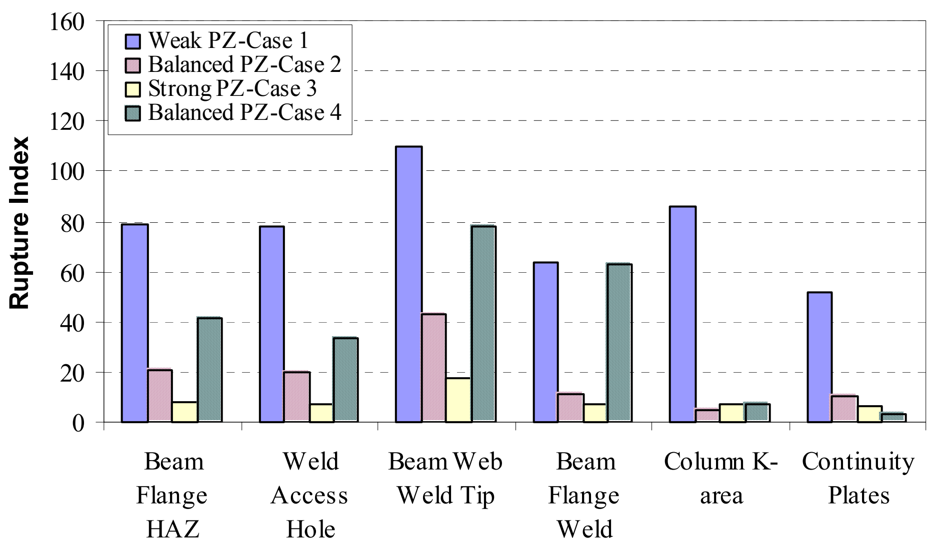

(b) 6% Story Drift

Figure 3.26 – Comparison of Rupture Index for different panel zone strength cases (Refer to Table 3.3 for case details)

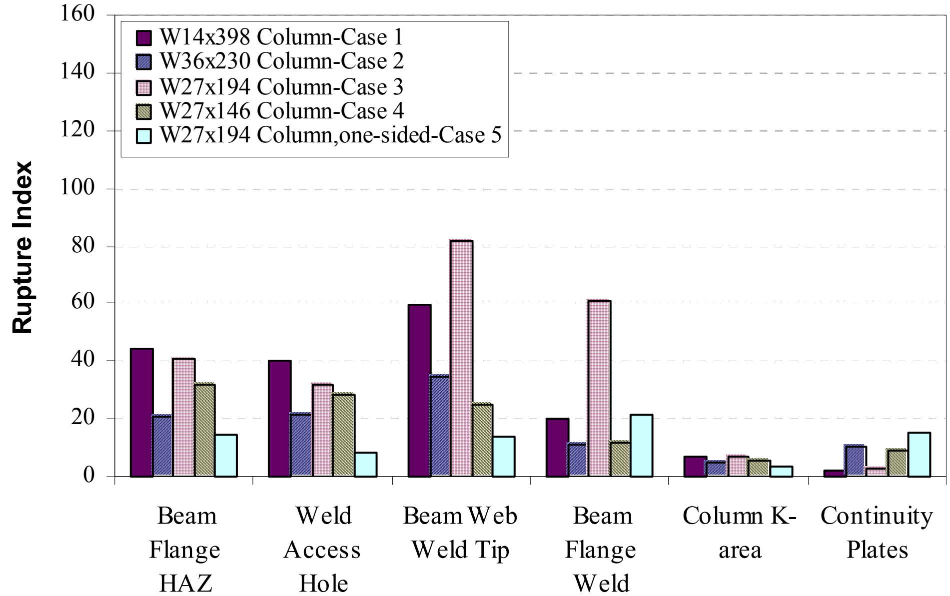

(a) 4% Story Drift

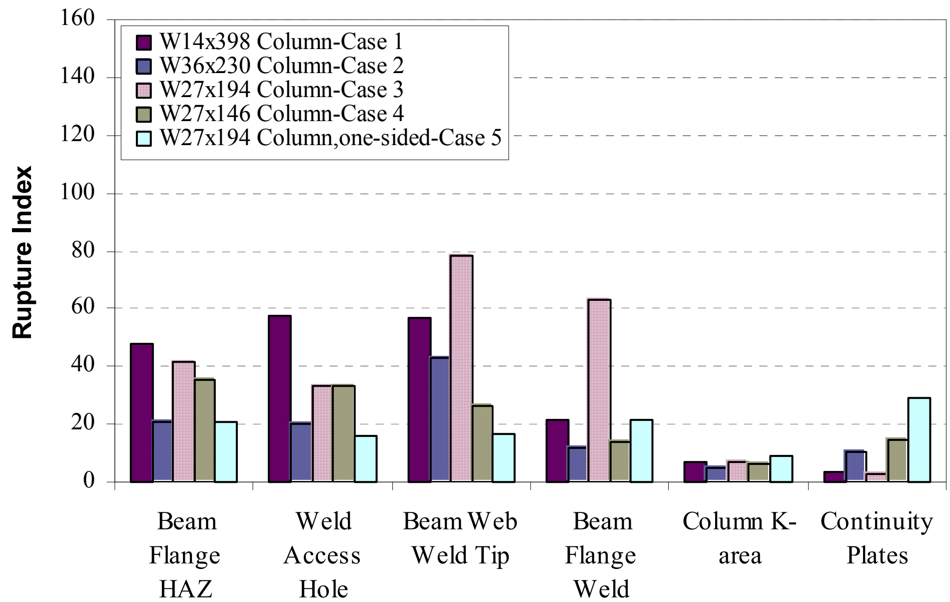

(b) 6% Story Drift

Figure 3.27 – Comparison of Rupture Index for different cases, RBS connection with selected column sizes (Refer to Table 3.4 for case details)

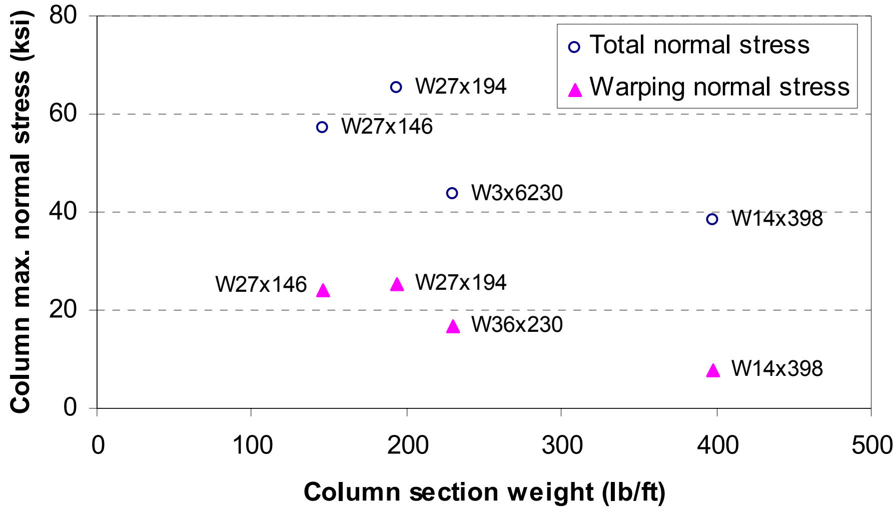

Note: except for the connection to a W27x146 column with W30x108 beams, all other connections to the column involved W36x150 beams

Figure 3.28 – Column total normal stress and warping normal stress vs. column section weight for RBS connections

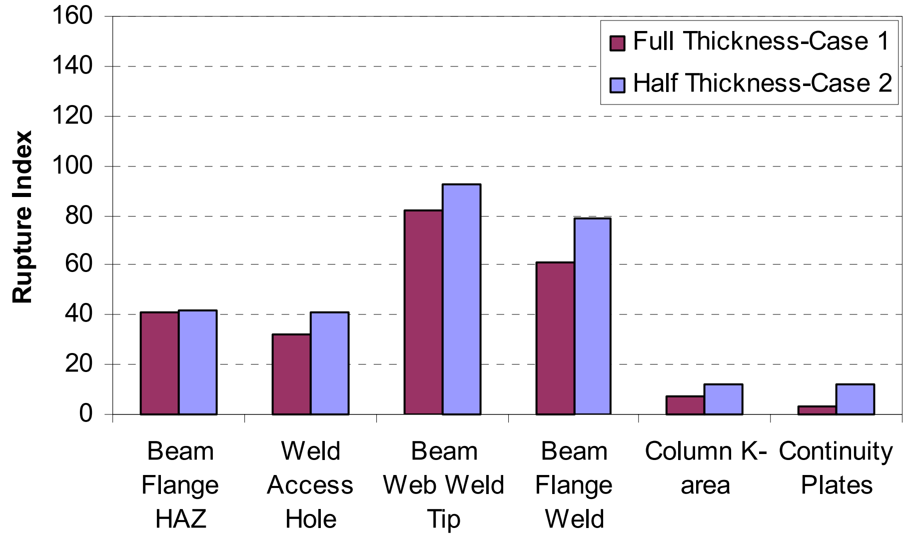

(a) 4% Story Drift

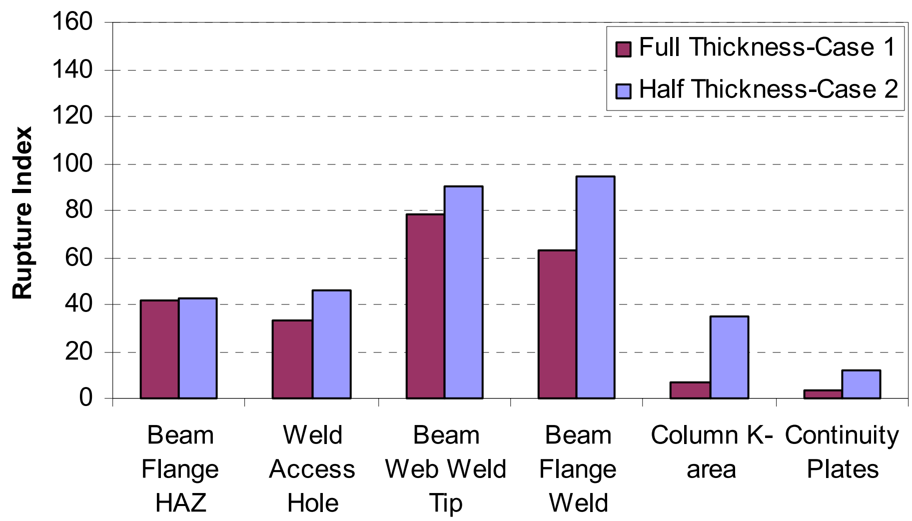

(b) 6% Story Drift

Figure 3.29 – Comparison of Rupture Index of continuity plate thickness effect on RBS connection to a deep column (Refer to Table 3.5 for case details)

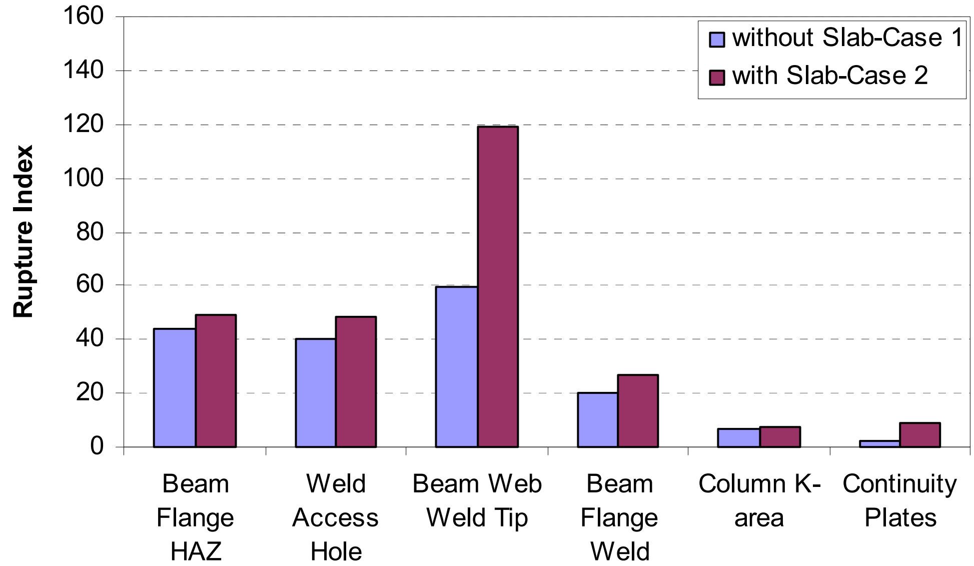

(a) 4% Story drift

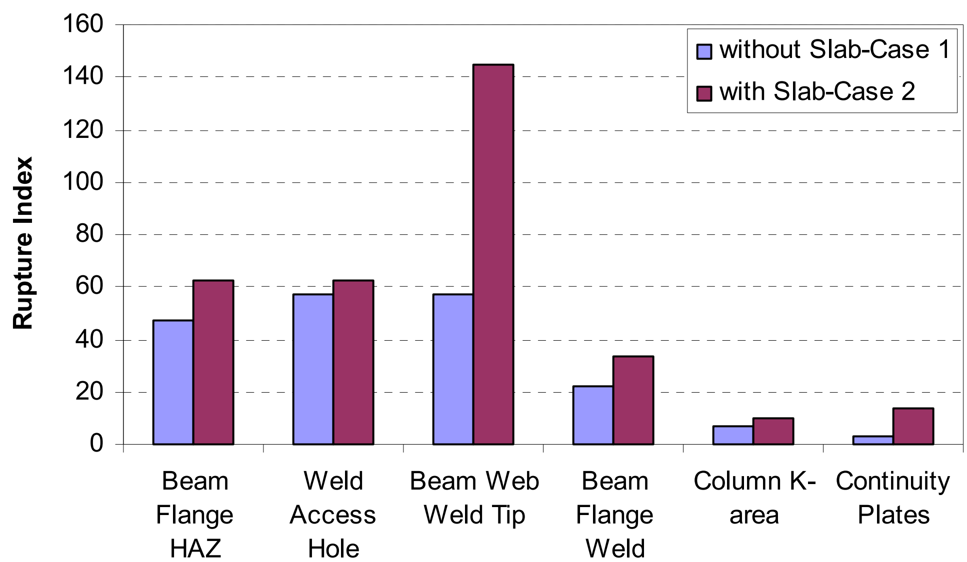

(b) 6% Story drift

Figure 3.30 – Comparison of Rupture Index for cases without and with composite floor slab (W14x398 column; W36x150 beams; refer to Table 3.6 for case details)

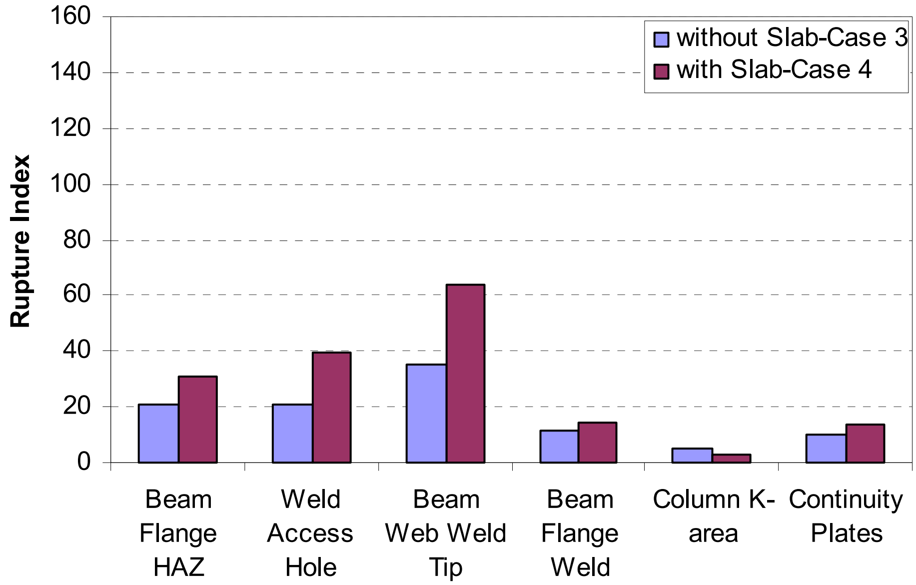

(a) 4% Story drift

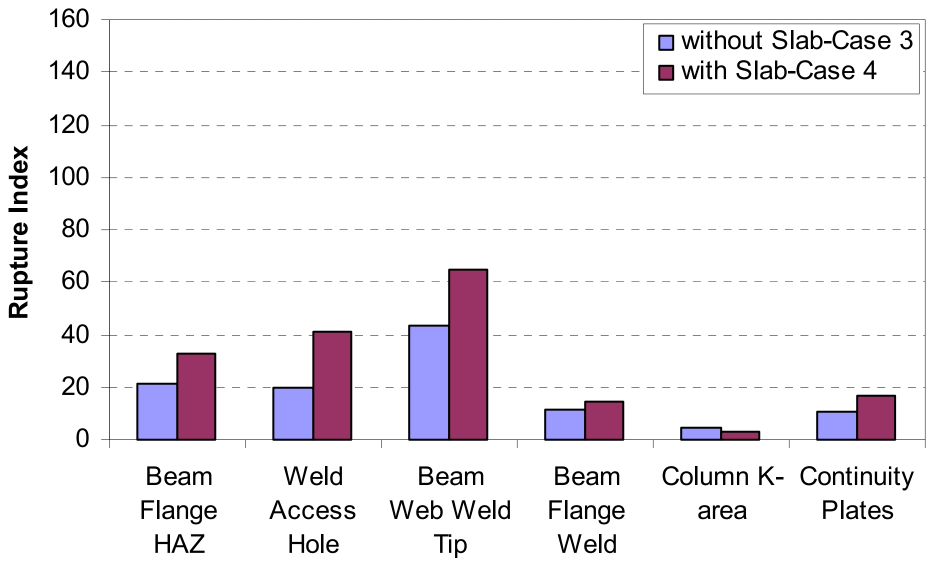

(b) 6% Story drift

Figure 3.31 – Comparison of Rupture Index for cases without and with composite floor slab (W36x230 column; W36x150 beams; refer to Table 3.6 for case details)

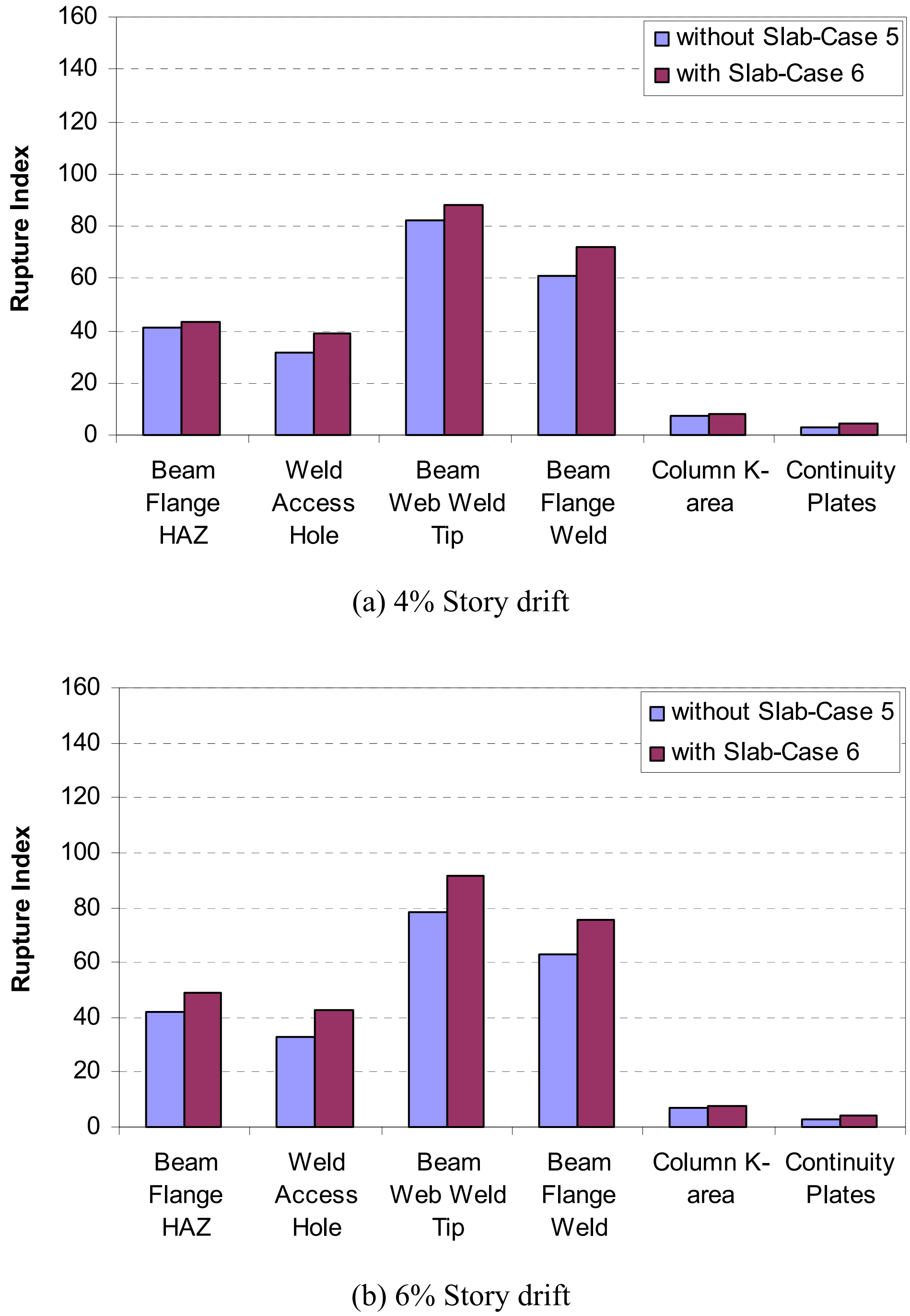

Figure 3.32 – Comparison of Rupture Index for cases without and with composite floor slab (W27x194 column; W36x150 beams; refer to Table 3.6 for case details)

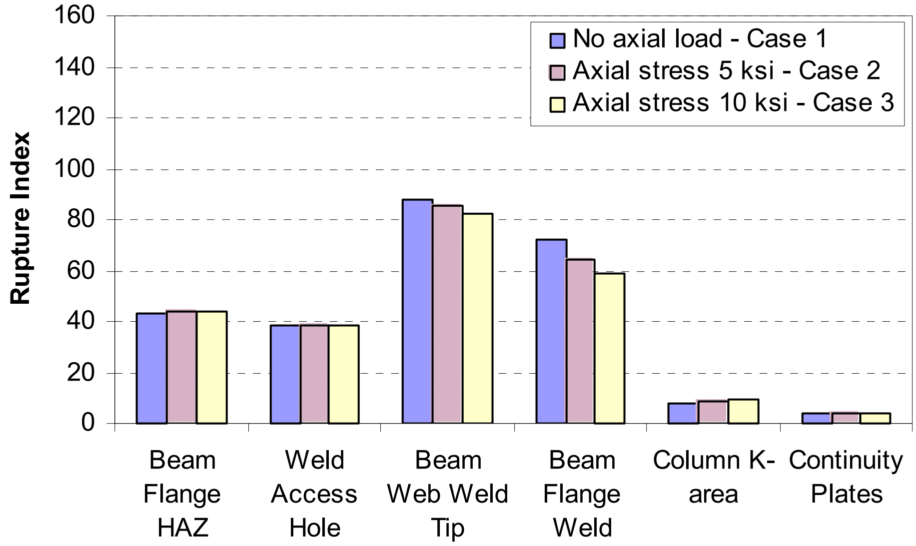

(a) 4% story drift

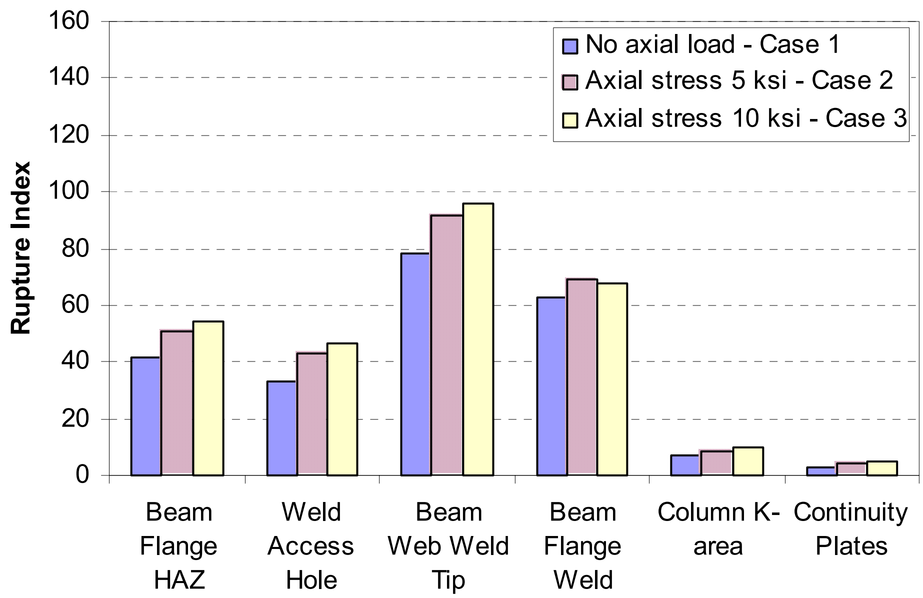

(b) 6% story drift

Figure 3.33 – Comparison of Rupture Index for cases with different values of axial load (W27x194 column, W36x150 beams; refer to Table 3.7 for case details)

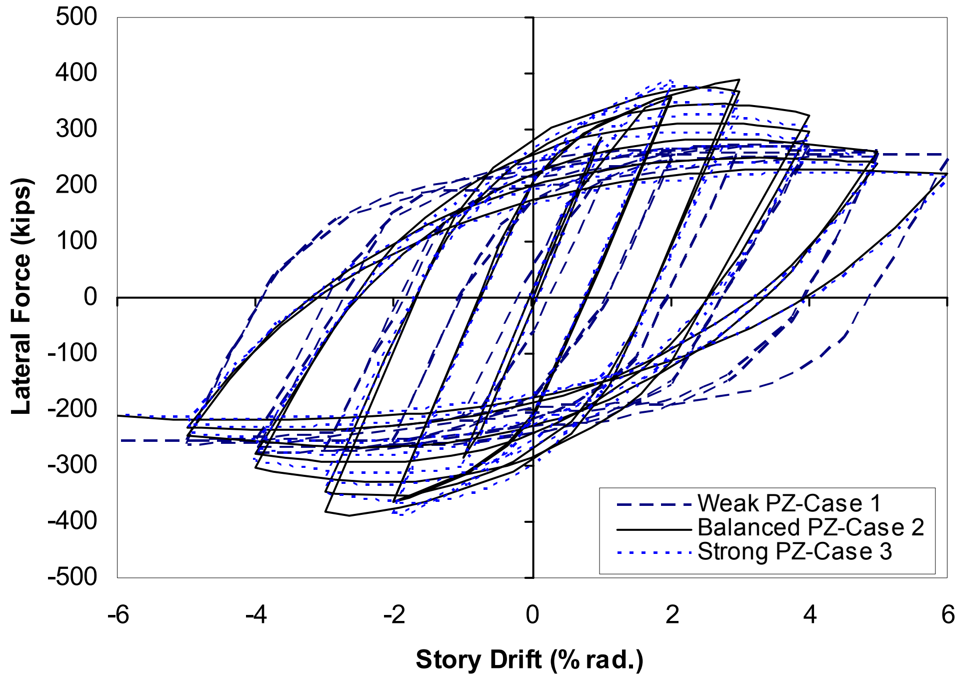

Figure 3.34 – Hysteretic response for connections with different panel zone strength (Refer to Table 3.8 for case details)

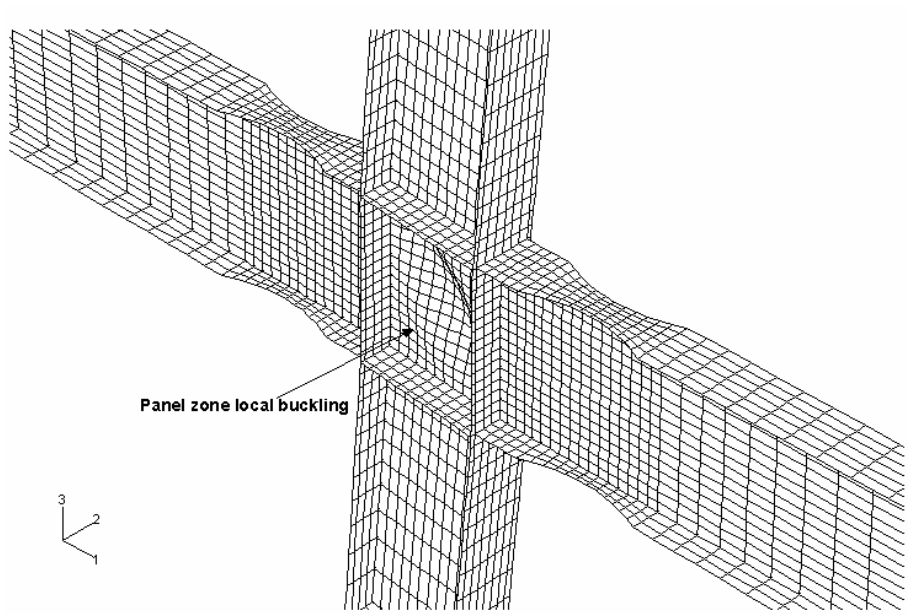

Figure 3.35 – Deformed shape and panel zone local buckling of connection with weak panel zone, at 4% story drift

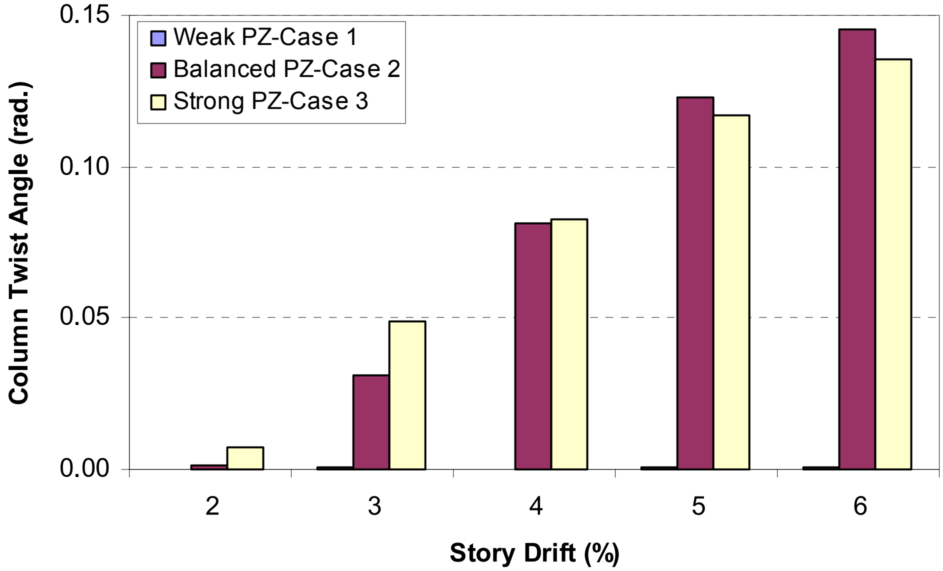

Figure 3.36 – Column twist angle for connections with different panel zone strength (Cases refer to Table 3.8)

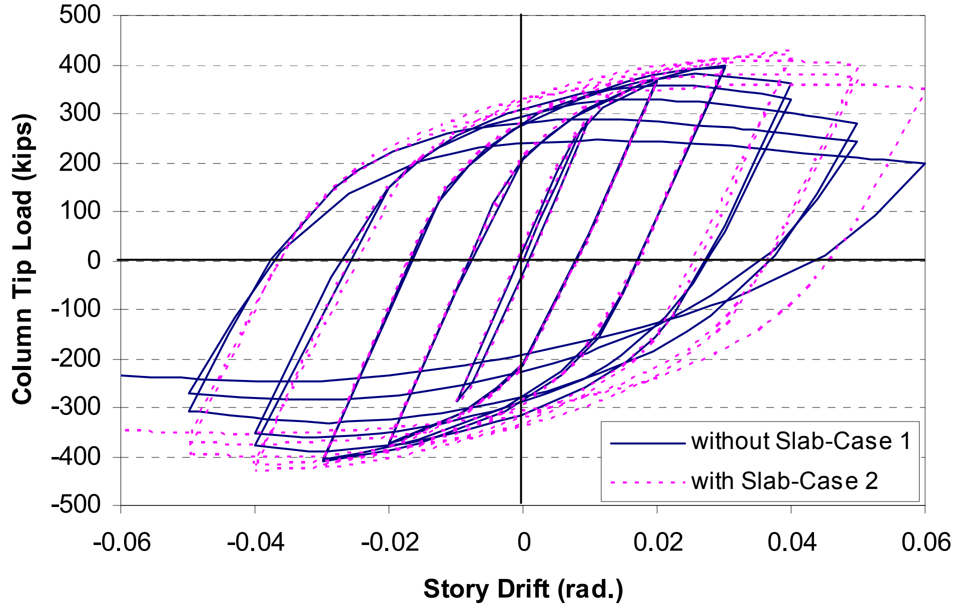

(a) W14x398 column; W36x150 beams

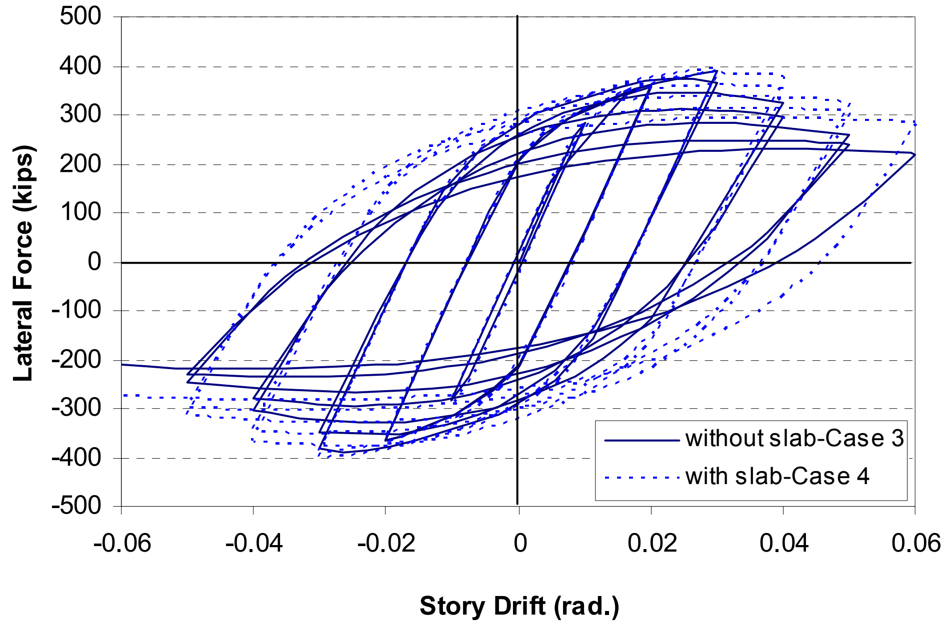

(b) W27x194 column; W36x150 beams

Figure 3.37 – Hysteretic response for RBS connection without and with a floor slab (Refer to Table 3.9 for case details)

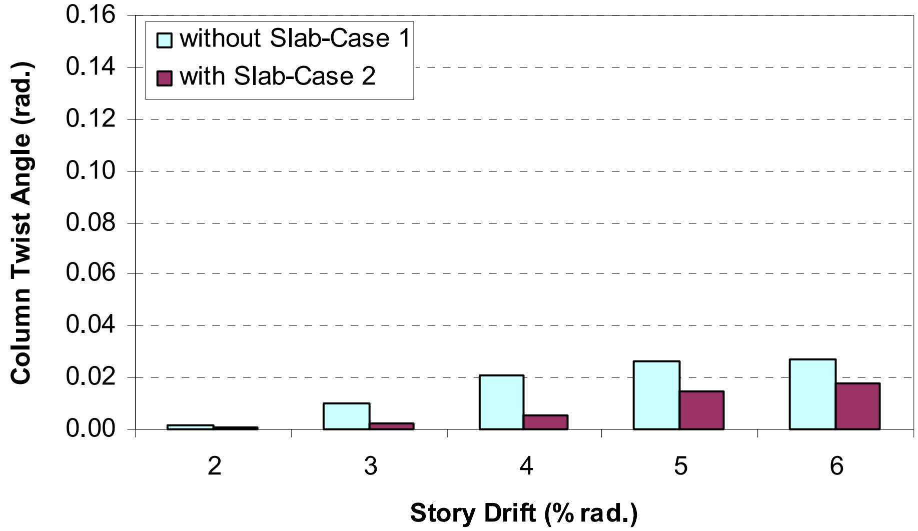

(a) W14x398 column; W36x150 beams

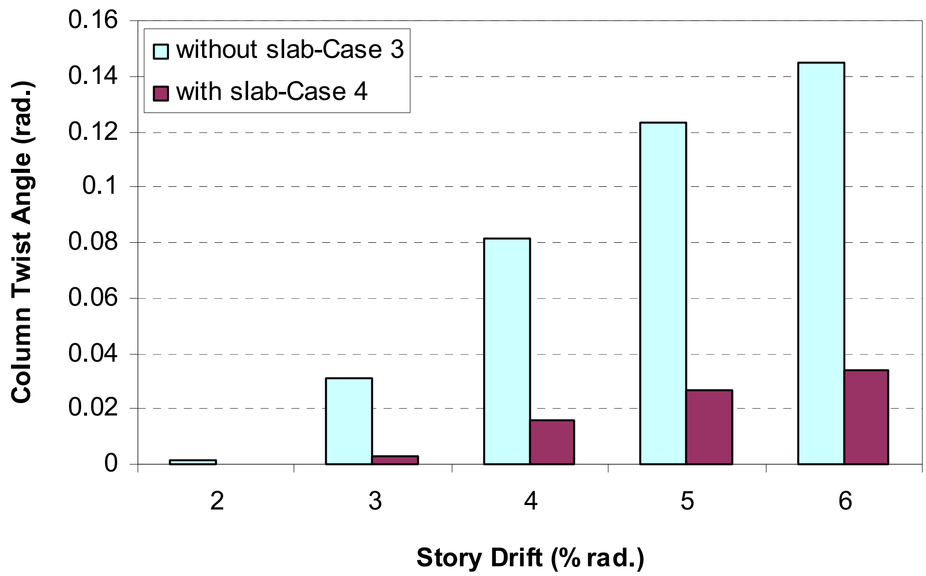

(b) W27x194 column; W36x150 beams

Figure 3.38 – Column twist angle for RBS connection without and with a floor slab (Refer to Table 3.9 for case details)

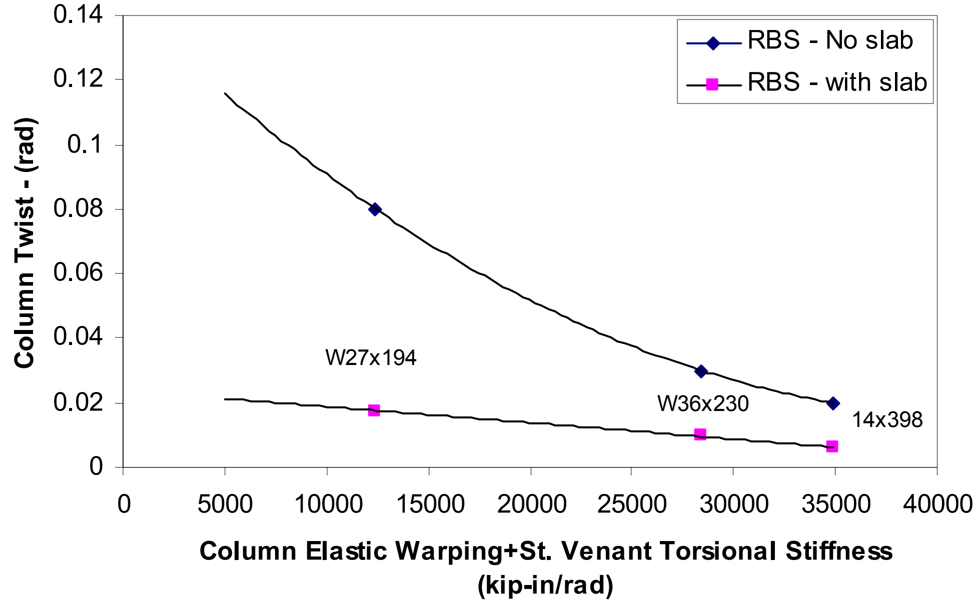

Figure 3.39 – Column twist vs. elastic torsional stiffness

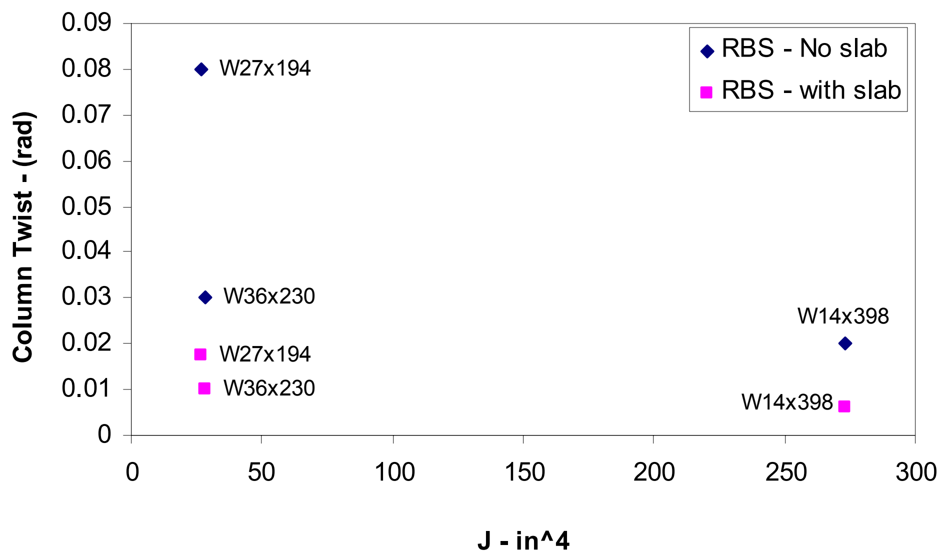

Figure 3.40 – Column twist in RBS connections to W36x150 beams plotted against the torsional constant J

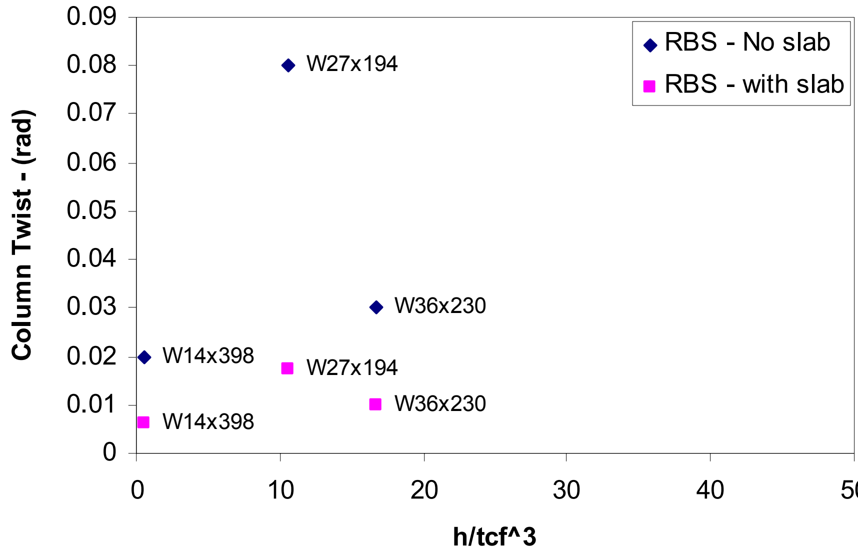

Figure 3.41 – Column twist in RBS connections to W36x150 beams plotted against the ratio h/t_{cf}^{3}

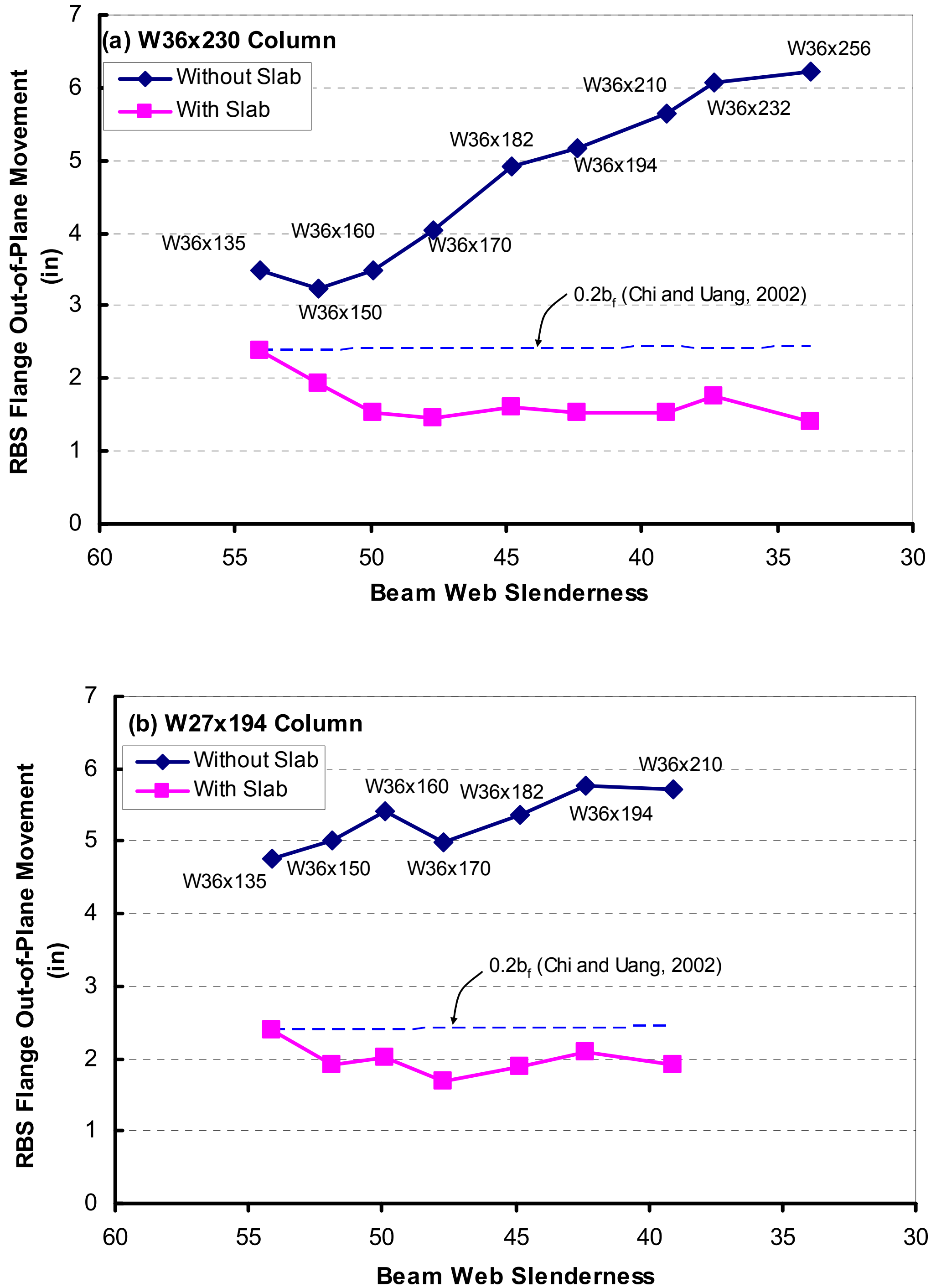

Figure 3.42 – Beam RBS bottom flange out-of-plane movement vs. beam web slenderness at 4% story drift

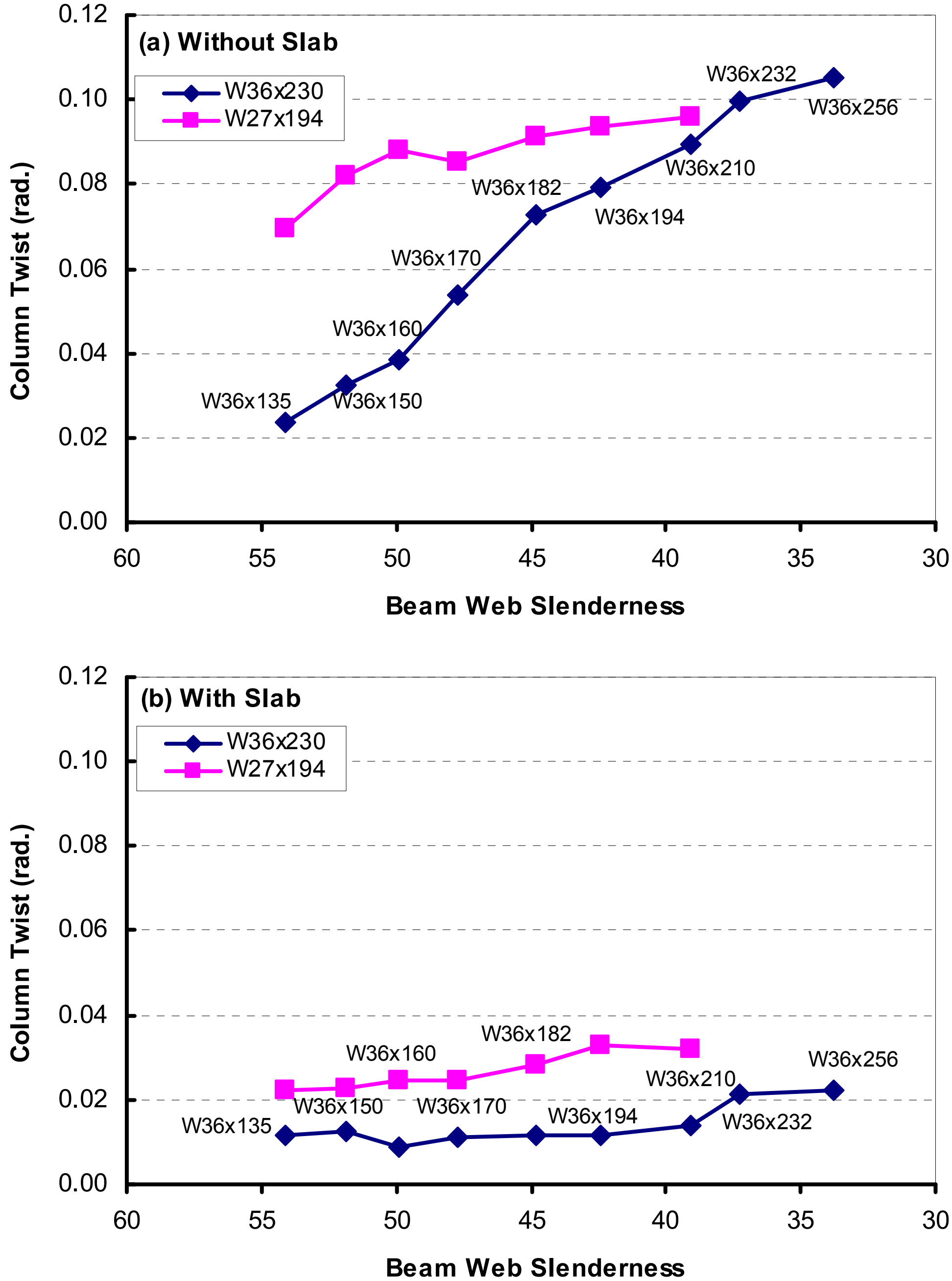

Figure 3.43 – Column twist vs. beam web slenderness at 4% story drift

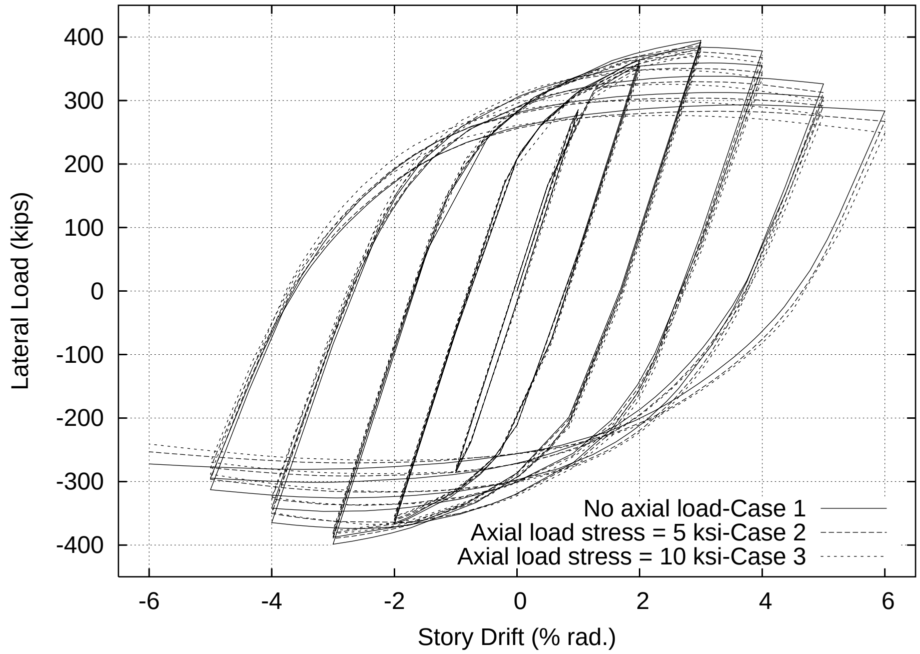

Figure 3.44 – Comparison of cyclic behavior for cases with different values of axial load (W27x194 column, W36x150 beams; refer to Table 3.11 for case details)

(This page is blank.)

CHAPTER 4 EXPERIMENTAL STUDY

The experimental program involved the testing of six full-scale RBS welded beam-to-deep column moment connection specimens. This chapter presents the details of the test matrix, connection detailing, specimen fabrication, test setup, instrumentation, and test procedure. The parameters investigated in the experimental program included: (1) column depth; (2) column weight; (3) beam size; (4) supplemental bracing; and (5) a composite floor slab.

4.1 Specimen Test Matrix

The specimen test matrix is given in Table 4.1. All specimens represented an interior RBS connection in a perimeter SMF. Each specimen had a composite floor slab except SPEC-6, the details of which are given later in this chapter. Each of the specimens was designed in accordance with the weak beam-strong column criteria in the AISC Seismic Provisions (AISC 2002). The values for the ratio of $\Sigma M^*_{pc}/\Sigma M^*_{pb}$ are given in Table 4.1, where ΣM^*_{pc} and ΣM^*_{pb} are defined in Section 9.6 of the AISC Seismic Provisions (AISC, 2002).

The columns for all specimens were fabricated from A992 steel. The column for SPEC-1 was a W36x230 section, while the columns for SPEC-2 and SPEC-3 were both a W27x194 section (from different heats). The column for SPEC-4 was a W36x150 section. The column for SPEC-5 was a W27x146 section and the column for SPEC-6 a W24x131 section. The member section sizes for each specimen are included in Table 4.1. The beams for first-four specimens were fabricated from a W36x150 section. The beams for SPEC-1 and SPEC-2 were from the same heat of A572 Gr. 50 steel, while the beams for SPEC-3 and SPEC-4 were from the same heat of A992 steel. The beams for SPEC-5 and SPEC-6 were fabricated from the same heat of A992 steel of a W30x108 section. The average measured section dimensions of the specimens are given in Tables 4.2.

In addition to the section dimensions, the out-of-flatness of the beam web in the RBS was measured. In this region of the web local buckling is expected to occur. The measured maximum out-of-flatness was 0.13 inches, equivalent to 20% of the beam web thickness.

The section sizes for each specimen were selected on the basis of inducing different degrees of torsional effects (as predicted by Chi and Uang's procedure (Chi and Uang 2002)), while also satisfying weak beam-strong column criteria. The predicted total column maximum normal flange stress f_{total} for each of the test specimens at 4% inter-story drift is plotted in Figure 4.1, where they are compared to the predicted total maximum normal flange stresses developed in the column of an RBS connection for a range of column sections. The components of normal warping stress f_{ws} and flexural stress f_{bx} for the test specimens are summarized in Table 4.3. The total column elastic normal stress f_{total} in Figure 4.1, is based on Equation (2-21), where the column elastic normal warping stress f_{ws} is determined using the procedure of Chi and Uang (2002), i.e., Equation (2-19), to evaluate the torque applied by the RBS of the beam to the column. It is evident in Figure 4.1 and Table 4.3 that SPEC-2, SPEC-4 and SPEC-5 have a total elastic stress in the column that exceeds the nominal yield stress of 50 ksi, which violates the recommendation by Chi and Uang, who suggest that the column be designed to remain elastic with f_{total} not to exceed ϕF_y, where $\phi = 0.90$. SPEC-3 has the lowest normal column stress (37.9 ksi) and SPEC-4 the highest normal column stress (88.3 ksi). SPEC-2 has a column normal stress of 64.3 ksi, while the supplemental brace in SPEC-3 at the end of the RBS reduces the column normal stress to 37.9 ksi (it is assumed that the RBS is adequately braced from lateral movement by the supplemental brace in SPEC-3 that the RBS does not induce torsion to the column. The same assumption is also applied to SPEC-6).

The connection and slab details for each specimen are shown in Figures 4.2 through 4.12. The RBS connection was designed in accordance with the recommendations by Engelhardt (1999) and FEMA 350 (FEMA 2000a), as discussed in Chapter 2. The RBS cut for the W36x150 beams was a circular radius cut of 27 inches in length, with 50% of the beam flange removed at the center section of the RBS. The RBS cut for the W30x108 beams was a circular radius cut of 22.5 inches in length, with 48% of the beam flange removed at the center of the RBS. The RBS was flame cut, with the burned surface ground to a surface roughness of 500 micro-inches in the longitudinal direction of the RBS, as recommended by FEMA 353 (FEMA 2000b). The edges of the flange within the RBS were also ground to remove sharp edges. The connection detail for each specimen included CJP groove welds between the beam flanges and the column, a beam web access hole geometry based on the modified weld access hole geometry shown in Figure 4.13 (Mao et al., 2001), and the beam web attachment consisting of a CJP groove weld between the beam web and the column flange with supplemental fillet welds around a shear tab. The shear tab was 5/8 inch thick, and was shop welded to the column. The shear tab served as an erection plate as well as a backing bar during erection. The beam web weld access hole was burned, and then ground to a surface roughness of 500 micro-inches, as required by FEMA 353 (FEMA 2000b) and the AISC Seismic Provisions (2002).

All specimens had A572 Grade 50 doubler plates whose design was based on the AISC Seismic Provisions (AISC 2002). The doubler plate was on only one side of the column web, and extended 3 inches above and below the beam. The values for the ratio of R_v/V_{pz} are given in Table 4.1, including both the nominal values for design and the values based on the measured dimensions and material properties. The top and bottom edges of the plate were fillet welded to the column web, where the fillet weld size was one-quarter inch, and the left and right vertical edges were groove welded to the column flanges (e.g., see Figure 4.2). All specimens had A572 Grade 50 full beam flange thickness continuity plates (one-inch thick for SPEC-1 to SPEC-4; three quarters of an inch thick for SPEC-5 and SPEC-6). The continuity plates were welded to the column flange using CJP groove welds and fillet welded to the column web. The fillet weld size was two-5/16 inches. The sizes of the doubler plate and continuity plates are noted in Table 4.1.

The beam-to-column CJP groove welds and supplemental fillet welds of each specimen were field welded in their normal upright position (to resemble prototype conditions). The welding details and procedure are discussed below in Section 4.2. A photograph of the connection region of SPEC-1 prior to testing is shown in Figure 4.14.

The composite concrete floor slab had a total thickness of 5.25 inches, and consisted of concrete cast on metal deck. The intended slab thickness was 5.5 inches, however, the availability of pour stops of 5.25 inch height necessitated the use of a 5.25 inch thick slab. The width of the floor slab was 4 ft on one side with a 12-inch overhang on the other side to simulate a perimeter SMF. The ribs of the decking ran parallel to the main beam of the test specimen. The metal decking was zinc coated and had a thickness of 20-gage. A 12-gage zinc coated pour stop was used for the side of the overhang and 16-gage zinc coated pour stops were used for the three remaining sides. To generate composite action, three-quarter inch diameter shear studs were placed at 12 inches on center to attach the deck to the main beams and W14x22 transverse floor beams placed perpendicular to the main beams, except for in the RBS region where no shear studs were located (see Figure 4.3). The floor slab had W4x4 welded wire mesh with the wire 6 inches on center in both directions. The 12-inch overhang of the floor slab had No. 3 and No. 4 Grade 60 reinforcement bars with the deck spot welded to the beam flange, see Figure 4.15. Photographs of the slab prior to placing the concrete are shown in Figure 4.16. The transverse No. 3 reinforcement bars were placed adjacent to the column flange for all specimens, as shown in Figure 4.16(b).

To investigate the effect of a safety harness eyebolt hole in the beam top flange near the RBS, a 1” diameter hole was drilled in the top flange of the east side beam of SPEC-6. The hole was centered 1⅜” from the south edge of the beam flange and 4” from the end of the RBS.

4.2 Weld Procedure Specification

The Weld Procedure Specification (WPS) for the test specimens are given in Appendix B. The WPS used in the fabrication are prequalified in accordance with AWS D1.1/D1.1M:2002 (AWS 2002). All welds conformed to the AWS 5.20-95 Specification (AWS 1995) and Section 4.2 of AWS D1.1/D1.1M:2002 (AWS 2002), and were performed using the flux core arc welding procedure. Three different types of electrodes, all of which were manufactured by Lincoln Electric, were utilized in the fabrication of the test specimens: E70T-1 (Lincoln Outershield® XLH-70) for the shop welds; E70T-6 (Lincoln Innershield® NR-305) for the beam flange-to-column flange CJP groove welds; and E71T-8 (Lincoln Innershield® NR-232) for the beam web-to-column flange CJP groove welds and beam web-to-shear tab supplemental fillet welds. The E70T-1 electrode is a gas shielded electrode, while the E70T-6 and E71T-8 electrodes are self shielded electrodes. The E70T-6 and E70T-1 electrodes each had a wire diameter of 3/32-inches, and the E71T-8 electrode a diameter of 0.068-inches.

The run-off tabs on the beam flanges were removed following placement of the CJP groove welds, and the weld at the edges of the beam flange were ground to a smooth transition (see Figure 4.17(a)). The backing bar of the beam top flange weld was left in place and a reinforcement fillet weld was provided between the bottom surface of the backing bar and the column flange using an E71T-8 electrode, see Figure 4.17(b). The beam bottom flange backing bar was removed using the air-arc process, back gouged, and reinforced with a fillet weld using an E71T-8 electrode. No run-off weld tabs were used for the vertical beam web CJP groove welds. Figure 4.17(c) shows a photograph of the end of the vertical beam web CJP groove weld, where the shear tab is shown extended beyond the beam web and served as a run-off tab. The ends of this weld were not ground.

The CJP groove welds for the beam flanges and web were inspected using the ultrasonic test procedure. Welds were considered to pass inspection if they satisfied the AWS D1.1 static loading criteria (AWS 2002). The UT inspection reports are given in Appendix C. All CJP groove welds passed inspection except for the beam web-to-column flange vertical CJP groove welds for SPEC-4. Each beam web vertical CJP weld of SPEC-4 was found to contain one defect that was not acceptable by AWS D1.1 UT Acceptance-Rejection Criteria (AWS 2002). The defects were in the vertical direction and parallel to the welds, and located near the neutral axis (mid-depth) of the beam. The demand on the weld at this location is low. The welds were therefore considered not to be located in a critical region, and then not repaired. These defects were subsequently found not to affect the performance of SPEC-4 during testing, which is reported in Chapter 5.

4.3 Specimen Material Properties

The mechanical properties of the steel sections and plates are given in Table 4.4. These properties were obtained from testing standard 8 inch gage length rectangular tensile coupons in accordance with ASTM standards E8-00 (ASTM 2000) and A370-97a

(ASTM 2002). The testing procedure was modified in accordance with Technical Memorandum No. 8 of the Guide to Stability Design Criteria for Metal Structures (Galambos, 1998) in order to measure the static yield stress. The static yield stress is a reliable and consistent measure of the value at which steel yields and is independent of testing procedures and testing machine behavior. It is typically less than the yield stress reported in mill reports, which are not static yield stress values.

The material test results in Table 4.4 indicate that most of the steel had a typical yield stress for Gr. 50 steel that slightly exceeded the nominal value of 50 ksi. Most of the flanges and web of the sections had a yield stress between 50 ksi to 55 ksi and 55 ksi to 60 ksi, respectively. SPEC-1 and SPEC-2 had a beam flange with the lowest value of static yield stress of 49.7 ksi. The measured static yield stress of the A572 Gr. 50 steel plate material ranged from 46.7 ksi (0.5 inch thick doubler plate for SPEC-6) to 64.7 ksi (0.375 inch thick doubler plate for SPEC-4).

The beam section flexural strength M_p is summarized in Table 4.5, and was calculated based on the measured section dimensions (Table 4.2) and the measured yield stress obtained from material tests (Table 4.4). Also included in Table 4.5 is the summary of the beam RBS flexural strength $M_{p,RBS}$, which was calculated based on the measured RBS section dimensions and the measured yield stress obtained from material tests (Table 4.4). Included in Table 4.5 are the nominal flexural capacity for the beam section, M_{pn}, and the RBS, $M_{pn,RBS}$.

The concrete strength for the floor slab versus the slab age of each specimen is shown in Figure 4.18. A normal weight concrete with a nominal compressive strength of 4 ksi was originally planned to construct the floor slab of each specimen. However, to expedite the test schedule in order that the specimens could be tested at 14 to 22 days (instead of 28 days) after placing of the concrete, a 28-day concrete compressive strength of 5 ksi was specified. The concrete compressive strength at the day of testing is given in Table 4.6 for each specimen, and ranged from 4.6 ksi to 5.6 ksi.

The strength and toughness of all the various type of weld metal were investigated before specimen fabrication. AWS A5.20-95 (AWS 1995) standard test plate and connection mock-ups were made. Standard 0.500-in. round tension test specimens were fabricated from the weld metal of the AWS standard test plate and tested in accordance with ASTM standards E8-00 (ASTM 2000). The mechanical properties from these coupon tests are reported in Table 4.7, where they are also compared to typical values. The stress-strain curves from the coupon tests are given in Appendix D.

The CVN specimens were taken from both AWS standard test plates and connection mock-ups, and manufactured in accordance with AWS A5.20-95 (AWS 1995). The CVN toughness test results are given in Figure 4.19, where they are shown to satisfy the requirements of both FEMA 350 (FEMA 2000a) and the AISC Seismic Provisions (AISC 2002). As noted in Chapter 2 (see Section 2.2.5) FEMA-350 requires the weld metal toughness to be at least 20 ft-lb at 0°F and 40 ft-lb at 70°F. The AISC Seismic Provisions require the weld metal toughness to be at least 20 ft-lb at -20°F and 40 ft-lb at 70°F. The results of numerous CVN toughness test for weld metal produced with different welding machine settings are given in Appendix E. It was found that care must be taken when adjusting the machine settings for applying E70T-6 electrode.

4.4 Test Setup, Instrumentation and Test Procedure

The specimens were tested in the setup shown in Figure 4.20. Each specimen represented a connection sub-assembly from a perimeter SMF where the ends of the members in the test setup were pin connected by using cylindrical bearing to simulate points of inflection in the prototype frame. The ends of each beam were supported by rigid links. The rigid links had pin connections at both ends that enabled horizontal movement of the end of each beam. In order to prevent out-of-plane movement of the beams and twisting near the ends of the column, lateral bracing was provided as shown in Figures 4.20 and 4.21. The beam bracing consisted of bracing at 10 ft (9 ft for SPEC-5 and SPEC-6, which had W30x108 beams) on center from the column, where the lateral brace detail is shown in Figure 4.22(a). The 10 ft (9 ft) distance satisfied the required spacing specified by the AISC Seismic Provisions (AISC 2002). The mid-height of the column was braced by a composite transverse framing beam using the detail shown in Figure 4.22(b). At the top and base of the column, the column was braced by a pair of W18x55 sections and the column base plate bolted to the clevis, respectively. The column base bracing detail was analyzed in Chapter 3 using finite element models to evaluate whether its rigidity would influence specimen behavior (see Section 3.2.4). As noted in Chapter 3, it was determined not to influence specimen behavior. Near the rigid links the beams were laterally braced in order to stabilize the rigid links from out-of-plane movement. Photographs of the beam and column bracing are shown in Figures 4.23.

SPEC-6 had no floor slab, with supplemental bracing placed at the end of the RBS. The test setup was modified to accommodate the lateral bracing, as shown in Figure 4.24. The modifications consisted of adding two additional "bracing columns" (labeled as Columns A and B in Figure 4.24(a)), in addition to a W36x150 beam that was placed parallel to the test specimen main beams (see Figures 4.24(a) and (b)). The far end of each transverse W14x22 bracing beam was connected to the W36x150 parallel beam using the detail shown in Figure 4.24(b). This parallel beam restrained the specimen's main beam lateral bracing from out-of-plane movement, which allowing the specimen to develop drift (horizontal movement). The parallel W36x150 beam sat on specially made brackets which were mounted on the bracing columns, and Teflon was glued on all contacting surfaces to reduce the friction so that the beam could freely slide horizontally with the specimen during testing. Photographs of the bracing are shown in Figure 4.25.

SPEC-3 had supplemental bracing at the end of RBS and a composite floor slab. The far end of each transverse W14x22 bracing beam was not attached to any part of the test setup. The W14x22 transverse bracing beams were connected to the composite floor slab by the shear studs. And the modification of the test setup for SPEC-6 was therefore not applied to SPEC-3.

Two parallel horizontal actuators were placed at the top of the column to impose story drift to the specimen. They were synchronized by the hydraulic control system. The story drift history followed the loading sequence given in Appendix S of the AISC Seismic Design Provisions (AISC 2002), which is the same as the SAC Protocol (SAC 1997). The story drift history is shown in Figure 4.26. A test was terminated when either fracture occurred, resulting in a significant loss of capacity, or after reaching a story drift of 6%.

The actuators and rigid links were both instrumented with calibrated load cells to enable the total applied load and reaction at the end of each beam to be measured. The measurement of these forces enabled the beam and column moments, as well as panel zone shear, to be determined.

Each specimen was carefully instrumented to also measure rotation, displacements, strain, and out-of-plane movement of the column and beam at the RBS. The general instrumentation layout for the strain gauges is shown in Figure 4.27 to Figure 4.29 for the test specimens. High elongation strain gauges were mounted to measure the strain in the beam flanges and web at the center section of the RBS, where the strain was expected to be large due to local buckling. Strain gauges were also mounted on the beam top and bottom flanges at a distance of 3 inches from the column face, and on the bottom flange at both ends of the RBS. Strain gauges were mounted on both sides of the continuity plates of the beam top and bottom flanges. Rosette stain gauges were mounted on both sides of the center of the column panel zone (see Figures 4.27(b), 4.28(b) and 4.29(b)). For SPEC-1 and SPEC-2 rosette strain gauges were also mounted on one side of the panel zone (on the doubler plate) near the column flange and the top continuity plate (see Figure 4.27(b)). Strain gauges were also mounted on the outside faces of the column flanges under the beam bottom flanges (see Figure 4.27(c)). For SPEC-3 and SPEC-4, as well as SPEC-5 and SPEC-6, additional strain gauges were placed on the column flanges above the beam top flanges (see Figures 4.28(c) and 4.29(c)).

The general instrumentation lay out for voltage devices (i.e., load cells, inclinometers, plastic slides, string potentiometers, and linear variable displacement transducers) are shown in Figure 4.30. As noted above, load cells (LC-1 and LC-2, see Figure 4.30(a)) were used to measure the applied load at the top of the column and the beam reaction forces (LC-3 and LC-4) developed in both rigid links. A string potentiometer (SP-1) was used to measure the lateral displacement at the top of the column. The panel zone deformation was measured by four rotation inclinometers (RT-1, RT-2, RT-3, and RT-4) placed at the top, bottom, left and right sides of the panel zone. A pair of diagonal linear variable displacement transducers (LVDTs) (LVDT-1 and LVDT-2) was also used to measure the panel zone deformation. Two string potentiometers (SP-2 and SP-3) were used to measure the horizontal movement (i.e., in the plain of Figure 4.30(a)) of the top and bottom of the panel zone. Two inclinometers (RT-5 and RT-6) were placed on the beam web at both ends of the RBS to measure the beam rotation over the length of the RBS. Any slippage in the beam reaction rigid links and slippage of the column base plate were measured by LVDTs mounted alongside the rigid links (LVDT-5 through LVDT-8) and in between the specimen column base plate and the clevis base plate (LVDT-9), respectively. These measurements were used to remove any rigid body motion from the measured story drift.

For SPEC-6, a built-up load cell was installed in the floor beam (W14x22 section) at the end of RBS of the east side beam in order to measure the axial force in the supplemental lateral bracing beam at the RBS. The built-up load cell was a Wheatstone bridge, which consisted of four pairs of bi-axial strain gauges placed symmetrically on the outside surfaces of both flanges of the W14x22 section (see Figure 4.31). The strain gauges were arranged in such a way that the bending effects by both the strong axis and by the weak axis were eliminated and only the axial force was measured. The built-up load cell was calibrated in a SATEC 600 kip test machine up to 50 kips before the test. Figure 4.32 gives the calibration curve. A photograph of the instrumented supplemental brace is given in Figure 4.25(a).

Prior to testing a specimen, the column, panel zone, and beams in the connection regions were white washed in order to provide visual evidence of any yielding during testing.

4.5 Measurements and Data Adjustments

The measured displacements and rotation enabled separate determinations of the panel zone deformation (γ), beam and column rotation (θ_{bm} and θ_{col}) and the story total drift θ_{total} using the following expressions:

$$\gamma = \frac{\Delta^+ - \Delta^-}{2}\frac{\sqrt{d_{pz}^2 + b_{pz}^2}}{d_{pz}b_{pz}} \tag{4.1}$$

$$\theta_{pz} = \gamma(1 - \frac{d_{bm}}{h} - \frac{d_{col}}{L}) \tag{4.2}$$

$$\theta_{col} = \theta_{total} - \frac{(\Delta_1 - \Delta_2)}{h} - \frac{\theta_1 + \theta_2}{2}(1 - \frac{d_{bm}}{h}) \tag{4.3}$$

$$\theta_{bm} = \theta_{total} - \theta_{pz} - \theta_{col} \tag{4.4}$$

$$\theta_{total} = \Delta_{total} / h \tag{4.5}$$

where Δ^+, Δ^- are the displacements measured from the two LVDTs (LVDT-1 and LVDT-2) located at the column panel zone, and d_{pz}, b_{pz} are the vertical and horizontal projection distances of the diagonal LVDTs in the panel zone (see Figure 4.30(d)), respectively. h is the distance between the column bottom pin center to the column top loading point, and L is the distance between two beam supports. d_{bm} and d_{col} are the depth of beam and column, respectively. Δ_{total}, Δ_1 and Δ_2 are the horizontal displacement at the top of the column (SP-1), beam top flange (SP-2), and beam bottom flange (SP-3), respectively. θ_1 and θ_2 are the rotations at the top and bottom of the panel zone (RT-1 and RT-2). The total plastic drift ($\theta_{p,total}$), plastic beam drift ($\theta_{p,bm}$), column drift ($\theta_{p,col}$) and panel zone drift ($\theta_{p,pz}$,) were obtained by subtracting the elastic components from Equations (4.5) (4.4), (4.3) and (4.2).

As an alternative to Equation (4.1), the panel zone deformation can be determined using:

$$\gamma = \frac{\theta_{RT-3} + \theta_{RT-4}}{2} - \frac{\theta_{RT-1} + \theta_{RT-2}}{2} \tag{4.6}$$

where θ_{RT-1}, θ_{RT-2}, θ_{RT-3}, and θ_{RT-4} are the rotations at the top, bottom, right and left edges of the panel zone, respectively. In this report the panel zone deformation are based on Equation (4.1).

The rotation over the length of the RBS, θ_{RBS}, was determined by the following relationship:

$$\theta_{RBS} = \theta_{RT-6} - \theta_{RT-5} \tag{4.7}$$

where θ_{RT-5} and θ_{RT-6} are the rotation at the ends of the RBS (see Figure 4.30(a)).

As noted above, rigid body motions were removed by subtracting out the rigid body rotation of the specimen caused by any slippage in the beam reaction rigid links. The measured slip at the column base was found to be small and negligible. The rigid body rotation was removed from the horizontal displacement at the top of the column by the following equation:

$$\Delta_{total} = \Delta - \frac{h}{L}(\delta_w - \delta_e) \tag{4.8}$$

In Equation (4.8) Δ and Δ_{total} are the uncorrected lateral displacement and corrected lateral displacement, respectively, at the top of the column. δ_e and δ_w are the vertical motion (i.e., slippage in the beam reaction rigid links) at the east and west beam support, respectively. Both δ_e and δ_w are positive for upward motion, and Δ_{total} and Δ are positive when the column moves towards the east (to the right in Figure 4.30(a)). These movements were measured by LVDT-5 and LVDT-6 for the east beam support, and LVDT-7 and LVDT-8 for the west beam support (see Figure 4.30(a)).

In the test setup there is a distance *e* between the pin at the end of the actuators and the column centerline (see Figure 4.33), which is caused by the assembly of components that connects the actuators to the column of the test specimen. As the column depth increases, this distance becomes larger. When the specimen undergoes lateral displacement (i.e., drift), the lateral actuators become inclined and a vertical component of force is produced (see Figure 4.33). This vertical component of the actuator force has a significant effect on the results. Therefore, the lateral force was corrected by the equilibrium of the test specimen using the following equation:

$$H = \frac{L}{h}(R_w - R_e) \tag{4.9}$$

where R_e and R_w are the measured beam reaction forces from the east and west side beam reaction rigid links, respectively. R_e and R_w are positive when the link force is tension, and H is positive when the actuator force is pointing to the east (to the right in Figure 4.30(a)).

To calculate the beam moment at the column face, the inclination of the beam reaction rigid links needs to be considered (see Figure 4.34). This was done by decomposing each force measured in the beam reaction rigid links into horizontal and vertical components. The following equations were used to compute the beam moment at the column face:

$$M_e = R_e\left(\frac{(L-d_{col})}{2}\cos\theta + e_2\sin\theta\right) \tag{4.10}$$

$$M_w = R_w\left(\frac{(L-d_{col})}{2}\cos\theta - e_2\sin\theta\right) \tag{4.11}$$

where R_e, R_w, L and d_{col} are defined above. θ is the inclination angle of the beam reaction rigid link, and e_2 is the distance between the center of the beam reaction rigid link top pin and the centerline of the beam (see Figure 4.34).

Table 4.1 – Test specimen matrix

SPEC	Conn. type	Column size	Beam size	Doubler plate (in)	Continuity plate (in)	Floor slab	Supp. lat. brace @ RBS	$\frac{\Sigma M^*_{pc}}{\Sigma M^*_{pb}}$	R_v/V_{pz} (nom.)	R_v/V_{pz} (act.)
1	RBS	W36x230	W36x150	¼x31½x42	1x6x33³/₈	Yes	No	2.03	1.09	1.26
2	RBS	W27x194	W36x150	½x24x42	1x6x25½	Yes	No	1.39	1.05	1.14
3	RBS	W27x194	W36x150	½x24x42	1x6x25½	Yes	Yes	1.39	1.05	1.28
4	RBS	W36x150	W36x150	⅜x32⅛x42	1x5½x34	Yes	No	1.25	1.04	1.24
5	RBS	W27x146	W30x108	⅜x24x36	¾x6½x25½	Yes	No	1.63	1.05	1.21
6	RBS	W24x131	W30x108	½x21x36	¾x6x22½	No	Yes	1.32	1.05	1.03

Note: 1. All specimens were fabricated using FCAW (E70T-6 electrode) for the beam flange-to-column flange CJP groove welds;
2. All columns are A992 steel;
3. SPEC-1 and SPEC-2 are A572 Grade 50 steel beams; SPEC-3, SPEC-4, SPEC-5 and SPEC-6 are A992 steel beams;
4. ΣM^*_{pc} = sum of the column nominal plastic moment capacity extrapolated to the intersection of the beam and column centerlines;
ΣM^*_{pb} = sum of the beam expected plastic moment capacity extrapolated to the intersection of the beam and column centerlines;
5. R_v = Panel zone shear strength, Equation (2.3);
V_{pz} = Panel shear force, based on beam moment from Equation (2.14);
6. nom.: nominal values; act.: actual values based on measured dimensions and material properties.

Table 4.2 – Measured specimen dimensions for rolled sections

Section	t_w (in.)	d (in.)	t_f (in.)	b_f (in.)	Z_x (in^3.)
W36x150[1]	0.607	35.987	0.928	11.995	567.1
W36x150[2]	0.602	35.901	1.005	11.956	592.2
W36x230[3]	0.768	36.078	1.213	16.531	916.4
W27x194[4] – Heat 1	0.775	28.313	1.302	14.023	621.2
W27x194[5] – Heat 2	0.783	28.365	1.330	14.133	637.4
W30x108[6]	0.558	29.875	0.725	10.625	337.2
W27x146[7]	0.598	27.625	0.964	14.063	459.9
W24x131[8]	0.581	24.604	0.966	12.836	367.7

Note:
1. Beams for SPEC-1 and SPEC-2;
2. Beams for SPEC-3 and SPEC-4; column for SPEC-4;
3. Column for SPEC-1;
4. Column for SPEC-2;
5. Column for SPEC-3;
6. Beams for SPEC-5 and SPEC-6;
7. Column for SPEC-5;
8. Column for SPEC-6.

Table 4.3 – Specimen column maximum normal elastic design stress per Chi and Uang (2002)

Specimen	Normal Stress		
	Warping stress, f_{ws} (ksi)	Flexural stress, f_{bx} (ksi)	Total stress, f_{total} (ksi)
SPEC-1	16.9	26.9	43.8
SPEC-2	26.4	37.9	64.3
SPEC-3	0	37.9	37.9
SPEC-4	42.0	46.3	88.3
SPEC-5	24.1	31.2	57.3
SPEC-6	0	38.5	40.8

Table 4.4 – Material properties of test specimens

Material		Yield stress (ksi)		Tensile strength (ksi)		Elongation (%)	
		Mill	Coupon (Static)	Mill	Coupon	Mill	Coupon
W36x150 [1]	Flange	N.A.	49.7	N.A.	69.3	N.A.	27.7
	Web	N.A.	54.8	N.A.	71.4	N.A.	24.8
W36x150 [2]	Flange	57.1	53.0	70.1	73.7	28.0	31.6
	Web	61.2	57.4	72.7	73.4	22.3	22.9
W36x230 [3]	Flange	57.1	51.6	73.2	71.9	24.0	28.5
	Web		57.0		74.5		25.6
W27x194 [4]	Flange	57.5	53.9	74.0	75.4	24.0	28.5
	Web		56.8		72.8		25.0
W27x194 [5]	Flange	56.5	51.7	74.0	72.1	24.0	29.4
	Web		58.5		75.6		24.3
W30x108 [6]	Flange	55.0	49.9	70.0	68.3	25.0	26.2
	Web		51.2		68.0		27.8
W27x146 [7]	Flange	57.5	52.7	73.0	72.5	27.0	28.0
	Web		57.8		74.4		25.0
W24x131 [8]	Flange	56.5	48.5	72.5	72.3	26.4	26.9
	Web		52.1		71.5		26.2
Continuity plate (1")	SPEC-1 SPEC-2	N.A.	52.6	N.A.	74.8	N.A.	24.1
	SPEC-3	N.A.	56.0	N.A.	80.7	N.A.	25.5
	SPEC-4	63.6	54.4	83.1	80.3	17.4	25.8
Continuity plate (¾")	SPEC-5 SPEC-6	N.A.	53.4	N.A.	78.4	N.A.	24.5
Doubler plate (¼")	SPEC-1	N.A.	58.2	N.A.	82.5	N.A.	20.6
Doubler plate (½")	SPEC-2	N.A.	47.5	N.A.	67.6	N.A.	24.8
	SPEC-3	63.0	59.3	73.0	75.6	20.0	19.9
	SPEC-6	N.A.	46.7	N.A.	73.1	N.A.	25.5
Doubler plate (⅜")	SPEC-4	61.0	64.7	86.0	92.7	21.0	18.8
	SPEC-5	N.A.	57.7	N.A.	82.1	N.A.	22.3

Note:
1. Beams for SPEC-1 and SPEC-2;
2. Beams for SPEC-3 and SPEC-4 and column for SPEC-4;
3. Column for SPEC-1;
4. Column for SPEC-2;
5. Column for SPEC-3;
6. Beams for SPEC-5 and SPEC-6;
7. Column for SPEC-5;
8. Column for SPEC-6;
9. N.A.: not available.

Table 4.5 – Specimen measured beam moment capacity

Specimen		M_p (k-in)	M_{pn} (k-in)	$M_{p,RBS}$ (k-in)	$M_{pn,RBS}$ (k-in)	$\frac{M_p}{M_{pn}}$	$\frac{M_{p,RBS}}{M_{pn,RBS}}$
SPEC-1	East	29,216	29,050	19,215	19,205	1.01	1.00
	West	29,203				1.01	
SPEC-2	East	29,326		19,846		1.01	1.03
	West	29,519				1.02	
SPEC-3	East	31,835		21,068		1.10	1.09
	West	32,060				1.10	
SPEC-4	East	32,363		21,262		1.11	1.10
	West	32,522				1.12	
SPEC-5	East	16,950	17,300	11,625	11,775	0.98	0.99
	West	16,997				0.98	
SPEC-6	East	17,001		11,667		0.98	0.99
	West	16,948				0.98	

Note: 1. M_p and $M_{p,RBS}$ were calculated based on the measured dimensions and the material yield strength from tensile coupon test;
2. M_{pn} was calculated based on the Z_x in AISC LRFD manual and the nominal yield strength of 50 ksi; $M_{pn,RBS}$ was calculated based on the design Z_{RBS} and the nominal yield strength of 50 ksi.

Table 4.6 – Specimen measured floor slab concrete compressive strength on date of testing

Specimen	Compressive Strength, f_c' (psi)
SPEC-1	5,270
SPEC-2	5,430
SPEC-3	4,646
SPEC-4	4,828
SPEC-5	5,593

Note: Concrete compressive strength on the date of testing was determined by interpolating between two concrete cylinder test results before and after specimen test.

Table 4.7 – Specimen weld metal mechanical properties

Electrode	Yield strength (ksi)		Tensile strength (ksi)		Elongation (%)	
	Typical [1]	Measured	Typical [1]	Measured	Typical [1]	Measured
E70T-6	65.9	70.1 [2]	82.6	86.5	27	22.7
E70T-1	77.3	78.5	83.5	93.1	28	26.2
E71T-8	64.9	64.4	84.7	80.2	28	15.7 [3]

Note:
1. Based on test reports by Lincoln Electric;
2. Yield strength of E70T-6 electrode were scattered, the results from three test plates were 70.3, 80.7 and 59.3, respectively;
3. Defects were found in the tensile coupons after test, this might affect the elongation.

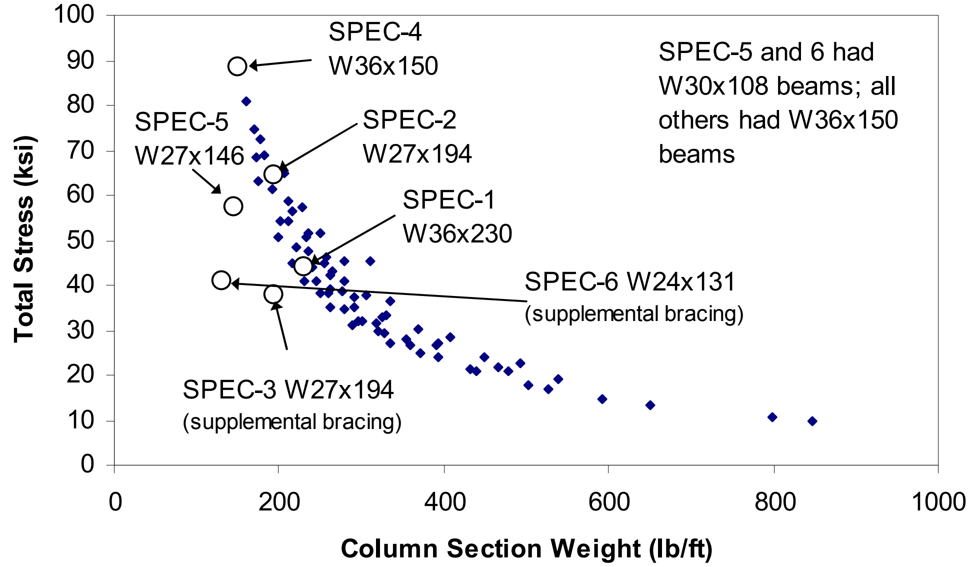

Figure 4.1 – Column maximum normal flange stress vs. section weight

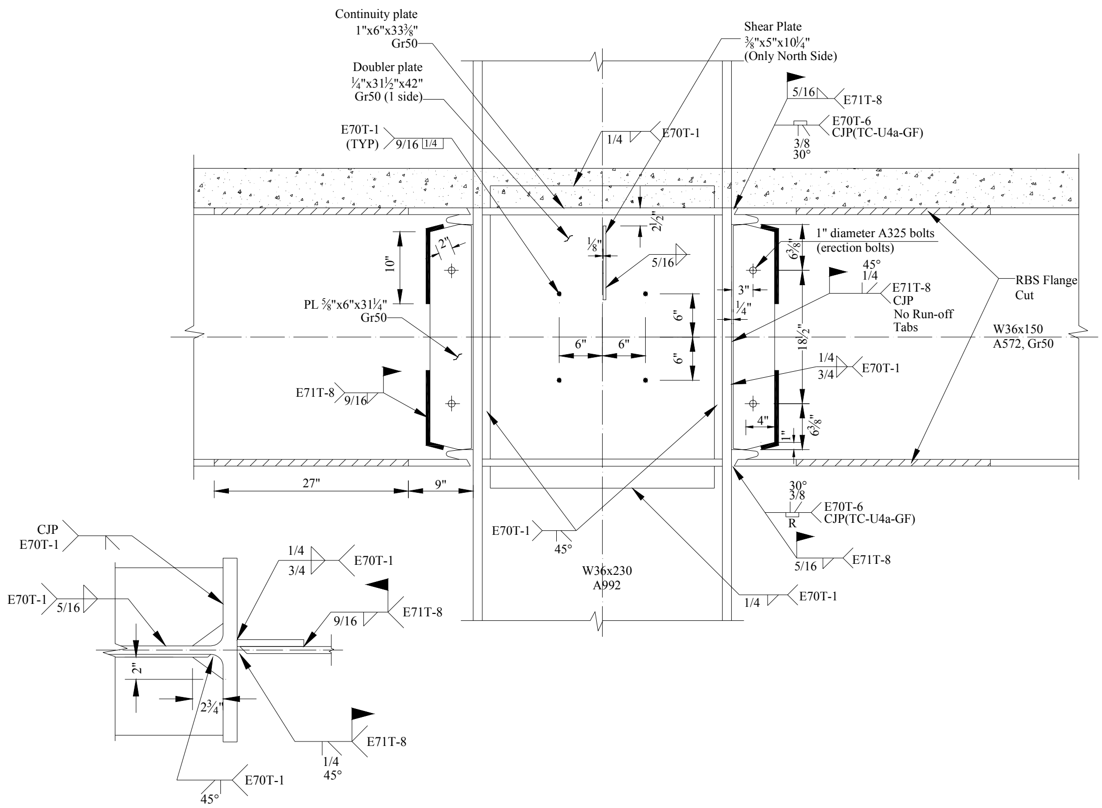

Figure 4.2 – SPEC-1 connection detail

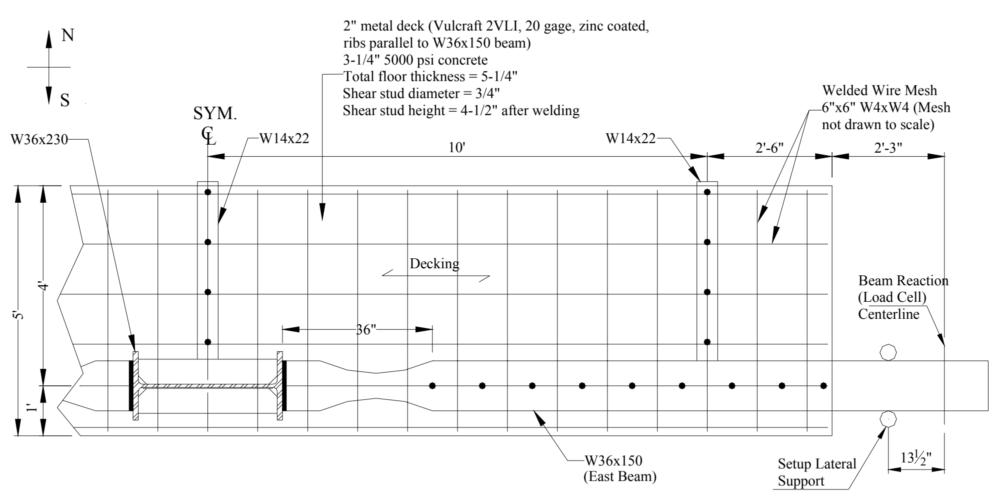

Figure 4.3 – SPEC-1 floor slab detail

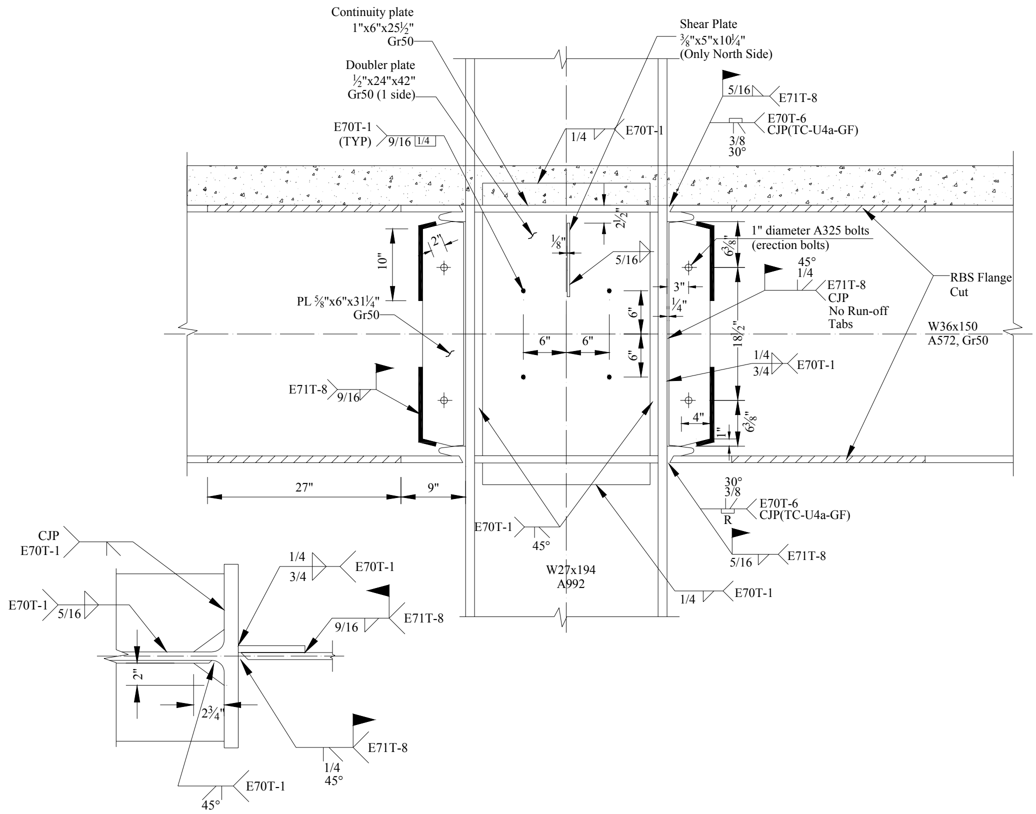

Figure 4.4 – SPEC-2 connection detail

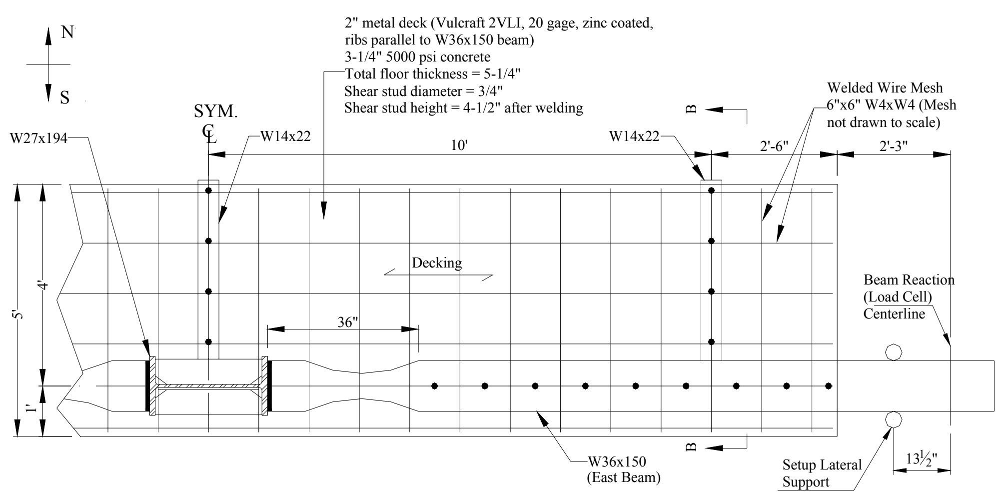

Figure 4.5 – SPEC-2 floor slab detail

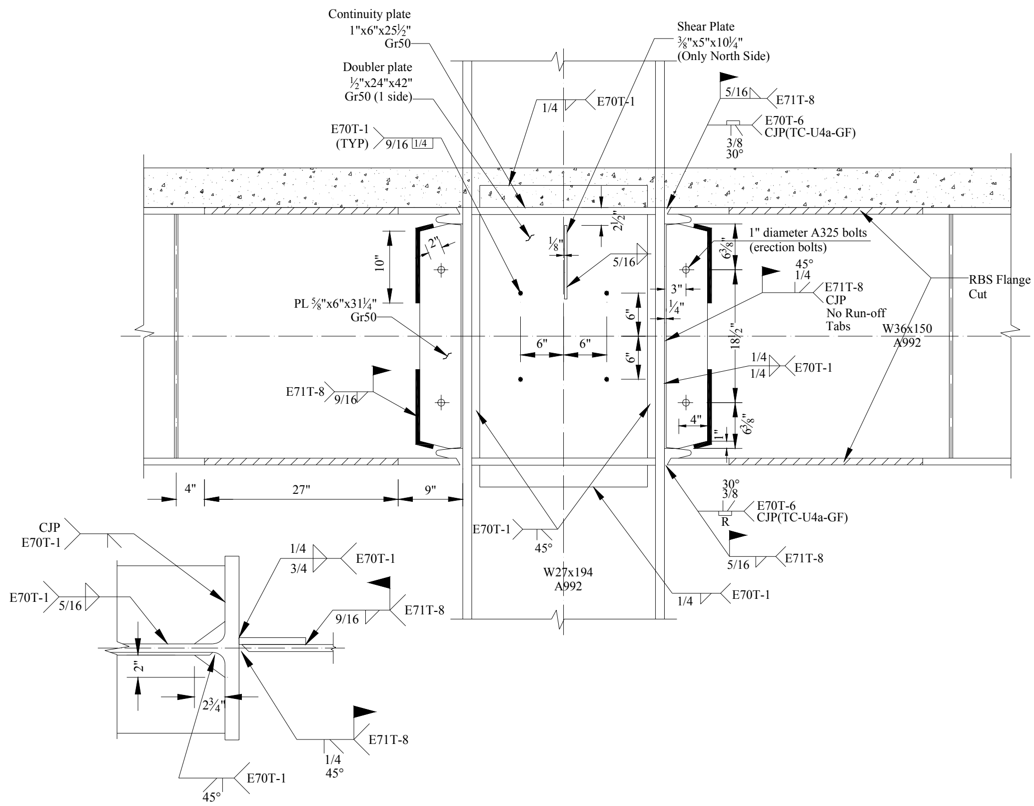

Figure 4.6 – SPEC-3 connection detail

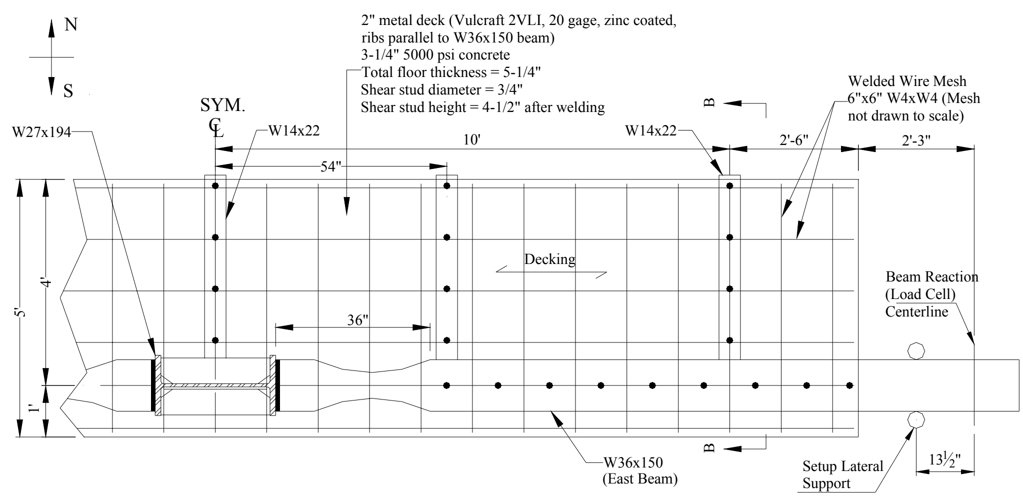

Figure 4.7 – SPEC-3 floor slab detail

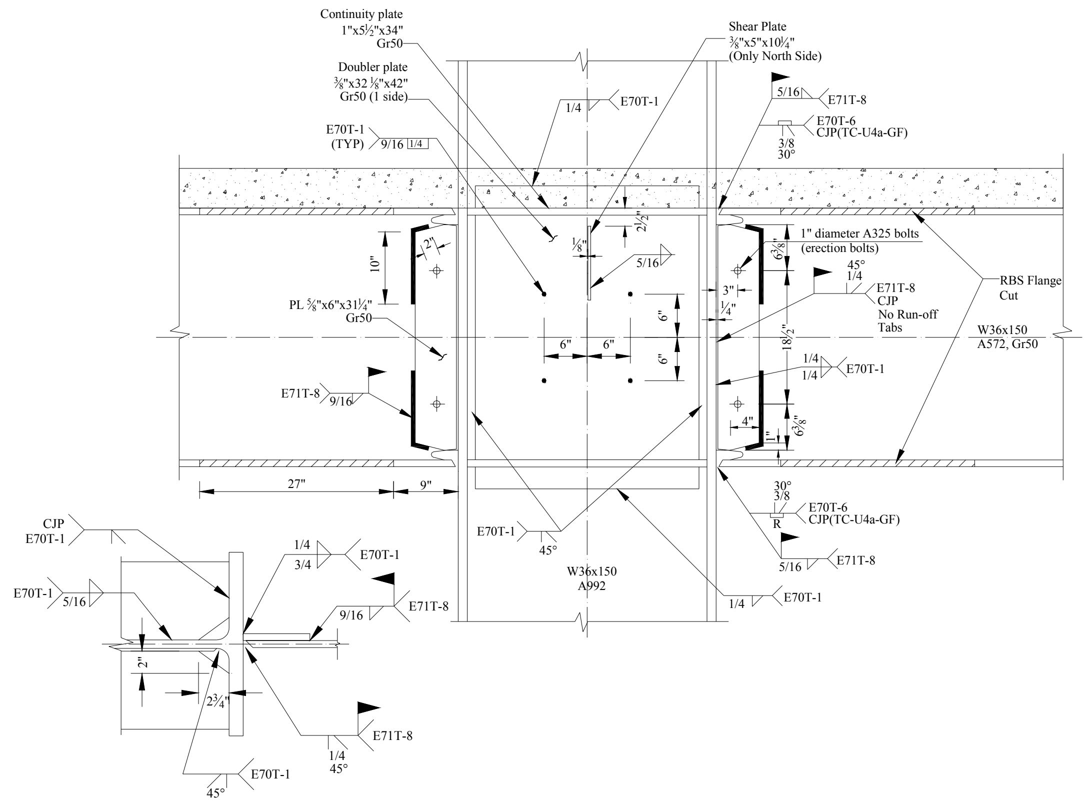

Figure 4.8 – SPEC-4 connection detail

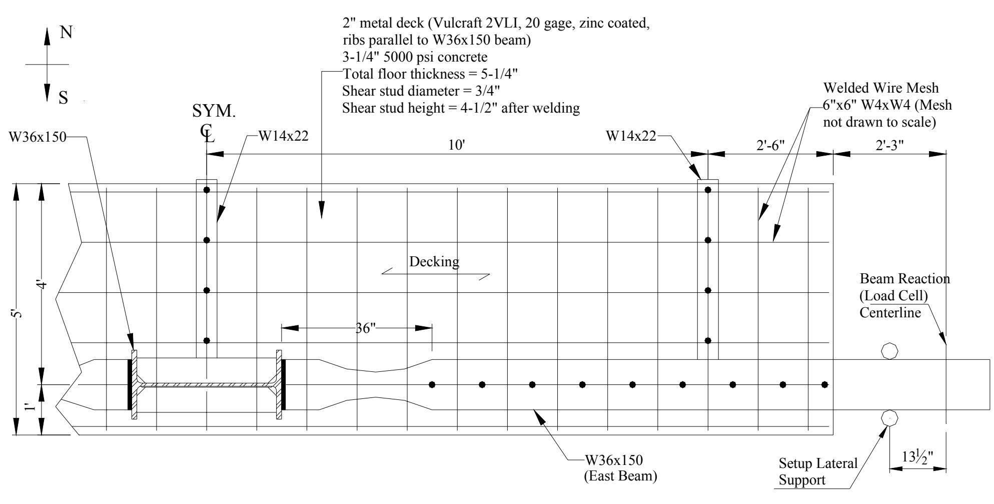

Figure 4.9 – SPEC-4 floor slab detail

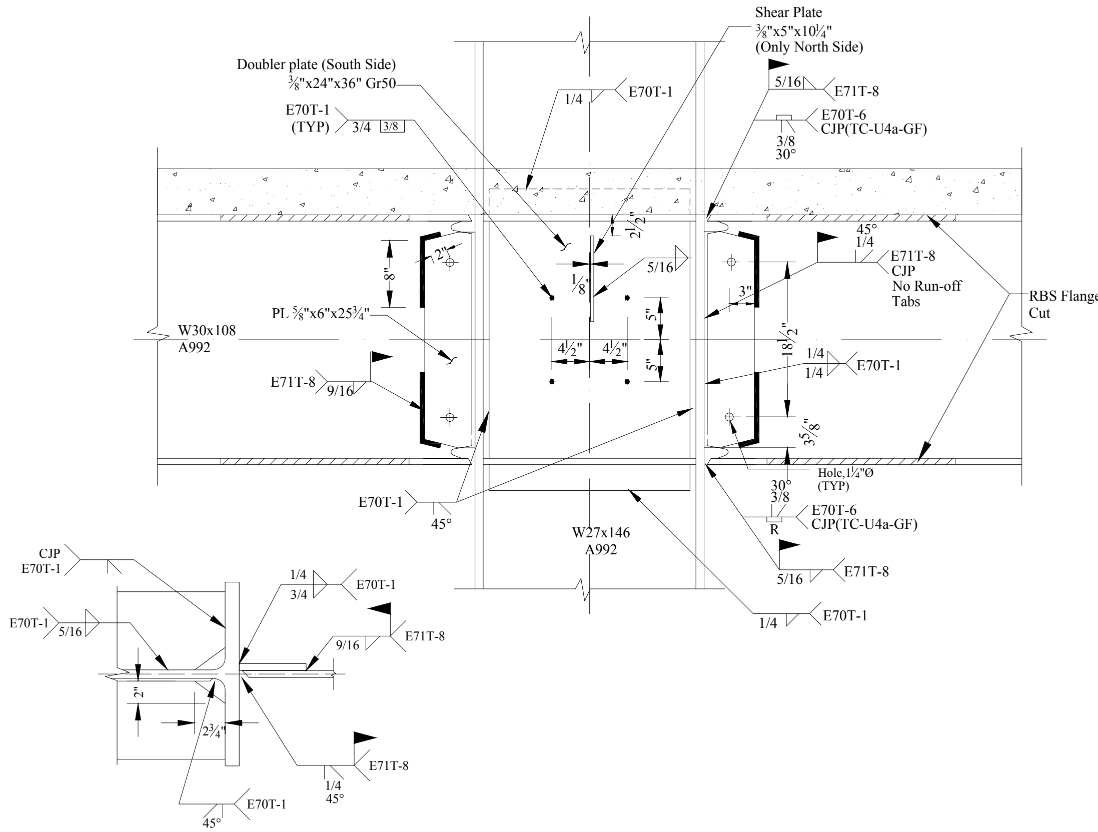

Figure 4.10 – SPEC-5 connection detail

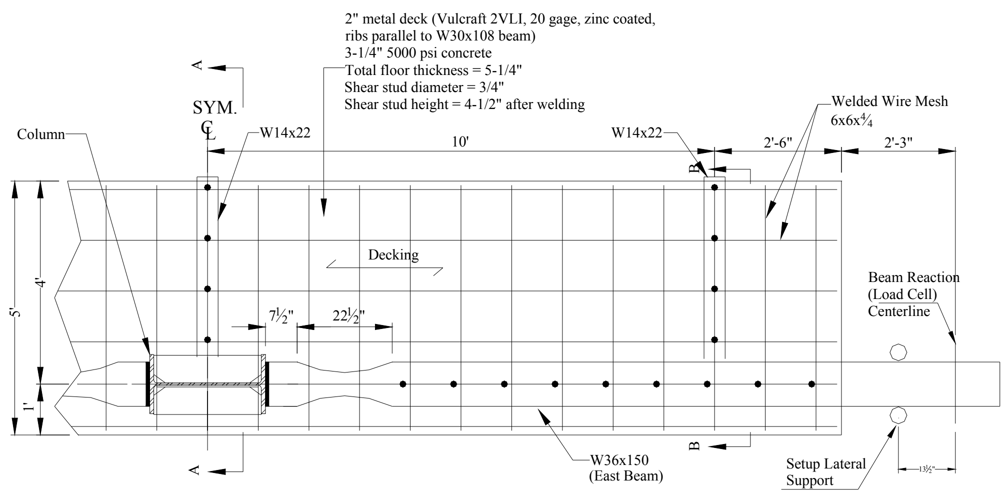

Figure 4.11 – SPEC-5 floor slab detail

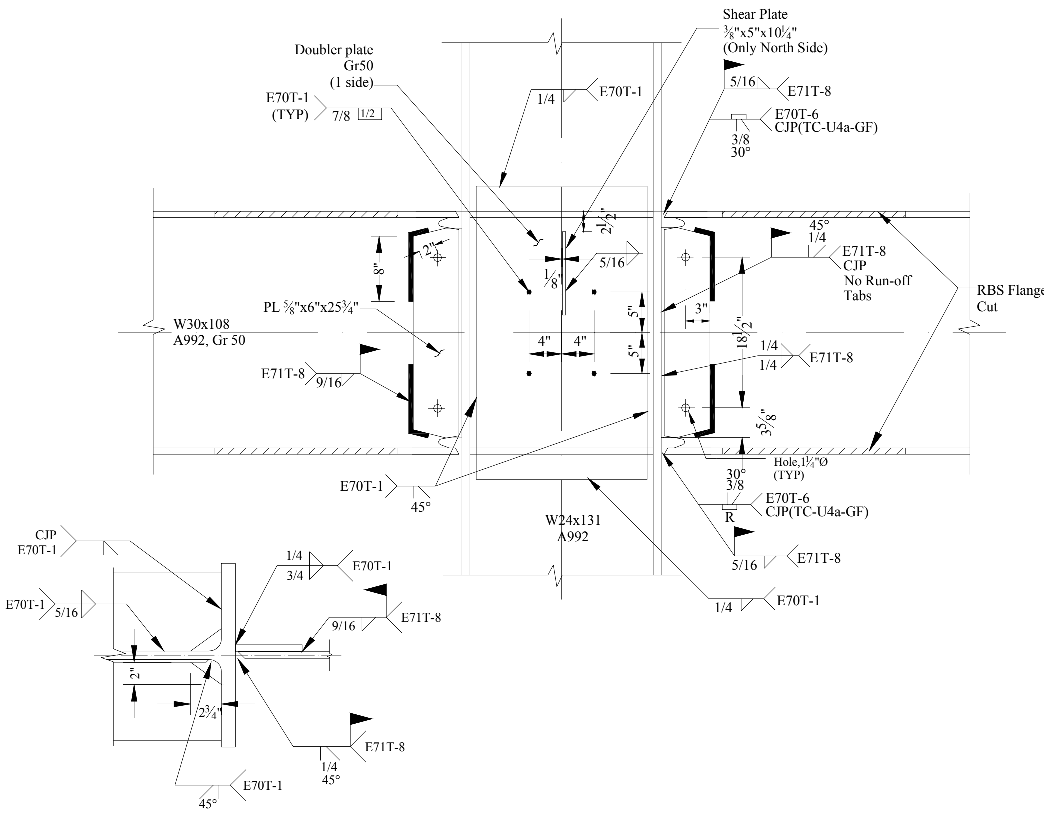

Figure 4.12 – SPEC-6 connection detail

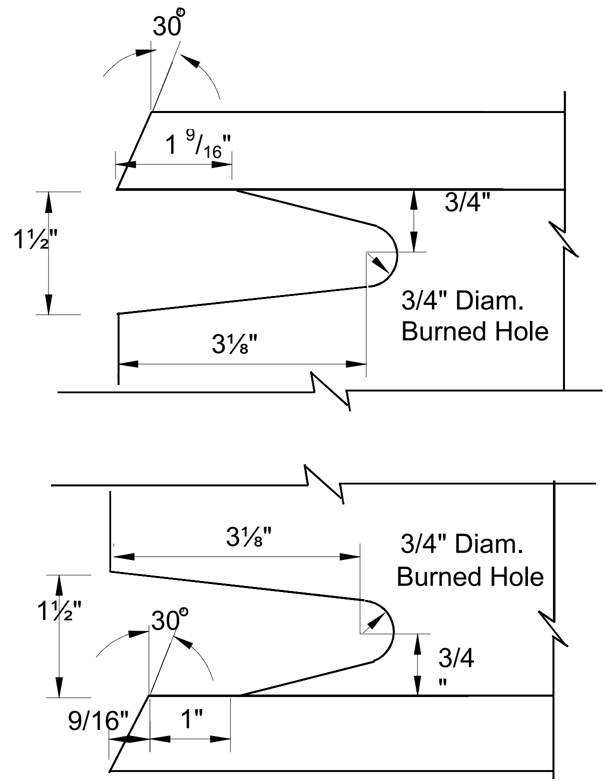

Note: all flame cut surface were ground smooth to a surface roughness of 500 micro-inches

Figure 4.13 – Modified weld access hole details

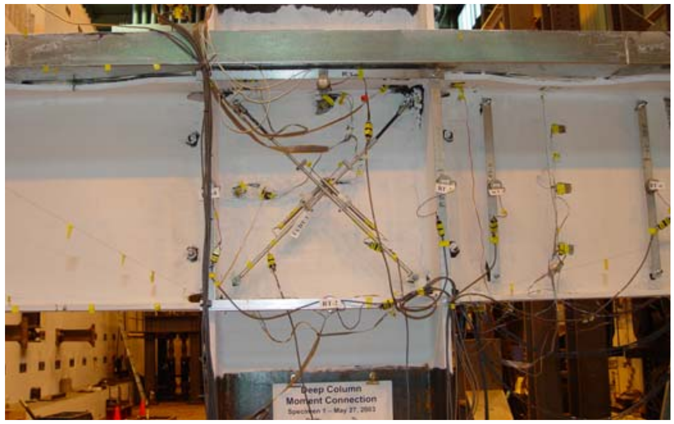

(a) South side

(b) North side

Figure 4.14 – Photos of SPEC-1 connection prior to testing

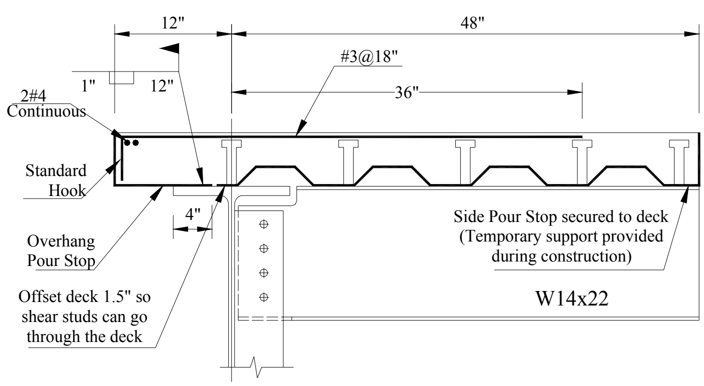

Figure 4.15 – Composite floor slab details

(a)

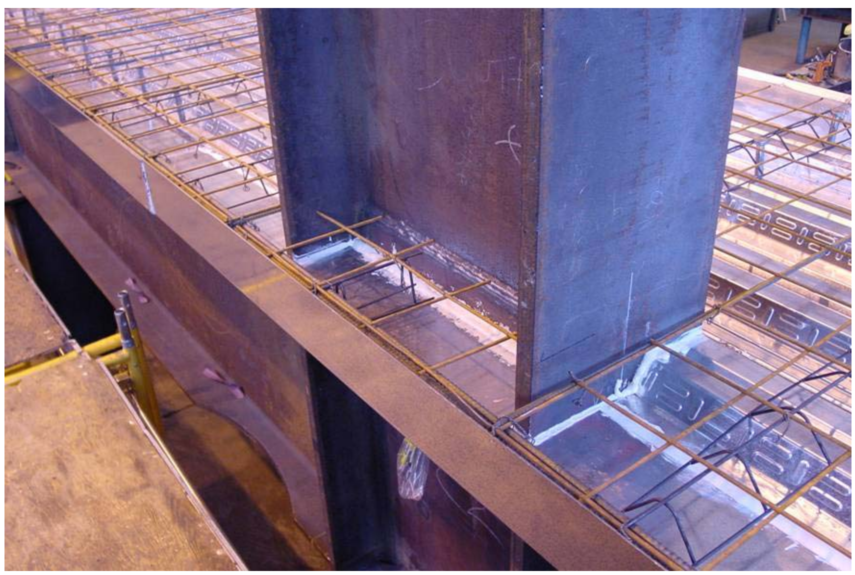

(b)

Figure 4.16 – SPEC-1 slab prior to concrete placement

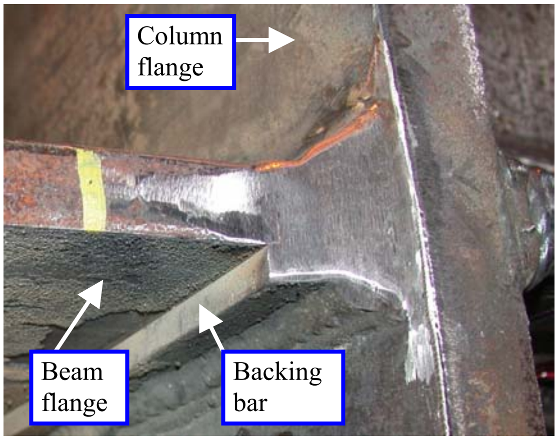

(a) Edge of beam flange CJP groove weld, top flange

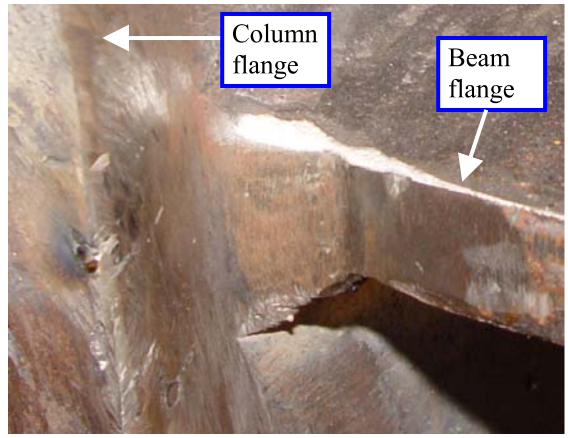

(b) Edge of beam flange CJP groove weld, bottom flange

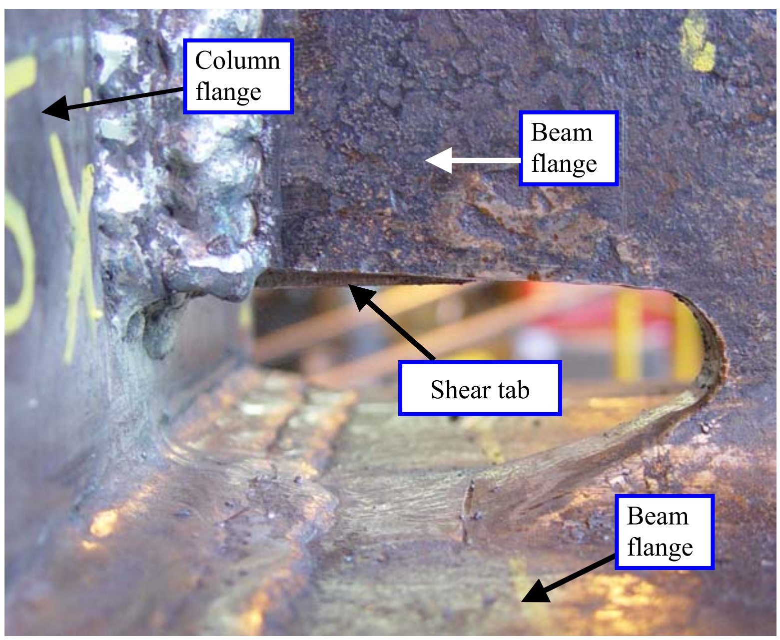

(c) End of beam web-to-column flange CJP groove weld

Figure 4.17 – Beam web and flange groove welds

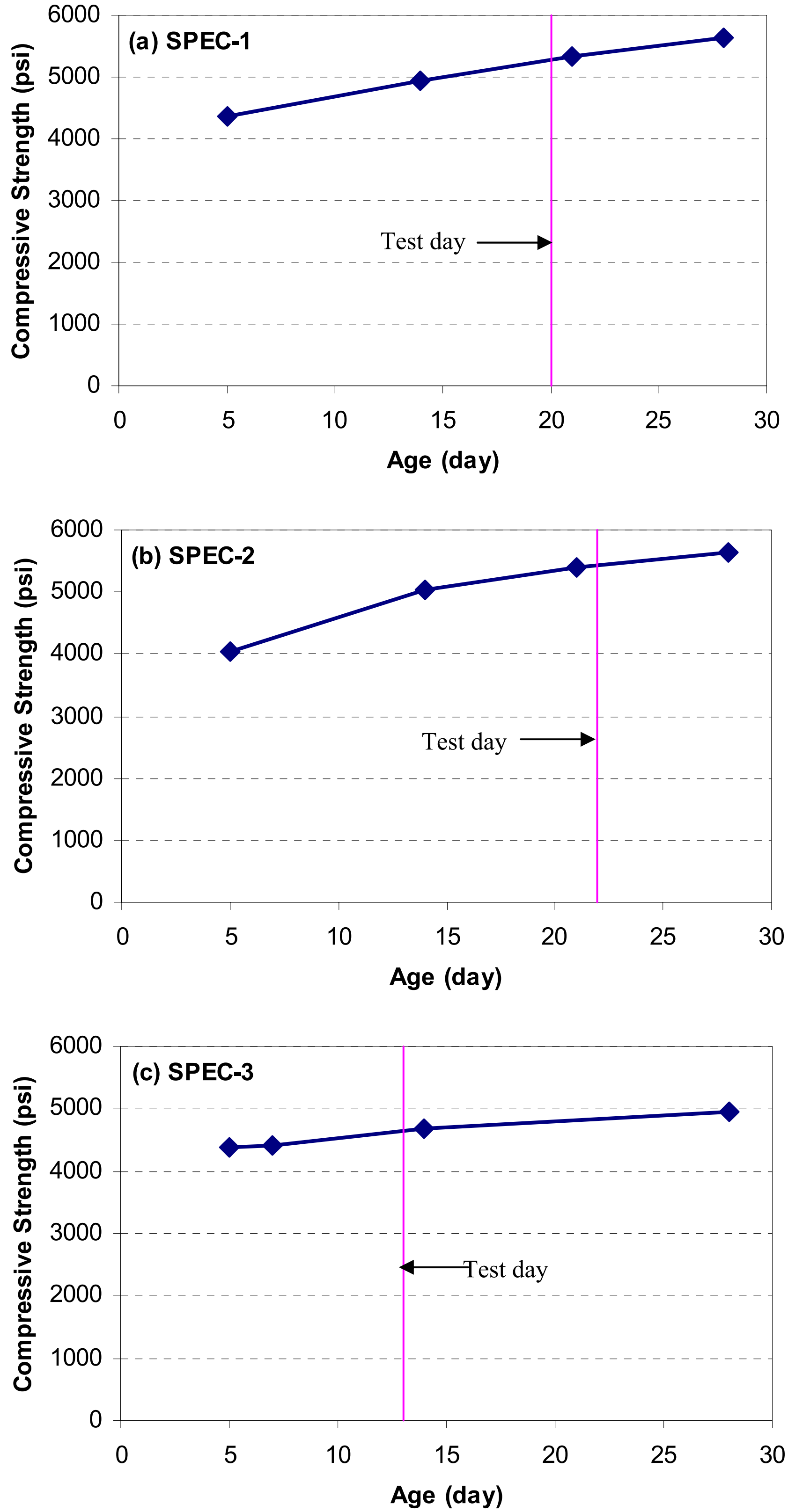

Figure 4.18 – Specimen floor slab concrete strength (Continued)

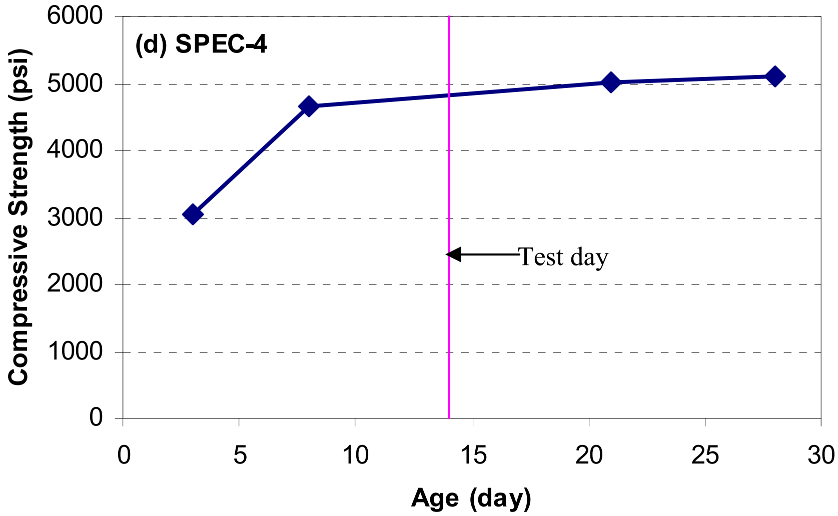

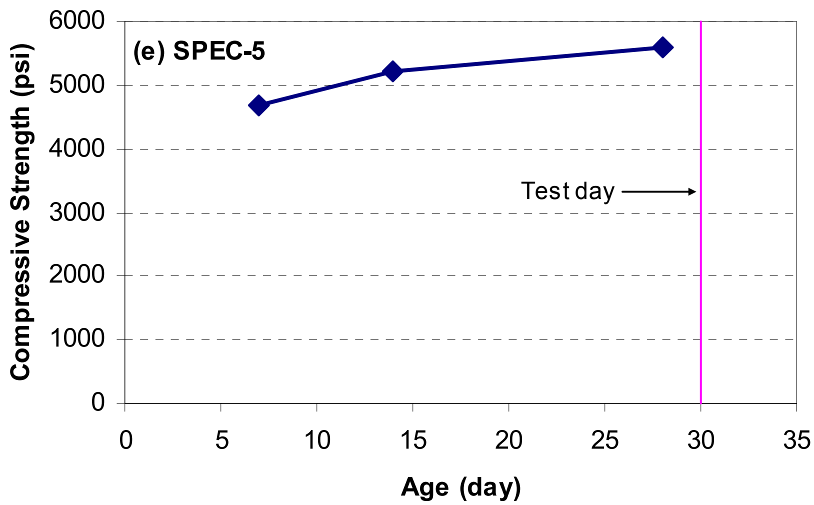

Figure 4.18 – Specimen floor slab concrete strength

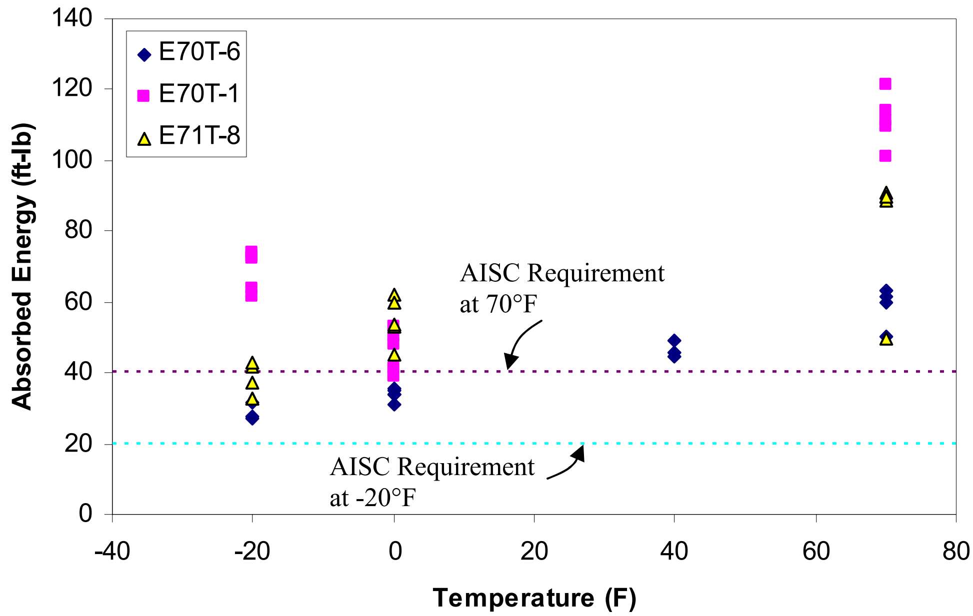

Figure 4.19 – CVN test results for weld metal

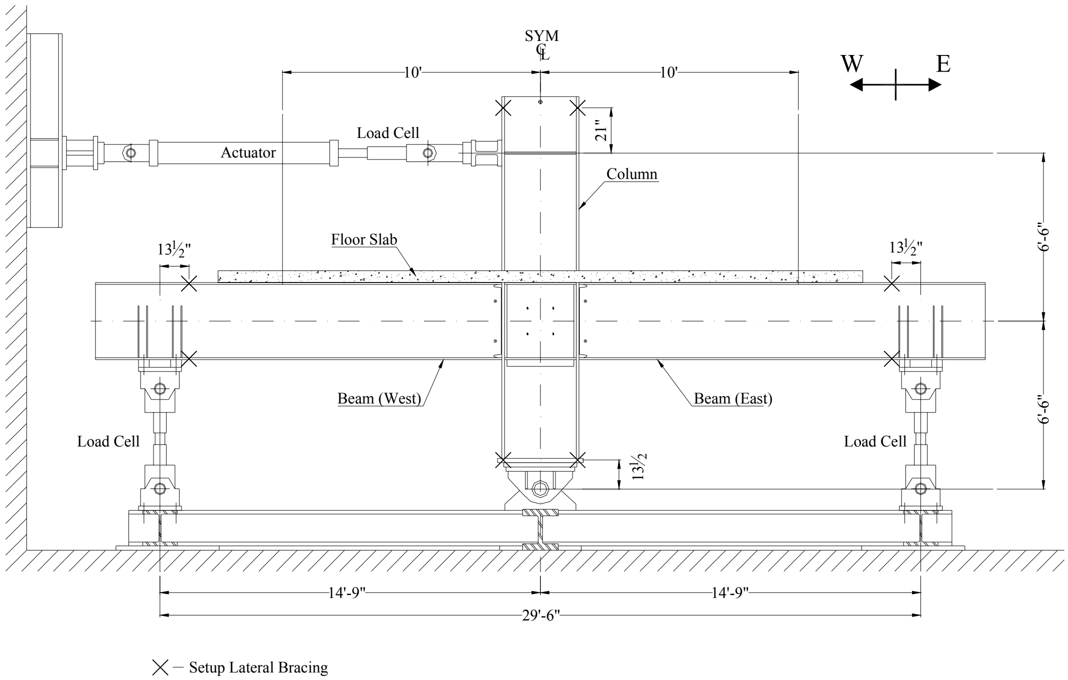

(a) South side

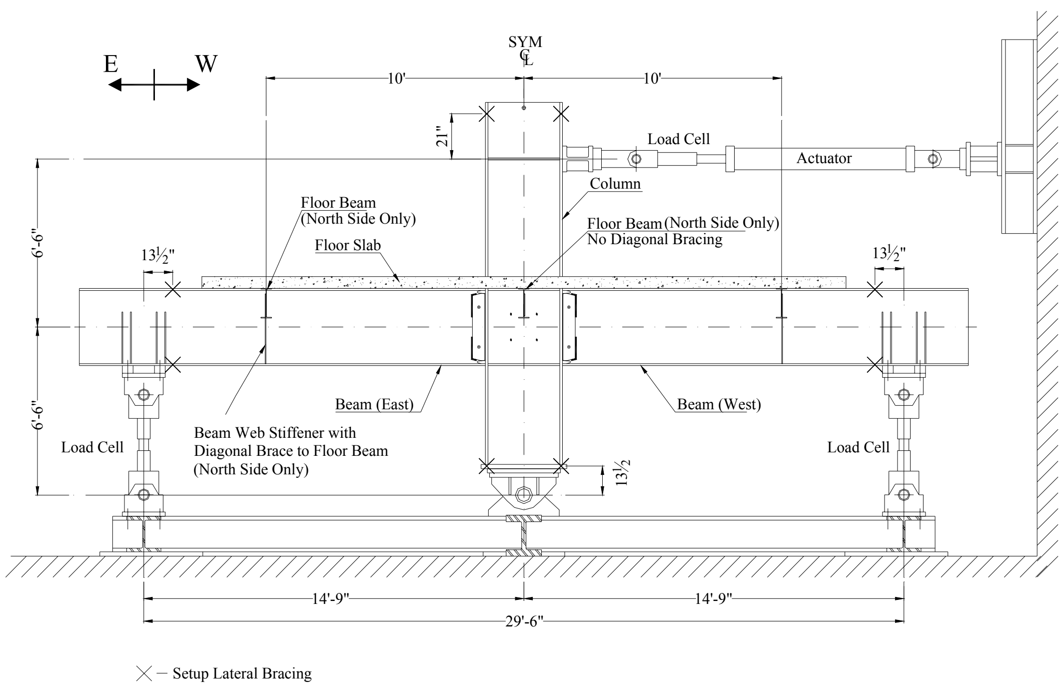

Note: SPEC-3 had supplemental bracing at ends of both RBS (not shown)

(b) North Side

Figure 4.20 – Test setup (Continued)

(c) Photograph of south side

(d) Photograph of north side

Figure 4.20 – Test Setup

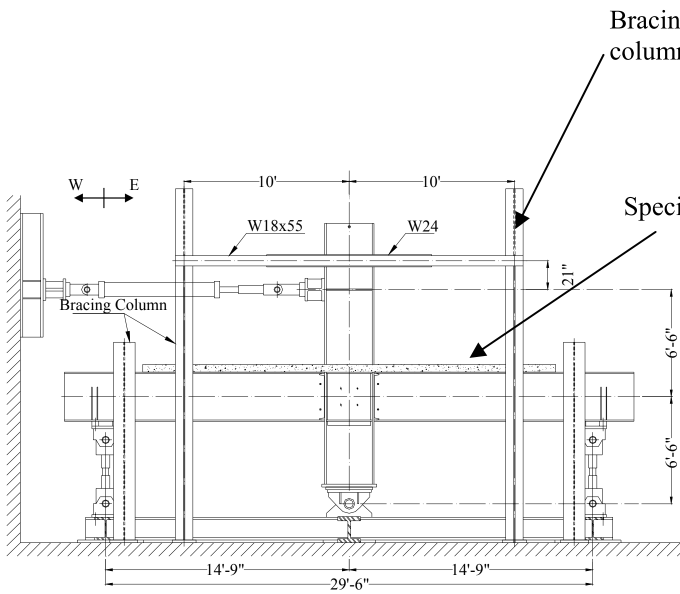

(a) South elevation

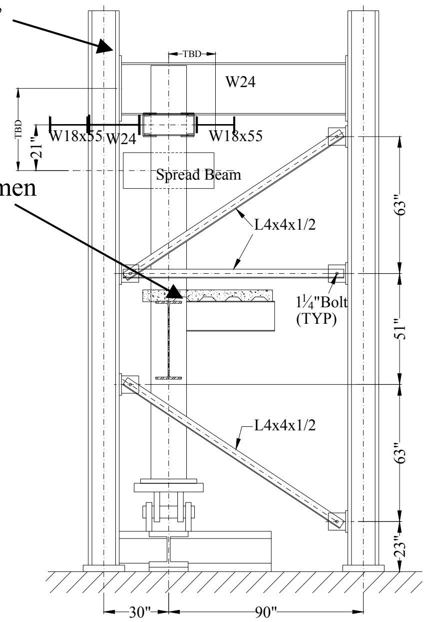

(b) Side (east) view

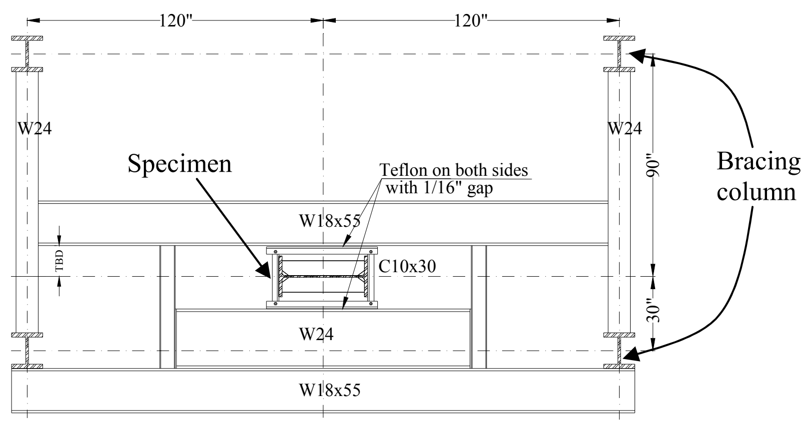

(c) Top view

Figure 4.21 – Specimen test set-up bracing details

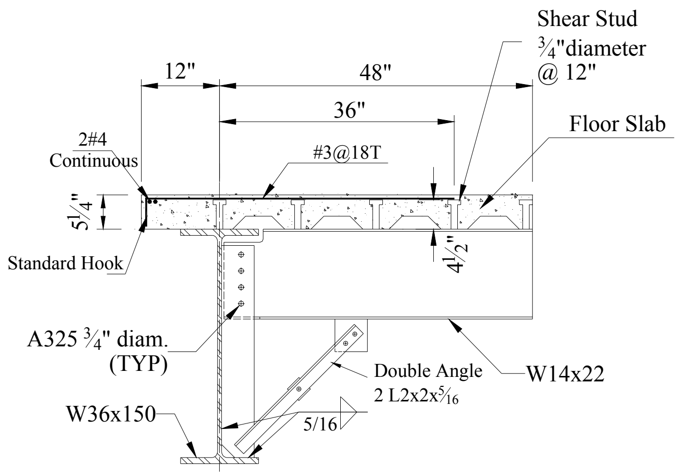

(a) Beam lateral bracing detail

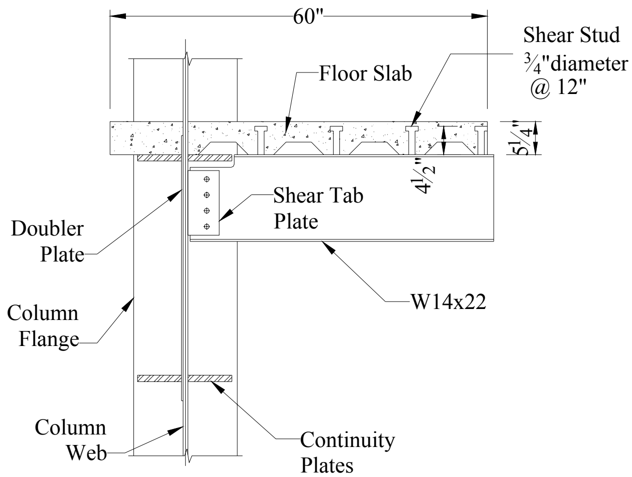

(b) Column lateral bracing at mid-height
Figure 4.22 – Bracing details

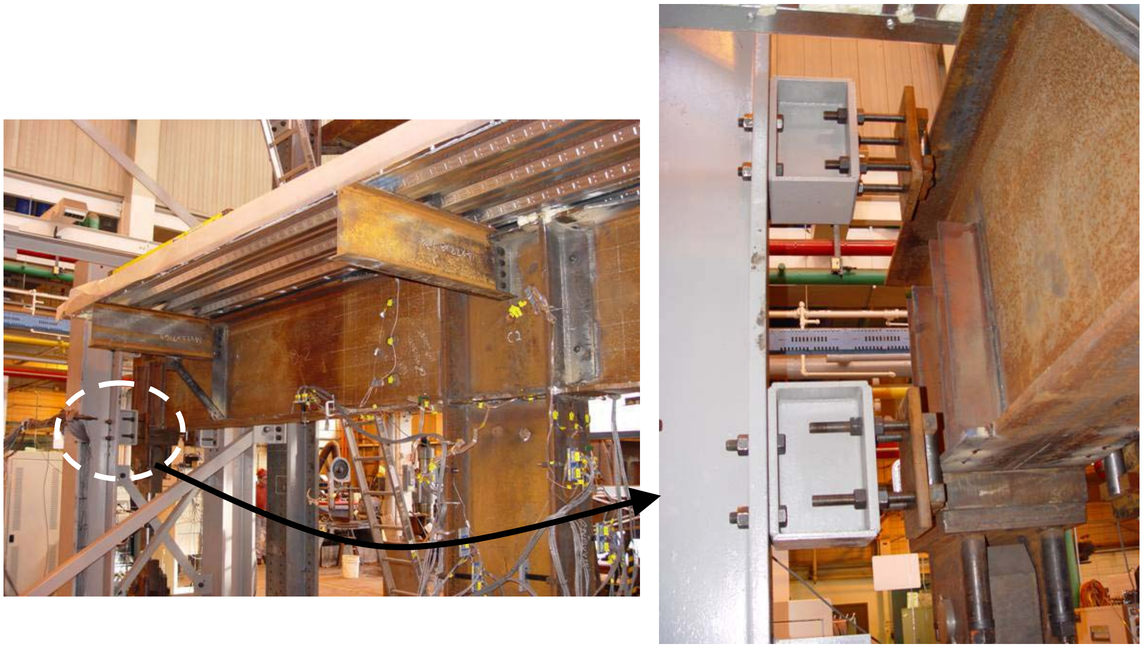

(a) Beam lateral bracing

(b) Test setup lateral bracing for beam

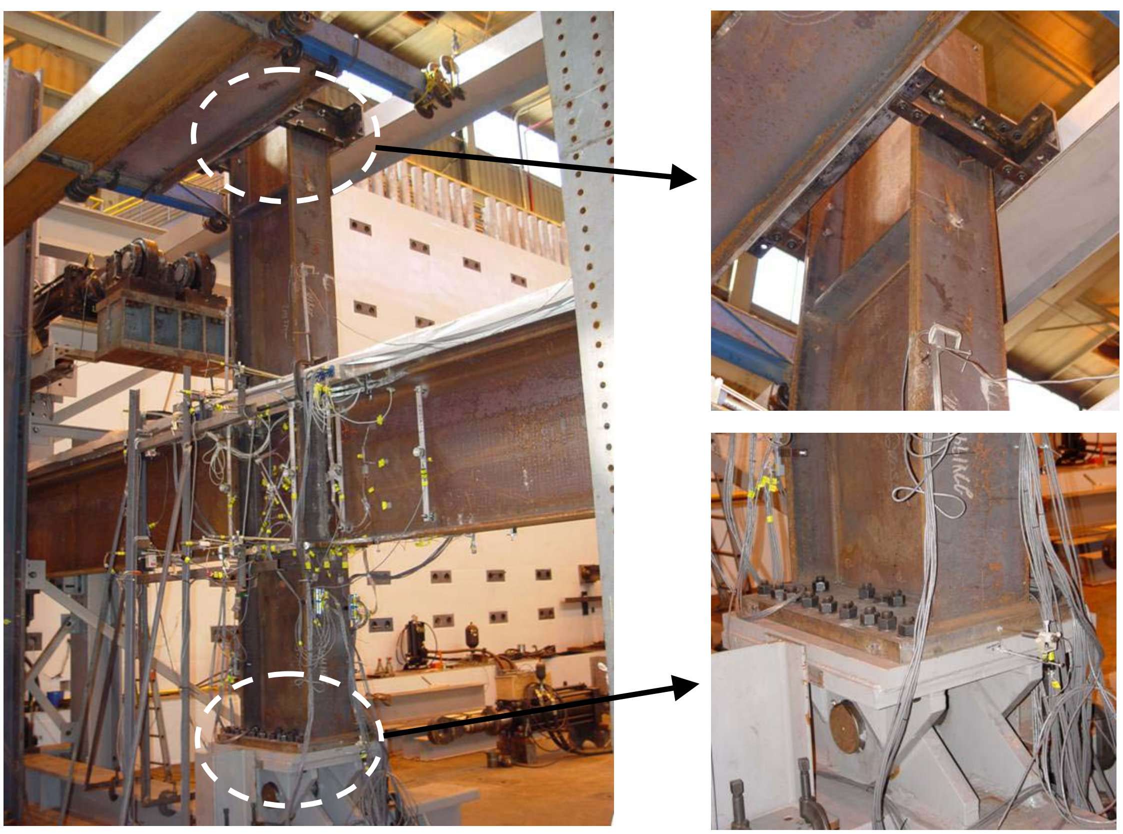

(c) Column lateral bracing

Figure 4.23 – Photos of beam and column lateral bracing

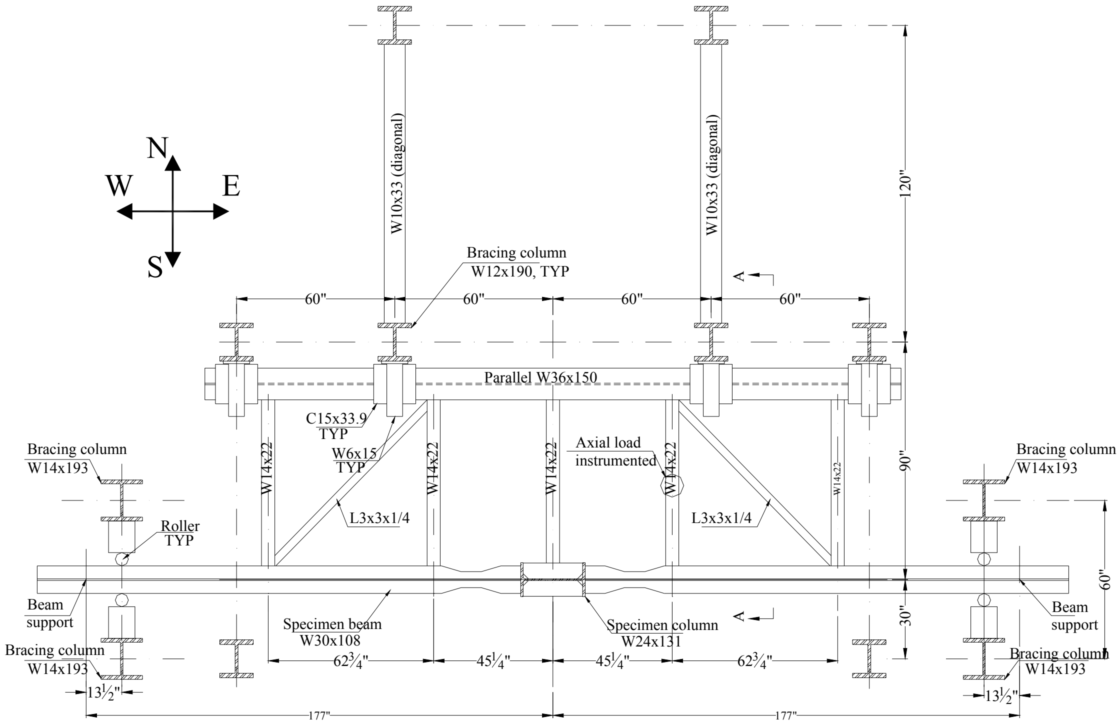

(a) Plane

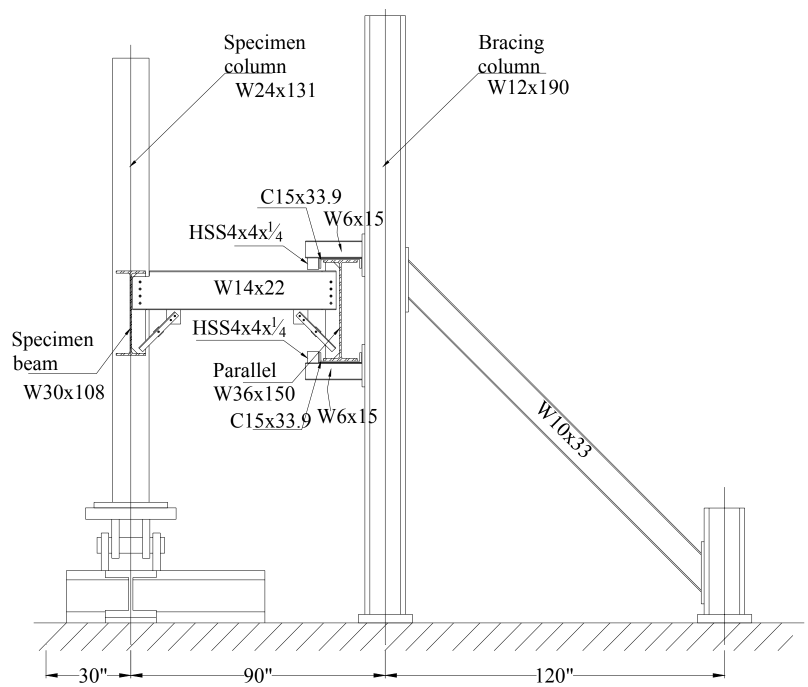

(b) Section A-A: Additional bracing column

Figure 4.24 – SPEC-6 setup additional bracing details
(Bracing details in Figure 4.21 remained, not shown for clarity)

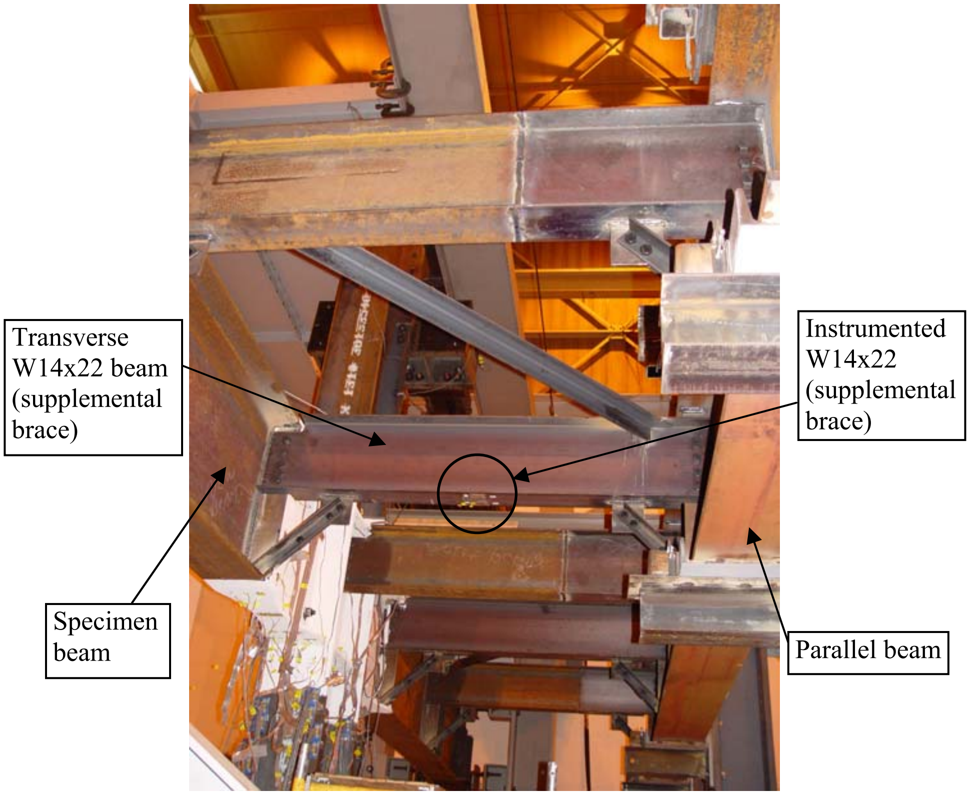

(a) Overview

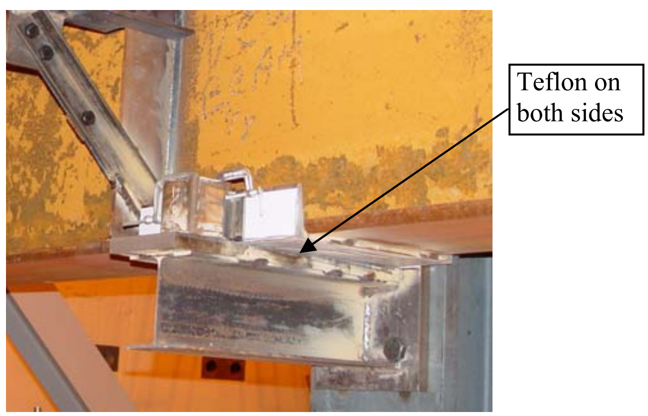

(b) Bracket

Figure 4.25 – Photos of SPEC-6 bracing

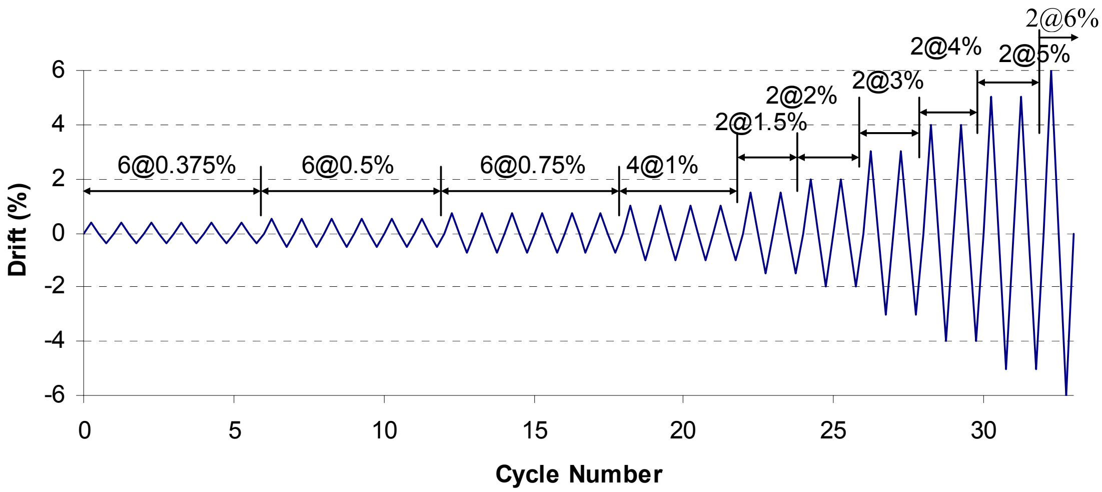

Figure 4.26 – Loading protocol

Normal Elongation

High Elongation

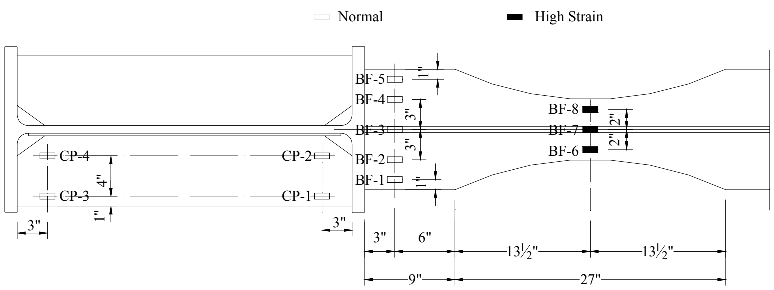

Top view of beam top flange

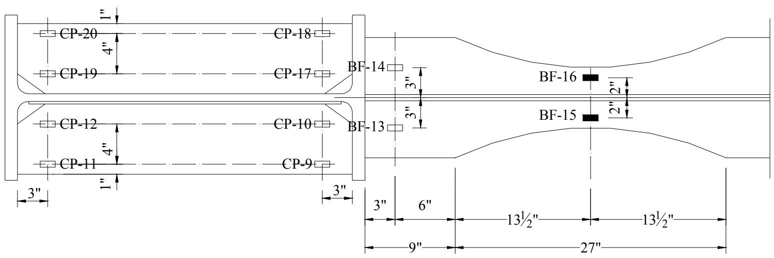

Top view of beam bottom flange

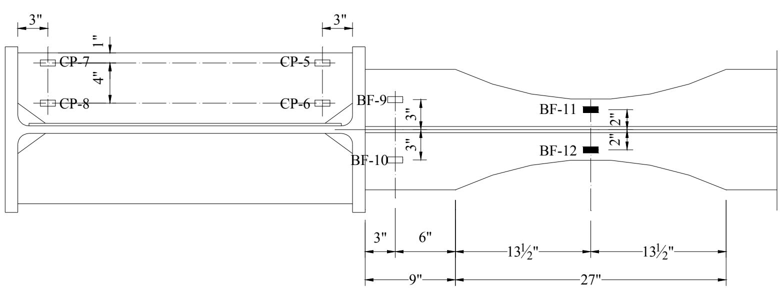

Bottom view of beam top flange

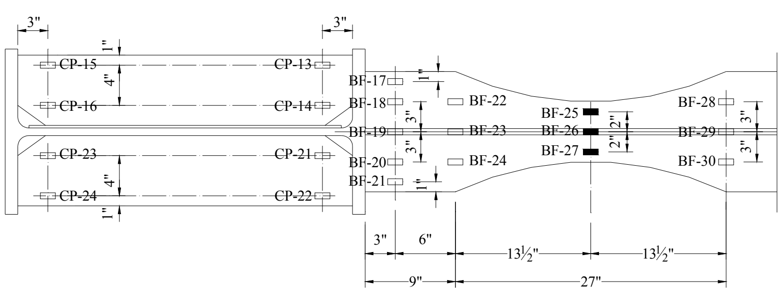

Bottom view of beam bottom flange

(a) Strain gauges on beam flanges

Figure 4.27 – Strain gauge layout for SPEC-1 and SPEC-2 (Continued)

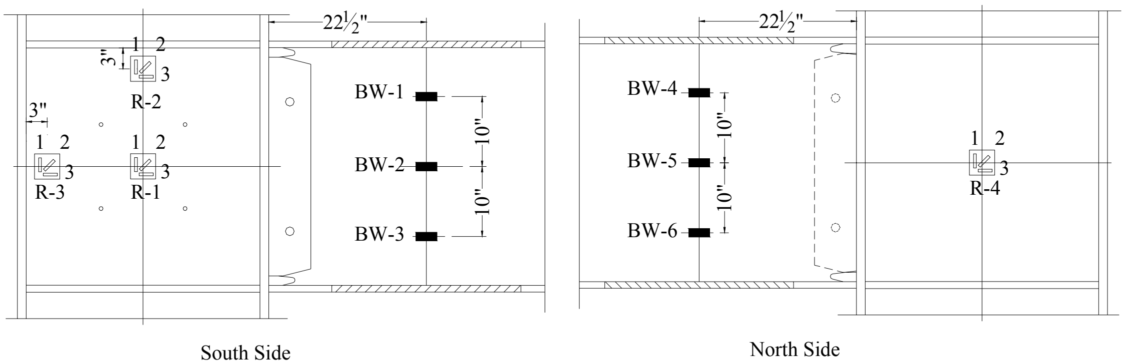

(b) Strain gauges on beam web and column panel zone

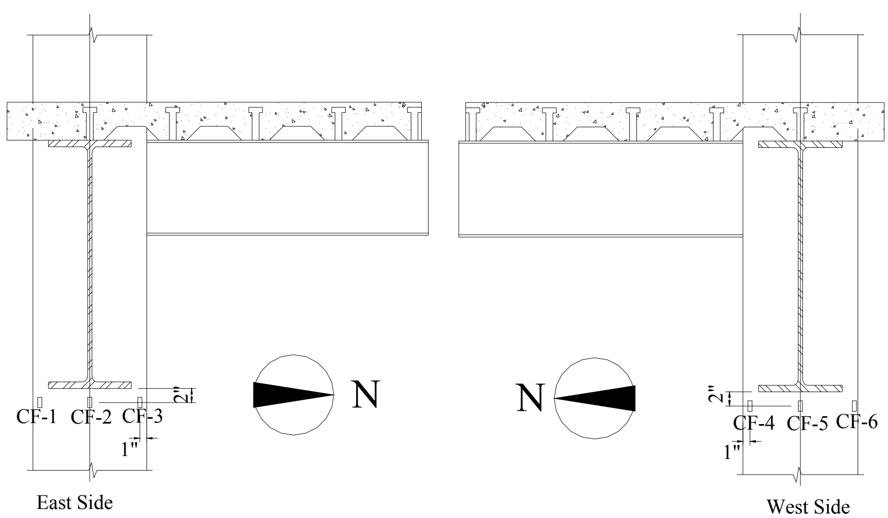

(c) Strain gauges on column flanges at beam-to-column connection

Figure 4.27 – Strain gauge layout for SPEC-1 and SPEC-2

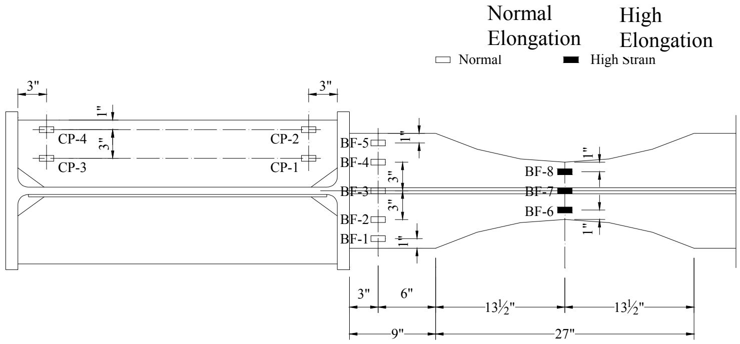

Top view of beam top flange

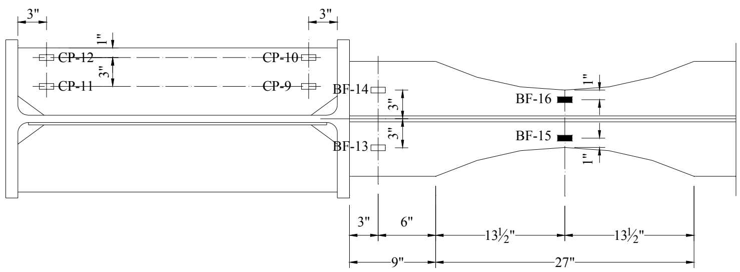

Top view of beam bottom flange

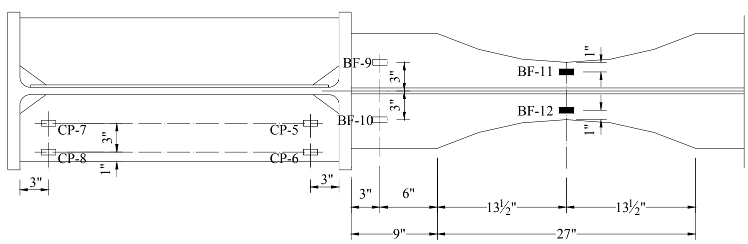

Bottom view of beam top flange

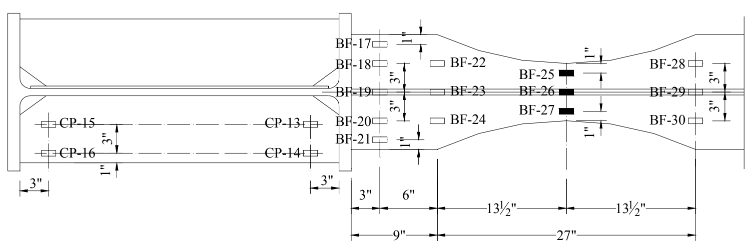

Bottom view of beam bottom flange

(a) Strain Gauges on Beam Flanges

Figure 4.28 – Strain gauge layout for SPEC-3 and SPEC-4 (Continued)

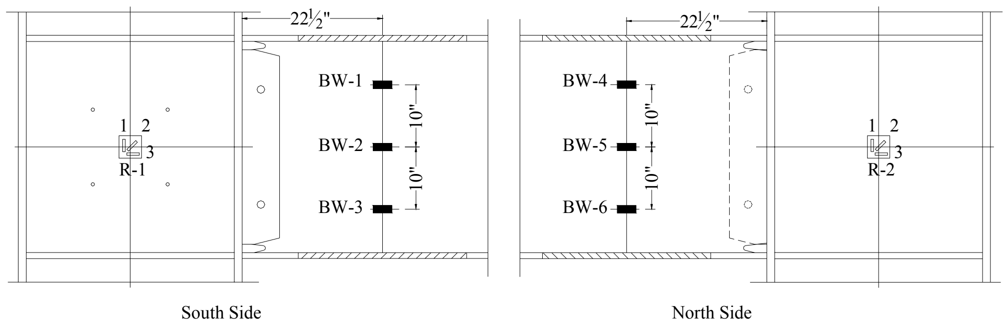

(b) Strain gauges on beam web and column panel zone

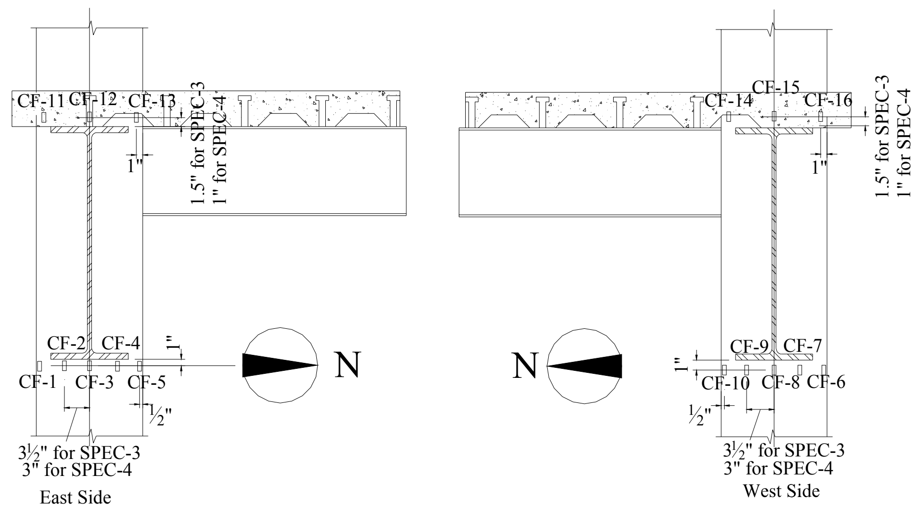

(c) Strain Gauges on Column Flanges

Figure 4.28 – Strain gauge layout for SPEC-3 and SPEC-4

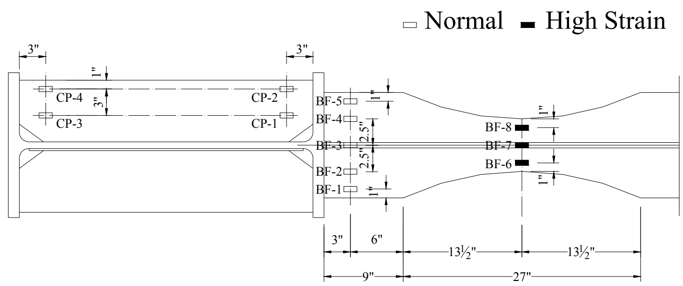

Top view of beam top flange

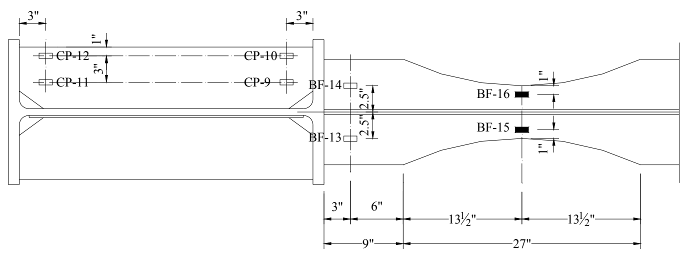

Top view of beam bottom flange

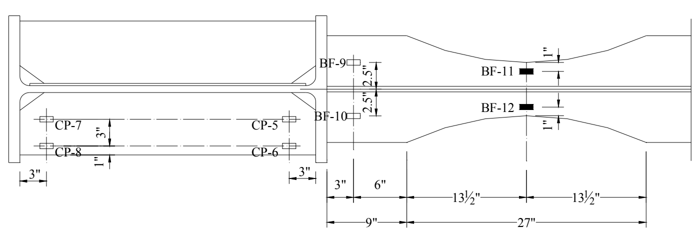

Bottom view of beam top flange

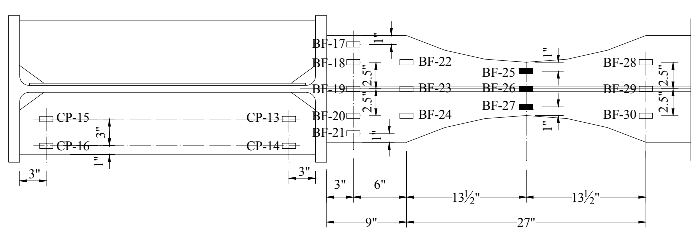

Bottom view of beam bottom flange

(a) Strain gauges on beam flanges

Figure 4.29 – Strain gauge layout for SPEC-5 and SPEC-6 (Continued)

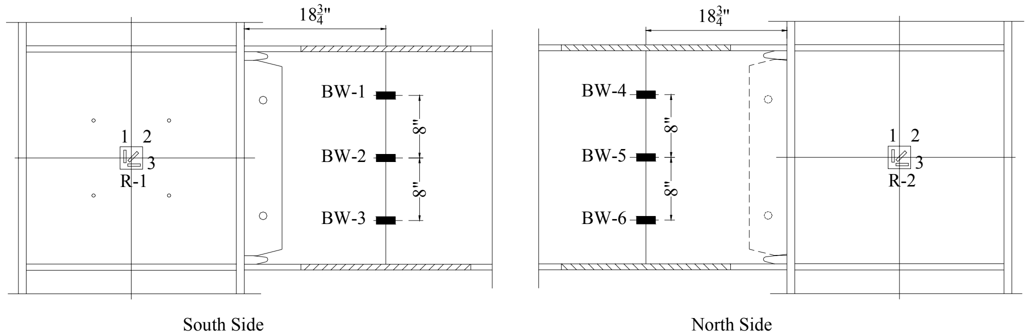

(b) Strain gauges on beam web and column panel zone

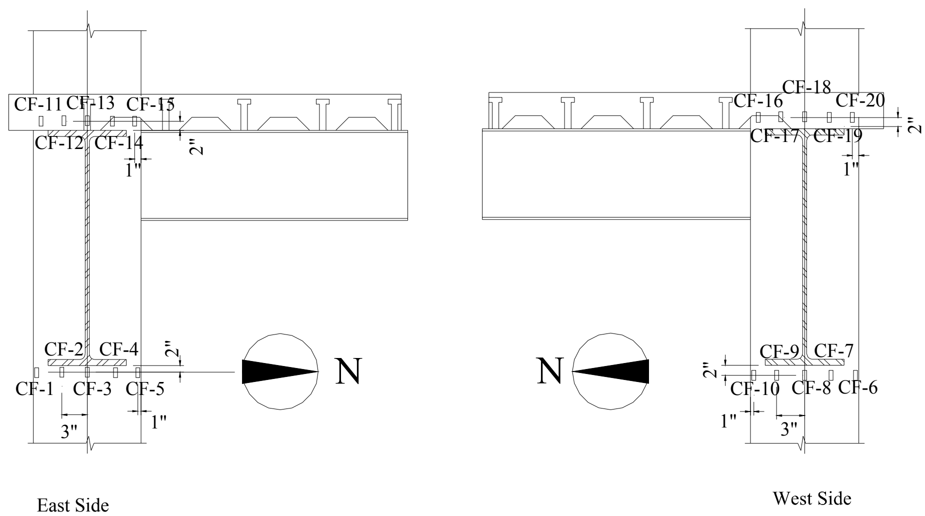

(c) Strain gauges on column flanges

Figure 4.29 – Strain gauge layout for SPEC-5 and SPEC-6

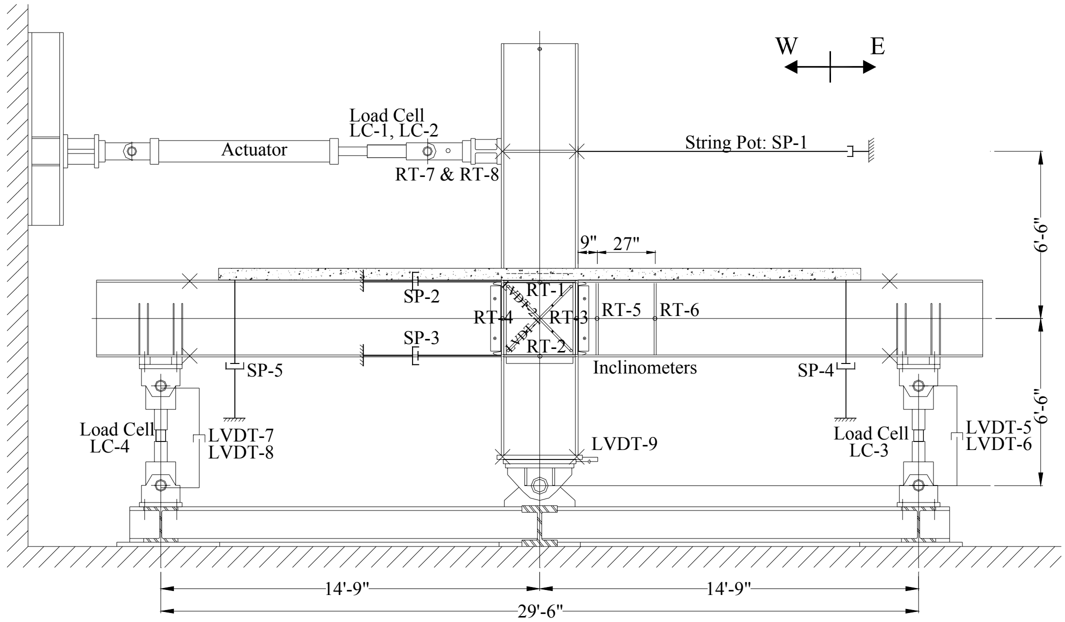

(a) Over view

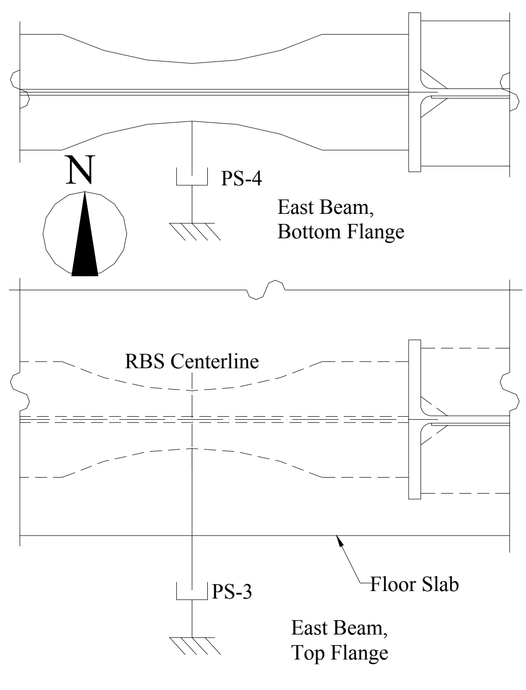

(b) RBS out-of-plane movement

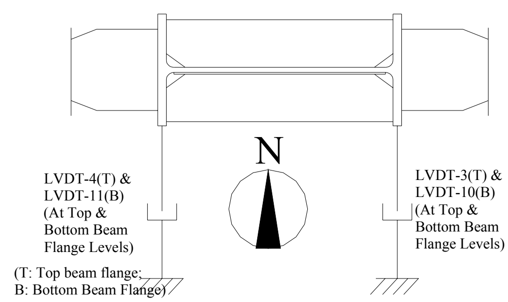

(c) Column twisting

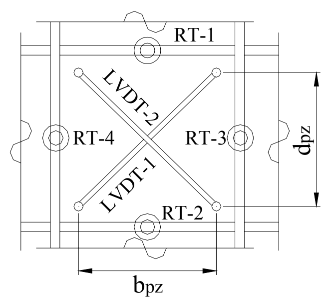

(d) Panel zone

Figure 4.30 – Voltage instruments layout

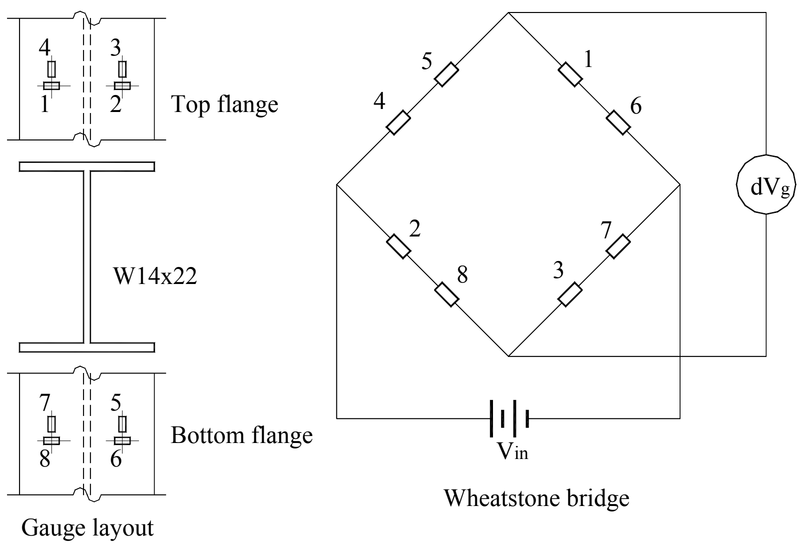

Figure 4.31 – Strain gauge layout and Wheatstone bridge connection for the built-up load cell on supplemental bracing of SPEC-6

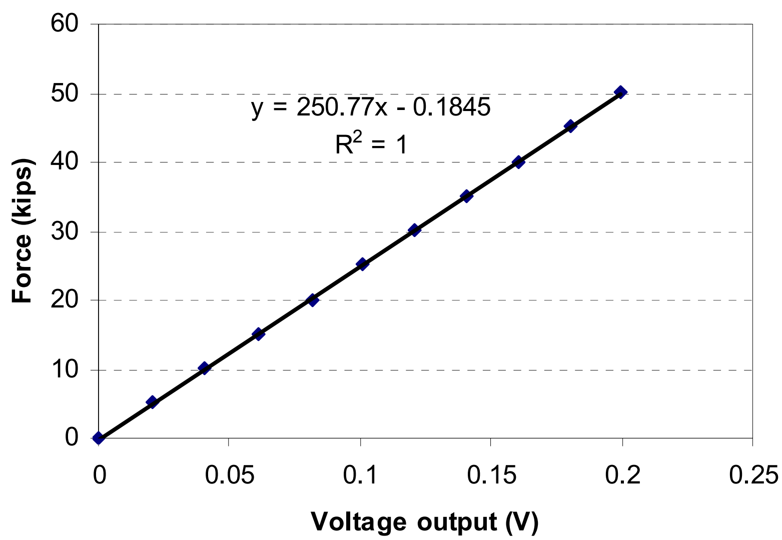

Figure 4.32 – Calibration curve for the axial load instrument on SPEC-6 supplemental bracing beam

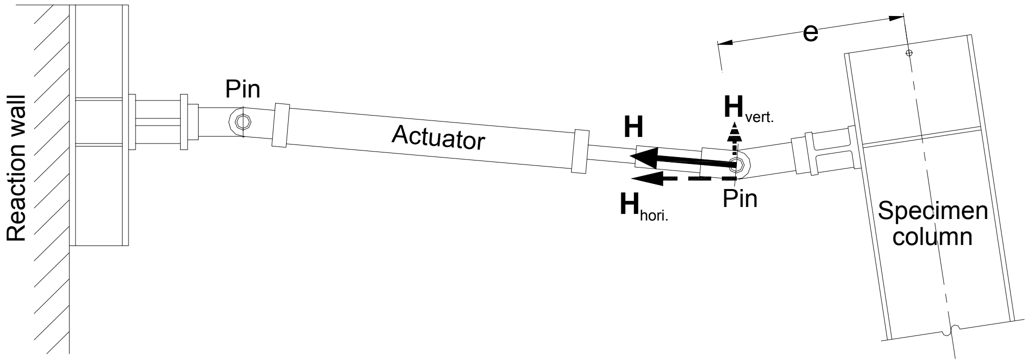

Figure 4.33 – Illustration of actuator inclination due to test setup

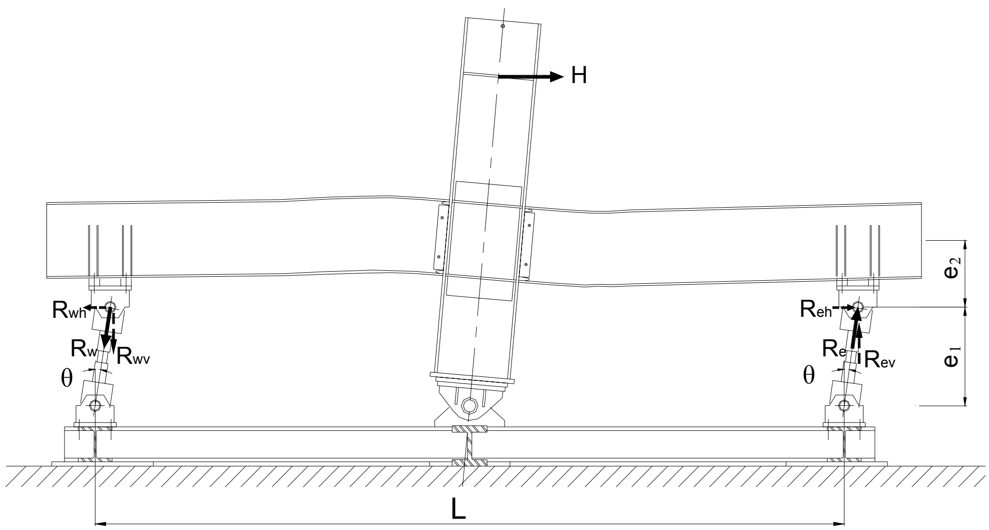

Figure 4.34 – Force components of measured beam reactions

(This page left blank)

CHAPTER 5 EXPERIMENTAL RESULTS

The general behavior of each specimen is discussed in this chapter.

5 .1 Experimental Observations of Specimen Performance

The discussion of the experimental observations of each test specimen utilizes five plots. These include plots of the relationships for: (1) lateral load-total story drift (H-θ_{total}); (2) lateral load-total plastic drift (H-$\theta_{p,total}$), (3) lateral load-panel zone drift (H-θ_{pz}), (4) lateral load-beam drift (H-θ_{bm}); and (5) lateral load-column plastic drift (H-θ_{col}). Photographs and discussion of specimen performance at 4% story drift and at the end of the testing are included. A summary of measured specimen performance results is given in Table 5.1. The measured specimen performance includes maximum total drift, maximum plastic drift, and components of maximum plastic drift. These values of drift are based on the maximum values achieved during the testing of each specimen. The maximum values of drift associated with the last successfully completed cycle are reported in Chapter 6. The last successful cycle is defined as the last cycle completed with neither a fracture nor specimen strength deterioration below 80% of the nominal specimen capacity occurred.

5.1.1 SPEC-1

The lateral load-story drift (H-θ) and lateral load-plastic drift hysteretic response for SPEC-1 are shown in Figure 5.1. The value of 0.8 times nominal lateral load capacity H_{pn} is marked in Figure 5.1(a). H_{pn} was calculated based on the nominal flexural capacity of the beam section developing at the column face. A summary of measured performance quantities is included in Table 5.1. SPEC-1 was observed to develop first yielding in the beam bottom flanges in the RBS and in between the RBS and column face during the 0.5% story drift cycles. Flexural cracking of the concrete in the floor slab also occurred. During the 1.0% story drift yielding of the doubler plate and column web in the panel zone occurred, and the beam flange yielding in the RBS had become more extensive. The concrete began crushing against the column flanges, both on the inside and outside faces, during the 1.5% story drift cycles. The damage to the floor slab in the vicinity of the column became more pronounced as the testing progressed. Initial beam web local buckling was observed in the RBS during the second cycle of 2% story drift. Minor beam flange local buckling occurred in the beam bottom flanges of the RBS during the first cycle of 3% story drift, which became more pronounced during the second cycle of 3% story drift. The specimen maximum capacity of H= 411 kips (see Table 5.1) was achieved during the first half of the 3% story drift cycle. The beam web and flange local buckling in the RBS became more pronounced during the 3% story drift cycles, causing the beam bottom flanges (when in compression) to begin to move laterally in the RBS region. The beam bottom flange in the RBS region straightened out when it went into tension. The cyclic local buckling and beam lateral flange movement in the RBS caused the specimen to develop a deterioration in capacity, which continued with each subsequent cycle throughout the remaining cycles of testing. This is evident in Figure 5.1.

During the 4% story drift cycles, the beam web and flange local buckling became more extensive, as did the lateral movement of the beam bottom flanges in the RBS region. This local buckling and lateral movement continued to become more pronounced with each remaining cycle in the test. Pinging sounds, indicating a possible shearing fracture of the shear studs attached to the beams, were heard during the cycles of 4% story drift. The beam top flanges in the RBS then began to also move laterally when in compression, and straighten out when in tension. The lateral movement was in the opposite direction of the other beam whose bottom flange was in compression. Photographs of the specimen at the end of the second cycle of 4% story drift are shown in Figure 5.2. The specimen capacity H at the first cycle of 4% story drift had deteriorated by 67 kips. The reduction in capacity was 16% below the specimen maximum capacity. The specimen capacity at 4% story drift corresponded to 0.83 times the nominal lateral load capacity H_{pn}. The beam bottom flanges in compression had buckled out laterally around 2.5 inches. Very little column twisting was observed.

A fracture occurred in the east side beam bottom flange of the RBS at the end of the first cycle of 5% story drift. The fracture occurred near the center of the RBS and extended completely across the beam flange. The fracture was due to low cycle fatigue as a result of the occurrence of repeated cyclic local flange buckling in the RBS. The test was terminated immediately after the fracture occurred. SPEC-1 had deteriorated to 38% below its maximum capacity of 411 kips, which is also equal to 0.62 times the nominal capacity H_{pn} of SPEC-1. Photographs of SPEC-1 after testing are shown in Figure 5.3. No cracks were found to initiate near the connection region, including the weld access hole.

Following the completion of the test, the slab was removed from the specimen revealing that most of the shear studs connecting the floor slab to the main beams had fractured, while the shear studs connecting the floor slab to the transverse floor beams remained intact.

The maximum total plastic drift achieved in SPEC-1 during the test was 0.043 radians, with the beams contributing to the majority of the plastic drift (0.038 radians). The maximum panel zone plastic drift was 0.006 radians. Although beam and panel zone yielding initiated about the same time, plastic deformation was concentrated in the beams, and primarily due to the buckling in the RBS. The deterioration in specimen capacity resulted in the panel zone unloading elastically from its inelastic state as the beam plastic hinges formed. The column slightly yielded, contributing 0.004 radians of plastic drift. The measured maximum total rotation across the east beam RBS was 0.043 radians, and was determined using Equation (4-7).

5.1.2 SPEC-2

The lateral load-story drift (H-θ) and lateral load-plastic drift hysteretic response for SPEC-2 are shown in Figure 5.4. A summary of measured specimen performance results is included in Table 5.1. Cracks in the concrete floor slab of SPEC-2 occurred near the column at the end the cycles of 0.375% story drift, and continued to develop and become more extensive near the column throughout the test. Yielding initiated in the beam flanges of the RBS and near the column face and in the panel zone at 1% story drift. The concrete slab started crushing against the column flanges and in region between the column flanges during the cycles 1.5% story drift. Minor column flange yielding below the beam bottom flange was observed during the 2% story drift cycles. Beam web local buckling occurred in the RBS region during the first cycle of 2% story drift, which became more extensive in subsequent cycles. Beam flange local buckling followed by a lateral movement of the beam bottom flange in the RBS (when in compression) was observed to initiate during the cycles of 3% story drift, and become more extensive in latter cycles. The beam flanges straighten out when in tension and buckled laterally when in compression. During the 4% story drift cycles, the local buckling in the beam web became extensive, causing the beam top flange in the RBS (when in compression) to also begin to develop lateral movement. The lateral movement was in the opposite direction of the other beam whose bottom flange was in compression. The beam top flange in the RBS region also straightened out when tension. Pinging sounds, indicating a possible shearing fracture of the shear studs attached to the beams, were heard during the cycles of 4% story drift. SPEC-2 developed its maximum capacity of H= 412 kips during the first cycle of 4% story drift (see Figure 5.4), whereupon a deterioration in capacity occurred in the subsequent cycles throughout the remaining cycles of the test. During these subsequent cycles the amplitude of local buckling and lateral movement of the beam compression flange in the RBS grew as the story drift amplitude was increased.

Photographs of SPEC-2 at the end of the second cycle of 4% story drift are shown in Figure 5.5. The specimen lateral load capacity at the end of the first cycle of 4% story drift had deteriorated by 22 kips. The reduction in capacity was 5% below the specimen maximum capacity, which corresponded to 0.96 times the nominal capacity. The beam bottom flanges in compression had buckled out laterally around 1.25-inches. Very little column twisting was observed.

At the end of the first 5% story drift cycle a fracture occurred in the top flange of the west side beam near the center of the RBS. The fracture went completely across the beam flange, and extended down into the beam web about 6.5-inch. The fracture was due to low cycle fatigue as a result of the occurrence of repeated cyclic local flange buckling in the RBS. The fracture initiated from a 0.0232-inch deep punch mark in the RBS that was placed during fabrication. The test was terminated immediately after the fracture occurred. SPEC-2 had deteriorated to 27% below its maximum capacity of 412 kips, which is 0.79 times the nominal capacity of SPEC-2. Photographs of SPEC-2 after testing are shown in Figure 5.6. No cracks were found to initiate near the connection region, including the weld access hole.

Following the completion of the test, the slab was removed from the specimen revealing that a number of the shear studs connecting the floor slab to the main beams had fractured, while the shear studs connecting the floor slab to the transverse floor beams remained intact.

The total plastic drift reached in the first 5% story drift cycle before fracture occurred was 0.04 radians. Similar to SPEC-1, the beams of SPEC-2 accounted for a majority of the specimen plastic story drift. The maximum beam plastic drift was 0.037 radians. The column panel zone contributed more to the total plastic drift than in SPEC-1, with the maximum plastic drift in SPEC-2 equal to 0.013 radians. The column slightly yielded, developing a maximum plastic drift of 0.004 radians. The measured maximum total rotation across the east beam RBS was 0.05 radians.

5.1.3 SPEC-3

The lateral load-story drift (H-θ) and lateral load-plastic drift hysteretic response for SPEC-3 are shown in Figure 5.7. A summary of measured specimen performance results is included in Table 5.1. Cracking of the concrete floor slab of SPEC-3 occurred in the vicinity of the column at the end of 0.375% story drift cycles, which continued to develop and become more extensive throughout the test. Yielding initiated in the beam bottom flanges and in the beam web near the flanges at the RBS at 1.0% story drift. The concrete slab also began to crush against the face of the column flanges and in the region between the column flanges during the cycles of 1.0% story drift. Panel zone yielding was observed to initiate during the story drift cycles of 1.5%. Beam web local buckling occurred in the RBS region during the first cycle of 2% story drift. During the first cycle of 3% story drift beam flange local buckling occurred in the RBS, as the maximum capacity of 407 kips was developed. In the second cycle of 3% story drift the beam web local buckling became more extensive, causing the beam bottom flange when in compression to move laterally and deterioration in specimen capacity to occur. During the cycles of 4% story drift the top flange of the beam at the RBS was observed to begin to move laterally when in compression. The lateral movement was in the opposite direction of the other beam whose bottom flange was in compression. The amplitudes of buckling and lateral movement grew and the capacity of the specimen deteriorated further in the remaining cycles of the test. Both the top and bottom flanges of the beam at the RBS would straighten out when in tension.

Photographs of SPEC-3 at the end of the second cycle of 4% story drift are shown in Figure 5.8. The specimen lateral load capacity at the end of the first cycle of 4% story drift had deteriorated by 32 kips. The reduction in capacity was 8% below the specimen maximum capacity, with the capacity corresponding to a value of 0.93 times the nominal lateral load capacity H_{pn}. Although the beam bottom flanges in compression had buckled out laterally around 1.25 inches, very little column twisting was observed.

During the first cycle of 5% story drift low cycle fatigue cracks were observed to initiate at the edge of the beam flange near the center of the RBS. Under repeated local beam flange buckling, the cracks steadily propagated across the beam bottom flanges of both beams during the remaining cycles of the test in a ductile manner. At the end of the first cycle of 6% story drift the fatigue cracks had caused a ductile tearing of the flange in the RBS of the east beam bottom, which extended almost complete across the flange and up into the web. Ductile tearing also occurred in the bottom flange of the west beam at the RBS. The ductile tearing of the beam flanges had caused the specimen capacity to deteriorate to 40% below its maximum capacity of 407 kips, which is 0.60 times the nominal capacity of SPEC-3. As a result, the test was terminated. Photographs of SPEC-3 after testing are shown in Figure 5.9. No cracks were found to initiate near the connection region, including the weld access hole. The shear studs all appeared to remain intact.

The total plastic drift developed in SPEC-3 during the test was 0.052 radians (see Table 5.1). Similar to SPEC-1 and SPEC-2, the beam accounted for a majority of the plastic story drift. The maximum plastic drift for the beam and panel zone were 0.051 radians and 0.004 radians, respectively. The column yielded slightly, developing 0.002 radians of plastic drift. The measured maximum total rotation across the east beam RBS was 0.056 radians.

5.1.4 SPEC-4

The lateral load-story drift (H-θ) and lateral load-rotation hysteretic response for SPEC-4 are shown in Figure 5.10. A summary of measured specimen performance results is included in Table 5.1. Cracking in the concrete floor slab initiated around the column of SPEC-4 at the end of the cycles of 0.375% story drift and become more extensive throughout the test. At 0.75% story drift minor yielding initiated in the beam bottom flanges at the RBS and near the column face, as well as in the panel zone. The concrete slab started crushing against the faces of the column flanges and in the region between the column flanges at a story drift of 1.0%. The yielding of the beam flange in the RBS and panel zone became more extensive. Minor column flange yielding below the beam bottom flange was observed during the cycles of story drift of 1.5%. Beam web local buckling occurred in the RBS region during the first cycle of 2% story drift, which became more extensive in subsequent cycles. During the 3% story drift cycles beam flange local buckling occurred, as the specimen maximum capacity of 406 kips developed. The beam web local buckling became extensive, causing the beam bottom compression flange to begin to move laterally in the RBS. During the story drift cycles of 4% the beam top flange in the RBS were subsequently observed to begin to move laterally when in compression. The lateral movement was in the opposite direction of the other beam whose bottom flange was in compression. Both the top and bottom flanges of the beam in the RBS would straighten out when in tension. The amplitude of buckling and lateral flange movement grew in subsequent cycles, and the specimen capacity deteriorated. The metal decking was found to locally buckle beneath where extensive floor slab concrete crushing had occurred.

Photographs of SPEC-4 at the end of the second cycle of 4% story drift are shown in Figure 5.11. The specimen capacity at the end of the first cycle of 4% story drift had deteriorated by 32 kips. The reduction in capacity was 8% below the specimen maximum capacity, and equal to a capacity of 0.90 times the nominal lateral load capacity H_{pn}. The beam bottom flanges in compression had moved laterally about 1.25-inches. Very little column twisting was observed.

Low cycle fatigue cracks were found to initiate in the beam flanges near the center of the RBS at 5% story drift. Ductile tearing of the west beam bottom flange at the RBS occurred near the end of the first half cycle of 6% story drift. The tearing occurred where severe local buckling had developed and led to low cycle fatigue. Upon completing the first half cycle of 6% story drift, the ductile tearing of the beam flange caused the specimen capacity to deteriorate to 48% below its maximum capacity of 406 kips, which was equivalent to 0.51 times the nominal lateral load capacity H_{pn} of SPEC-4.

The test was then terminated. Photographs of SPEC-3 after testing are shown in Figure 5.12. No cracks were found to initiate near the connection region, including the weld access hole. All of the shear studs appeared to remain intact.

The total plastic drift reached when the ductile fracture occurred in the first 6% story drift cycle was 0.053 radians. The maximum beam plastic drift was 0.056 radians, and like the other specimens the beam accounted for a majority of the total plastic drift. The maximum plastic drift of the panel zone was 0.008 radians. The column slightly yielded, developing 0.008 radians of plastic drift. The maximum total rotation across the beam in the RBS was 0.068 radians.

5.1.5 SPEC-5

The lateral load-story drift (H-θ) and lateral load-plastic drift hysteretic response for SPEC-5 are shown in Figure 5.13. A summary of measured specimen performance results is included in Table 5.1. Cracking of the concrete floor slab of SPEC-5 occurred in the vicinity of the column during the 0.375% story drift cycles, which continued to develop and become more extensive throughout the test. Yielding initiated in the beam bottom flanges and in the panel zone at 0.75% story drift. Yielding was observed in the beam top flanges and web at the RBS at 1% story drift. The concrete slab began to crush against the face of the column flanges and in the region between the column flanges during the cycles of 1.5% story drift. Beam web local buckling occurred in the RBS region during the first cycle of 3% story drift, at which time the maximum lateral load capacity of 258 kips developed. Minor column flange yielding was observed during the cycles of 3% story drift. During the first cycle of 4% story drift beam flange local buckling occurred in the RBS. The beam web local buckling then became more extensive, causing the beam bottom flange when in compression to move laterally and a deterioration in specimen capacity to occur. Local buckling of the panel zone doubler plate occurred between the plug welds at 4% story drift cycles. During the cycles of 5% story drift the top flange of the beam at the RBS was observed to begin to move laterally when in compression. The lateral movement was in the opposite direction of the other beam whose bottom flange was in compression. Both the top and bottom flanges of the beam at the RBS would straighten out when in tension. The amplitudes of buckling and lateral movement grew, and the capacity of the specimen deteriorated further in the remaining cycles of the test.

Photographs of SPEC-5 at the end of the second cycle of 4% story drift are shown in Figure 5.14. The specimen lateral load capacity at the end of the first cycle of 4% story drift had deteriorated by 12 kips. The reduction in capacity was 5% below the specimen maximum lateral load capacity, with the capacity corresponding to a value of 1.02 times the nominal lateral load capacity H_{pn}. Although the beam bottom flanges in compression had buckled out laterally to approximately 1 inch, very little column twisting was observed.

During the first cycle of 5% story drift low cycle fatigue cracks were observed to initiate at the edge of the beam flange near the center of the RBS (where cyclic local flange buckling had been occurring). A fracture occurred in the east side beam bottom flange of the RBS at the beginning of second cycle of 6% story drift. The fracture occurred near the center of the RBS and extended completely across the beam flange. The fracture was due to low cycle fatigue crack growth as a result of the occurrence of repeated cyclic local flange buckling in the RBS. The test was terminated after the fracture occurred. The capacity of SPEC-5 had deteriorated to 36% below its maximum lateral load capacity of 258 kips, which is 0.69 times the nominal lateral load capacity H_{pn} of SPEC-5. Photographs of SPEC-5 after testing are shown in Figure 5.15. No cracks were found to initiate near the connection region, including the weld access hole. The shear studs all appeared to remain intact.

The maximum total plastic drift developed in SPEC-5 during the test was 0.050 radians (see Table 5.1). Similar to other specimens, the beam accounted for a majority of the plastic story drift. The maximum plastic drift for the beam and panel zone were 0.043 radians and 0.013 radians, respectively. The column yielded slightly, developing 0.002 radians of plastic drift. The measured maximum total rotation across the east beam RBS was 0.056 radians.

5.1.6 SPEC-6

The lateral load-story drift (H-θ) and lateral load-plastic drift hysteretic response for SPEC-6 are shown in Figure 5.16. A summary of measured specimen performance results is included in Table 5.1. Yielding initiated in the beam flanges at the RBS and in the panel zone at 0.75% story drift. The yielding in the beam flanges spread over the length of the RBS region and in the region between the RBS and column flange at 1.5% story drift. The yielding in the panel zone became more extensive, and continued to do so throughout the remainder of the test. Yielding around the safety harness eyebolt hole was observed at 1.5% story drift. The column flanges began to yield at the 2% story drift cycles, with yielding occurring in the column web near the continuity plates during the 3% story drift cycles. Minor beam web local buckling occurred in the RBS region during the first cycle of 3% story drift, however, the magnitude was small and remained so during the 4% story drift cycles. The lateral load continued to increase when the story drift was increased. Neither beam flange local buckling nor beam flange lateral movement were visible, and very little column twisting was observed. The panel zone had developed extensive yielding. Cracks were found to initiate at the root of the beam bottom flange reinforcement fillet welds during the 4% story drift cycles (see Figure 5.17(d)). Yielding in the weld metal and in the HAZ at the ends of the beam web-to-column flange CJP groove welds was observed during 4% story drift cycles.

Photographs of SPEC-6 at the end of the second cycle of 4% story drift are shown in Figure 5.17. The specimen developed a maximum lateral load capacity of 240 kips (during the first 5% story drift), which corresponded to a value of 1.01 times the nominal lateral load capacity H_{pn}. The specimen capacity did not deteriorate until the fracture occurred. The beam RBS bottom flanges in compression remained fairly straight, for beam web local buckling was minor and little column twisting was observed.

A fracture occurred in the west side beam bottom flange HAZ near the weld root at the end of the first 5% story drift cycle. The fracture initiated from the crack at the center of the beam bottom flange reinforcement fillet weld root. The fracture went completely across the beam flange.

As seen in the last column of Table 4.1, SPEC-6 had a weaker panel zone than all the other specimens (the measured value of R_v/V_{pz} was equal to 1.03). It was found in Chapter 3 from the finite element study that RBS connections with a weak panel zone will not develop beam web and flange local buckling, nor a deterioration in capacity.

However, a weak panel zone can raise the ductile fracture potential in the connection region. More discussion is presented in Chapter 7 regarding the effect of the weaker panel zone of SPEC-6 on the specimen performance.

Because the beam local buckling and lateral buckling did not occur during the testing, large cyclic plastic strain demands were imposed on the connection, which caused low cycle fatigue cracks to develop and grow. The lack of beam local and lateral buckling resulted in no deterioration in specimen capacity prior to fracture. The growth of the low cycle fatigue cracks and high stress in the beam flanges eventually caused the fracture. More details about the fracture are discussed in Section 5.2.

The test was terminated at the end of first 5% story drift cycle after the fracture occurred. Photographs of SPEC-6 after testing are shown in Figure 5.18. Low cycle fatigue cracks were also observed at the ends of the beam web CJP groove welds. No cracks were found to initiate in the weld access hole region.

The total maximum plastic drift developed in SPEC-6 during the test was 0.040 radians (see Table 5.1). Unlike the other specimens, the panel zone accounted for a majority of the plastic story drift. This was due to the fact that SPEC-6 had a weaker panel zone and plastic deformation was concentrated in the panel zone. The maximum plastic drift for the beam and panel zone were 0.017 radians and 0.024 radians, respectively. The column yielded slightly, developing 0.004 radians of plastic drift. The measured maximum total rotation across the east beam RBS was 0.014 radians, which is much smaller compared to the other specimens.

After releasing the support and the bracing of the fractured west side beam, SPEC-6 was continued as a one-sided connection test for the remaining loading cycles of 5% and 6% story drift. Figure 5.19 shows the lateral load-story drift hysteresis loops for the testing of SPEC-6 as a one-sided connection. Releasing of the west side beam reduced half of the panel force V_{pz} while the panel zone strength R_v remained unchanged. Hence, the panel zone became relatively stronger to the demand. The east side beam began to locally buckle in the web and flanges immediately after the one-sided connection test started and in the subsequent cycles to failure (see Figure 5.20(a)). The beam flanges developed out-of-plane movement after beam web and flange local buckling (see Figure 5.20(b)). The lateral load capacity began to deteriorate due to the beam local and lateral buckling. The low cycle fatigue crack at the center of the east beam bottom flange reinforcement fillet weld, which was observed in earlier cycles (during the two-sided connection test), became stable and didn't propagate to cause any fracture. Fracture occurred in the beam top flange near the center of the RBS and went across the width of the flange (see Figure 5.20(c)), and penetrated into the web about 1½". This fracture was due to low cycle fatigue crack growth causing by cyclic local flange buckling in the RBS, similar to that observed in the other test specimens.

The yielding around the safety harness eyebolt hole did not become any more extensive during the testing of SPEC-6 as a one-sided connection (see Figure 5.20(d)). This is due to the fact that the lateral load capacity of the specimen deteriorated, causing the stress around the safety harness eyebolt hole to reduce.

5.2. Fracture Surfaces

After the testing was completed, the fractured sections of the RBS of SPEC-1 (east beam bottom flange), SPEC-2 (west beam top flange) and SPEC-6 (west beam bottom flange in HAZ near the beam flange CJP groove weld) were removed to examine their fracture surface under a scanning electron microscope (A summary of all photographs from this examination is given in Appendix F). Selected photographs of the fracture surfaces of SPEC-1 and SPEC-2 are shown in Figure 5.21.

In SPEC-1, the fracture across the width of the beam flange was initiated from low cycle fatigue crack growth. The crack length was rather small before the crack went into cleavage fracture. In SPEC-2, a low cycle fatigue crack was initiated at a punch mark placed during fabrication. After a small amount of crack growth, the crack went into cleavage fracture and abruptly propagated across the width of the beam flange. The Charpy V-notch toughness of the base metal in the RBS of SPEC-2 after testing is compared to the elastic material at the end of the beam near the reaction in Figure 5.22. The comparison shows that the toughness of the base metal has degraded due to the cyclic plasticity demand in the RBS, causing it to be more susceptible to cleavage fracture, particularly near the edge of the flange. A comparison of the measured stress-strain relationships from coupon tests of the base metal in the RBS after testing with virgin base metal from coupon tests is shown in Figure 5.23. The comparison shows that the steel in RBS region went through large amount of plasticity during the testing of SPEC-2, causing the steel ductility capacity in the RBS to be dramatically reduced.

Photographs of the fracture surface in west side beam bottom flange of SPEC-6 are shown in Figure 5.24. The fracture originated in the center of the weld root, where small weld defects (porosity, fish-eyes) were found (see Figure 5.24(e)). Low cycle fatigue cracks grew as the specimen was cyclically loaded. The fracture surface can be divided into two parts. One side appeared to be ductile fracture in the HAZ, see left-side, Figure 5.24(a). The fracture surface was inclined and parallel to the fusion line. The other side appeared to be a cleavage fracture which extended into the base metal, where the chevron marks were visible, see right side, Figure 5.24(b). The fracture surface was vertical and right to the principal stress in the flange. Part of the ductile fracture surface was removed (Figure 5.24(d)) and examined under the scanning electron microscope, SEM (Figure 5.24(f)), where the presence of small dimples shows the characteristics of a ductile fracture surface.

After the completion of the test of the SPEC-6, the center portion of east side beam flange was removed (see Figure 5.25), and the cut section was polished and nital etched to investigate the crack growth. The beam local and lateral buckling that occurred resulted in a deterioration in specimen capacity, which arrested the crack growth.

As noted in Chapter 4, the beam sections of SPEC-1 and SPEC-2 were both rolled from A572 Grade 50 steel, while the beams of the remaining specimens were fabricated from A992 steel. The A992 steel of the beams for SPEC-3 and SPEC-4 was produced from a different mill than the A572 Grade 50 steel of the beams for SPEC-1 and SPEC-2 and the A992 steel of the beams for SPEC-5 and SPEC-6. The beams of SPEC-3 and SPEC-4 did not go into cleavage fracture.

Table 5.1 – Summary of Connection Specimen Performance

Specimen		SPEC-1	SPEC-2	SPEC-3	SPEC-4	SPEC-5	SPEC-6
Peak Actuator Force (kips)		411	412	407	406	258	240
Maximum Total Drift (% rad.)		5.0	5.0	6.0	6.0	6.0	5.0
Maximum Total Plastic Drift (% rad.)		4.3	4.0	5.2	5.3	5.0	4.0
Beam Maximum Plastic Drift (% rad.)		3.8	3.7	5.1	5.6	4.3	1.7
Panel Zone Maximum Plastic Drift (% rad.)		0.6	1.3	0.4	0.8	1.3	2.4
Column Maximum Plastic Drift (% rad.)		0.4	0.4	0.2	0.8	0.2	0.4
Accumulated Total Plastic Drift (% rad.)		78.4	66.6	109	98.0	107	60.7
Maximum Total Rotation Across East Beam RBS (% rad.)		4.3	5.0	5.6	6.8	5.6	1.4
Beam Plastic Moment $\mathbf{M_p}^*$ (k-in.)	East Beam	29,216	29,326	31,835	32,363	16,950	17,001
	West Beam	29,203	29,519	32,060	32,522	16,997	16,948
Maximum $\mathbf{M_f/M_p}^*$ (M_f at Column Face)	East Beam	0.95	1.00	0.97	0.92	1.21	1.01
	West Beam	1.03	1.10	1.12	1.03	1.19	1.03
Total Accumulated Dissipated Energy (k-in.)		29,536	27,203	40,086	36,621	28,230	16,232
Location of Fracture (All fractures occurred in the RBS except SPEC-6)		Beam bottom flanges	Beam top flanges	Beam bottom flange	Beam bottom flange	Beam bottom flange	Beam bottom flange HAZ

Note: 1. M_f = Beam moment at column face;
M_p = Beam plastic moment capacity based on measured dimensions and material properties;
2. Drift values are based on measurements at the end of test.

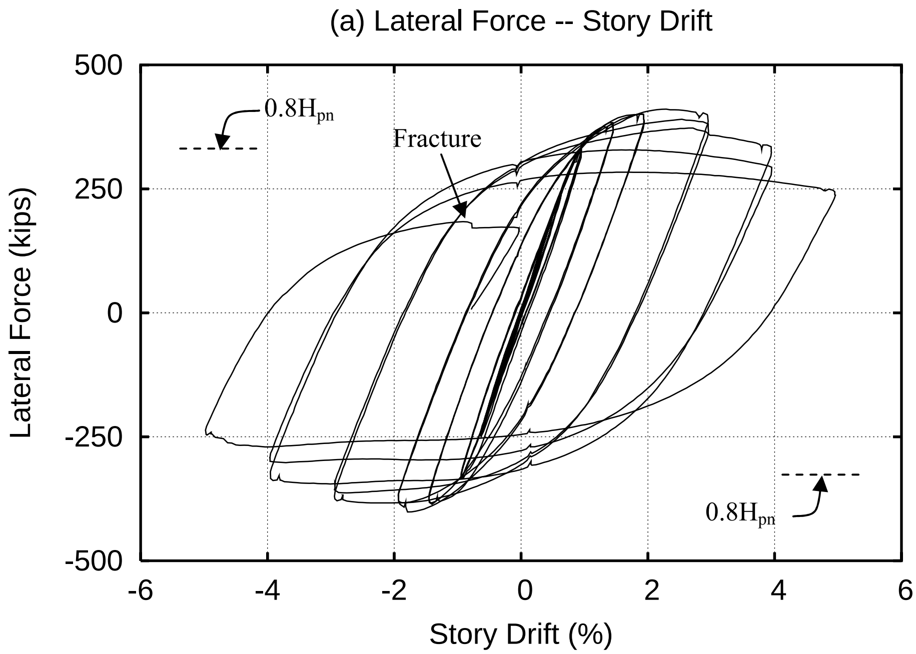

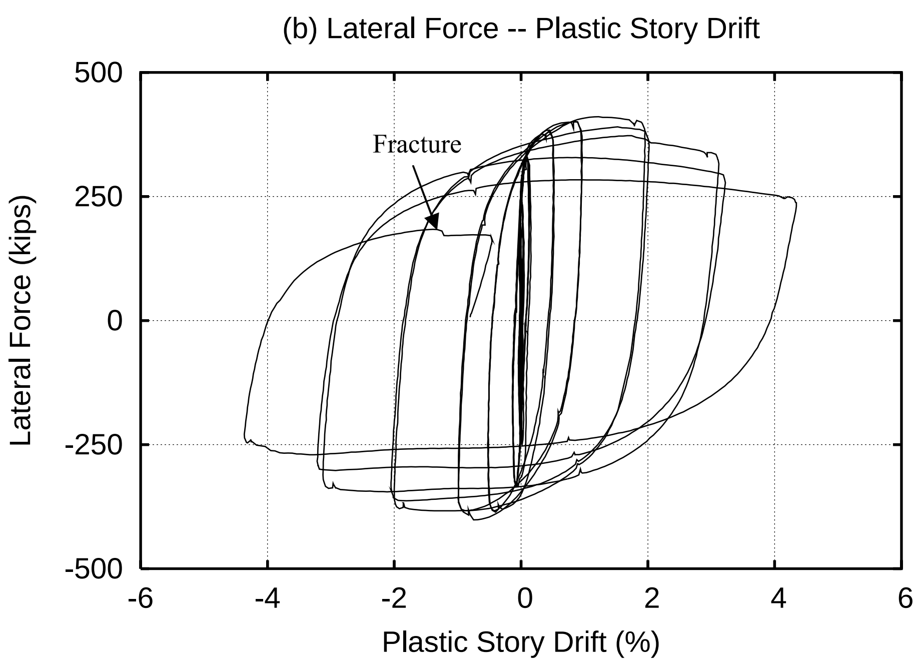

Figure 5.1 – Test Results of SPEC-1 (Continued)

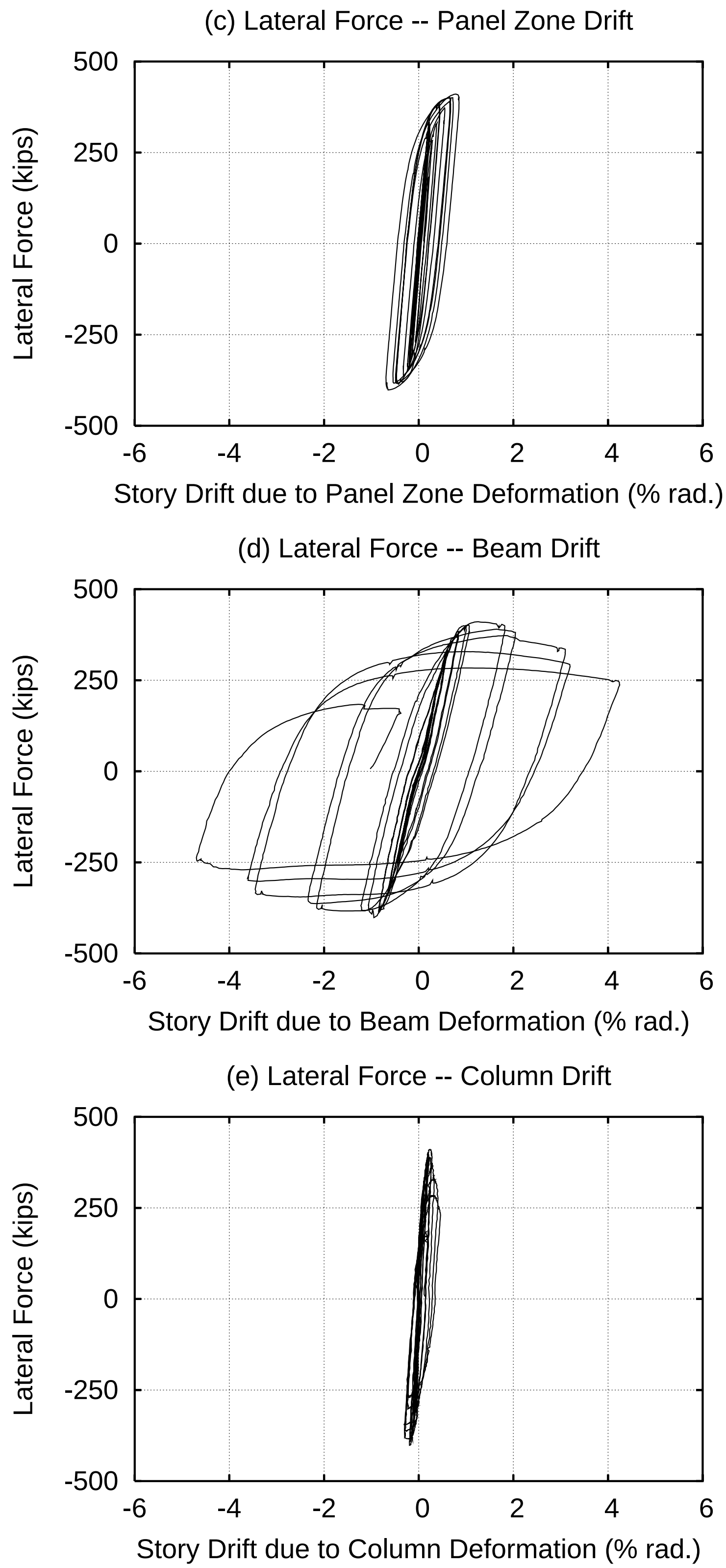

Figure 5.1 – Test Results of SPEC-1

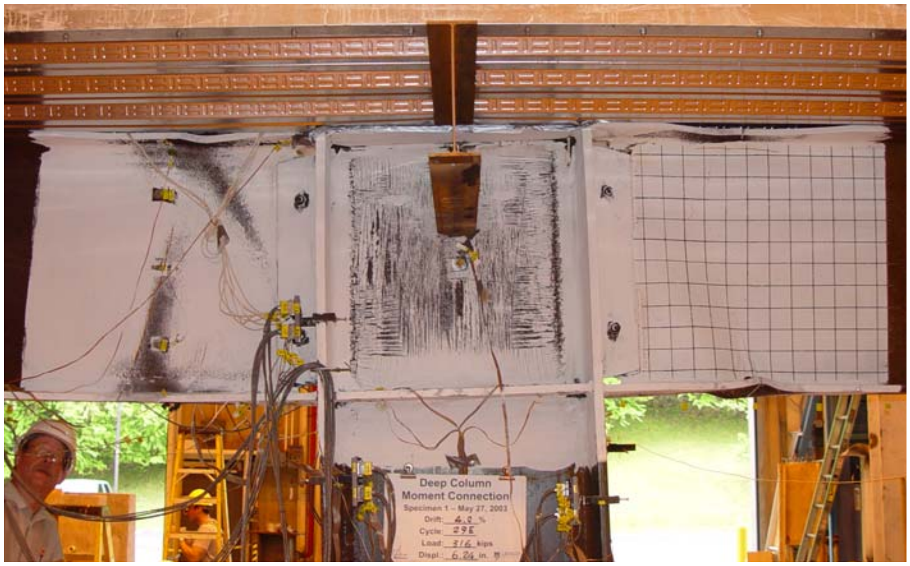

(a) Yielding and buckling in connection region

(b) RBS bottom flange out-of-plane movement

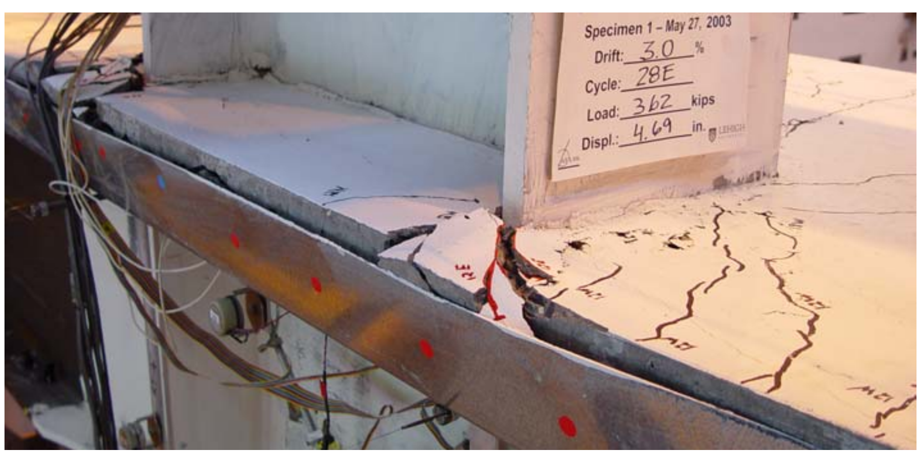

(c) Slab concrete crushing near column flanges
(Picture taken at 3% story drift, at 4% story drift slab damage was similar)

Figure 5.2 – Photos of SPEC-1 at 4% story drift

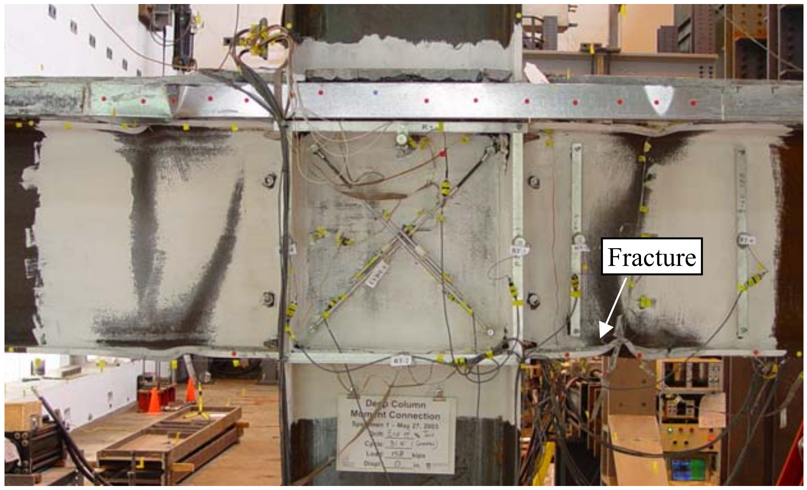

(a) Pronounced beam yielding and local buckling at RBS; fracture in the east beam bottom flange at center of RBS

(b) Beam Web and Flange Local Buckling

Figure 5.3 – Photos of SPEC-1 after Testing (Continued)

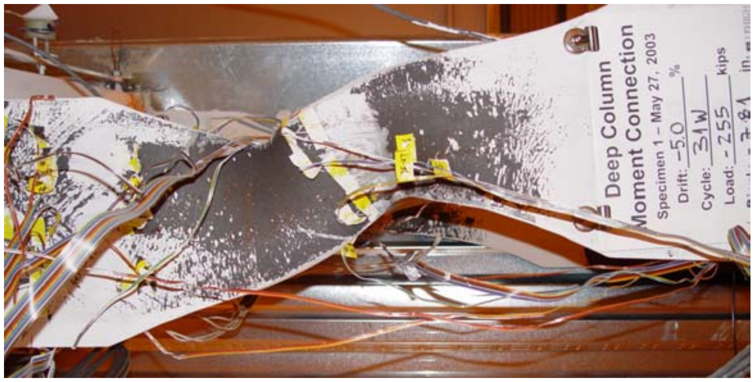

(c) RBS bottom flange out-of-plane movement


(d) Close-up of east beam flange fracture at RBS


(e) Concrete composite floor slab cracking

Figure 5.3 – Photos of SPEC-1 after Testing

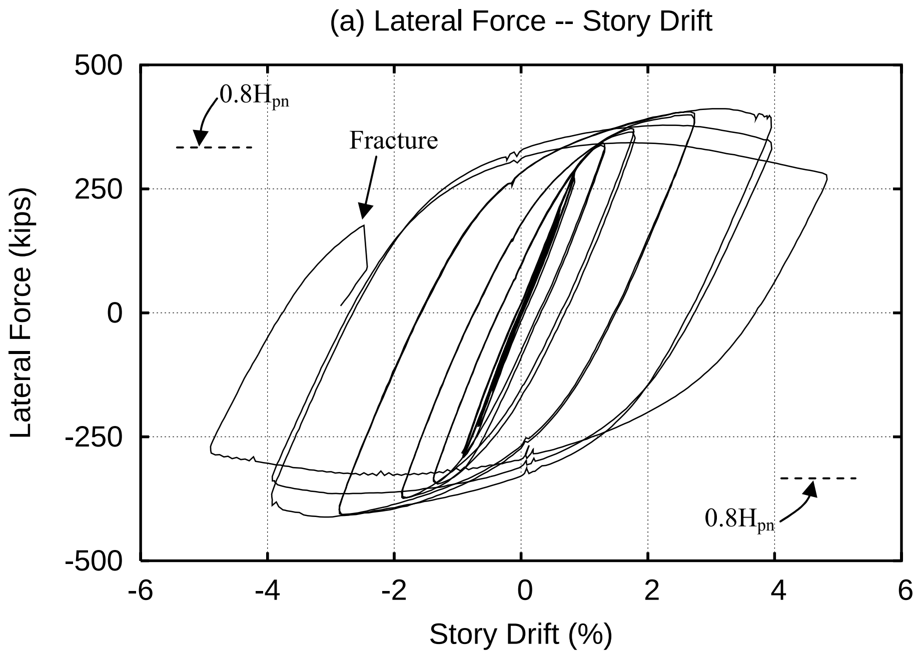

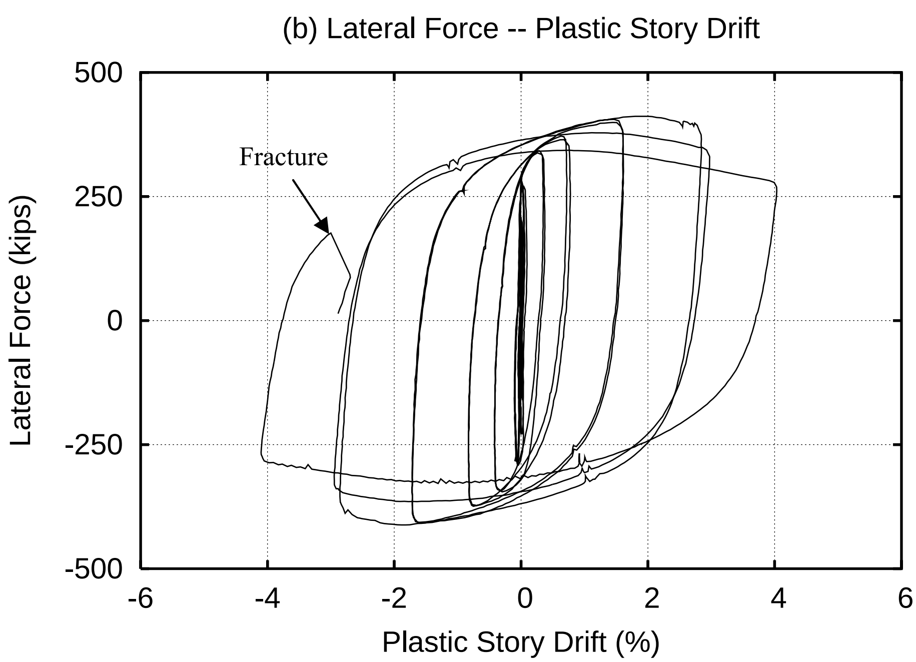

Figure 5.4 – Test Results of SPEC-2 (Continued)

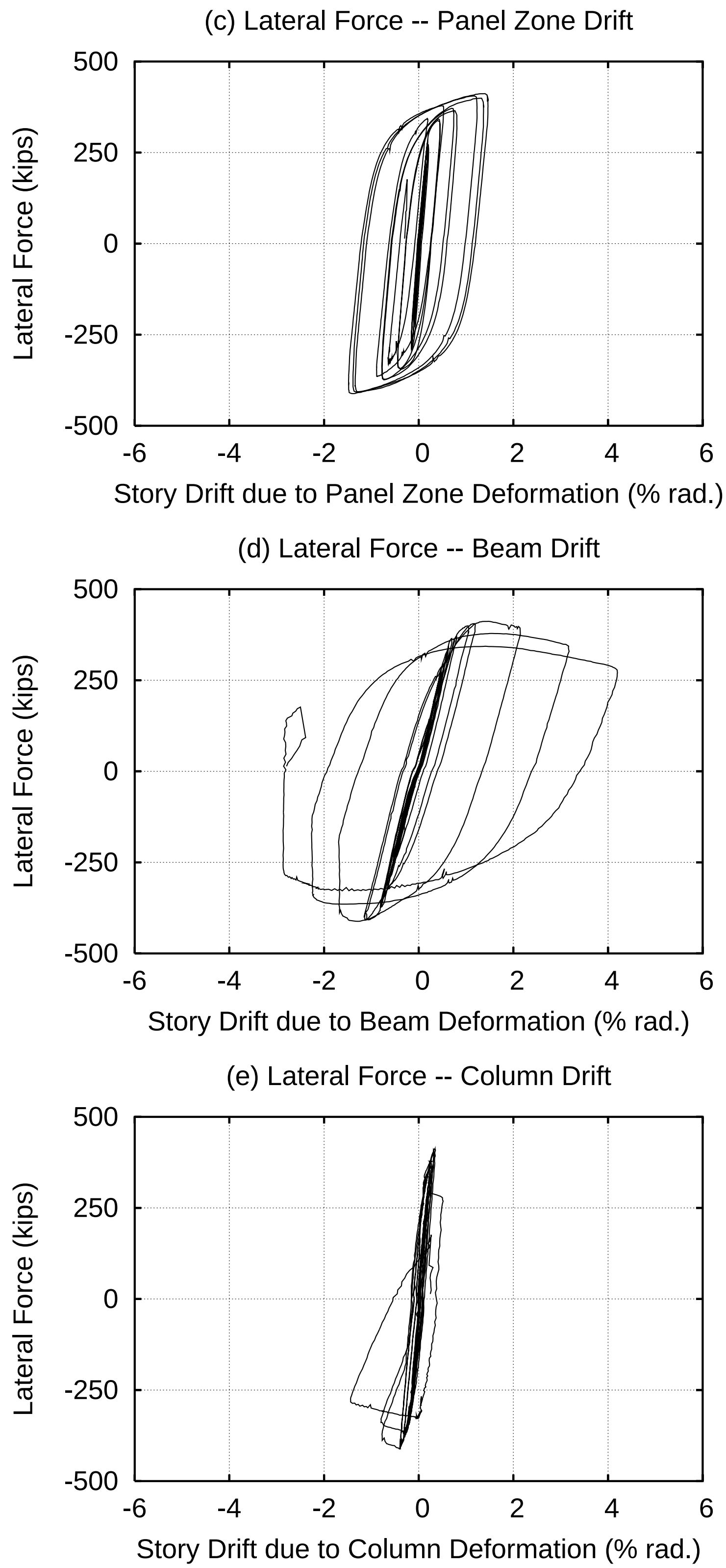

Figure 5.4 – Test Results of SPEC-2

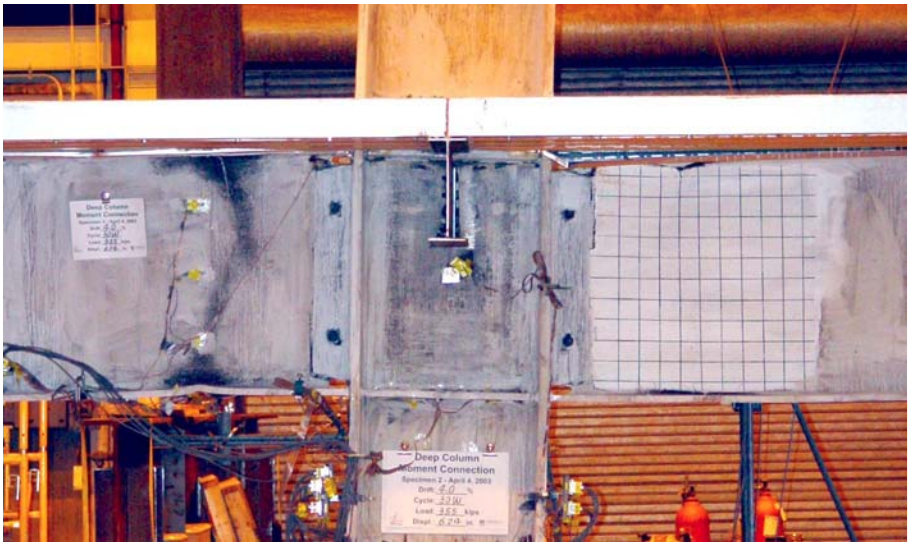

(a) Yielding and buckling in connection regions

(b) RBS bottom flange out-of-plane movement

(c) Slab concrete crushing near column flanges

Figure 5.5 – Photos of SPEC-2 at 4% drift

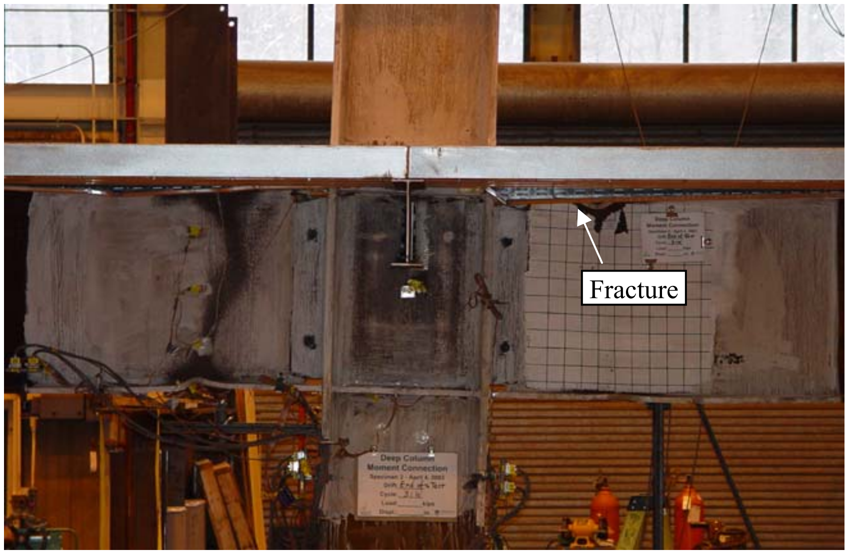

(a) Pronounced beam yielding and local buckling at RBS; fracture in the west beam top flange at center of RBS

(b) Beam web and flange local buckling

Figure 5.6 – Photos of SPEC-2 after Testing (Continued)

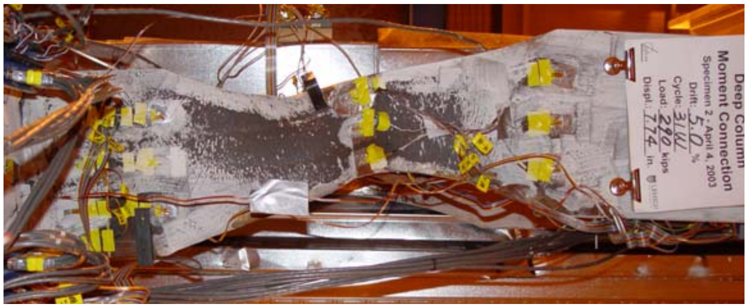

(c) RBS bottom flange out-of-plane movement

(d) Close-up of beam flange fracture at RBS

(e) Concrete composite floor slab cracking

Figure 5.6 – Photos of SPEC-2 after Testing

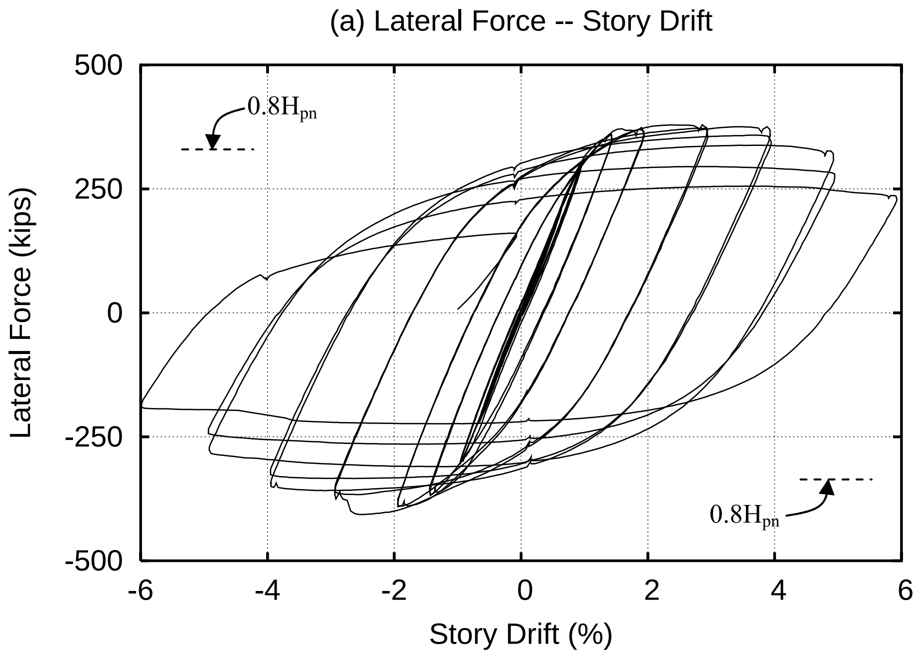

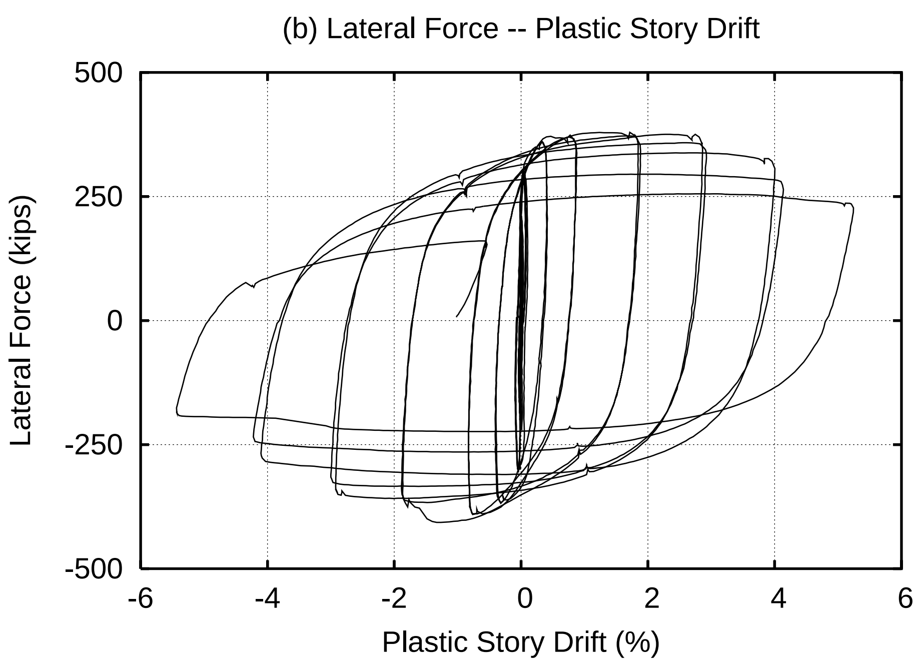

Figure 5.7 – Test Results of SPEC-3 (Continued)

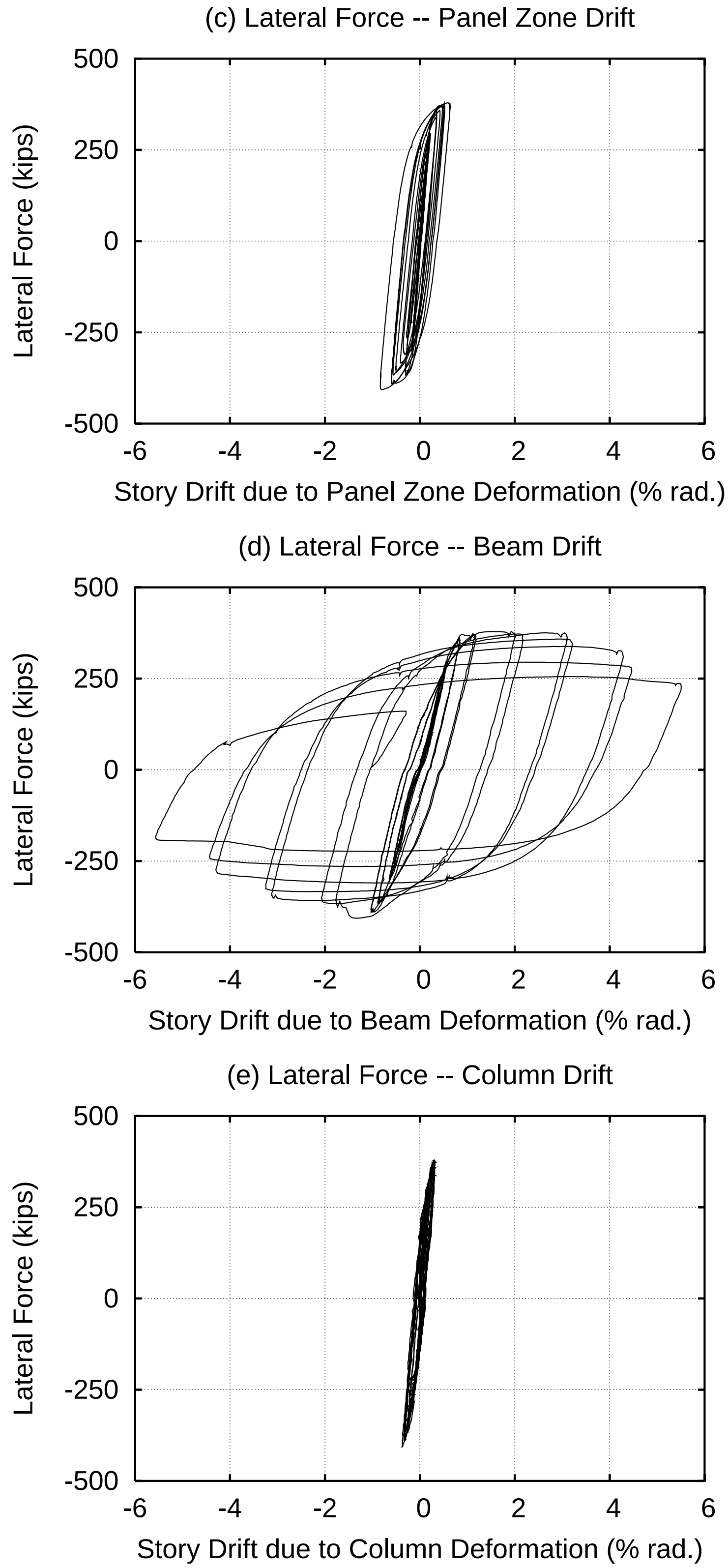

Figure 5.7 – Test Results of SPEC-3

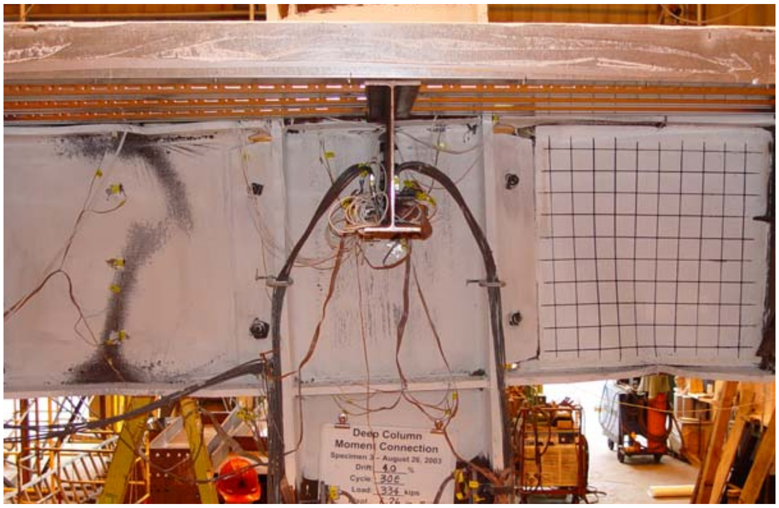

(a) Yielding and buckling in connection region

(b) RBS out-of-plane movement

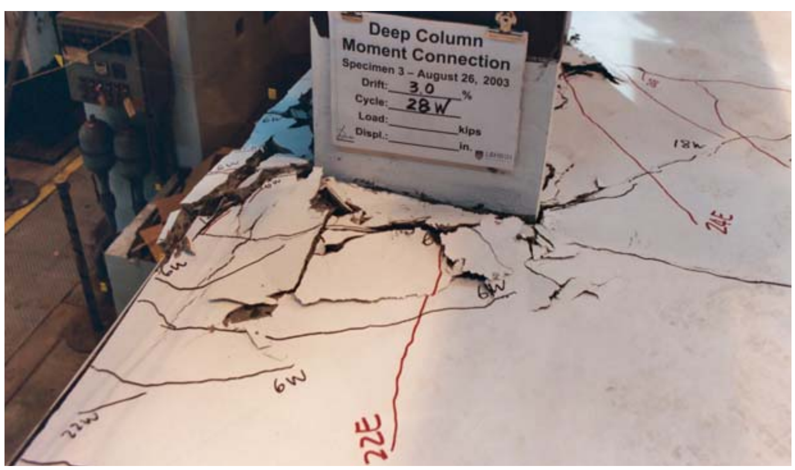

(c) Slab concrete crushing near column flanges
(Picture taken at 3% story drift, at 4% story drift slab damage was similar)
Figure 5.8 – Photos of SPEC-3 at 4% story drift

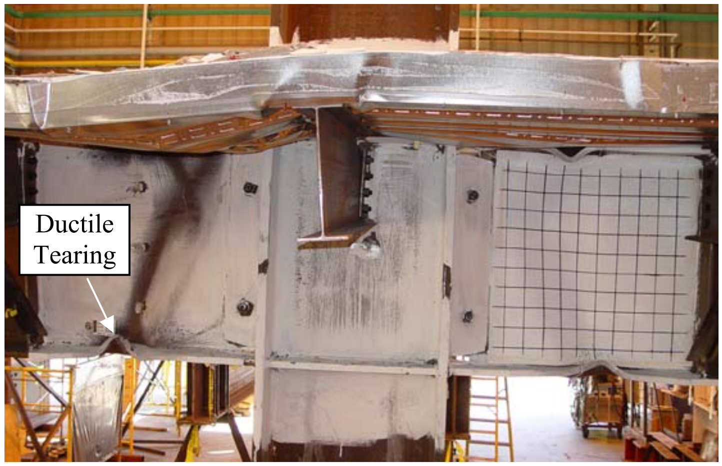

(a) Pronounced beam yielding and local buckling at RBS; Ductile tearing in the east beam bottom flange at center of RBS

(b) Beam web and flange local buckling

(c) RBS bottom flange out-of-plane movement

Figure 5.9 – Photos of SPEC-3 after Testing (Continued)

(d) Ductile tearing of east beam bottom flange at RBS

(e) Low cycle fatigue crack growth in west beam bottom flange at RBS

(e) Concrete composite floor slab cracking and crushing

Figure 5.9 – Photos of SPEC-3 after Testing

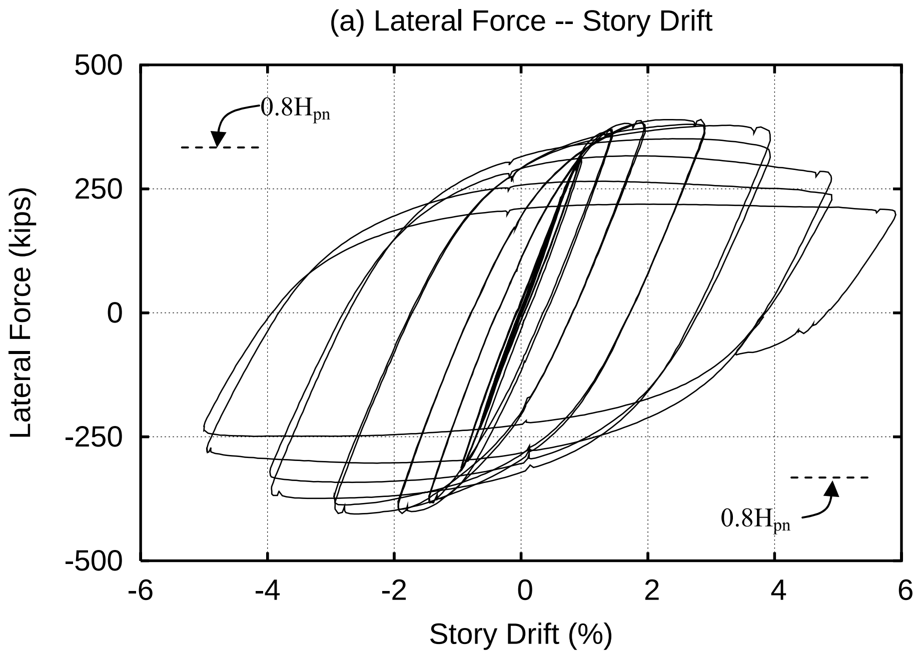

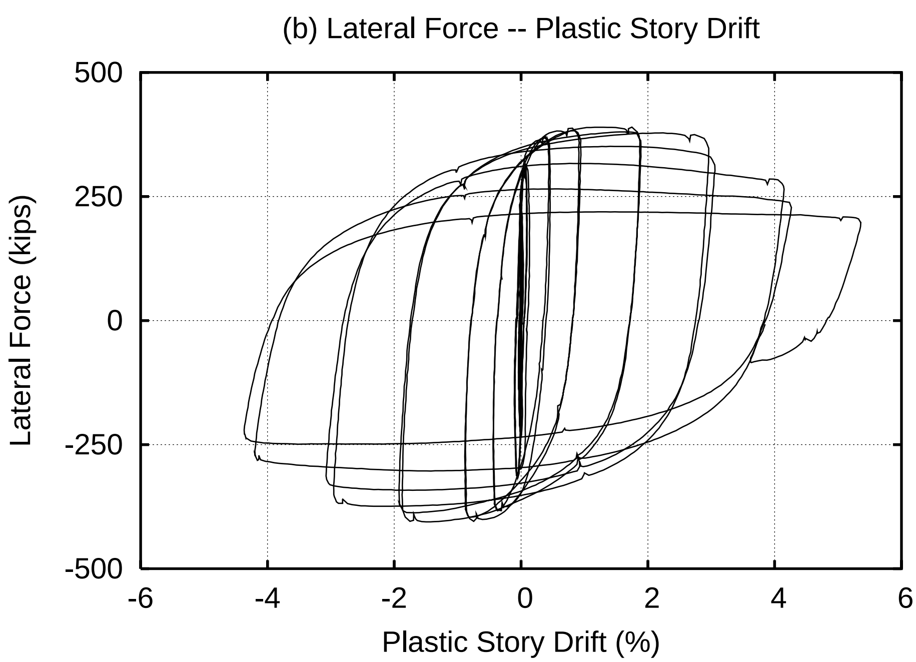

Figure 5.10 – Test Results of SPEC-4 (Continued)

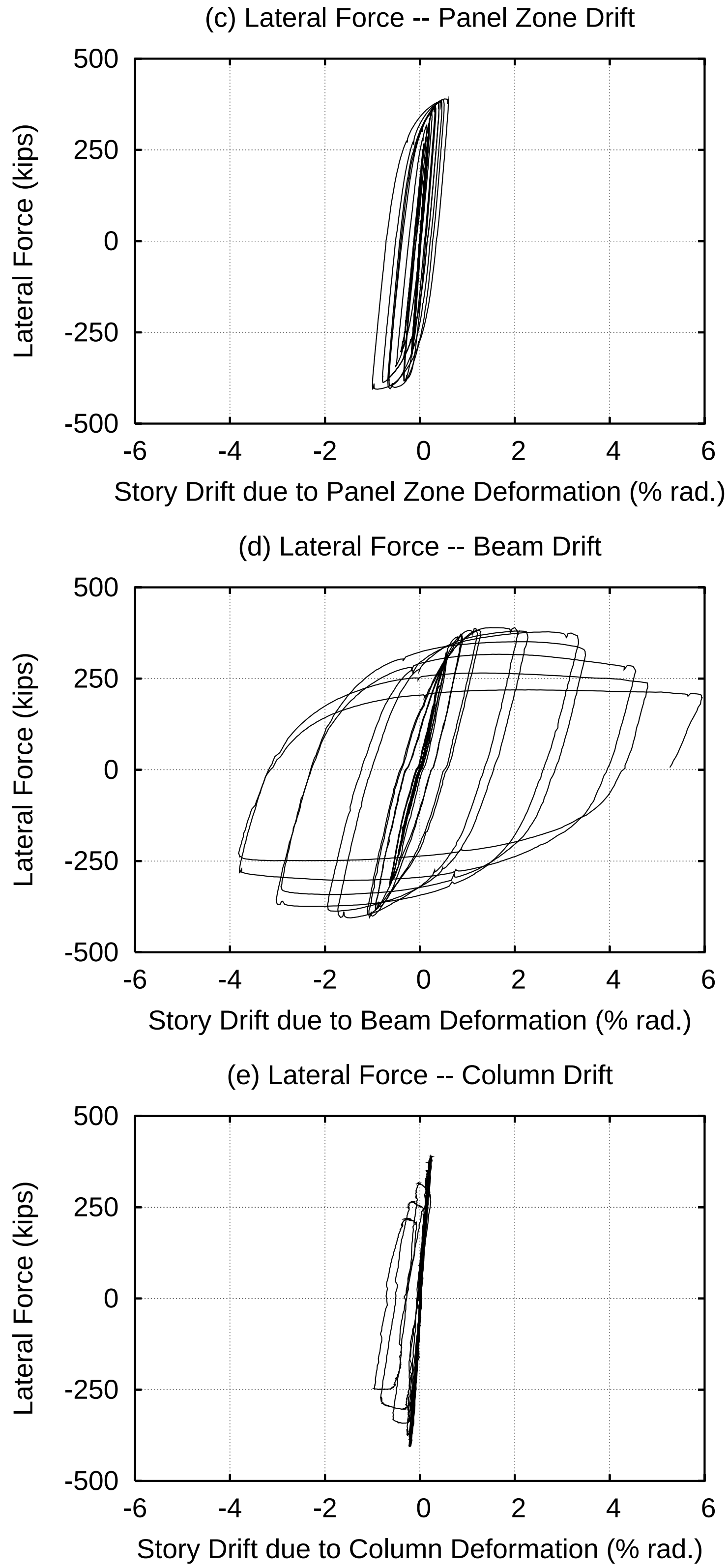

Figure 5.10 – Test Results of SPEC-4

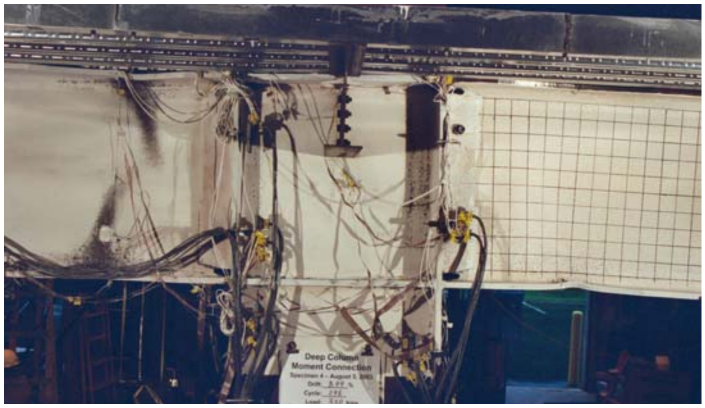

(a) Yielding and local buckling in connection region

(b) RBS bottom flange out-of-plane movement

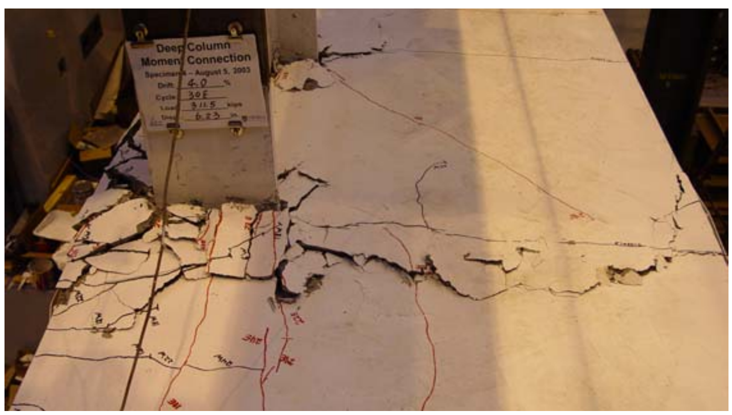

(c) Slab concrete crushing near column flanges

(d) Deck local buckling

Figure 5.11 – Photos of SPEC-4 at 4% story drift

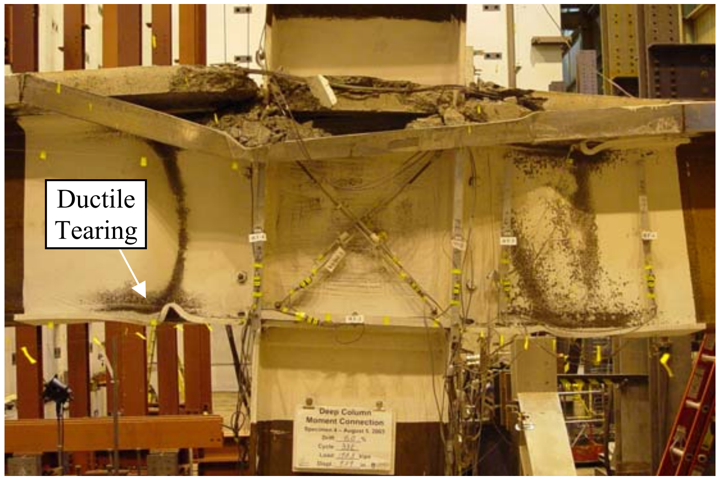

(a) Pronounced beam yielding and local buckling at RBS; Ductile tearing in the west beam bottom flange at center of RBS

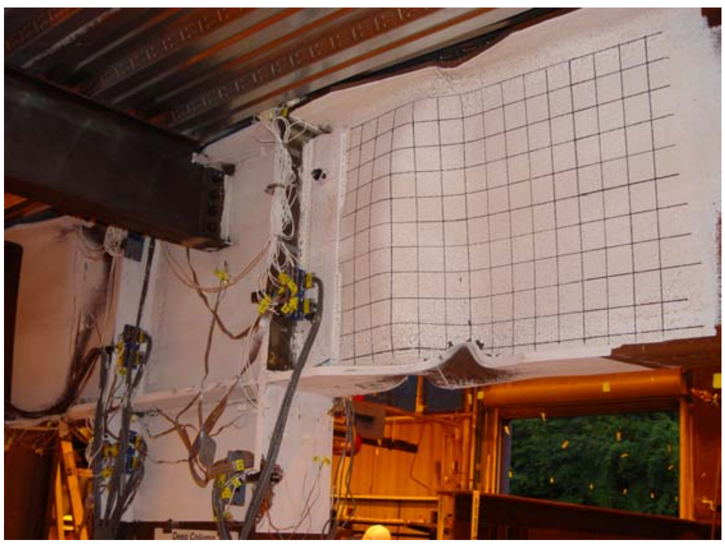

(b) Beam web and flange local buckling

(c) RBS bottom flange out-of-plane movement

Figure 5.12 – Photos of SPEC-4 after testing (Continued)

(c) Ductile tearing of west beam bottom flange at RBS

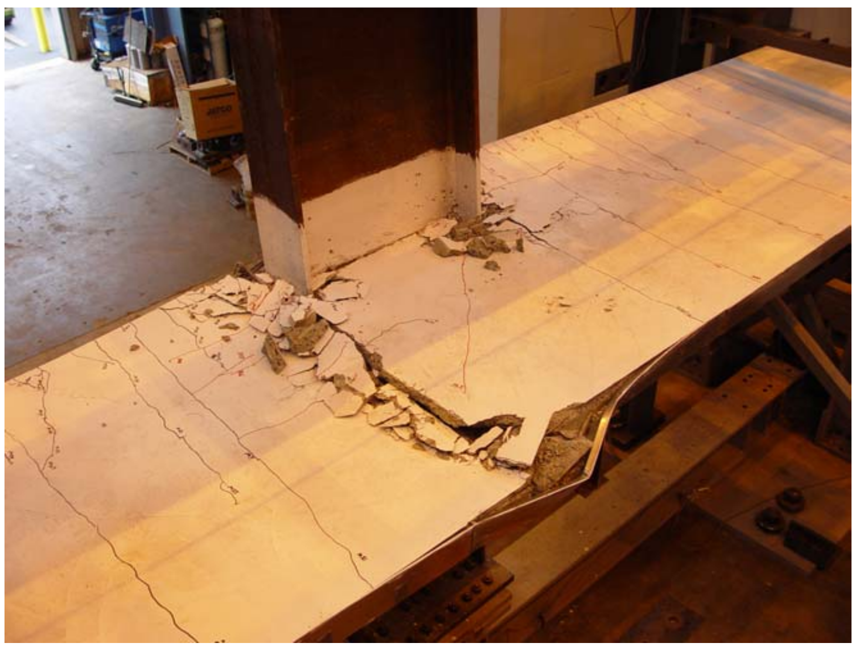

(d) Concrete composite floor slab cracking and crushing

Figure 5.12 – Photos of SPEC-4 after testing

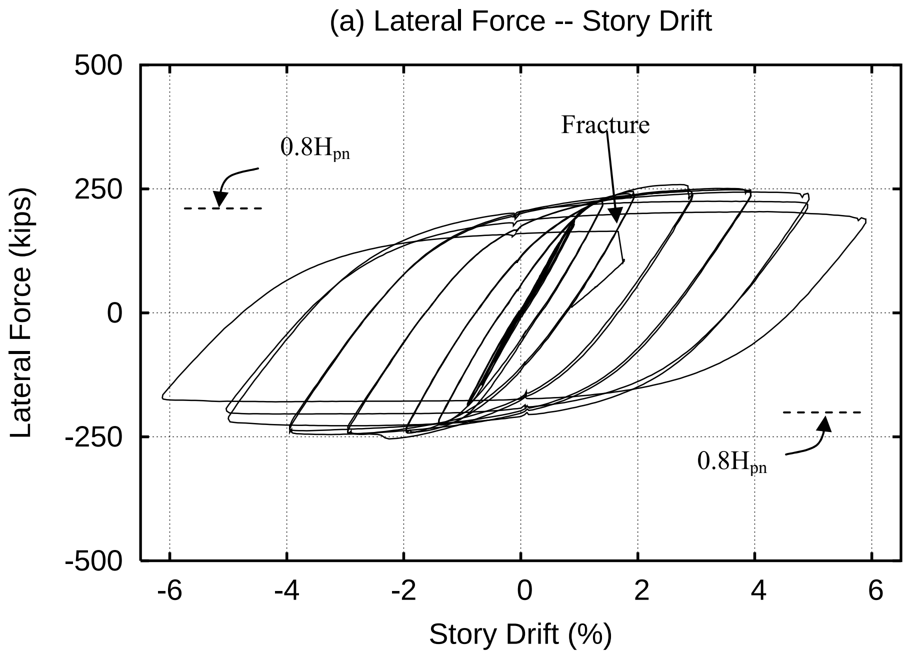

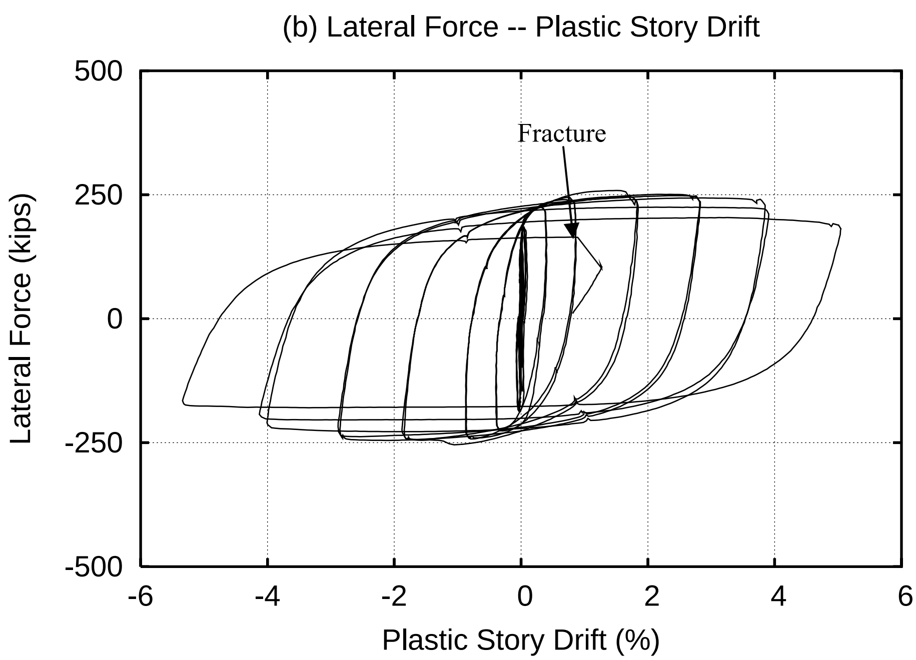

Figure 5.13 – Test results of SPEC-5 (Continued)

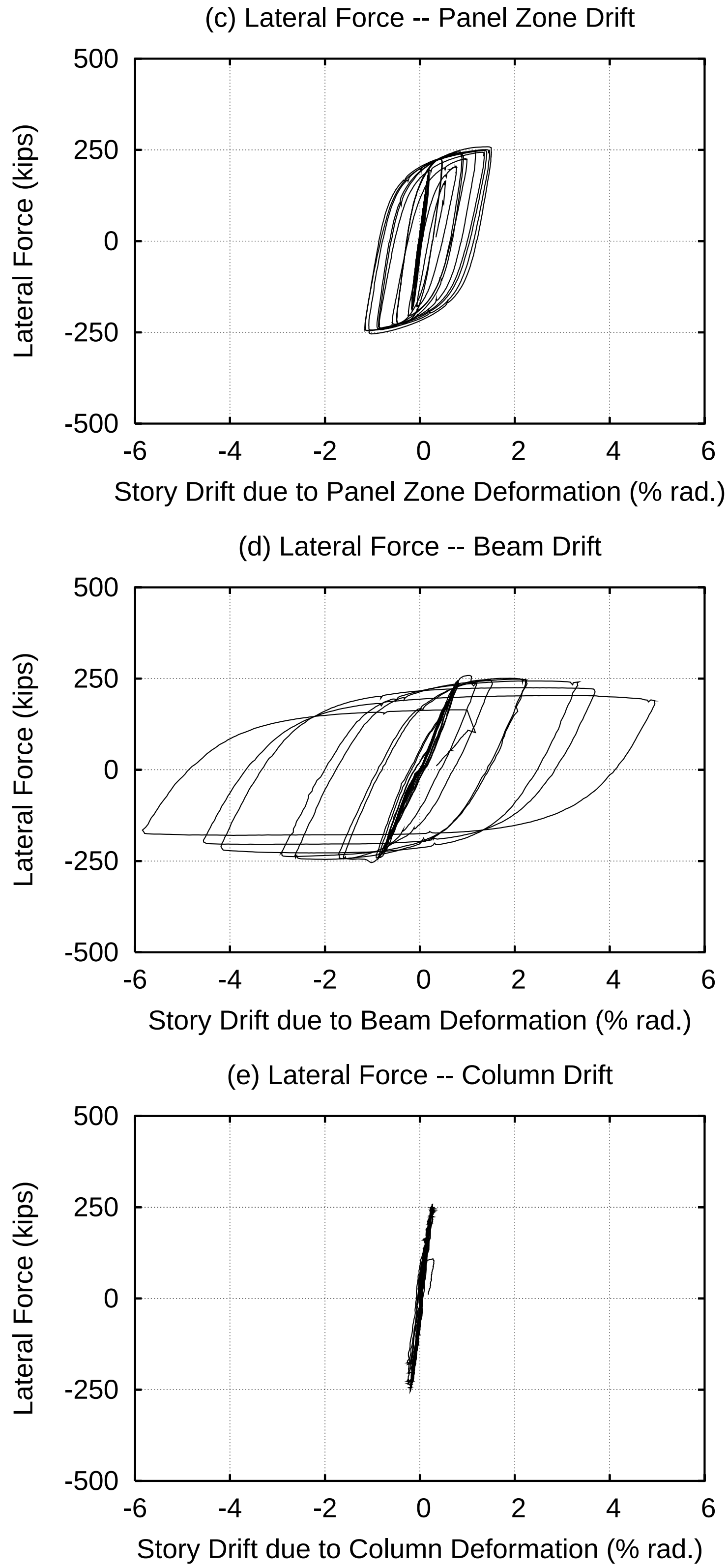

Figure 5.13 – Test results of SPEC-5

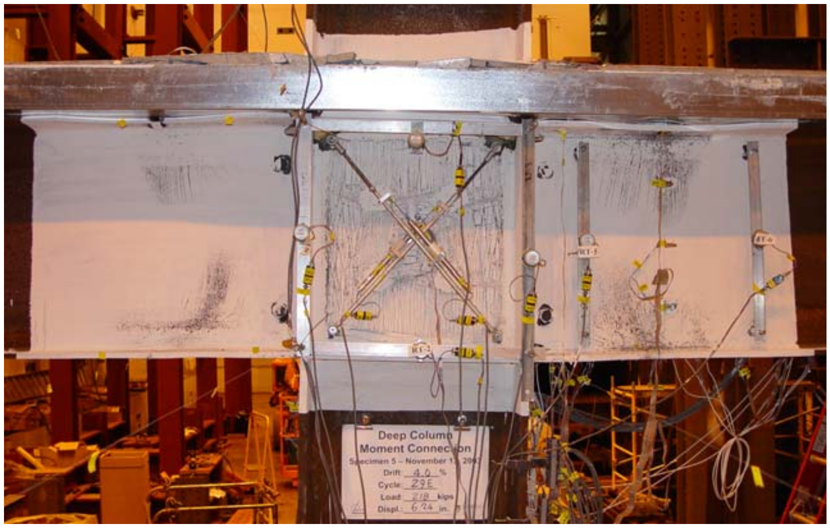

(a) Yielding and local buckling in connection region

(b) RBS bottom flange out-of-plane movement

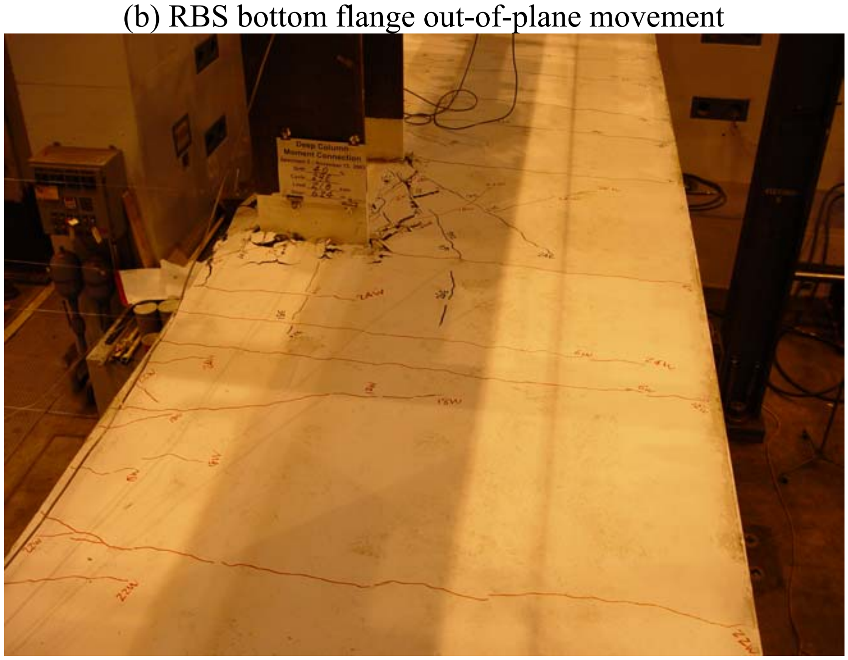

(c) Floor slab concrete cracking and crushing

Figure 5.14 – Photos of SPEC-5 at 4% story drift

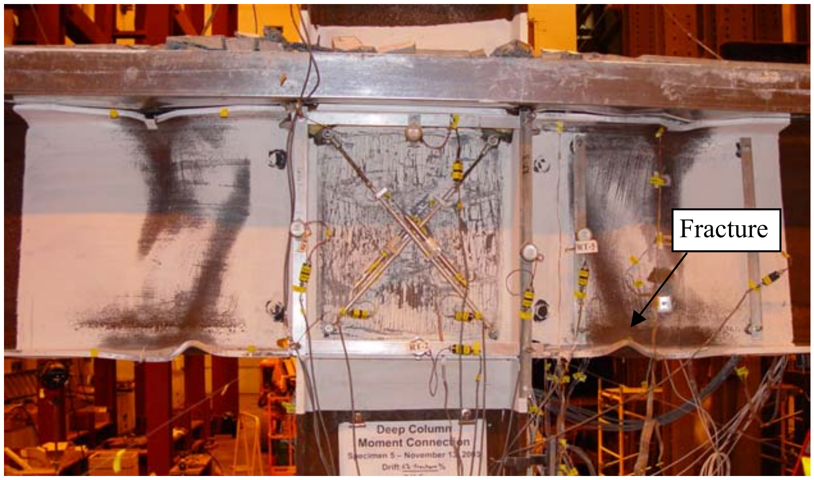

(a) Pronounced beam yielding and local buckling at RBS; fracture in the east beam bottom flange at center of RBS

(b) Beam web and flange local buckling

(c) RBS bottom flange out-of-plane movement

Figure 5.15 – Photos of SPEC-5 at the end of test (continued)

(d) Fracture of east beam bottom flange near the center of RBS

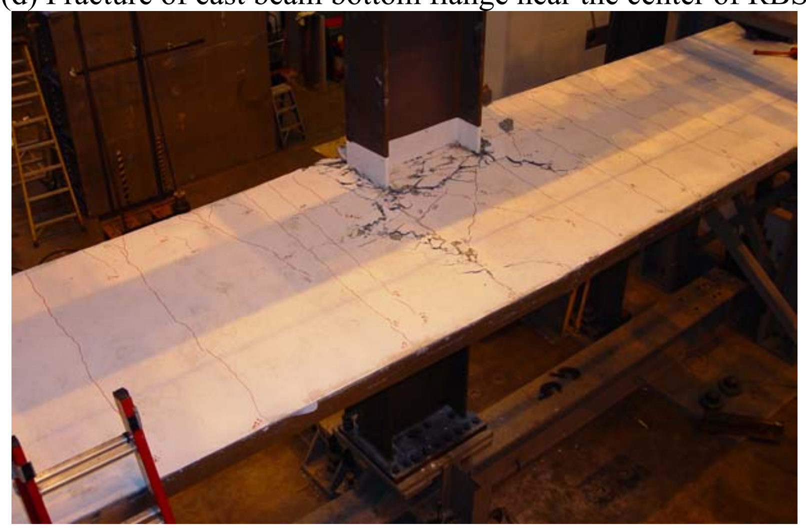

(e) Overall view of floor slab after test

Figure 5.15 – Photos of SPEC-5 at the end of test

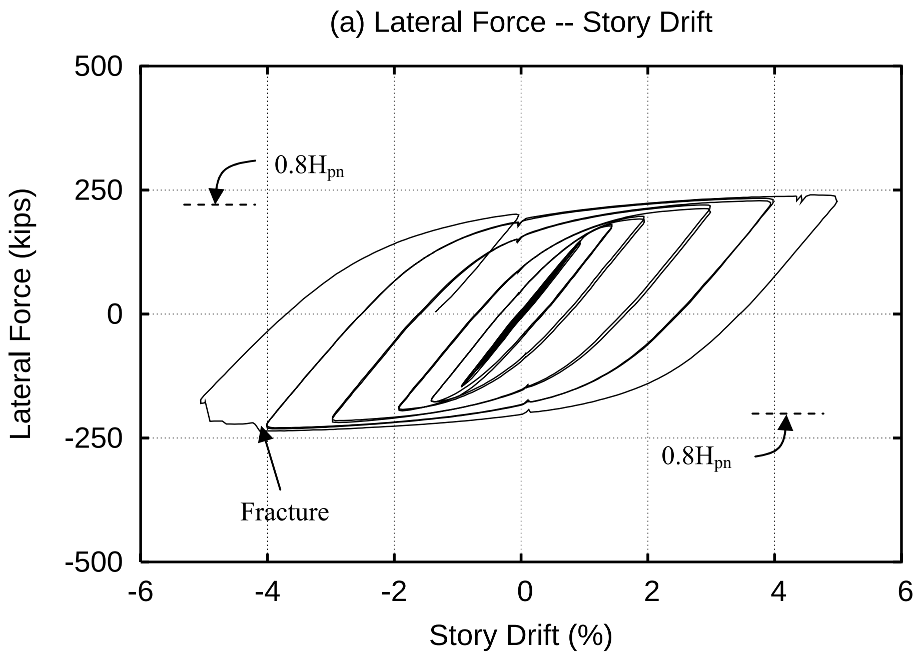

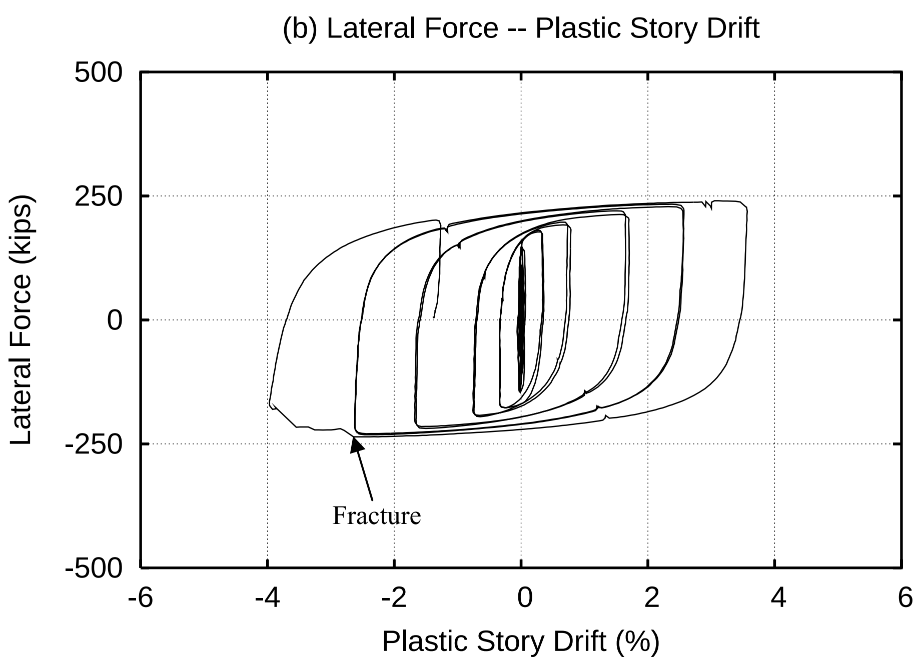

Figure 5.16 – Test results of SPEC-6 (continued)

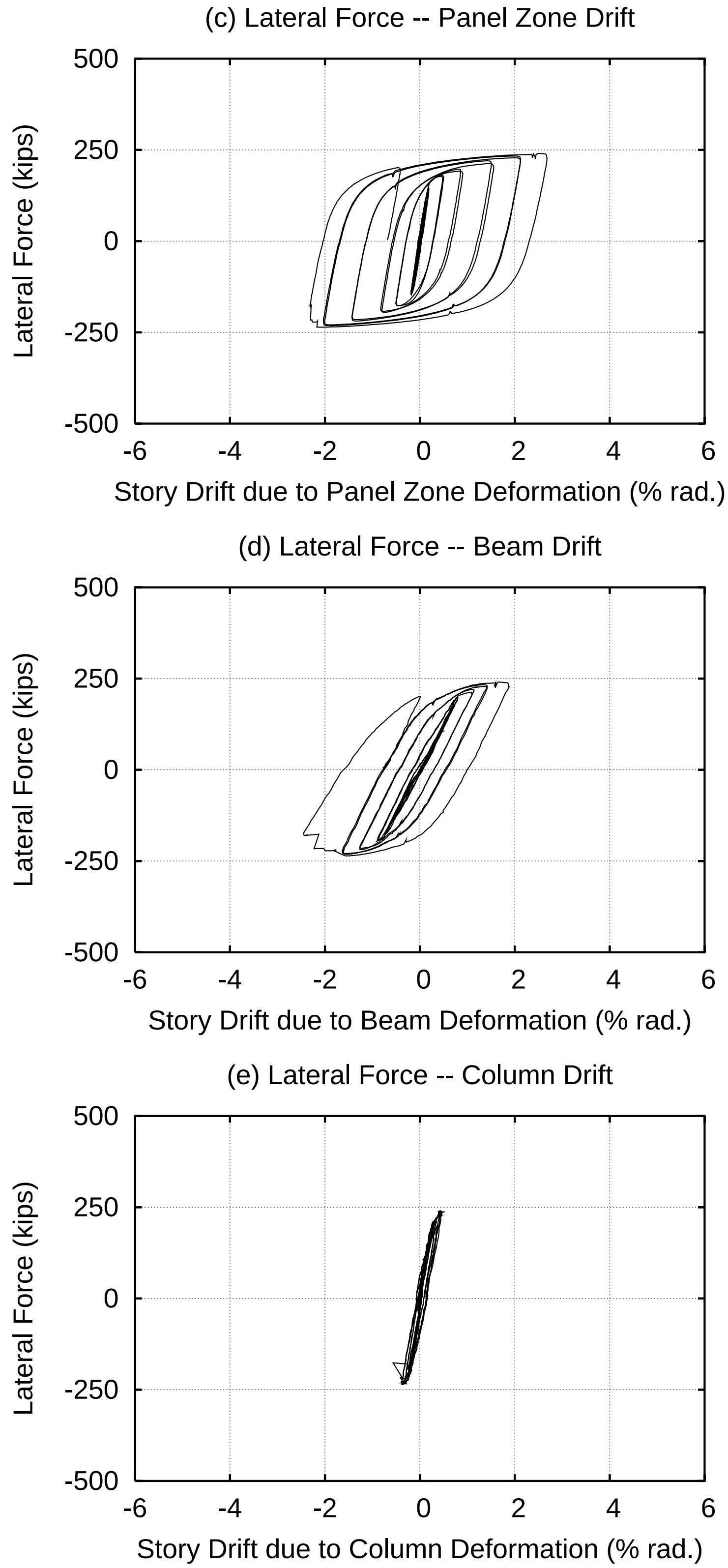

Figure 5.16 – Test results of SPEC-6

(a) Yielding in the connection region

(b) RBS bottom flange out-of-plane movement

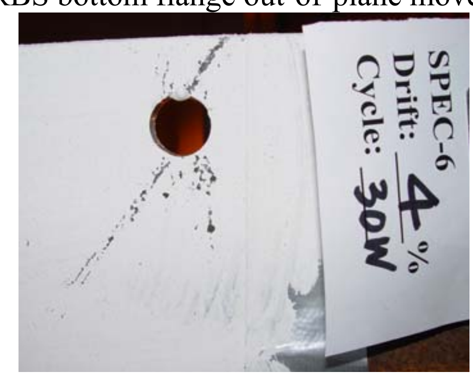

(c) Yielding around the safety harness eyebolt hole

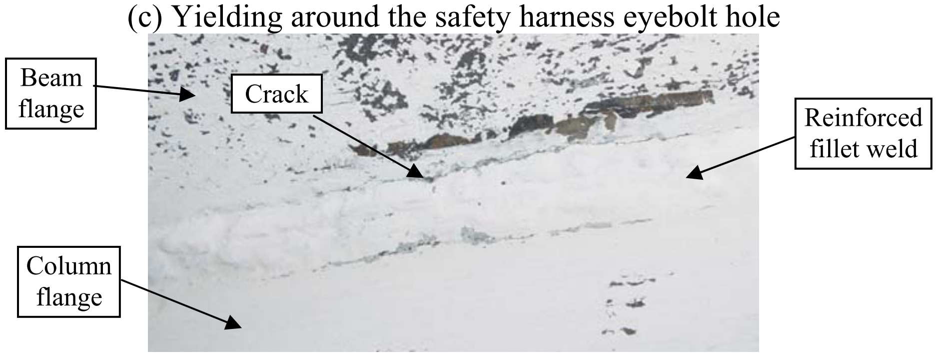

(d) Crack developing near the center of the beam bottom flange reinforced fillet weld root

Figure 5.17 – Photos of SPEC-6 at 4% story drift

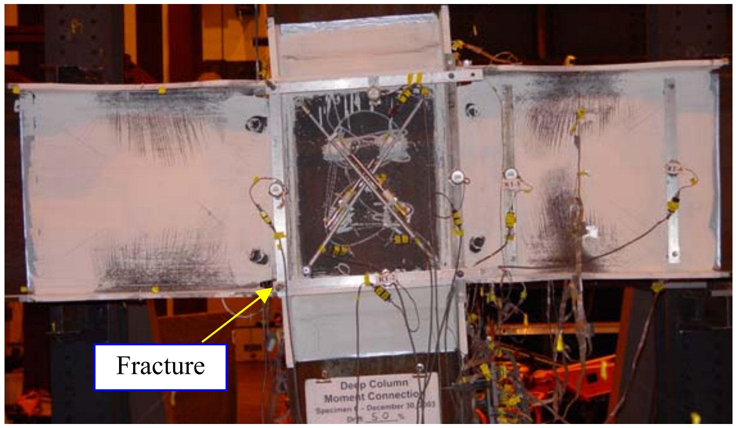

(a) Pronounced yielding in panel zone and connection region

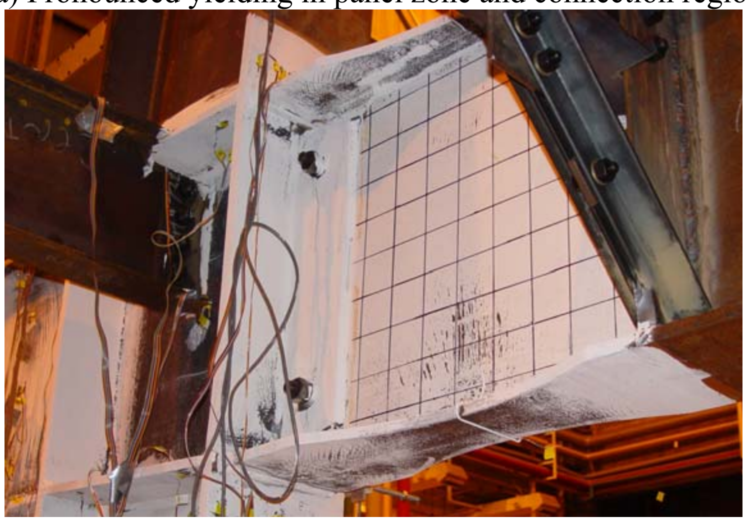

(b) Beam web and flange remained straight

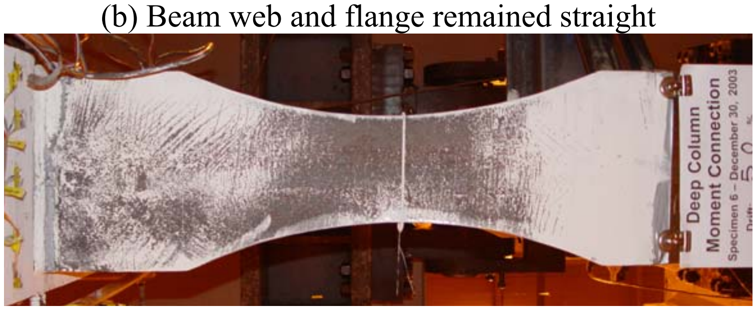

(c) Beam flange at RBS remained straight

Figure 5.18 – Photos of SPEC-6 at the end of test (continued)

(d) Yielding around the safety harness eyebolt hole

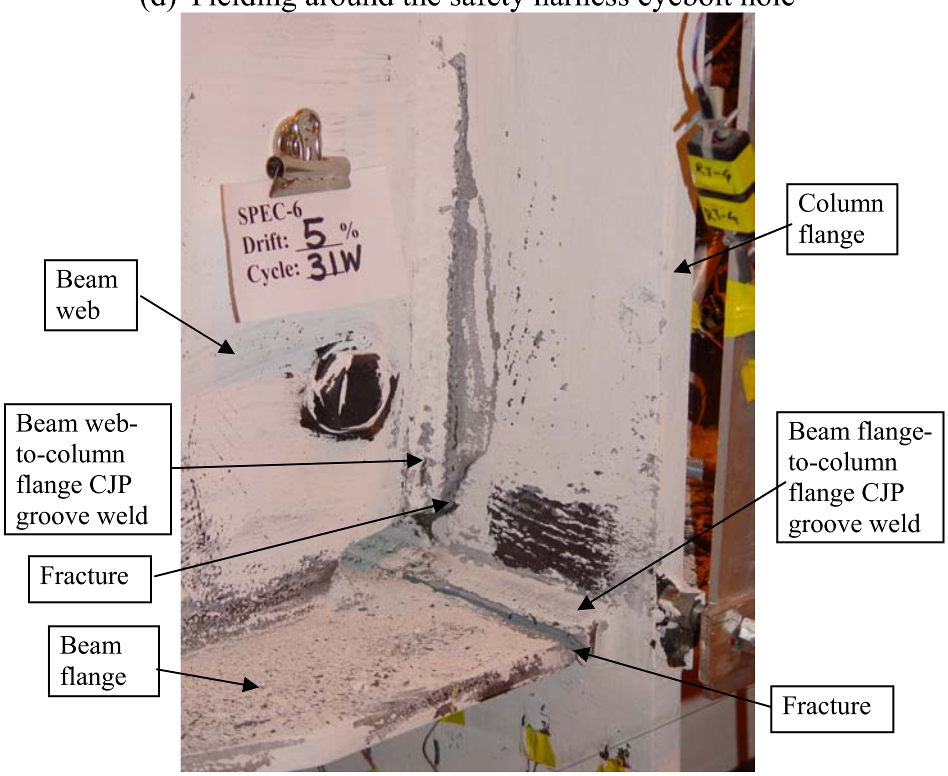

(e) Fracture in the west beam bottom flange HAZ and column flange adjacent to beam web CJP groove weld

Figure 5.18 – Photos of SPEC-6 at the end of test

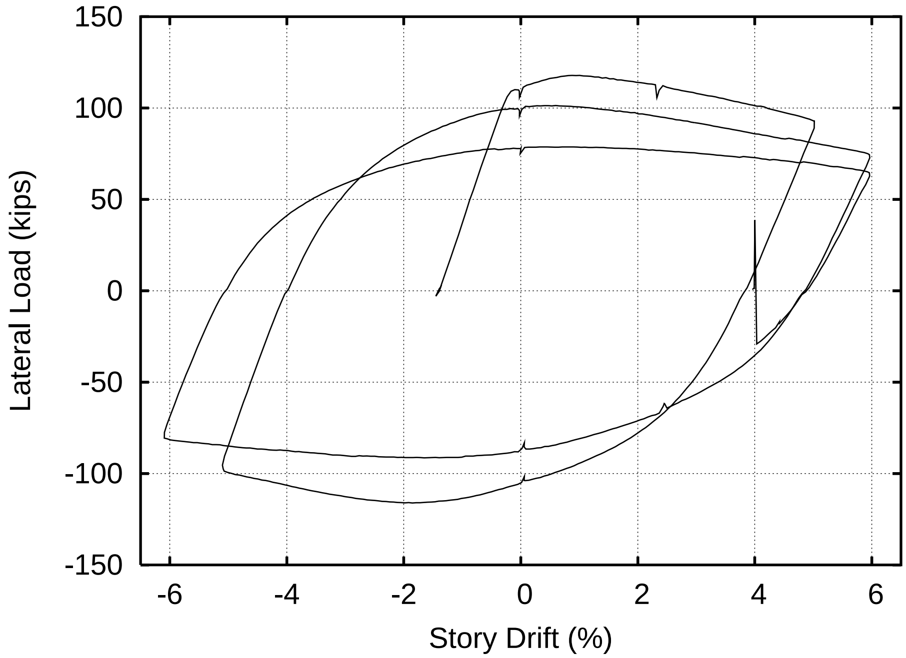

Figure 5.19 – Lateral load vs. story drift curve of SPEC-6, continued testing as a one-sided connection

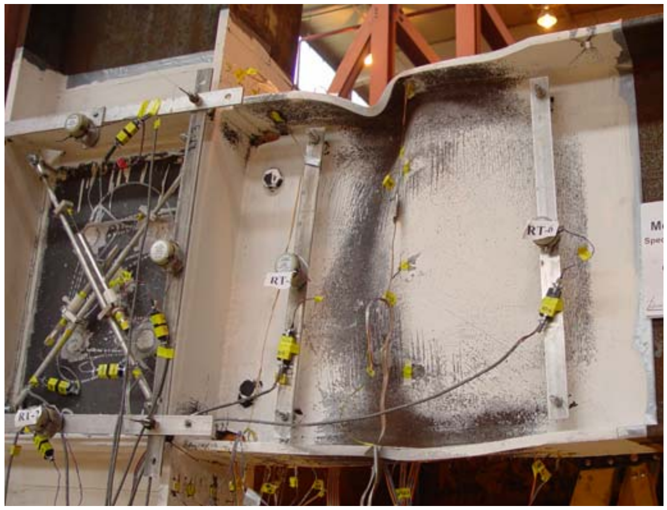

(a) East side beam yielding and local buckling

(b) East side beam bottom flange out-of-plane movement

(c) Fracture in east side beam top flange at the center of RBS

Figure 5.20 – Photos of SPEC-6, after completion of testing as a one-sided connection (continued)

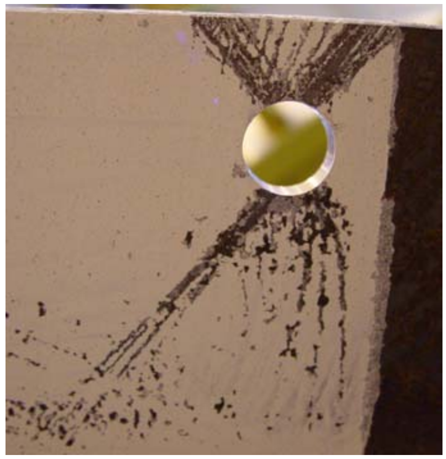

(d) Safety harness eyebolt hole

Figure 5.20 – Photos of SPEC-6, after completion of testing as a one-sided connection

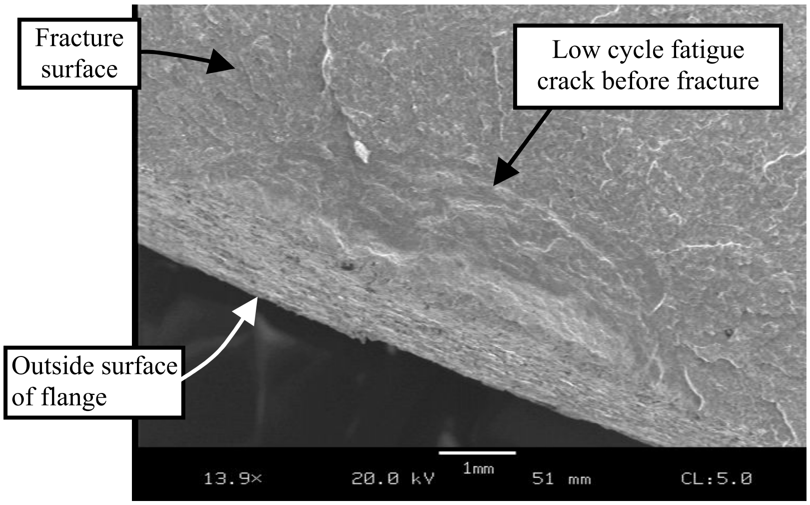

(a) SPEC-1

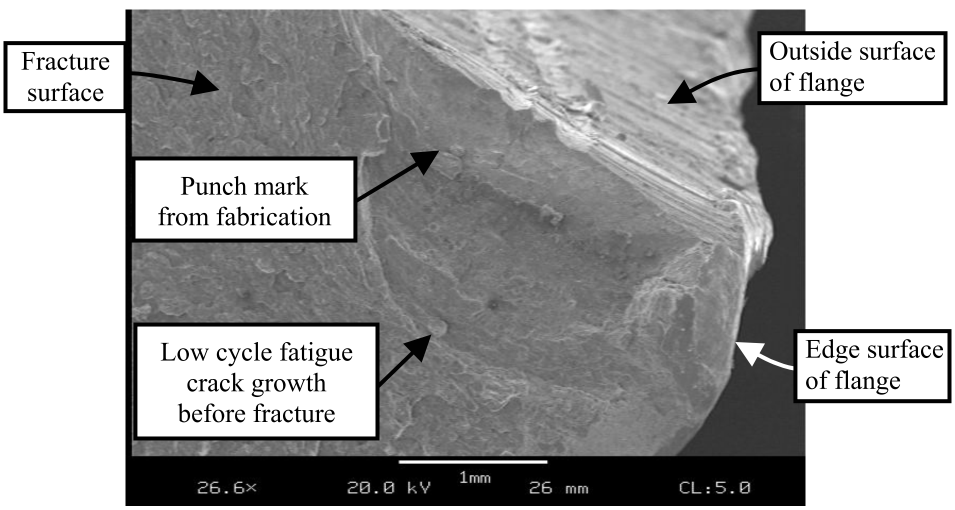

(b) SPEC-2

Figure 5.21 – SEM photographs of RBS flange fracture surfaces of SPEC-1 and SPEC-2

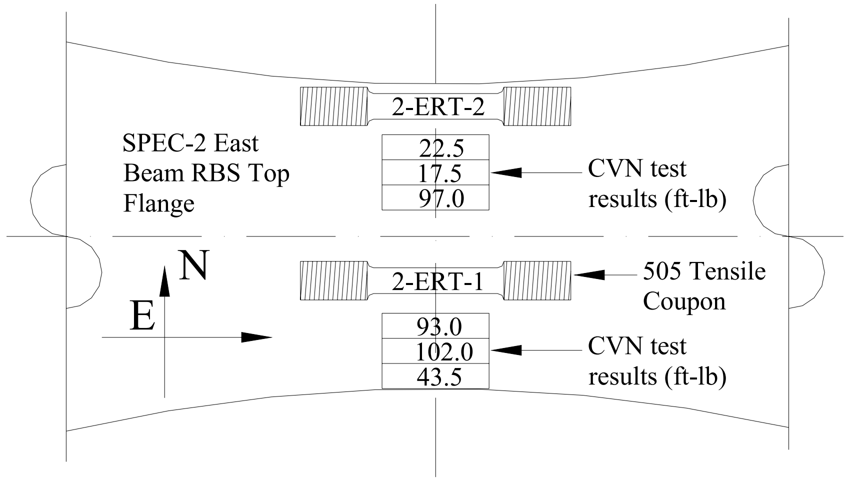

(a) RBS

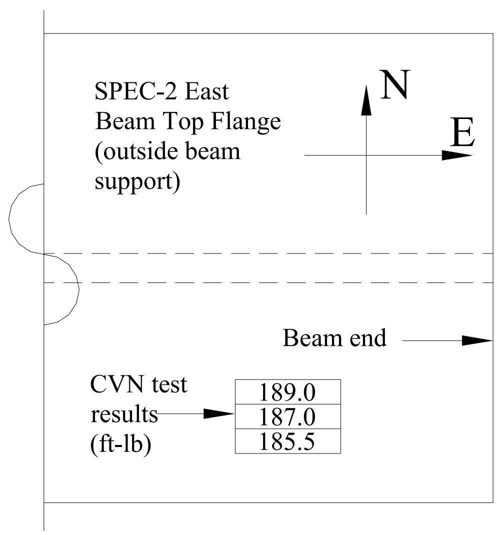

(b) Beam end (elastic material)

Figure 5.22 – CVN toughness results of SPEC-2 after test

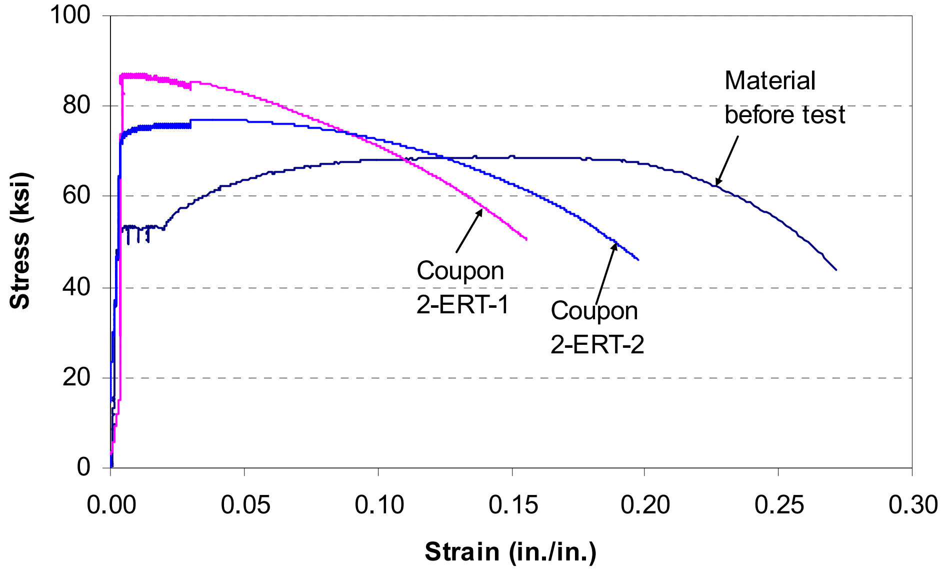

Figure 5.23 – Comparison of stress-strain curves of material in RBS after test and the original material before test for SPEC-2

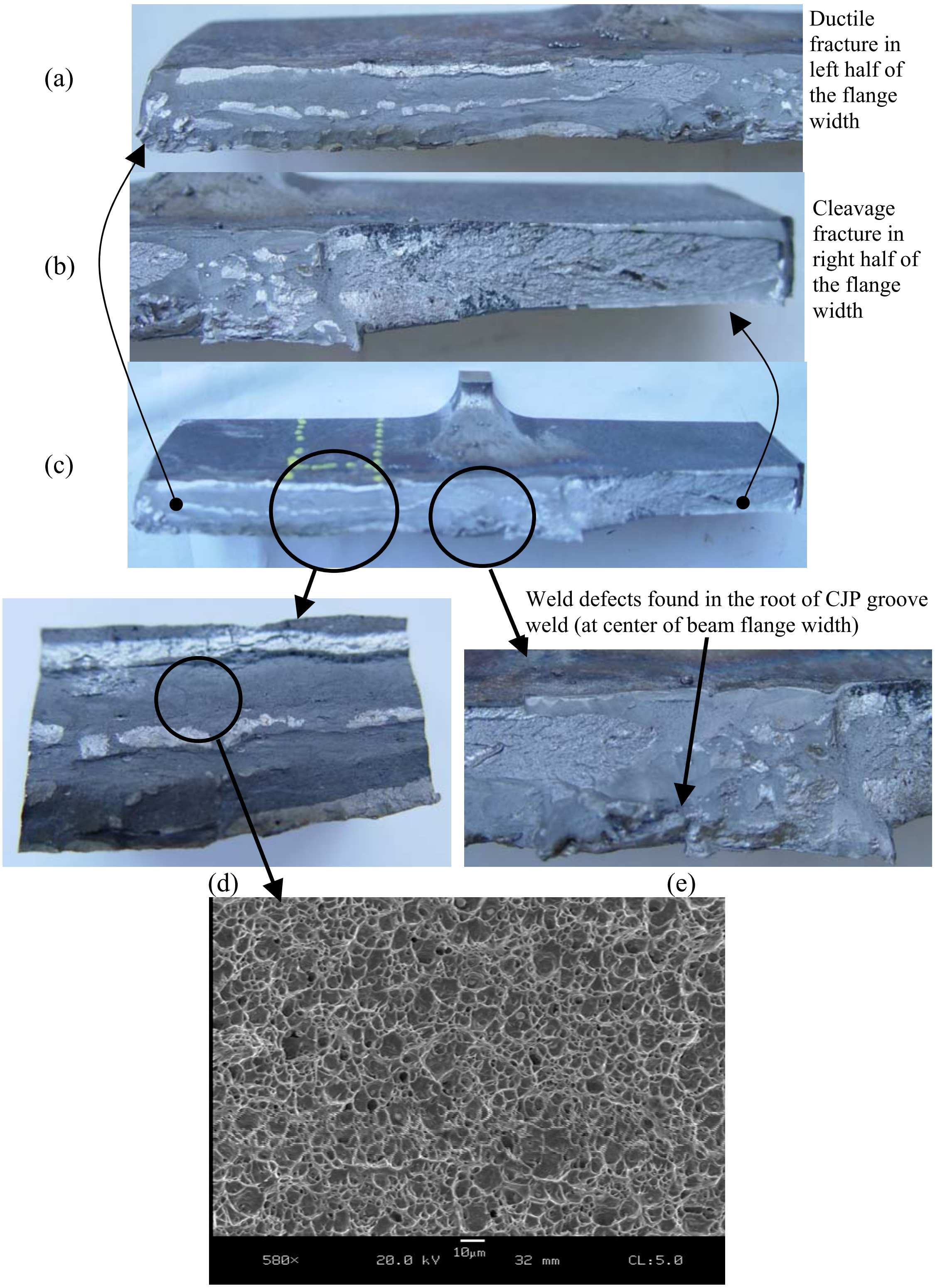

(f) SEM photo of ductile fracture

Figure 5.24 – Photographs of fracture surface of SPEC-6

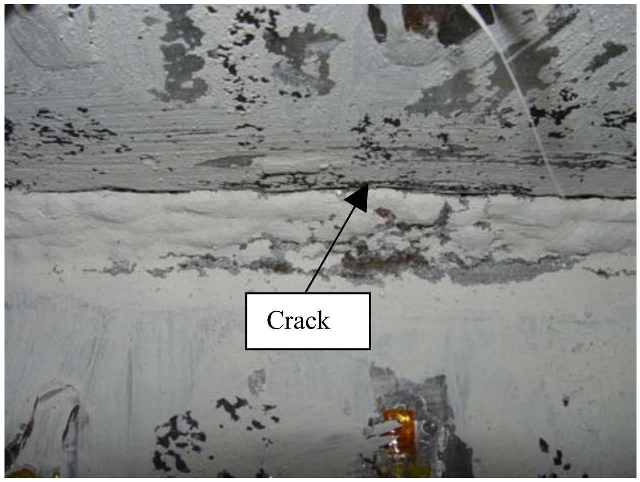

(a) Low cycle fatigue crack observed near the center of weld root

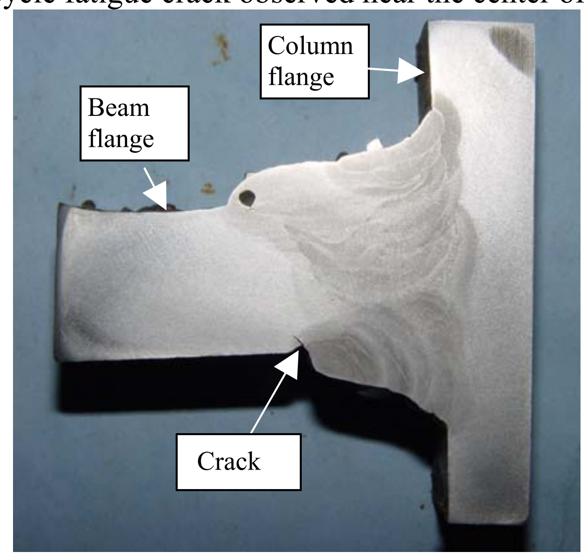

(b) Section cut at the center of the flange width

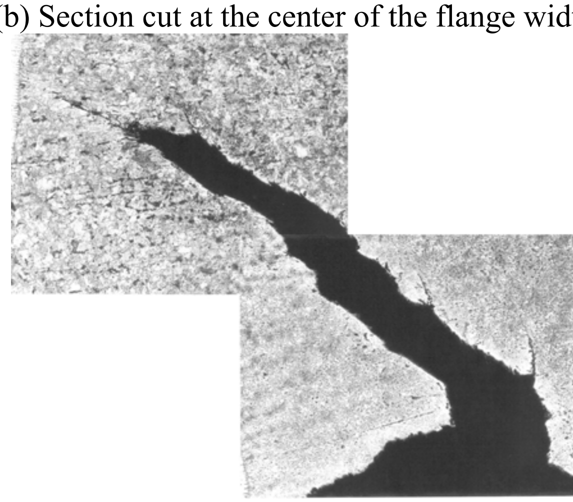

(c) Crack under microscope

Figure 5.25 – Photos of SPEC-6 east beam flange near weld low cycle fatigue crack

CHAPTER 6 TEST DATA ANALYSIS

6.1 Analysis of Test Data

Discussed in this chapter is the analysis and comparison of the data from the measurements of the testing, including: (1) total and plastic story drift; (2) story drift components by the beams, panel zone and column; (3) energy dissipation and its components; (4) RBS out-of-plane movement and column twist; (5) beam moment at the column face; (6) beam and column flange strain profiles; (7) beam web strain; and (8) axial force in the supplemental brace at the RBS.

6.1.1 Total and Plastic Story Drift

Figure 6.1 shows the maximum total story drift θ_{max} and the plastic story drift $\theta_{p,max}$ that each specimen achieved in a cycle prior to any fracture (i.e., the drift amplitude of the last successfully completed cycle prior to any fracture) or strength deterioration to below 80% of the nominal plastic moment of the beam at the column face. θ_{max} and $\theta_{p,max}$ were controlled by strength deterioration to 80% M_{pn} of the nominal capacity, see Figure 6.9, where the hysteretic relationship between the beam moment at the column face and the story drift is shown for each beam of all the specimens. The value of 80% of the beam nominal flexural capacity (i.e., $0.8M_{pn}$) is identified in the figure. The beam moment at the column face for each specimen will be discussed later in this chapter. These results are also summarized in Table 6.1. The AISC Seismic Provisions (2002) Section 9.2a, Item (2) states that: "The required flexural strength of the connection, determined at the column face, must equal at least 80 percent of the nominal plastic moment of the connected beam at an Interstory Drift Angle of 0.04 radians." All six specimens thus met or exceeded the current AISC Seismic Provisions (AISC 2002) requirement for qualifying a connection for seismic use. The test results therefore indicate that the RBS connection to a deep column, where a floor slab or supplemental brace at the RBS is present, can be qualified for SMF applications.

6.1.2 Story Drift Components

Figures 6.2 shows plots of the components of the story drift from the beams, panel zone, and column over the course of testing. The maximum values of each component are summarized in Table 6.1. Near the end of the test (i.e., at 4% story drift and beyond) the column is seen to have the smallest contribution to the story drift for all of the specimens, with most of the contribution to story drift coming from the beams and the panel zone. This is due to the fact that the design of each specimen followed the weak beam-strong column philosophy. With the panel zones designed according to the AISC Seismic Provisions (AISC 2002), the panel zone contribution to total story drift during the test was relatively small in the specimens SPEC-1, SPEC-3 and SPEC-4,,somewhat larger in specimens SPEC-2 and SPEC-5, while in SPEC-6, the panel zone contribution to the total story drift exceeded that of the beam.

Figure 6.3 shows a summary of the contribution of the beam, column and panel zone to the plastic story drift at selected story drift levels. Except for SPEC-6, Figure 6.3 shows that the panel zone contributes a major portion to the plastic drift during the cycles 2% and 3% story drift. For all the specimens except SPEC-6, with buckling in the RBS occurring followed by a deterioration in specimen capacity, the panel zone shear decreased and the panel zone deformation began to drop as most of the plastic rotation developed in the RBS. For SPEC-6, a majority of the plastic deformation was concentrated in the panel zone due to it having a weaker panel zone.

Figure 6.2 shows that for all the specimens except SPEC-6, which didn't have extensive beam local buckling, the panel zone deformation decreased after reaching a maximum value, typically either during the 3% story drift cycles (SPEC-1, SPEC-3, and SPEC-4) or 4% story drift cycles (SPEC-2 and SPEC-5), when severe beam local buckling began to deteriorate the beam flexural capacity and concentrate significant plastic deformations in the RBS.

The values of the R_v/V_{pz} ratio calculated based on the measured dimensions and material properties are tabulated in the last column of Table 4.1. The portion of the panel zone contribution to the total story drift is related to the values of the measured R_v/V_{pz} ratio (see Table 4.1). SPEC-1, SPEC-3 and SPEC-4 had the largest values of R_v/V_{pz} ratio among all the specimens, which is 1.26, 1.28 and 1.24, respectively. Hence, the contribution from the panel zone to the story drift was small in these specimens. On the contrary, SPEC-6 had the lowest value of R_v/V_{pz} ratio (and thus, had a weaker panel zone compared to the other specimens), so the panel zone contribution to the story drift is the largest among all the specimens. In SPEC-6, the panel zone contribution to the story drift is more than that of the beams. For SPEC-2 and SPEC-5, the values of R_v/V_{pz} ratio are intermediate, which are 1.14 and 1.21, respectively. Therefore, the panel zone contribution to the story drift for SPEC-2 and SPEC-5 is larger than that for SPEC-1, SPEC-3 and SPEC-4, but smaller than that for SPEC-6.

For SPEC-5, because of the smaller depth of the beams, composite action have a greater effect on enhancing the RBS flexural capacity, and thus effectively reducing the value of R_v/V_{pz}.

The ratio R_v/V_{pz} for SPEC-6 was considerably lower than that of the other specimens due to the actual yield stress and column thickness for the specimen. The static yield stress of the doubler plate for SPEC-6 was 46.7 ksi (see Table 4.4), less than the nominal yield stress of 50 ksi. The column web static yield stress for SPEC-6 was 52.1 ksi, which is lower than all other specimens, and the column web thickness was 0.581 inch (see Table 4.2), less than the nominal value of 0.605 inch. The column web yield stresses for all the other specimens were comparable, ranging in value from 56.8 ksi (SPEC-2) to 58.5 ksi (SPEC-3). The static yield strength of the doubler plate for SPEC-2 was 47.5 ksi, also less than the nominal yield strength of 50 ksi. The doubler plates for the other specimens (i.e., excluding SPEC-2 and SPEC-6) ranged from 58.2 ksi (SPEC-1) to 64.7 ksi (SPEC-4).

6.1.3 Energy Dissipation

The accumulated energy dissipated by the components (i.e., column, panel zone, and the beam) of each specimen during testing is shown in Figure 6.4. A summary of the total accumulated energy dissipated by the components of each specimen is given in Figure 6.5, with specimen overall energy dissipation tabulated in Table 5.1. Among specimens with W36x150 beams, SPEC-3 dissipated the largest amount of energy, while SPEC-2 had the smallest amount of energy dissipation. Since these two specimens are identical, except that SPEC-3 has a supplemental brace at the RBS, this observation indicates that the supplemental lateral bracing improves the energy dissipation capacity of the connection. SPEC-5 and 6 both had W30x108 section for the beams, with the former having a W27x146 column section and the latter a W24x131 column section. SPEC-5 had a stronger panel zone than SPEC-6, and greater lateral load capacity. Consequently, SPEC-5 is shown in Figure 6.5 to dissipate more total energy than SPEC-6, and dissipate more energy in the beams.

For SPEC-1, SPEC-3 and SPEC-4, it is shown in Figure 6.4 that prior to the onset of the deterioration in specimen capacity (at 3% story drift) that the panel zone accounts for about 33% of the total energy dissipated by each specimen. SPEC-2, which had a panel zone with R_v/V_{pz} equal to 1.14, had the panel zone account for 65% of the energy dissipated by the specimen when its capacity began to deteriorate at 4% story drift. SPEC-5 had an intermediate value of the R_v/V_{pz} ratio, which was 1.21, and a greater composite action of the floor slab (see Section 6.1.5). The panel zone thus contributed more to the energy dissipation, similar to SPEC-2. SPEC-6, which had a weaker panel zone (with the value of the R_v/V_{pz} ratio equal to 1.03) and the supplemental lateral bracing. SPEC-6 had 73% total dissipated energy in the panel zone at 4% story drift. A major portion of the energy dissipated following the onset of the deterioration in specimen capacity occurs in the beams. At the end of testing, the panel zone and the beams of SPEC-2 dissipated 43% and 49% of the overall total energy, respectively, while the panel zone and the beams of SPEC-6 dissipated 70% and 26% of the total energy dissipation, respectively (see Figure 6.5). For the remaining specimens the beams accounted for a major portion of the overall total energy dissipated by the specimen at the end of testing. For these specimens the panel zone dissipated 10% (SPEC-3) to 30% (SPEC-5) of the total energy, while the beams dissipated about 69% (SPEC-5) to 86% (SPEC-3) of the total energy. For all specimens, the energy dissipated by the column was 1% (SPEC-5) to 8% (SPEC-2) of the total energy dissipated. This is consistent with the weak beam-strong column design philosophy.

6.1.4 RBS Lateral Movement and Column Twist

The measured RBS flange out-of-plane movement and column twist of each specimen are shown plotted against story drift in Figures 6.6 and 6.7, respectively. These quantities were measured at the elevations of both the beam top and bottom flanges (see Figure 4.30). The data is plotted at the peak story drift during each cycle. The measured relationship for column twist-RBS out of plane movement of the beam bottom flange are plotted in Figure 6.8 for each specimen.

The beam bottom flange in the RBS of all the specimens except SPEC-6 is shown in Figure 6.6 to develop out-of-plane movement at 2% story drift, corresponding to about when beam web buckling initiated in the RBS. Because the composite floor slab restrained the top flange of the beam at the end of the RBS, the lateral movement of the beam bottom flange in the RBS was much larger than that of the top flange. For SPEC-1 to SPEC-4, the beam top flange in the RBS did not develop an appreciable out-of-plane movement until a story drift of 3% was imposed, and the lateral movement of the beam top flange remained smaller than that of the bottom flange (by a factor of two or more). In the latter part of testing the out-of-plane movement tended to increase in the second cycle of each selected story drift compared to that measured during the first cycle**.** SPEC-5 had the same composite floor slab as the first four specimens, but a shallower and lighter beam (W30x108 compared to W36x150). The effect of the slab restraint on the beam top flange of SPEC-5 is seen in Figure 6.6(e) to be significantly enhanced. The movement of the top flange at the RBS was small. The difference in beam depth (W30 vs. W36) and in beam web slenderness ratio h/t_w (49.0 for W30x108, 52.0 for W36x150) also reduced the RBS bottom flange out-of-plane movement for SPEC-5. With the relatively stiffer lateral bracing and a weaker panel zone, SPEC-6 had little RBS out-of-plane movement in both the beam top and bottom flanges (see Figure 6.6(f)).

A comparison of the response of SPEC-2 with SPEC-3 indicates that the supplemental bracing reduced the out-of-plane movement of the beam bottom flange in the test specimen, but did not fully restrain the lateral movement of the beam flange at the middle of the RBS. However, by comparing the results of SPEC-5 and SPEC-6, it is seen that supplemental lateral bracing combined with a weaker panel zone can prevent beam local and lateral buckling, and thus RBS out-of-plane movement. However, it also imposes additional demand on the connection, as discussed in Section 3.4.1.2.

An examination of the out-of-plane movement of the beam bottom flange at 4% drift for all of the test specimens in Figure 6.6 indicates that the movement is less than 20% of the beam flange width (i.e., $0.2b_f$), which is the value used in the design procedure proposed by Chi and Uang (2002) to determine the torque applied to the column.

Figure 6.7 shows that the column twist developed in the specimens was less than 0.012 radians before the story drift cycles of 4% were imposed. The columns continued to develop an increase in column twist as the amplitude of story drift was increased beyond 4%. This is due to the increase in the RBS out-of-plane movement and damage to the slab around the column (see Figure 6.8, where the measured column twist is shown to steadily increase with the development of RBS out-of-plane movement of the beam bottom flange). As seen in Figure 6.7, by the end of the test, SPEC-4 at 4% story drift had the largest amount of column twist (0.037 radians) among all of the specimens. This is attributed to the fact that the column for SPEC-4 (W36x150) is the one of the more torsionally flexible among the specimens, as well as being the most highly stressed. SPEC-1 had the smallest amount of column twist (0.02 radians) among the specimens with W36x150 beams and without a supplemental brace (i.e., SPEC-1, SPEC-2, and SPEC-4). This is attributed to the fact that the column for SPEC-1 (W36x230) has the largest torsional stiffness of all of the specimen columns. SPEC-3, which had a supplemental brace, had the smallest column twist (0.015 radians) among all the specimens with W36x150 beams. The maximum column twist in SPEC-3 was less than one-half the maximum column twist of 0.035 radians that developed in companion specimen SPEC-2, showing the effectiveness of the supplemental lateral bracing in reducing column twist. Although the column for SPEC-5 is lighter and has a smaller torsional stiffness compared to SPEC-1 to SPEC-4, SPEC-5 had less column twist than all of the first four specimens. This shows that column twist is not only related to the column torsional stiffness, but also related to the driving force (i.e., beam flange force). SPEC-6 had the smallest column twist due to the supplemental lateral bracing and lack of local and lateral buckling in the beams at the RBS.

6.1.5 Beam Moment at Column Face and the Effect of Composite Action

Figure 6.9 shows the beam moment at the column face vs. total story drift for both beams of all six specimens. The value of $0.8M_{pn}$ is marked in the figures, which was used to examine the specimen flexural capacity deterioration, and thus to determine the last successfully completed cycle to achieve a capacity of $0.8M_{pn}$. The results were reported in Section 6.1.1. For all specimens except SPEC-6, the maximum moment when the beam top flange is in compression is slightly higher than the maximum moment when the beam bottom flange is in compression. This indicates that there is some composite action from the slab. Also, it is found that for specimens with a composite floor slab that when the beam top flange is in compression the beam moment at the column face didn't deteriorate as quickly as when the beam bottom flange is in compression. This is due to the slab's restraint on beam local and lateral buckling. The composite floor slab prevents the beam top flange in the RBS, when in compression, from laterally buckling and thus reduces the deterioration from occurring in the beam. SPEC-6 had a weaker panel zone, and as a result developed smaller beam moments.

Figure 6.10 compares the measured beam maximum moment $M_{f,exp}$ developed at the column face for all of the test specimens, where the ratio of $M_{f,exp}$ to beam expected plastic flexural capacity M_{pe} is plotted. The beam expected plastic flexural capacity is based on the expected yield stress, where $M_{pe}=Z_bR_yF_y$. Included are some RBS specimens tested by Engelhardt et al. (2000). Table 6.3 summarizes the beam and column sizes of the specimens tested by Engelhardt et al. Results are plotted in Figure 6.10. These specimens consisted of W14 column sections, including two specimens without a floor slab (Specimens DBBW and DBWW) and two with a floor slab (Specimens DBBWC and DBWWC). Figure 6.10 shows that the specimens with a composite floor slab (i.e., SPEC-1 to SPEC-5, DBBWC and DBWWC) developed a larger beam moment at the column face than those without a floor slab (i.e., SPEC-6, DBBW and DBWW), both for shallow and deep columns. This is attributed to the composite action by the floor slab.

Table 6.2 shows the values for the ratios of $M_{f,design}/R_yZ_bF_y$, $M_{f,design}/M_{pn}$, $M_{f,exp}/M_{f,design}$, and $M_{f,exp}/M_{pn}$. $M_{f,design}$ is the design value of the maximum beam moment developed at the column face, based on Equation (2.13). $M_{f,exp}$ is the maximum beam moment developed at the column face from test results. M_{pn} is the beam nominal flexural capacity, which is equal to Z_bF_y. The design of the RBS intended to have the beam develop $0.97M_{pn}$ at the column face, which corresponds to $0.88Z_bR_yF_y$. The RBS design complied with the design recommendation (Equation (2.13) in Section 2.2.4.1). As noted in Section 2.2.4.1, composite action is not considered in the design procedure. Based on the RBS design, the maximum beam moment at the face of the column should not exceed M_{pn}. However, the experimental results shown in Table 6.2 indicate that the maximum beam moment at the column face exceeds M_{pn} for all of the specimens except SPEC-6, whose maximum measured beam moment was equal to M_{pn}. $M_{f,exp}$ exceeded $M_{f,design}$ by average of 14%. SPEC-6, which did not have a floor slab, had the smallest value (1.03) of the ratio of $M_{f,exp}/M_{f,design}$. SPEC-5, which had a composite slab and W30x108 beams, had the largest value (1.23) for the ratio of $M_{f,exp}/M_{f,design}$. SPEC-5 appears to be more affected by the floor slab since it has the smallest beam section.

It can be seen that the design procedure (Equation (2.13)) underestimates the maximum beam moment at the column face when a composite floor slab is present. The composite action from a composite floor slab increases the beam flexural capacity, causing the beam to become more inelastic at the column face. Composite action appears to become greater as the beams get smaller. The increase of the beam flexural capacity by the composite action also imposes more demand on the panel zone, thus making it weaker than designed (i.e., the R_v/V_{pz} ratio becomes smaller).

6.1.6 Beam and Column Flange Strain Profiles

Figures 6.11 through 6.16 show the longitudinal strain distribution across the beam top and bottom flanges at various story drift values. The results shown are related to the first cycle of the indicated story drifts of 1% through 5%. Due to a strain gauge malfunction, the strains for the beam top flange of SPEC-4 are only shown for story drift cycles of up to 3%. The strain gauges used to measure the strain were located on the beam flange outer surface, at three inches from the column face (see Figures 4.27 to 4.29). For SPEC-1 to SPEC-5, the strain plots show a concentration of strain to develop in the latter cycles at one edge of the bottom flange, where a strain gradient developed across the beam flange near the column face. This is due to the effects of beam bottom flange local buckling and lateral buckling in the RBS. Compared to the beam bottom flanges, the beam top flange strains are more uniform, and is due to the top flange is more restrained by the composite floor slab from local and lateral buckling. It is also observed that the beam flange strains begin to decrease after the 3% or 4% drift cycles when the specimen capacity began to deteriorate due to local and lateral buckling in the RBS. Thus, it appears that this buckling reduced the strain near the interface of the weld and base metal. In all of the specimens except for SPEC-6, cracks were not found at the interface of the beam flange welds and base metal, and fracture of the beam flange occurred in the region of local buckling. The strain distribution in the beam flanges of SPEC-6 are shown in Figure 6.16. The strains are fairly uniform across the beam flanges, indicating that there was little local and lateral buckling in the beams.

The longitudinal strain distribution across the column flange, just below the beam bottom flange, is shown in Figures 6.17 through 6.22 for the test specimens. Among the specimens having W36x150 beams, SPEC-1 had the stiffest and strongest column, and consequently the column flange strains are shown in Figure 6.17 to be the lowest among the specimens. On the contrary, SPEC-4 had the smallest value for column-to-beam flexural capacity ratio M^*_{pc}/M^*_{pb} (see Table 4.1) (i.e., the weakest column relative to the beams) and is shown in Figure 6.20 to have the largest column flange strain. SPEC-5 and SPEC-6 both had W30x108 beams. In Figures 6.21 and 6.22, it can be seen that SPEC-5 has lower strains than SPEC-6 because the column of SPEC-5 (W27x146) has higher stiffness and strength than the column of SPEC-6 (W24x131), and therefore a larger value for the column-to-beam flexural capacity ratio (see Table 4.1). Except for SPEC-4 and SPEC-6, the column flange strain for all specimens is rather small and barely exceeds the yield strain ε_y marked in Figure 6.17 through 6.22. The columns of SPEC-4 and SPEC-6 showed evidence of developing more appreciable yielding than the other specimens, locally beneath the beam flanges. In SPEC-4, this is due to the specimen having the smallest value of column-to-beam flexural capacity ratio (see Table 4.1), resulting in some column yielding from flexure. For SPEC-6, the significant panel zone deformation caused significant local bending (i.e., kinking) of the column flanges just outside the panel zone.

The measured column flange strain distribution for the specimens shows no strong evidence of the presence of any appreciable column torsional warping normal stress (strain) that is predicted by the design procedure of Chi and Uang (2002), where a stress (strain) gradient across the column flange would have been present.

6.1.7 Beam Web Strain

As discussed in Chapter 4, high elongation strain gauges were mounted on opposite sides of the web of the east beam (see Figure 4.27 to 4.29). Figures 6.23 through 6.28 show for each specimen the beam web strains measured from each pair of these strain gauges during testing. For all the specimens except SPEC-6, a separation of strain is observed to occur between the two gages in the each pair of strain gages. This indicates that the occurrence of web local buckling observed in the test had commenced. The strain gage readings indicate that web local buckling started at a story drift of 2% for SPEC-1, SPEC-3, and SPEC-4, and 3% for SPEC-2 and SPEC-5. For SPEC-6, the strains in the beam web were very small compared to other specimens and no strain separation occurred (see Figure 6.28). This supports the observation made during testing that the beams of SPEC-6 did not have appreciable local buckling occur before the specimen failed.

6.1.8 Bracing Force

As noted in Chapter 4, the axial force in the east side supplemental brace (a W14x22 section) for SPEC-6 was measured. The relationship of measured axial force in the brace vs. specimen story drift is shown in Figure 6.29. The results in Figure 6.29 show that the axial brace force increased as the story drift developed, and cyclically reversed signs (i.e., reversed from tension to compression as the cyclic drift displacements were imposed). The maximum value of the axial brace force was about 45 kips, at 5% story drift as a two-sided connection. This amount of force corresponds to 15.9% of the beam flange area at the RBS times its nominal yield stress ($A_{flg,RBS}F_y$). The maximum value of the axial brace force at the end of the first 4% story drift cycle was about 37 kips. The value of 37 kips corresponds to $0.13A_{flg,RBS}F_y$, where F_y is the nominal yield stress.

In Section 9.8 of the AISC Seismic Provisions (AISC 2002), it is stated that: "…The Required Strength of lateral bracing provided adjacent to plastic hinges shall be at least 6 percent of the expected Nominal Strength of the beam flange computed as $R_yF_yb_ft_f$." If the reduced flange width at the RBS is considered, the expected nominal strength of the beam RBS flange is 229 kips, and the required bracing strength shall be at least 13.7 kips. If the whole beam width is used, the expected nominal strength of the beam whole flange is 438 kips, and the required bracing strength shall be at least 26.3 kips.

The measured brace force in the supplemental brace of SPEC-6 thus exceeded the brace design force recommended by the AISC Seismic Provisions (2002). The maximum value of the measured axial force in the brace at 4% story drift is 2.7 times and 1.4 times the value using the beam RBS flange width and the beam whole flange width, respectively.

6.2 Summary and Conclusions

Based on the test results and evaluation of the data, the following conclusions are noted:

(1) The deep column RBS connection test specimens, having a composite floor slab or a proper lateral bracing, have sufficient ductility for seismic application. The specimens meet the qualification criteria required by Appendix S of the AISC Seismic Provisions (AISC 2002) for use in SMFs in seismic regions.

(2) The E70T-6 electrode appears to perform adequately when the AISC Seismic Provisions for weld metal toughness are satisfied.

(3) The restraint by the concrete composite floor slab reduces the lateral movement of the beam bottom flange in the RBS. Hence it enhances the performance of the connection by reducing the strength deterioration due to lateral buckling of the beam top flange and the resulting twisting moment subjected to the column from this beam flange. It was shown that the same thickness composite floor slab had more restraint effect on shallower and ligher beams (W30x108) than deeper and heavier beams (W36x150).

(4) The observed out-of-plane movement of the beam bottom flange at 4% drift in the test specimens is less than the value of $0.2b_f$ suggested by Chi and Uang (2002) to determine the torque applied to the column.

(5) The beams in all the specimens except SPEC-6 accounted for most of the plastic drift and energy dissipation of the specimens. The panel zone designed according to the current AISC Seismic Provisions appears to work well, enabling the beams to fully develop plastic hinges in the RBS. In SPEC-6, due to the low yield stress of the doubler plate and undersize of the column web, the panel zone had a reduced strength, which resulted in a larger portion of the plastic deformation to be concentrated in the panel zone.

(6) The supplemental bracing for SPEC-3 and SPEC-6 reduced the column twisting and out-of-plane movement of the beam bottom flange in the test specimens. In SPEC-3, which had a stronger panel zone and thereby local buckling in the RBS, the supplemental brace did not fully restrain the lateral movement of the beam flange at the middle of the RBS.

(7) The current design recommendation for RBS connections to a deep column over-estimates the column torsional warping stress due to twisting.

(8) The current fabrication requirements for grinding the RBS in accordance with FEMA 353 (FEMA 2000b) appear to be adequate for the specimens with A992 steel beams. The specimens with beams fabricated from A572 Grade 50 steel W36x150 sections (SPEC-1 and SPEC-2) and A992 steel W30x108 sections (SPEC-5) went into cleavage fracture in the RBS, while the specimens with beams fabricated from A992 steel W36x150 sections (SPEC-3 and SPEC-4) developed ductile tearing in the RBS. Further studies are needed to understand all of the causes for this.

(9) With a composite floor slab, the beams have developed a larger moment capacity and less deterioration when the beam top flange is in compression, compared to when the beam bottom flange is in compression. The RBS design procedure recommended by Engelhardt (1999) and that by AISC Draft of *Prequalified Connections for Special and Intermediate Steel Moment Frames for Seismic Applications* (2003) both underestimate the maximum moment developed in the beam at the column face when

a composite floor slab is present. This phenomenon is due to the increase in the RBS flexural capacity because of composite action.

(10) The axial brace force in the supplemental brace at the RBS was found to be larger than the design value recommended by the AISC Seismic Provisions (2002). Further studies are needed to possibly consider whether to revise the brace design force.

Table 6.1 Maximum cyclic drift achieved in test specimens prior to any fracture or strength deterioration below 80% of the nominal capacity of the specimen

SPEC	θ_{max} (% rad.)	$\theta_{p,max}$ (% rad.)	$\theta_{bm,pmax}$ (% rad.)	$\theta_{pz,pmax}$ (% rad.)	$\theta_{col,pmax}$ (% rad.)	R_v / V_{pz}
1	4.0	3.1	2.9	0.6	0.2	1.26
2	4.0	2.9	1.4	1.3	0.6	1.14
3	5.0	4.1	3.7	0.6	0.2	1.28
4	4.0	3.0	2.7	0.8	0.1	1.24
5	5.0	4.0	3.5	1.3	0.2	1.21
6	4.0	2.6	0.8	1.9	0.2	1.03

Note: The values of the R_v/V_{pz} ratio were based on the measured dimensions and material properties.

Table 6.2 Comparison of the design values and experimental results for the maximum beam moment at the column face

SPEC	$\frac{M_{f,design}}{R_y Z_b F_y}$	$\frac{M_{f,design}}{M_{pn}}$	$\frac{M_{f,\exp}}{M_{f,design}}$	$\frac{M_{f,\exp}}{M_{pn}}$
1	0.88	0.97	1.06	1.03
2	0.88	0.97	1.17	1.13
3	0.88	0.97	1.19	1.15
4	0.88	0.97	1.14	1.11
5	0.88	0.97	1.23	1.20
6	0.88	0.97	1.03	1.00

Table 6.3 Test specimen matrix by Engelhardt et al. (2000)

Specimen	Beam	Column	Floor slab
DBBW	W36x150	W14x398	No
DBWW	W36x150	W14x398	No
DBBWC	W36x150	W14x398	Yes
DBWWC	W36x150	W14x398	Yes

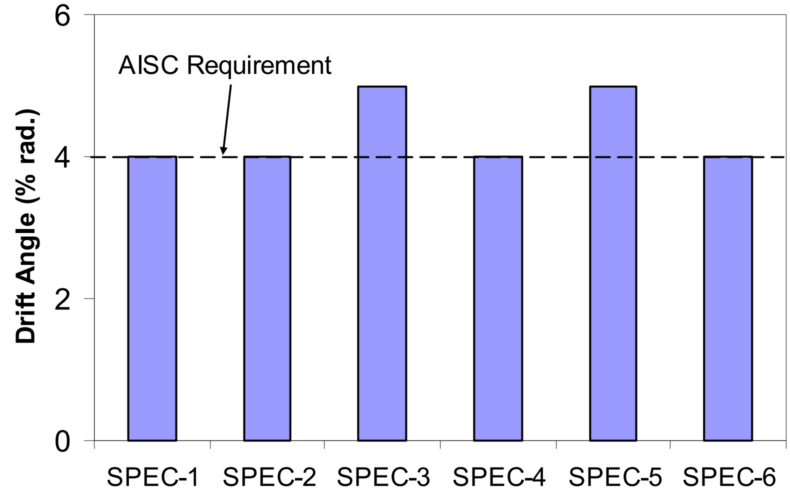

(a) Total Story Drift

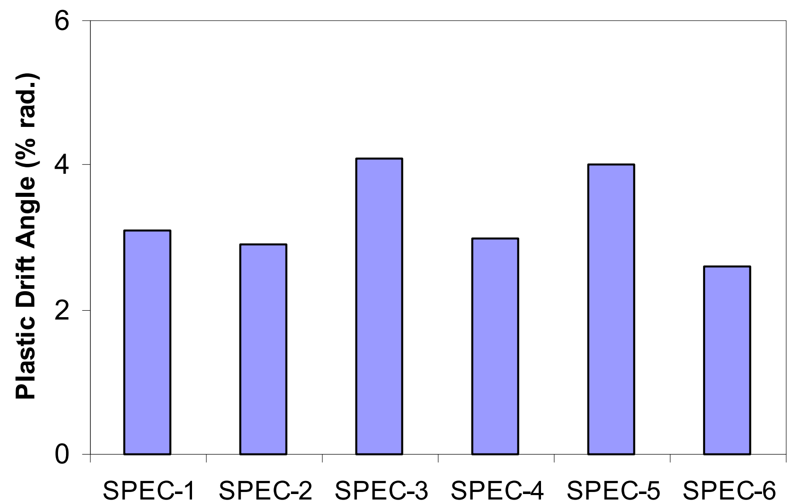

(b) Plastic Story Drift

Figure 6.1 – Total and plastic story drift achieved for specimens (Based on last successfully completed cycle prior to any fracture or strength deterioration below 80% of the nominal capacity)

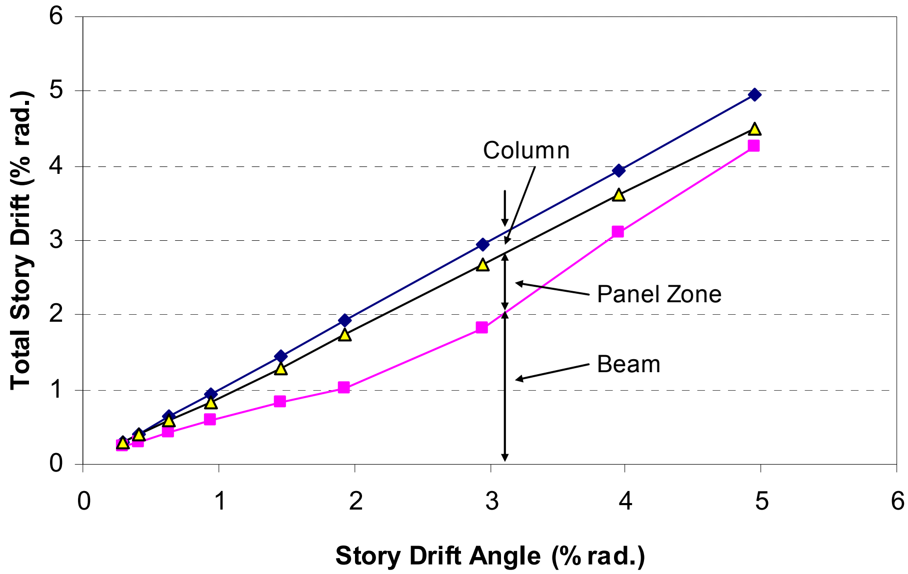

(a) SPEC-1

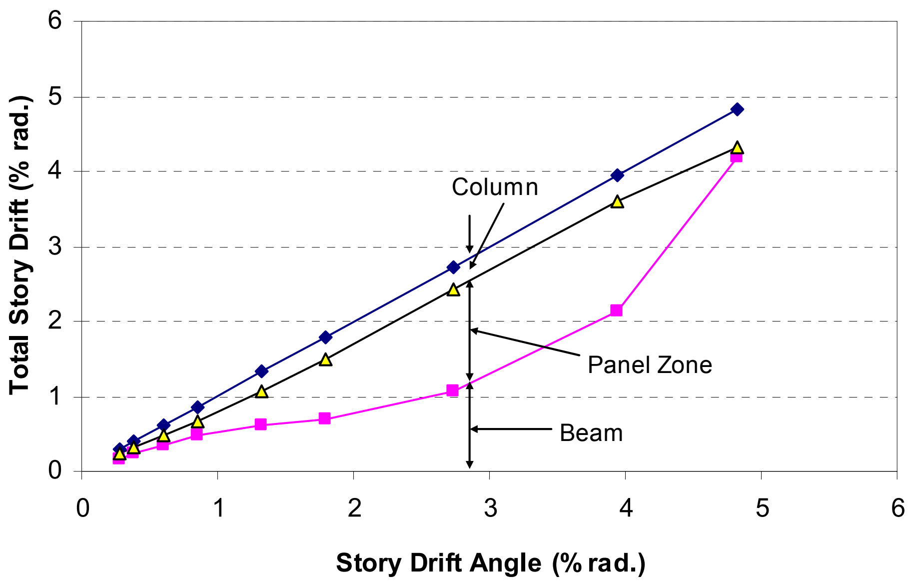

(b) SPEC-2

Figure 6.2 – Drift components of test specimens (Continued)

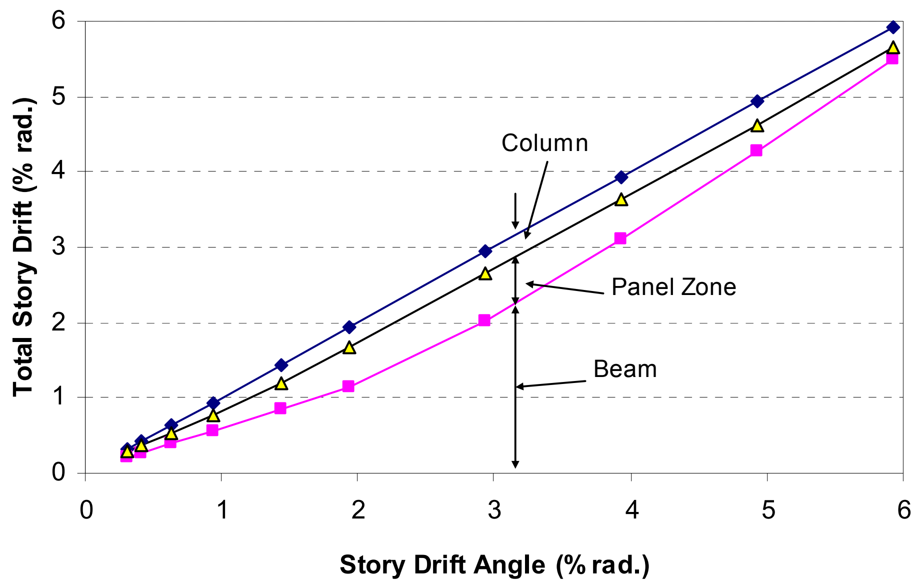

(c) SPEC-3

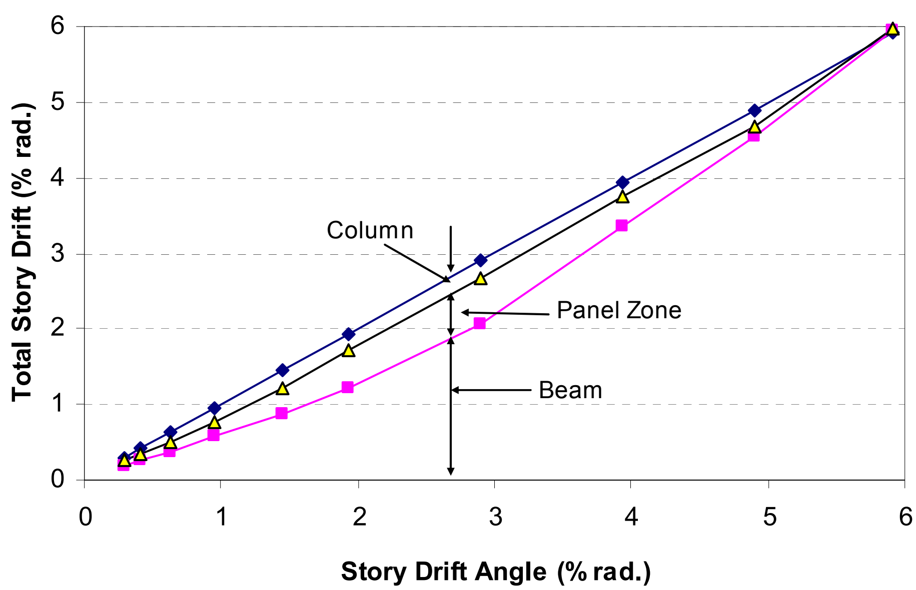

(d) SPEC-4

Figure 6.2 – Drift components of test specimens (continued)

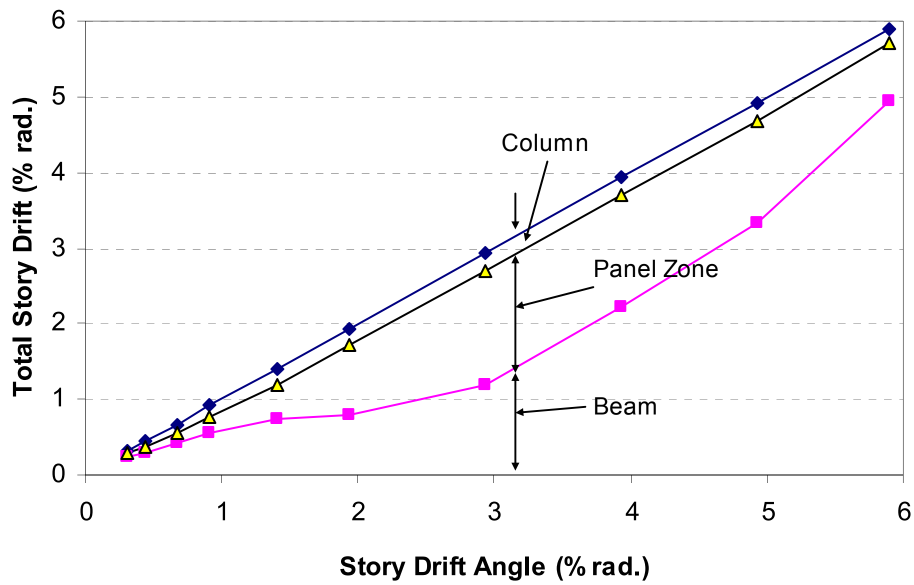

(e) SPEC-5

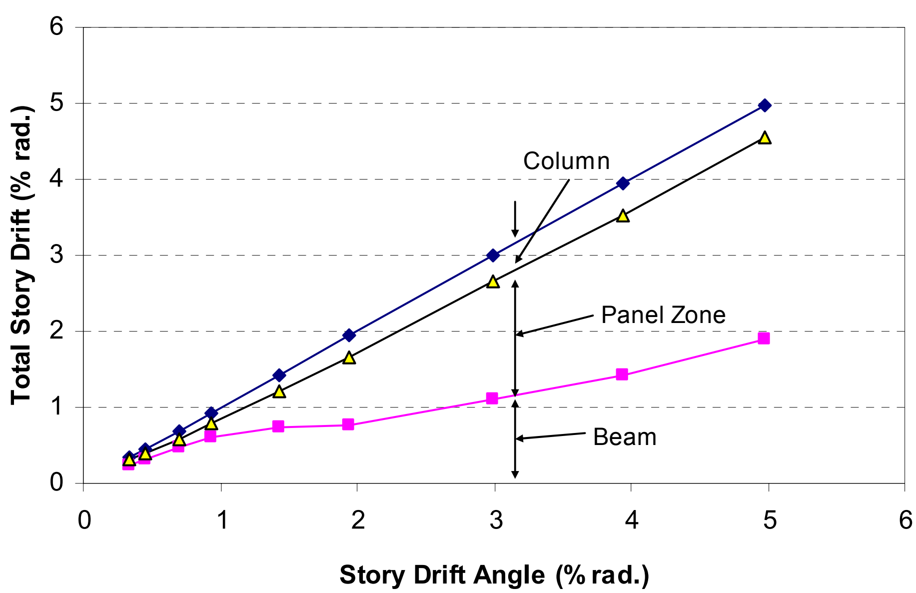

(f) SPEC-6

Figure 6.2 – Drift components of test specimens

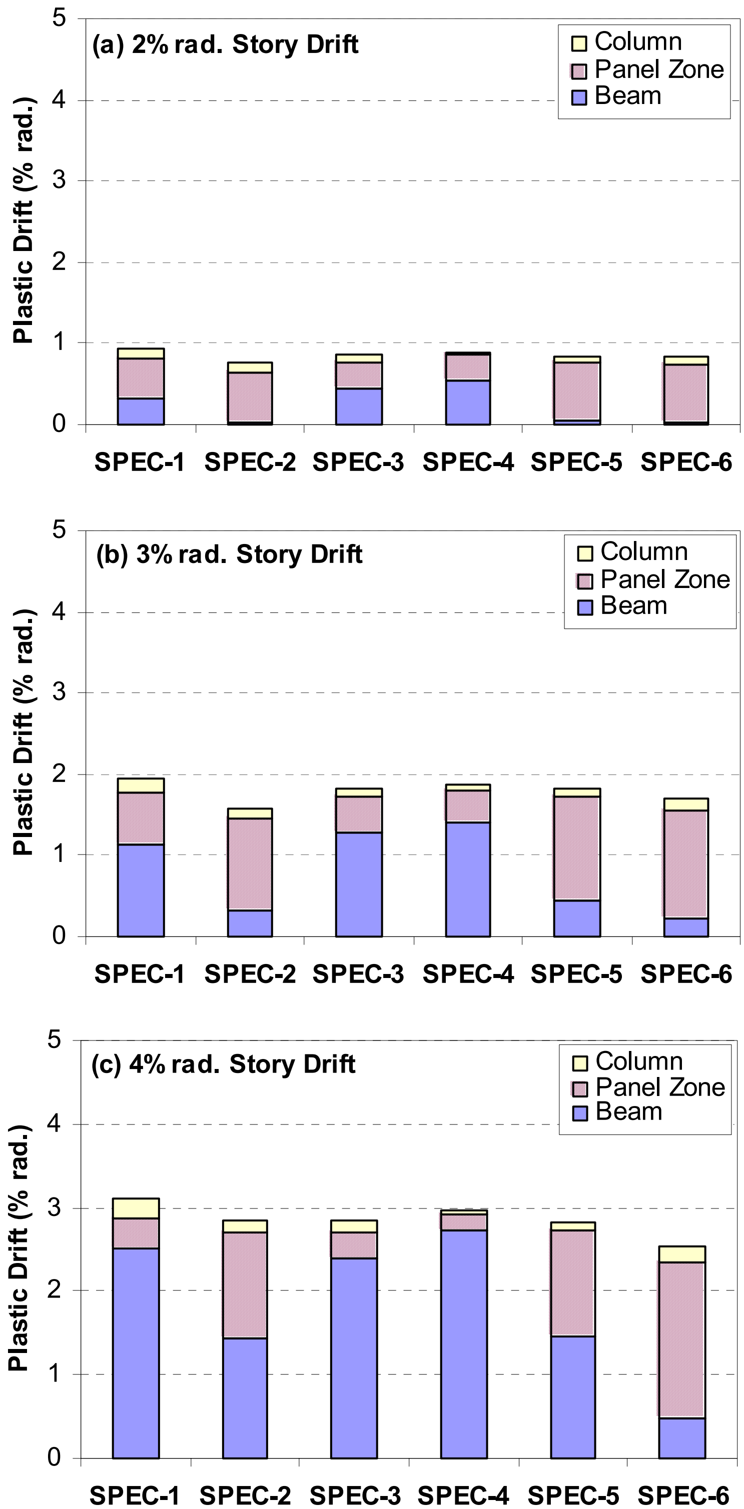

Figure 6.3 – Summary of specimen plastic story drift components at selected drift levels (continued)

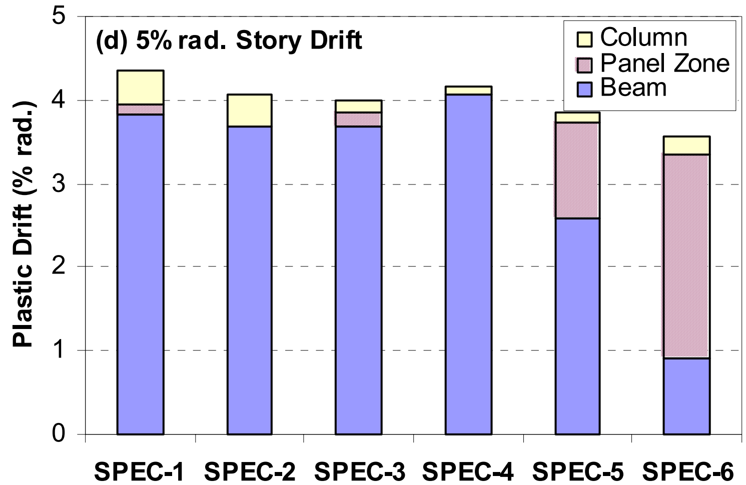

Figure 6.3 – Summary of specimen plastic story drift components at selected drift levels

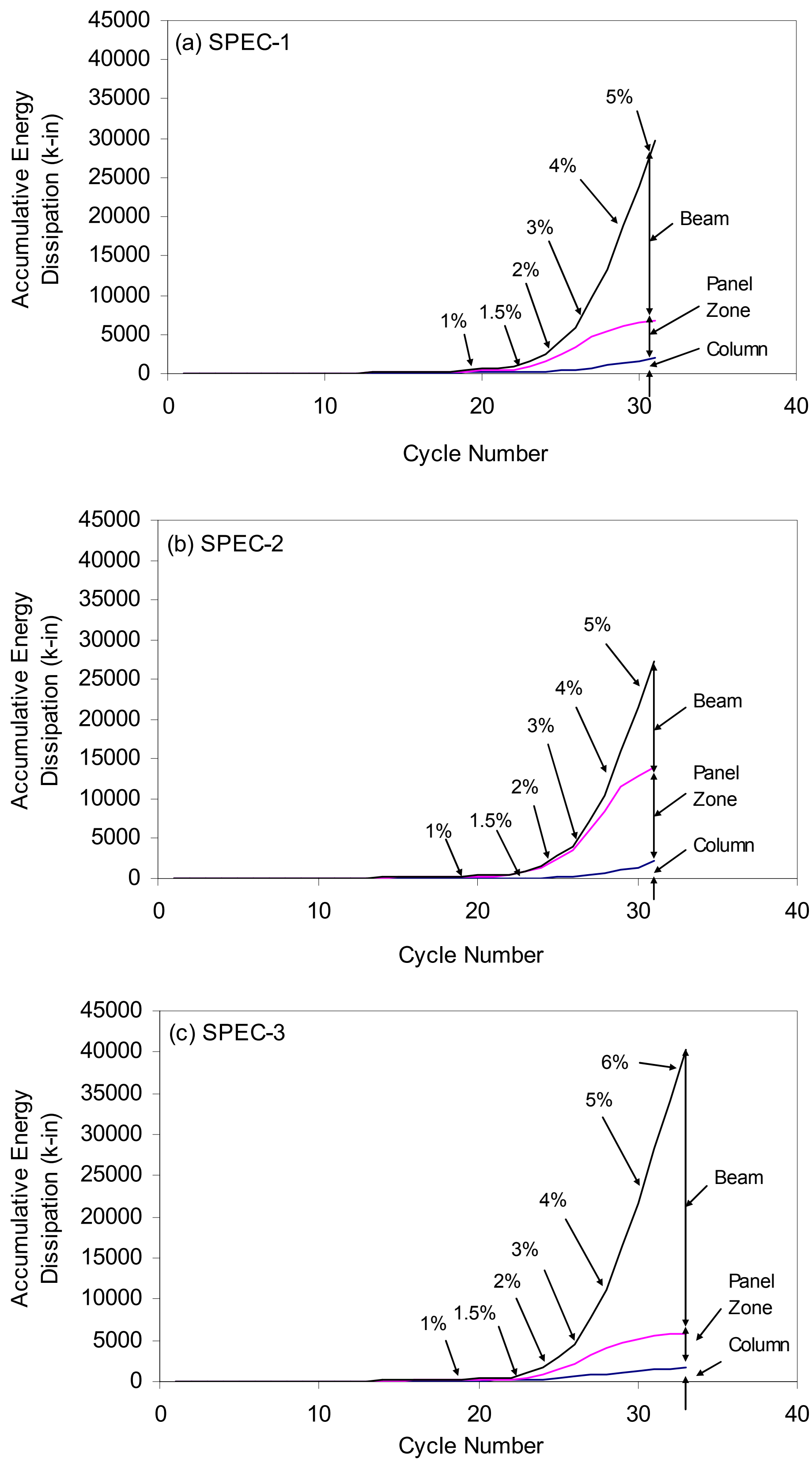

Figure 6.4 – Energy dissipated by components of test specimens (Continued)

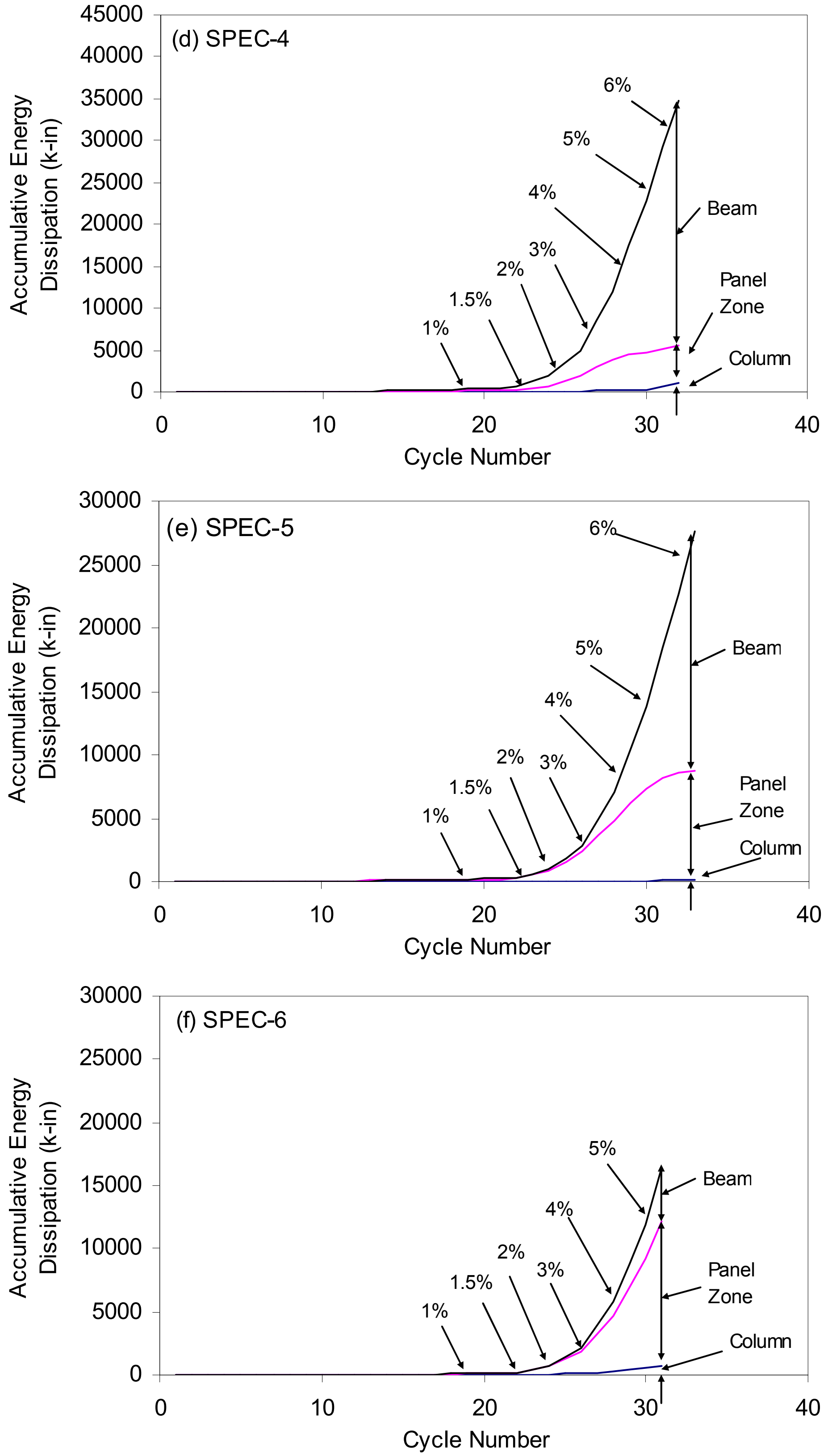

Figure 6.4 – Energy dissipated by components of test specimens

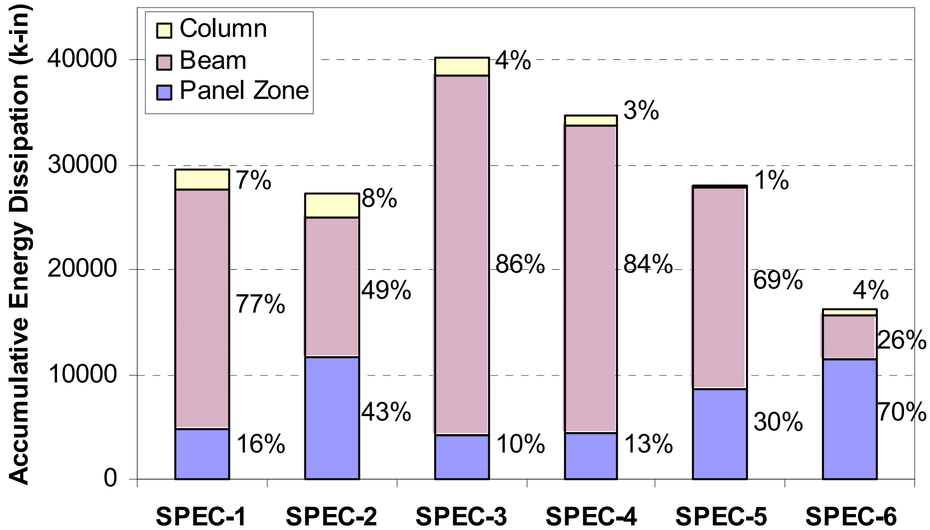

Figure 6.5 – Summary of specimen components contribution to total energy dissipation

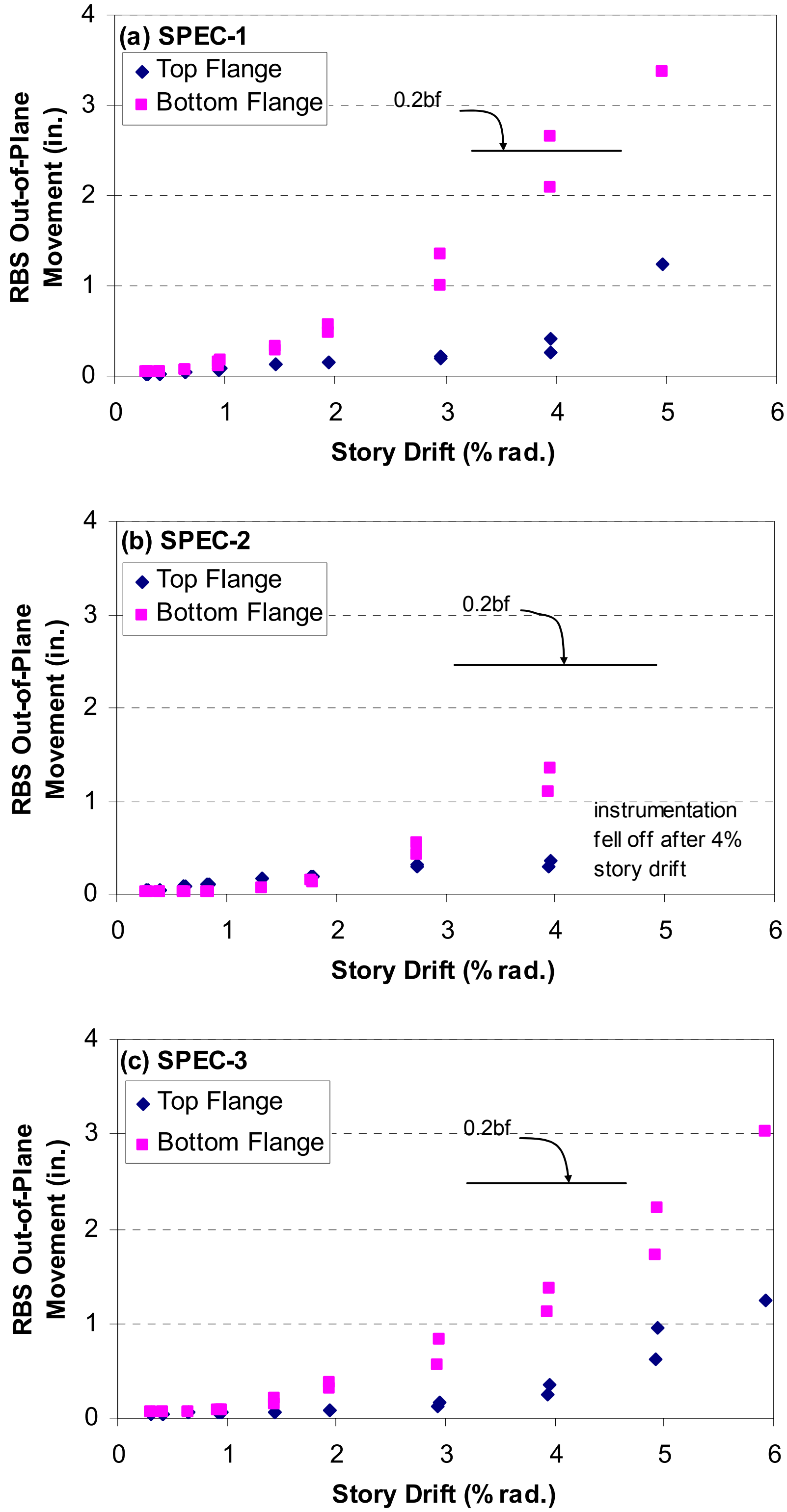

Figure 6.6 – Magnitude of RBS beam flange out-of-plane movement (Continued)

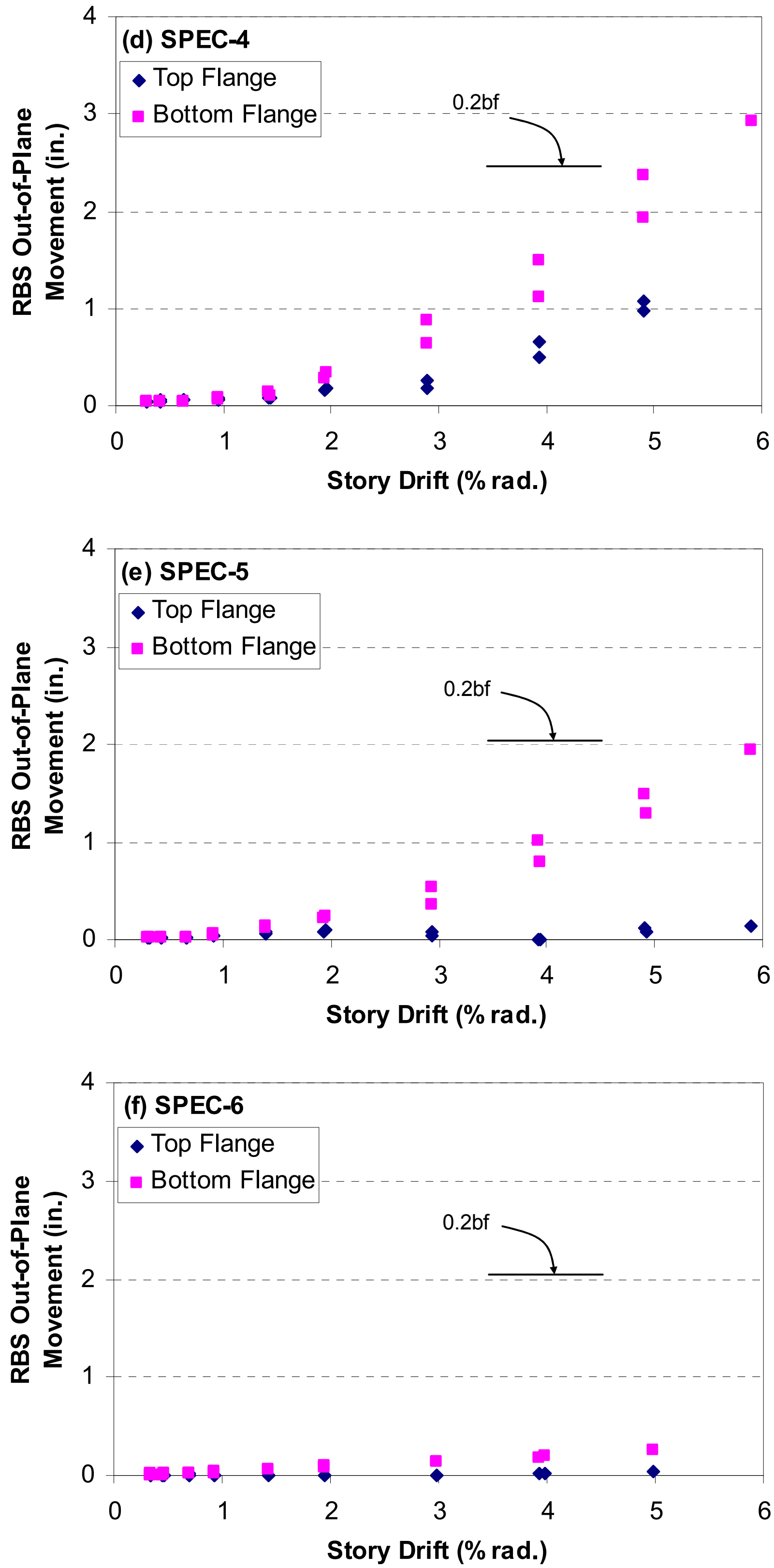

Figure 6.6 – Magnitude of RBS beam flange out-of-plane movement

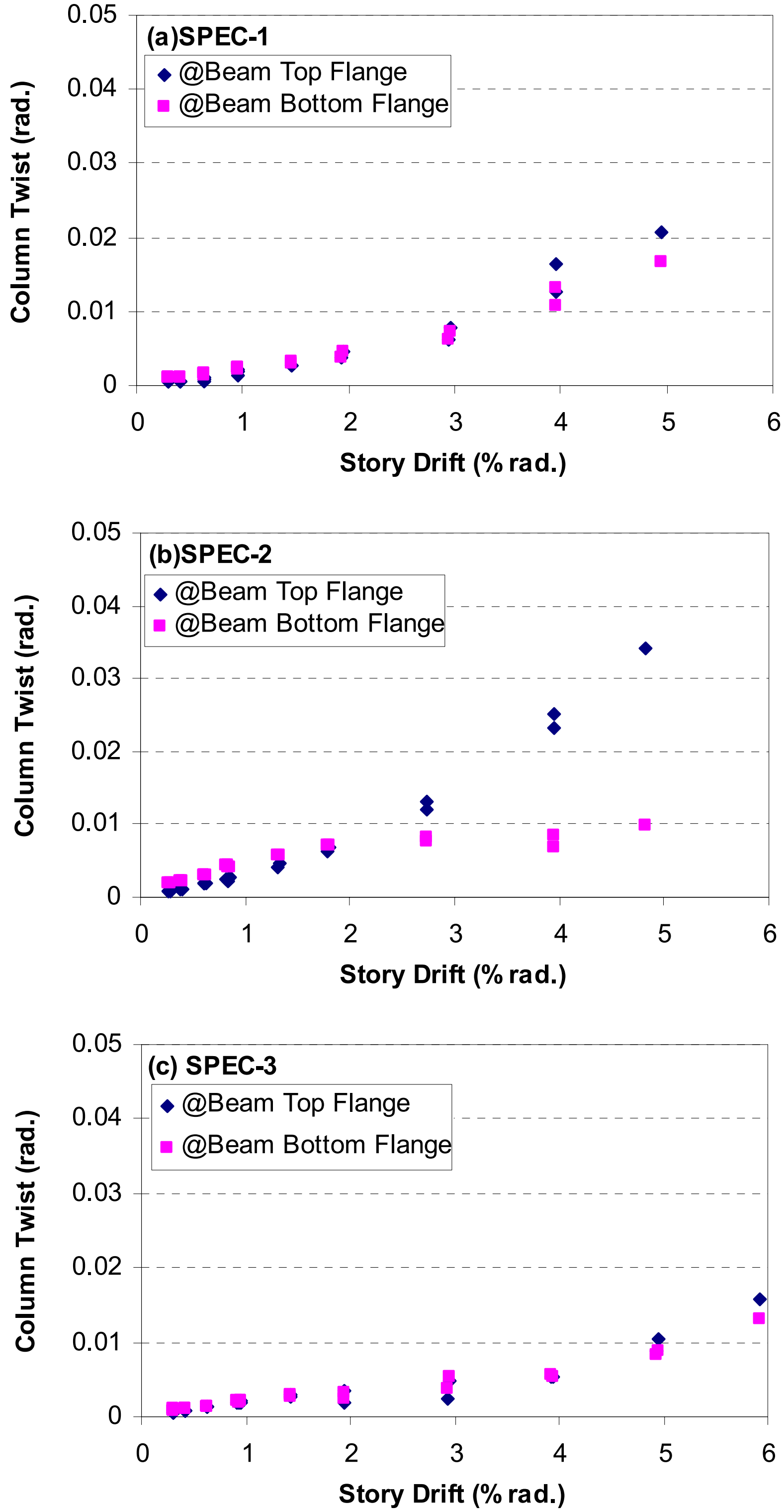

Figure 6.7 – Column twist (Continued)

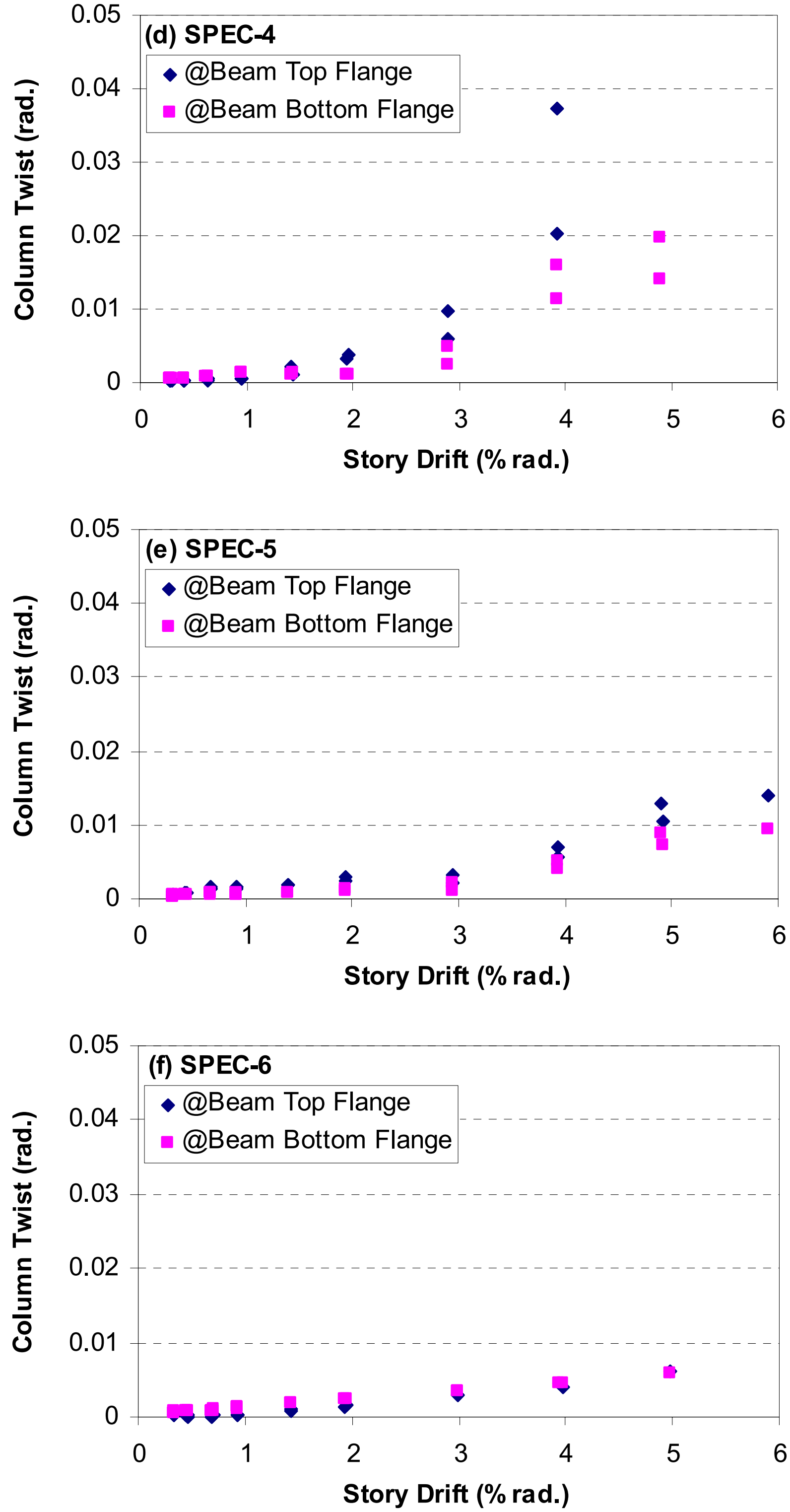

Figure 6.7 – Column twist

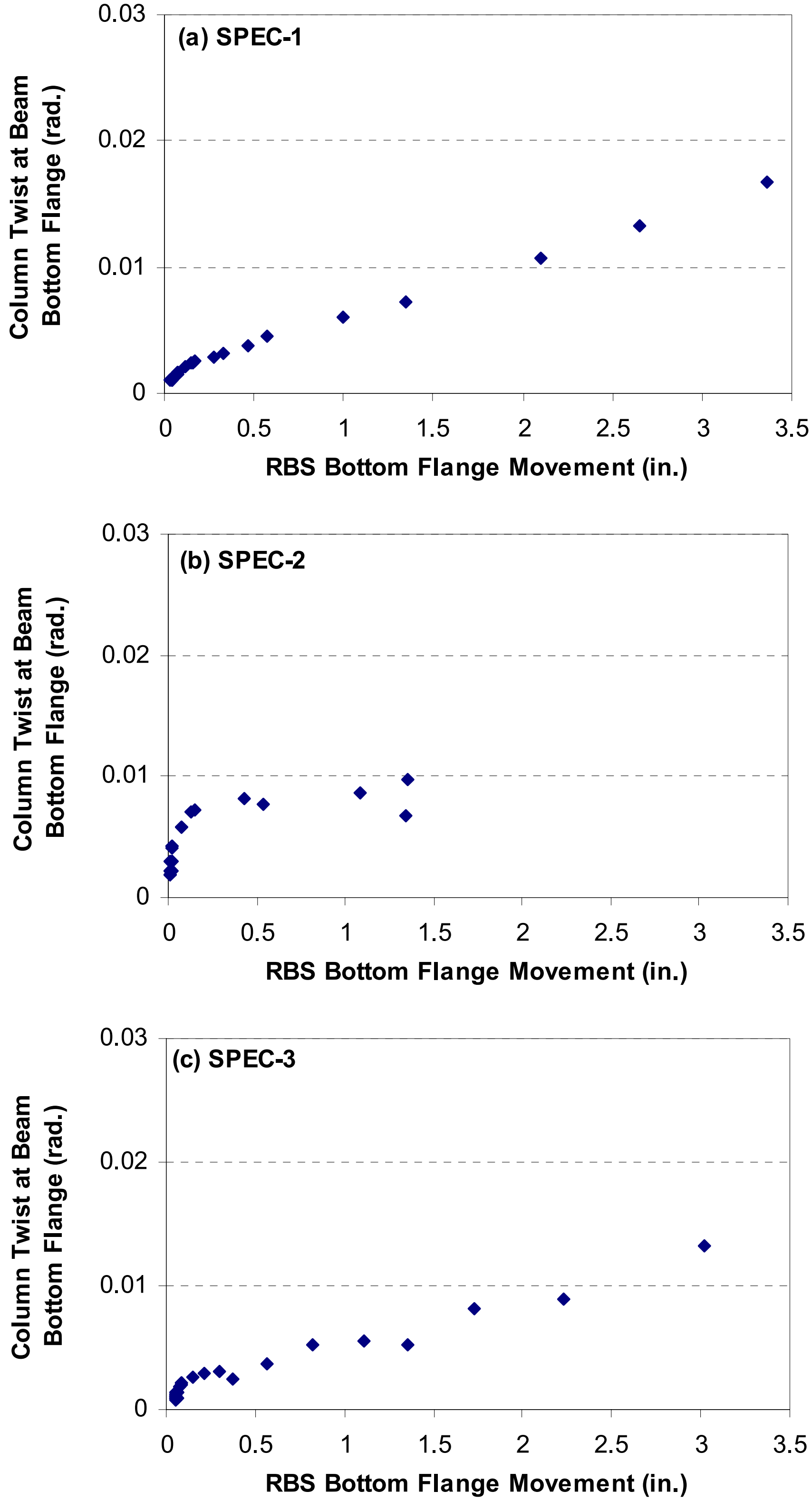

Figure 6.8 – Column twist vs. RBS lateral movement (Continued)

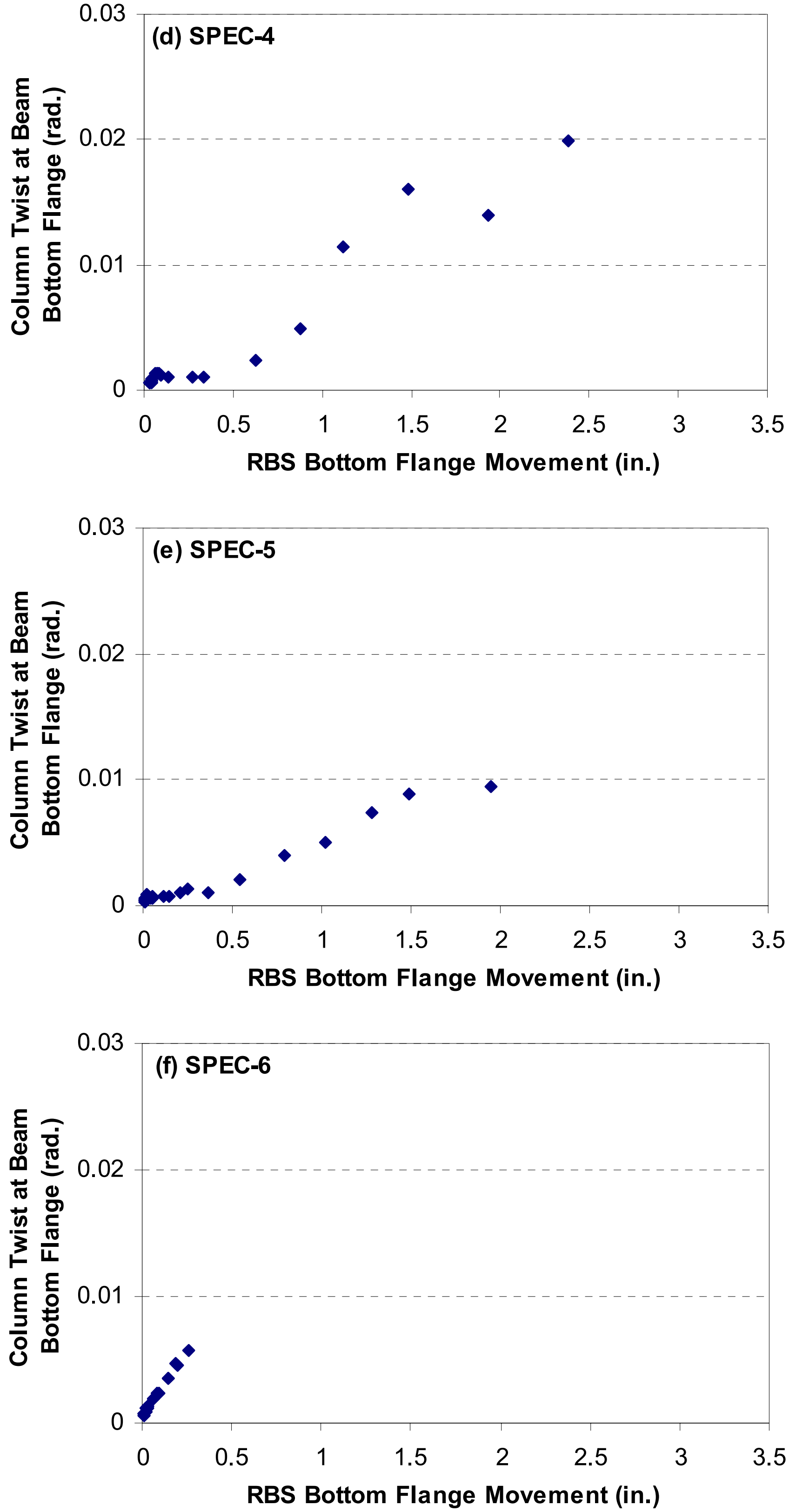

Figure 6.8 – Column twist vs. RBS lateral movement

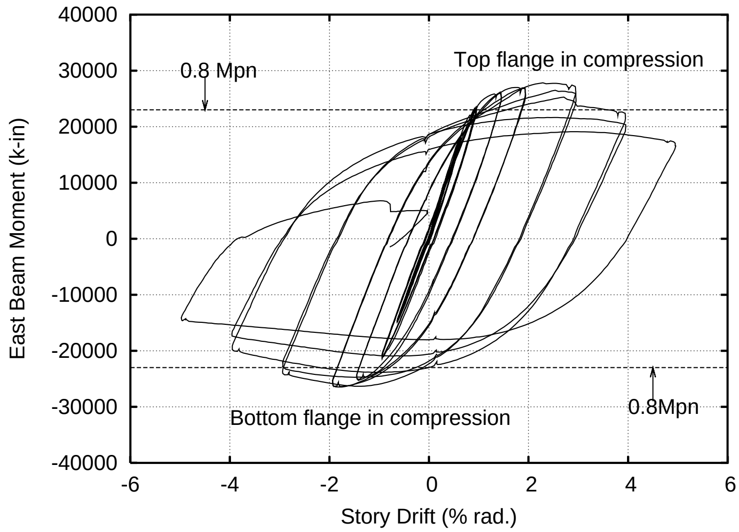

(a) SPEC-1 east beam moment at column face vs. story drift

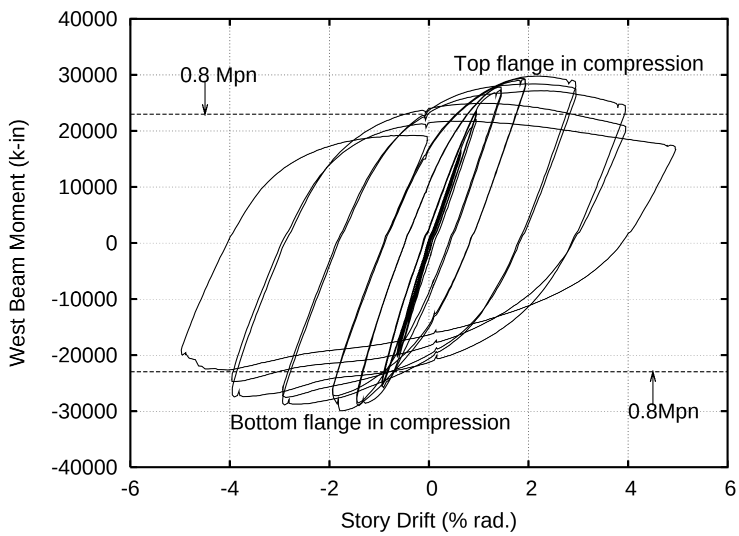

(b) SPEC-1 west beam moment at column face vs. story drift

Figure 6.9 – Beam moment at column face (continued)

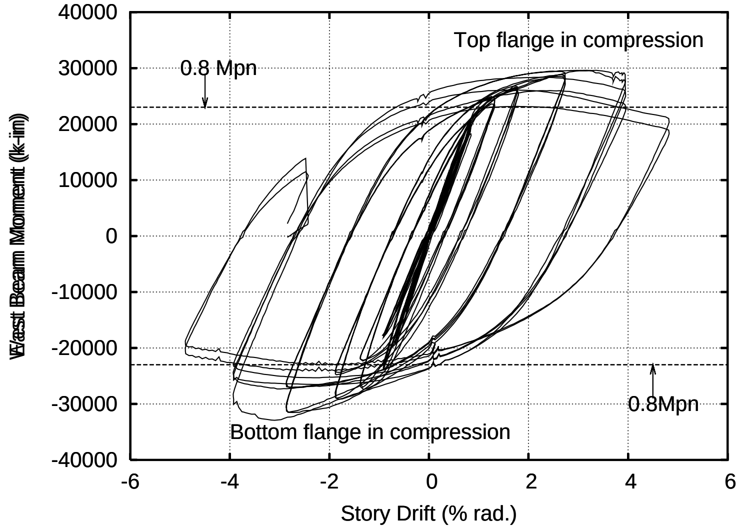

(c) SPEC-2 east beam moment at column face vs. story drift

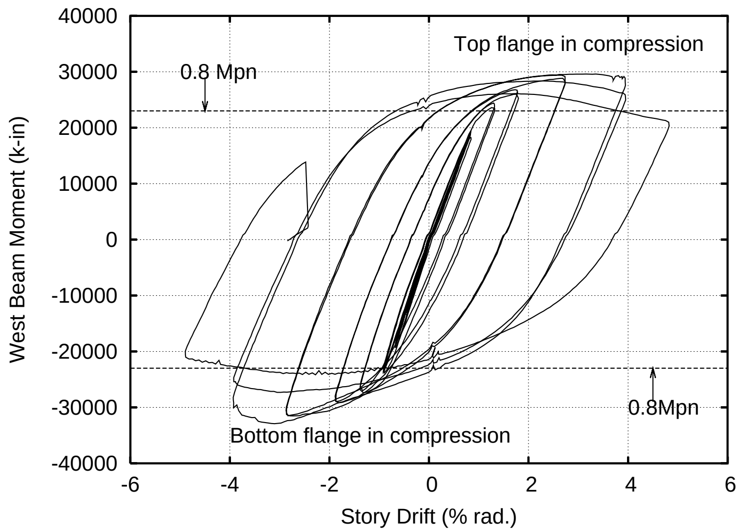

(d) SPEC-2 west beam moment at column face vs. story drift

Figure 6.9 – Beam moment at column face (continued)

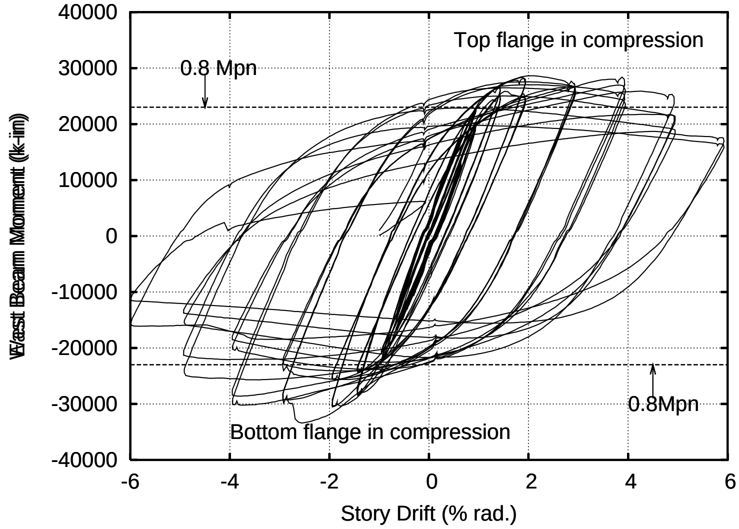

(e) SPEC-3 east beam moment at column face vs. story drift

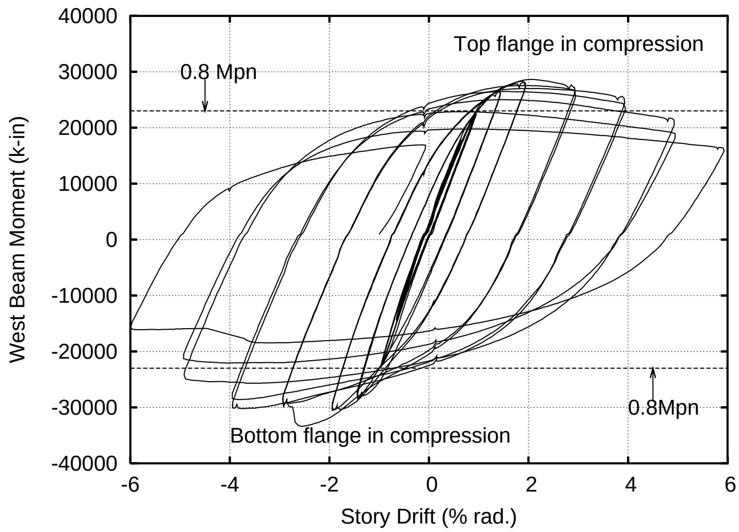

(f) SPEC-3 west beam moment at column face vs. story drift

Figure 6.9 – Beam moment at column face (continued)

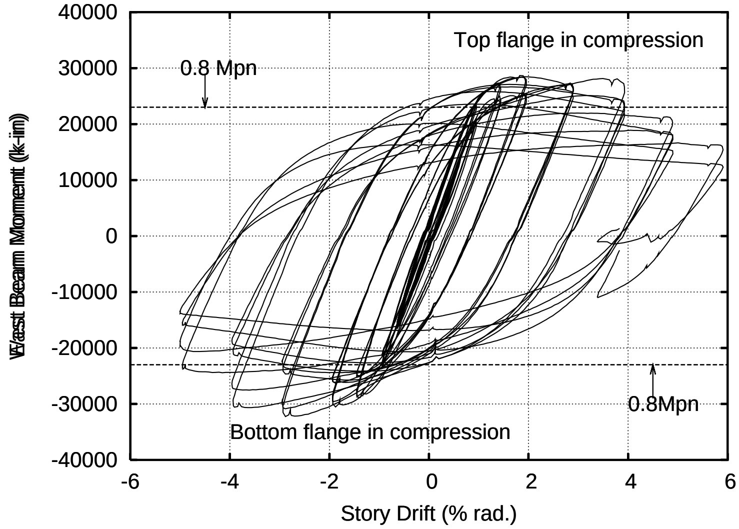

(g) SPEC-4 east beam moment at column face vs. story drift

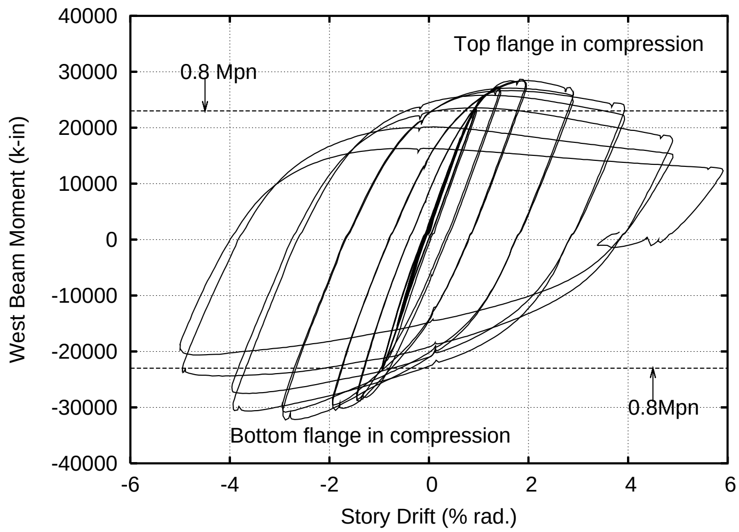

(h) SPEC-4 west beam moment at column face vs. story drift

Figure 6.9 – Beam moment at column face (continued)

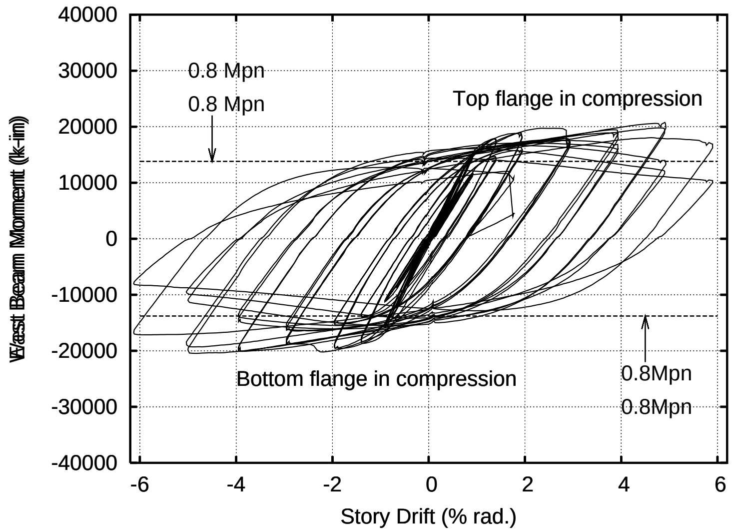

(i) SPEC-5 east beam moment at column face vs. story drift

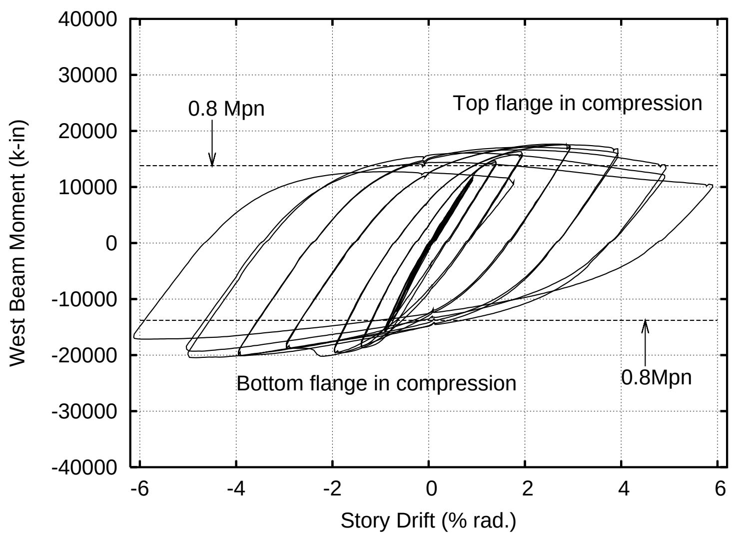

(j) SPEC-5 west beam moment at column face vs. story drift

Figure 6.9 – Beam moment at column face (continued)

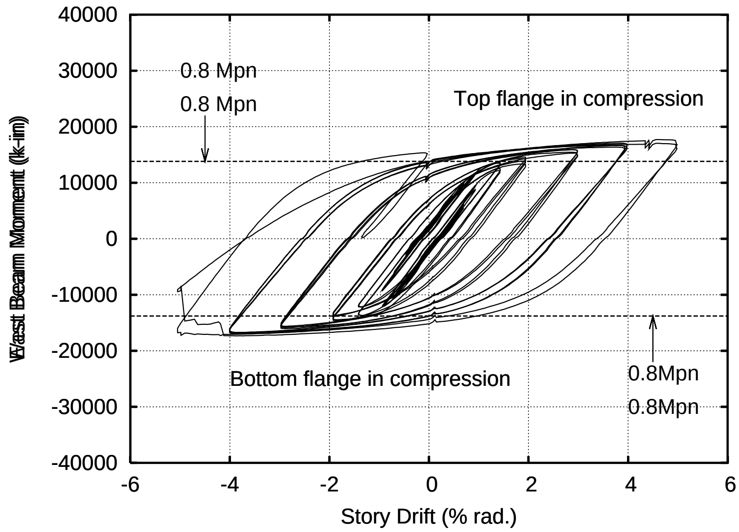

(k) SPEC-6 east beam moment at column face vs. story drift

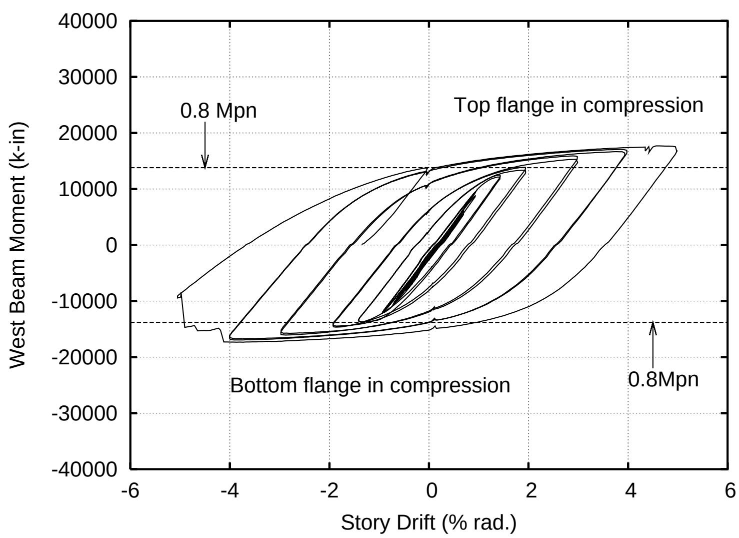

(l) SPEC-6 west beam moment at column face vs. story drift

Figure 6.9 – Beam moment at column face
(M_{pn}: beam nominal flexural capacity)

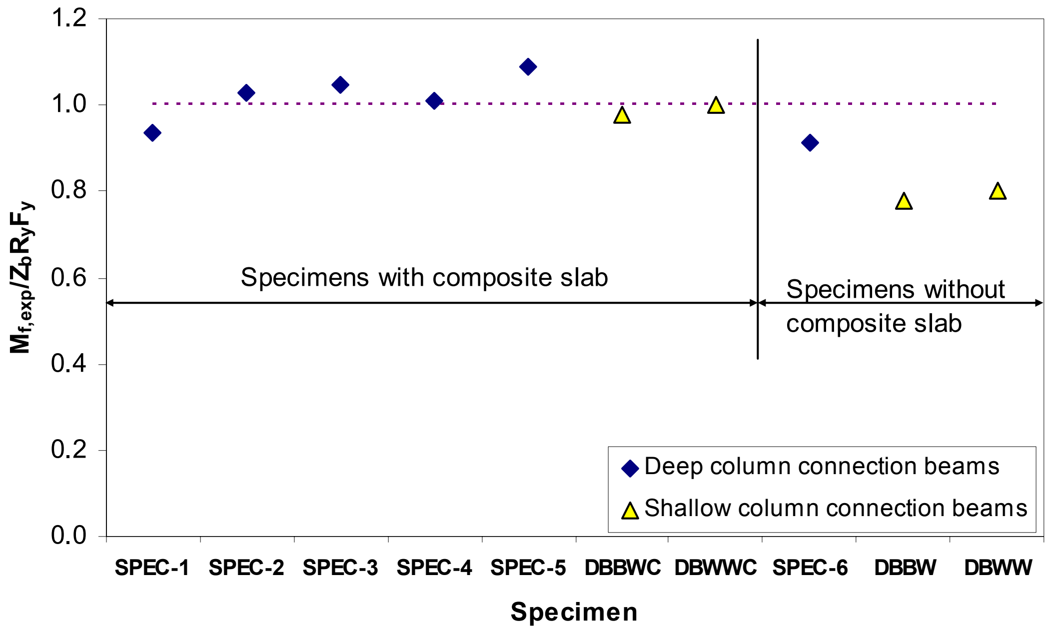

Figure 6.10 – Maximum beam moment achieved in test at column face
(Data for the shallow column specimens are from Engelhardt et al. 2000)

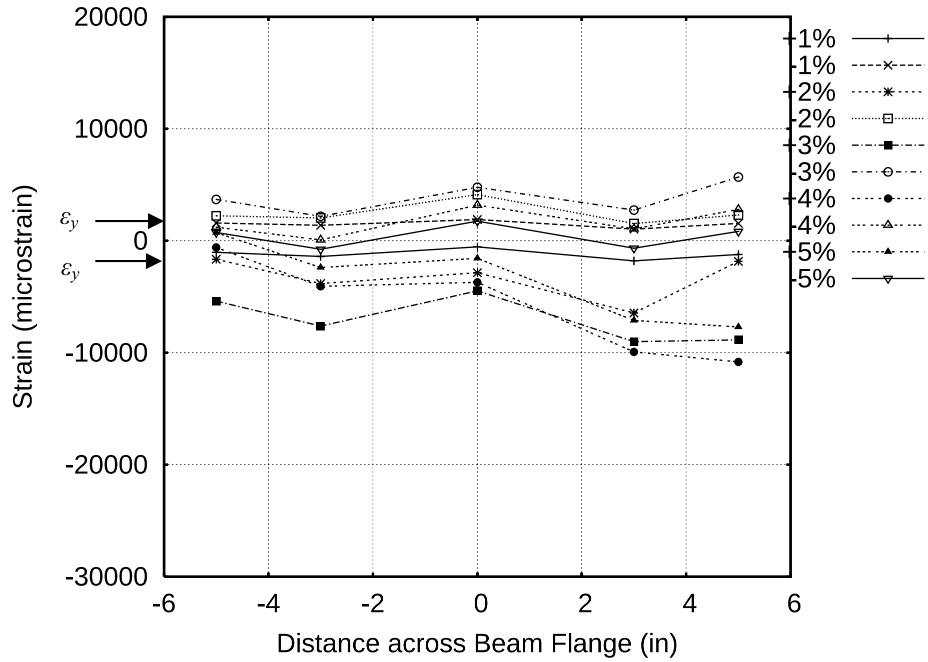

(a) Beam Top Flange

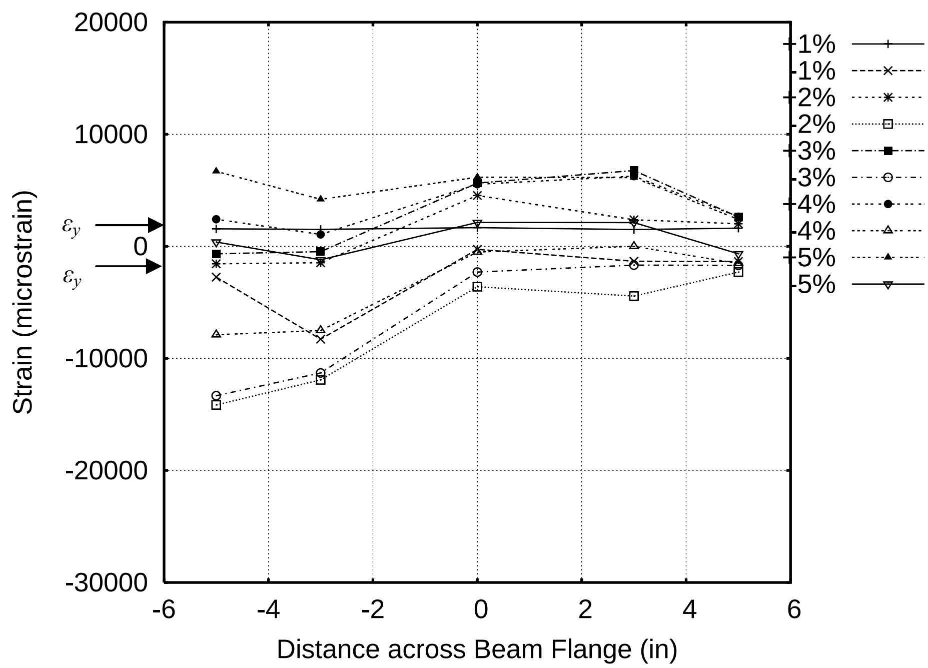

(b) Beam Bottom Flange

Figure 6.11 – Strain profile across the beam top and bottom flanges of SPEC-1
(ε_y= 1.714 x 10^{-3})

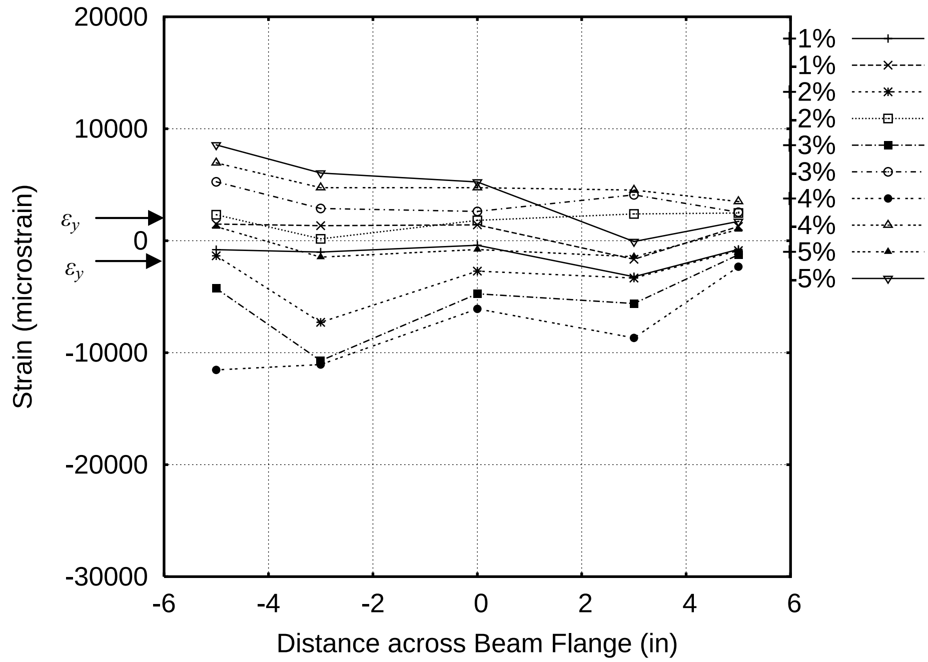

(a) Beam Top Flange

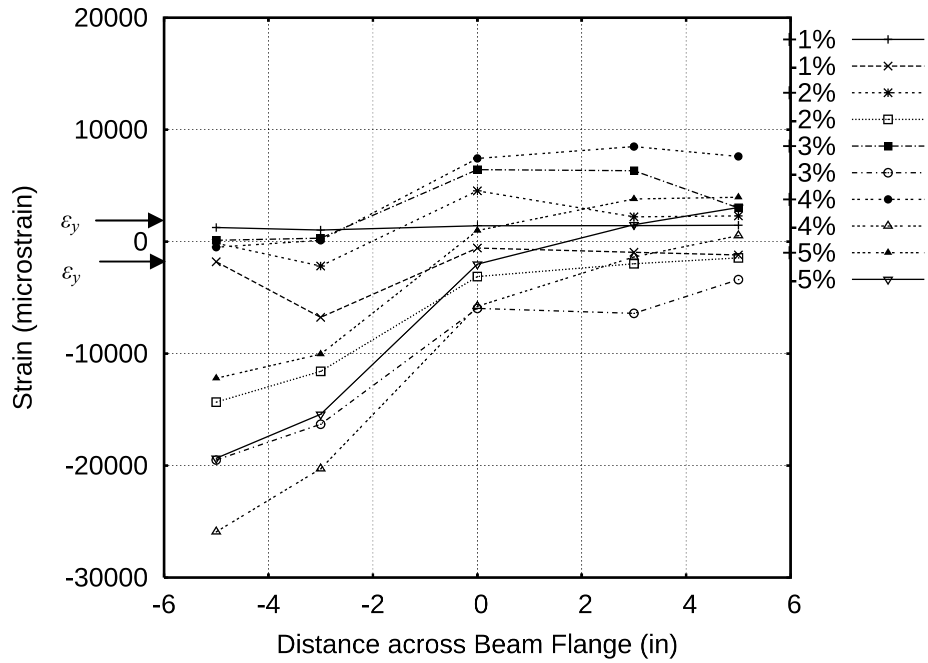

(b) Beam Bottom Flange

Figure 6.12 – Strain profile across the beam top and bottom flanges of SPEC-2
(ε_y= 1.714 x 10^{-3})

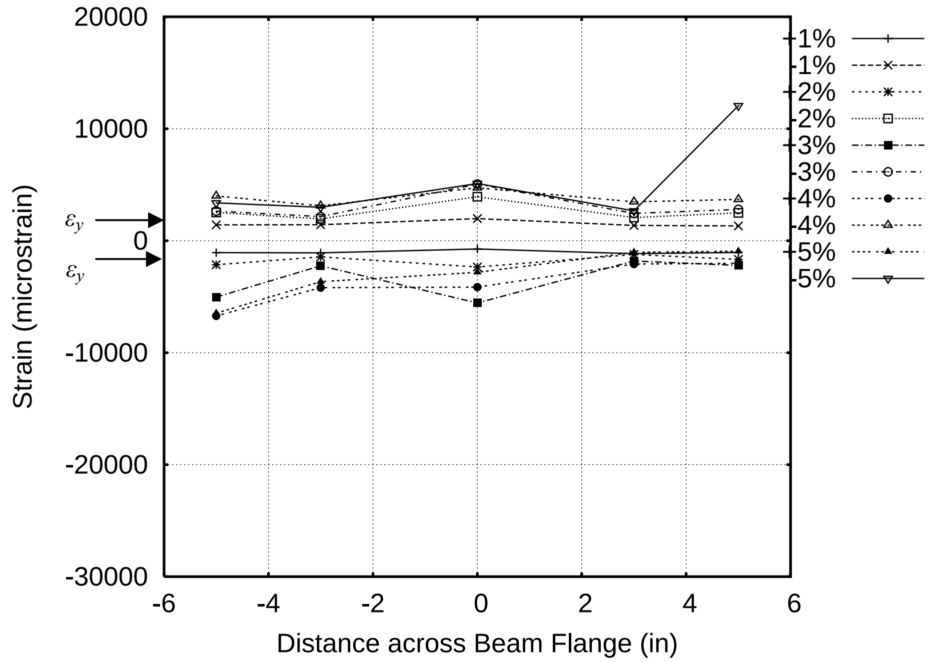

(a) Beam Top Flange

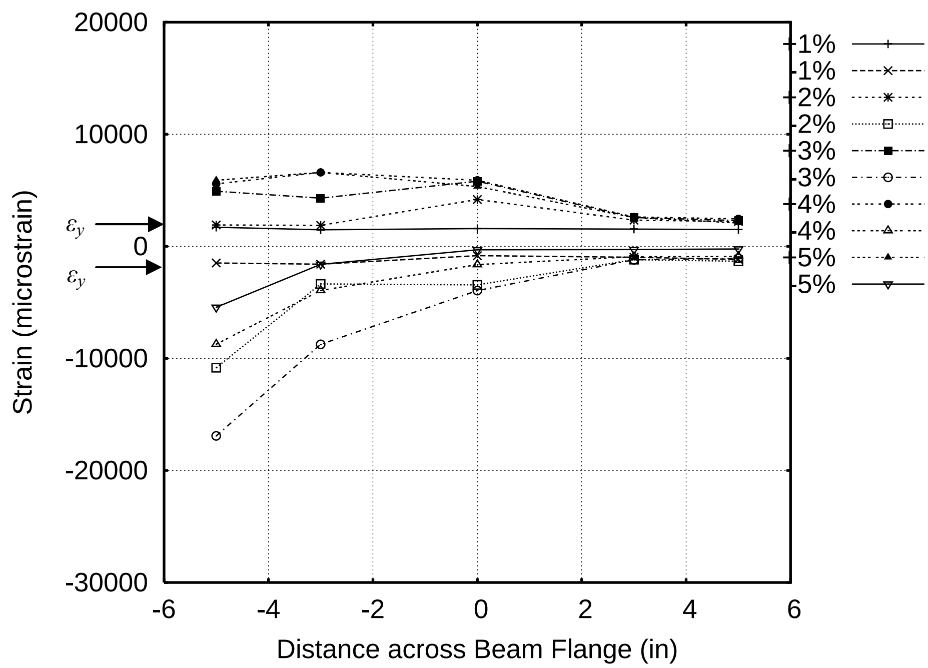

(b) Beam Bottom Flange

Figure 6.13 – Strain profile across the beam top and bottom flanges of SPEC-3 (ε_y= 1.828 x 10^{-3})

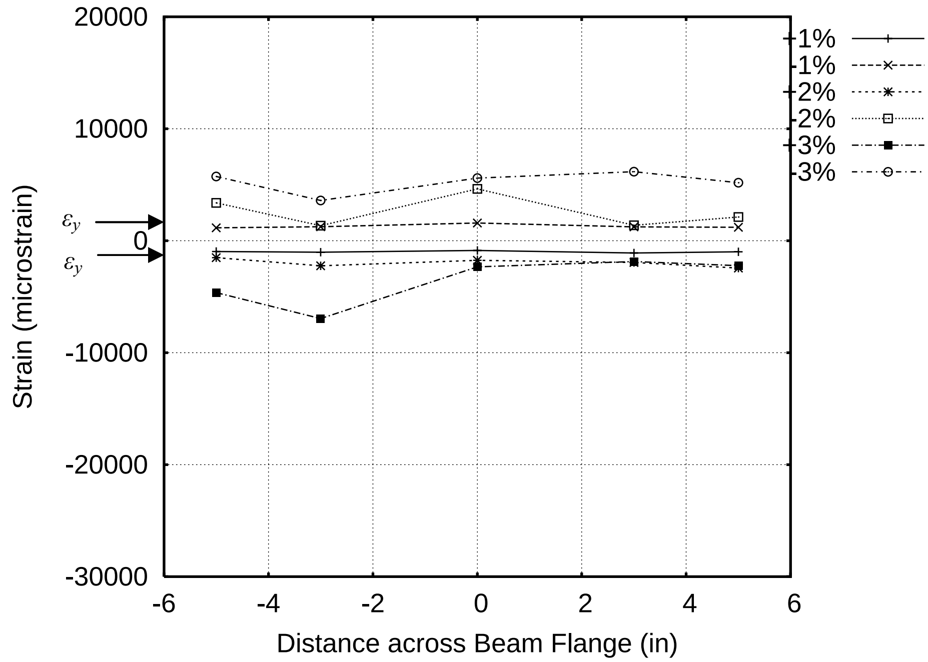

(a) Beam Top Flange

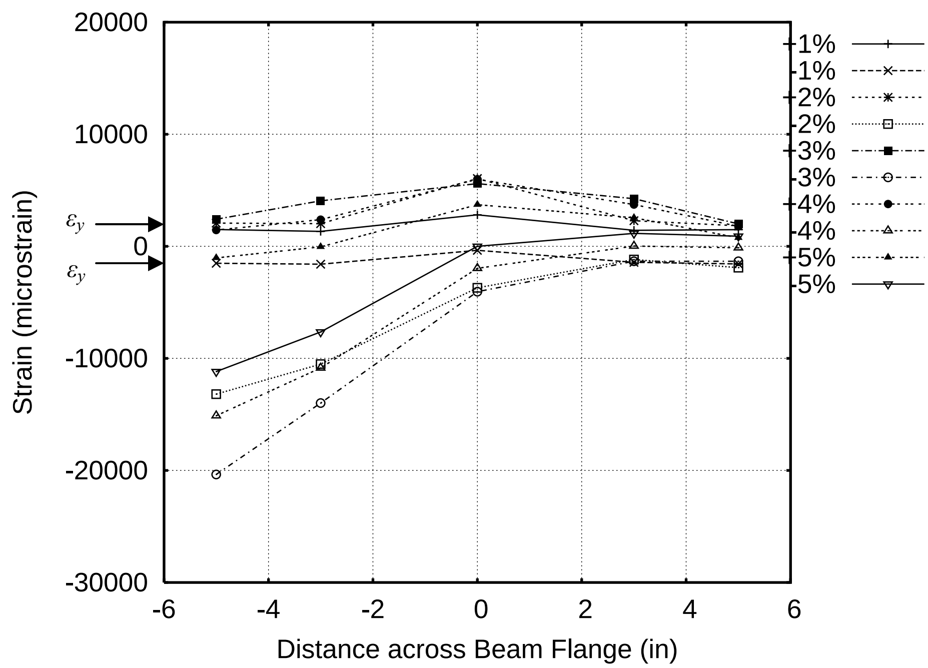

(b) Beam Bottom Flange

Figure 6.14 – Strain profile across the beam top and bottom flanges of SPEC-4 (ε_y= 1.828 x 10^{-3})

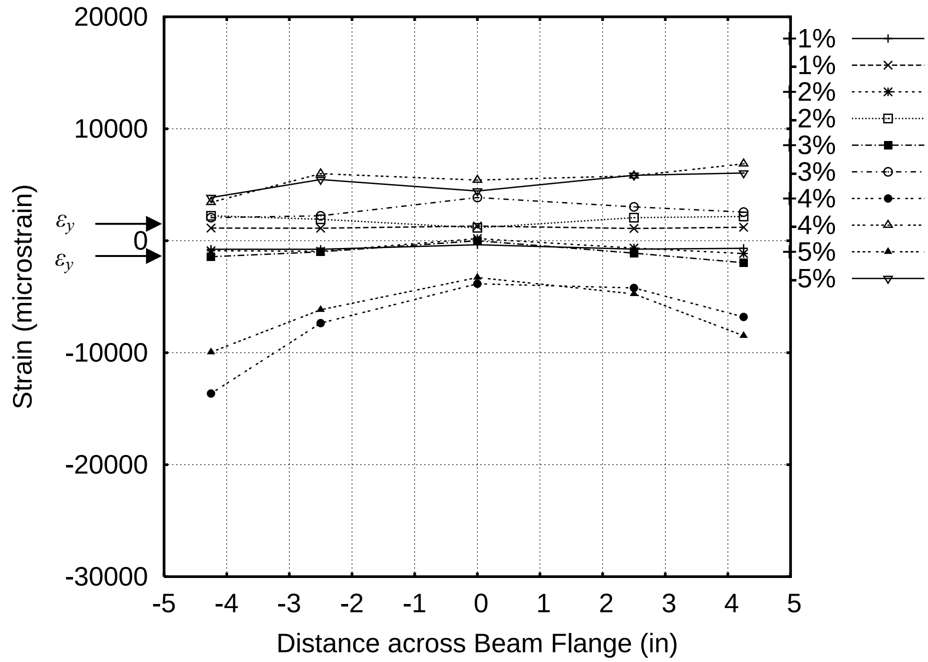

(a) Beam top flange

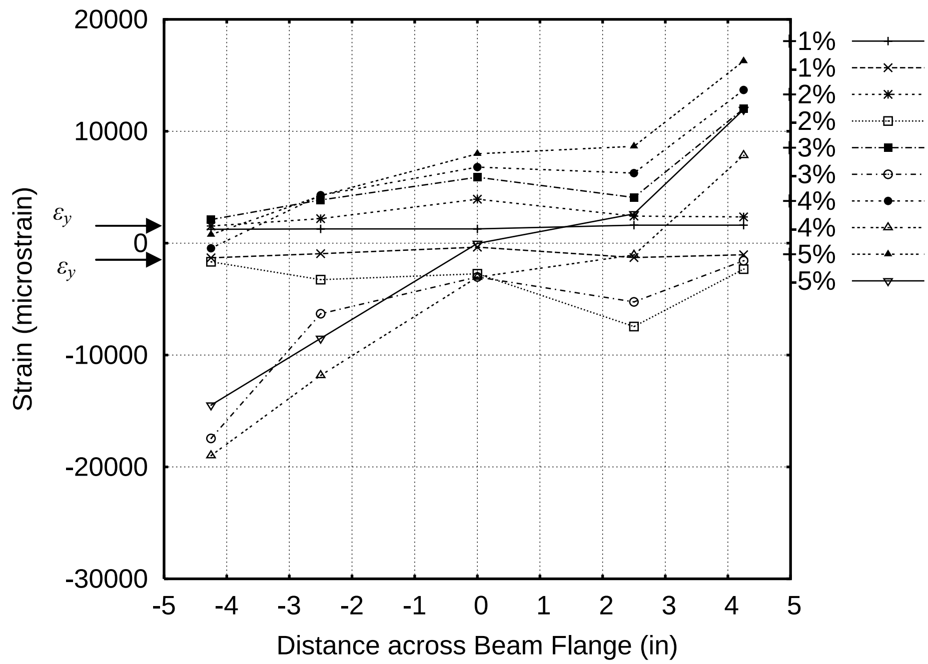

(b) Beam bottom flange

Figure 6.15 – Strain profile across the beam top and bottom flanges of SPEC-5 (ε_y= 1.721 x 10^{-3})

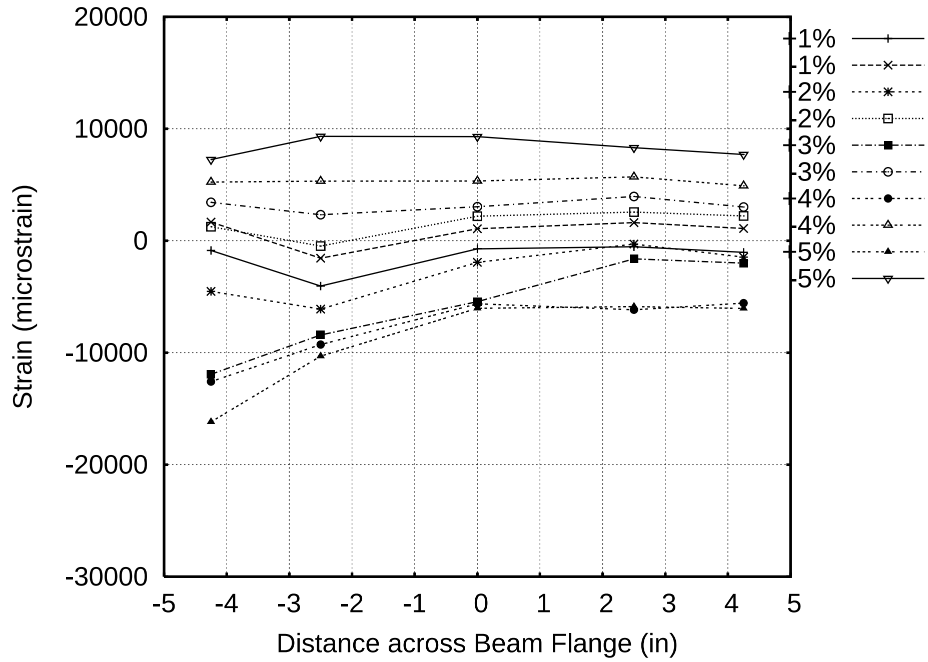

(a) Beam top flange

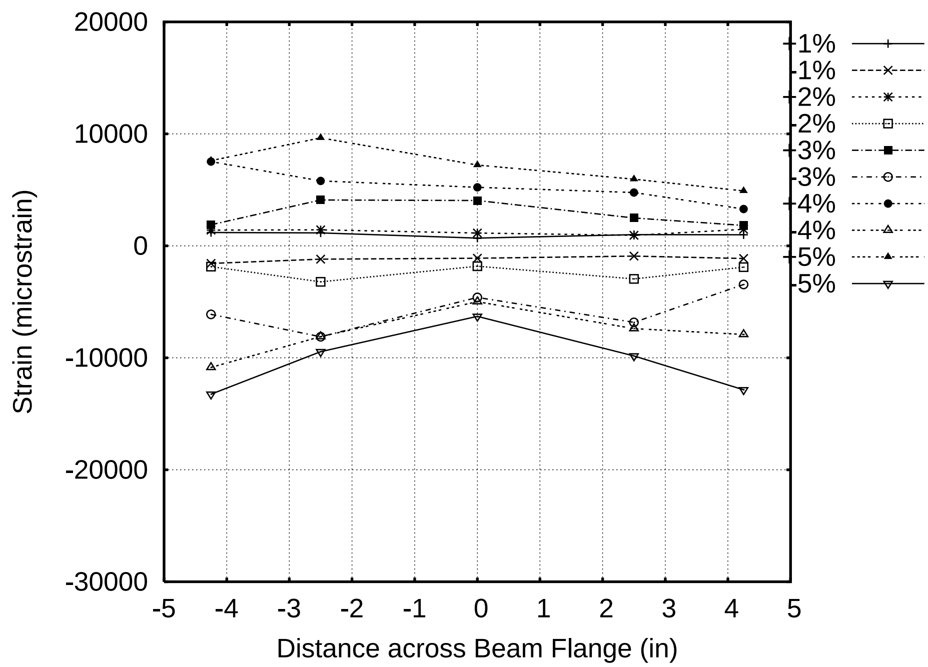

(b) Beam bottom flange

Figure 6.16 – Strain profile across the beam top and bottom flanges of SPEC-6

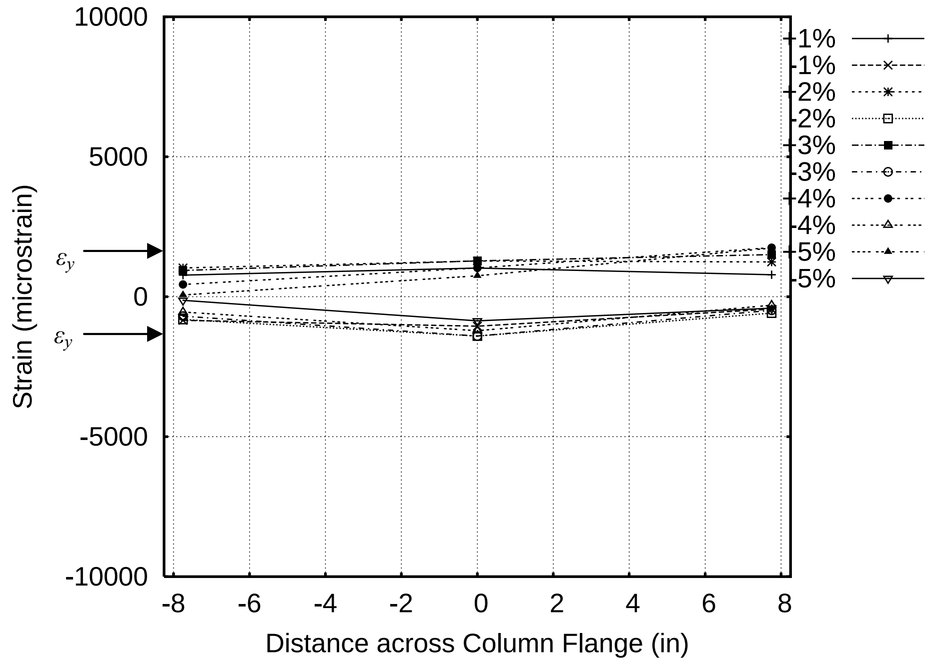

(a) East Face Column Flange

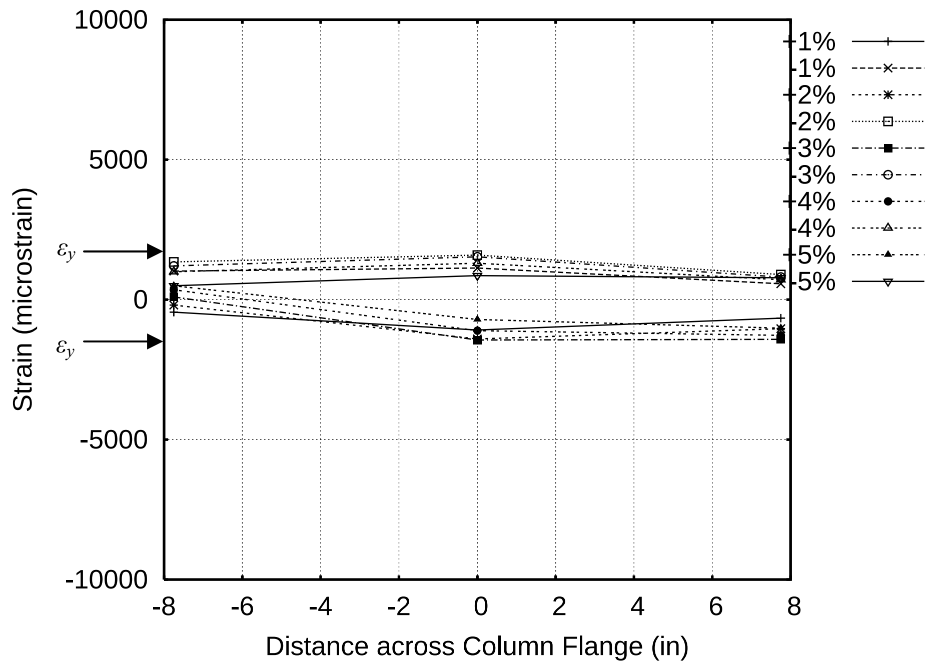

(b) West Face Column Flange

Figure 6.17 – Strain profile across column flanges of SPEC-1
(ε_y= 1.779 x 10^{-3})

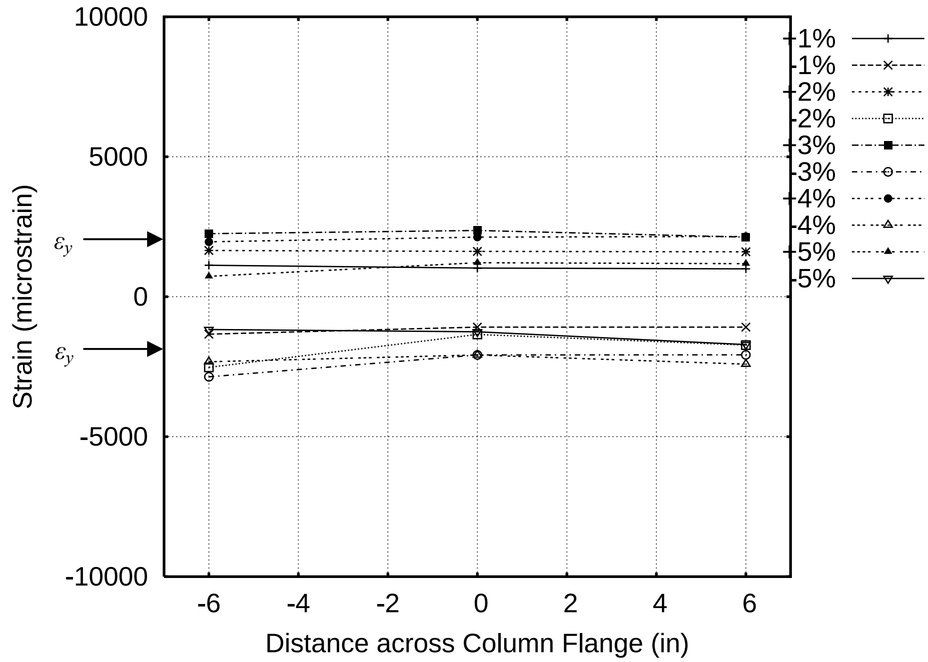

(a) East Face Column Flange

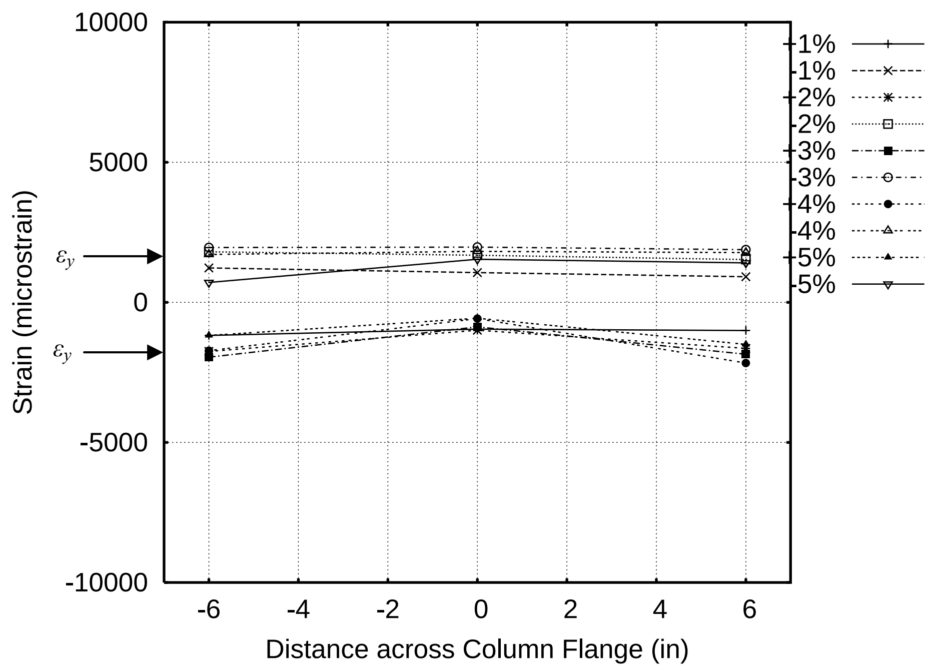

(b) West Face Column Flange

Figure 6.18 – Strain profile across column flanges of SPEC-2
(ε_y= 1.859 x 10^{-3})

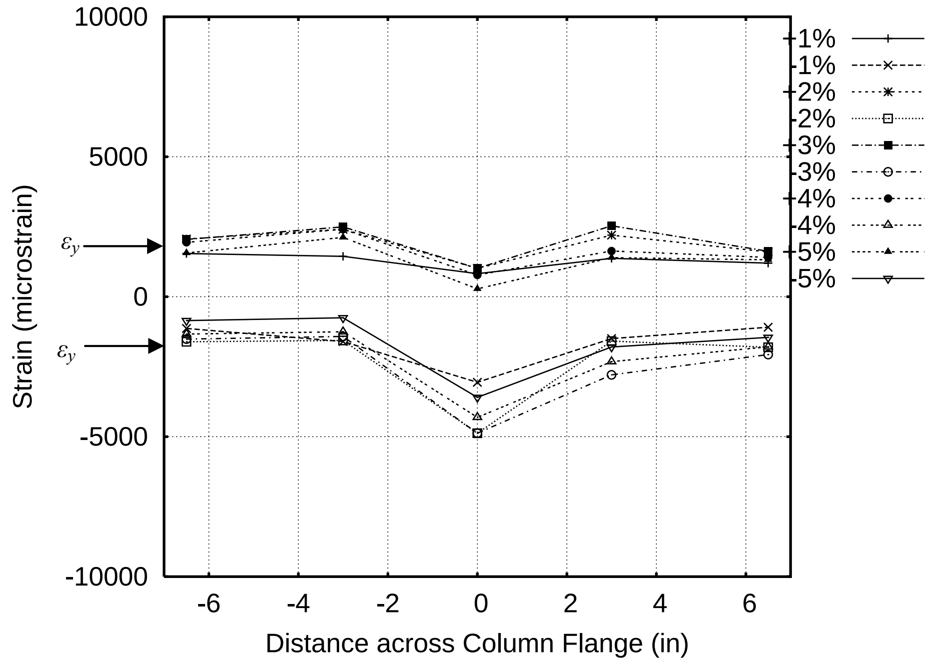

(a) East Face Column Flange

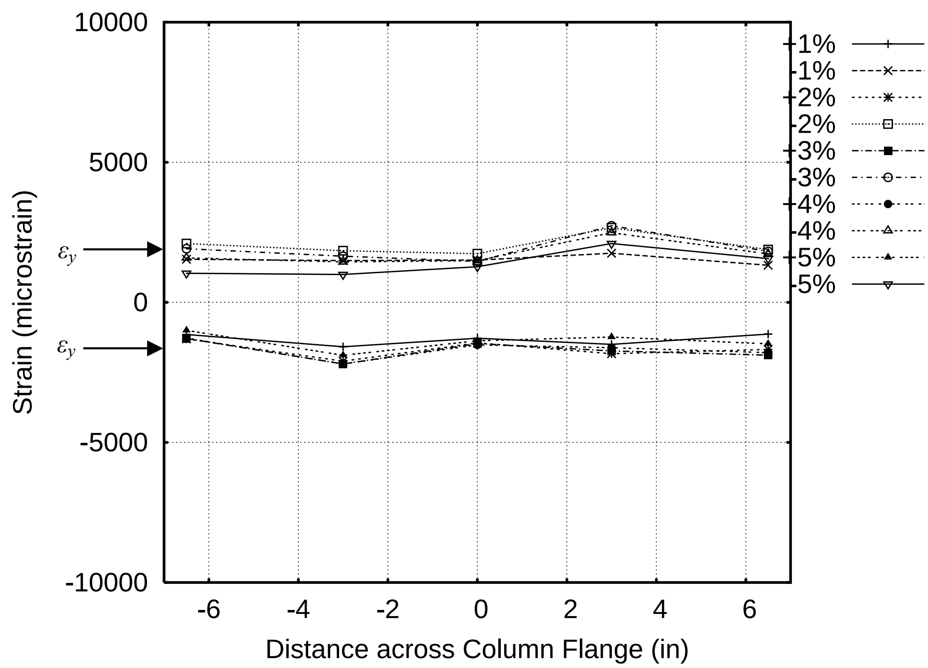

(b) West Face Column Flange

Figure 6.19 – Strain profile across column flanges of SPEC-3
(ε_y= 1.783 x 10^{-3})

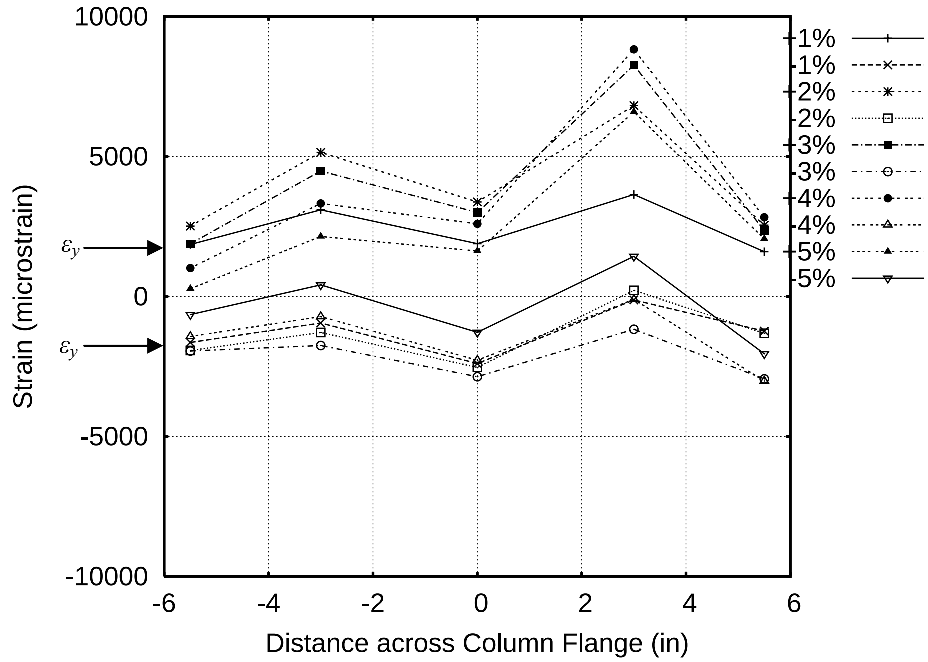

(a) East Face Column Flange

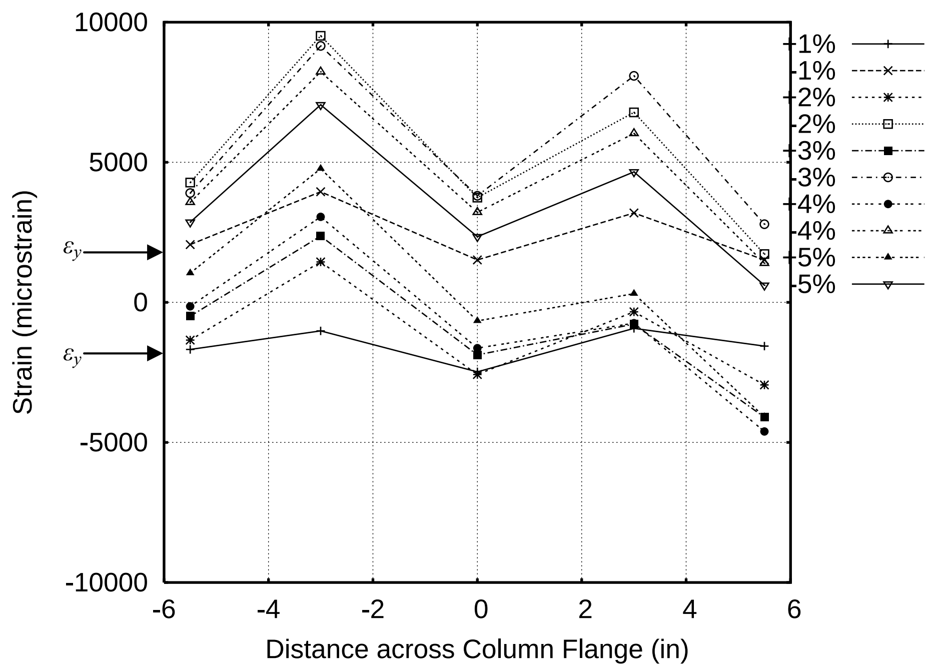

(b) West Side Column Flange

Figure 6.20 – Strain profile across column flanges of SPEC-4
(ε_y= 1.828 x 10^{-3})

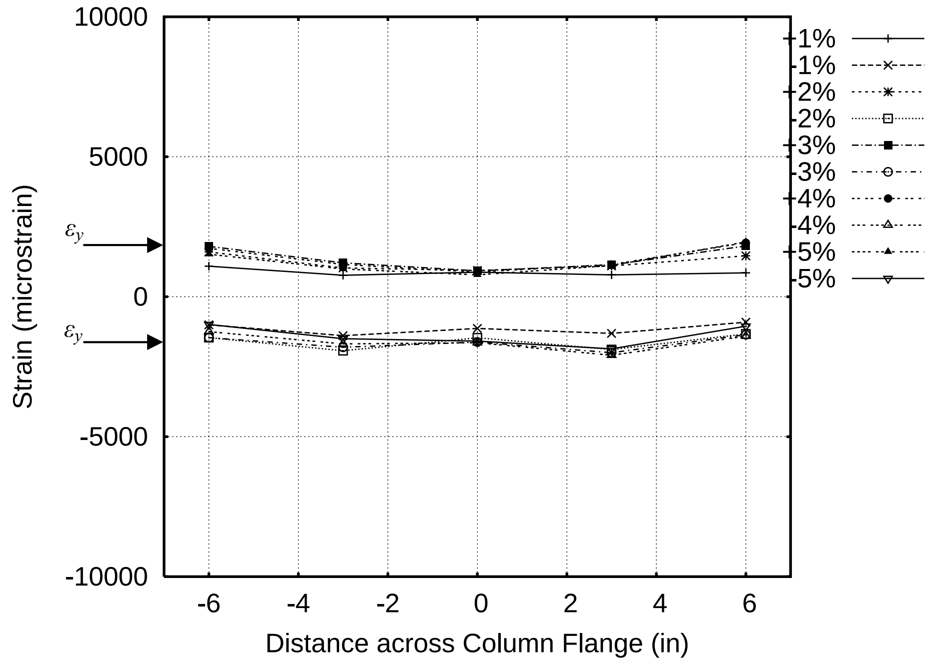

(a) East Face Column Flange

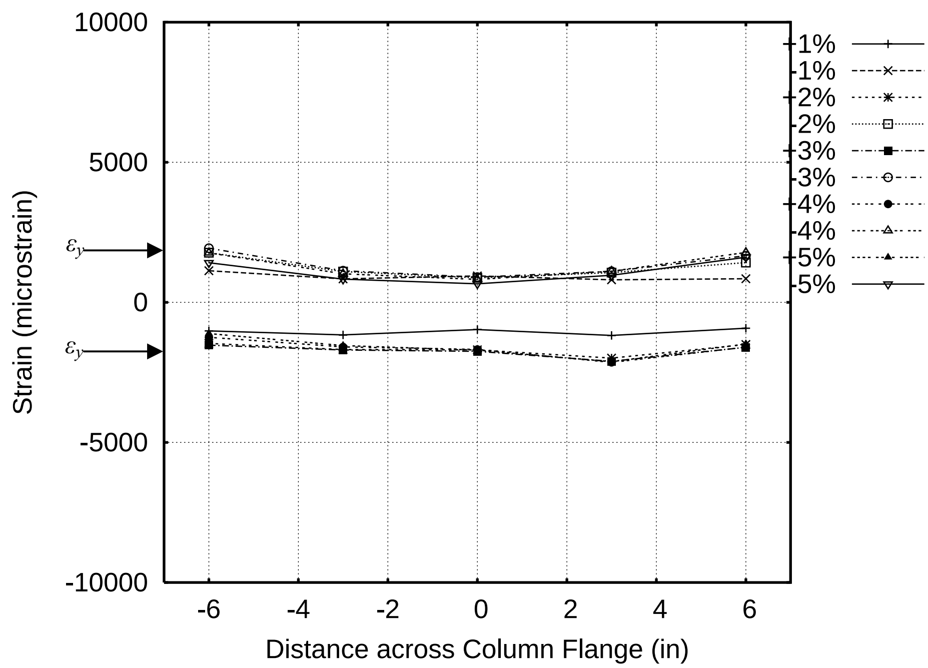

(b) West Side Column Flange

Figure 6.21 – Strain profile across column flanges of SPEC-5
(ε_y= 1.817 x 10^{-3})

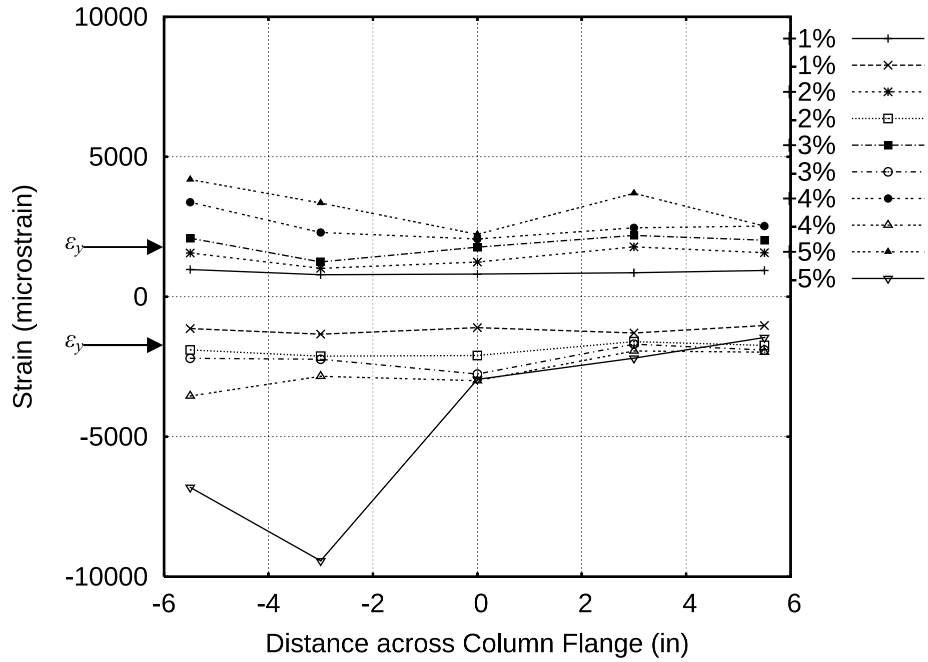

(a) East Face Column Flange

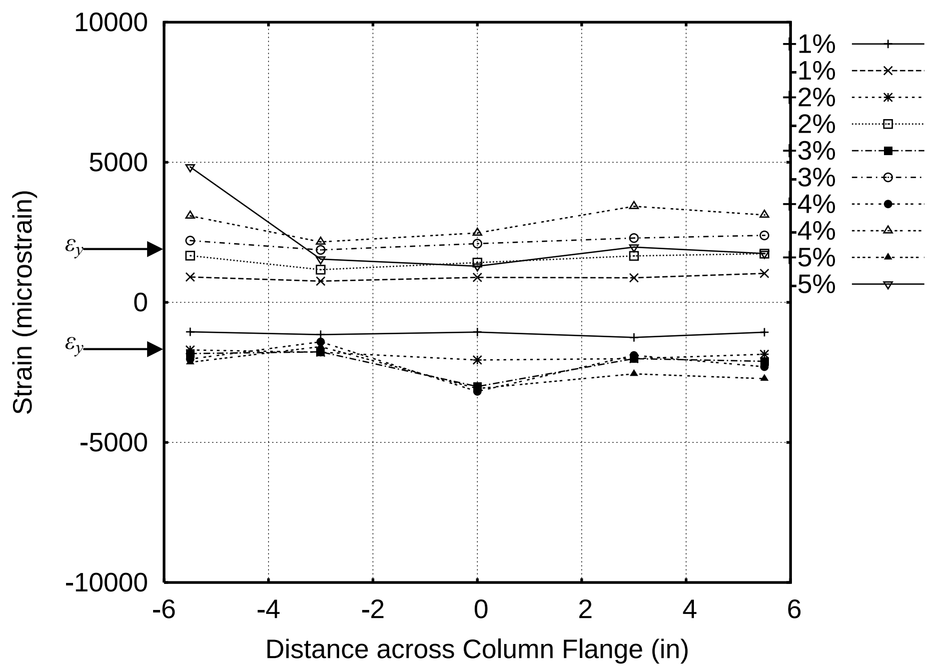

(b) West Side Column Flange

Figure 6.22 – Strain profile across column flanges of SPEC-6
(ε_y= 1.672 x 10^{-3})

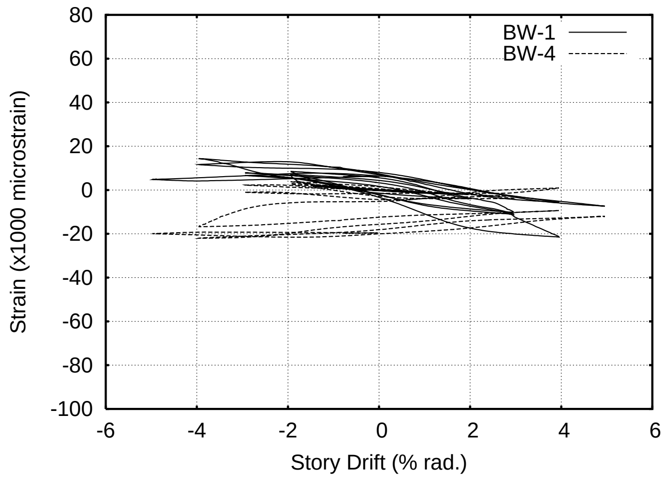

(a) BW-1 vs. BW-4

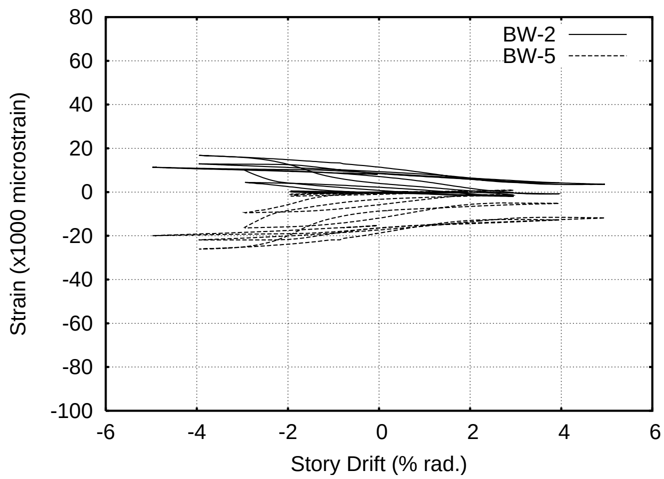

(b) BW-2 vs. BW-5

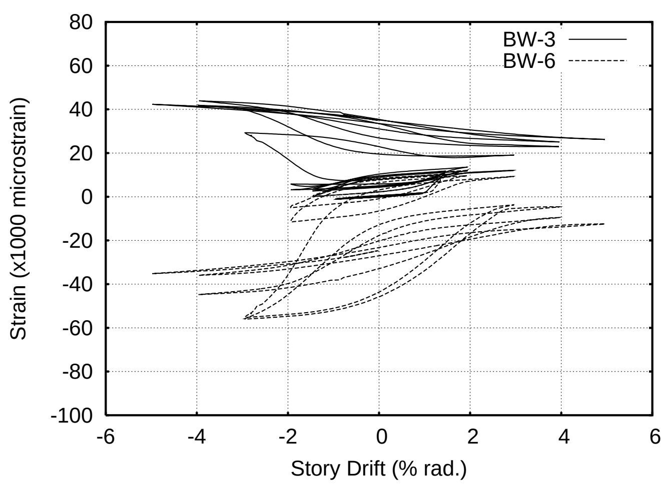

(c) BW-3 vs. BW-6

Figure 6.23 – Beam web strains showing web local buckling of SPEC-1

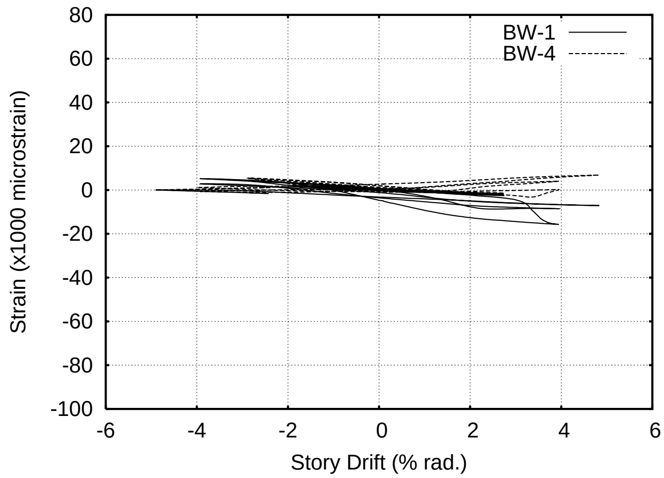

(a) BW-1 vs. BW-4

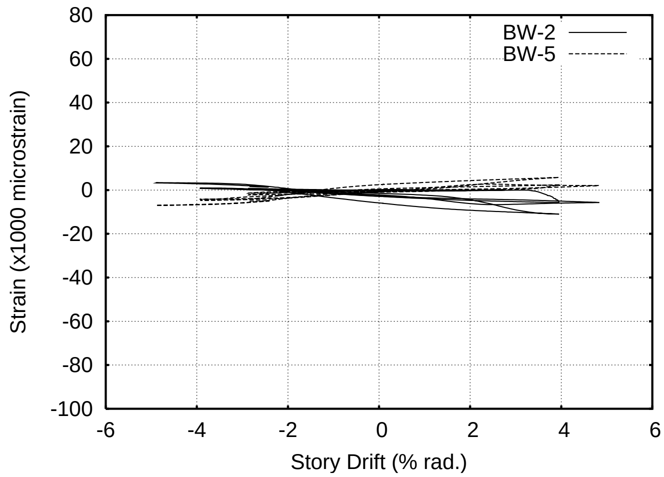

(b) BW-2 vs. BW-5

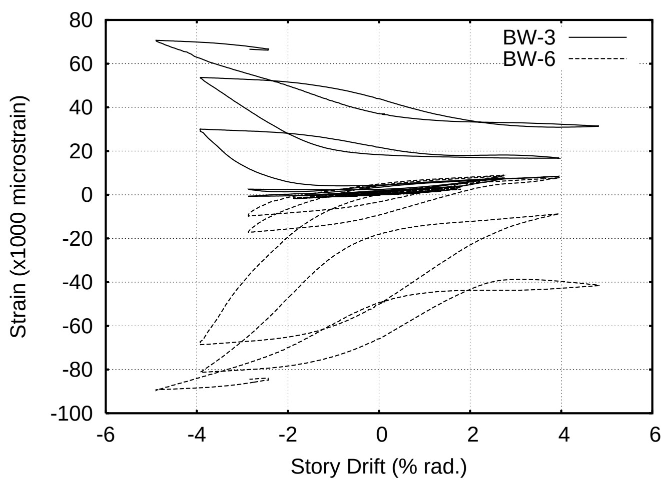

(c) BW-3 vs. BW-6

Figure 6.24 – Beam web strains showing web local buckling of SPEC-2

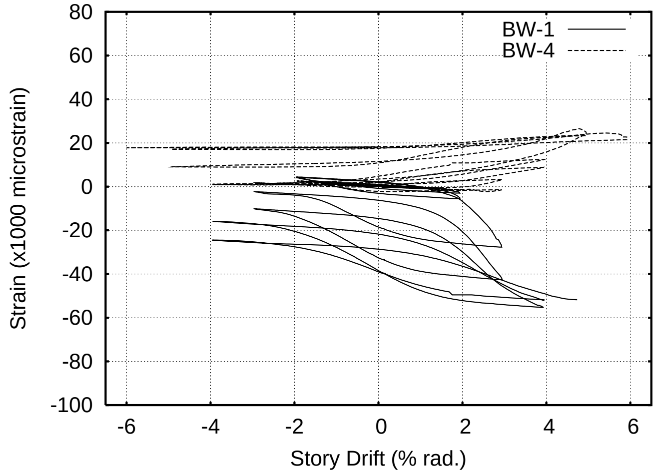

(a) BW-1 vs. BW-4

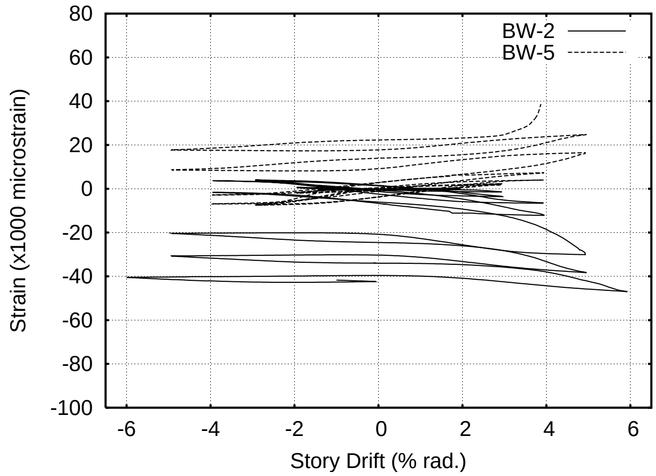

(b) BW-2 vs. BW-5

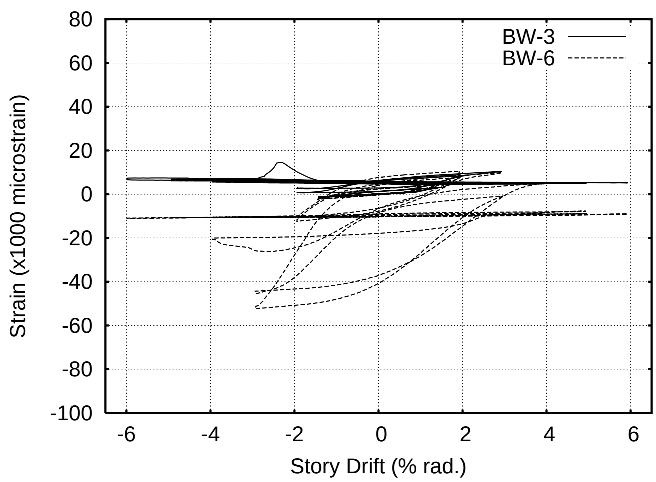

(c) BW-3 vs. BW-6

Figure 6.25 – Beam web strains showing web local buckling of SPEC-3

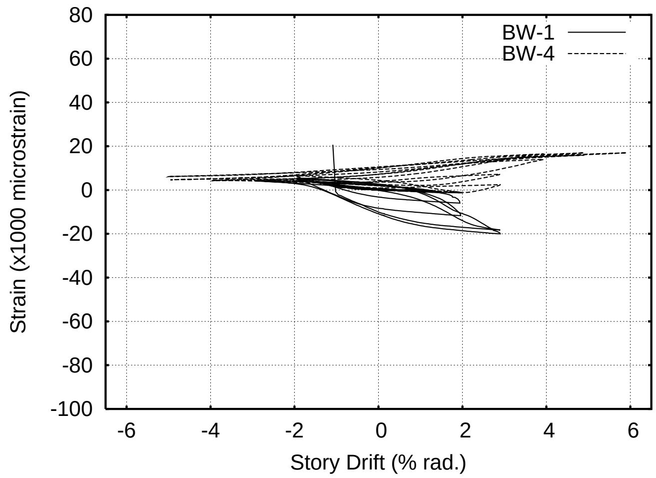

(a) BW-1 vs. BW-4

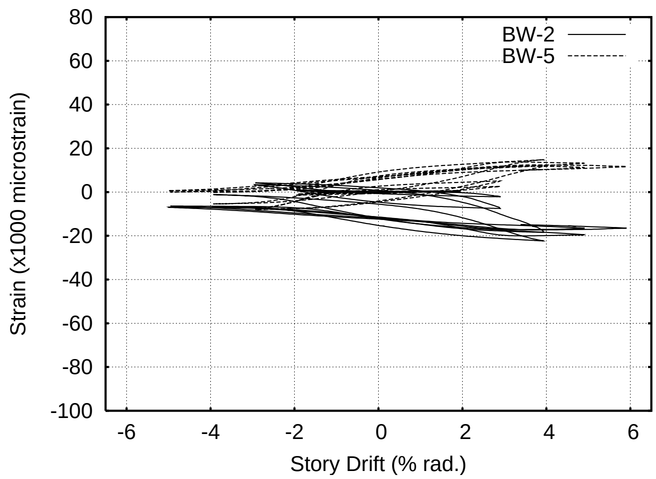

(b) BW-2 vs. BW-5

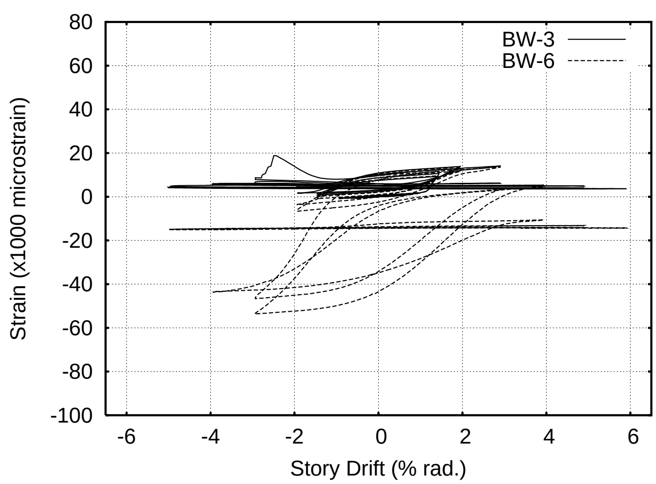

(c) BW-3 vs. BW-6

Figure 6.26 – Beam web strains showing web local buckling of SPEC-4

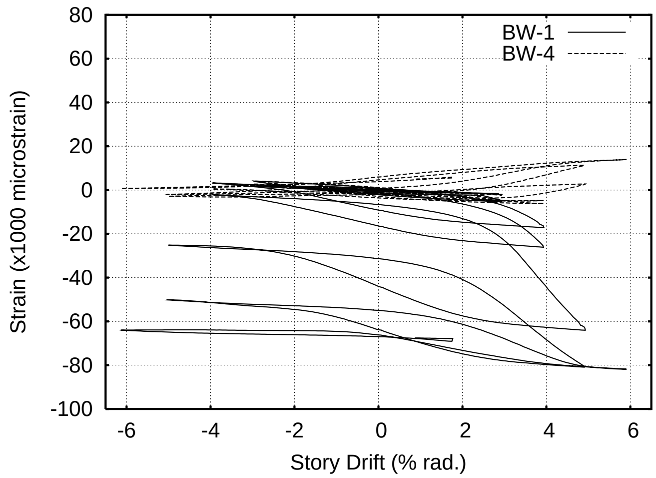

(a) BW-1 vs. BW-4

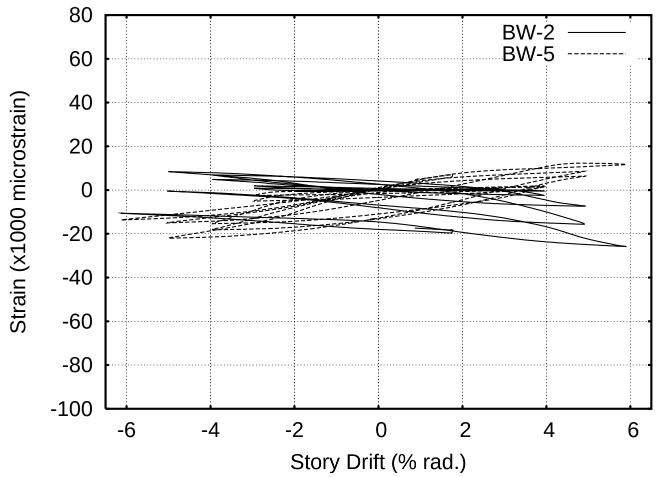

(b) BW-2 vs. BW-5

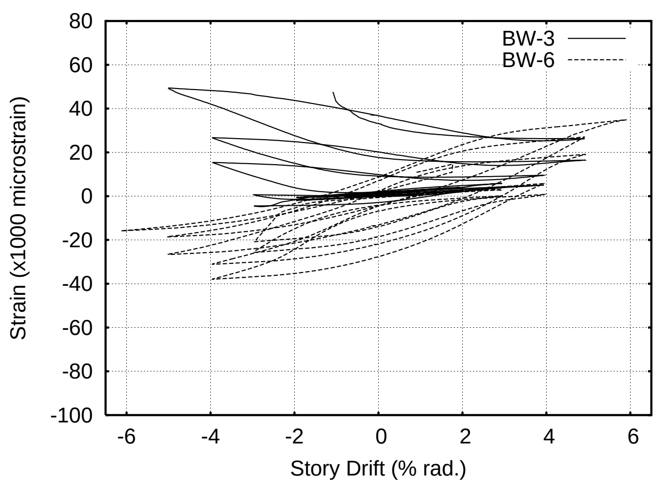

(c) BW-3 vs. BW-6

Figure 6.27 – Beam web strains showing web local buckling of SPEC-5

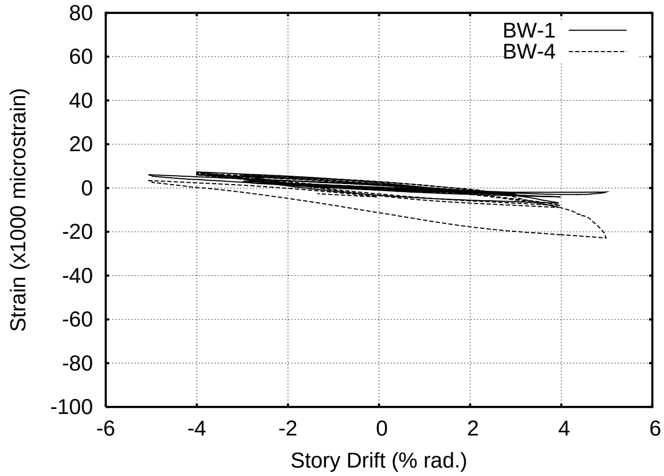

(a) BW-1 vs. BW-4

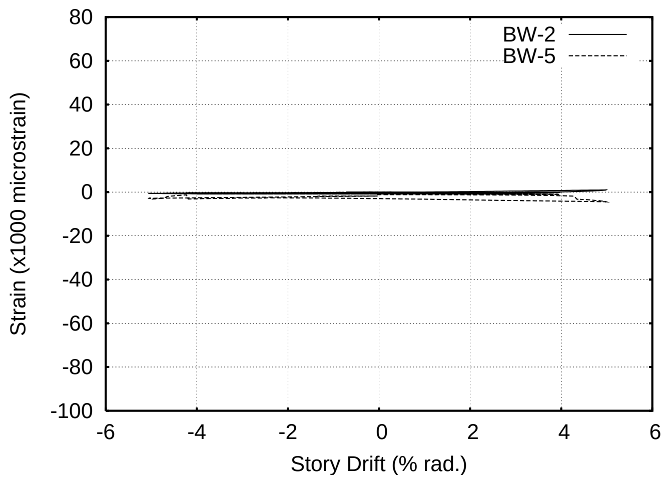

(b) BW-2 vs. BW-5

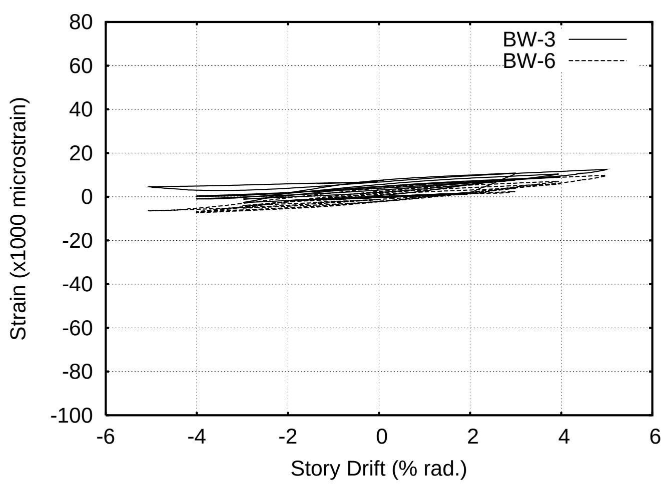

(c) BW-3 vs. BW-6

Figure 6.28 – Beam web strains of SPEC-6

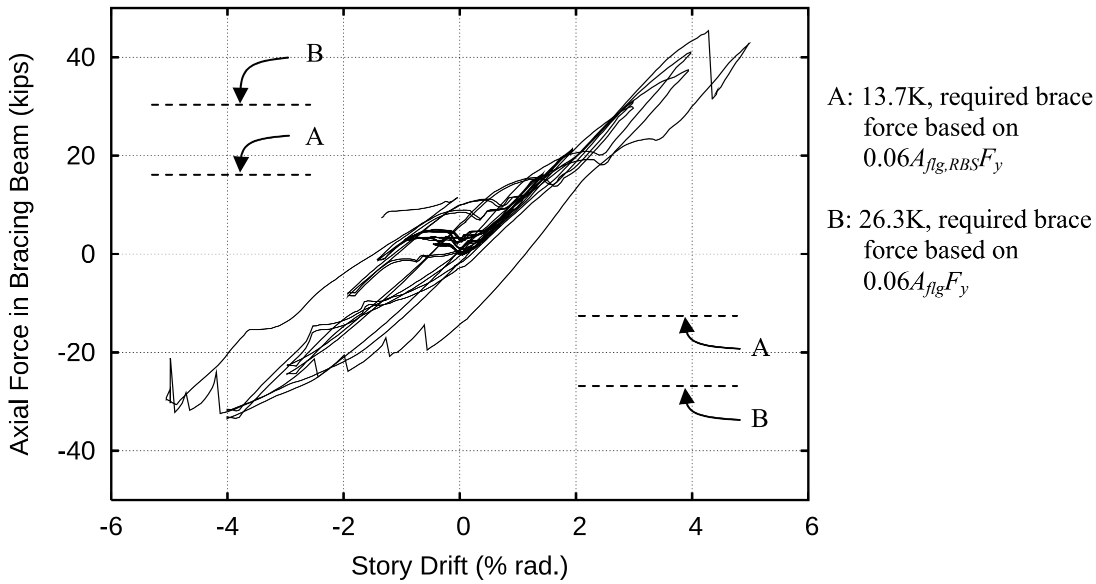

Figure 6.29 – Axial force in the supplemental bracing beam of SPEC-6

(This page is blank.)

CHAPTER 7 COMPARISON OF FEA RESULTS WITH SPECIMEN TEST RESULTS

7.1 General

This chapter discusses the comparison of the finite element analysis (FEA) and the test results in order to further evaluate the accuracy of the finite element models described in Chapter 3. Finite element models for all test specimens were developed and the specimens analyzed before the test to predict the test specimen behavior. For each test specimen, material tensile coupon test results were used to determine the material properties for the ABAQUS finite element models. In the cyclic analysis the displacement history applied at the top of column in the model was the same as that applied to the test specimen, except that the elastic test cycles prior to 1% story drift and two cycles of 1.5% story drift were omitted in the analysis.

7.2 Predicted vs. Measured Specimen Response

The comparison of cyclic behavior of specimen tests and finite element models is shown in Figures 7.1 to 7.6. Good agreement exists between the test and FEA results. Overall, it was determined that the finite element models correctly predicted the limit states and their sequence that occurred in the test specimens, which included: (1) yielding in the RBS beam web and flanges; (2) panel zone yielding; (3) local buckling of the beam web and flanges in the RBS; (4) lateral movement of the beam flanges in the RBS; (5) strength degradation following local buckling and lateral flange movement of the beam in the RBS; and, (6) column twisting due to torsional loading caused by buckling in the RBS.

Values for the initial stiffness, peak loading, and connection strength degradation (as a percentage of the peak loading) at 4% story drift of each test specimen are summarized in Table 7.1. The initial stiffness, peak load, and strength degradation in the finite element model show good agreement with the test results. The initial stiffness from the FEA is slightly lower than the test results for all six specimens. However, the difference is less than 4% for most cases and for SPEC-3 the difference is about 8%. The only exception is SPEC-5, which is about 19%. The peak loading predicted by the finite element models is within 4% of the test results for all specimens with the exception of SPEC-5, for which the difference is about 8%. SPEC-5 had the same composite floor slab system but shallower and lighter beams (W30x108) than SPEC-1 to SPEC-4 (W36x150). There was a greater degree of composite action in SPEC-5 than the other specimens with a floor slab. The finite element model for SPEC-5 is seen in Figure 7.5 to underestimate the stiffness and the strength of the test specimen at the early stage of the testing.

The strength degradation starts after 3% story drift is reached (see Figures 7.1 through 7.5) for SPEC-1 to SPEC-5. Specimen strength degradation occurred in the analysis, and shows good agreement with the test results. The strength degradation predicted by the finite element models at 4% story drift is within 3% of that which occurred in the test specimens. As noted in Chapters 3 and 5, the degradation of the strength is associated with beam local web and flange buckling and lateral movement of the beam flange in the RBS.

Figure 7.7 shows the pattern of beam local buckling developed in the test specimen and finite element model for SPEC-2. SPEC-2 had a W27x194 column and W36x150 beams. It can be seen that the finite element analysis results resembles the test results very well, where both have the same buckling pattern. These results were typical for the analysis of the test specimens. The types of shell elements therefore used in the finite element model (S4 and S4R in the ABAQUS element library) are suitable for capturing local buckling and performing post-buckling analysis.

As discussed in Chapters 5 and 6, SPEC-6 had little beam buckling and no strength deterioration before it fractured. This behavior was also captured in the FEA results (see Figure 7.6), and is attributed to the weaker panel zone of SPEC-6 (where the measured R_v/V_{pz} = 1.03). As noted in Chapter 6, the panel zone accounted for 80% of the inelastic story drift at a story drift of 0.04 radians. The larger plastic deformations developed in the region of the connection with a weaker panel zone may cause fracture in the connection, as occurred during the testing of SPEC-6. It was found through the finite element analysis that a ratio for R_v/V_{pz} of about 1.15 or greater is required to have more equal balance of inelastic panel zone and beam plastic deformation. Figure 7.8 shows the comparison of the FEA results for the as-tested configuration and that of a model of SPEC-6 with R_v/V_{pz} = 1.13. For this latter model the beams developed local and lateral buckling, followed by strength deterioration. The panel zone in this latter model accounts for 37% of the inelastic story drift at a story drift of 0.04 radians.

The contribution of the beams, panel zone, and column to the total drift of the model of SPEC-1 are shown in Figure 7.9, where they are compared to the test results. SPEC-1 had a W36x230 column and W36x150 beams. Good agreement is seen in Figure 7.9 between the test and FEA results. Figure 7.10 shows a comparison of the column twist for SPEC-1 from test measurements and FEA results at selected story drift levels. Good correlation is again shown between the test and FEA results. The above same comparisons for SPEC-6 are shown in Figures 7.11 and 7.12, where as noted above SPEC-6 had a weaker panel zone. The finite element results and the experimental results for SPEC-6 agree very well, except for the last half cycle at 5% story drift, where the specimen developed a fracture during testing. The agreement of the FEA results with the test results shown in Figures 7.9 and 7.12 is typical for all specimens.

Overall, the FEA results show good correlation with the test results. The comparison of the analysis and test results further verifies that the finite element modeling approach, described in Chapter 3 and used in the parametric study, provides reasonably accurate results.

Table 7.1 Comparison of test results and FEA results

Specimen		Initial stiffness (k/in.)	Peak loading (kips)	Strength degradation at 4% story drift (% of peak loading)
SPEC-1	Test	232.7	411	16
	FEA	225.4	406	15
SPEC-2	Test	202.1	412	14
	FEA	194.2	399	11
SPEC-3	Test	212.1	407	8
	FEA	194.3	415	9
SPEC-4	Test	211.0	406	16
	FEA	208.6	423	16
SPEC-5	Test	136.0	258	4
	FEA	109.6	235	5
SPEC-6	Test	102.0	240	0
	FEA	98.3	228	0

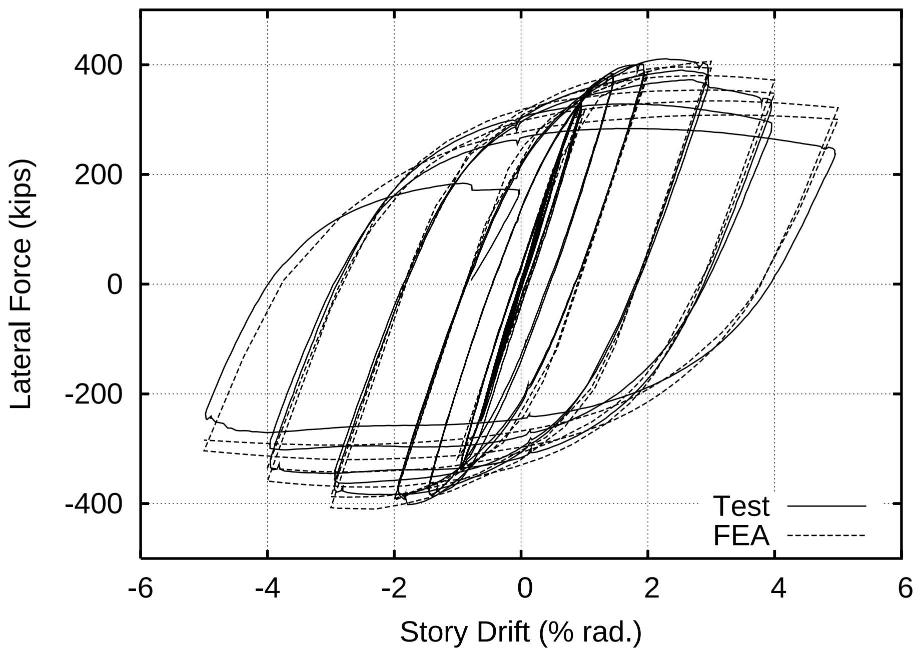

Figure 7.1 – Comparison between test and FEA results for lateral force-story drift of SPEC-1

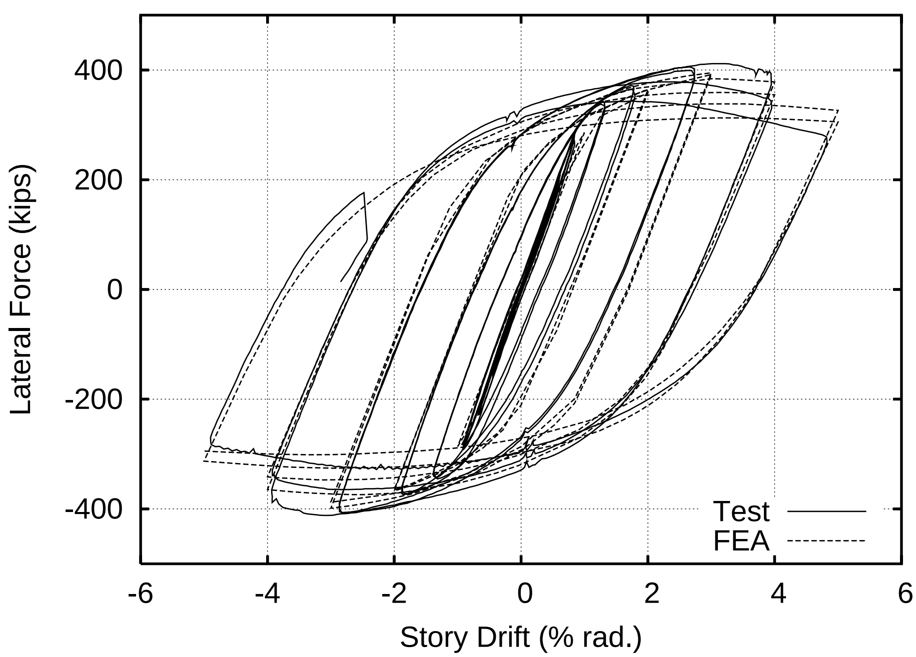

Figure 7.2 – Comparison between test and FEA results for lateral force-story drift of SPEC-2

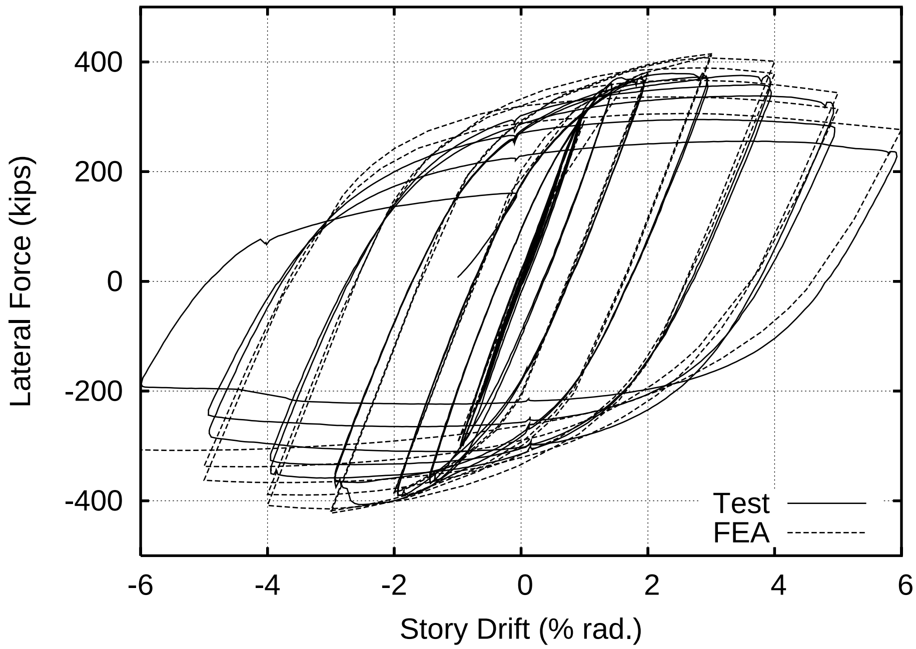

Figure 7.3 – Comparison between test and FEA results for lateral force-story drift of SPEC-3

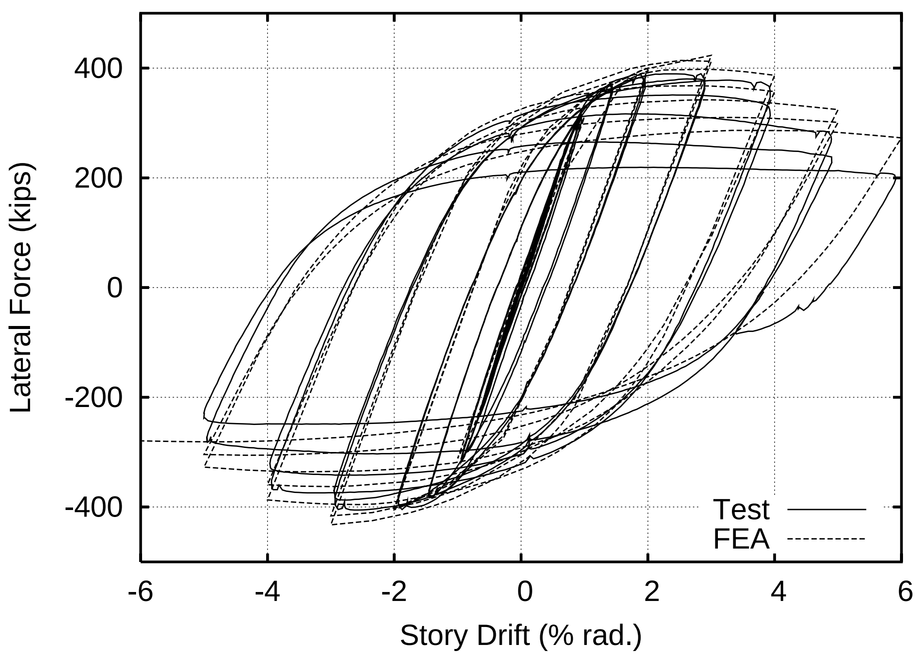

Figure 7.4 – Comparison between test and FEA results for lateral force-story drift of SPEC-4

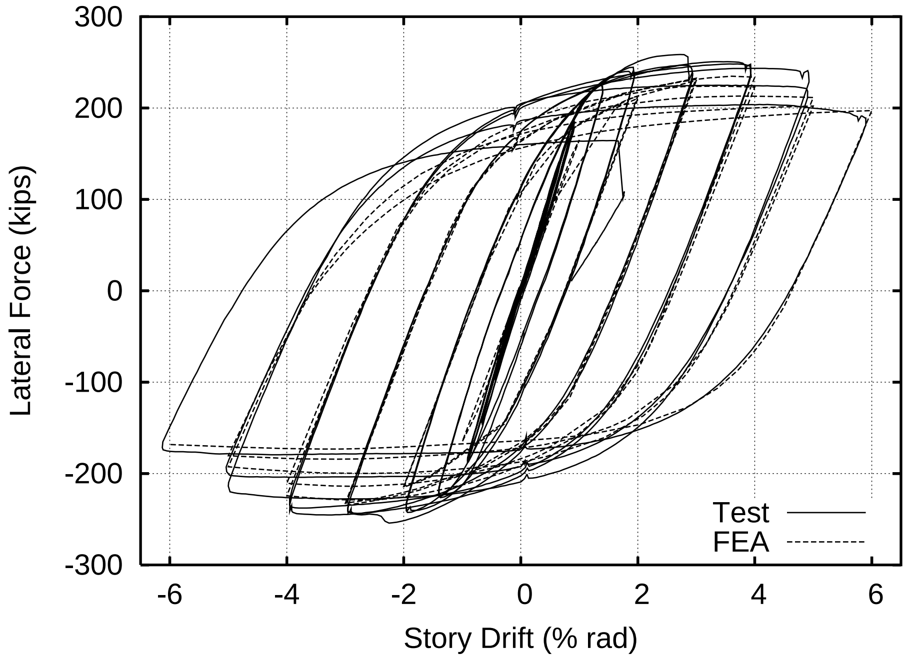

Figure 7.5 – Comparison between test and FEA results for lateral force-story drift of SPEC-5

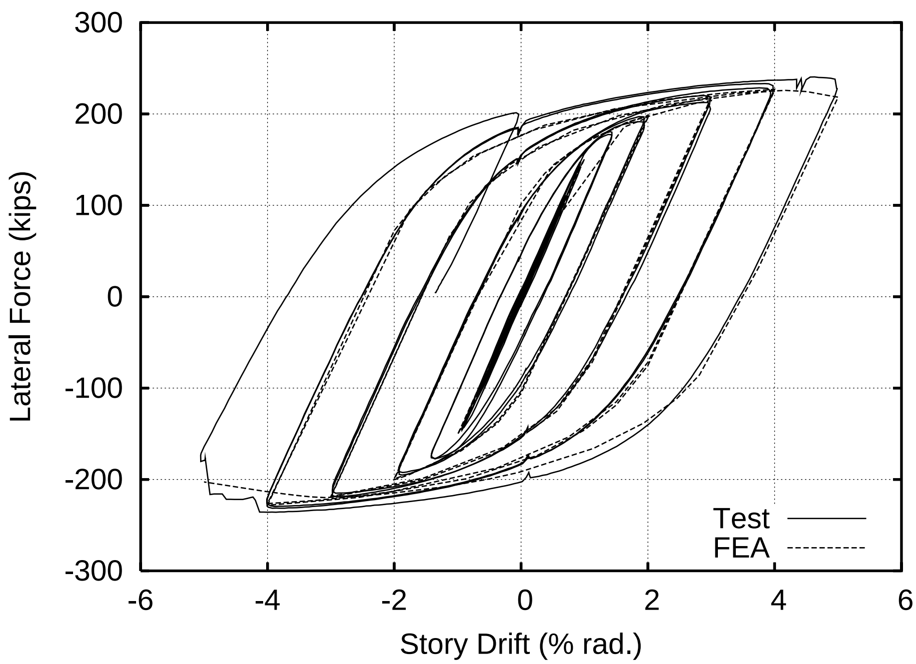

Figure 7.6 – Comparison between test and FEA results for lateral force-story drift of SPEC-6

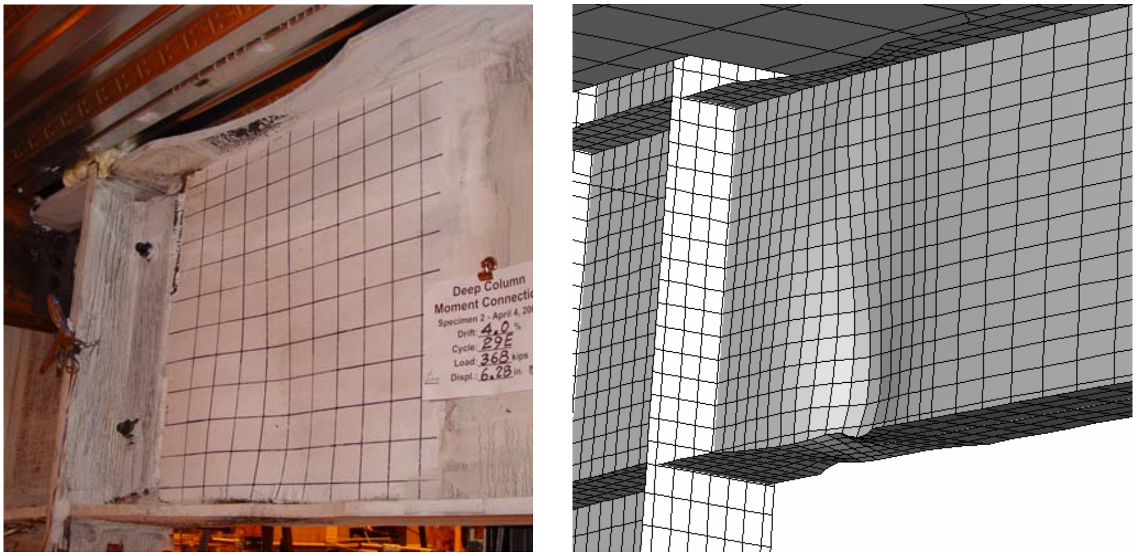

(a) Photograph of test specimen (b) FEA model

Figure 7.7 – Beam local buckling, SPEC-2 at 4% story drift

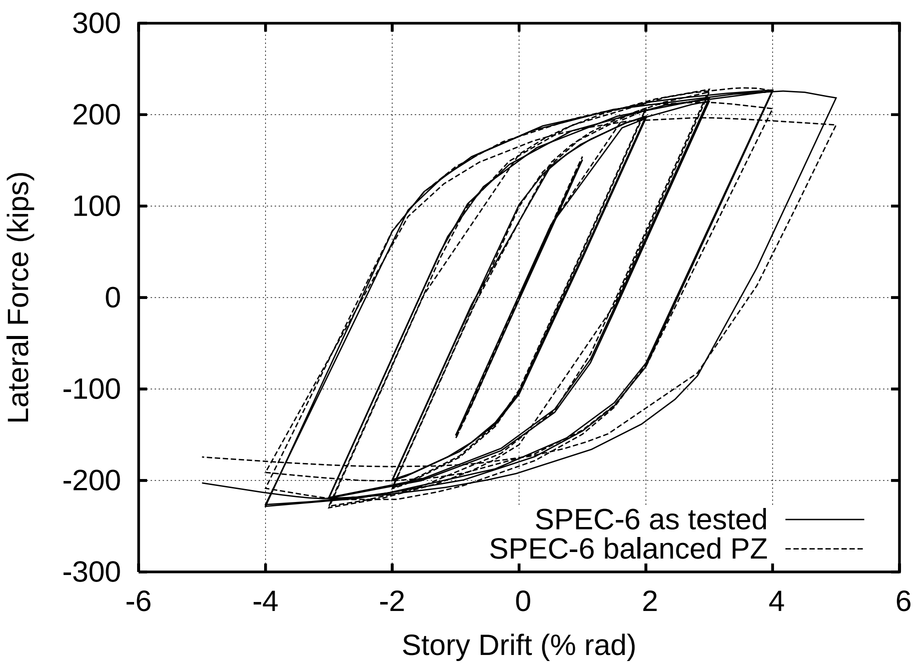

Figure 7.8 – Comparison of FEA results for different panel zone strength of SPEC-6

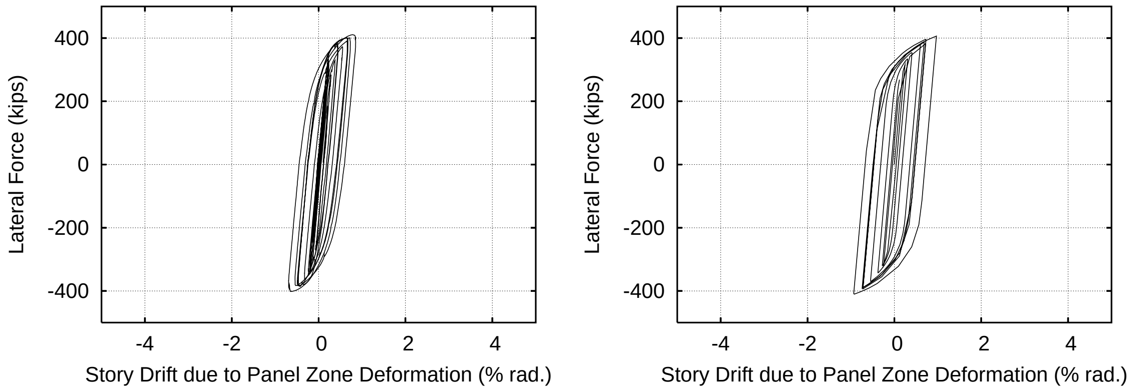

Test FEA

(a) Panel zone contribution to story drift

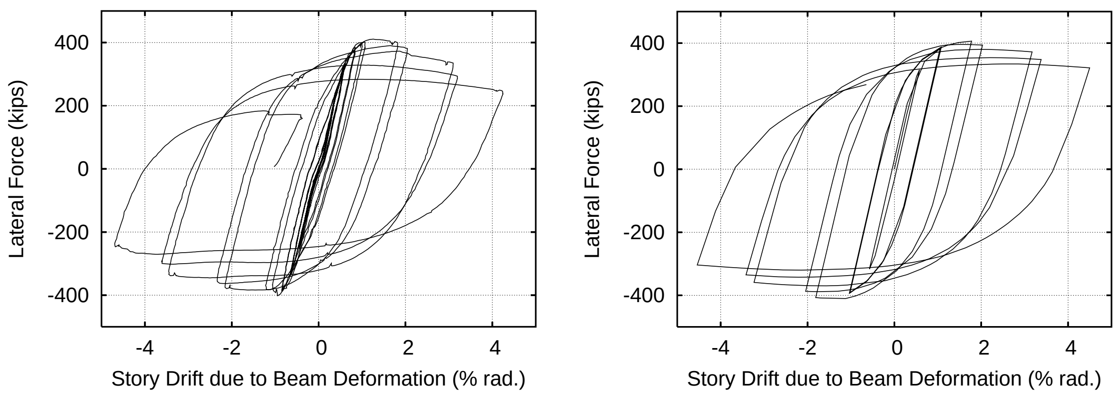

Test FEA

(b) Beam contribution to story drift

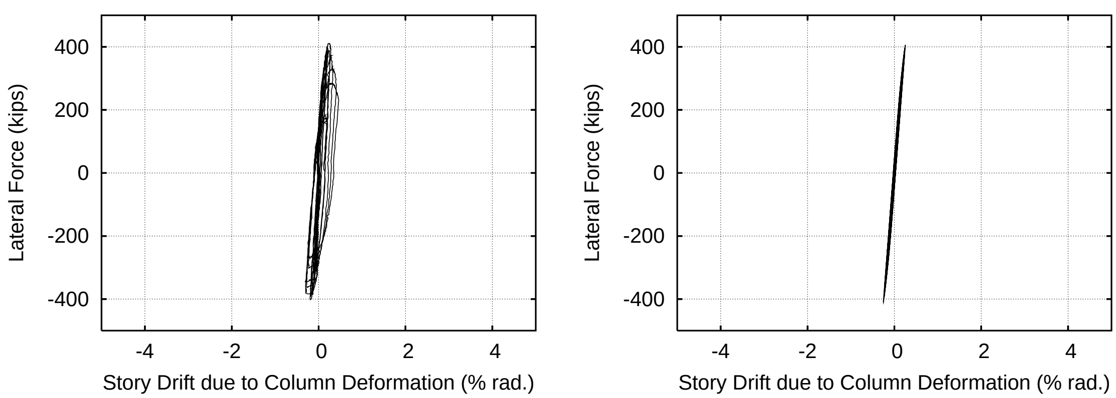

Test FEA

(c) Column contribution to story drift

Figure 7.9 – Comparison of test and FEA results for story drift components of SPEC-1

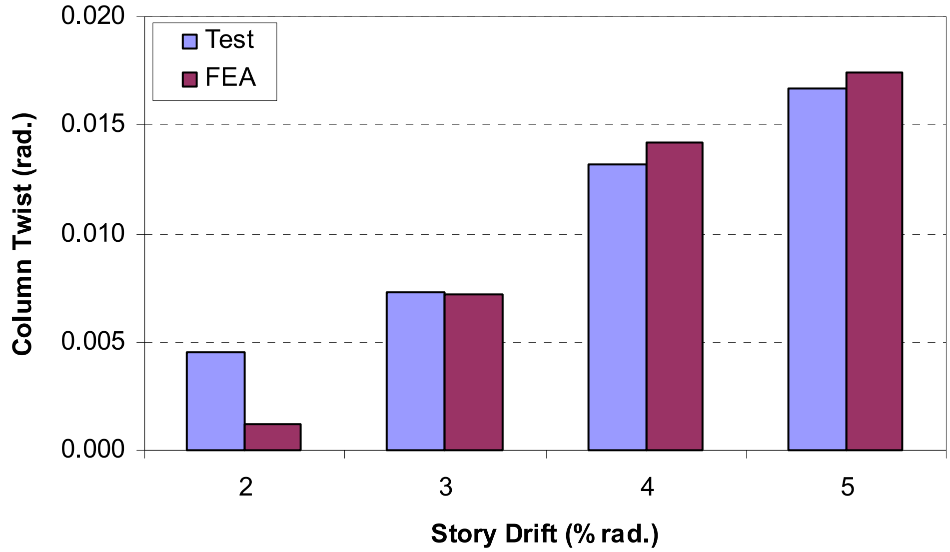

Figure 7.10 – Comparison of test and FEA results for column twist, SPEC-1

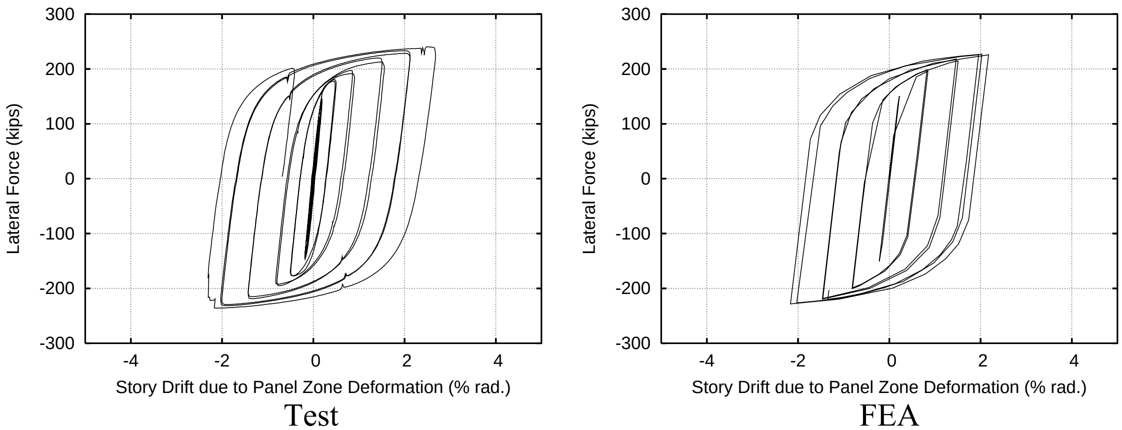

(a) Panel zone contribution to story drift

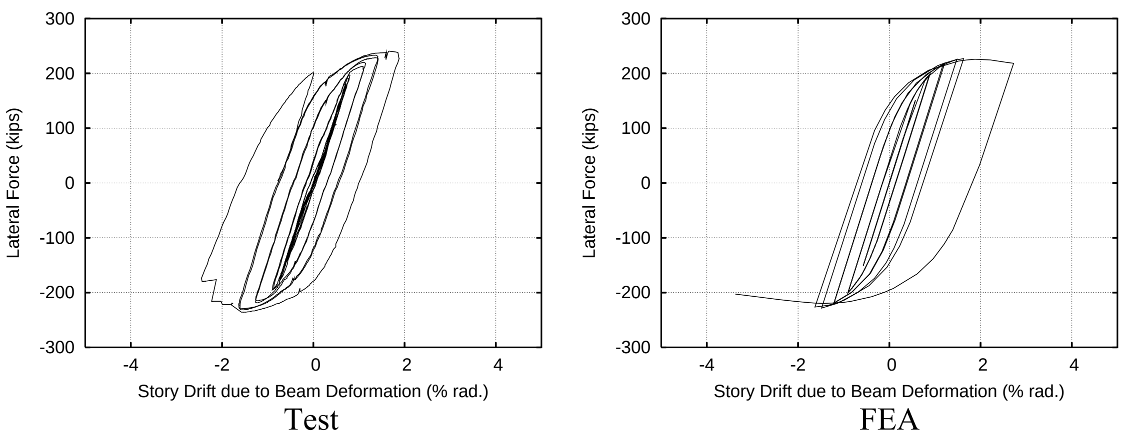

(b) Beam contribution to story drift

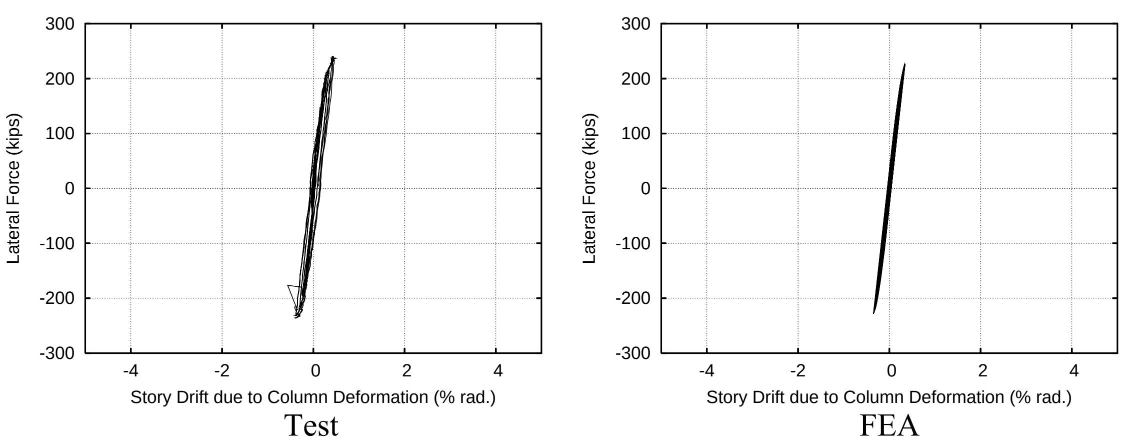

(c) Column contribution to story drift

Figure 7.11 – Comparison of test and FEA results for story drift components of SPEC-6

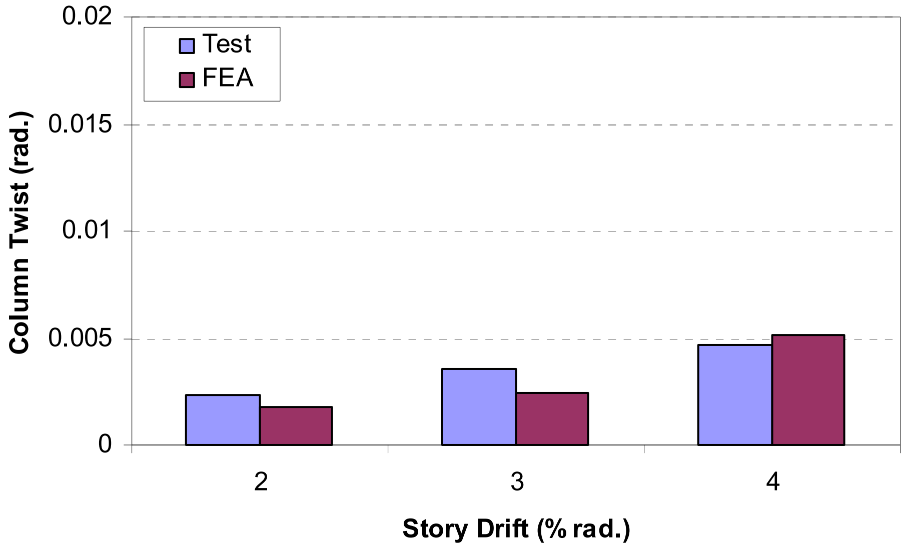

Figure 7.12 – Comparison of test and FEA results for column twist, SPEC-6

CHAPTER 8 DESIGN RECOMMENDATIONS

8.1 Introduction

The analytical and experimental studies reported in the prior chapters indicate that the current design recommendation by Chi and Uang (2002) over-estimates the column warping stress in the design of a deep column-to-beam RBS moment connection. This chapter presents a newly developed procedure for the design of moment connections between beams and a deep column.

8.2 Beam Flange Stress and Strain Distribution

The main idea behind the proposed design procedure is that the torsion imposed to the column by the compression flanges of the beams is based on the stress distribution in the beam compression flanges at the column face. This stress distribution across the beam flange is influenced by the local and lateral buckling in the RBS. This stress distribution can be determined from measured strains of the test specimens and the finite element results.

8.2.1 Beam Flange Strain Distribution from Experimental Results

Figure 8.1 shows the measured strain distributions across the beam bottom flanges near the column at 4% story drift for SPEC-1 to SPEC-5. All of the specimens developed extensive beam local buckling and RBS out-of-plane movement at 4% story drift during testing. The strains were measured using strain gauges that were placed across the east side beam flange width at three inches from the column face (see Figures 4.27, 4.28 and 4.29). The strains in Figure 8.1 are plotted when the east-side beam bottom flange was in compression at 4% story drift. A strain gradient is seen in the figure, which is caused by the bending of the beam compression flange about the beam weak axis as the result of the RBS out-of-plane movement, as well as local buckling of the beam at the RBS. For SPEC-6, the beam buckling at 4% story drift was minor and there was no visible RBS out-of-plane movement. The strain distribution was thus rather uniform along the beam width (see Figure 6.16), and not included in Figure 8.1.

Shown in Figure 8.2 is the stress distribution across the beam flange, which was determined from the strain distribution shown in Figure 8.1. The stress calculation was based on the assumption of a uniaxial relationship between strain and stress. It can be seen in Figure 8.2 that approximately two-thirds of the flange width in the specimens (excluding SPEC-1) has developed the yield stress (which ranged from 49.7 ksi to 53.0 ksi, see Table 4.4), with the stress rapidly diminishing at one edge of the flange.

8.2.2 Beam Flange Stress Distribution from Finite Element Analysis Results

To investigate further the stress distribution in the beam compression flange, nonlinear finite element analysis (FEA) were performed. Cyclic analysis was used along with sub-modeling to investigate the stress in the beam compression flange, following the loading protocol in the AISC Seismic Provisions (AISC 2002) shown in Figure 4.26. SPEC-2, which had a W27x194 column and W36x150 beams, was chosen for the analysis. The dimensions and material properties are given in Chapter 4 that were used in the model. Shown in Figure 8.3 is part of the sub-model, which consists of the beam flange and portions of the beam web. Figure 8.4 shows the longitudinal stress distribution at 4% story drift in the beam bottom flange along the path that is across the beam flange, three inches from the face of the column flange (see Figure 8.3). The results in Figure 8.4 show similarities to the stress distribution in Figure 8.2. These results confirm that due to the RBS out-of-plane movement that the longitudinal stress in the beam flange redistributes accordingly. In the FEA results a majority of the flange width (around two-thirds) is fully yielded in compression with a slight amount of strain hardening. Over the remaining flange width there is a nearly linear distribution to the edge of the flange where the stress is approximately zero.

As noted already, the stress distribution patterns in the beam bottom compression flange from the test results and FEA results both show consistency. Over the course of cyclic loading, the beam flange becomes fully yielded as the beam reaches its plastic moment at 2% story drift, as shown in Figure 8.5(a). Then, at 3% story drift the beam flange starts to locally buckle and the beam moment starts to drop after achieving a maximum value. At 4% story drift, the out-of-plane movement of the beam compression flange in the RBS introduces a moment T about the beam weak axis, which applies a torque to the column. The moment about the beam weak axis causes the stress in the beam compression flange to redistribute as illustrated in Figure 8.5(b). The beam flange starts to unload from the tension side of this moment T.

Shown in Figures 8.6 and 8.7 is the longitudinal stress distribution in the beam bottom flange when in compression near the column face (along the path shown in Figure 8.3), for a RBS connection with supplemental bracing and a WUF connection, respectively. These results are based on nonlinear cyclic finite element analysis, and are shown plotted at a story drift of 4%. The RBS connection has a W27x194 column and W36x150 beams with the supplemental bracing at the RBS, and corresponds to test specimen SPEC-3. The WUF connection has a W36x230 column and W36x150 beams, with material properties and dimensions similar to SPEC-1. It can be seen from the Figure 8.6 that the RBS connection with supplemental bracing has a different stress distribution than the RBS connection without the supplemental bracing (Figure 8.4). About one-sixth of the width of the beam flange is below the beam flange yield stress (53 ksi), where at the edge of the beam flange the stress is about one half the yield stress. The rest of the flange remains fully plastic. In the WUF connection, shown in Figure 8.7, the stress distribution is more uniform. A small portion of the width of the beam flange (about one-sixth of the flange width) is below the beam flange yield stress (49.7 ksi), where at the edge of the beam flange the stress decreases to around two-thirds of the maximum stress. It is noted that the WUF connection has a greater amount of strain-hardening develop in the beam flange than in the RBS connections.

Integrating the stresses across the beam flange width (shown in Figures 8.4, 8.6 and 8.7) gives an eccentricity of the beam flange stress resultant force with respect to the centerline of the beam (column) of $0.0811b_f$, $0.0214b_f$, and $0.0108b_f$, for an RBS connection without supplemental bracing, an RBS connection with supplemental bracing, and an WUF connection, respectively, where b_f is the beam flange width. The corresponding torque T applied to the column by the beam flange is $0.075F_{ye}b^2_ft_f$, $0.021F_{ye}b^2_ft_f$, and $0.011C_{pr}F_{ye}b^2_ft_f$, respectively, where F_{ye} is the expected yield stress of the beam flange, b_f is the width of the beam flange, t_f is the thickness of the beam flange, and C_{pr} has a value of 1.15.

8.3 Design Recommendation

The design procedure is based on a simplified stress distribution in the beam compression (bottom) flange. The following are the basic assumptions that lead to the proposed design procedure.

8.3.1 Assumptions

1. The torque imposed to the column by the beam compression (bottom) flanges comes from the eccentricity of the beam compression flange force with respect to the column;
2. A floor slab is present;
3. The beam tension flanges have a uniform stress distribution, where there is no eccentricity of the tension flange force with respect to the column;
4. Before lateral buckling in the RBS occurs, the compression beam flange is in uniform compression; as the RBS undergoes out-of-plane movement, the longitudinal stresses in the beam compression flange redistribute (see Figure 8.8), which leads to an eccentricity of the beam flange force;
5. Based on the results from the experimental and finite element studies that were discussed above, the beam bottom flange compressive stress distribution shown in Figure 8.8(a) is assumed for an RBS connection without a supplemental brace at the RBS. The eccentricity e of the beam compression (bottom) flange longitudinal stress resultant with respect to the column and the corresponding torque on the column T are equal to

$$e = \frac{11}{120} b_f \approx 0.0917 b_f \tag{8.1}$$

$$T = \frac{11}{150} F_{ye} b_f^2 t_f \approx 0.073 F_{ye} b_f^2 t_f \tag{8.2}$$

where e = the eccentricity of the resultant force of the beam compression (bottom) flange longitudinal stresses;

T = the torque applied to the column by the resultant force of the beam compression (bottom) flange longitudinal stresses;

F_{ye} = expected yield stress, equal to R_yF_y, where F_y is the specified minimum yield stress of the beam flange, and R_y is the ratio of the expected yield stress to the specified minimum yield stress;

b_f = beam flange width;

t_f = beam flange thickness.

6. For an RBS connection with a supplemental brace at the end of the RBS, the compression stress distribution across the beam bottom flange shown in Figure 8.8(b) is assumed, and the eccentricity e of the beam compression (bottom) flange longitudinal stress resultant force with respect to the column and the corresponding torque T are equal to

$$e = \frac{13}{570} b_f \approx 0.0228 b_f \tag{8.3}$$

$$T = \frac{13}{600} F_{ye} b_f^2 t_f \approx 0.022 F_{ye} b_f^2 t_f \tag{8.4}$$

7. For an WUF connection, the beam bottom flange compressive stress distribution shown in Figure 8.8(c) is assumed. Strain hardening is not considered for the RBS connections, while it is considered for an WUF connection. This is due to the fact that the beam flange near the column in an WUF connection undergoes more cyclic strain hardening than that in a RBS connection. The eccentricity e of the beam compression (bottom) flange longitudinal stress resultant force with respect to the column and the corresponding torque T are equal to

$$e = \frac{2}{153} b_f \approx 0.0131 b_f \tag{8.5}$$

$$T = \frac{1}{81} C_{pr} F_{ye} b_f^2 t_f \approx 0.012 C_{pr} F_{ye} b_f^2 t_f \tag{8.6}$$

The above assumed stress distributions resulted in similar values of the eccentricity e and torque T compared to the finite element analysis results, with the comparison shown in Table 8.1. Based on the above assumptions, the design procedure is presented below.

8.3.2 Design Procedure

The design procedure given below assumes an interior connection with two beams and a floor slab. If no floor slab is present, then the torque T computed below needs to be doubled for an interior connection. If an exterior connection with no floor slab is present, then the torque is not doubled and the value T is used as calculated below. The design requires having a supplemental lateral brace at the end of the RBS when a floor slab is not present.

1. Determine the torque T according to the assumed stress distribution in the beam compression (bottom) flange:

   For an RBS connection without supplemental bracing, Equation (8.2) is used; for an RBS connection with supplemental bracing, Equation (8.4) is used; and for an WUF connection, Equation (8.6) is used.

2. Calculate the maximum warping normal stress f_w in the column flange due to the applied torque T:

   $$f_w = EW_{n0}\theta'' \tag{8.7}$$

   where E = modulus of elasticity;

   W_{n0} = normalized warping function at column flange tip;

   θ" = second derivative of the angle of column twist θ with respect to longitudinal distance of the column, dependent on the value of torque T applied to column and as well column torsional flexibility. θ" can be obtained from either the charts in Appendix B or analytical solution in Appendix C of the AISC *Torsional Analysis of Structural Steel Members* (Seaburg and Carter 1997). See Appendix G of this report.

3. Calculate the column bending stress f_b:

   $$f_b = \frac{M_{col}}{S_x} \tag{8.8}$$

   where M_{col} = in-plane bending moment in column at beam bottom flange level;

   S_x = column elastic section modulus.

The value for M_{col} should be based on the column resisting the moments developed in the beams adjacent to the connection at 4% story drift. Table 8.2 shows the beam moment $M_{f,exp4\%}$ at the column face at a story drift of 4%. Included in Table 8.2 is a comparison of $M_{f,exp4\%}$ with the beam's nominal flexural capacity M_{pn}. For RBS connections without a supplemental brace the average value for $M_{f,exp4\%}/M_{pn}$ is equal to 0.93; for RBS connections with asupplemental brace at the RBS (SPEC-3 and SPEC-6) the average value of $M_{f,exp4\%}/M_{pn}$ is equal to 0.97. Prior WUF connection test results (Ricles et al., 2000) indicated that at 4% story drift an WUF connection deteriorated below its maximum developed capacity to an average value of about 1.1 times the beam expected flexural capacity (which in turn is equal to $1.21M_{pn}$). Thus, for the proposed design procedure recommended values for the beam moment at 4% story drift are $0.9M_{pn}$, M_{pn}, and $1.2M_{pn}$ for RBS connections without a supplemental brace, RBS connections with a supplemental brace, and WUF connections, respectively. Note that if significant out-of-plane bending in the column exists, then the effect on the column bending stress should be included.

4. Calculate the axial stress f_a due to the axial load on the column:

$$f_a = \frac{P_u}{A} \tag{8.9}$$

where P_u = factored axial load on column considering P-Δ effects at 4% story drift;

A = column section area.

5. Determine the total stress f_{total} and check to ensure this required strength does not exceed the design strength. The design strength is based on Equation (H2-1) in the AISC LRFD Specification (AISC 2001), where the combined stress is limited to the design yield stress (ϕF_y) of the column:

$$f_{total} = f_a + f_w + f_b \le \phi F_y \tag{8.10}$$

where F_y = specified minimum yield stress of the column steel;

$\phi = 0.9$.

8.4 Verification of the Design Procedure

The proposed design procedure (for RBS connections) described above was verified by comparing the column stresses computed in accordance with this procedure to the test results. SPEC-6 did not have a slab and therefore the torque is applied by both of the beams to the column. Thus a value of 2T was used for the torque in SPEC-6. Shown in Table 8.3 is a comparison between the calculated column stresses by the current design approach, the proposed design method, and the test results. No axial load was present. The experimental stresses f_{exp} were based on the strains from the strain gauges placed closest to the edge of the column flange tip, one to two inches below the beam bottom flanges (see Figure 4.27 – 29). The experimental stresses f_{exp} were calculated using the steel's elastic modulus and the measured strain. If the stress exceeded the yield stress, the yield stress was used instead. Chi and Uang's (2002) procedure does not provide any guidance for calculating the column flange normal warping stress for an RBS connection with a supplemental brace. Therefore, for SPEC-3 and SPEC-6 no comparisons are made.

Summarized in Table 8.4 is a comparison of the values for the ratio of the total stress f_{total} to the experimental measured column flange stress f_{exp} for both the current (Chi and Uang 2002) and the proposed design method. The values shown in Table 8.4 are also plotted in Figure 8.9. The ratio of f_{total}/f_{exp} for the proposed design method is close to 1 for most specimens except SPEC-4 and SPEC-6. Significant yielding in the column flanges was observed during testing of these two specimens, as discussed in Chapters 5 and 6. For SPEC-1, SPEC-2, SPEC-3 and SPEC-5, the average value for the f_{total}/f_{exp} ratio by the proposed design approach is equal to 1.04, while the average value for the f_{total}/f_{exp} ratio by the current design method is equal to 1.30 (this value of 1.30 excludes SPEC-3). It can be seen in Table 8.4 and Figure 8.9 that the proposed approach more accurately predicts the column stresses in the test specimens than the procedure recommended by Chi and Uang (2002). Also, in most cases the procedure recommended by Chi and Uang (2002) overestimates the column flange stress.

SPEC-4 and SPEC-6 both met the connection deformation requirement in AISC Seismic Provisions (2002), Appendix S of 4% story drift during testing. SPEC-4 had a W36x150 section for both the column and beams, while SPEC-6 had a weaker panel zone that resulted in significant panel zone yielding, along with kinking and yielding in the column flanges. The fact that these specimens successfully met the requirements in Appendix S of the AISC Seismic Provisions (2002) and thus qualify for seismic use, and that the design stress f_{total} based on the newly proposed procedure exceeds $(\phi=0.9)F_y$ in these specimens, implies that the first yield criteria in Section H2 of the AISC LRFD Specification is conservative. To remove this conservativeness, an ultimate strength format is needed. This approach is beyond the scope of this study since there is a lack of data on ultimate strength of wide flange shapes under combined torsion, flexure and axial force.

8.5 Summary

The design procedure presented in this chapter is based on both the experimental and analytical results for the stress distribution in the beam compression (bottom) flange, and utilizes the design method in the AISC LRFD Specification for Structural Steel Buildings (AISC 2001) for a column under combined flexural and torsional loading. The newly proposed procedure was found to be more accurate than that recommended by Chi and Uang (2002). Both the newly proposed procedure and that by Chi and Uang are based on first yield criteria, which was found to be conservative. A review of the literature revealed that currently there is a lack of experimental data and research on the ultimate strength of wide-flange columns subjected to the combined loading of torsion, flexure, and axial force. Further studies are needed if designers want to use an ultimate strength design method for a column subjected to these combined forces.

This project did not address connections with the reinforced beam flanges, where the plastic hinge forms at a distance further from the column face. The AISC Seismic Provisions (2002), Section 9.8 states that: "In addition, lateral braces shall be placed near concentrated forces, change in cross-section and other locations where analysis indicates that a plastic hinge will form during inelastic deformation of the SMF." Torsional loading to the column by the beam for these types of connections is likely reduced by the restraint of the lateral bracing that is required at the plastic hinge for these types of connections.

Table 8.1 Comparison between the FEA results and the beam flange stress distribution assumed for design

Connection	e/b_f		$T/F_{ye}b^2_f t_f$	
	FEA	Design	FEA	Design
RBS with no supplemental brace	0.0811	0.0917	0.075	0.073
RBS with supplemental brace	0.0214	0.0228	0.021	0.022
WUF	0.0108	0.0131	0.011	0.012

Table 8.2 Beam moment at column face at 4% story drift, $M_{f,exp4\%}$

SPEC	$M_{f,\exp 4\%}$	$\frac{M_{f,\exp 4\%}}{M_{pn}}$
1	25,284	0.87
2	26,547	0.91
3	28,376	0.98
4	26,652	0.92
5	17,553	1.01
6	16,659	0.96

Note: $M_{pn} = F_y Z_b$, nominal plastic flexural capacity of beam section.

Table 8.3 Predicted and experimental column flange stresses

SPEC	Column	Beam	Axial load stress f_a (ksi)	Bending stress f_b (ksi)	Warping stress f_w (ksi)		Total normal stress f_{total} (ksi)		Experimental results	
					Chi and Uang	Pro-posed	Chi and Uang	Pro-posed	Strain (με)	Stress (ksi)
1	W36x230	W36x150	0	27.5	18.6	9.5	46.1	37.0	1277	37.0
2	W27x194		0	43.3	26.4	14.6	69.7	57.9	2151	53.9(2)
3	W27x194		0	48.1	- (1)	4.3	- (1)	52.4	1797	51.7(2)
4	W36x150		0	48.9	46.5	23.7	95.4	72.6	3296	53.0(2)
5	W27x146	W30x108	0	36.5	26.1	13.8	62.6	50.3	1598	46.3
6	W24x131		0	50.3	- (1)	10.5	- (1)	60.8	2525	48.5(2)

Note: (1) Chi and Uang provide no recommendation for RBS connections with a supplemental brace;
(2) yield stress of the column flange.

Table 8.4 Comparison of predicted and experimental column flange stress

SPEC	$f_{total} / f_{\exp}$	
	Chi and Uang	Proposed
1	1.25	1.00
2	1.29	1.07
3	- (1)	1.01
4	1.80	1.37
5	1.35	1.09
6	- (1)	1.25

Note: (1) Chi and Uang provide no recommendation for RBS connections with a supplemental brace.

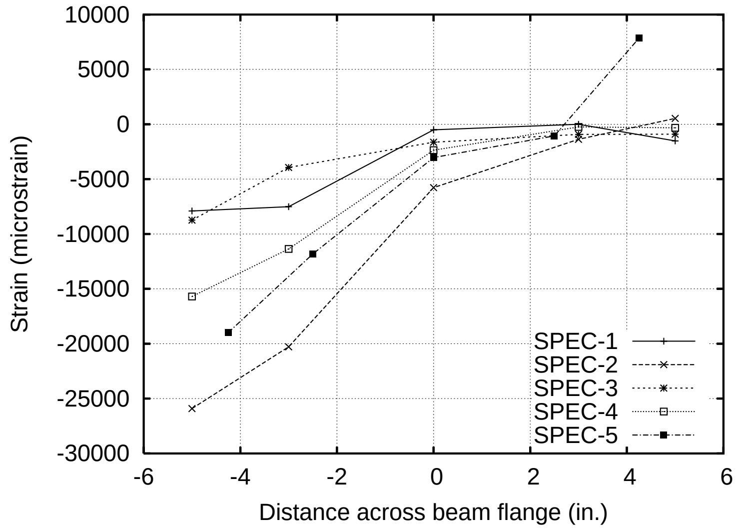

Figure 8.1 – Measured compressive strain distribution across the beam bottom flange at 4% story drift

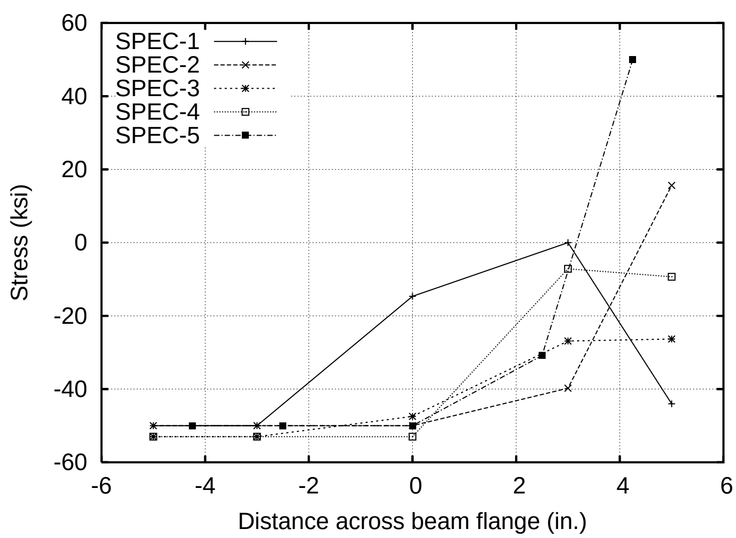

Figure 8.2 – Stress distribution from measured strains across the beam bottom flange at 4% story drift

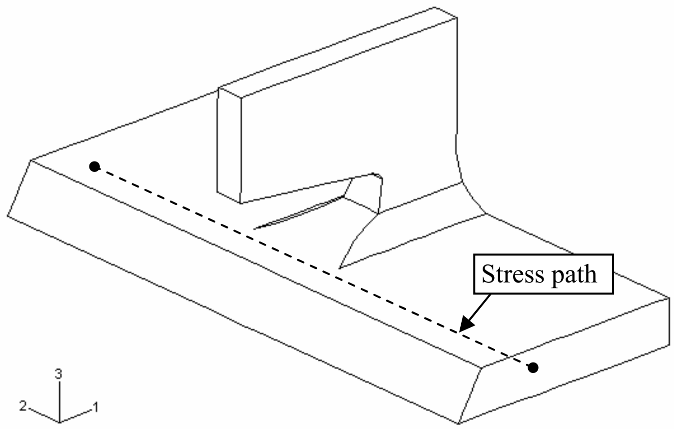

Figure 8.3 – Part of the FEA sub-model with a path across the beam bottom flange width near the column where the longitudinal stress is extracted and plotted

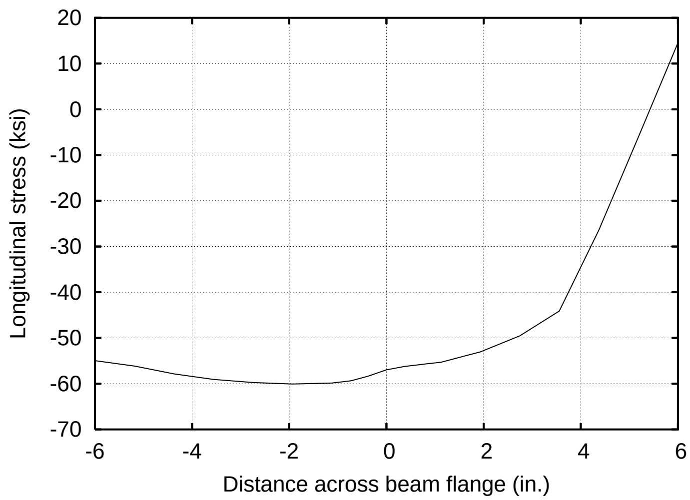

Figure 8.4 – Longitudinal stress distribution across beam compression flange from FEA sub-model results for a RBS connection (W27x194 column, W36x150 beam, with floor slab)

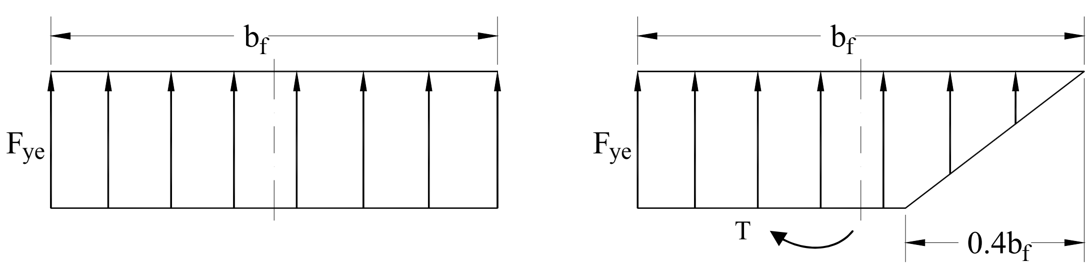

(a) Stress distribution at 2% story drift (b) Stress distribution at 4% story drift
Figure 8.5 – Illustration of compressive stress redistribution across beam bottom flange

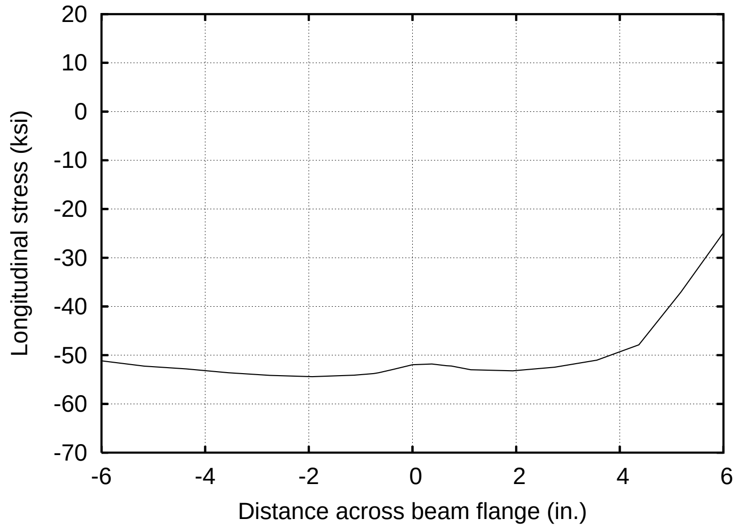

Figure 8.6 – Longitudinal stress distribution across beam compression flange from FEA sub-model results for a RBS connection with supplemental bracing (W27x194 column, W36x150 beam, with floor slab and supplemental bracing)

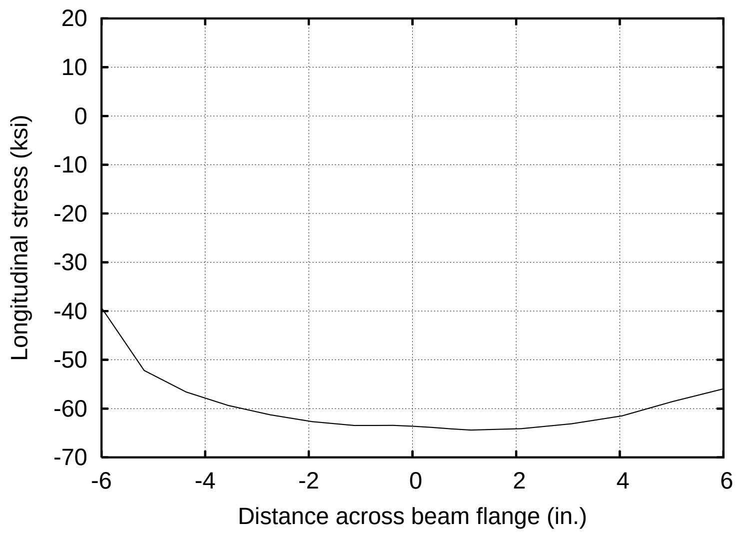

Figure 8.7 – Longitudinal stress distribution across beam compression flange from FEA sub-model results for a WUF connection (W36x230 column, W36x150 beam, with floor slab)

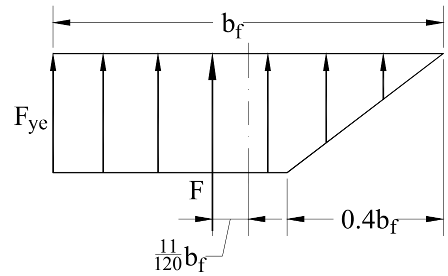

(a) RBS connection without supplemental bracing

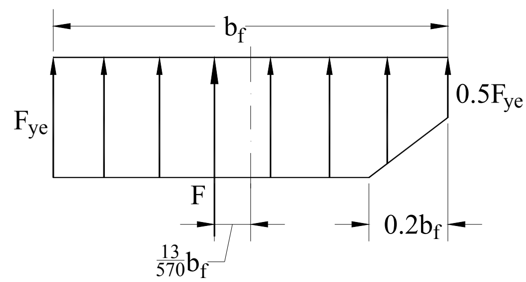

(b) RBS connection with supplemental bracing

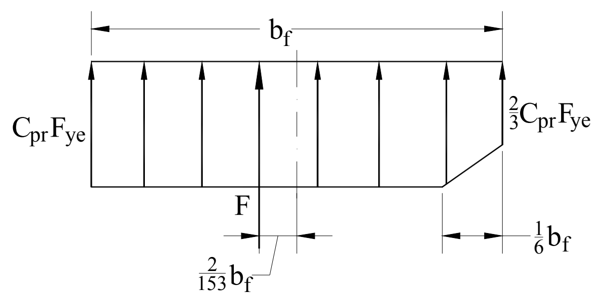

(c) WUF connection

Figure 8.8 – Idealized compression stress distribution across beam bottom flange recommended for design

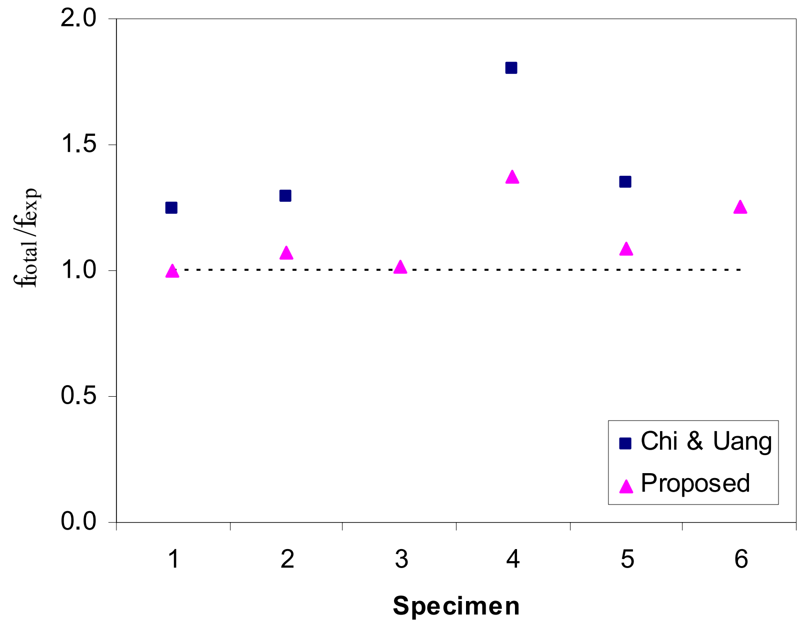

Note: SPEC-4 and SPEC-6 experienced significant yielding in the column flanges during testing.

Figure 8.9 – Comparison of the predicted f_{total} and the experimental f_{exp} column maximum flange normal stresses

CHAPTER 9 SUMMARY AND CONCLUSIONS

9.1 Summary

A study was performed with the objective of evaluating the effect of a floor slab on the behavior of a beam-to-column moment connection involving a deep column and to compare the results with current design criteria. Emphasis was placed on the RBS type of connection, because of its current popularity and the fact that recent research suggests the need for further investigations.

The study involved three main tasks. These tasks included: (1) performing analytical parametric studies using nonlinear finite element models to evaluate the effect of various selected parameters on connection behavior; (2) conducting an experimental program to experimentally access the effects of selected parameters on connection performance and to examine whether RBS connections to a deep column can be qualified for seismic use in accordance with the standards in Appendix S of the AISC Seismic Provisions (2002); and, (3) use the results from the analytical and experimental studies to assess current design criteria and develop new design procedures for moment connections to a deep column, if required.

The finite element parametric study involved examining the following parameters: connection type, column section size, beam section size, panel zone strength; continuity plate thickness; beam web slenderness, composite floor slab, and axial load. Global models of connection subassemblies were developed and used to determine response under monotonic and cyclic loading. Sub-models of the local connection region were developed and used to determine the potential for ductile fracture of the connection.

The experimental program involved full-scale connection tests, where five RBS connection specimens with a composite floor slab and one without a composite floor slab and a supplemental lateral brace at the RBS were fabricated and tested. The main parameters in the experimental study were the column section, beam section, composite floor slab and a supplemental brace.

The assessment of the current design criteria for RBS connections involved comparing the results of the analytical and experimental studies with predicted response based on the design procedure. This includes the lateral movement of the RBS beam bottom flange and the warping normal stresses in the column flanges. A new design procedure was developed for beam-to-column moment connections involving a deep column. The new procedure is similar to that proposed by Chi and Uang (2002) for determining the total elastic normal stress in a column attached to an RBS, with one major difference. This difference is in the calculation of the torque applied by the beam compression flange.

9.2 Conclusions

9.2.1 Finite Element Study

Based on the finite element parametric study performed, the following conclusions are noted:

(1) The finite element studies indicate that RBS connections have less potential for ductile fracture at the connection region than WUF connections.

(2) The fracture potential and column twist in an RBS connection depends on the section modulus and torsional rigidity of the column section, where larger stresses in the column flange can lead to a higher ductile fracture potential in the connection as well as column twist. An RBS connection with a deeper column can have a smaller ductile fracture potential than an RBS connection to a shallower column, if the deeper column has lower stresses in the column flanges.

(3) Panel zone strength plays an important role in RBS connections to deep columns. Weaker panel zones have an increase in the ductile fracture potential in the connection. Stronger panel zones result in an increase in the column twist and degradation in connection capacity under cyclic loading due to beam local buckling in the RBS. A balanced panel zone strength is recommended, which can be designed by the current AISC Seismic Provisions (AISC 2002).

(4) The finite element analysis results show that a composite floor slab provides restraint to the top flange of the beams, whereby the magnitude of beam top and bottom flange lateral movement in the RBS, as well as the column twist are reduced. Strength degradation due to beam instability in the RBS is also reduced by the restraint effect

obtained from the floor slab. However, the floor slab increases the fracture potential of the connection, particularly at the end of the beam web-to-column flange CJP groove weld. This increase is more pronounced in shallower columns.

(5) With the presence of a floor slab, out-of-plane movement of the RBS bottom flange and column twist are not sensitive to the beam section size and beam web slenderness. Without the floor slab, the RBS lateral movement and column twist tend to increase with an increase in beam section size. Heavier beam sections have a smaller web slenderness, which can improve the beam stability; but at the same time the driving force for the column twist gets larger since the beam flange area increases. The lateral movement of the beam bottom flange in the presence of a floor slab is less than the value of 20% of the beam flange width proposed by Chi and Uang (2002).

(6) Reducing the thickness of the continuity plates increases the ductile fracture potential of an RBS connection to a deep column. The critical location with the largest Rupture Index remains at the end of the beam web-to-column flange CJP groove weld; however, there is an increase in the Rupture Index in the beam flange-to-column flange CJP groove welds when the continuity plate thickness is reduced.

(7) The column total normal elastic stresses based on the procedure proposed by Chi and Uang (2002) does not show consist trends with the fracture potential based on the Rupture Index for the RBS connections. Thus, column total elastic stress is not a reliable indicator of the fracture potential of the connection, and hence performance. The value of the elastic warping normal stress appears to be highly conservative based on the procedure proposed by Chi and Uang.

(8) The best indicator for column twist is the column elastic torsional stiffness, considering both the effects of St. Venant and Warping Torsion. No clear trend was found to exist between the column twist from the finite element analyses and the ratio of h / t_{cf}^3 for the column.

(9) The axial load does not have a significant effect on the connection behavior. Within the practical range of axial load, the axial load does not increase the potential for fracture at 4% story drift, although it does increase the value of Rupture Index by a

small amount at 6% story drift. The axial load increases the deterioration of the connection capacity at larger story drift levels, where the P-Δ effect becomes more pronounced.

9.2.2 Experimental Study

Based on the test results and evaluation of the data, the following conclusions are noted:

(1) The deep column RBS connection test specimens, having a composite floor slab or adequate lateral bracing, have sufficient ductility for seismic application. The specimens meet the qualification criteria required by Appendix S of the AISC Seismic Provisions (AISC 2002) for use in SMFs in seismic regions.

(2) The E70T-6 electrode appears to perform adequately when the AISC Seismic Provisions for weld metal toughness are satisfied.

(3) The restraint by the concrete composite floor slab reduces the lateral movement of the beam bottom flange in the RBS. Hence it enhances the performance of the connection by reducing the strength deterioration due to lateral buckling of the beam top flange and the resulting torque subjected to the column from this beam flange. It was shown that for the same thickness of composite floor slab that the slab has a greater restraint effect on shallower and lighter beams (W30x108) than deeper and heavier beams (W36x150).

(4) The observed out-of-plane movement of the beam bottom flange at 4% drift in the test specimens is less than the value of $0.2b_f$ suggested by Chi and Uang (2002) to determine the torque applied to the column.

(5) The beams in all the specimens except SPEC-6 accounted for most of the plastic drift and energy dissipation of the specimens. The panel zone designed according to the current AISC Seismic Provisions appears to work well when the design uses a 15% overstrength in the panel zone resistance R_v, enabling the beams to fully develop plastic hinges in the RBS. In SPEC-6, due to the low yield strength for the doubler plate and undersize of the column web thickness, the panel zone strength to shear force ratio R_v/V_{pz} based on the AISC Seismic Provisions was close to 1.0. This

resulted in a larger portion of the plastic deformation to be concentrated in the panel zone.

(6) The supplemental bracing for SPEC-3 and SPEC-6 reduced the column twisting and out-of-plane movement of the beam bottom flange in the test specimens. In SPEC-3, which had a stronger panel zone and thereby local buckling in the RBS, the supplemental brace did not fully restrain the lateral movement of the beam flange at the middle of the RBS.

(7) The current design recommendation for RBS connections to a deep column over-estimates the column torsional warping stress due to twisting.

(8) The current fabrication requirements for grinding the RBS in accordance with FEMA 353 (FEMA 2000b) appear to be adequate for the specimens with A992 steel beams. The specimens with beams fabricated from A572 Grade 50 steel W36x150 sections (SPEC-1 and SPEC-2) and A992 steel W30x108 sections (SPEC-5) went into cleavage fracture in the RBS, while the specimens with beams fabricated from A992 steel W36x150 sections (SPEC-3 and SPEC-4) developed ductile tearing in the RBS. Further studies are needed to fully understand all of the causes for this.

(9) With a composite floor slab, the beam developed a larger moment capacity and less deterioration when the beam top flange is in compression, compared to when the beam bottom flange is in compression. The RBS design procedure recommended by Engelhardt (1999) and that by AISC Draft of *Prequalified Connections for Special and Intermediate Steel Moment Frames for Seismic Applications* (2003) both underestimate the maximum moment developed in the beam at the column face when a composite floor slab is present. This phenomenon is due to the increase in the RBS flexural capacity because of composite action.

(10) The axial brace force in the supplemental brace at the RBS was found to be larger than the design value recommended by the AISC Seismic Provisions (2002). More studies are needed to further evaluate the design for the bracing force at the RBS.

9.2.3 Overall Conclusions and Recommendations

An evaluation of the results from both the experimental studies led to the following conclusions:

(1) The use of the value for the ratio h / t_{cf}^3 by itself, or column depth d_c by itself, is not a clear indicator of the effects of an RBS on a deep column. Consideration must be given to the torsional and flexural properties of the column section, as well as the beam section size in the beam-to-column moment connection. Larger beams will result in a greater amount of stress applied to the column.

(2) The current design procedure for determining the torque caused by the RBS lateral movement of the beam bottom flange needs revisions, for it overestimates the warping stresses developed in the column when a floor slab is present. Three of the test specimens were predicted to not perform adequately by the current design procedure of Chi and Uang (2002); however, all of the test specimens performed well, meeting the qualification criteria set forth in Appendix S of the AISC Seismic Provisions. The finite element studies show that the potential for ductile fracture is not consistent with the performance anticipated based on the current design procedure.

(3) All of the connection test specimens qualified for seismic use. Based on the column and beam section sizes in the test matrix, it appears that an RBS connection with a floor slab or a supplemental brace at the RBS and a column section size that satisfies the weak beam-strong column criteria will perform adequately. A RBS connection to a deep column with a floor slab does not appear to require any special considerations beyond checking the column for stresses. Torsional stresses should be included, but the current method recommended by Chi and Uang (2002) for calculating the column torque is too conservative.

(4) RBS connections to a deep column appear to perform better than WUF-W connections to a deep column. The finite element parametric study shows that WUF-W connections develop a larger plastic strain in the connection, resulting in it having a greater potential for ductile fracture than an RBS connection. Because of this, the test results based on the RBS connections to a deep column cannot be extrapolated to a WUF connection to a deep column. The test results can be used to pre-qualify RBS

connections (with a floor slab) to columns that are W36x150 sections and heavier that are attached to W36x150 beams, W27x194 column sections and heavier that are attached to W36x150 beams, W27x146 column sections and heavier that are attached to W30x108 beams, as well as W24x131 column sections and heavier that are attached to W30x108 beams. Any smaller column section size or larger beam size will need to be evaluated. One evaluation approach would be to check the stresses in the column, as discussed above.

(5) A new procedure is presented in this report, based on the stress and strain distribution in the beam flange from the analytical and experimental results. This proposed design procedure shows better accuracy in predicting the column flange normal stresses.

(This page left blank)

REFERENCES

AISC (1997). "Seismic Provisions for Structural Steel Buildings," (including Supplemental No.1 (1999) and Supplemental No.2 (2000)), American Institute of Steel Construction, Chicago, Illinois

AISC (2001). "Load and Resistance Factor Design Specification for Structural Steel Buildings,", American Institute of Steel Construction, Chicago, Illinois

AISC (2002). "Seismic Provisions for Structural Steel Buildings," American Institute of Steel Construction, Chicago, Illinois

AISC (2003). "Prequalified Connections for Special and Intermediate Steel Moment Frames for Seismic Applications (DRAFT)," American Institute of Steel Construction, Chicago, Illinois

ASTM (2000). "Annual Book of ASTM Standards, 2000, section three, Metals Test Methods and Analytical Procedures," volume 03.01, West Conshohocken, Pennsylvania

ASTM (2002). "Annual Book of ASTM Standards, 2002, section one, Iron and Steel Products," volume 01.04, West Conshohocken, Pennsylvania

AWS (1995). "Specification for Carbon Steel Electrodes for Flux Cored Arc Welding," *ANSI/AWS A5.20-95*, AWS, Miami, Florida

AWS (2002). "Structural Welding Code – Steel," *AWS D1.1/D1.1M:2002*, AWS, Miami, Florida

Chi, B. and Uang, C.-M. (2002). "Cyclic Response and Design Recommendations of Reduced Beam Section Moment Connections with Deep Columns," *Journal of Structural Engineering*, ASCE, Vol. 128, Issue 4, pp. 464-473

Deierlein, G. G. and Chi, W-M (1999). "Integrative Analytical Investigations on the Fracture Behavior of Welded Moment Resisting Connections," *Report No. SAC/BD-99/15*, SAC Joint Venture, Sacramento, California.

El-Tawil, S., Mikesell, T., Vidarsson, E., and Kunnath, S. (1998). "Strength and Ductility of FR Welded-Bolted Connections," *Report No. SAC/BD-98/01*, SAC Joint Venture, Sacramento, California.

Engelhardt, M. D. (1999). "The 1999 T. R. Higgins Lecture: Design of Reduced Beam Section Moment Connections," *Proceedings: 1999 North American Steel Construction Conference*, American Institute of Steel Construction, Toronto, Canada, pp. 1-1 to 1-29, May 1999

Engelhardt, M. D., Venti, M., Fry, G. T. and Holiday, S. (2000). "Behavior and Design of Radius Cut Reduced Beam Section Connections," *Report No. SAC/BD-00/17*, SAC Joint Venture, Sacramento, California

FEMA (2000a). "Recommended Seismic Design Criteria For New Steel Moment-Frame Buildings," *Report No. FEMA 350*, FEMA, Washington D. C., July 2000

FEMA (2000b). "Recommended Specifications and Quality Assurance Guidelines for Steel Moment-Frame Construction for Seismic Applications," *Report No. FEMA 353*, FEMA, Washington D. C., July 2000

FEMA (2000c). "State of the Art Report on Connection Performance," *Report No. FEMA-353*, FEMA, Washington D. C., September, 2000

Galambos, T. V. (1998). *Guide to Stability Design Criteria for Metal Structures*, 5th Edition, John Wile & Sons, Inc.

Gilton, C., Chi, B. and Uang, C.-M. (2000). "Cyclic Response of RBS Moment Connections: Weak-Axis Configuration and Deep Column Effects," *Report No. SAC/BD-00/23*, SAC Joint Venture, Sacramento, California

Hancock, J.W. and MacKenzie, A.C. (1976). "On the Mechanisms of Ductile Failure in High-Strength Steels Subjected to Multi-Axial Stress-States," J. Mech. Phys. Solids, 1976, vol.24. pp. 147-169

HKS (2001). *ABAQUS User's Manual*, Version 6.1, Hibbit, Karlsson & Sorenson, Inc., Pawtucket, Rhode Island

Jones, S. L., Fry, G. T. and Engelhardt, M. D. (2002). "Experimental Evaluation of Cyclically Loaded Reduced Beam Section Moment Connections," *Journal of Structural Engineering*, ASCE, Vol. 128, Issue 4, pp. 441-451

Kaufmann, E.J., Pense, A.W. (1999). "Characterization of Cyclic Inelastic Strain Behavior on Properties of A572 Gr.50 and A913 Rolled Sections," AISC-PITA Project Progress Report, ATLSS Research Center, Lehigh University, May

Lee, S., and Lu, L. (1989). "Cyclic Tests of Full-Scale Composite Joint Subassemblages," *Journal of Structural Engineering,* ASCE, Vol. 115, No. 8, pp. 1977-1998

Mao, C., Ricles, J. M., Lu, L.-W. and Fisher, J. W. (2001). "Effect of Local Details on Ductility of Welded Moment Connections," Journal of Structural Engineering, ASCE, Vol. 127, Issue 9, pp. 1036-1044

Ricles, J. M., Mao, C., Lu, L.-W. and Fisher, J. W. (2000). "Development and Evaluation of Improved Details for Ductile Welded Unreinforced Flange Connections," *Report No. SAC/BD-00/24*, SAC Joint Venture, Sacramento, California

Ricles, J. M., Mao, C., Lu, L.-W. and Fisher, J. W. (2002). "Inelastic Cyclic Testing of Welded Unreinforced Moment Connections," *Journal of Structural Engineering*, ASCE, Vol. 128, Issue 4, pp.429-440

Roeder, C. W. (2000). "Connection Performance State of Art Report," *Report No. FEMA-355D*, FEMA, Washington, D.C.

SAC Joint Venture (SAC) (1997). "Protocol for Fabrication, Inspection, Testing, and Documentation of Beam-Column Connection Tests and Other Experimental Specimens," *Report No. SAC/BD-97/02*, SAC Joint Venture, Sacramento, California

SAC (1999). The SAC Steel Project Website Search Connection Database. http://www.sacsteel.org/connections/, The SAC Steel Project, Richmond, California

Salmon, C. G., and Johnson J. E. (1996). "Steel Structures: Design and Behavior, Emphasizing Load and Resistance Factor Design," Fourth ed., HarperCollins, New York

Seaburg and Carter (1997). "Torsional Analysis of Structural Steel Members," Steel Design Guide Series 9, American Institute of Steel Construction, Chicago, Illinois

Shen, J.-H. J., Astaneh-Asl, A. and McCallen, D. B. (2002). "Use of Deep Columns In Special Steel Moment Frames," Technical Information and Product Service, Structural Steel Education Council, AISC, Chicago, Illinois

Uang, C.-M. and Fan, C.-C. (2001). "Cyclic Stability Criteria for Steel Moment Connections with Reduced Beam Section," *Journal of Structural Engineering*, ASCE, Vol. 127, Issue 9, pp.1021-1027

Youssef, N. F. G, Bonowitz, D., and Gross, J. L. (1995). "A Survey of Steel Moment Resisting Frame Buildings Affected by the 1994 Northridge Earthquake," NIST, NISTIR 5625, Gaithersburg, MD 20899

Yu, Q. S., Gilton, C. and Uang, C.-M. (2000). "Cyclic Response of RBS Moment Connections: Loading Sequence and Lateral Bracing Effects," *Report No. SAC/BD-00/22*, SAC Joint Venture, Sacramento, California

(This page left blank)

Appendix A

Specimen Test Summaries

(This page left blank)

Deep Column Moment Connection Experimental Study

TEST SUMMARY OF SPEC-1

Specimen ID	SPEC-1
Key Words	Deep column; RBS connection; E70T-6 electrode; modified weld access hole; composite floor slab
Test Location	ATLSS Research Center, Lehigh University
Test Date	May 27, 2003
Investigators	James M. Ricles, John W. Fisher, Le-Wu Lu and Xiaofeng Zhang
Main References	FEMA 350, FEMA 353, AISC Seismic Provisions 2002
Sponsors	AISC, PITA

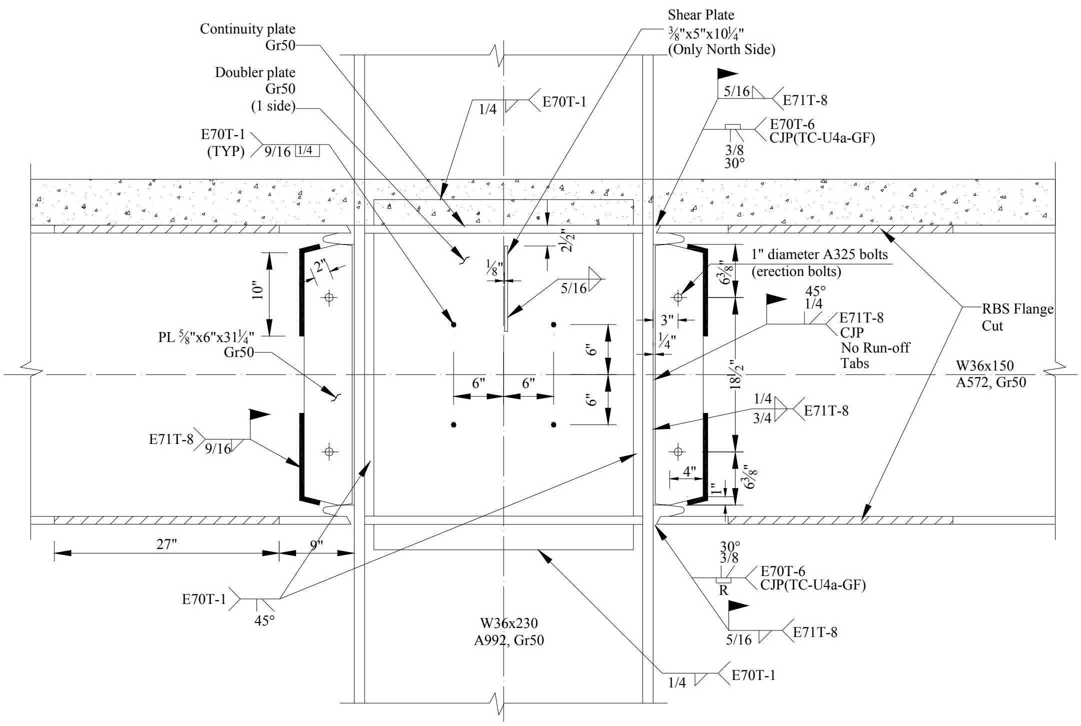

Connection Details

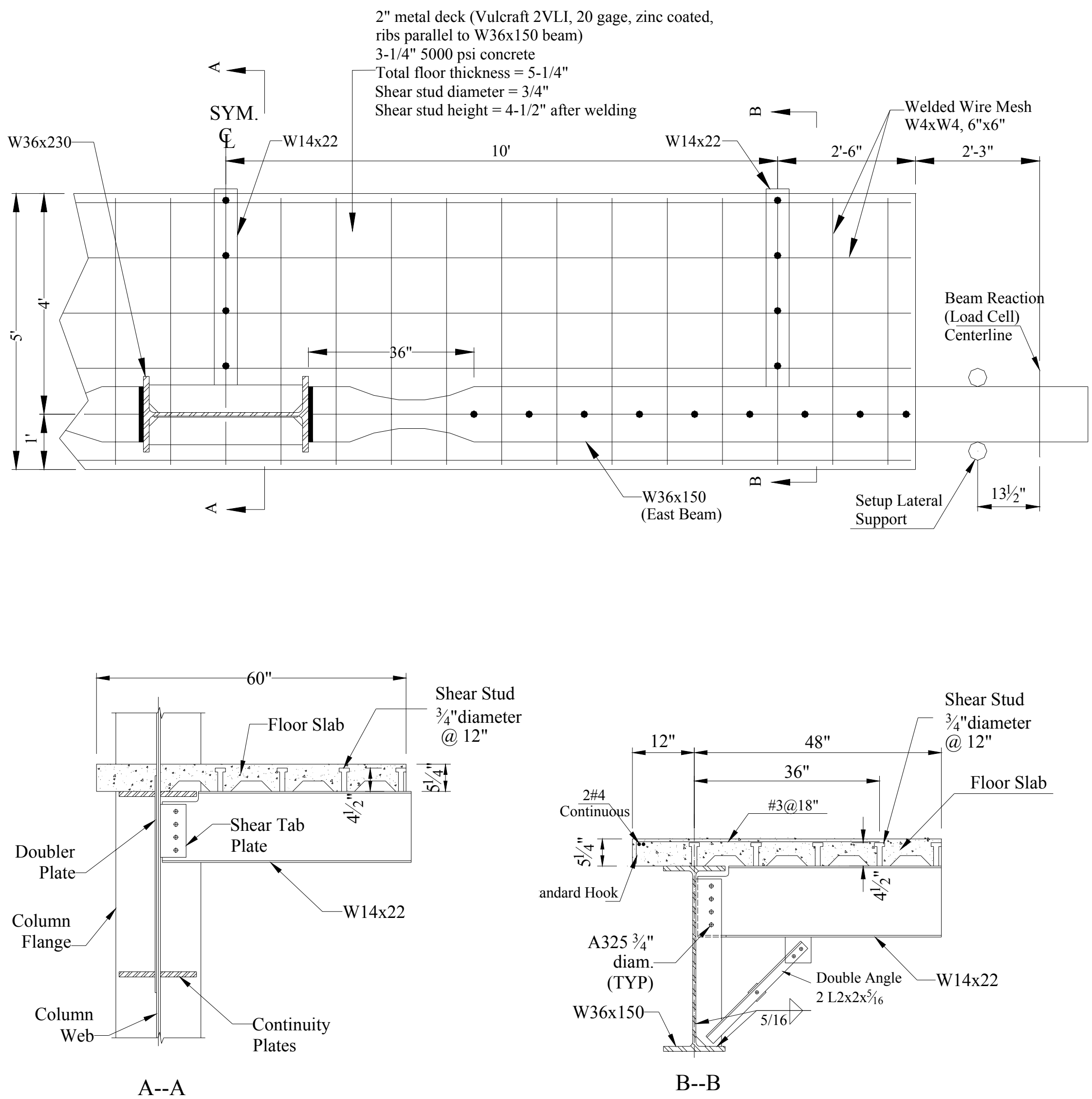

Floor Slab Details

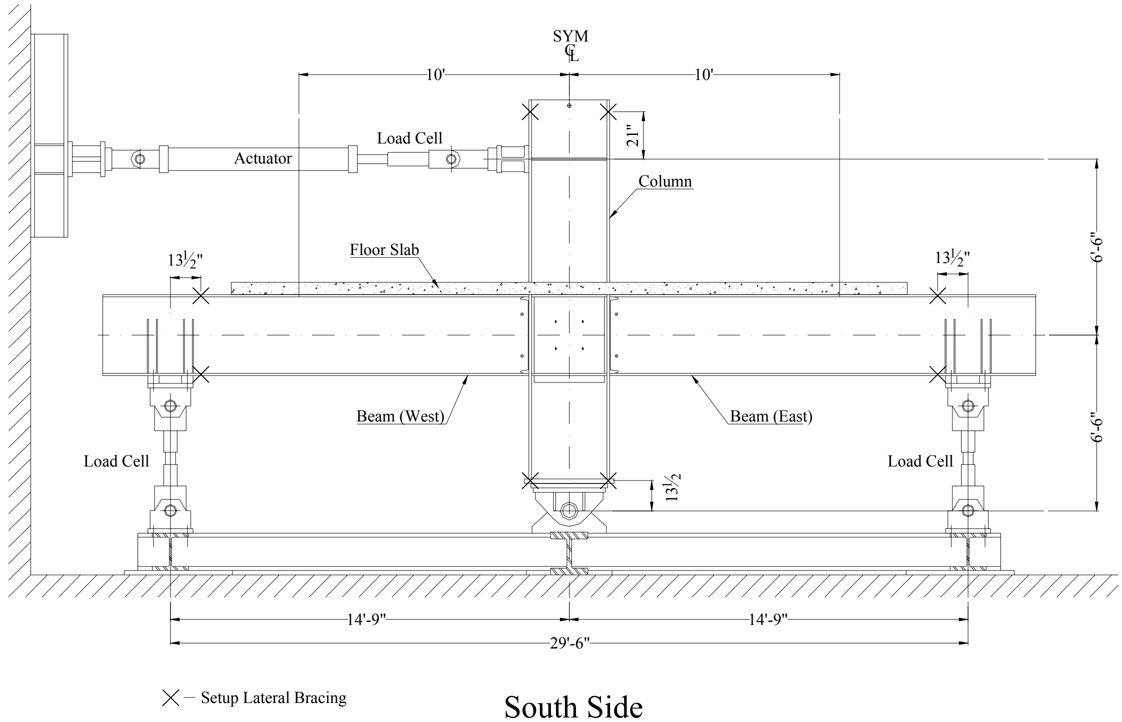

South Side

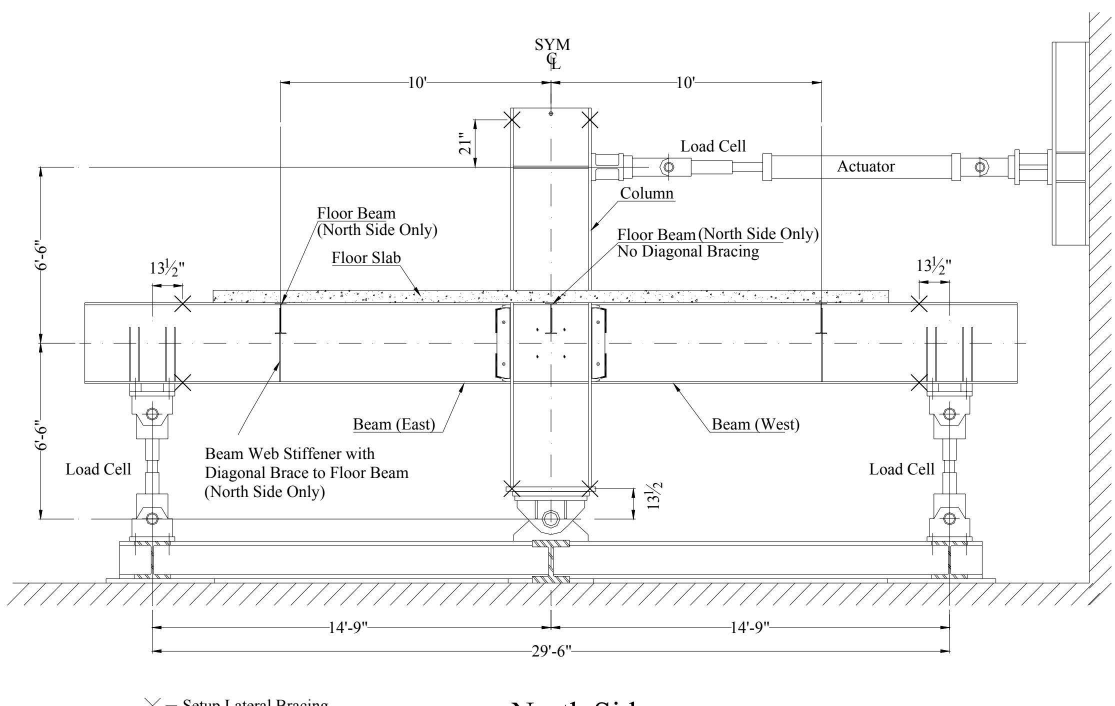

North Side

Test Setup

MATERIAL PROPERTIES AND SPECIMEN DETAILS

<table>
<tr><td rowspan="2">Member</td><td rowspan="2">Size</td><td rowspan="2">Grade</td><td colspan="2">Yield Stress (ksi)</td><td colspan="2">Ultimate Stress (ksi)</td></tr>
<tr><td>Mill Cert.</td><td>Coupon Test</td><td>Mill Cert.</td><td>Coupon Test</td></tr>
<tr><td>Beam</td><td>W36x150</td><td>A572 Gr.50</td><td>N.A</td><td>49.7 Flange
54.8 Web</td><td>N.A</td><td>69.3 Flange
71.4 Web</td></tr>
<tr><td>Column</td><td>W36x230</td><td>A992</td><td>57.1</td><td>51.6 Flange
57.0 Web</td><td>73.2</td><td>71.9 Flange
74.5 Web</td></tr>
<tr><td>Doubler Plate</td><td>¼"x31½" x42"</td><td>A572 Dr.50</td><td>N.A</td><td>58.2</td><td>N.A</td><td>82.5</td></tr>
<tr><td>Continuity Plate</td><td>1"x6" x33$^3/_8$"</td><td>A572 Dr.50</td><td>N.A</td><td>52.6</td><td>N.A</td><td>74.8</td></tr>
<tr><td>Concrete Slab</td><td colspan="6">5¼" composite slab, with 2” metal deck
f_c' = 5,633 psi (28 days); f_c' = 5,326 psi (21 days); tested at 20 days of age</td></tr>
<tr><td>Welding Procedure Specification</td><td colspan="6">CJP Groove Weld: FCAW-SS, 3/32” diameter AWS E70T-6 electrode for beam flange, 0.068” diameter AWS E71T-8 electrode for beam web; Complying with AWS A5.20 Classification and AWS D1.1/D1.1M:2002 Specification.
Fillet weld: FCAW-SS, 0.068” diameter AWS E71T-8 electrode; Complying with AWS A5.20 Classification and AWS D1.1/D1.1M:2002 Specification.</td></tr>
<tr><td>Shear Tab</td><td colspan="6">Fillet welded to the column flange, serving as a backing bar for beam web CJP groove weld. Supplemental fillet welds are placed between shear tab and beam web.</td></tr>
<tr><td>Doubler Plate</td><td colspan="6">One-sided doubler plate. Groove welded to column flanges on both sides and fillet welded to column web on top and bottom.</td></tr>
<tr><td>Continuity Plate</td><td colspan="6">Full beam flange thickness continuity plates. Single V-bevel groove welded to column flanges and fillet welded to column web/doubler plate.</td></tr>
<tr><td>Composite Floor Slab</td><td colspan="6">Decking: Vulcraft 2VLI, 20 gage, zinc coated, ribs parallel to W36x150 beam; 12 gage side pour stop on the overhang side; 16 gage side and end pour stop on remaining sides;
Wire-mesh: W4xW4, 6"x6"</td></tr>
<tr><td>Boundary Condition</td><td colspan="6">Two-sided test with floor slab; no axial force applied to the column; Column was pinned at the bottom and laterally loaded on the top, beam ends were connected to rigid links to simulate roller boundary conditions.</td></tr>
<tr><td>Other Details</td><td colspan="6">The run-off tabs on the beam flanges were removed; no run-off tabs were used for beam web groove weld. Beam top flange backing bar remained and a reinforcing fillet weld was provided between the bottom surface of the backing bar and the column flange using AWS E71T-8 electrode. The bottom beam flange backing bar was removed using the air-arc process, back gouged and reinforced with a fillet weld using AWS E71T-8 electrode.</td></tr>
</table>

DISPLACEMENT HISTORY AND KEY EXPERIMENTAL OBSERVATIONS

Applied Displacement History

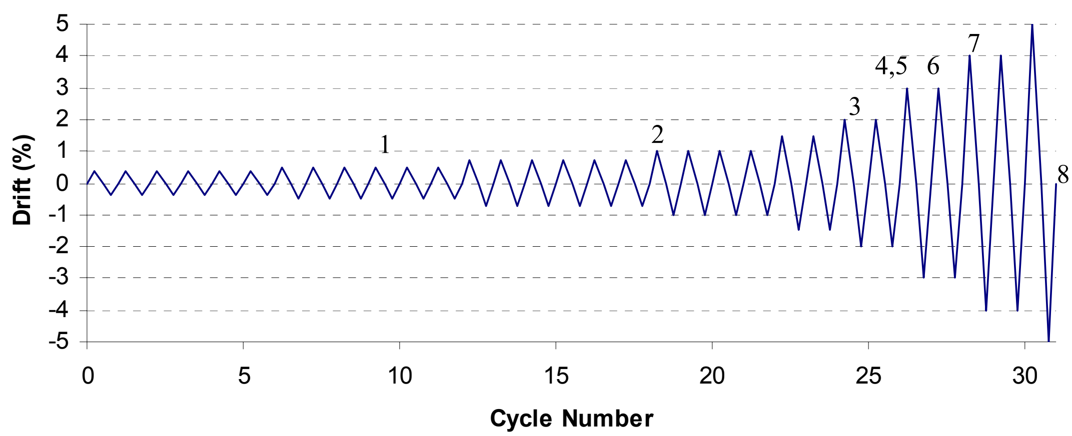

Key Observations during the Test

1	Minor yielding of beam flange in RBS. Concrete floor slab cracking around column.
2	More extensive beam flange yielding in RBS; panel zone yielding. Crushing of concrete at column flanges.
3	Onset of beam web local buckling at RBS. More crushing of concrete on the face of column flanges and inside the flange region.
4	Onset of beam flange local buckling in RBS. Beam web local buckling became more severe.
5	Maximum specimen capacity achieved.
6	Beam flanges laterally displaced.
7	Fracture of some shear studs.
8	Fracture of east side beam bottom flange at RBS. Fracture initiated from low cycle fatigue cracks on the edge of beam flanges.

TEST RESULTS

			Maximum
Force/Displacement	Peak Actuator Force (kips)		411
	Column Top Displacement (in.)		7.7
	Experimental Yielding Displacement (in.)		1.6
Moment	Beam Plastic Moment $\mathbf{M_p}^*$ (k-in.)	East Beam	29,216
		West Beam	29,203
	$\mathbf{M_f/M_p}^*$ (M_f at column face)	East Beam	0.95
		West Beam	1.03
Rotation Capacity	Total Plastic Drift (% rad.)		4.3
	Total Rotation across RBS, East Beam (% rad.)		4.3
	Panel Zone Plastic Drift (% rad.)		0.6
	Cumulative Total Plastic Drift (% rad.)		78.4
Energy Dissipation	Cumulative Energy Dissipation (k-in.)		29,536

Note: M_f = Beam moment at column face;
M_p = Beam plastic moment capacity based on measured dimensions and material properties.

TEST OBSERVATION

Specimen SPEC-1 first yielded in the beam bottom flanges at the RBS and in between the RBS and column region during the 0.5% story drift cycles. The concrete slab also developed cracking. Panel zone yielding and concrete crushing in the floor slab against the column flanges and inside the flange regions initiated during the 1% story drift cycles. Beam web local buckling in the RBS was observed during the second cycle of 2% drift. Minor flange local buckling occurred in the beam bottom flanges at the RBS during the first cycle of 3% story drift, which became more pronounced during the second cycle of 3% story drift. The specimen developed its maximum capacity during the first half cycle of 3% story drift. Beam web buckling in the RBS also became more extensive during the 3% story drift cycles, which caused the beam bottom flanges to move laterally in the RBS. Extensive beam web and flange local buckling occurred during 4% story drift cycles. The beam bottom flange in the RBS had moved laterally about 2.5-inches at the end of the 4% story drift cycles, with column twist visible. Fracture occurred at the end of first cycle of 5% story drift in the east side beam bottom flange at the RBS. Low cycle fatigue cracks were found in the beam flange at the RBS.

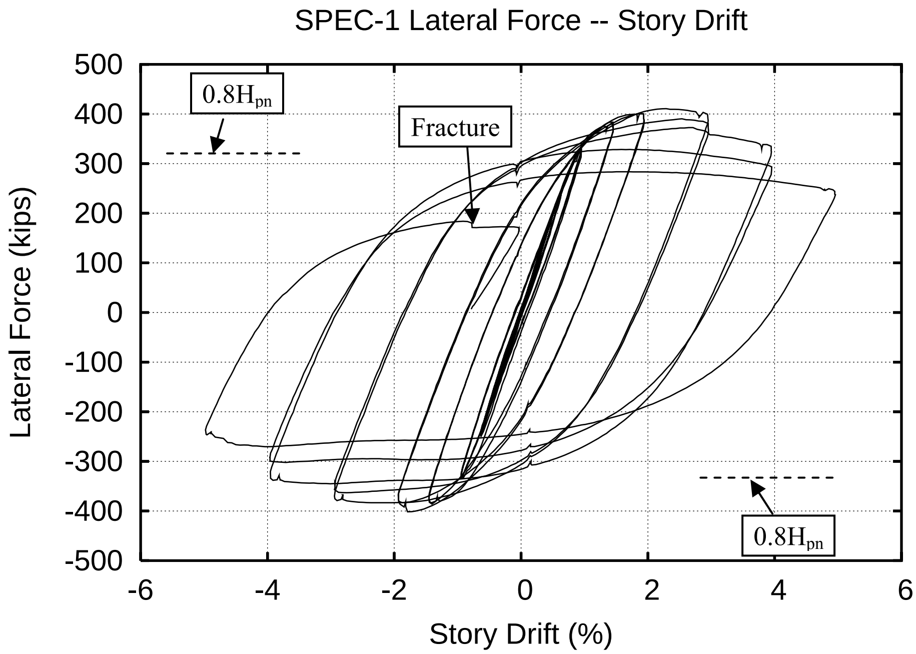
SPEC-1 Lateral Force -- Story Drift
0.8Hpn
Fracture
0.8Hpn
Lateral Force (kips)
Story Drift (%)
500
400
300
200
100
0
-100
-200
-300
-400
-500
-6
-4
-2
0
2
4
6

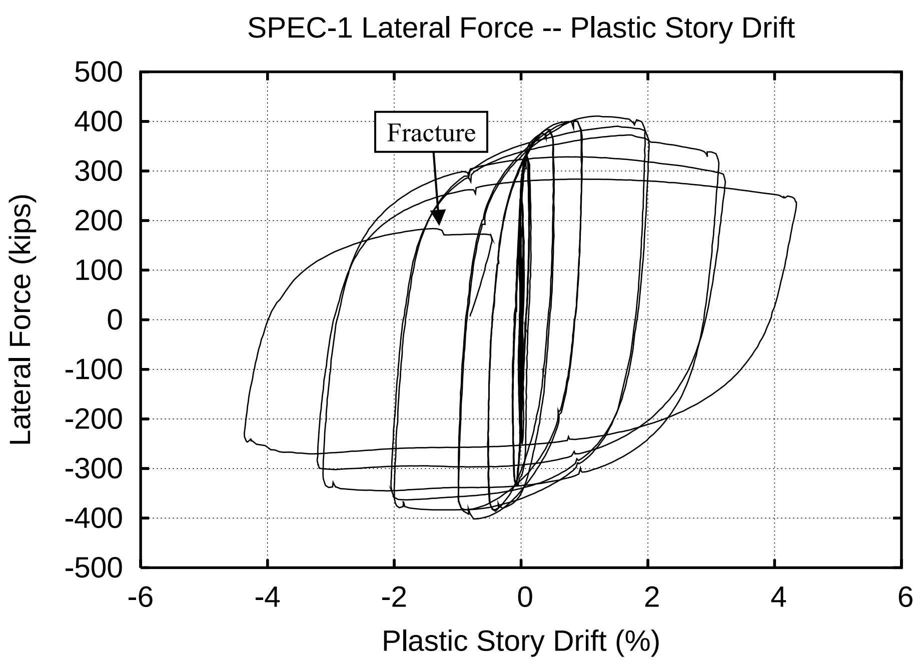
SPEC-1 Lateral Force -- Plastic Story Drift
Fracture
Lateral Force (kips)
Plastic Story Drift (%)
500
400
300
200
100
0
-100
-200
-300
-400
-500
-6
-4
-2
0
2
4
6

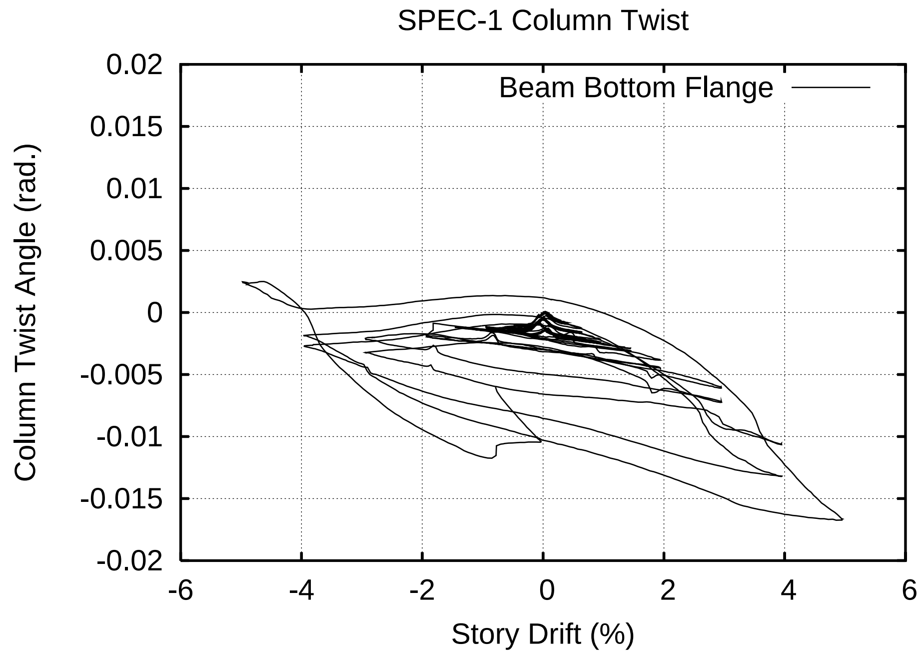
SPEC-1 Column Twist
Beam Bottom Flange
Column Twist Angle (rad.)
0.02
0.015
0.01
0.005
0
-0.005
-0.01
-0.015
-0.02
-6
-4
-2
0
2
4
6
Story Drift (%)

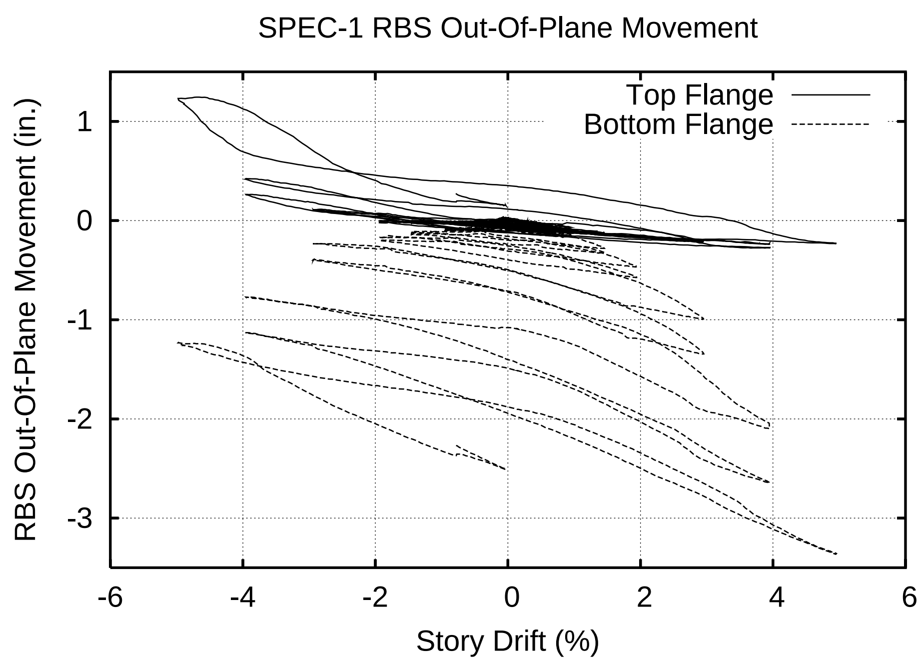
SPEC-1 RBS Out-Of-Plane Movement
Top Flange
Bottom Flange
RBS Out-Of-Plane Movement (in.)
1
0
-1
-2
-3
-6
-4
-2
0
2
4
6
Story Drift (%)

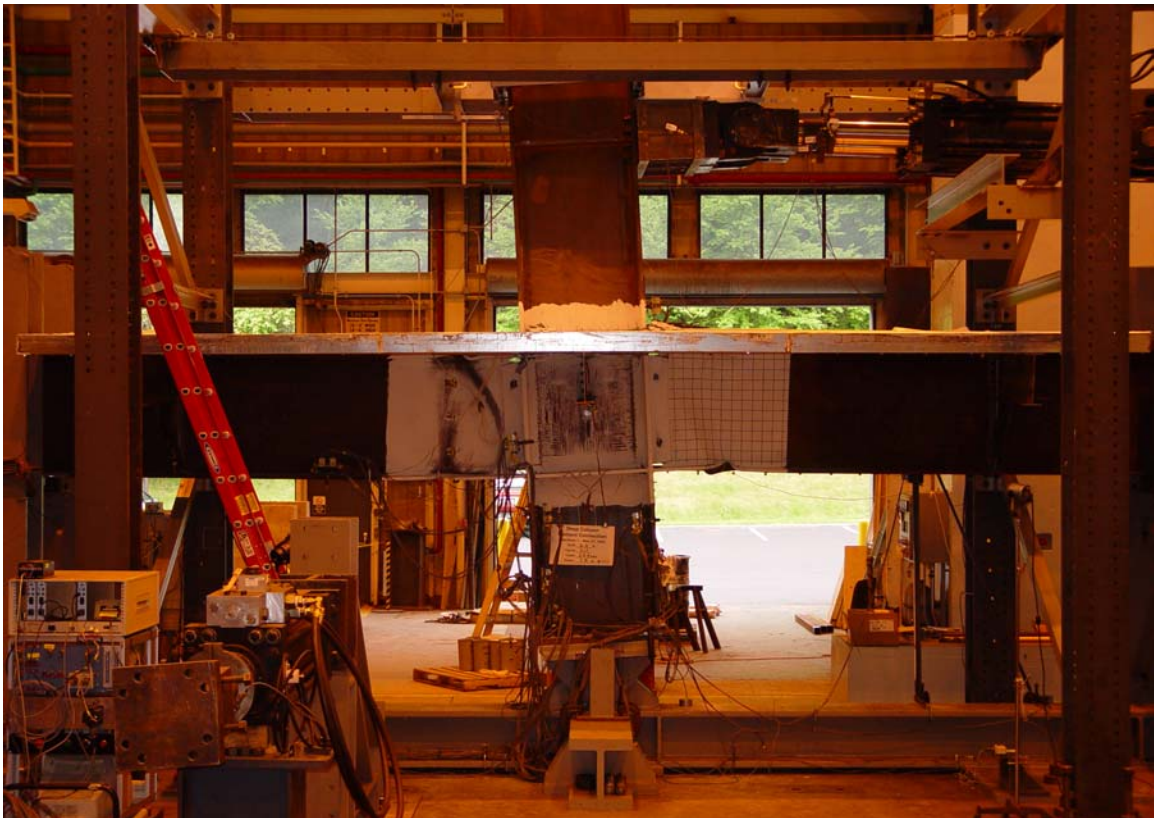

SPEC-1 at 5% story drift

Beam bottom flange lateral movement in RBS, 5% story drift

East beam bottom flange fracture

Deep Column Moment Connection Experimental Study

TEST SUMMARY OF SPEC-2

Specimen ID	SPEC-2
Key Words	Deep column; RBS connection; E70T-6 electrode; modified weld access hole; balanced panel zone; composite floor slab
Test Location	ATLSS Research Center, Lehigh University
Test Date	April 4, 2003
Investigators	James M. Ricles, John W. Fisher, Le-Wu Lu and Xiaofeng Zhang
Main References	FEMA 350, FEMA 353, AISC Seismic Provisions 2002
Sponsors	AISC, PITA

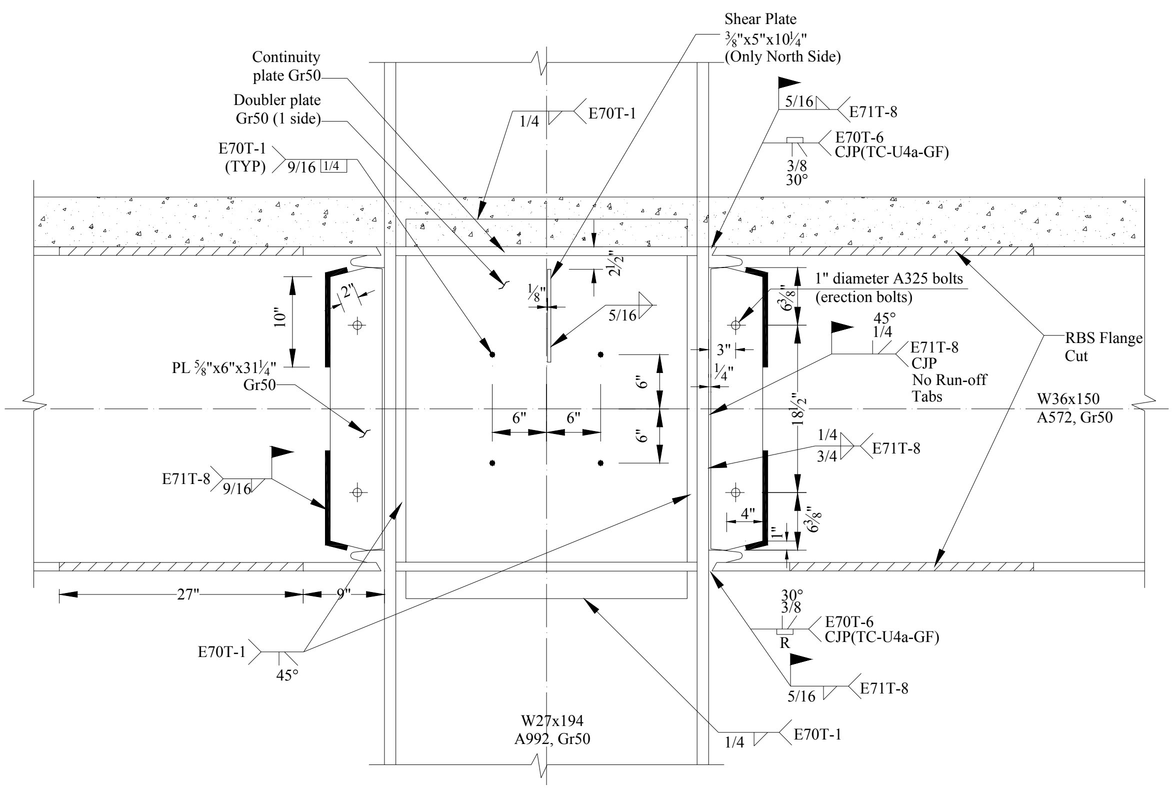

Connection Details

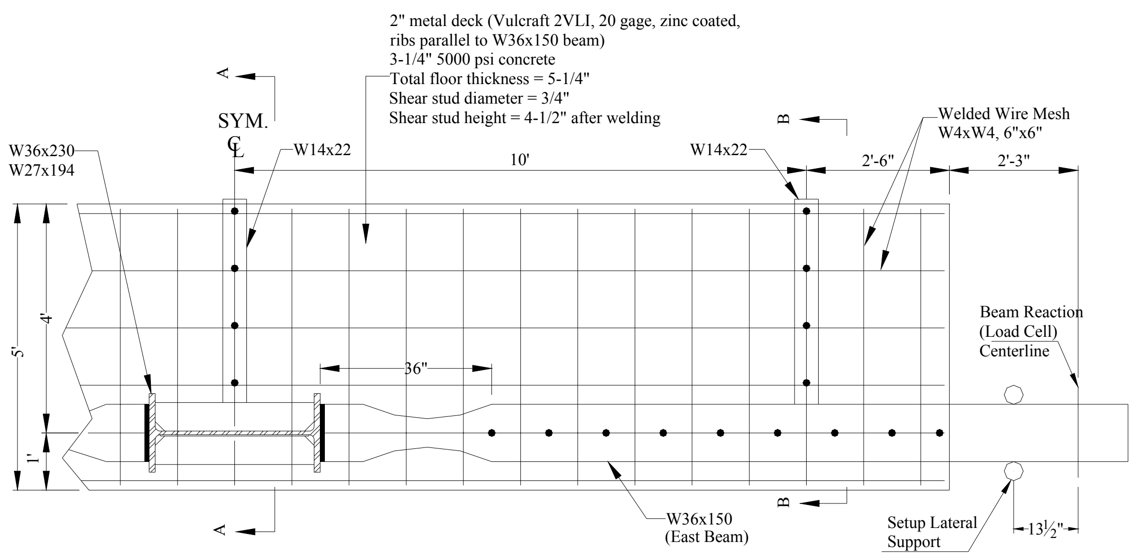

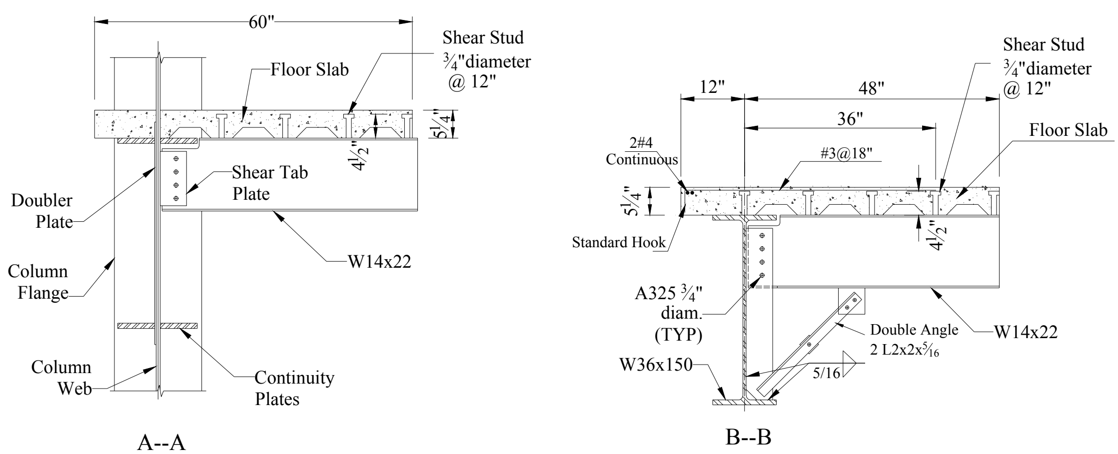

Floor Slab Details

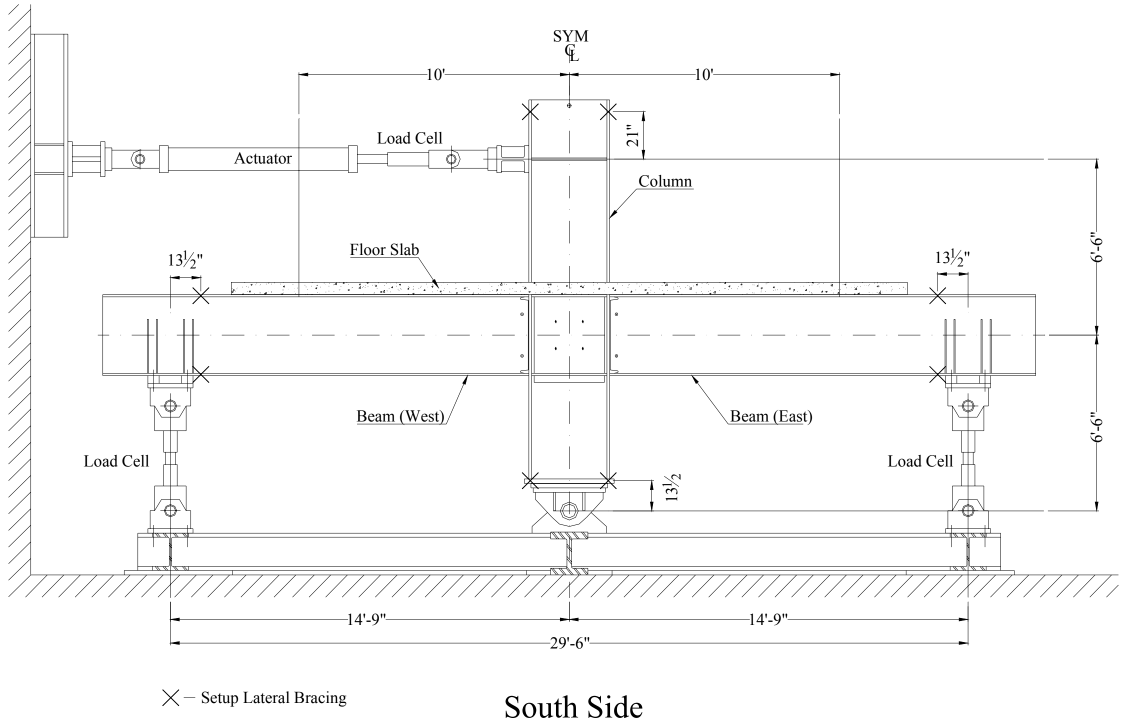

South Side

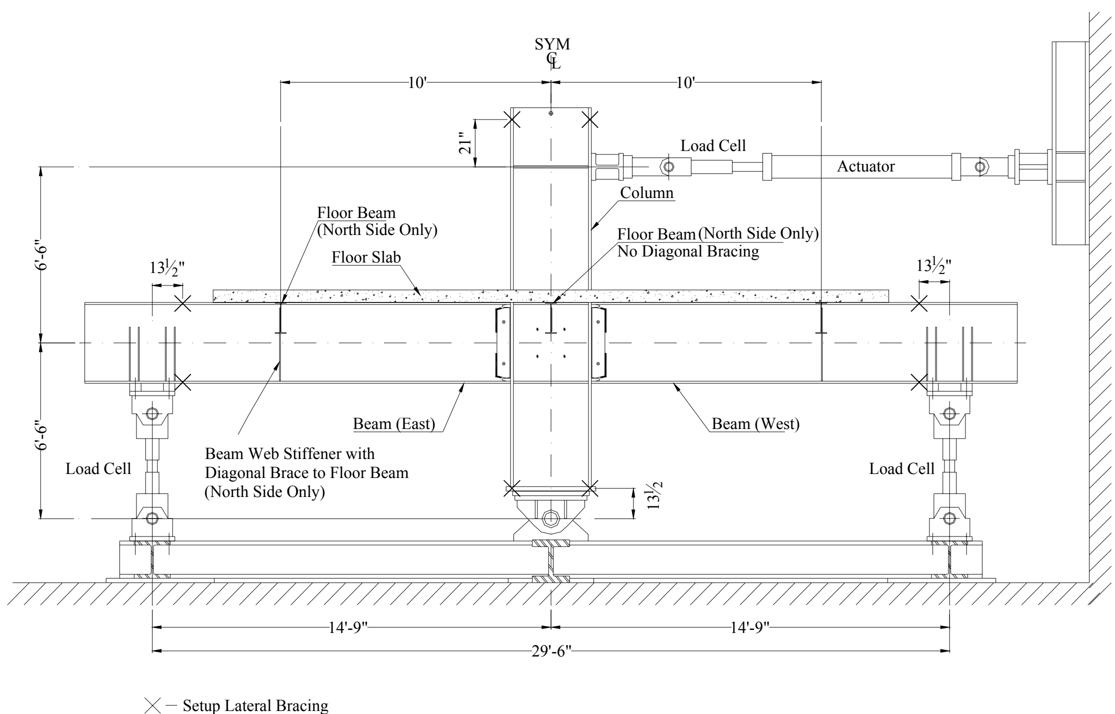

North Side

Test Setup

MATERIAL PROPERTIES AND SPECIMEN DETAILS

<table>
<tr><td rowspan="2">Member</td><td rowspan="2">Size</td><td rowspan="2">Grade</td><td colspan="2">Yield Stress (ksi)</td><td colspan="2">Ultimate Stress (ksi)</td></tr>
<tr><td>Mill Cert.</td><td>Coupon Test</td><td>Mill Cert.</td><td>Coupon Test</td></tr>
<tr><td>Beam</td><td>W36x150</td><td>A572 Gr.50</td><td>N.A.</td><td>49.7 Flange
54.8 Web</td><td>N.A.</td><td>69.3 Flange
71.4 Web</td></tr>
<tr><td>Column</td><td>W27x194</td><td>A992</td><td>57.5</td><td>53.9 Flange
56.8 Web</td><td>74.0</td><td>75.4 Flange
72.8 Web</td></tr>
<tr><td>Doubler Plate</td><td>½"x24"x42"</td><td>A572 Gr.50</td><td>N.A.</td><td>47.5</td><td>N.A.</td><td>67.6</td></tr>
<tr><td>Continuity Plate</td><td>1"x6"x25½"</td><td>A572 Gr.50</td><td>N.A.</td><td>52.6</td><td>N.A.</td><td>74.8</td></tr>
<tr><td>Concrete Slab</td><td colspan="6">5¼" composite slab, with 2” metal deck
f_c' = 5,648 psi (28 days); f_c' = 5,394 psi (21 days); tested at 22 days of age</td></tr>
<tr><td>Welding Procedure Specification</td><td colspan="6">CJP Groove Weld: FCAW-SS, 3/32” diameter AWS E70T-6 electrode for beam flange, 0.068” diameter AWS E71T-8 electrode for beam web; Complying with AWS A5.20 Classification and AWS D1.1/D1.1M:2002 Specification.
Fillet weld: FCAW-SS, 0.068” diameter AWS E71T-8 electrode; Complying with AWS A5.20 Classification and AWS D1.1/D1.1M:2002 Specification.</td></tr>
<tr><td>Shear Tab</td><td colspan="6">Fillet welded to the column flange, serving as a backing bar for beam web CJP groove weld. Supplemental fillet welds are placed between shear tab and beam web.</td></tr>
<tr><td>Doubler Plate</td><td colspan="6">One-sided doubler plate. Groove welded to column flanges on both sides and fillet welded to column web on top and bottom. Plug welded to the column web.</td></tr>
<tr><td>Continuity Plate</td><td colspan="6">Full beam flange thickness continuity plates. Single V-bevel groove welded to column flanges and fillet welded to column web/doubler plate.</td></tr>
<tr><td>Composite Floor Slab</td><td colspan="6">Decking: Vulcraft 2VLI, 20 gage, zinc coated, ribs parallel to W36x150 beam; 12 gage side pour stop on the overhang side; 16 gage side and end pour stop on remaining sides;
Wire-mesh: W4xW4, 6"x6"</td></tr>
<tr><td>Boundary Condition</td><td colspan="6">Two-sided test with floor slab; no axial force applied to the column; Column was pinned at the bottom and laterally loaded on the top, beam ends were connected to rigid links to simulate roller boundary conditions.</td></tr>
<tr><td>Other Details</td><td colspan="6">The run-off tabs on the beam flanges were removed; no run-off tabs were used for beam web groove weld. Beam top flange backing bar remained and a reinforcing fillet weld was provided between the bottom surface of the backing bar and the column flange using AWS E71T-8 electrode. The bottom beam flange backing bar was removed using the air-arc process, back gouged and reinforced with a fillet weld using AWS E71T-8 electrode.</td></tr>
</table>

DISPLACEMENT HISTORY AND KEY EXPERIMENTAL OBSERVATIONS

Applied Displacement History

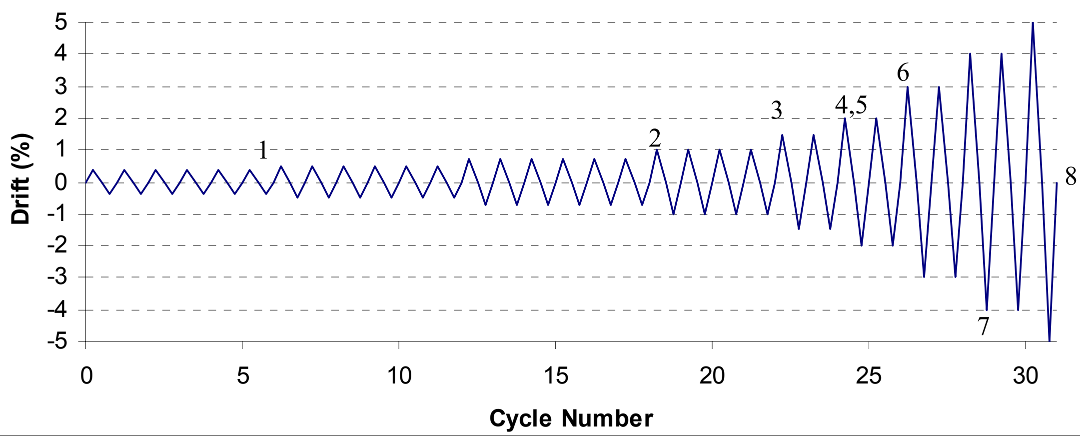

Key Observations during the Test		
	1	Concrete slab cracking.
	2	Yielding in beam flanges at RBS and in panel zone.
	3	Crushing of concrete at column flanges on column face as well as inside column flange region.
	4	Yielding on column flange below beam bottom flanges.
	5	Onset of beam web local buckling at RBS.
	6	Onset of beam flange local buckling at RBS. Beam flanges laterally displaced.
	7	Specimen maximum capacity achieved.
	8	Fracture of the west side beam top flange at RBS. Fracture initiated from a punch mark placed during fabrication.

TEST RESULTS

			Maximum
Force/Displacement	Peak Actuator Force (kips)		412
	Column Top Displacement (in.)		7.5
	Experimental Yield Displacement (in.)		1.6
Moment	Beam Plastic Moment $\mathbf{M_p}$ (k-in.)	East Beam	29,326
		West Beam	29,519
	$\mathbf{M_f/M_p}$	East Beam	0.99
		West Beam	1.10
Rotation Capacity	Total Plastic Drift (% rad.)		4.0
	Total Rotation across RBS, East Beam (% rad.)		5.1
	Panel Zone Plastic Drift (% rad.)		1.3
	Cumulative Total Plastic Drift (% rad.)		66.4
Energy Dissipation	Cumulative Energy Dissipation (k-in.)		27,203

Note: M_f = Beam moment at column face;
M_p = Beam plastic moment capacity based on measured dimensions and material properties.

TEST OBSERVATIONS

Cracks in the concrete floor slab of SPEC-2 occurred near the column at the end of 0.375% story drift cycles and continued to develop and become more extensive throughout the test. Yielding initiated in the beam bottom flanges in the RBS and near the column face, as well as in the panel zone at 1% story drift. The concrete slab started crushing against the column flanges and inside the column flanges region during the 1.5% story drift cycles. Minor column flange yielding below the beam bottom flange was observed during the 2% story drift cycles. Beam web local buckling occurred in the RBS region during the first cycle of 2% story drift and became more extensive in subsequent cycles. Beam flange local buckling, followed by the onset of beam bottom flange lateral movement in the RBS began during the 3% story drift cycles. At the end of the first cycle of 4% story drift the specimen developed its maximum capacity, followed by a deterioration in strength. The beam bottom flange had displaced laterally about 1.2 inches at 4% story drift, with no noticeable column twist. The buckling amplitudes grew as the displacement amplitude increased. Fracture occurred at the end of the first 5% story drift cycle. The fracture occurred in the top flange of the west side beam near the center of the RBS. The fracture extended down into the column web about 6.5-inches. Low cycle fatigue cracks were found in the beam bottom flanges at the RBS. The fracture initiated from a 0.023-inch deep punch mark.

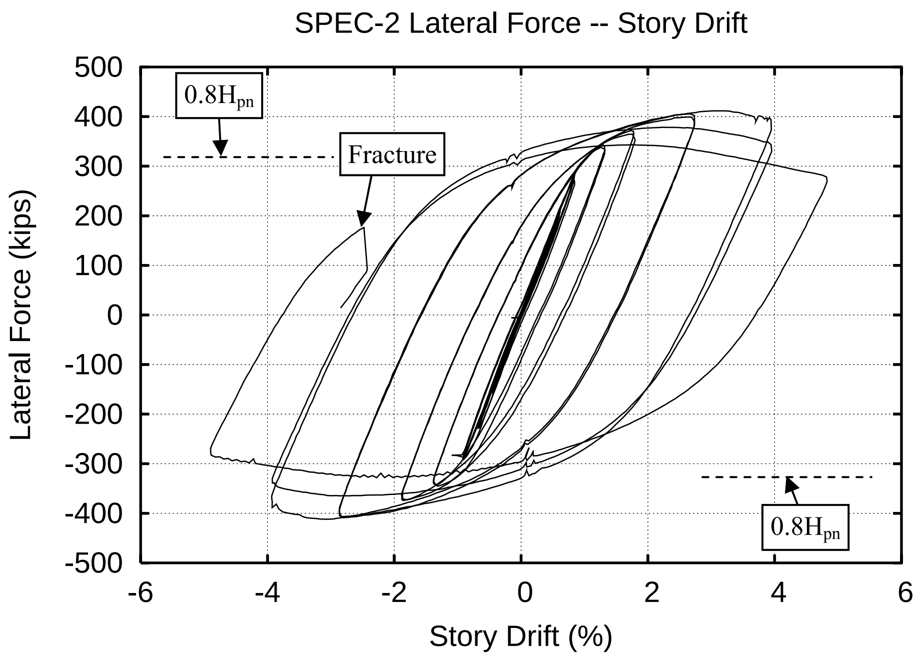
SPEC-2 Lateral Force -- Story Drift
Lateral Force (kips)
Story Drift (%)
0.8H_{pn}
Fracture
0.8H_{pn}

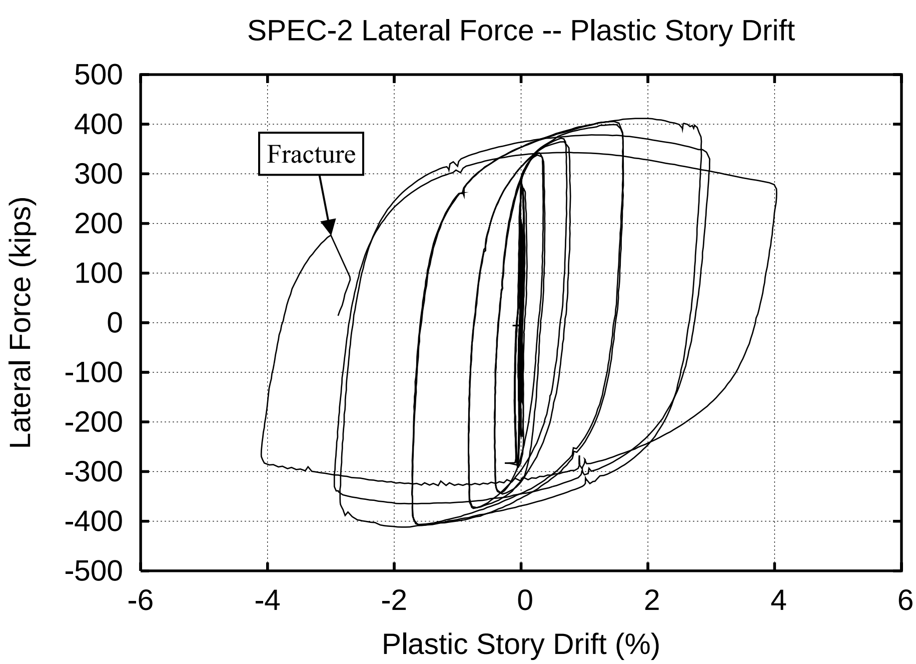
SPEC-2 Lateral Force -- Plastic Story Drift
Lateral Force (kips)
Plastic Story Drift (%)
Fracture

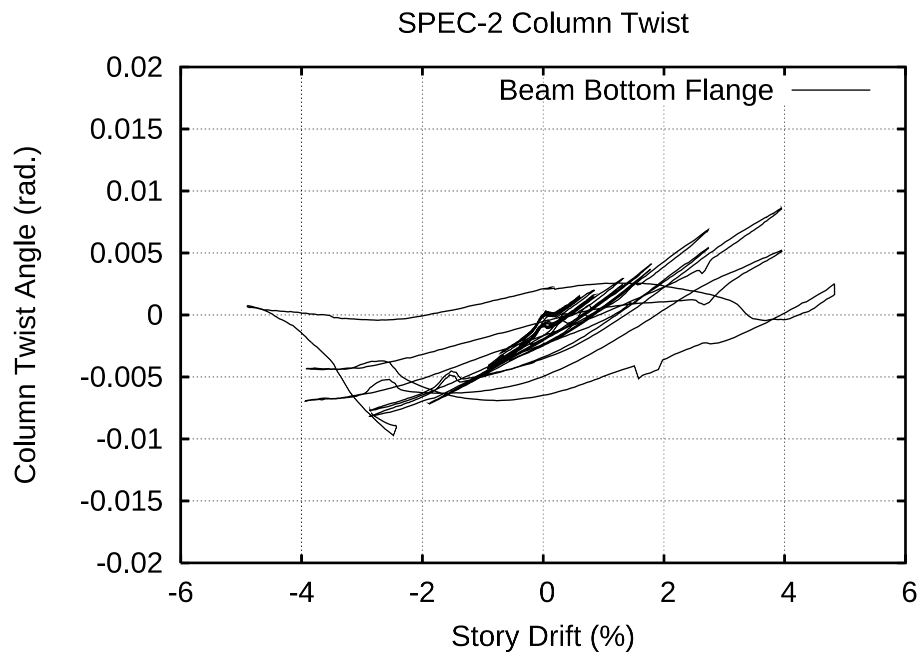
SPEC-2 Column Twist
Beam Bottom Flange
Column Twist Angle (rad.)
0.02
0.015
0.01
0.005
0
-0.005
-0.01
-0.015
-0.02
-6
-4
-2
0
2
4
6
Story Drift (%)

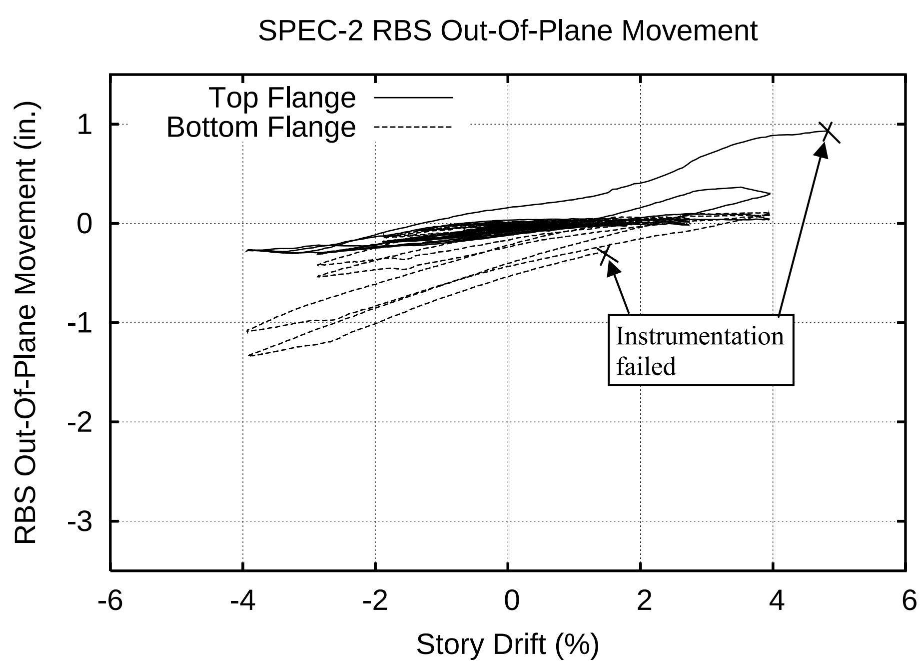
SPEC-2 RBS Out-Of-Plane Movement
Top Flange
Bottom Flange
RBS Out-Of-Plane Movement (in.)
1
0
-1
-2
-3
-6
-4
-2
0
2
4
6
Story Drift (%)
Instrumentation failed

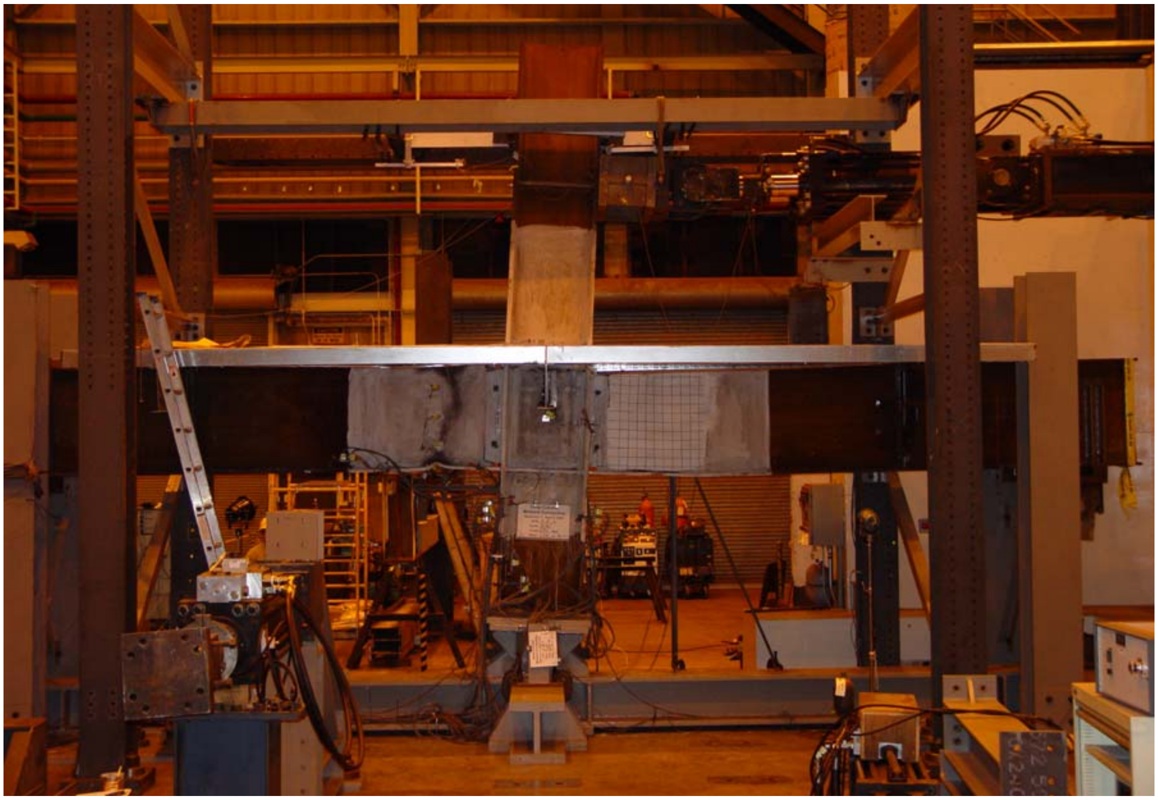

SPEC-2 at 5% story drift

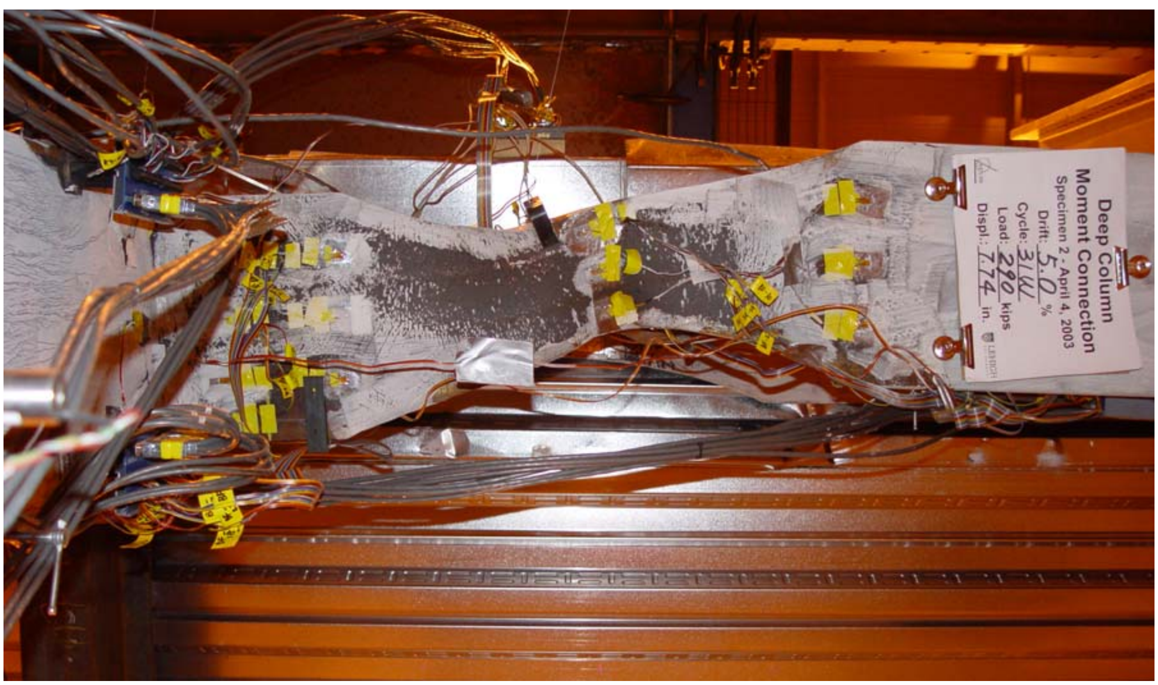

Beam bottom flange lateral movement in RBS, 5% story drift

West beam top flange fracture

Deep Column Moment Connection Experimental Study

TEST SUMMARY OF SPEC-3

Specimen ID	SPEC-3
Key Words	Deep column; RBS connection; E70T-6 electrode; modified weld access hole; composite floor slab
Test Location	ATLSS Research Center, Lehigh University
Test Date	August 26, 2003
Investigators	James M. Ricles, John W. Fisher and Le-Wu Lu and Xiaofeng Zhang
Main References	FEMA 350, FEMA 353, AISC Seismic Provisions 2002
Sponsors	AISC, PITA

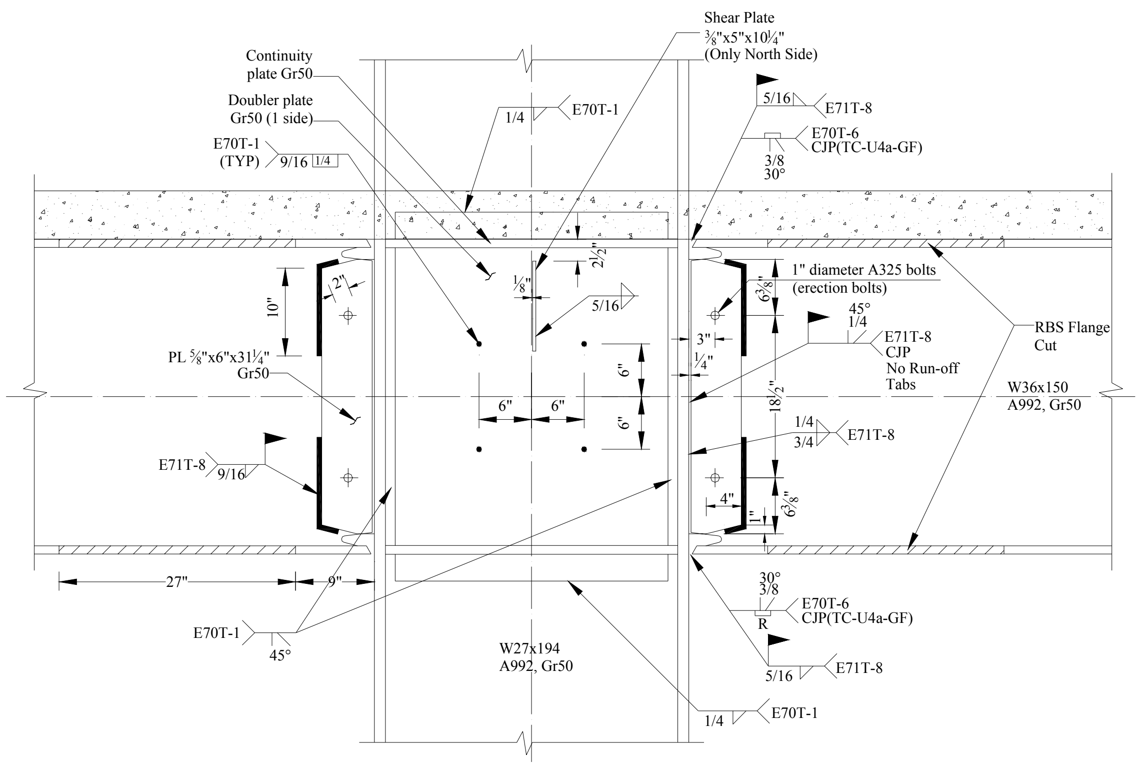

Connection Details

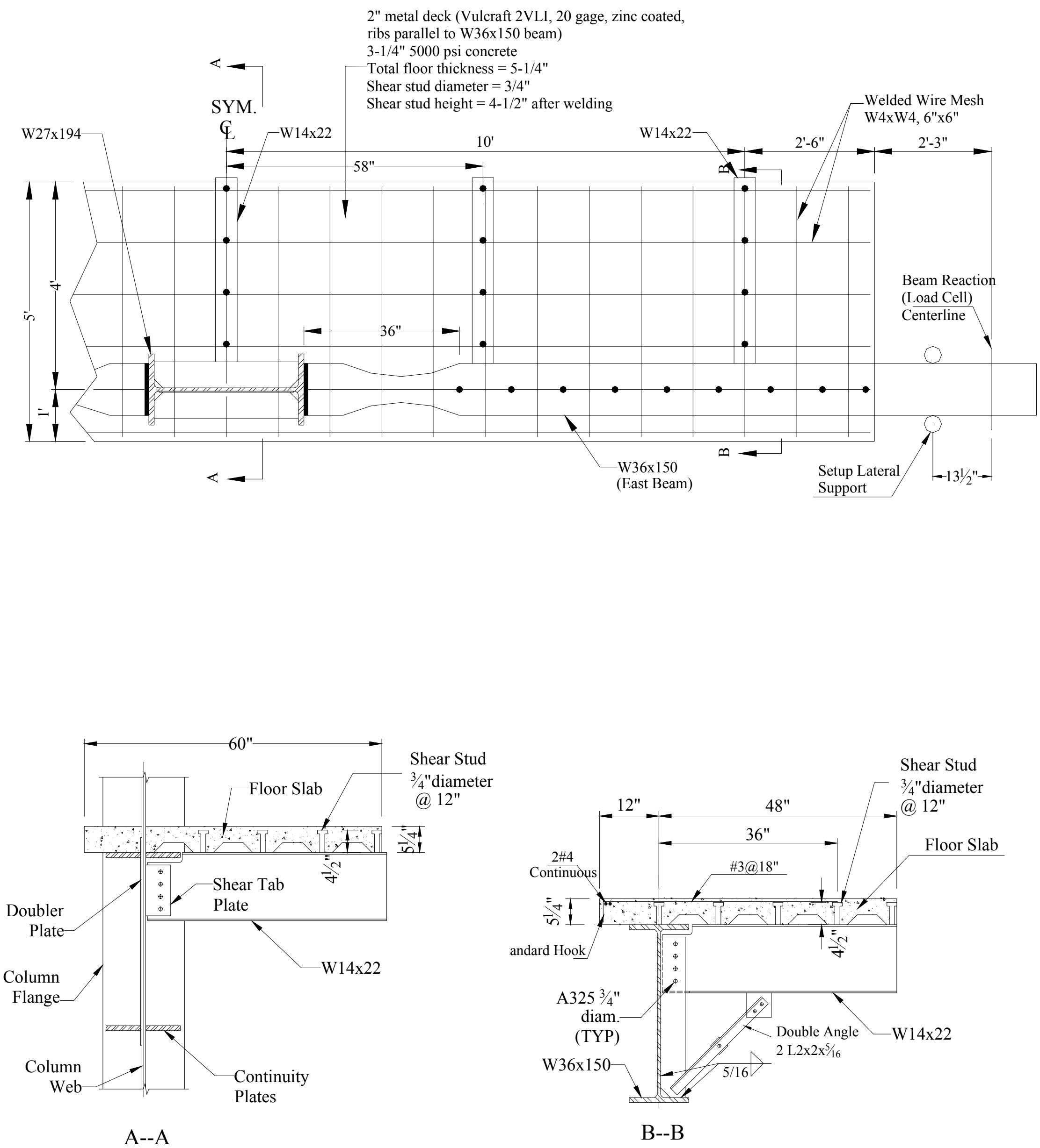

Floor Slab Details

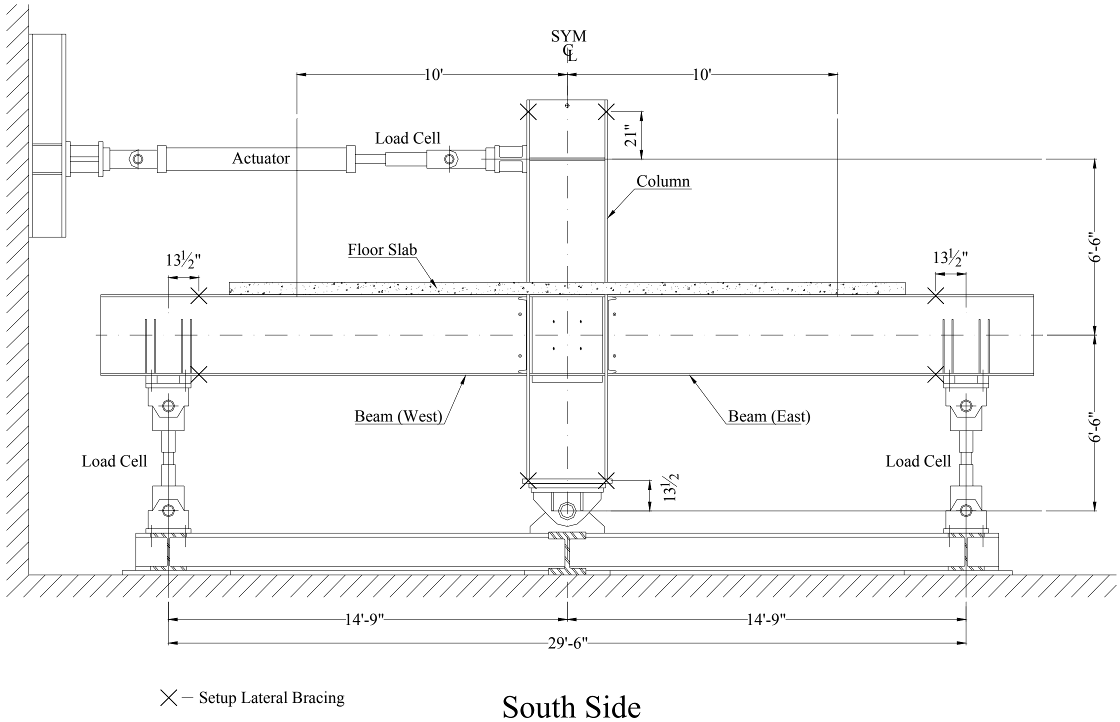

South Side

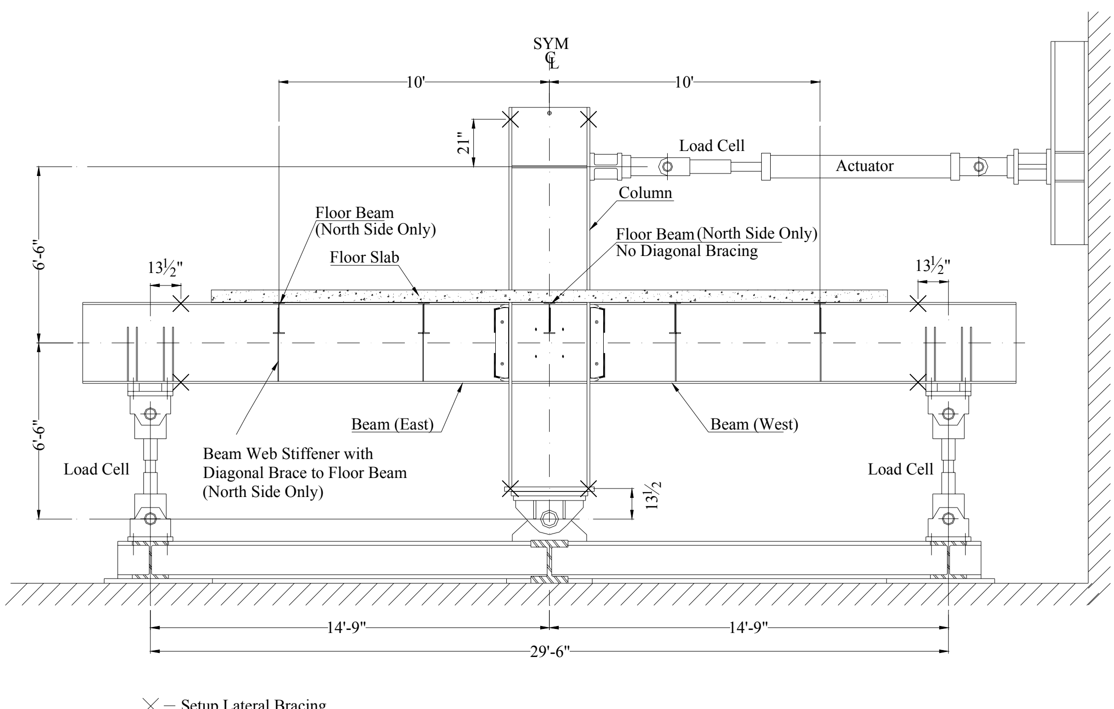

North Side

Test Setup

MATERIAL PROPERTIES AND SPECIMEN DETAILS

Member	Size	Grade	Yield Stress (ksi)		Ultimate Stress (ksi)	
			Mill Cert.	Coupon Test	Mill Cert.	Coupon Test
Beam	W36x150	A992	57.1 Flange 61.2 Web	53.0 Flange 57.4 Web	70.1 Flange 72.7 Web	73.7 Flange 73.4 Web
Column	W27x194	A992	56.5	51.7 Flange 58.5 Web	74.0	72.1 Flange 75.6 Web
Doubler Plate	½"x24"x42"	A572 Gr.50	63.0	59.3	73.0	75.6
Continuity Plate	1"x6"x25½"	A572 Gr.50	N.A.	56.0	N.A.	80.7
Concrete Slab	5¼" composite slab, with 2" metal deck f_c' = 4,958 psi (28 days); f_c' = 4,686 psi (14 days); tested at 13 days of age					

Welding Procedure Specification	*CJP Groove Weld*: FCAW-SS, 3/32" diameter AWS E70T-6 electrode for beam flange, 0.068" diameter AWS E71T-8 electrode for beam web; Complying with AWS A5.20 Classification and AWS D1.1/D1.1M:2002 Specification. *Fillet weld*: FCAW-SS, 0.068" diameter AWS E71T-8 electrode; Complying with AWS A5.20 Classification and AWS D1.1/D1.1M:2002 Specification.
Shear Tab	Fillet welded to the column flange, serving as a backing bar for the beam web CJP groove weld. Supplemental fillet welds are put between the shear tab and beam web.
Doubler Plate	One-sided doubler plate. Groove welded to column flanges on both sides and fillet welded to column web on top and bottom. Plug welded to the column web.
Continuity Plate	Full beam flange thickness continuity plates. Single V-bevel groove welded to column flanges and fillet welded to column web/doubler plate.
Composite Floor Slab	Decking: Vulcraft 2VLI, 20 gage, zinc coated, ribs parallel to W36x150 beam; 12 gage side pour stop on the overhang side; 16 gage side and end pour stop on remaining sides; Wire-mesh: W4xW4, 6"x6"
Boundary Condition	Two-sided test with floor slab; no axial force applied to the column; Column was pinned at the bottom and laterally loaded on the top, beam ends were connected to rigid links to simulate roller boundary conditions.
Other Details	The run-off tabs on the beam flanges were removed; no run-off tabs were used for beam web groove weld. Beam top flange backing bar remained and a reinforcing fillet weld was provided between the bottom surface of the backing bar and the column flange using an AWS E71T-8 electrode. The bottom beam flange backing bar was removed using the air-arc process, back gouged and reinforced with a fillet weld using AWS E71T-8 electrode.

DISPLACEMENT HISTORY AND KEY EXPERIMENTAL OBSERVATIONS

Applied Displacement History

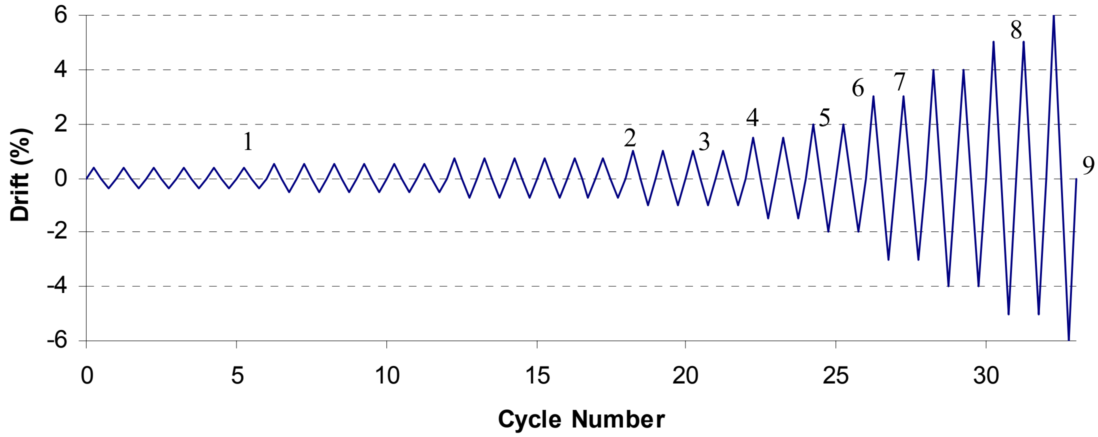

Key Observations during the Test		
	1	Concrete slab cracking.
	2	Yielding in beam flanges and webs at RBS.
	3	Crushing of concrete at column flanges on column face as well as inside column flange region.
	4	Yielding in panel zone.
	5	Onset of beam web local buckling at RBS.
	6	Onset of beam flange local buckling at RBS. Maximum specimen capacity achieved.
	7	Beam flange laterally displaced.
	8	Low cycle fatigue cracks developed in beam bottom flanges at RBS.
	9	Ductile material tearing of the east side beam top flange at RBS occurred at the end of first 6% cycle, which developed from low cycle fatigue cracks.

TEST RESULTS

			Maximum
Force/Displacement	Peak Actuator Force (kips)		407
	Column Top Displacement (in.)		9.3
	Experimental Yield Displacement (in.)		1.6
Moment	Beam Plastic Moment **M_p** (k-in.)	East Beam	31,835
		West Beam	32,060
	M_f/M_p	East Beam	0.97
		West Beam	1.12
Rotation Capacity	Total Plastic Drift (% rad.)		5.2
	Total Rotation across RBS, East Beam (% rad.)		5.6
	Panel Zone Plastic Drift (% rad.)		0.4
	Cumulative Total Plastic Drift (% rad.)		109
Energy Dissipation	Cumulative Energy Dissipation (k-in.)		40,086

Note: M_f = Beam moment at column face;
M_p = Beam plastic moment capacity based on measured dimensions and material properties.

TEST OBSERVATIONS

Cracking in the concrete floor slab of SPEC-3 occurred at the end of the 0.375% story drift cycles, which continued to develop and become more extensive throughout the test. Yielding initiated in the beam bottom flanges at the RBS and near the column face and in the beam webs near the flanges at 1.0% story drift. The concrete slab also started crushing against the column flanges and inside the column flanges region at the 1.0% story drift cycles. Panel zone yielding was observed during the 1.5% story drift cycles. Beam web local buckling occurred in the RBS region during the first cycle of 2% story drift and became more extensive in subsequent cycles. During the 3% story drift cycles, beam flange local buckling occurred. The beam web local buckling became extensive, causing the beam bottom flange to develop lateral movement. The specimen capacity then began to deteriorate. The buckling amplitudes grew as the test continued beyond 3% story drift. At 4% story drift the beam bottom flanges in compression had moved laterally about 1.2-inches in the RBS; very little column twisting was observed. Low cycle fatigue cracks were found to initiate during the 5% story drift cycles. Ductile material tearing of the bottom flange at the RBS of both beams occurred near the end of the first cycle of 6% story drift. Several low cycle fatigue cracks were found in the beam bottom flanges at the end of test.

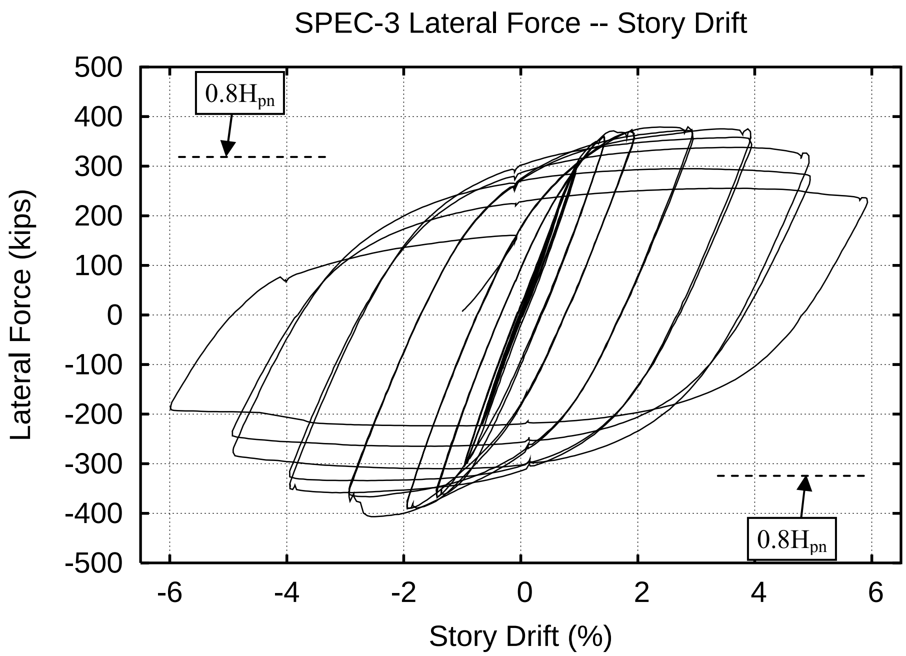
SPEC-3 Lateral Force -- Story Drift
Lateral Force (kips)
Story Drift (%)
0.8H
pn
0.8H
pn
500
400
300
200
100
0
-100
-200
-300
-400
-500
-6
-4
-2
0
2
4
6

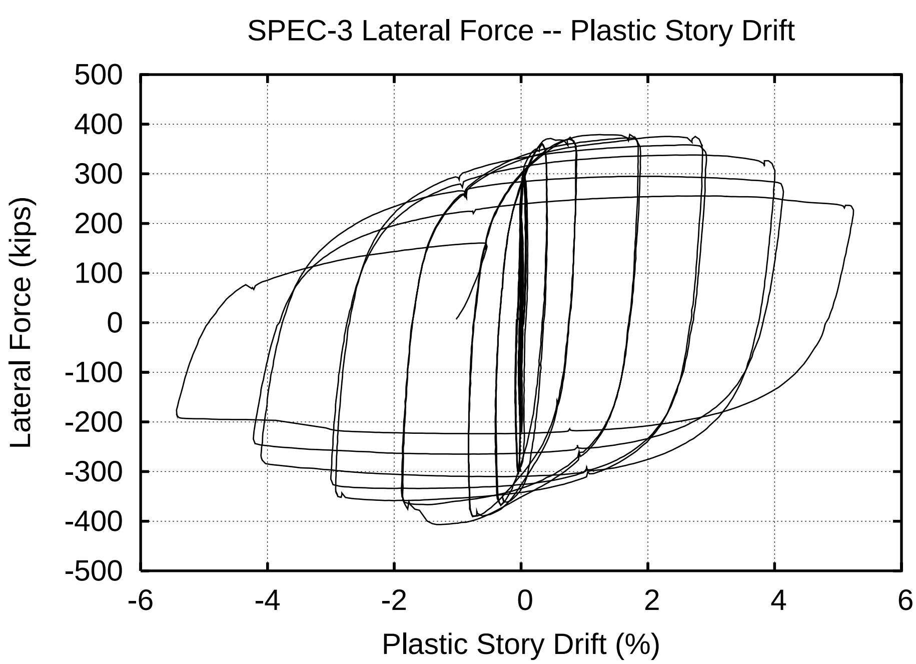
SPEC-3 Lateral Force -- Plastic Story Drift
Lateral Force (kips)
Plastic Story Drift (%)
500
400
300
200
100
0
-100
-200
-300
-400
-500
-6
-4
-2
0
2
4
6

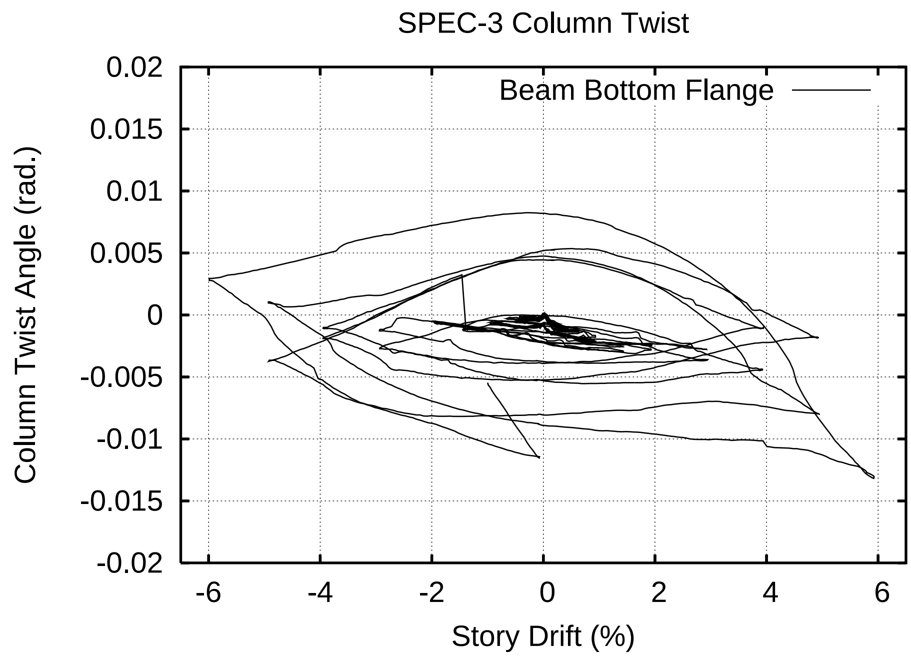
SPEC-3 Column Twist
Beam Bottom Flange
Column Twist Angle (rad.)
0.02
0.015
0.01
0.005
0
-0.005
-0.01
-0.015
-0.02
-6
-4
-2
0
2
4
6
Story Drift (%)

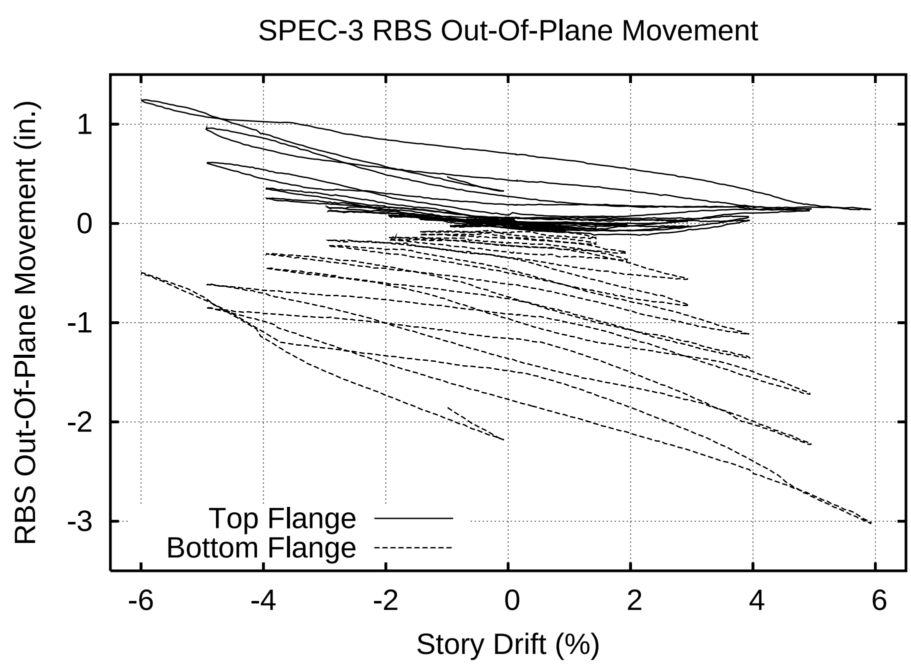
SPEC-3 RBS Out-Of-Plane Movement
RBS Out-Of-Plane Movement (in.)
1
0
-1
-2
-3
Top Flange
Bottom Flange
-6
-4
-2
0
2
4
6
Story Drift (%)

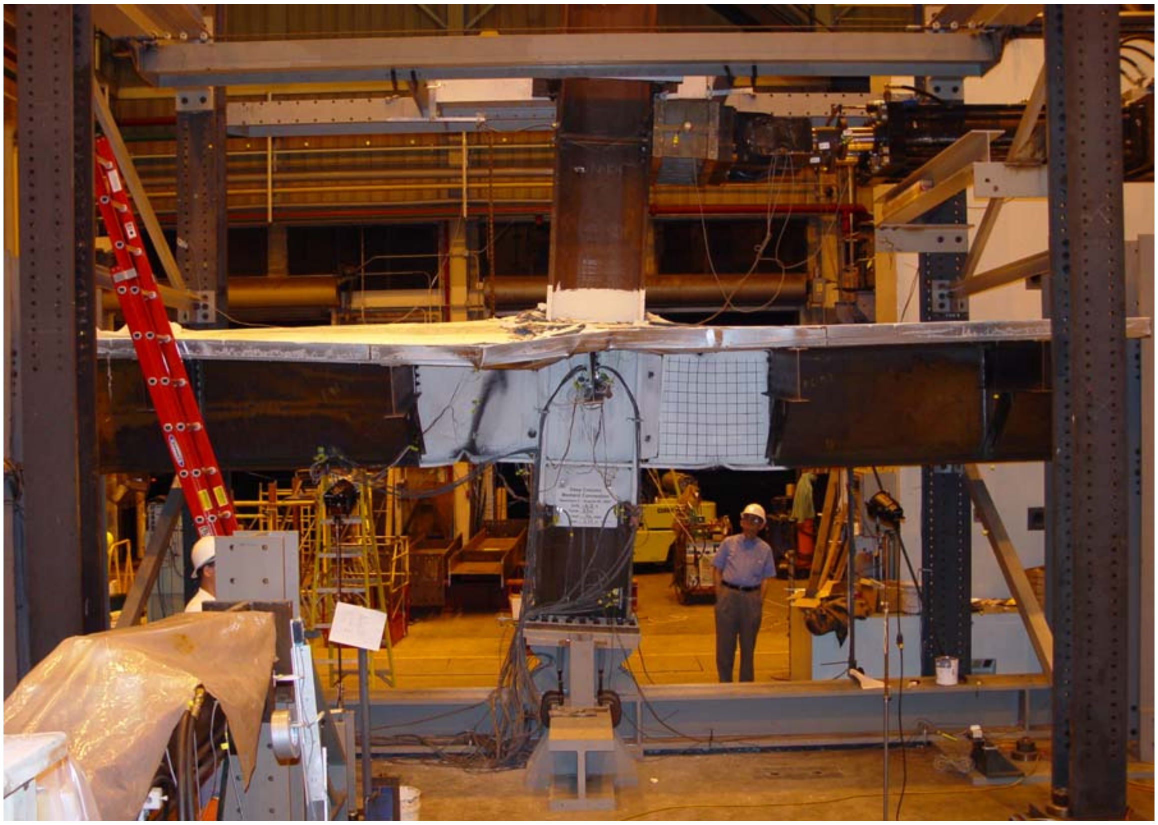

SPEC-3 at 6% story drift

Beam bottom flange lateral movement in RBS, 5% story drift

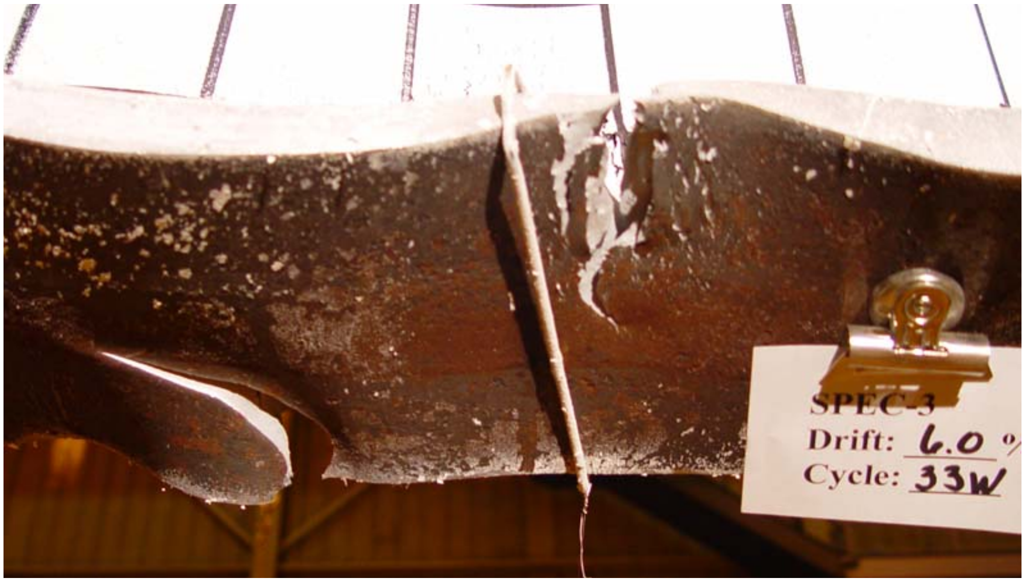

Low cycle fatigue cracking of beam bottom flange, 6% story drift

Deep Column Moment Connection Experimental Study

TEST SUMMARY OF SPEC-4

Specimen ID	SPEC-4
Key Words	Deep column; RBS connection; E70T-6 electrode; modified weld access hole; balanced panel zone; composite floor slab
Test Location	ATLSS Research Center, Lehigh University
Test Date	August 5, 2003
Investigators	James M. Ricles, John W. Fisher, Le-Wu Lu and Xiaofeng Zhang
Main References	FEMA-350, FEMA-353, AISC Seismic Provisions 2002
Sponsors	AISC, PITA

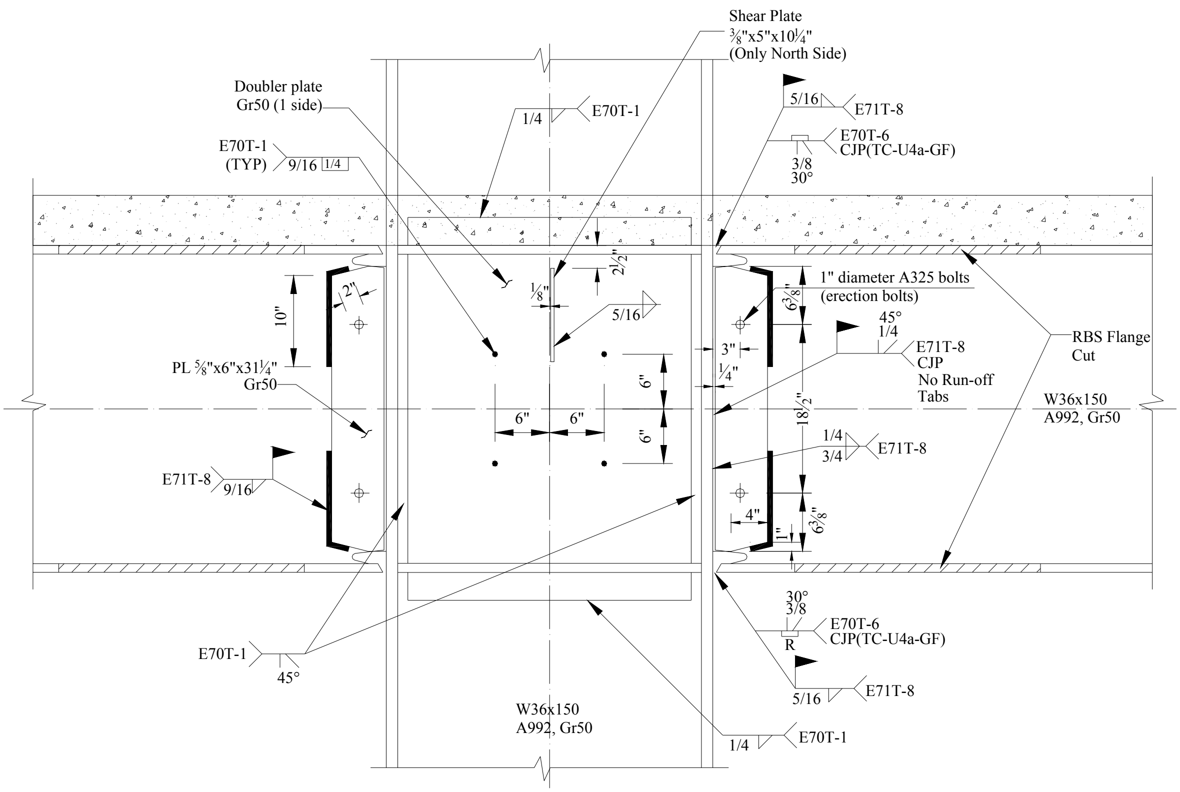

Connection Details

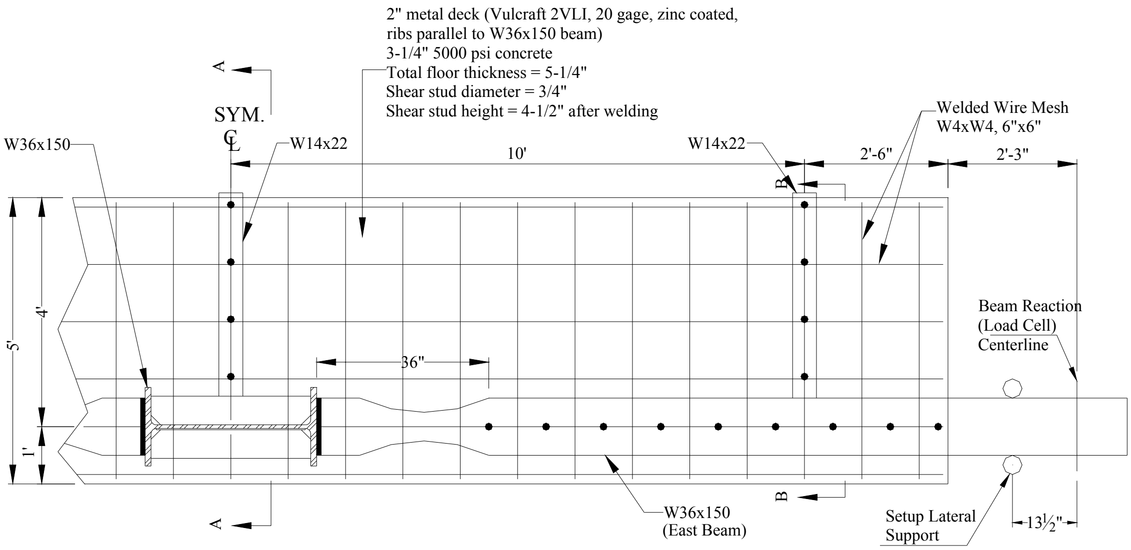

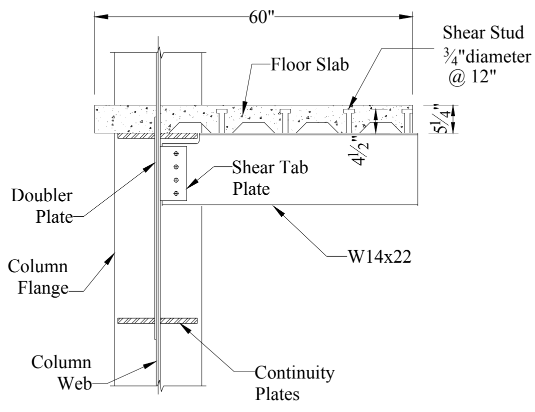

A--A

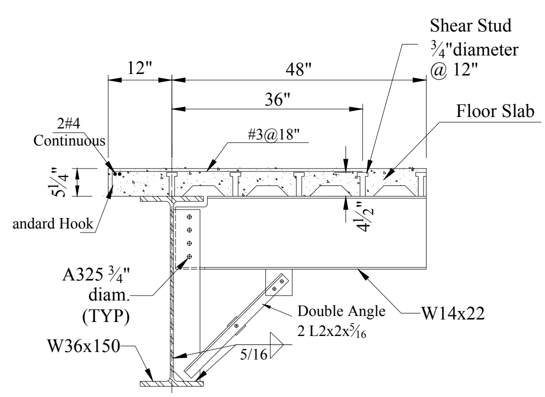

B--B

Floor Slab Details

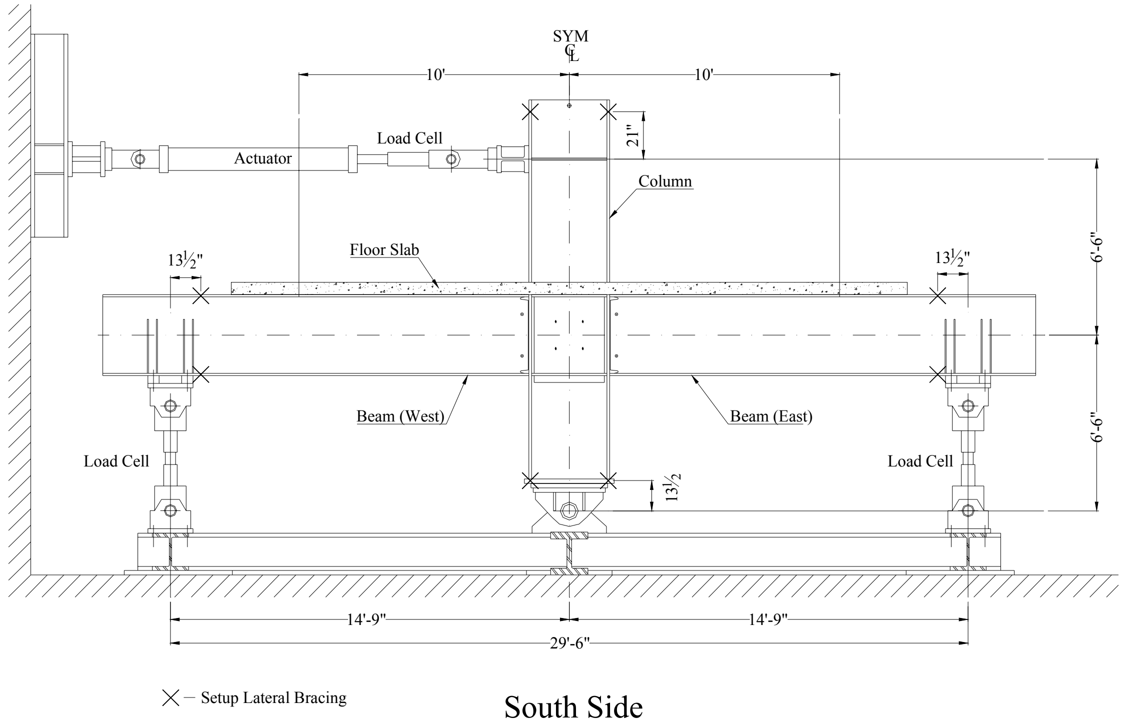

South Side

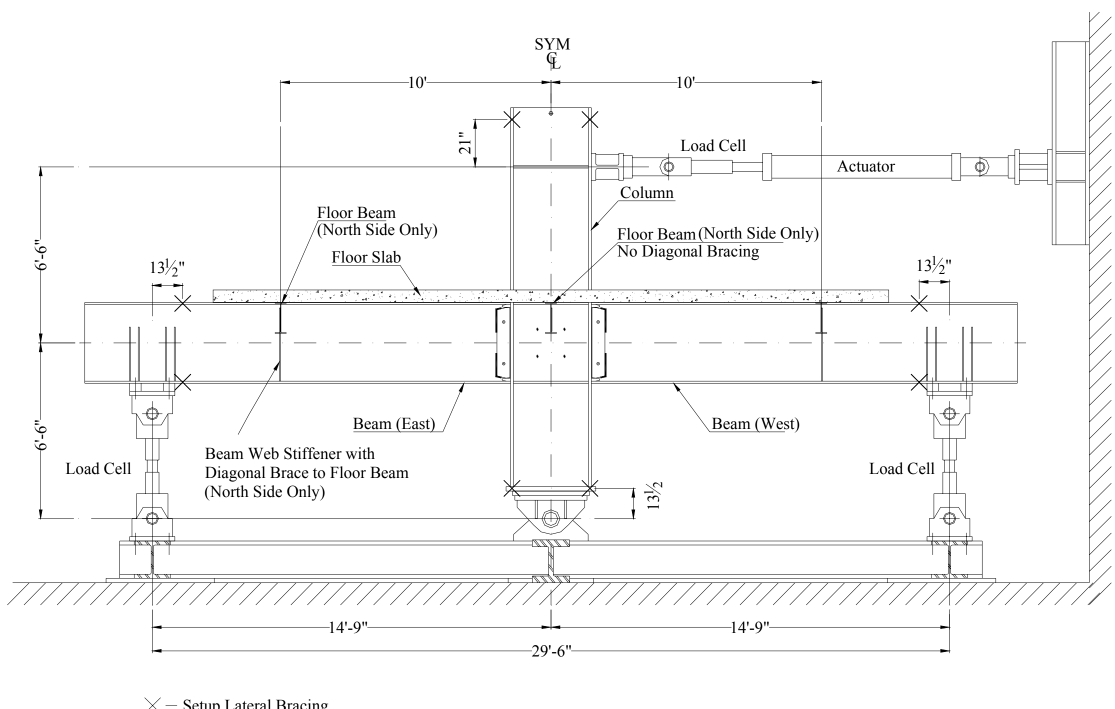

North Side

Test Setup

MATERIAL PROPERTIES AND SPECIMEN DETAILS

Member	Size	Grade	Yield Stress (ksi)		Ultimate Stress (ksi)	
			Mill Cert.	Coupon Test	Mill Cert.	Coupon Test
Beam	W36x150	A992	57.1 Flange 61.2 Web	53.0 Flange 57.4 Web	70.1 Flange 72.7 Web	73.7 Flange 73.4 Web
Column	W36x150	A992	57.1 Flange 61.2 Web	53.0 Flange 57.4 Web	70.1 Flange 72.7 Web	73.7 Flange 73.4 Web
Doubler Plate	⅜"x32⅛" x42"	A572 Gr.50	61.0	64.7	86.0	92.7
Continuity Plate	1"x5½"x34"	A572 Gr.50	63.6	54.4	83.1	80.3
Concrete Slab	5¼" composite slab, with 2" metal deck f_c' = 5,095 psi (28 days); f_c' = 4,660 psi (8 days); tested at 14 days of age					

Welding Procedure Specification	*CJP Groove Weld*: FCAW-SS, 3/32" diameter AWS E70T-6 electrode for beam flange, 0.068" diameter AWS E71T-8 electrode for beam web; Complying with AWS A5.20 Classification and AWS D1.1/D1.1M:2002 Specification. *Fillet weld*: FCAW-SS, 0.068" diameter AWS E71T-8 electrode; Complying with AWS A5.20 Classification and AWS D1.1/D1.1M:2002 Specification.
Shear Tab	Fillet welded to the column flange, serving as a backing bar for beam web CJP groove weld. Supplemental fillet welds are put between shear tab and beam web.
Doubler Plate	One-sided doubler plate. Groove welded to column flanges on both sides and fillet welded to column web on top and bottom. Plug welded to the column web.
Continuity Plate	Full beam flange thickness continuity plates. Single V-bevel groove welded to column flanges and fillet welded to column web/doubler plate.
Composite Floor Slab	Decking: Vulcraft 2VLI, 20 gage, zinc coated, ribs parallel to W36x150 beam; 12 gage side pour stop on the overhang side; 16 gage side and end pour stop on remaining sides; Wire-mesh: W4xW4, 6"x6"
Boundary Condition	Two-sided test with floor slab; no axial force applied to the column; Column was pinned at the bottom and laterally loaded on the top, beam ends were connected to rigid links to simulate roller boundary conditions.
Other Details	The run-off tabs on the beam flanges were removed; no run-off tabs were used for beam web groove weld. Beam top flange backing bar remained and a reinforcing fillet weld was provided between the bottom surface of the backing bar and the column flange using AWS E71T-8 electrode. The bottom beam flange backing bar was removed using the air-arc process, back gouged and reinforced with a fillet weld using AWS E71T-8 electrode.

DISPLACEMENT HISTORY AND KEY EXPERIMENTAL OBSERVATIONS

Applied Displacement History

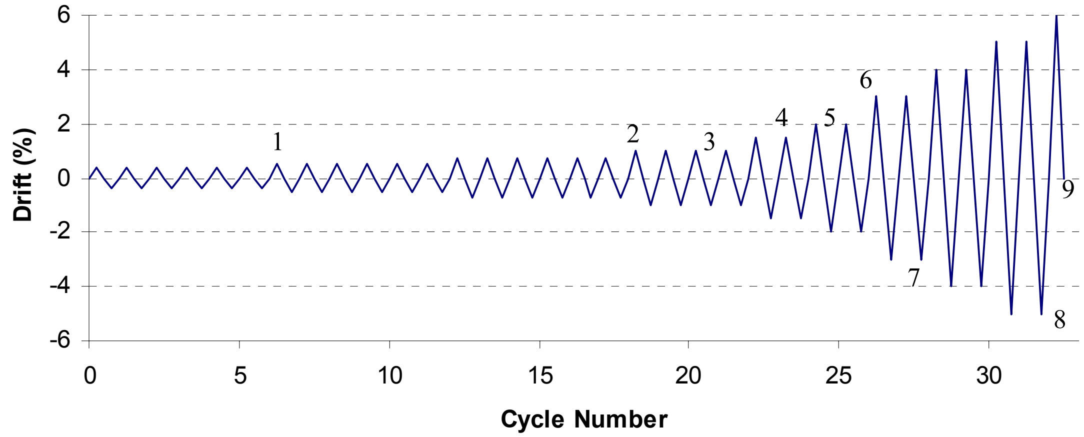

Key Observations during the Test		
	1	Concrete slab cracking.
	2	Yielding in beam flanges at RBS and in panel zone.
	3	Crushing of concrete at column flanges on column face as well as inside column flange region.
	4	Minor yielding in column flange below beam bottom flanges.
	5	Onset of beam web local buckling at RBS.
	6	Onset of beam flange local buckling at RBS. Beam flanges displaced laterally.
	7	Onset of deterioration in specimen capacity
	8	Low cycle fatigue cracks developed in beam bottom flanges at RBS.
	9	Ductile material tearing of the west side beam bottom flange at the RBS, initiating from low cycle fatigue cracks.

TEST RESULTS

			Maximum
Force/Displacement	Peak Actuator Force (kips)		406
	Column Top Displacement (in.)		9.2
	Experimental Yield Displacement (in.)		1.6
Moment	Beam Plastic Moment $\mathbf{M_p}$ (k-in.)	East Beam	32,363
		West Beam	32,522
	$\mathbf{M_f/M_p}$	East Beam	0.92
		West Beam	1.03
Rotation Capacity	Total Plastic Drift (% rad.)		5.3
	Total Rotation across RBS, East Beam (% rad.)		6.8
	Panel Zone Plastic Drift (% rad.)		0.8
	Cumulative Total Plastic Drift (% rad.)		98.0
Energy Dissipation	Cumulative Energy Dissipation (k-in.)		36,621

Note: M_f = Beam moment at column face;
M_p = Beam plastic moment capacity based on measured dimensions and material properties.

TEST OBSERVATIONS

Cracking in the concrete floor slab of SPEC-4 occurred at the end of 0.375% story drift cycles and continued to develop and become more extensive throughout the rest of the test. Yielding initiated in beam bottom flanges at the RBS and near the column face as well as in the panel zone at 0.75% story drift. The floor slab started crushing against the column flanges and inside the column flanges region during the story drift cycles of 1.0%. Minor column flange yielding below the beam bottom flange was observed during the 1.5% story drift cycles. Beam web local buckling occurred in the RBS region during the first cycle of 2% story drift, which became more extensive in subsequent cycles. During the 3% story drift cycles beam flange local buckling occurred. The beam web local buckling became extensive causing beam bottom flange lateral movement in the RBS to occur. The buckling amplitudes grew as the test continued and the specimen capacity deteriorated. Although the beam bottom flanges buckled in compression laterally about 1.5-inches, no noticeable twisting of the column had occurred. Ductile tearing of the west beam bottom flange in the RBS occurred near the end of the first half cycle of 6% story drift which had initiated from low cycle fatigue cracks. More low cycle fatigue cracks were found in the beam bottom flanges at the end of test.

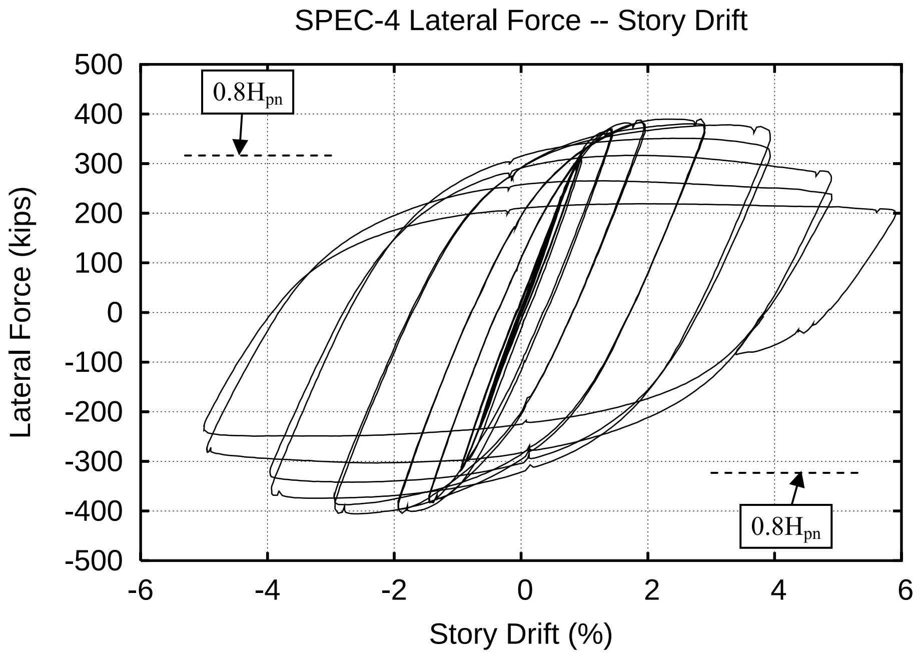
SPEC-4 Lateral Force -- Story Drift
0.8H$_{pn}$
0.8H$_{pn}$
Lateral Force (kips)
Story Drift (%)
500
400
300
200
100
0
-100
-200
-300
-400
-500
-6
-4
-2
0
2
4
6

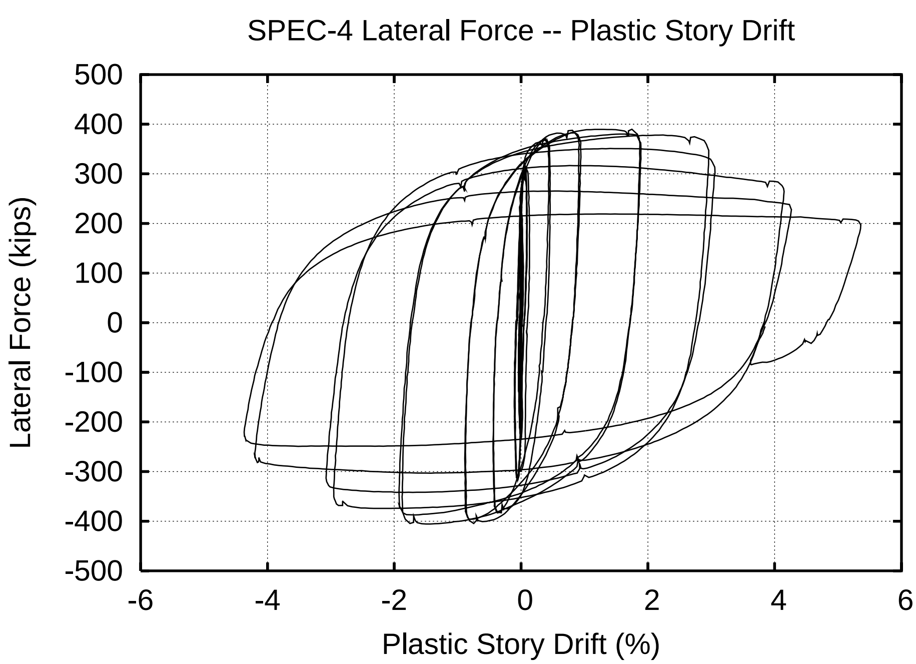
SPEC-4 Lateral Force -- Plastic Story Drift
Lateral Force (kips)
Plastic Story Drift (%)
500
400
300
200
100
0
-100
-200
-300
-400
-500
-6
-4
-2
0
2
4
6

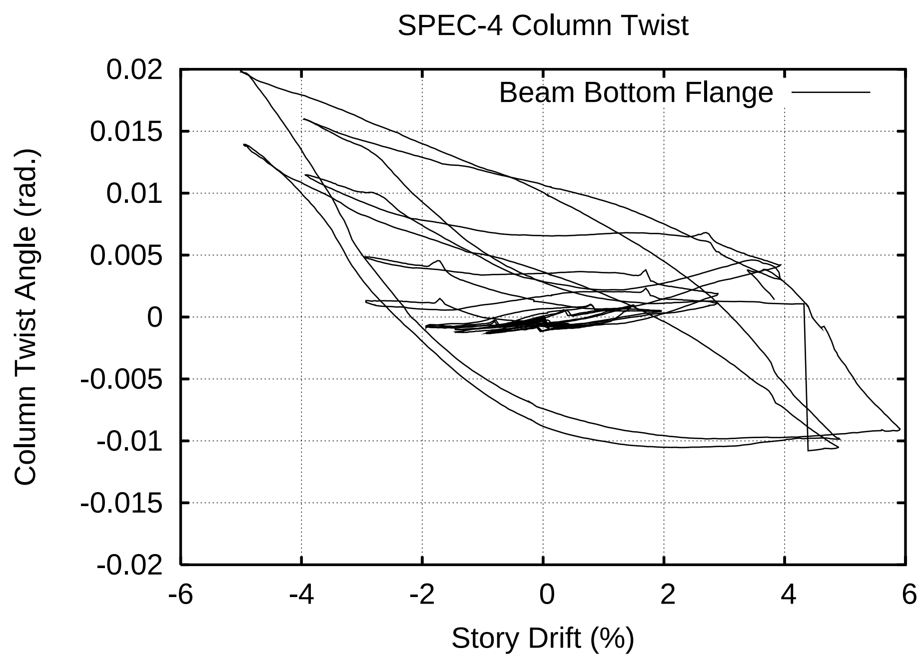
SPEC-4 Column Twist
Beam Bottom Flange
Column Twist Angle (rad.)
0.02
0.015
0.01
0.005
0
-0.005
-0.01
-0.015
-0.02
-6
-4
-2
0
2
4
6
Story Drift (%)

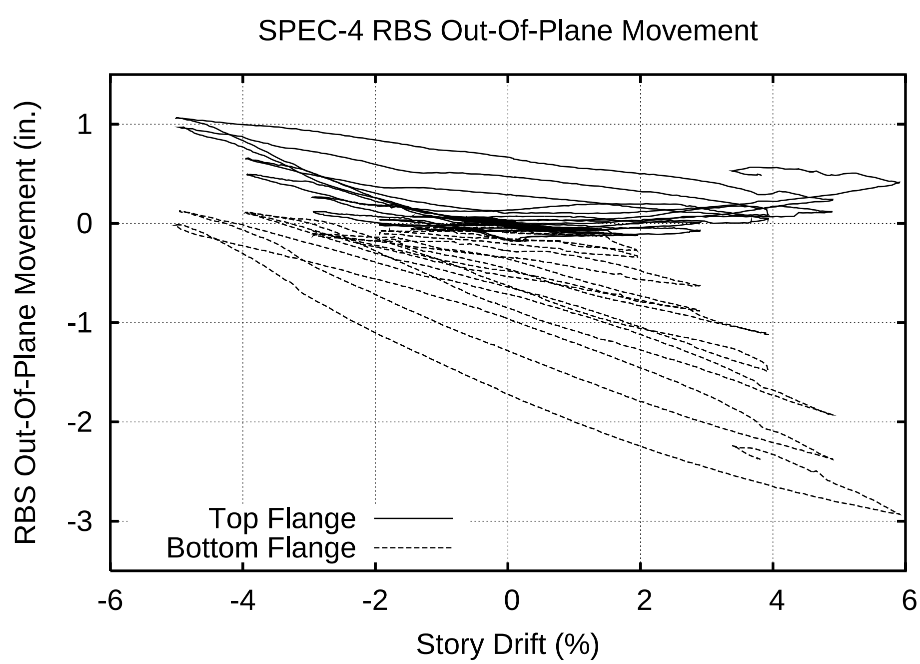
SPEC-4 RBS Out-Of-Plane Movement
RBS Out-Of-Plane Movement (in.)
1
0
-1
-2
-3
Top Flange
Bottom Flange
-6
-4
-2
0
2
4
6
Story Drift (%)

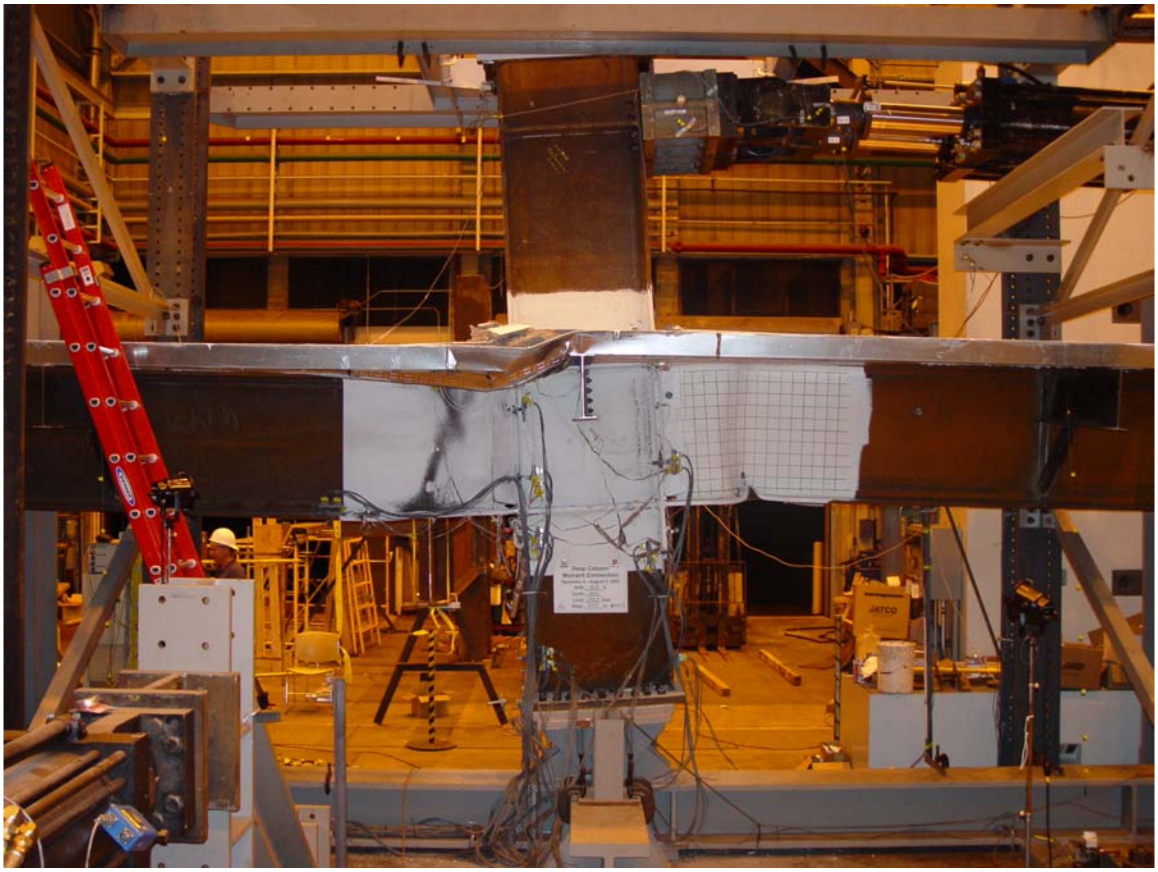

SPEC-4 at 6% story drift

Beam bottom flange lateral movement in RBS, 6% story drift

Low cycle fatigue crack propagation in beam bottom flange of RBS, after test

Low cycle fatigue crack propagation west beam bottom flange, after test

Deep Column Moment Connection Experimental Study

TEST SUMMARY OF SPEC-5

Specimen ID	SPEC-5
Key Words	Deep column; RBS connection; E70T-6 electrode; modified weld access hole; composite floor slab
Test Location	ATLSS Research Center, Lehigh University
Test Date	November 13, 2003
Investigators	James M. Ricles, John W. Fisher and Le-Wu Lu and Xiaofeng Zhang
Main References	FEMA 350, FEMA 353, AISC Seismic Provisions 2002
Sponsors	AISC, PITA

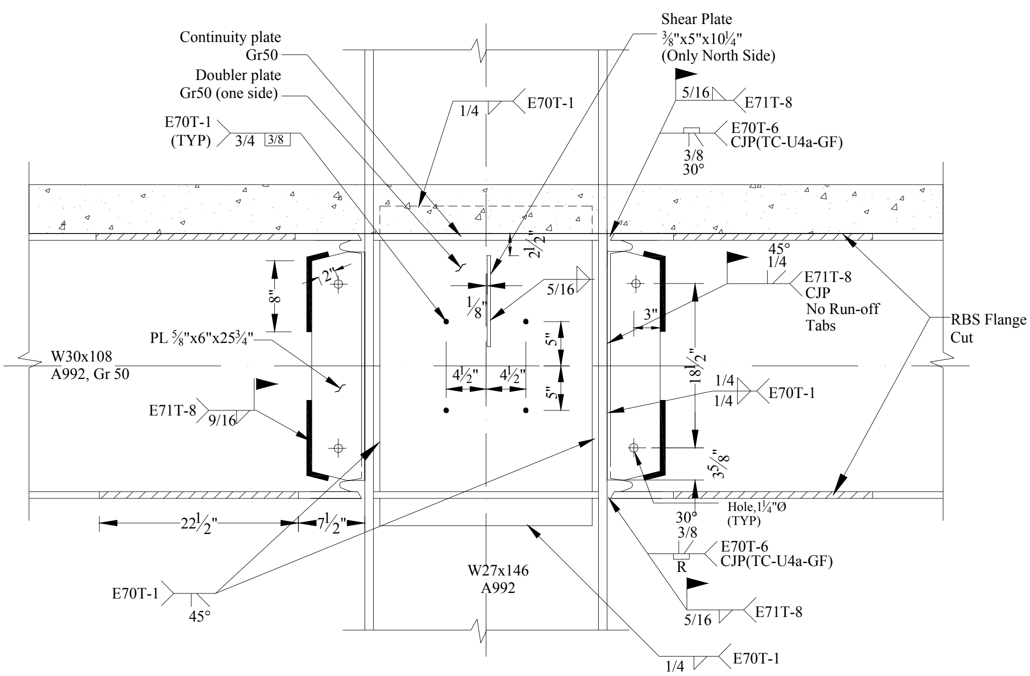

Connection Details

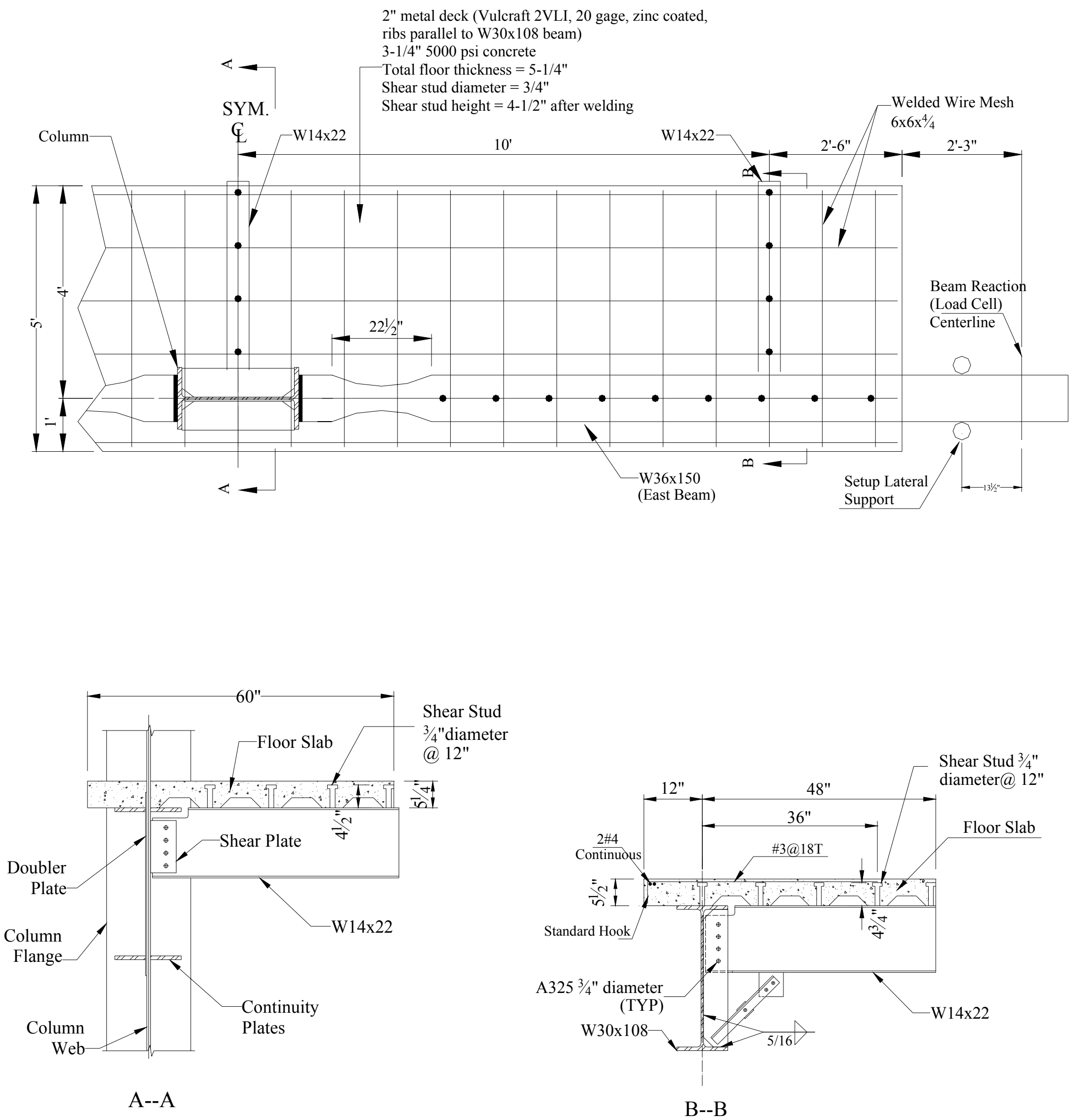

Floor Slab Details

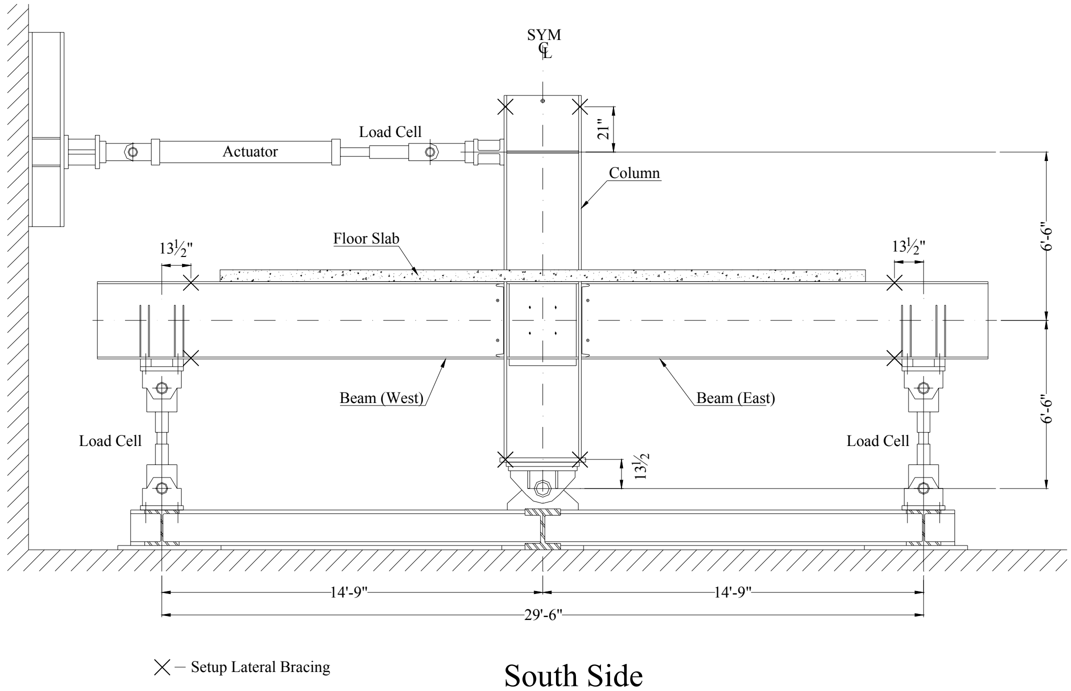

South Side

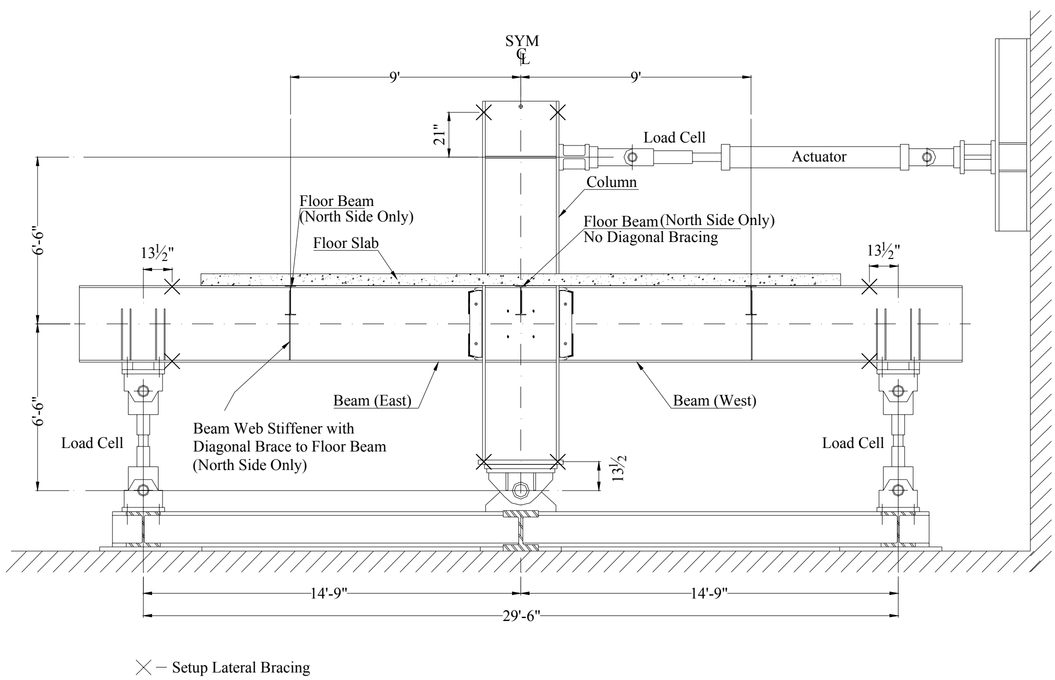

North Side

Test Setup

MATERIAL PROPERTIES AND SPECIMEN DETAILS

Member	Size	Grade	Yield Stress (ksi)		Ultimate Stress (ksi)	
			Mill Cert.	Coupon Test	Mill Cert.	Coupon Test
Beam	W30x108	A992	55.0	49.9 Flange 51.2 Web	70.0	68.3 Flange 68.0 Web
Column	W27x146	A992	57.5	52.7 Flange 57.8 Web	73.0	72.5 Flange 74.4 Web
Doubler Plate	⅜"x24"x36"	A572 Gr.50	N.A.	57.7	N.A.	82.1
Continuity Plate	¾"x6"x25½"	A572 Gr.50	N.A.	53.4	N.A.	78.4
Concrete Slab	5¼" composite slab, with 2" metal deck f_c' = 5,593 psi (28 days); tested at 30 days of age					
Welding Procedure Specification	*CJP Groove Weld*: FCAW-SS, 3/32" diameter AWS E70T-6 electrode for beam flange, 0.068" diameter AWS E71T-8 electrode for beam web; Complying with AWS A5.20 Classification and AWS D1.1/D1.1M:2002 Specification. *Fillet weld*: FCAW-SS, 0.068" diameter AWS E71T-8 electrode; Complying with AWS A5.20 Classification and AWS D1.1/D1.1M:2002 Specification.					
Shear Tab	Fillet welded to the column flange, serving as a backing bar for the beam web CJP groove weld. Supplemental fillet welds are placed between the shear tab and beam web.					
Doubler Plate	One-sided doubler plate. Groove welded to column flanges on both sides and fillet welded to column web on top and bottom. Plug welded to the column web.					
Continuity Plate	Full beam flange thickness continuity plates. Single V-bevel groove welded to column flanges and fillet welded to column web/doubler plate.					
Composite Floor Slab	Decking: Vulcraft 2VLI, 20 gage, zinc coated, ribs parallel to W36x150 beam; 12 gage side pour stop on the overhang side; 16 gage side and end pour stop on remaining sides; Wire-mesh: W4xW4, 6"x6"					
Boundary Condition	Two-sided test with floor slab; no axial force applied to the column; Column was pinned at the bottom and laterally loaded on the top, beam ends were connected to rigid links to simulate roller boundary conditions.					
Other Details	The run-off tabs on the beam flanges were removed; no run-off tabs were used for beam web groove weld. Beam top flange backing bar remained and a reinforcing fillet weld was provided between the bottom surface of the backing bar and the column flange using an AWS E71T-8 electrode. The bottom beam flange backing bar was removed using the air-arc process, back gouged and reinforced with a fillet weld using AWS E71T-8 electrode.					

DISPLACEMENT HISTORY AND KEY EXPERIMENTAL OBSERVATIONS

Applied Displacement History

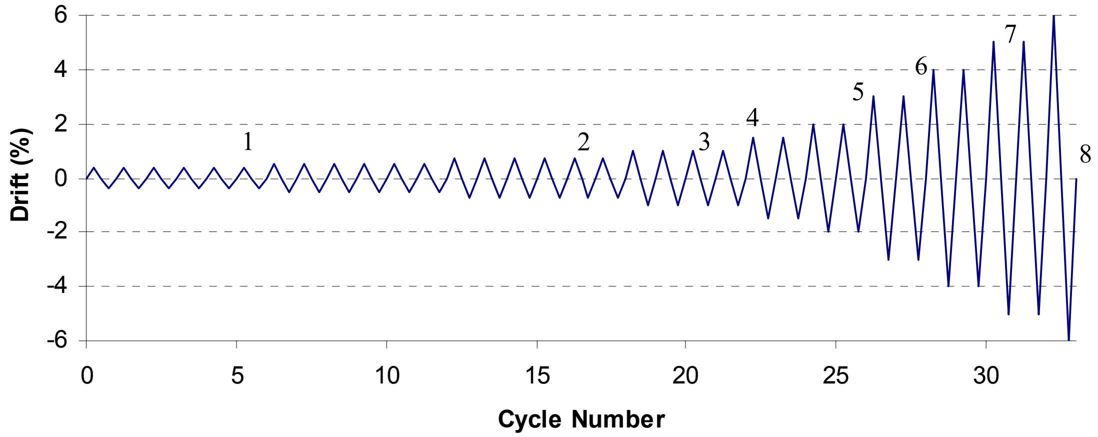

Key Observations during the Test	
1	Concrete slab cracking around column.
2	Yielding in beam bottom flanges at RBS and in panel zone.
3	Yielding in beam top flanges and web at RBS.
4	Crushing of concrete at column flanges on column face as well as inside column flange region.
5	Onset of beam web local buckling at RBS. Maximum specimen capacity achieved.
6	Onset of beam flange local buckling at RBS. Beam flange laterally displaced. Panel zone locally buckled in between plug welds..
7	Low cycle fatigue cracks developed in beam bottom flanges at RBS.
8	Fracture of the east side beam bottom flange at RBS occurred at the beginning of second 6% cycle, which initiated from low cycle fatigue cracks.

TEST RESULTS

			Maximum
Force/Displacement	Peak Actuator Force (kips)		258
	Column Top Displacement (in.)		9.38
	Experimental Yield Displacement (in.)		1.56
Moment	Beam Plastic Moment $\mathbf{M_p}$ (k-in.)	East Beam	16,950
		West Beam	16,997
	$\mathbf{M_f/M_p}$	East Beam	1.21
		West Beam	1.19
Rotation Capacity	Total Plastic Drift (% rad.)		5.1
	Total Rotation across RBS, East Beam (% rad.)		5.6
	Panel Zone Plastic Drift (% rad.)		1.2
	Cumulative Total Plastic Drift (% rad.)		107
Energy Dissipation	Cumulative Energy Dissipation (k-in.)		28,230

Note: M_f = Beam moment at column face;
M_p = Beam plastic moment capacity based on measured dimensions and material properties.

TEST OBSERVATIONS

Cracking in the concrete floor slab of SPEC-5 occurred at the end of the 0.375% story drift cycles, which continued to develop and become more extensive throughout the test. Yielding initiated in the beam bottom flanges at the RBS and near the column face and in the panel zone at 0.75% story drift. Yielding was observed in the beam top flanges and the web at the RBS at 1% story drift. The concrete slab also started crushing against the column flanges and inside the column flanges region at the 1.5% story drift cycles. Beam web local buckling occurred in the RBS region during the first cycle of 3% story drift, which became more extensive in subsequent cycles. The maximum lateral load was reached during the first cycle of 3% story drift. During the first cycle of 4% story drift, beam flange local buckling occurred. The panel zone doubler plate buckled at 4% story drift cycles. The beam web local buckling became extensive, causing the beam bottom flange to develop lateral movement. The specimen capacity then began to deteriorate. The buckling amplitudes grew as the test continued beyond 4% story drift. At 4% story drift the beam bottom flanges in compression had moved laterally about 1 inch in the RBS. Very little column twisting was observed. Low cycle fatigue cracks were found to initiate during the 5% story drift cycles. SPEC-5 successfully underwent the full first cycle of 6% story drift. Fracture of the east beam bottom flange at the RBS occurred at the beginning of the second cycle of 6% story drift. Several low cycle fatigue cracks were found in the beam bottom flanges at the end of the test.

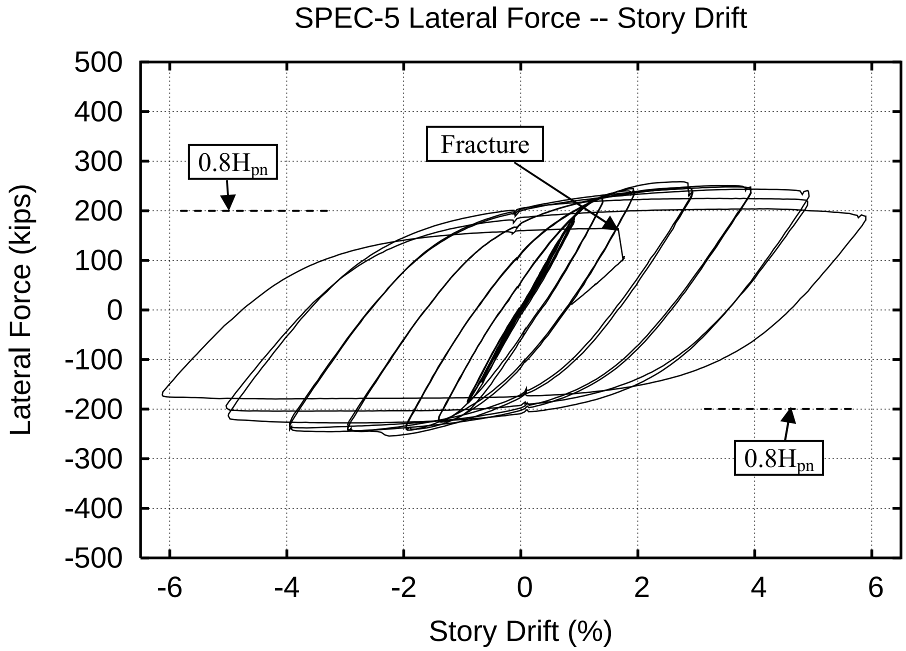
SPEC-5 Lateral Force -- Story Drift
Fracture
0.8H$_{pn}$
0.8H$_{pn}$
Lateral Force (kips)
Story Drift (%)
500
400
300
200
100
0
-100
-200
-300
-400
-500
-6
-4
-2
0
2
4
6

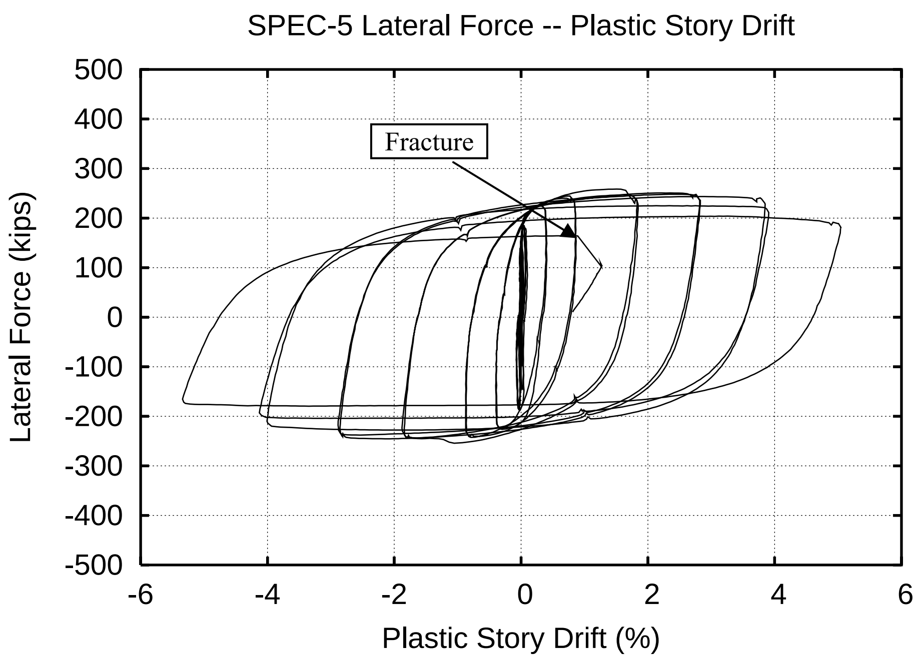
SPEC-5 Lateral Force -- Plastic Story Drift
Fracture
Lateral Force (kips)
Plastic Story Drift (%)
500
400
300
200
100
0
-100
-200
-300
-400
-500
-6
-4
-2
0
2
4
6

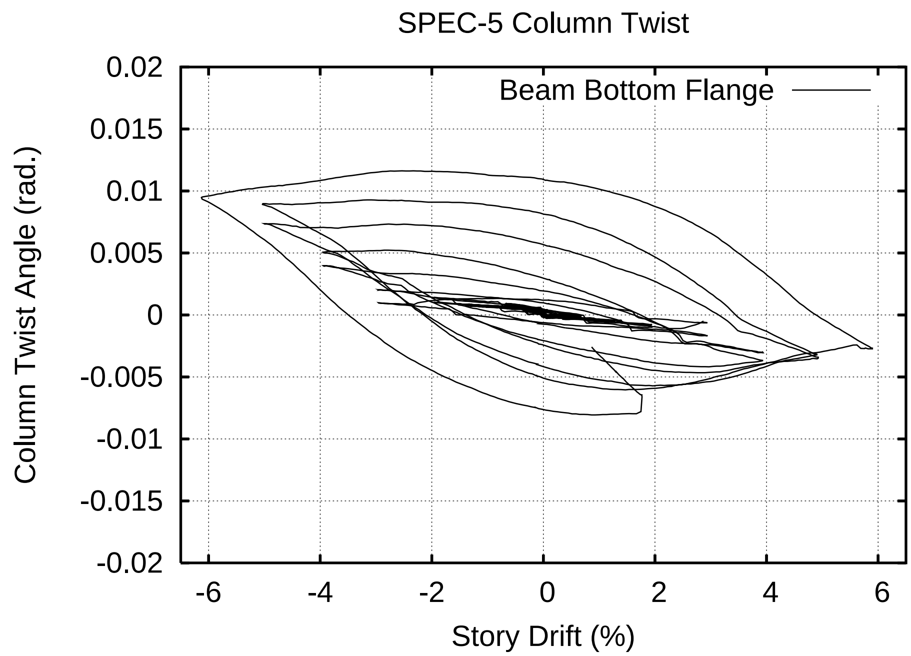
SPEC-5 Column Twist
Beam Bottom Flange
Column Twist Angle (rad.)
0.02
0.015
0.01
0.005
0
-0.005
-0.01
-0.015
-0.02
-6
-4
-2
0
2
4
6
Story Drift (%)

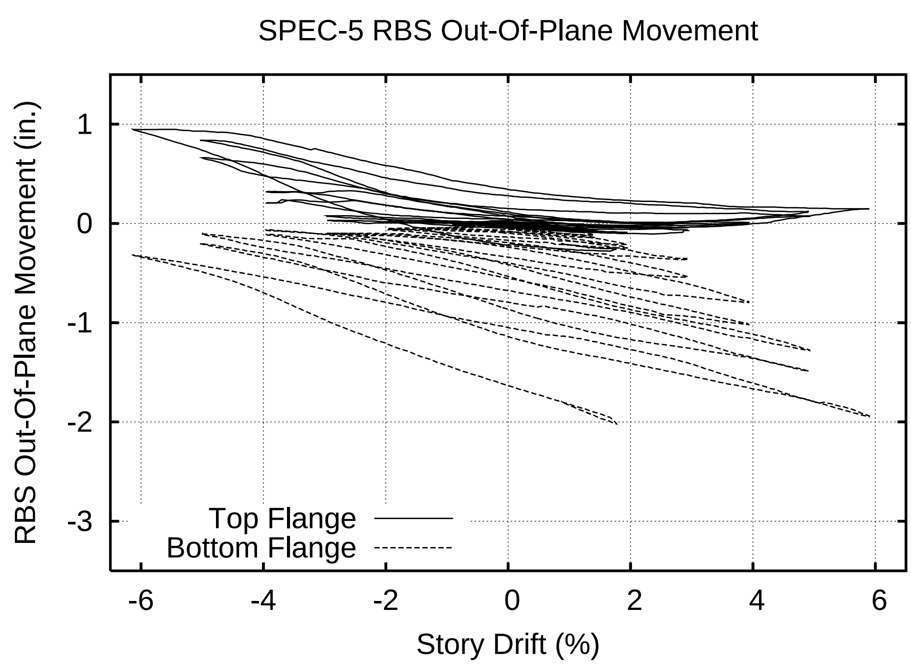
SPEC-5 RBS Out-Of-Plane Movement
RBS Out-Of-Plane Movement (in.)
1
0
-1
-2
-3
Top Flange
Bottom Flange
-6
-4
-2
0
2
4
6
Story Drift (%)

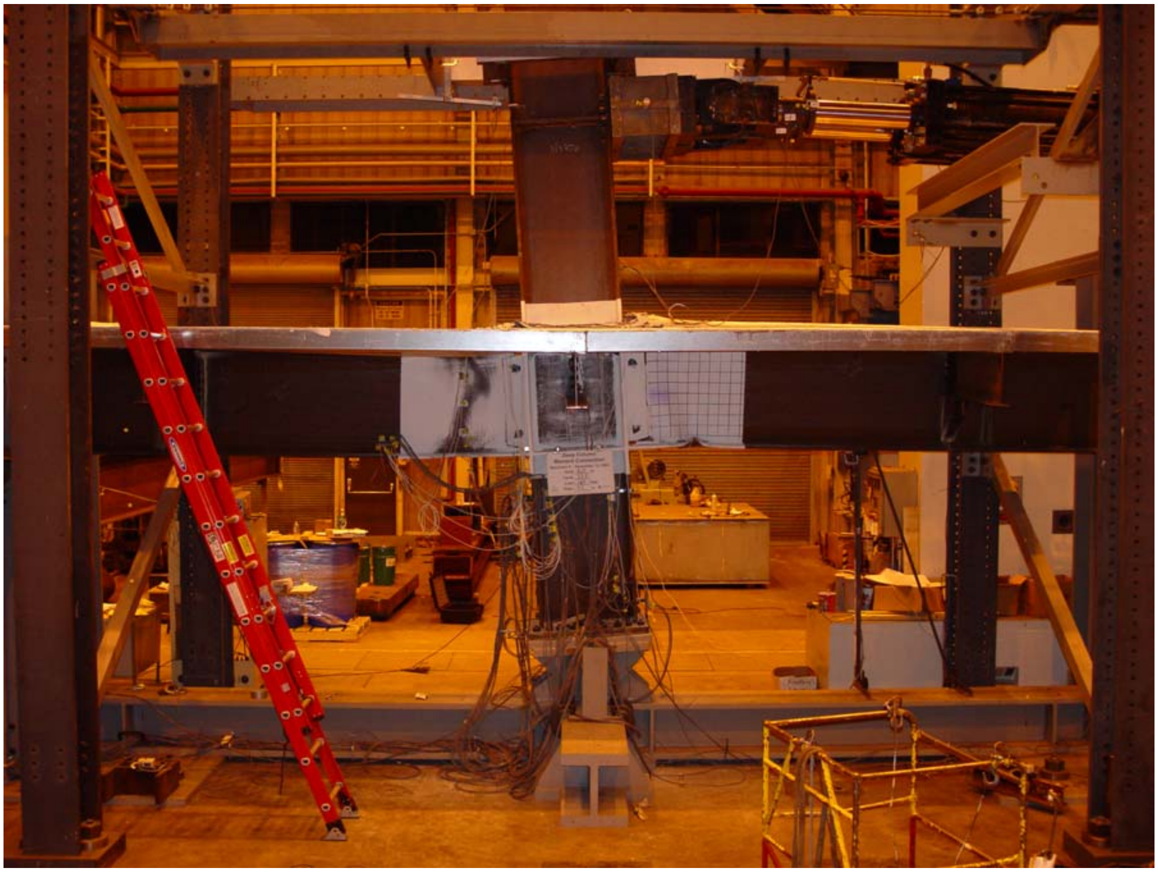

SPEC-5 at 6% story drift

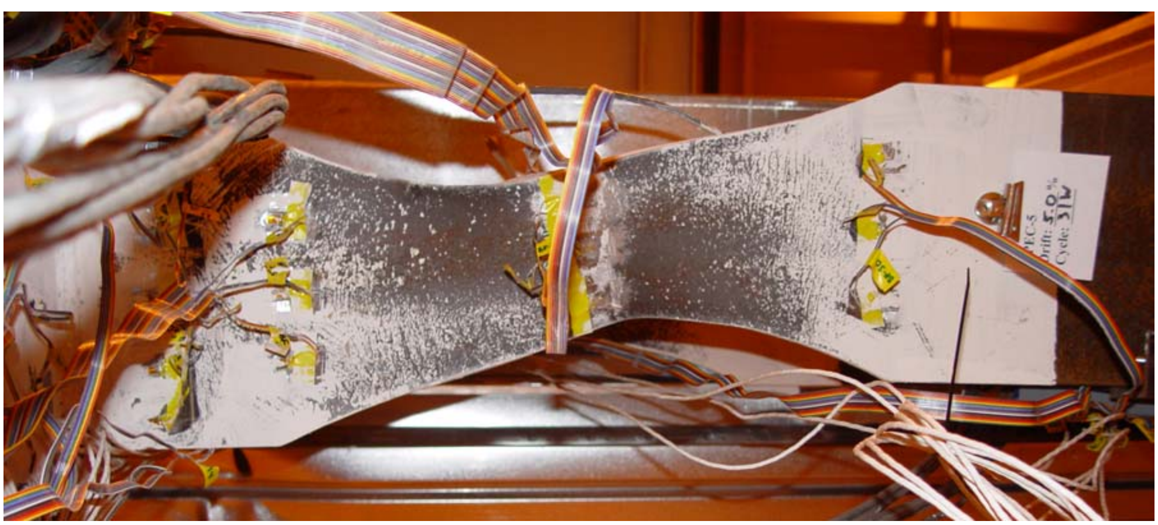

Beam bottom flange lateral movement in RBS, 5% story drift

East beam bottom flange fracture, after achieving 6% story drift

Deep Column Moment Connection Experimental Study

TEST SUMMARY OF SPEC-6

Specimen ID	SPEC-6
Key Words	Deep column; RBS connection; E70T-6 electrode; modified weld access hole; supplemental lateral bracing
Test Location	ATLSS Research Center, Lehigh University
Test Date	December 30, 2003
Investigators	James M. Ricles, John W. Fisher and Le-Wu Lu and Xiaofeng Zhang
Main References	FEMA 350, FEMA 353, AISC Seismic Provisions 2002
Sponsors	AISC, PITA

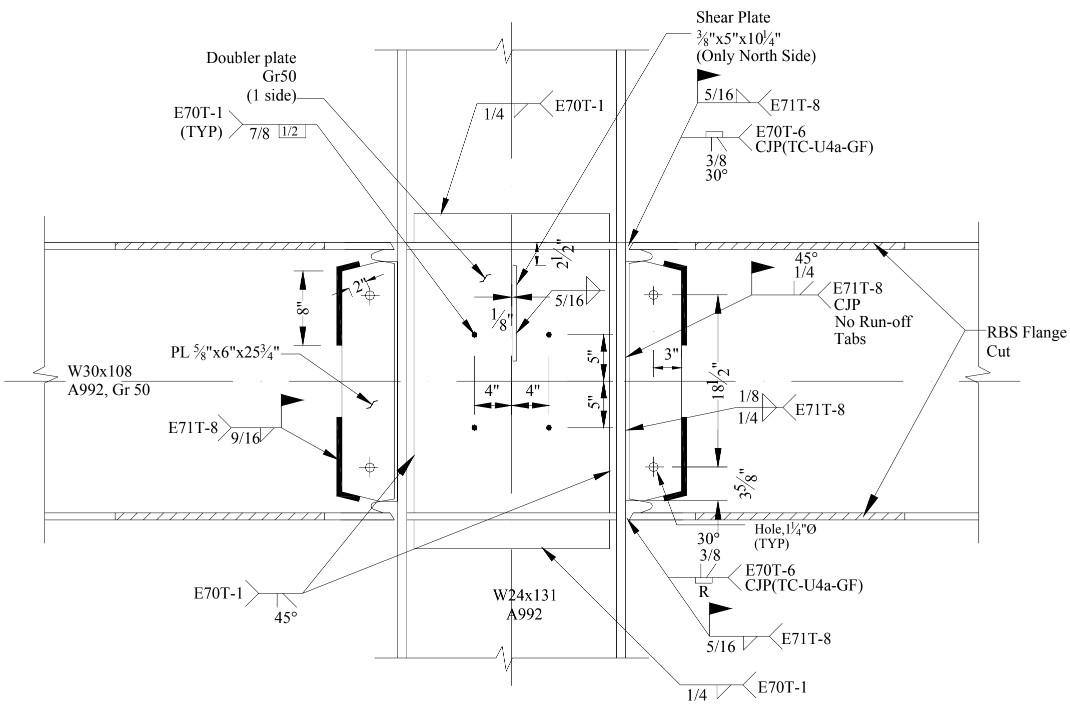

Connection Details

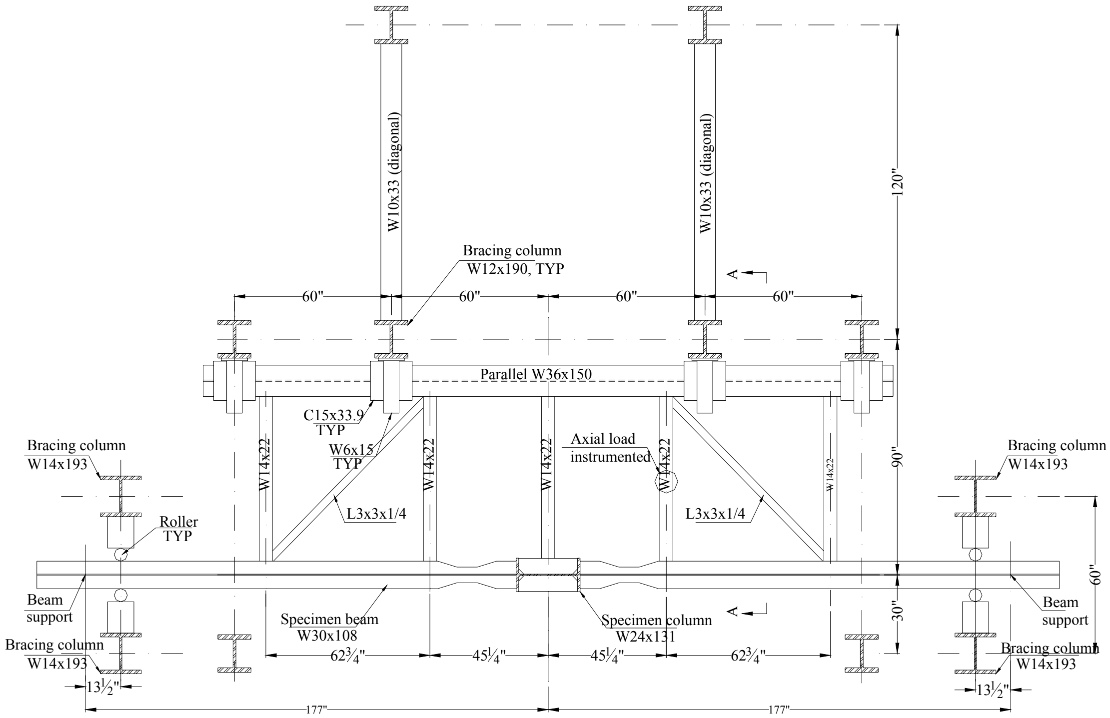

Bracing plan

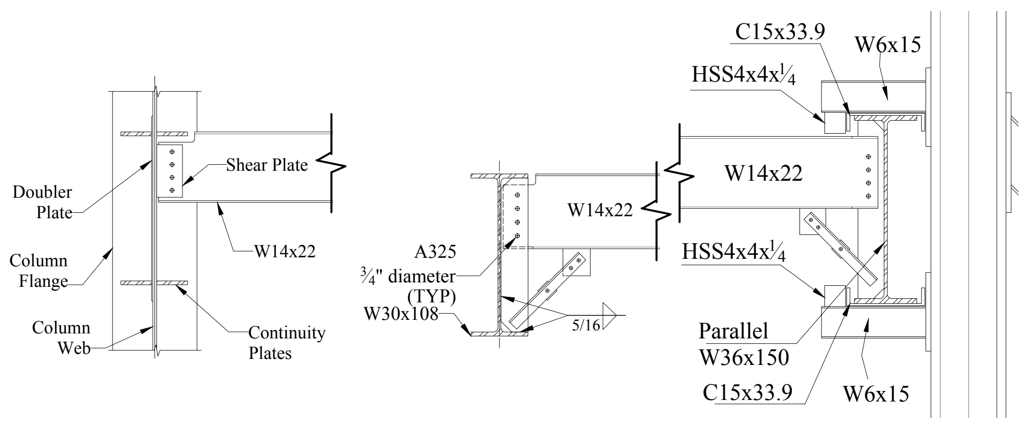

Bracing beam details

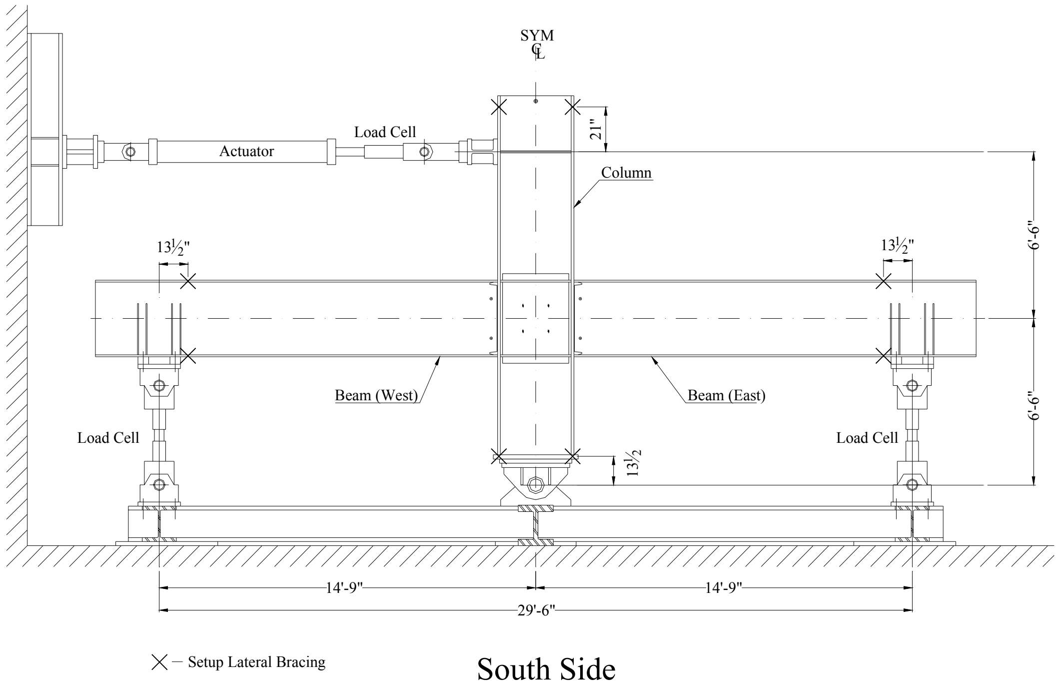

South Side

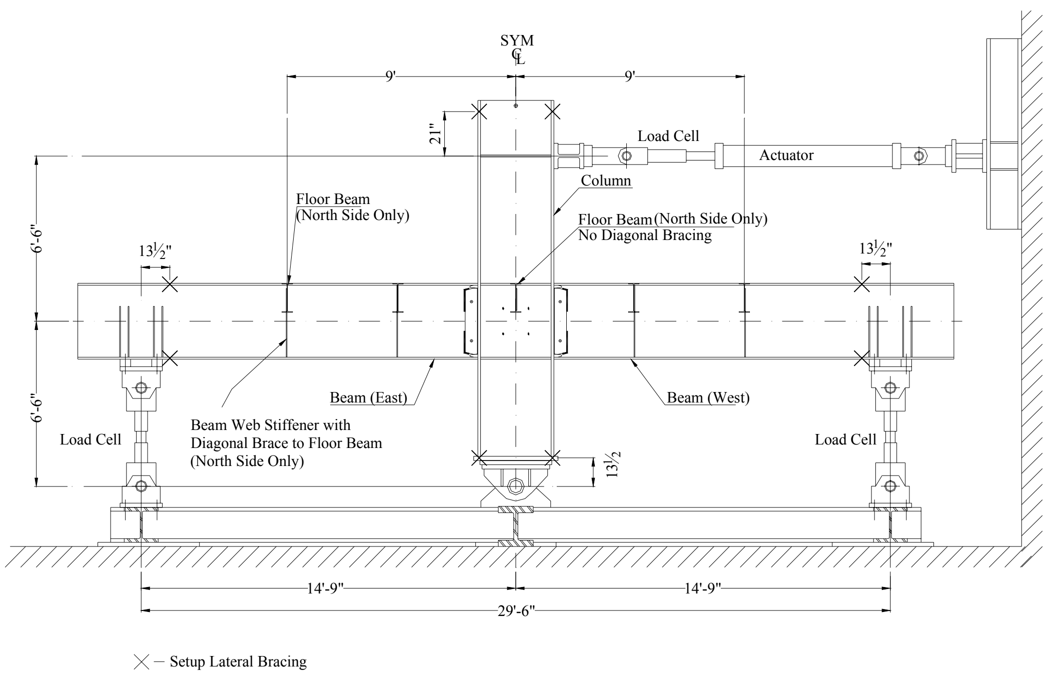

North Side

Test Setup

MATERIAL PROPERTIES AND SPECIMEN DETAILS

Member	Size	Grade	Yield Stress (ksi)		Ultimate Stress (ksi)	
			Mill Cert.	Coupon Test	Mill Cert.	Coupon Test
Beam	W30x108	A992	55.0	49.9 Flange 51.2 Web	70.0	68.3 Flange 68.0 Web
Column	W24x131	A992	56.5	48.5 Flange 52.1 Web	72.5	72.3 Flange 71.5 Web
Doubler Plate	½"x24"x36"	A572 Gr.50	N.A.	46.7	N.A.	73.1
Continuity Plate	¾"x6"x25½"	A572 Gr.50	N.A.	53.4	N.A.	78.4
Concrete Slab	None					

Welding Procedure Specification	*CJP Groove Weld*: FCAW-SS, 3/32" diameter AWS E70T-6 electrode for beam flange, 0.068" diameter AWS E71T-8 electrode for beam web; Complying with AWS A5.20 Classification and AWS D1.1/D1.1M:2002 Specification. *Fillet weld*: FCAW-SS, 0.068" diameter AWS E71T-8 electrode; Complying with AWS A5.20 Classification and AWS D1.1/D1.1M:2002 Specification.
Shear Tab	Fillet welded to the column flange, serving as a backing bar for the beam web CJP groove weld. Supplemental fillet welds are placed between the shear tab and beam web.
Doubler Plate	One-sided doubler plate. Groove welded to column flanges on both sides and fillet welded to column web on top and bottom. Plug welded to the column web
Continuity Plate	Full beam flange thickness continuity plates. Single V-bevel groove welded to column flanges and fillet welded to column web/doubler plate.
Composite Floor Slab	None.
Boundary Condition	Two-sided connection; no axial force applied to the column; Column was pinned at the bottom and laterally loaded on the top, beam ends were connected to rigid links to simulate roller boundary conditions.
Other Details	The run-off tabs on the beam flanges were removed; no run-off tabs were used for beam web groove weld. Beam top flange backing bar remained and a reinforcing fillet weld was provided between the bottom surface of the backing bar and the column flange using an AWS E71T-8 electrode. The bottom beam flange backing bar was removed using the air-arc process, back gouged and reinforced with a fillet weld using AWS E71T-8 electrode.

DISPLACEMENT HISTORY AND KEY EXPERIMENTAL OBSERVATIONS

Applied Displacement History

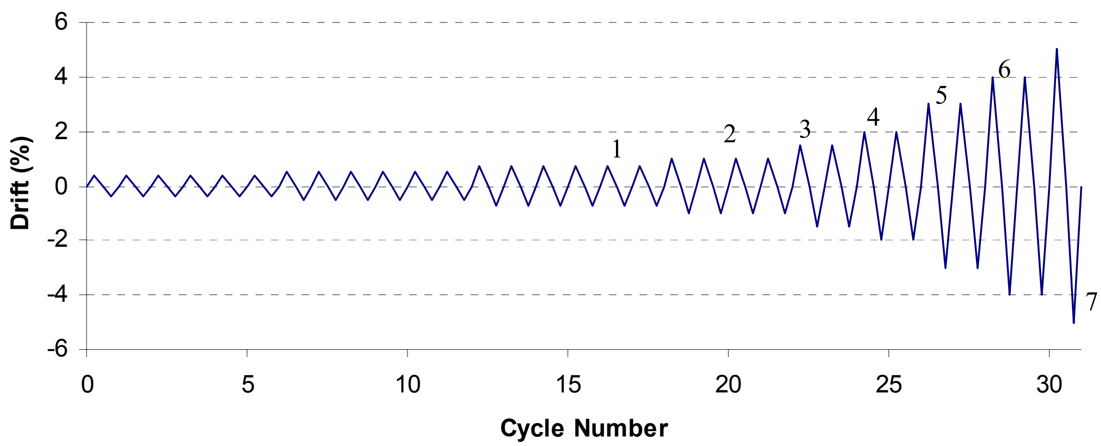

Key Observations during the Test		
	1	Yielding in beam flanges at RBS and in the panel zone.
	2	Yielding in beam web at RBS.
	3	Yielding in the beam flanges spread throughout the RBS and regions between the RBS and column face. Yielding around the safety harness eyebolt hole.
	4	Minor yielding in the column flanges.
	5	Minor yielding in the column web above and below the panel zone. Small magnitude of beam web local buckling was observed.
	6	Minor yielding in the continuity plates. Crack was observed at the root of the beam bottom flange reinforcement fillet welds. Onset of yielding of weld metal of the beam web CJP welds.
	7	Fracture in the west side beam bottom flange HAZ.

TEST RESULTS

			Maximum
Force/Displacement	Peak Actuator Force (kips)		240
	Column Top Displacement (in.)		7.78
	Experimental Yield Displacement (in.)		1.56
Moment	Beam Plastic Moment $\mathbf{M_p}$ (k-in.)	East Beam	17,001
		West Beam	16,948
	$\mathbf{M_f/M_p}$	East Beam	1.01
		West Beam	1.03
Rotation Capacity	Total Plastic Drift (% rad.)		4.0
	Total Rotation across RBS, East Beam (% rad.)		1.4
	Panel Zone Plastic Drift (% rad.)		2.3
	Cumulative Total Plastic Drift (% rad.)		60.7
Energy Dissipation	Cumulative Energy Dissipation (k-in.)		16,232

Note: M_f = Beam moment at column face;
M_p = Beam plastic moment capacity based on measured dimensions and material properties.

TEST OBSERVATIONS

Minor yielding initiated in the beam flanges at the RBS and in the panel zone at 0.75% story drift. Yielding was observed in the beam web at the RBS at 1% story drift. Yielding in the beam flanges spread throughout the RBS and in the beam region between the RBS and column flange at 1.5% story drift. The panel zone yielding became more pronounced. Yielding around the safety harness eyebolt hole was observed at 1.5% story drift. The column flanges started to yield at the 2% story drift cycles. Yielding occurred in the column web above and below continuity plates at 3% story drift cycles. Minor beam web local buckling occurred in the RBS region during the first cycle of 3% story drift, and remained small in the 4% story drift cycles. The lateral load kept increasing when story drift increased as the panel zone continued to yield and develop significant shear deformation. No visible beam flange buckling was observed and neither was the beam flange lateral movement. Very little column twisting was observed. Cracks were found to initiate at the root of the beam bottom flange reinforcement fillet welds during the 4% story drift cycles. Yielding in the weld metal and in the HAZ at the bottom and top ends of beam web CJP groove welds was observed during 4% story drift cycles. SPEC-6 successfully underwent the first half cycle of 5% story drift. Fracture in the HAZ of west beam bottom flange occurred when the specimen tried to complete the first 5% story drift cycle. The specimen capacity did not deteriorate prior to fracture.

After releasing the support and the bracing of the fractured west side beam, the testing of SPEC-6 was continued for the remaining loading cycles of 5% and 6% story drift. Releasing the west side beam made the panel zone stronger relative to the beam capacity. The east side beam started to develop pronounced web and flange local buckling in the 5% drift cycles. Fracture occurred in the beam top flange near the center of RBS and went through the width of the flange and penetrated to the web. This fracture was due to low cycle fatigue and similar to the other specimens.

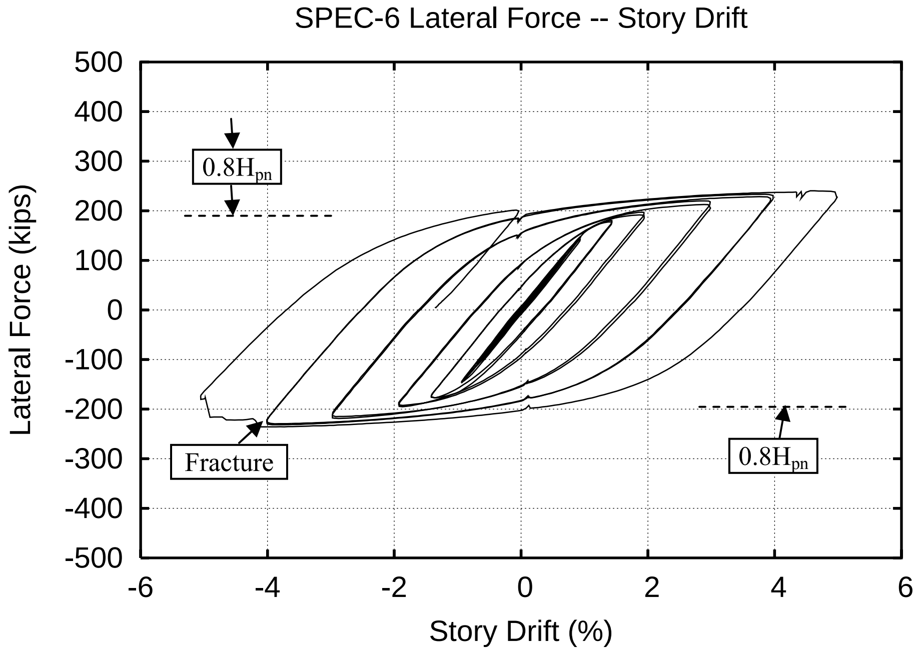
SPEC-6 Lateral Force -- Story Drift
Lateral Force (kips)
Story Drift (%)
0.8H_{pn}
Fracture
0.8H_{pn}
500
400
300
200
100
0
-100
-200
-300
-400
-500
-6
-4
-2
0
2
4
6

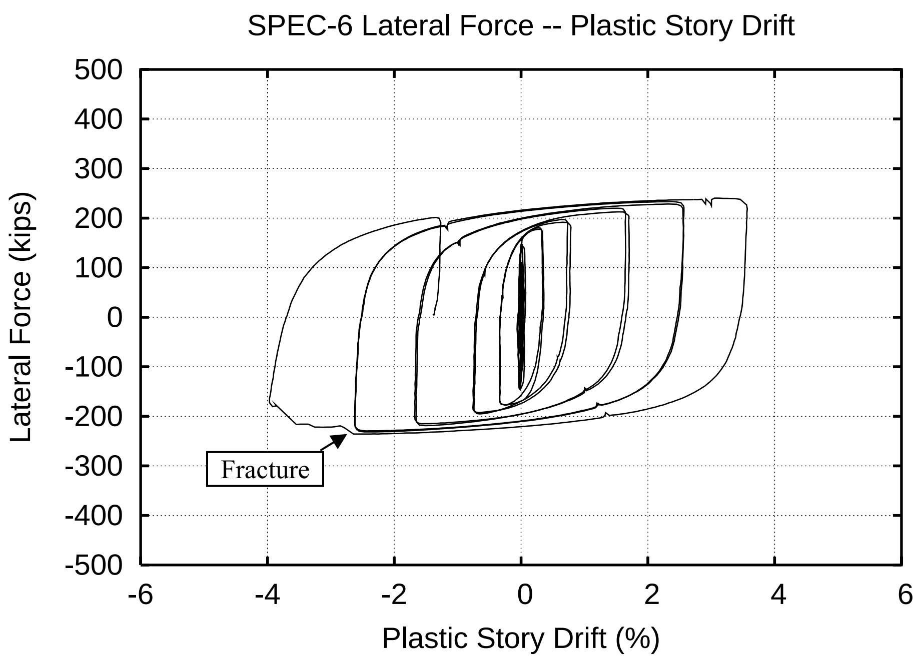
SPEC-6 Lateral Force -- Plastic Story Drift
Lateral Force (kips)
Plastic Story Drift (%)
Fracture
500
400
300
200
100
0
-100
-200
-300
-400
-500
-6
-4
-2
0
2
4
6

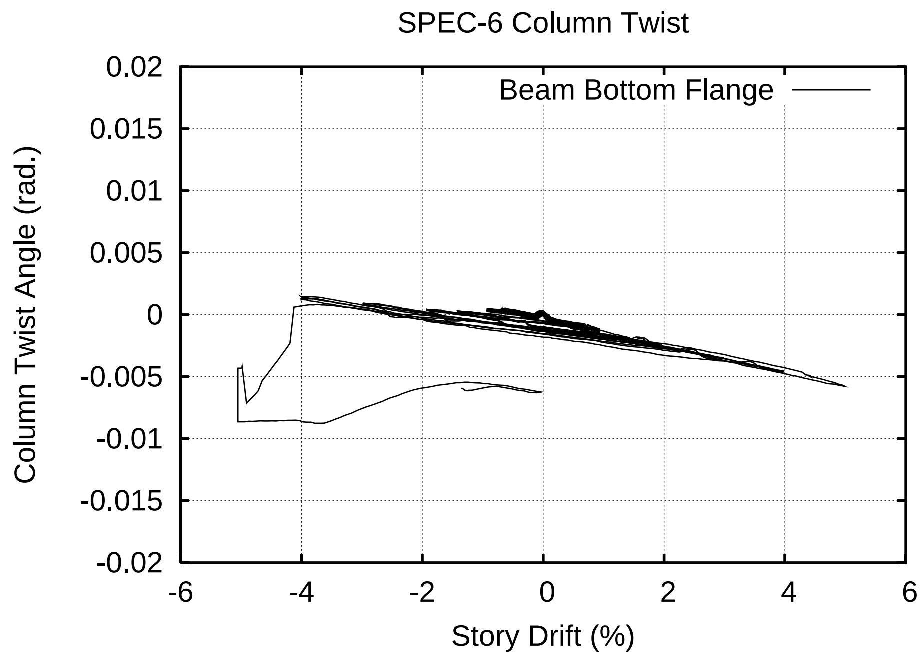
SPEC-6 Column Twist
Beam Bottom Flange
Column Twist Angle (rad.)
0.02
0.015
0.01
0.005
0
-0.005
-0.01
-0.015
-0.02
-6
-4
-2
0
2
4
6
Story Drift (%)

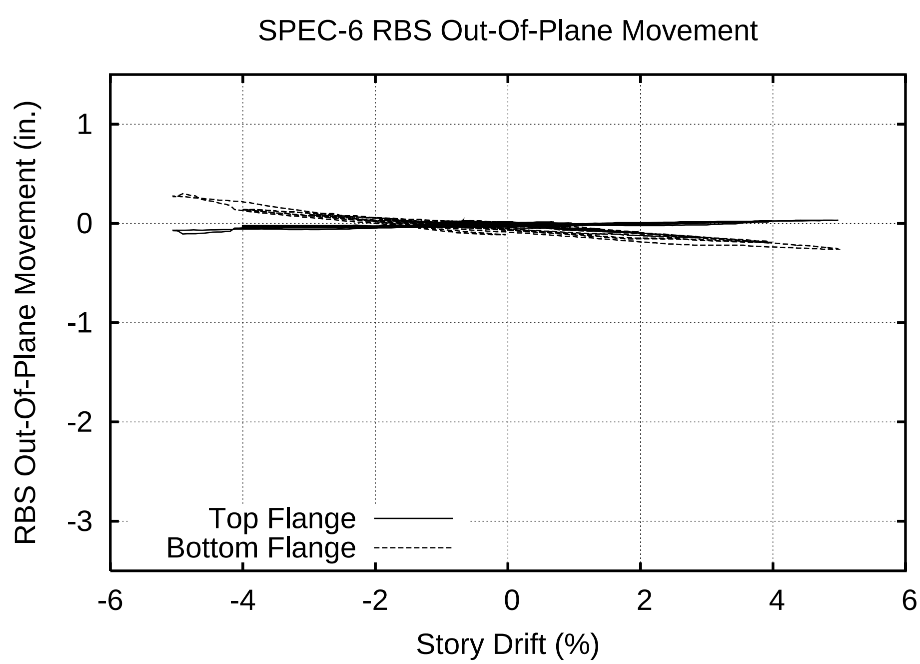
SPEC-6 RBS Out-Of-Plane Movement
RBS Out-Of-Plane Movement (in.)
1
0
-1
-2
-3
Top Flange
Bottom Flange
-6
-4
-2
0
2
4
6
Story Drift (%)

SPEC-6 at 5% story drift

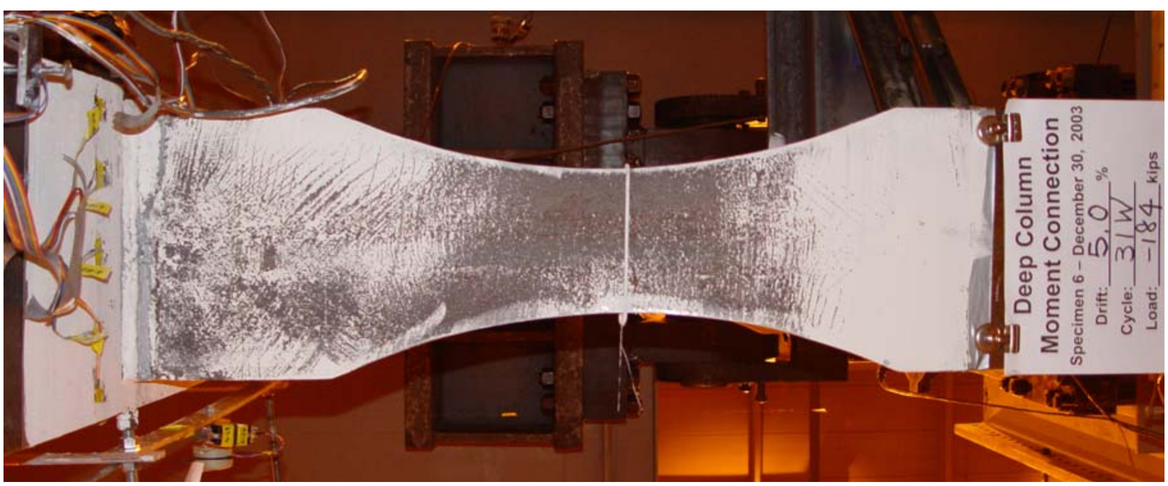

Beam bottom flange lateral movement in RBS, 5% story drift

West beam bottom flange fracture during first cycle of 5% story drift

APPENDIX B

WELD PROCEDURE SPECIFICATIONS

(This page left blank)

1. Beam Top Flange-to-Column Flange CJP Groove Weld

Welding Procedure Specification

Top flange

WPS No. ________ Date 2/13/03 By John Hoffner Type: Manual ☐ Machine ☐
Authorized By ________ Date ________ Revision ________ Semi-Auto ☒ Auto ☐
Welding Process(es) FCAWSS ________ Prequalified ☐
Supporting PQR(s) ________

JOINT
Type Single Bevel
Backing Yes ☒ No ☐ Single Weld ☐ Double Weld ☐
Backing Material 3/8"x1" A36
Root Opening 3/8 Root Face Dimension ____
Groove Angle 30° Radius ____
Back Gouge Yes ☐ No ☒
Method ________

JOINT DETAIL

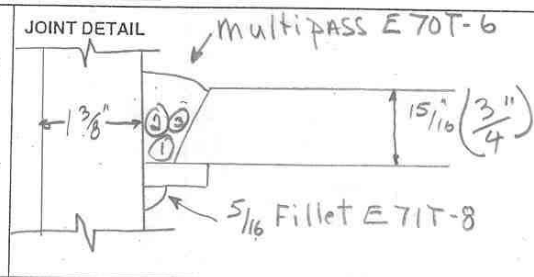

BASE METALS
Material Spec. A992 to ____
Type or Grade 50 to ____
Thickness: Groove 15/16 - ____
Fillet ____ - ____
Diameter (Pipe) ____ - ____

POSITION
Groove Flat Fillet overhead
Vertical Progression: ☐ Up ☐ Down

ELECTRICAL CHARACTERISTICS
Transfer Mode (GMAW):
Short Circuiting ☐ Globular ☐ Spray ☐
Current: AC ☐ DCEP ☐ DCEN ☐ Pulsed ☐
Other ________
Tungsten Electrode (GTAW):
Size ____ Type ____

FILLER METALS
AWS Specification E70T-6 Groove
AWS Classification E71T-8 overhead

SHIELDING
Flux: ____ Gas: None
Electrode-Flux(Class): ____ Composition: ____
________ Flow Rate ____
Gas Cup Size ____

TECHNIQUE
Stringer or Weave Bead Stringer
Multi-pass or Single Pass (per side) multi-pass
Number of Electrodes ____
Electrode Spacing: Longitudinal ____
Lateral ____
Angle ____
Contact Tube to Work Distance 1 1/2
Peening ____
Interpass Cleaning Chipping hammer, wire brush, grinding

PREHEAT
Preheat Temp., Min. 50
Thickness Up to 3/4", Temperature: 50°
Over 3/4" to 1-1/2" 50°
Over 1-1/2" to 2-1/2" 150
Over 2-1/2" 225
Interpass Temp., Min. 275° Max. 325° (?550°)

POSTWELD HEAT TREATMENT PWHT Required ☐
Temp. ____ Time ____

WELDING PROCEDURE

Layer/Pass	Process	Filler Metal Class	Diameter	Current Type	Amps or WFS	Volts	Travel Speed
multipass groove	FCAWSS	E70T-6	3/32	DCEP	460 Amps	26	10 to 15 IPM
Overhead	FCAWSS	E71T-8	.068	DCEN	260 Amps	21	10 to 15 IPM

2. Beam Bottom Flange-to-Column Flange CJP Groove Weld

Welding Procedure Specification

Bottom Flange

WPS No. ______ Date 2/13/03 By John Hoffner Type Manual ☐ Machine ☐
Authorized By ______ Date ______ Revision ______ Semi-Auto ☒ Auto ☐
Welding Process(es) FCAWSS ______ Prequalified ☐
Supporting PQR(s) ______

JOINT
Type Single Bevel
Backing Yes ☒ No ☐ Single Weld ☐ Double Weld ☐
Backing Material 3/8" X 1" A36
Root Opening 3/8" Root Face Dimension ______
Groove Angle 30° Radius ______
Back Gouge Yes ☒ No ☐
Method Airarc

JOINT DETAIL

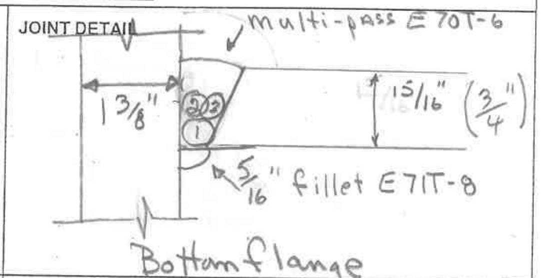

BASE METALS
Material Spec. A992 to ______
Type or Grade 50 to ______
Thickness: Groove 15/16" - ______
Fillet ______ - ______
Diameter (Pipe) ______ - ______

POSITION
Groove Flat Fillet OVERhead
Vertical Progression: ☐ Up ☐ Down

FILLER METALS
AWS Specification E70T-6 Groove
AWS Classification E70T-8 overhead fillet

ELECTRICAL CHARACTERISTICS
Transfer Mode (GMAW):
Short Circuiting ☐ Globular ☐ Spray ☐
Current: AC ☐ DCEP ☒ DCEN ☐ Pulsed ☐
Other ______
Tungsten Electrode (GTAW):
Size ______ Type ______

SHIELDING
Flux: ______ Gas: None
Electrode-Flux(Class): ______ Composition: ______
Flow Rate ______
Gas Cup Size ______

TECHNIQUE
Stringer or Weave Bead Stringer
Multi-pass or Single Pass (per side) ______
Number of Electrodes ______
Electrode Spacing: Longitudinal ______
Lateral ______
Angle ______
Contact Tube to Work Distance 1 1/2
Peening ______
Interpass Cleaning Chipping hammer, wire brush and grinding

PREHEAT
Preheat Temp., Min. 50°
Thickness Up to 3/4", Temperature: 50
Over 3/4" to 1-1/2" 50
Over 1-1/2" to 2-1/2" 150
Over 2-1/2" 225
Interpass Temp., Min. 275° Max. 325°
? 550° ?

POSTWELD HEAT TREATMENT PWHT Required ☐
Temp. ______ Time ______

WELDING PROCEDURE

Layer/Pass	Process	Filler Metal Class	Diameter	Current Type	Amps or WFS	Volts	Travel Speed
multi-pass grove	FCAWSS	E70T-6	3/32	DCEP	460 Amps	26	10 to 15 IPM
OVERHead	FCAWSS	E71T-8	.068	DCEN	260	21	10 to 15 IPM

3. Beam Web-to-Column Flange CJP Groove Weld

Welding Procedure Specification

Column flange to beam Web

WPS No. ______ Date 2/13/03 By John Hoffner Type: Manual ☐ Machine ☐
Authorized By ______ Date ______ Revision ______ Semi-Auto ☒ Auto ☐
Welding Process(es) FCAW SS ______ Prequalified ☐
Supporting PQR(s) ______

JOINT
Type: Single Bevel
Backing: Yes ☒ No ☐ Single Weld ☐ Double Weld ☐
Backing Material: A572-50
Root Opening: 1/4" Root Face Dimension: ______
Groove Angle: 45° Radius: ______
Back Gouge: Yes ☐ No ☒
Method: ______

JOINT DETAIL

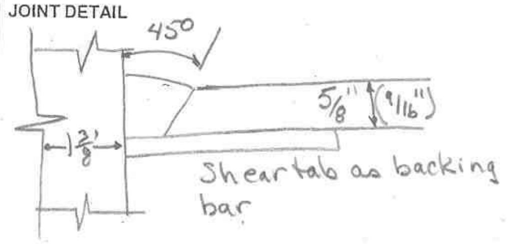

BASE METALS
Material Spec. A992 to ______
Type or Grade 50 to ______
Thickness: Groove 9/16 - ______
Fillet ______ - ______
Diameter (Pipe) ______ - ______

POSITION
Groove: 3G Fillet: ______
Vertical Progression: ☒ Up ☐ Down

FILLER METALS
AWS Specification: E 71T-8
AWS Classification: ______

ELECTRICAL CHARACTERISTICS
Transfer Mode (GMAW):
Short Circuiting ☐ Globular ☐ Spray ☐
Current: AC ☐ DCEP ☐ DCEN ☒ Pulsed ☐
Other ______
Tungsten Electrode (GTAW):
Size ______ Type ______

SHIELDING
Flux: ______ Gas: None
Electrode-Flux(Class): ______ Composition: ______
Flow Rate ______
Gas Cup Size ______

TECHNIQUE
Stringer or Weave Bead: Stringer
Multi-pass or Single Pass (per side): multipass
Number of Electrodes ______
Electrode Spacing: Longitudinal ______
Lateral ______
Angle ______
Contact Tube to Work Distance: 1/2" to 1"
Peening ______
Interpass Cleaning: Wire brush, Chipping hammer, Grinding

PREHEAT
Preheat Temp., Min. 50°
Thickness Up to 3/4", Temperature: 50°
Over 3/4" to 1-1/2": 50°
Over 1-1/2" to 2-1/2": 150°
Over 2-1/2": 225°
Interpass Temp., Min. 175° Max. 325 550°

POSTWELD HEAT TREATMENT PWHT Required ☐
Temp. ______ Time ______

WELDING PROCEDURE

Layer/Pass	Process	Filler Metal Class	Diameter	Current Type	Amps or WFS	Volts	Travel Speed
multipass groove	FCAWSS	E71T-8	.068	DCEN	195 to 270	19-21	8-12 IPM

(This page is blank.)

Appendix C

Weld UT Inspection Reports

(This page left blank)

1. SPEC-1

ANNEX D　　　　　　　　　　　　　　　　　　　　　　AWS D1.1/D1.1M:2002

Form D-11

REPORT OF UT OF WELDS

Project Deep Column Steel Moment Connection Project　　Report no. 2

Weld identification C1 Column Flange to flange Welds CJP

Material thickness 15/16" Flange to 1 5/16" Flange

Weld joint AWS TCU4a-GF

Welding process FCAW Self Shielded

Quality requirements—section no. AWS D1.1-02 table 6.2

Remarks

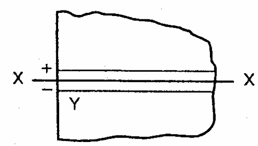

Line number	Indication number	Transducer angle	From Face	Leg[1]	Decibels: Indication level a	Reference level b	Attenuation factor c	Indication rating d	Discontinuity: Length	Angular distance (sound path)	Depth from "A" surface	Distance From X	From Y	Discontinuity evaluation	Remarks
1		70°	a	1	–	79	–	–							
2															
3		No Relevant indications found on all four flange to													
4															
5		flange CJP welds													
6															
7															
8		Calib performed on Standard IIW Type 1 Block R.L. 79dB													
9															
10		from .060" hole @ 50% FSH.													
11															
12															
13															
14															
15															
16															
17															
18															
19															
20															
21															
22															
23															
24															
25															
26															

We, the undersigned, certify that the statements in this record are correct and that the welds were prepared and tested in conformance with the requirements of Section 6, Part F of AWS D1.1/D1.1M, (2002) Structural Welding Code—Steel.
(year)

Test date 3-24-03　　　　Manufacturer or Contractor

Inspected by [signature] Lev II　　　　Authorized by

Date

General Note: This form is applicable to Section 2, Parts B or C (Statically and Cyclically Loaded Nontubular Structures). Do **NOT** use this form for Tubular Structures (Section 2, Part D).

Form D-11

2. SPEC-2

ANNEX D

AWS D1.1/D1.1M:2002

Form D-11

REPORT OF UT OF WELDS

Project: Deep Column Steel Moment Connection Project
Report no.: 1

Weld identification: C2 Column
Material thickness: 15/16" flange to 15/16" flange
Weld joint AWS: TC U4a - GF
Welding process: Self Shielded FCAW
Quality requirements—section no.: AWS D1.1 table 6.2/82-02
Remarks: No relevant indications

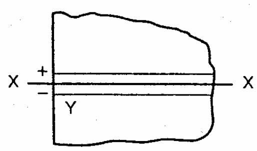

Line number	Indication number	Transducer angle	From Face	Leg[1]	Decibels: Indication level a	Reference level b	Attenuation factor c	Indication rating d	Discontinuity: Length	Angular distance (sound path)	Depth from "A" surface	Distance From X	Distance From Y	Discontinuity evaluation	Remarks
1	/	70°	a	1	/	79		/	/	2.74"	/	/	/		Each
2	/	70°	a	2	/	79		/	/	5.48"	/	/	/		flange
3	/	70°	b	1	/	79		/	/	2.74"	/	/	/		
4	/	70°	b	2	/	79		/	/	5.48"	/	/	/		
5															
6		No Relevant indications found on all four Flange													
7		welds													
8															
9															
10		Calib per IIW type 1 Block .060" SDH @ 50% FSH													
11		Reference Level 79 dB													
12															
13															
14															
15															
16															
17															
18															
19															
20															
21															
22															
23															
24															
25															
26															

We, the undersigned, certify that the statements in this record are correct and that the welds were prepared and tested in conformance with the requirements of Section 6, Part F of AWS D1.1/D1.1M, (2002) Structural Welding Code—Steel.
(year)

Test date: 3 March 03
Inspected by: Rob K. Wunderlin Level II

Manufacturer or Contractor: ______
Authorized by: ______
Date: ______

General Note: This form is applicable to Section 2, Parts B or C (Statically and Cyclically Loaded Nontubular Structures). Do **NOT** use this form for Tubular Structures (Section 2, Part D).

Form D-11

3. SPEC-3

WTTI

WELDER TRAINING & TESTING INSTITUTE, INC.
1144 N. Graham Street, Allentown, PA 18103-1263
Phone: (610) 820-9551 FAX: (610) 820-0271

REPORT OF ULTRASONIC TESTING OF WELDS

Project: Deep Column Steel Moment Connection Project Report no. 1

Weld identification: C-3 Column flange to flange CJP Weld
Material thickness: 15/16 flange to 1 5/16" flange
Weld joint AWS: TC-U4-a-GF
Welding process: FCAW - Self Shielded
Quality requirements — section no.: AWS D1.1 tab 6.2
Remarks:

X + − Y X

	Line number	Indication number	Transducer angle	From Face	Leg*	Decibels: Indication level (a)	Decibels: Reference level (b)	Decibels: Attenuation factor (c)	Decibels: Indication rating (d)	Discontinuity: Length	Discontinuity: Angular distance (sound path)	Discontinuity: Depth from "A" surface	Discontinuity: Distance From X	Discontinuity: Distance From Y	Discontinuity evaluation	Remarks
X-4	1	1	70°	A	1	75	69	2	+4	1.00"	1.9"	.89"	10.8"	0	Acceptable	
	2															
X-2	3	1	70°	A	1	75	69	2	+4	.75"	1.7"	.67"	6.0"	0	Acceptable	
	4															
	5															
	6															
	7															
	8															
	9															
	10															
	11															
	12															
	13															
	14															
	15															
	16															
	17															
	18															
	19															
	20															
	21															
	22															
	23															
	24															
	25															
	26															

We, the undersigned, certify that the statements in this record are correct and that the welds were prepared and tested in accordance with the requirements of section 6, Part C of ANSI/AWS D1.1, (2002 year) Structural Welding Code-Steel.

Test date: 8-6-03
Inspected by: Rob K. [illegible] Lev III

Manufacturer or contractor:
Authorized by:
Date:

Note: This form is applicable to sections 8 and 9 (Statically and Dynamically Loaded Structures). Do **NOT** use this form for Tubular Structures (section 10).

Form D-11

4. SPEC-4

JUL. 9.2003 1:41PM P 1

FROM :

WTTI

WELDER TRAINING & TESTING INSTITUTE, INC.
1144 N. Graham Street, Allentown, PA 18103-1263

Phone: (610) 820-9551 FAX: (610) 820-0271

REPORT OF ULTRASONIC TESTING OF WELDS

Project Deep Column Steel Moment Connection Project Report no. 1

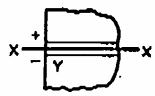

Weld identification C-4 Column flange to flange CJP Weld
Material thickness 15/16" flange to 1 3/16" flange
Weld joint AWS TC-U4a - GF
Welding process FCAW - Self Shielded
Quality requirements — section no. AWS D1.1 Tab. 6.2
Remarks 4-Flange to flange Welds X-1, X-2, X-3, X-4 Accepted
2-Web to flange welds had discontinuities X-5, X-6

	Line number	Indication number	Transducer angle	From Face	Leg*	Decibels: Indication level a	Decibels: Reference level b	Decibels: Attenuation factor c	Decibels: Indication rating d	Discontinuity: Length	Discontinuity: Angular distance (sound path)	Discontinuity: Depth from "A" surface	Discontinuity: Distance From X	Discontinuity: Distance From Y	Discontinuity evaluation	Remarks
X-5	1	1	70°	a	1	68	69	2	+1	1.00"	1.80"	.64"	15.00"	0	unacceptable	
	2															
X-6	3	1	70°	a	1	69	69	2	+2	.50"	1.80"	.64"	20.5"	0	unacceptable	
	4															
	5															
	6															
	7															
	8															
	9															
	10															
	11															
	12															
	13															
	14															
	15															
	16															
	17															
	18															
	19															
	20															
	21															
	22															
	23															
	24															
	25															
	26															

We, the undersigned, certify that the statements in this record are correct and that the welds were prepared and tested in accordance with the requirements of section 6, Part C of ANSI/AWS D1.1, (2002 year) Structural Welding Code-Steel.

Test date 7-9-03

Inspected by [illegible signature] Level II

Manufacturer or contractor

Authorized by

Date

Note: This form is applicable to sections 8 and 9 (Statically and Dynamically Loaded Structures). Do NOT use this form for Tubular Structures (section 10).

5. SPEC-5

WTTI

WELDER TRAINING & TESTING INSTITUTE, INC.
1144 N. Graham Street, Allentown, PA 18103-1263
Phone: (610) 820-9551 FAX: (610) 820-0271

REPORT OF ULTRASONIC TESTING OF WELDS

Project: Deep Column Steel Moment Connection Project
Report no. ______

Weld identification: C-5 Column to flange CJP Weld
Material thickness: .750" flange, .500" Web
Weld joint AWS: TCU 4a - GF
Welding process: FCAW Self Shielded
Quality requirements — section no.: AWS D1.1 tab 6.2
Remarks: 4 flange to flange X1, X2, X3, X4, Accepted
2 web to flange: X5, X6 Accepted

Line number	Indication number	Transducer angle	From Face	Leg*	Decibels: Indication level (a)	Reference level (b)	Attenuation factor (c)	Indication rating (d)	Discontinuity: Length	Angular distance (sound path)	Depth from "A" surface	Distance: From X	From Y	Discontinuity evaluation	Remarks
1		70°	a	1	No relevant indications found									Accepted	
2				+											
3				2											
4															
5															
6															
7															
8															
9															
10															
11															
12															
13															
14															
15															
16															
17															
18															
19															
20															
21															
22															
23															
24															
25															
26															

We, the undersigned, certify that the statements in this record are correct and that the welds were prepared and tested in accordance with the requirements of section 6, Part C of ANSI/AWS D1.1, (2002 year) Structural Welding Code-Steel.

Test date: 9-26-03
Inspected by: [signature] Lev II

Manufacturer or contractor ______
Authorized by ______
Date ______

Note: This form is applicable to sections 8 and 9 (Statically and Dynamically Loaded Structures). Do **NOT** use this form for Tubular Structures (section 10).

Form D-11

6. SPEC-6

WTTI

WELDER TRAINING & TESTING INSTITUTE, INC.
1144 N. Graham Street, Allentown, PA 18103-1263
Phone: (610) 820-9551 FAX: (610) 820-0271

REPORT OF ULTRASONIC TESTING OF WELDS

Project Deep Column Steel Moment Connection Project Report no. ____

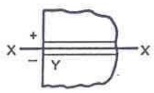

Weld identification C-6 Column Flange to flange CJP Weld
Material thickness .750" flange .500" Web
Weld joint AWS TCu 4a - GF
Welding process FCAW Self Shielded
Quality requirements — section no. AWS D1.1 tab. 6.2
Remarks 4-Flange to Flange welds Accepted X1, X2, X3, X4
2- Web to flange Welds Accepted X5, X6

Line number	Indication number	Transducer angle	From Face	Leg*	Decibels: Indication level (a)	Decibels: Reference level (b)	Decibels: Attenuation factor (c)	Decibels: Indication rating (d)	Discontinuity: Length	Discontinuity: Angular distance (sound path)	Discontinuity: Depth from "A" surface	Distance: From X	Distance: From Y	Discontinuity evaluation	Remarks
1		70°	A	1	No relevant indications found									Accepted	
2				4											
3				2											
4															
5															
6															
7															
8															
9															
10															
11															
12															
13															
14															
15															
16															
17															
18															
19															
20															
21															
22															
23															
24															
25															
26															

We, the undersigned, certify that the statements in this record are correct and that the welds were prepared and tested in accordance with the requirements of section 6, Part C of ANSI/AWS D1.1, (2002 year) Structural Welding Code-Steel.

Test date 9-26-03
Inspected by [signature] Lev II

Manufacturer or contractor ____
Authorized by ____
Date ____

Note: This form is applicable to sections 8 and 9 (Statically and Dynamically Loaded Structures). Do **NOT** use this form for Tubular Structures (section 10).

Form D-11

Appendix D

Specimen Material Tensile Coupon Stress – Strain Curves

(This page left blank)

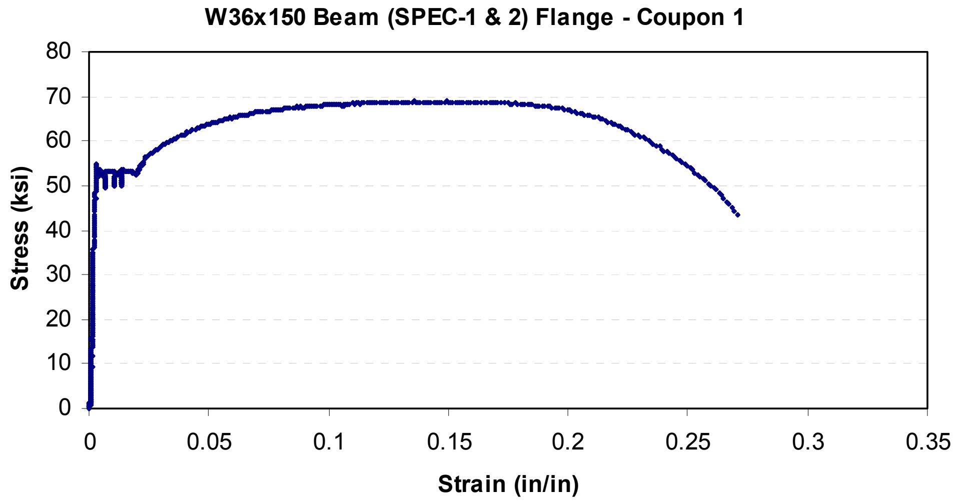
W36x150 Beam (SPEC-1 & 2) Flange - Coupon 1
Stress (ksi)
0
10
20
30
40
50
60
70
80
0
0.05
0.1
0.15
0.2
0.25
0.3
0.35
Strain (in/in)

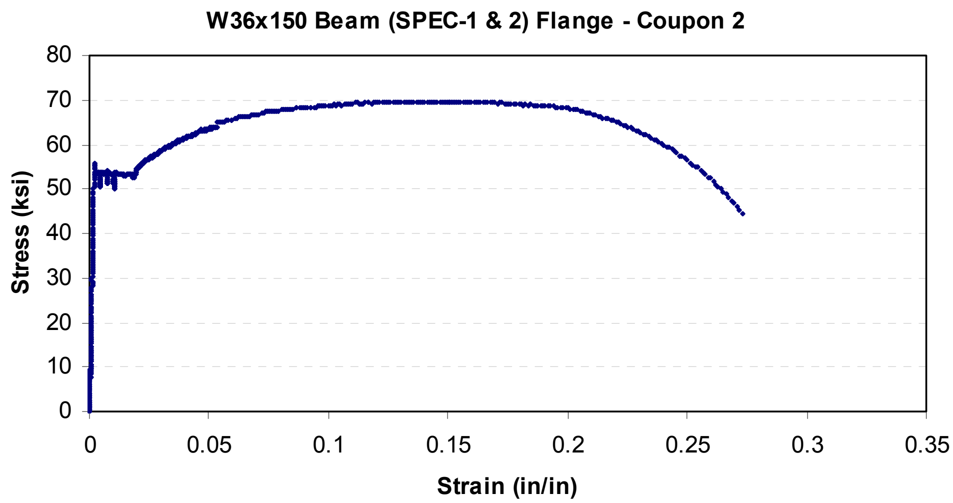
W36x150 Beam (SPEC-1 & 2) Flange - Coupon 2
Stress (ksi)
0
10
20
30
40
50
60
70
80
0
0.05
0.1
0.15
0.2
0.25
0.3
0.35
Strain (in/in)

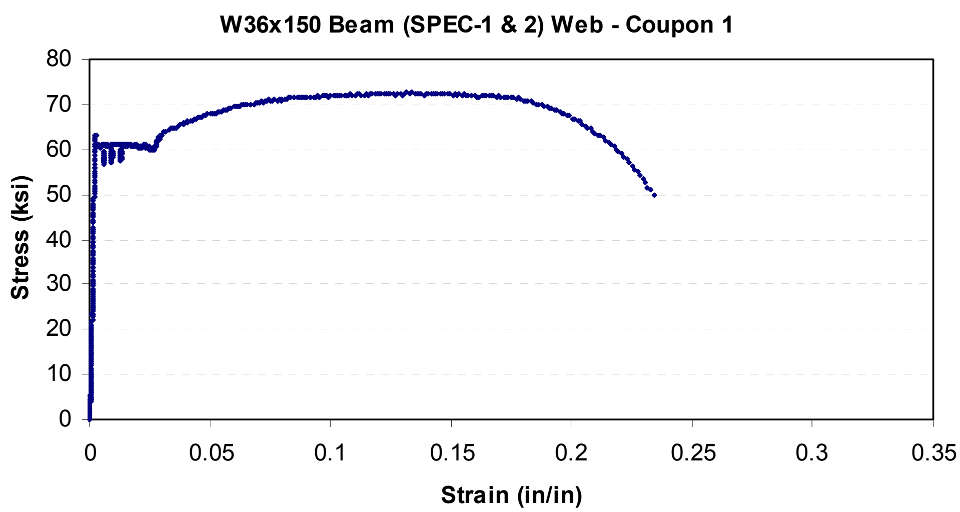
W36x150 Beam (SPEC-1 & 2) Web - Coupon 1
Stress (ksi)
0
10
20
30
40
50
60
70
80
0
0.05
0.1
0.15
0.2
0.25
0.3
0.35
Strain (in/in)

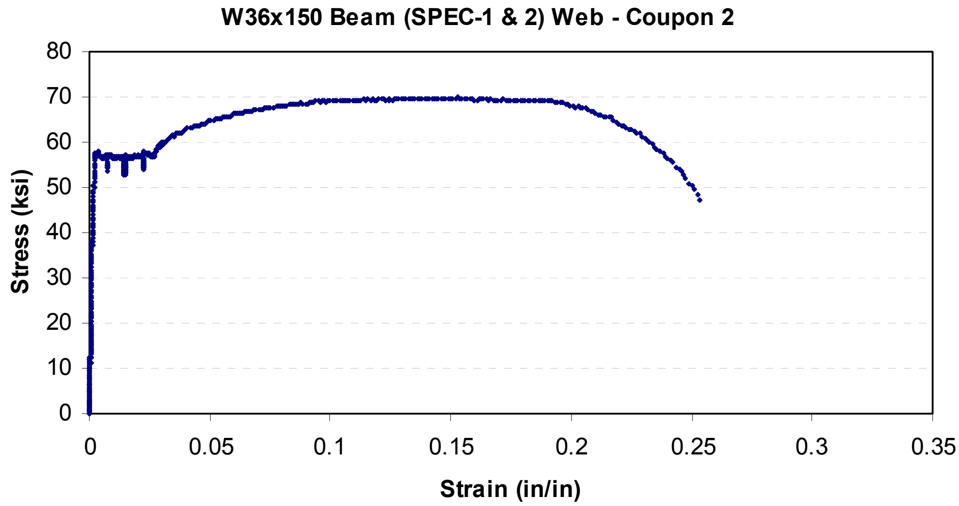
W36x150 Beam (SPEC-1 & 2) Web - Coupon 2
Stress (ksi)
Strain (in/in)
0
10
20
30
40
50
60
70
80
0.05
0.1
0.15
0.2
0.25
0.3
0.35

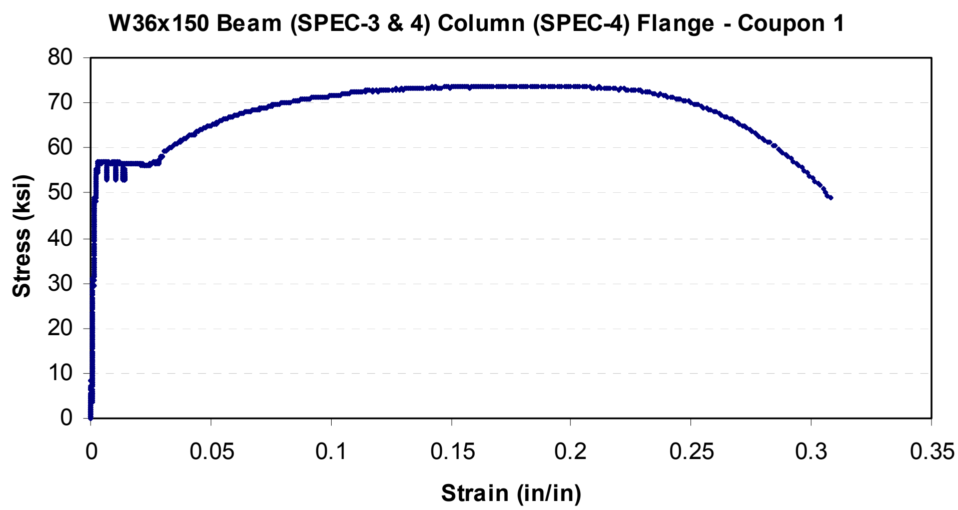
W36x150 Beam (SPEC-3 & 4) Column (SPEC-4) Flange - Coupon 1
Stress (ksi)
Strain (in/in)
0
10
20
30
40
50
60
70
80
0.05
0.1
0.15
0.2
0.25
0.3
0.35

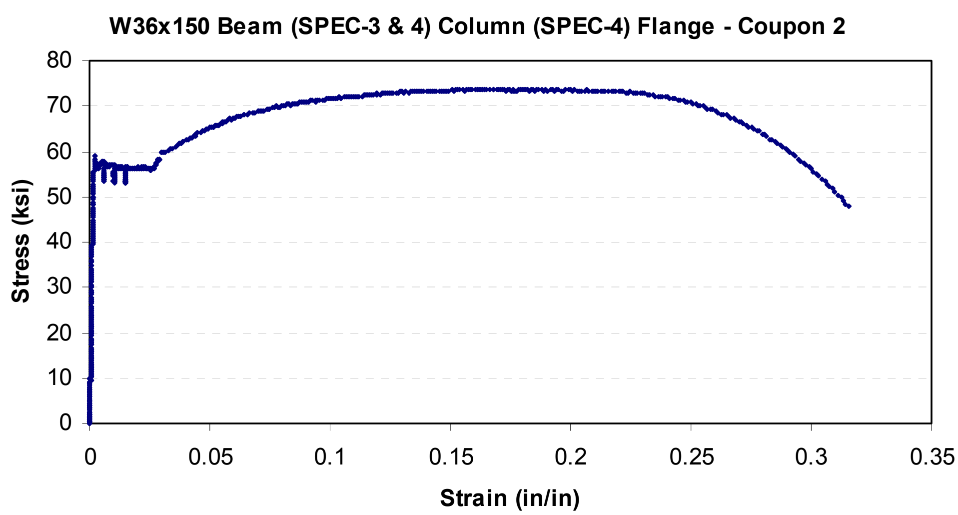
W36x150 Beam (SPEC-3 & 4) Column (SPEC-4) Flange - Coupon 2
Stress (ksi)
Strain (in/in)
0
10
20
30
40
50
60
70
80
0.05
0.1
0.15
0.2
0.25
0.3
0.35

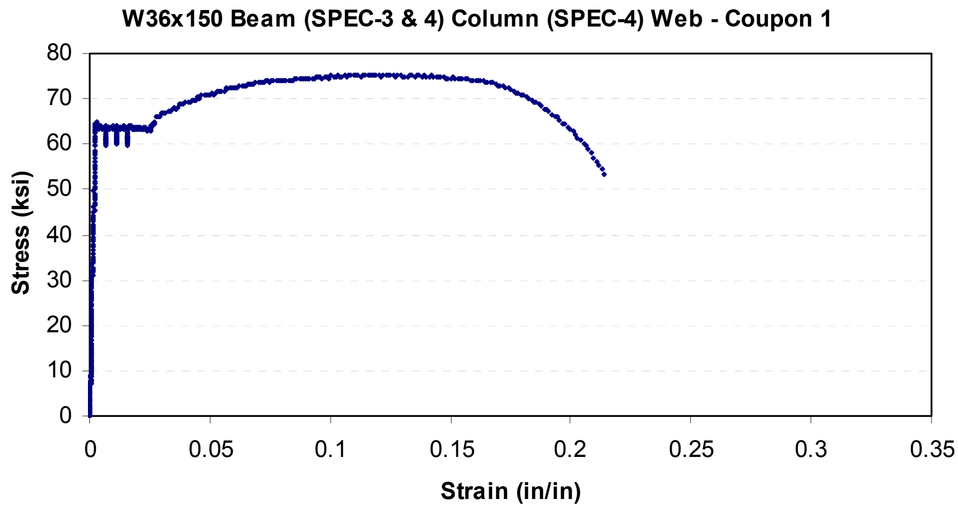
W36x150 Beam (SPEC-3 & 4) Column (SPEC-4) Web - Coupon 1
Stress (ksi)
0
10
20
30
40
50
60
70
80
0
0.05
0.1
0.15
0.2
0.25
0.3
0.35
Strain (in/in)

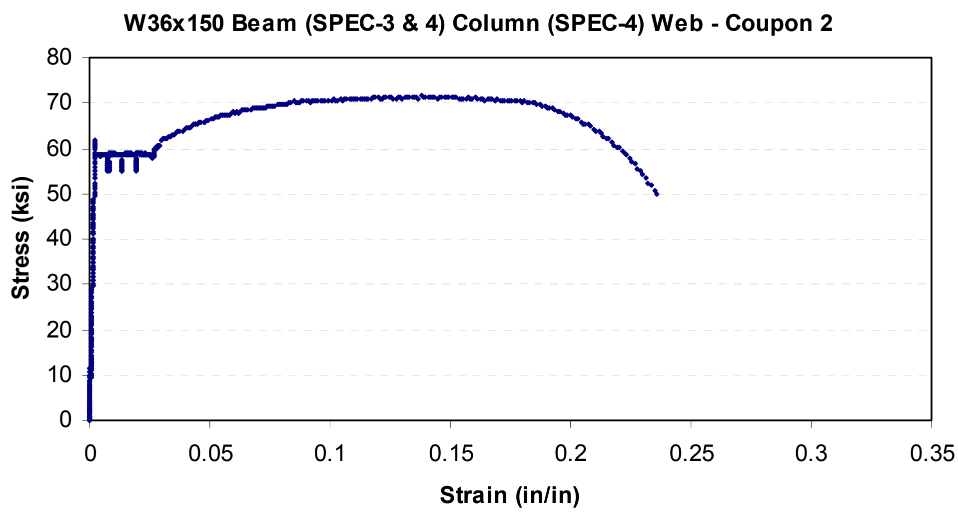
W36x150 Beam (SPEC-3 & 4) Column (SPEC-4) Web - Coupon 2
Stress (ksi)
0
10
20
30
40
50
60
70
80
0
0.05
0.1
0.15
0.2
0.25
0.3
0.35
Strain (in/in)

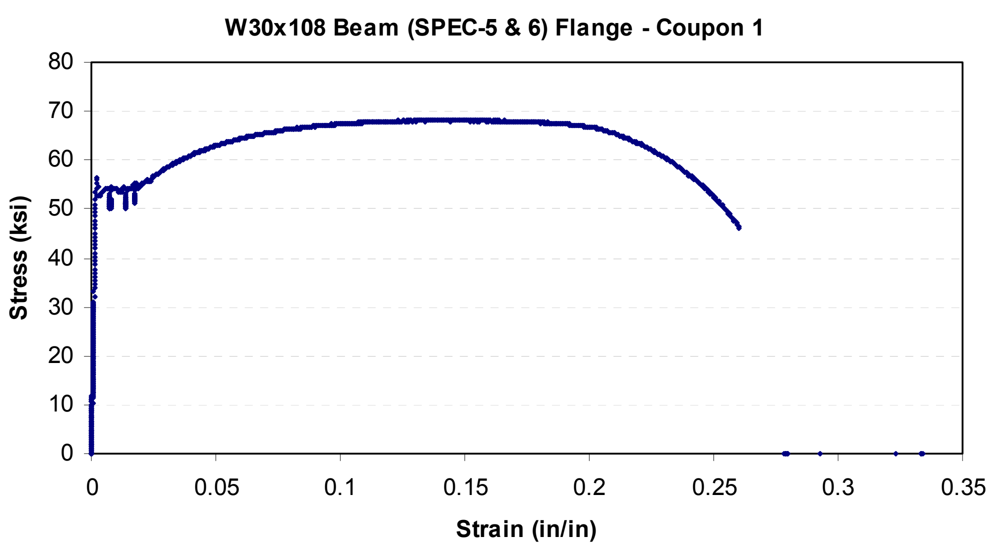
W30x108 Beam (SPEC-5 & 6) Flange - Coupon 1
Stress (ksi)
0
10
20
30
40
50
60
70
80
0
0.05
0.1
0.15
0.2
0.25
0.3
0.35
Strain (in/in)

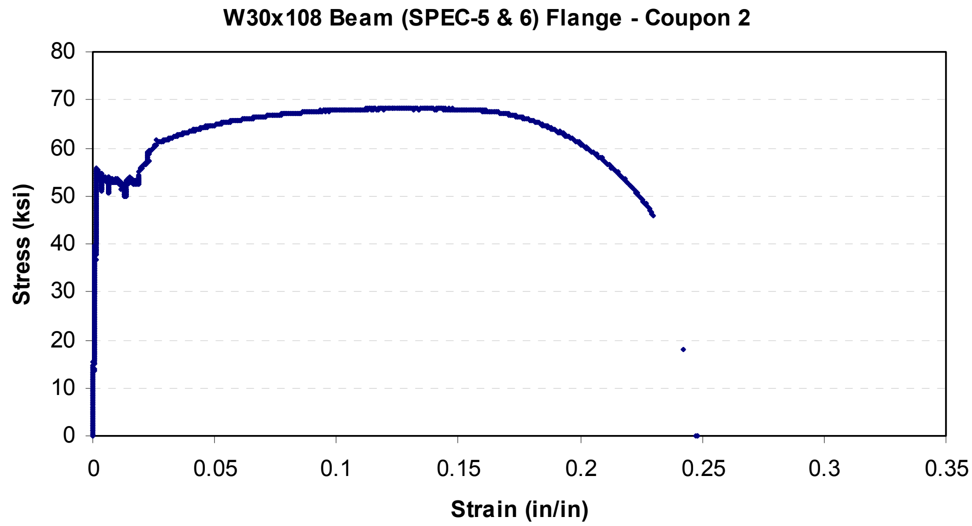
W30x108 Beam (SPEC-5 & 6) Flange - Coupon 2
Stress (ksi)
80
70
60
50
40
30
20
10
0
0
0.05
0.1
0.15
0.2
0.25
0.3
0.35
Strain (in/in)

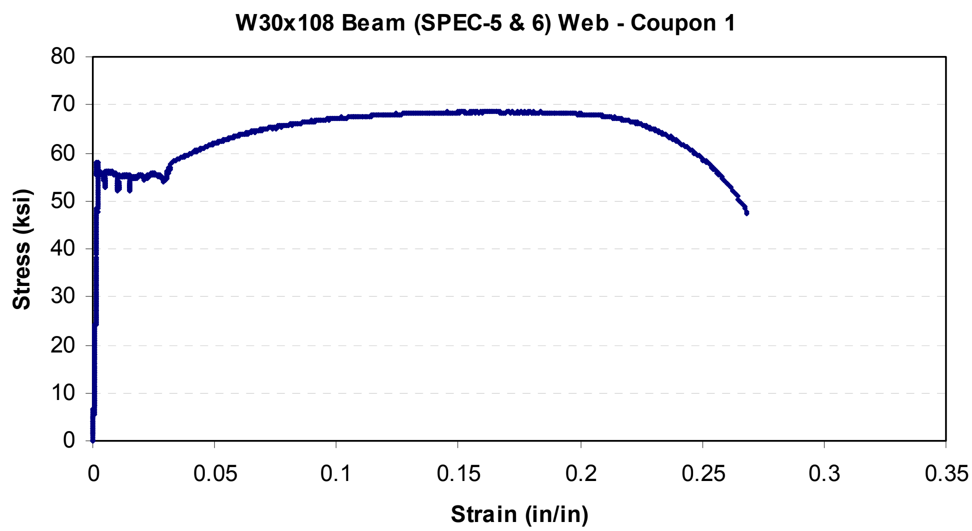
W30x108 Beam (SPEC-5 & 6) Web - Coupon 1
Stress (ksi)
80
70
60
50
40
30
20
10
0
0
0.05
0.1
0.15
0.2
0.25
0.3
0.35
Strain (in/in)

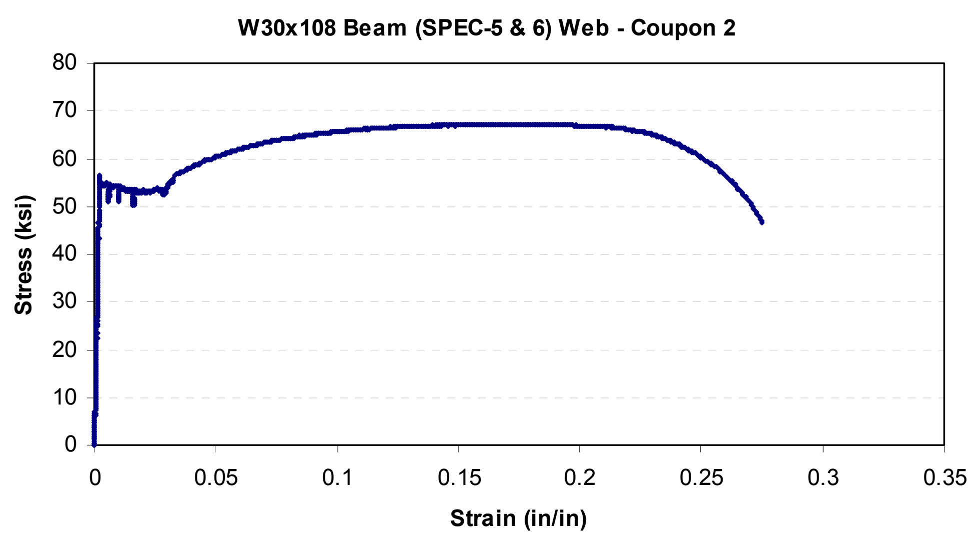
W30x108 Beam (SPEC-5 & 6) Web - Coupon 2
Stress (ksi)
80
70
60
50
40
30
20
10
0
0
0.05
0.1
0.15
0.2
0.25
0.3
0.35
Strain (in/in)

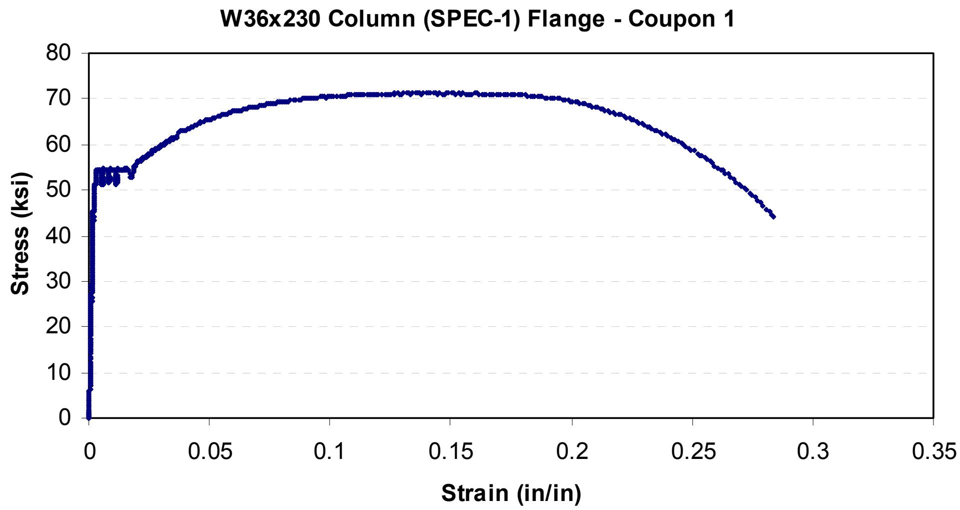
W36x230 Column (SPEC-1) Flange - Coupon 1
Stress (ksi)
80
70
60
50
40
30
20
10
0
0
0.05
0.1
0.15
0.2
0.25
0.3
0.35
Strain (in/in)

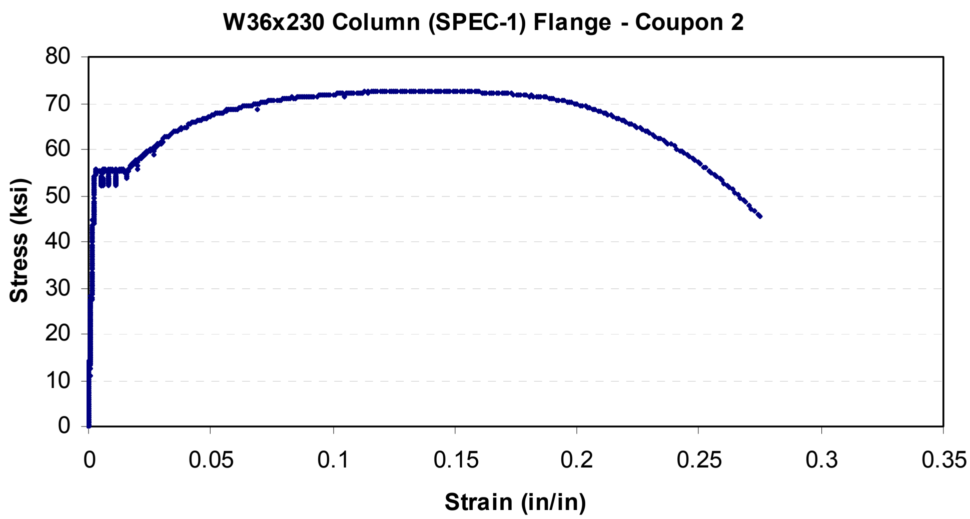
W36x230 Column (SPEC-1) Flange - Coupon 2
Stress (ksi)
80
70
60
50
40
30
20
10
0
0
0.05
0.1
0.15
0.2
0.25
0.3
0.35
Strain (in/in)

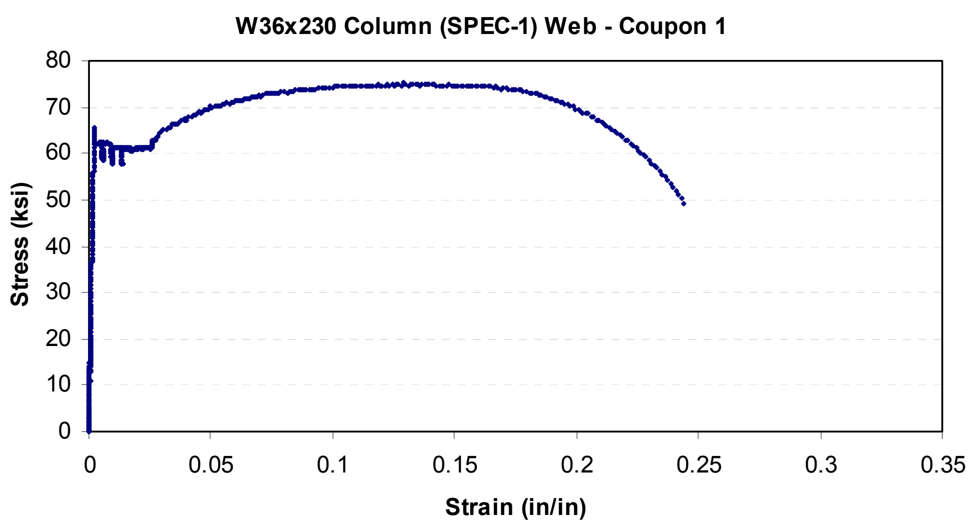
W36x230 Column (SPEC-1) Web - Coupon 1
Stress (ksi)
80
70
60
50
40
30
20
10
0
0
0.05
0.1
0.15
0.2
0.25
0.3
0.35
Strain (in/in)

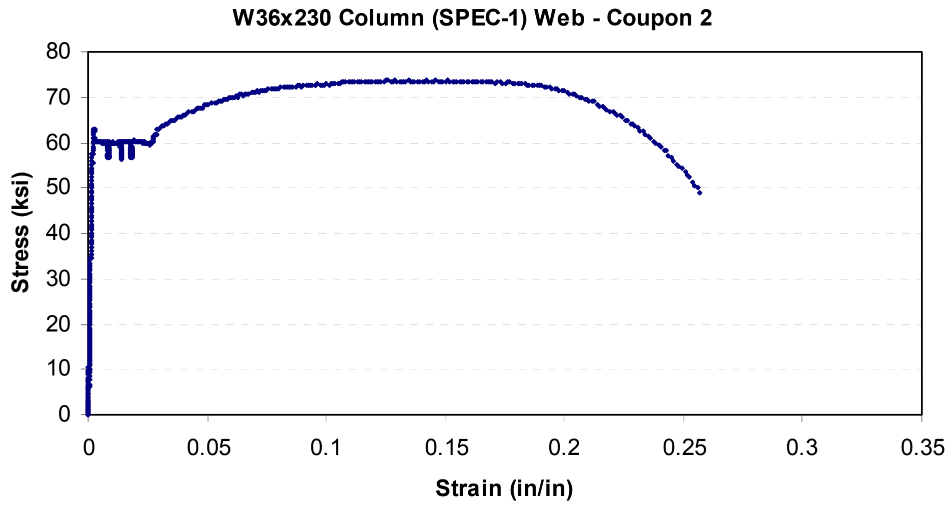
W36x230 Column (SPEC-1) Web - Coupon 2
Stress (ksi)
Strain (in/in)
0
10
20
30
40
50
60
70
80
0
0.05
0.1
0.15
0.2
0.25
0.3
0.35

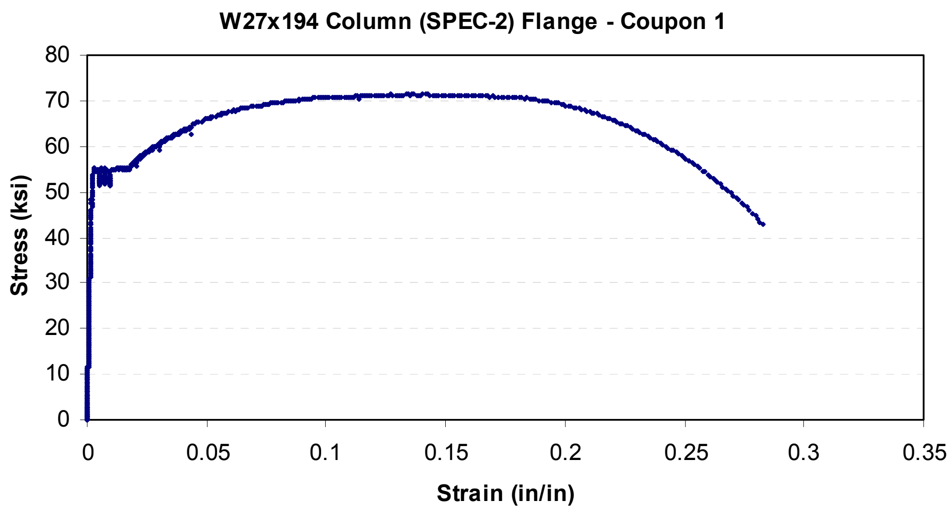
W27x194 Column (SPEC-2) Flange - Coupon 1
Stress (ksi)
Strain (in/in)
0
10
20
30
40
50
60
70
80
0
0.05
0.1
0.15
0.2
0.25
0.3
0.35

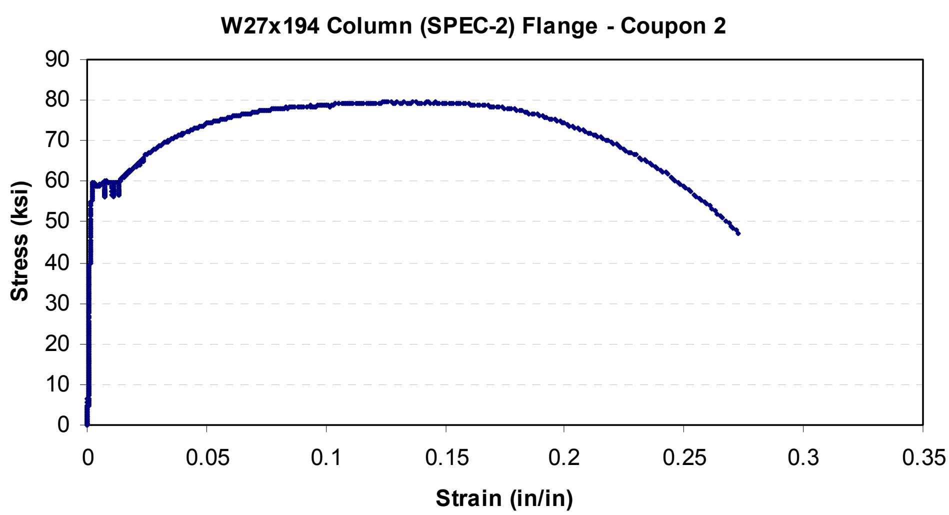
W27x194 Column (SPEC-2) Flange - Coupon 2
Stress (ksi)
Strain (in/in)
0
10
20
30
40
50
60
70
80
90
0
0.05
0.1
0.15
0.2
0.25
0.3
0.35

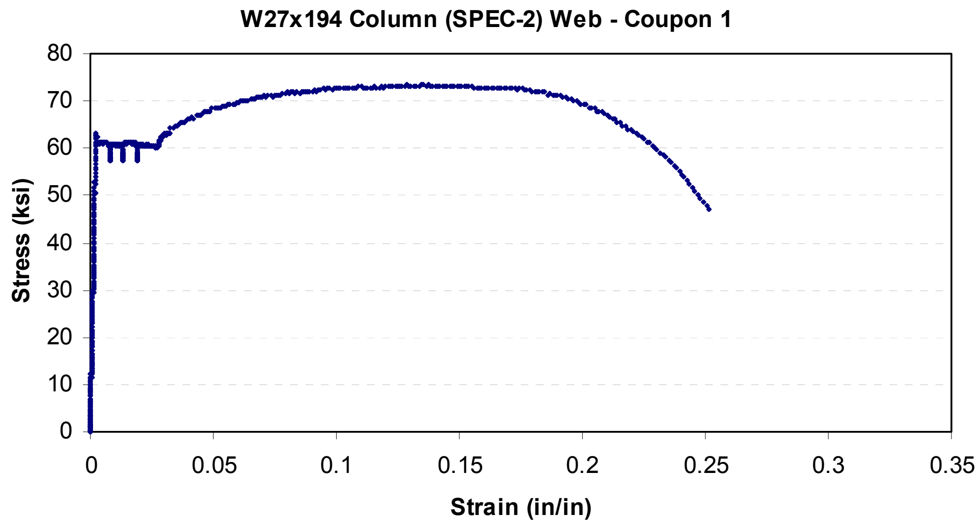
W27x194 Column (SPEC-2) Web - Coupon 1
Stress (ksi)
0
10
20
30
40
50
60
70
80
Strain (in/in)
0
0.05
0.1
0.15
0.2
0.25
0.3
0.35

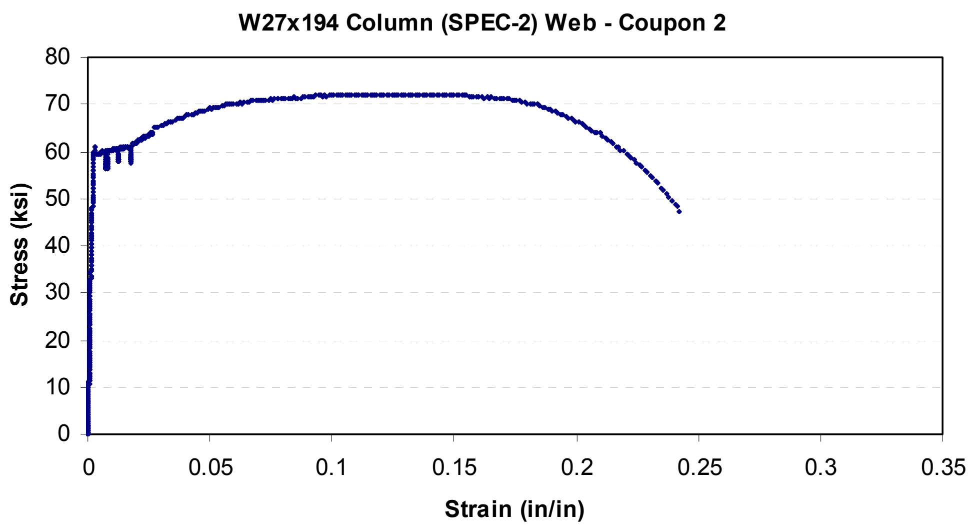
W27x194 Column (SPEC-2) Web - Coupon 2
Stress (ksi)
0
10
20
30
40
50
60
70
80
Strain (in/in)
0
0.05
0.1
0.15
0.2
0.25
0.3
0.35

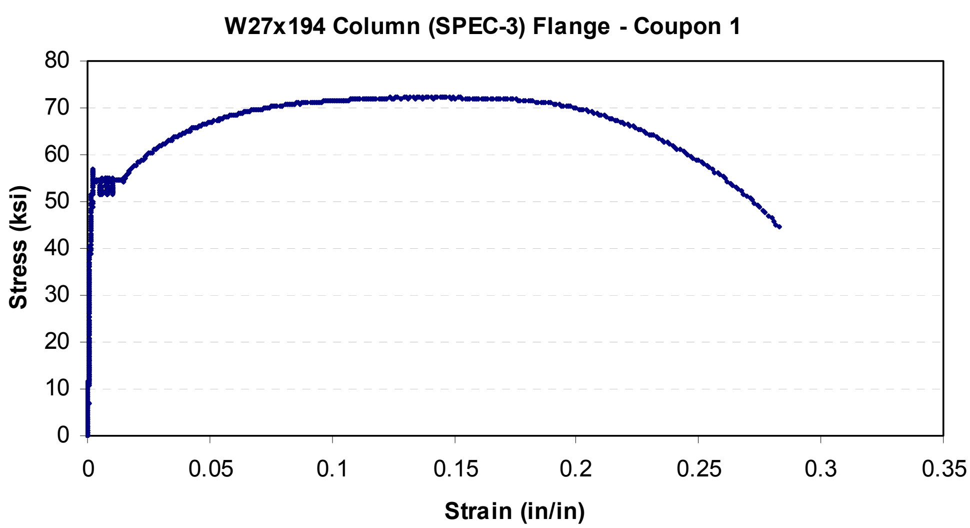
W27x194 Column (SPEC-3) Flange - Coupon 1
Stress (ksi)
0
10
20
30
40
50
60
70
80
Strain (in/in)
0
0.05
0.1
0.15
0.2
0.25
0.3
0.35

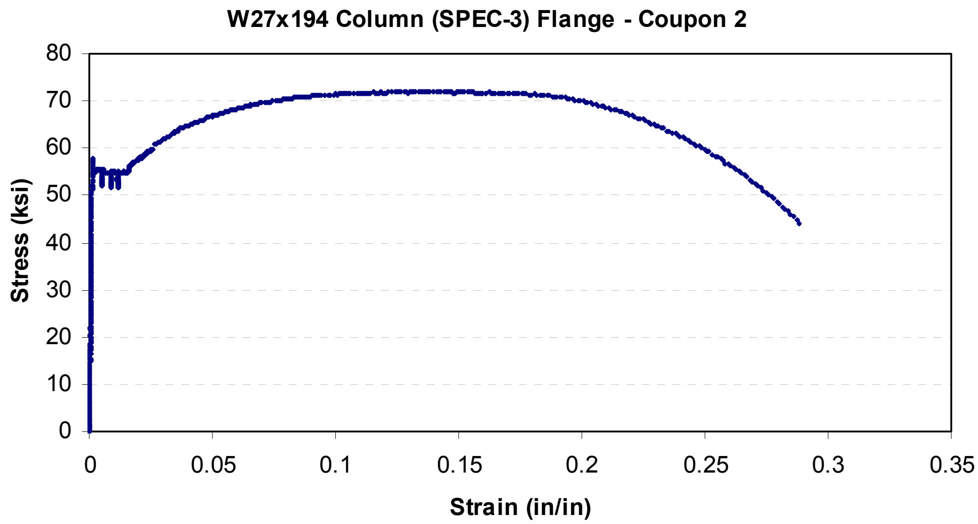
W27x194 Column (SPEC-3) Flange - Coupon 2
Stress (ksi)
0
10
20
30
40
50
60
70
80
0
0.05
0.1
0.15
0.2
0.25
0.3
0.35
Strain (in/in)

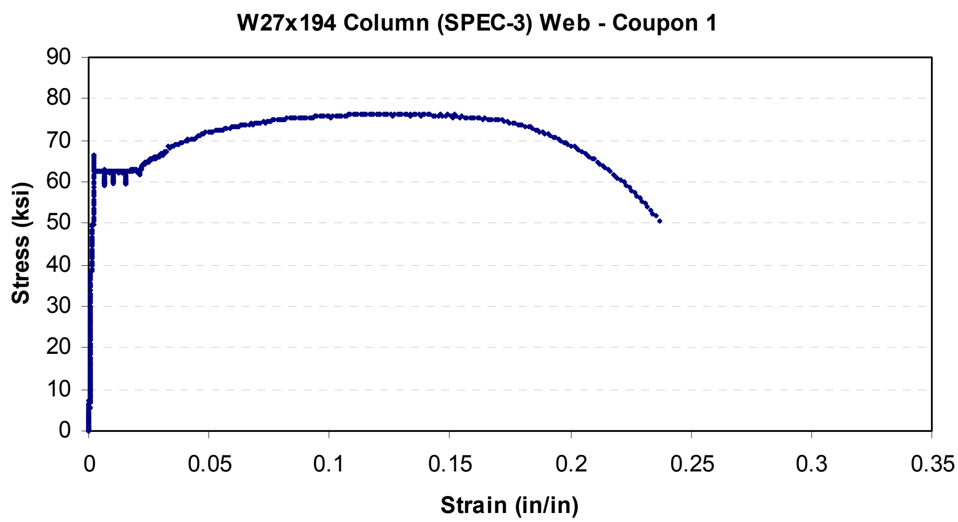
W27x194 Column (SPEC-3) Web - Coupon 1
Stress (ksi)
0
10
20
30
40
50
60
70
80
90
0
0.05
0.1
0.15
0.2
0.25
0.3
0.35
Strain (in/in)

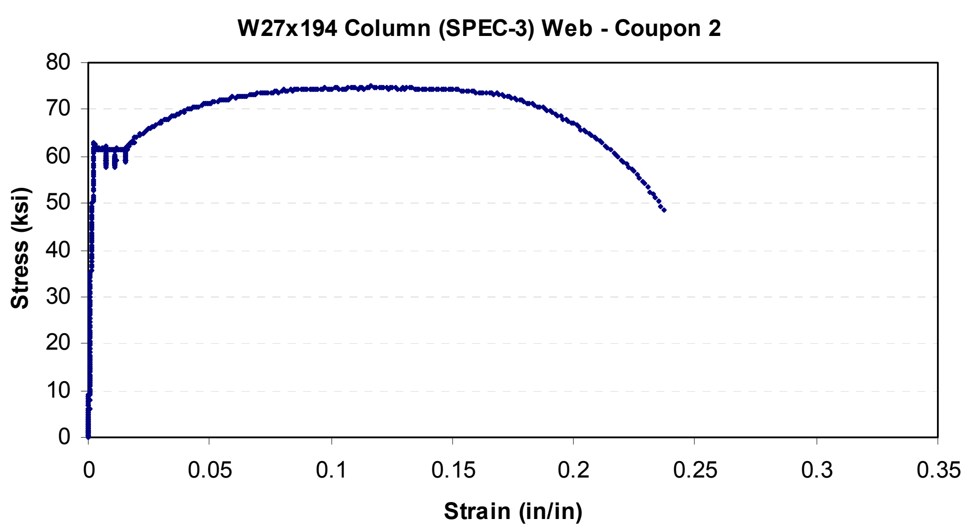
W27x194 Column (SPEC-3) Web - Coupon 2
Stress (ksi)
0
10
20
30
40
50
60
70
80
0
0.05
0.1
0.15
0.2
0.25
0.3
0.35
Strain (in/in)

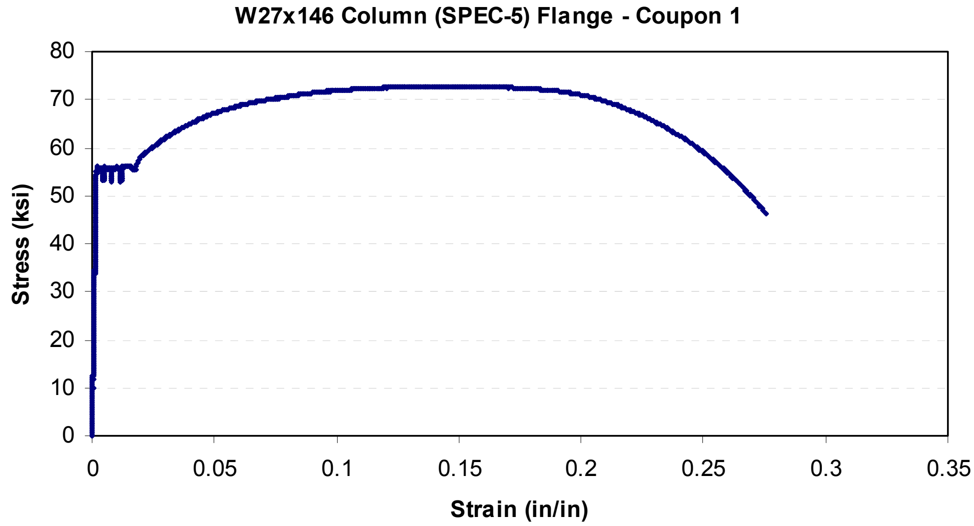
W27x146 Column (SPEC-5) Flange - Coupon 1
Stress (ksi)
0
10
20
30
40
50
60
70
80
0
0.05
0.1
0.15
0.2
0.25
0.3
0.35
Strain (in/in)

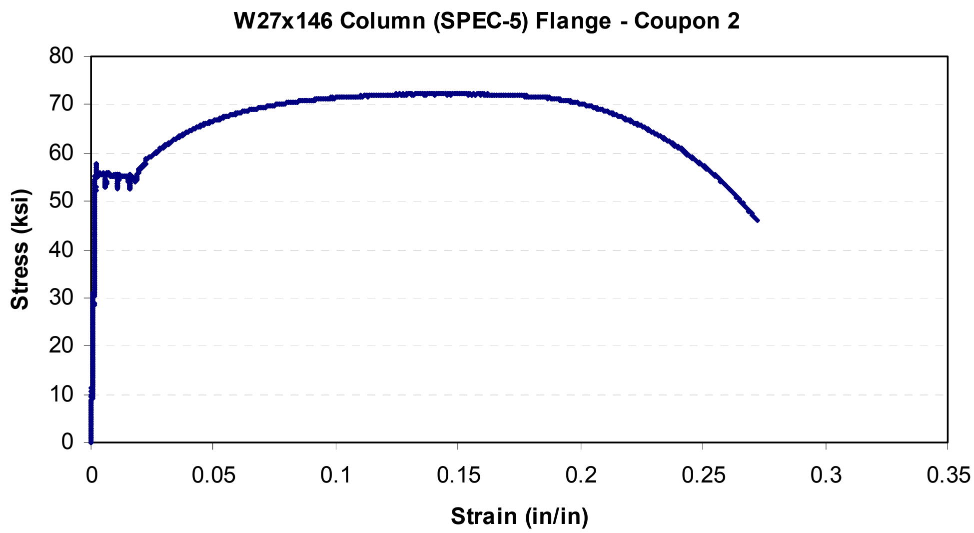
W27x146 Column (SPEC-5) Flange - Coupon 2
Stress (ksi)
0
10
20
30
40
50
60
70
80
0
0.05
0.1
0.15
0.2
0.25
0.3
0.35
Strain (in/in)

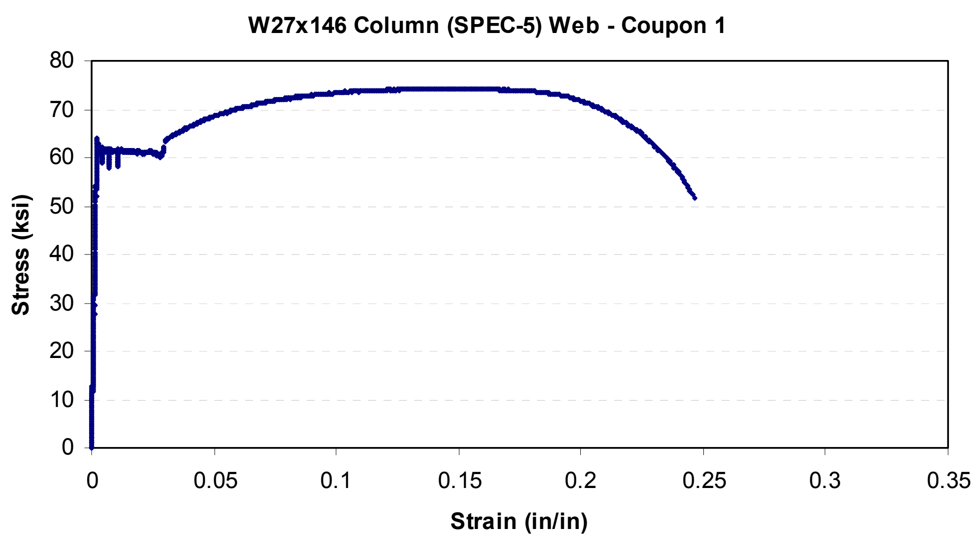
W27x146 Column (SPEC-5) Web - Coupon 1
Stress (ksi)
0
10
20
30
40
50
60
70
80
0
0.05
0.1
0.15
0.2
0.25
0.3
0.35
Strain (in/in)

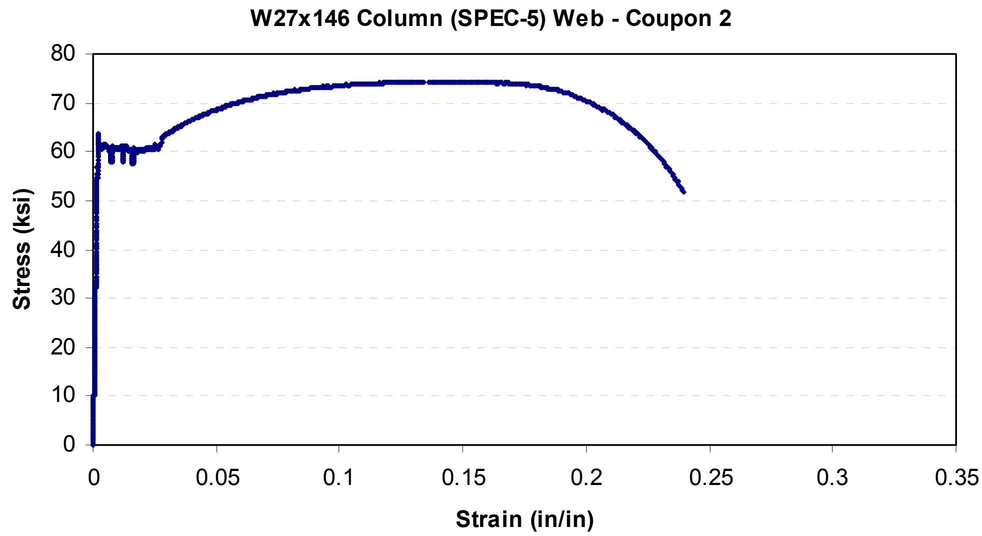
W27x146 Column (SPEC-5) Web - Coupon 2
Stress (ksi)
0
10
20
30
40
50
60
70
80
0
0.05
0.1
0.15
0.2
0.25
0.3
0.35
Strain (in/in)

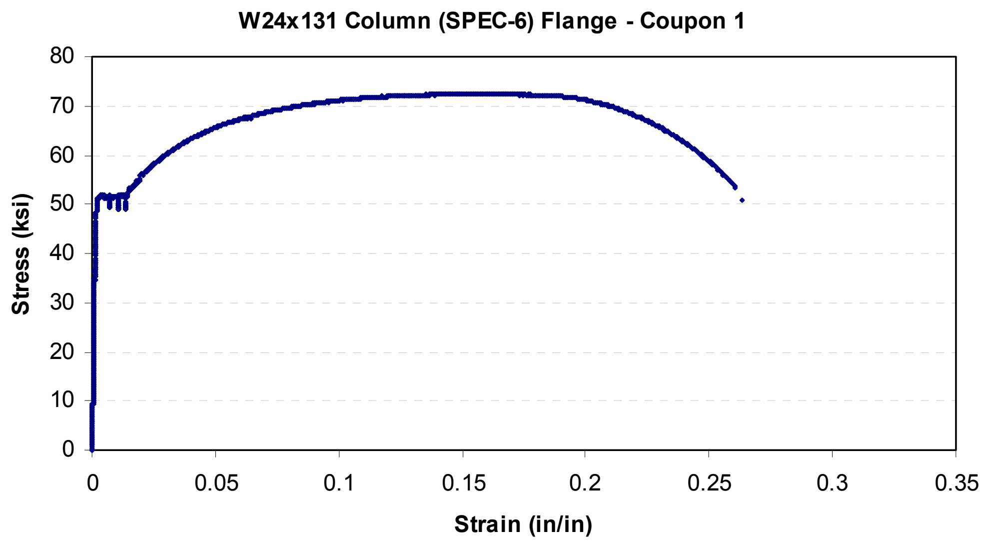
W24x131 Column (SPEC-6) Flange - Coupon 1
Stress (ksi)
0
10
20
30
40
50
60
70
80
0
0.05
0.1
0.15
0.2
0.25
0.3
0.35
Strain (in/in)

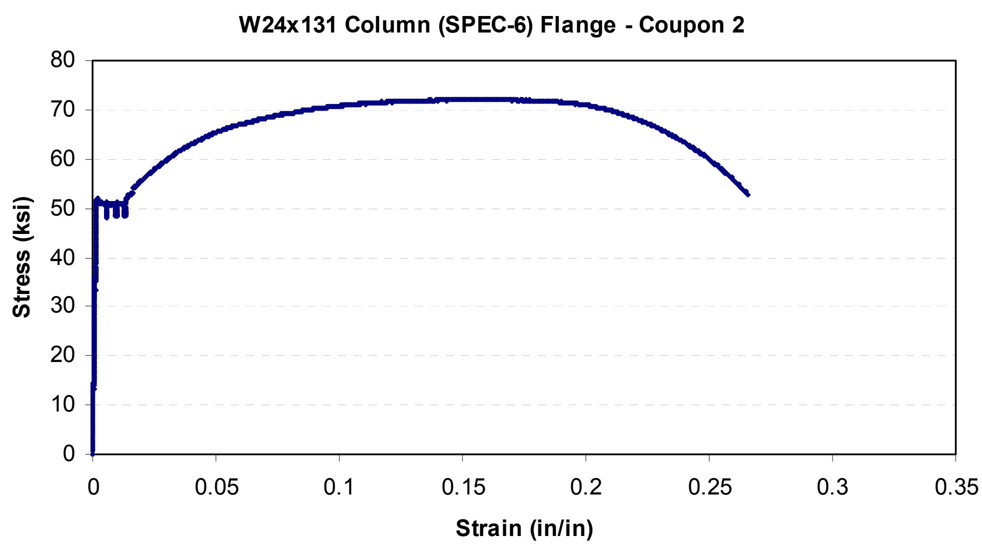
W24x131 Column (SPEC-6) Flange - Coupon 2
Stress (ksi)
0
10
20
30
40
50
60
70
80
0
0.05
0.1
0.15
0.2
0.25
0.3
0.35
Strain (in/in)

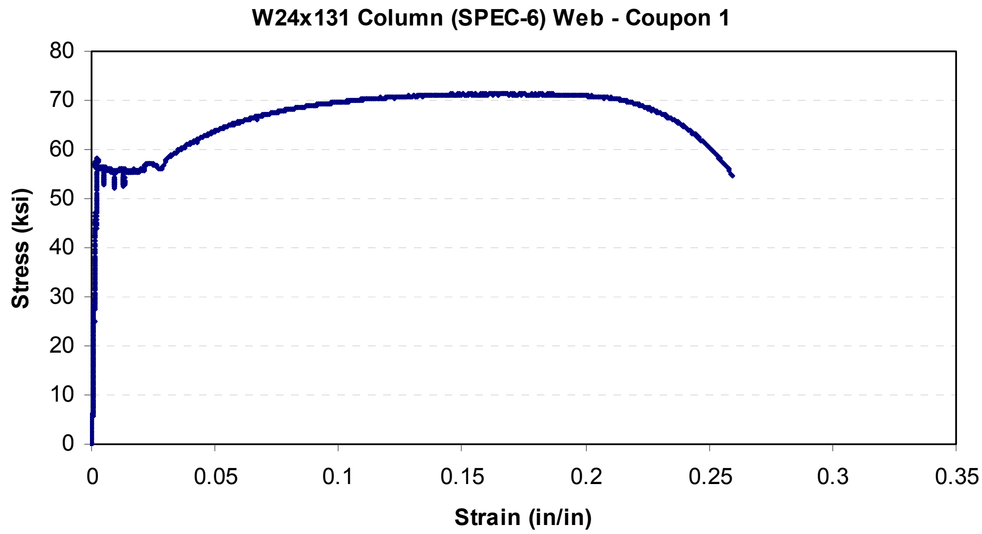
W24x131 Column (SPEC-6) Web - Coupon 1
Stress (ksi)
0
10
20
30
40
50
60
70
80
0
0.05
0.1
0.15
0.2
0.25
0.3
0.35
Strain (in/in)

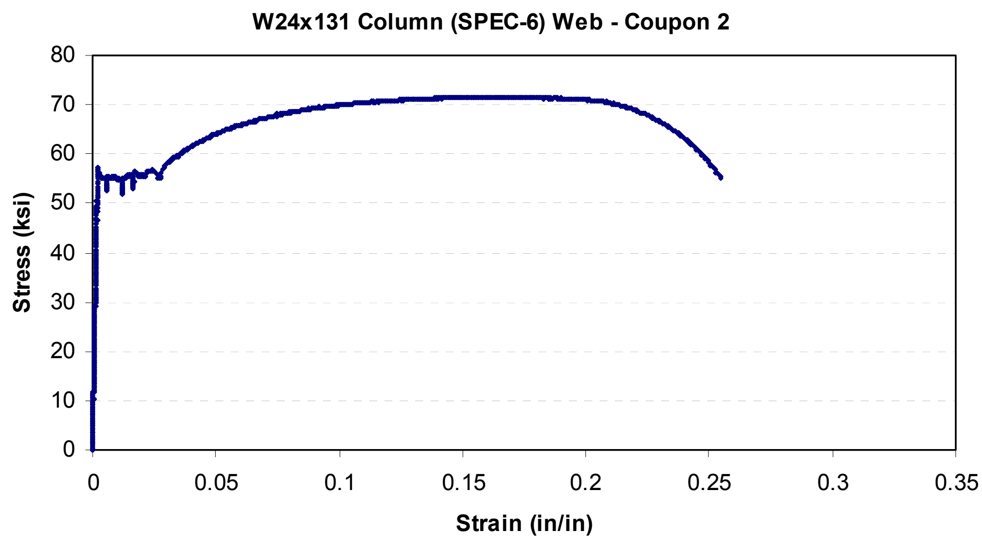
W24x131 Column (SPEC-6) Web - Coupon 2
Stress (ksi)
0
10
20
30
40
50
60
70
80
0
0.05
0.1
0.15
0.2
0.25
0.3
0.35
Strain (in/in)

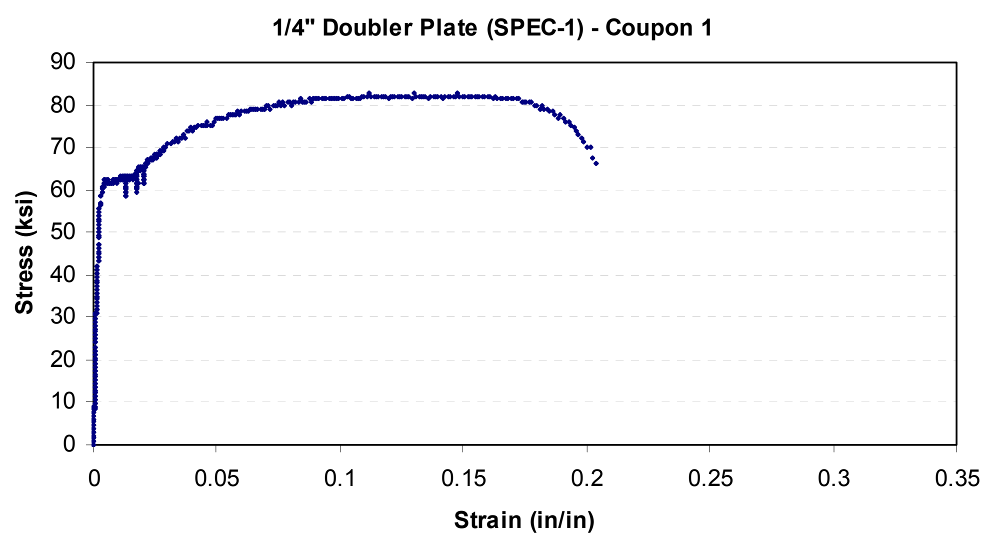
1/4" Doubler Plate (SPEC-1) - Coupon 1
Stress (ksi)
0
10
20
30
40
50
60
70
80
90
0
0.05
0.1
0.15
0.2
0.25
0.3
0.35
Strain (in/in)

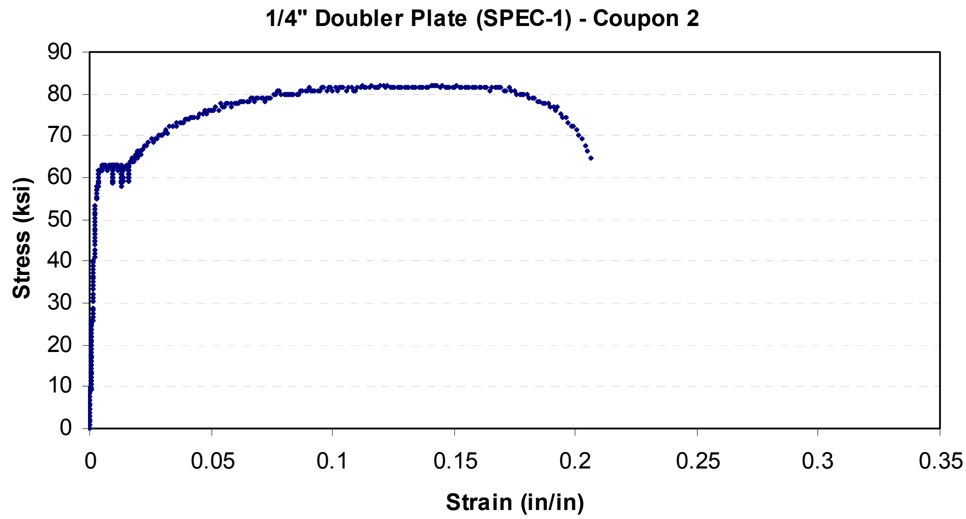
1/4" Doubler Plate (SPEC-1) - Coupon 2
Stress (ksi)
Strain (in/in)
0
10
20
30
40
50
60
70
80
90
0
0.05
0.1
0.15
0.2
0.25
0.3
0.35

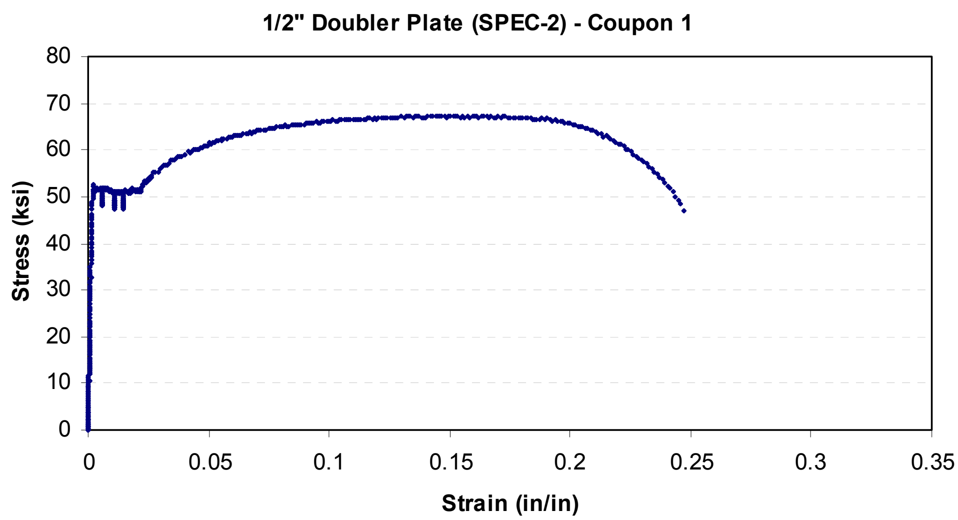
1/2" Doubler Plate (SPEC-2) - Coupon 1
Stress (ksi)
Strain (in/in)
0
10
20
30
40
50
60
70
80
0
0.05
0.1
0.15
0.2
0.25
0.3
0.35

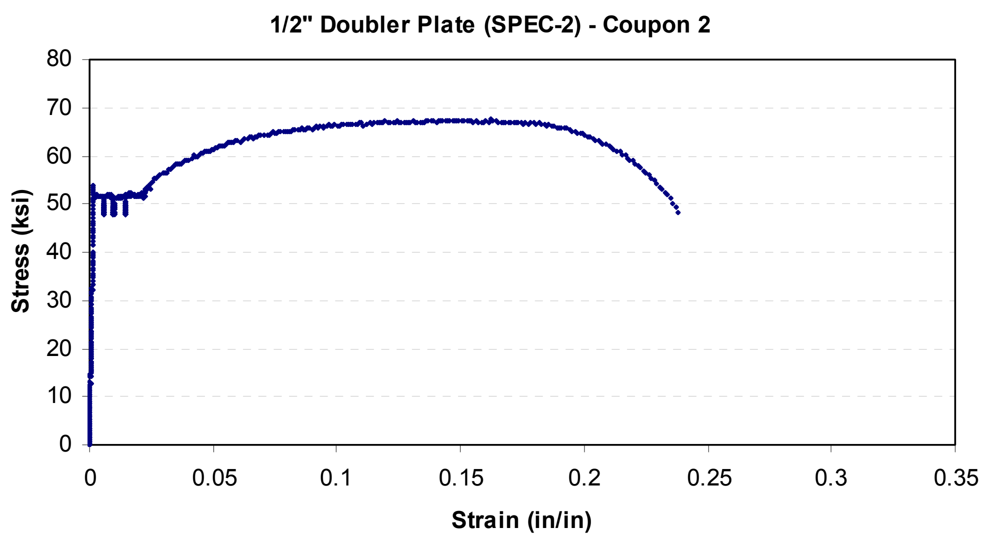
1/2" Doubler Plate (SPEC-2) - Coupon 2
Stress (ksi)
Strain (in/in)
0
10
20
30
40
50
60
70
80
0
0.05
0.1
0.15
0.2
0.25
0.3
0.35

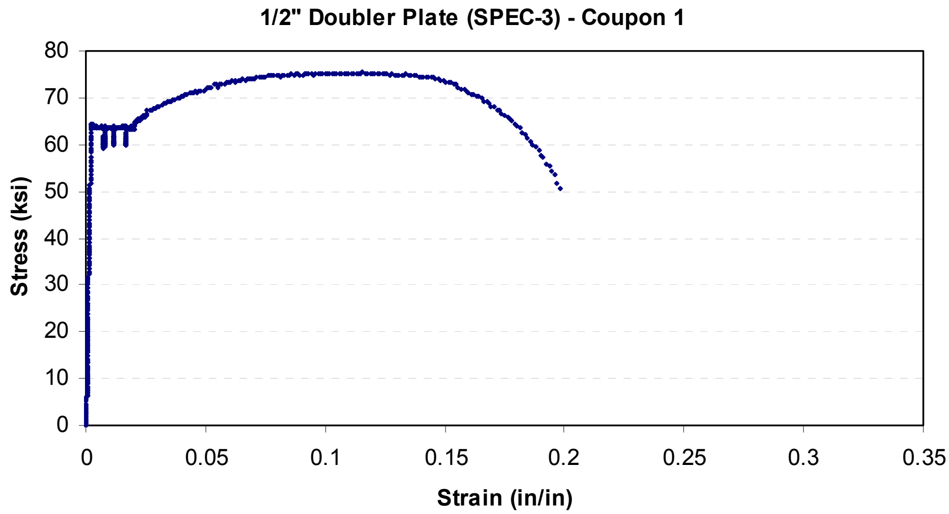
1/2" Doubler Plate (SPEC-3) - Coupon 1
Stress (ksi)
0
10
20
30
40
50
60
70
80
0
0.05
0.1
0.15
0.2
0.25
0.3
0.35
Strain (in/in)

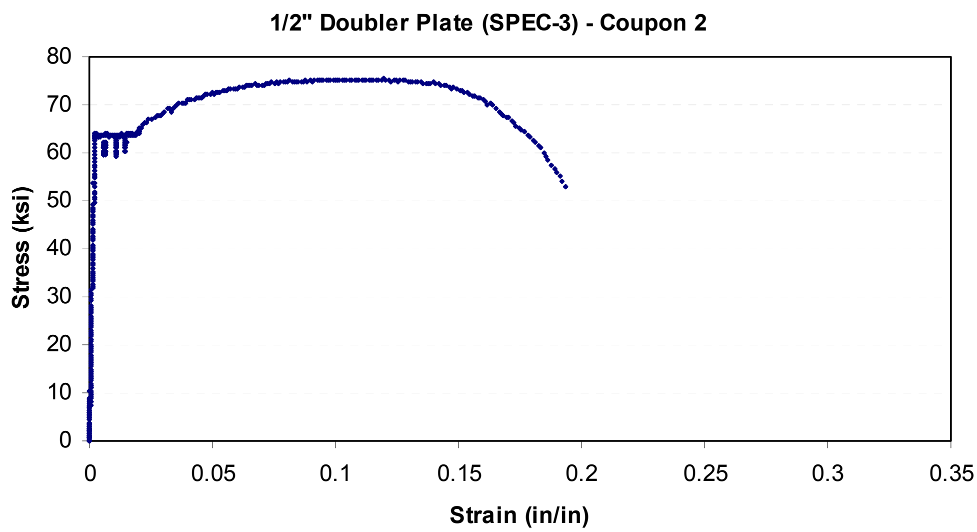
1/2" Doubler Plate (SPEC-3) - Coupon 2
Stress (ksi)
0
10
20
30
40
50
60
70
80
0
0.05
0.1
0.15
0.2
0.25
0.3
0.35
Strain (in/in)

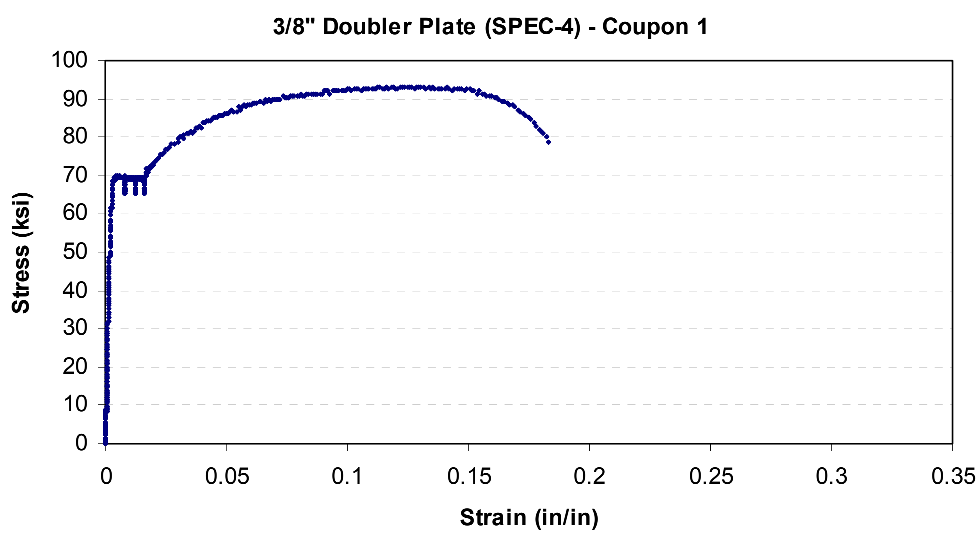
3/8" Doubler Plate (SPEC-4) - Coupon 1
Stress (ksi)
0
10
20
30
40
50
60
70
80
90
100
0
0.05
0.1
0.15
0.2
0.25
0.3
0.35
Strain (in/in)

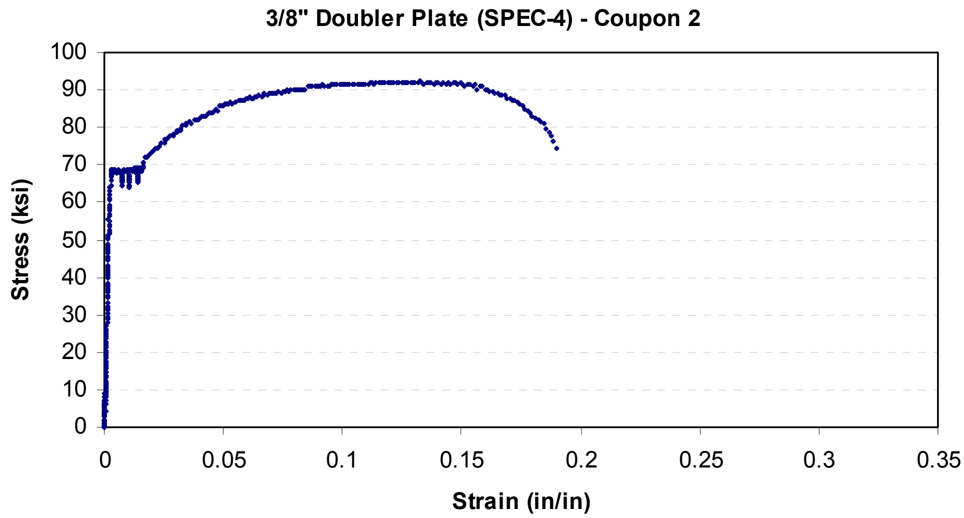
3/8" Doubler Plate (SPEC-4) - Coupon 2
Stress (ksi)
Strain (in/in)
0
10
20
30
40
50
60
70
80
90
100
0
0.05
0.1
0.15
0.2
0.25
0.3
0.35

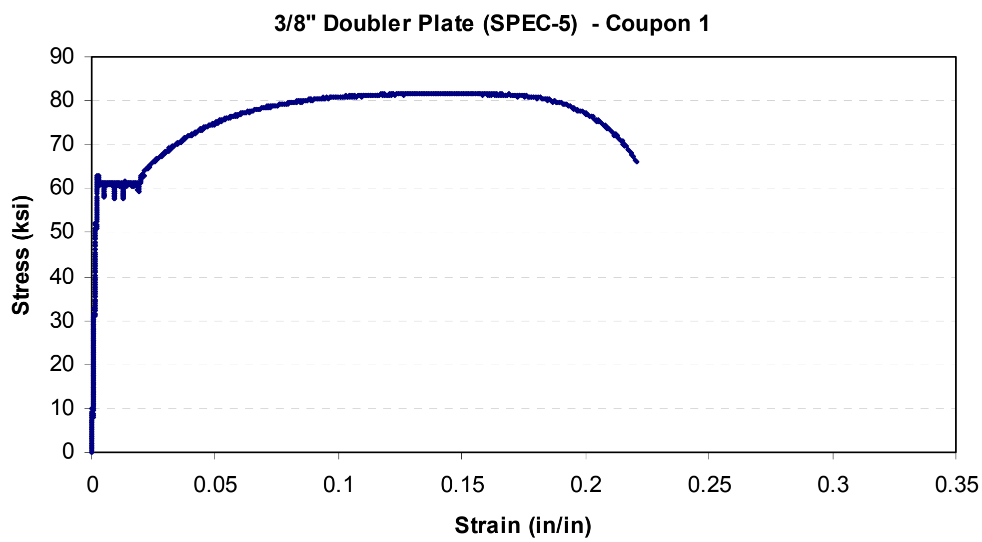
3/8" Doubler Plate (SPEC-5) - Coupon 1
Stress (ksi)
Strain (in/in)
0
10
20
30
40
50
60
70
80
90
0
0.05
0.1
0.15
0.2
0.25
0.3
0.35

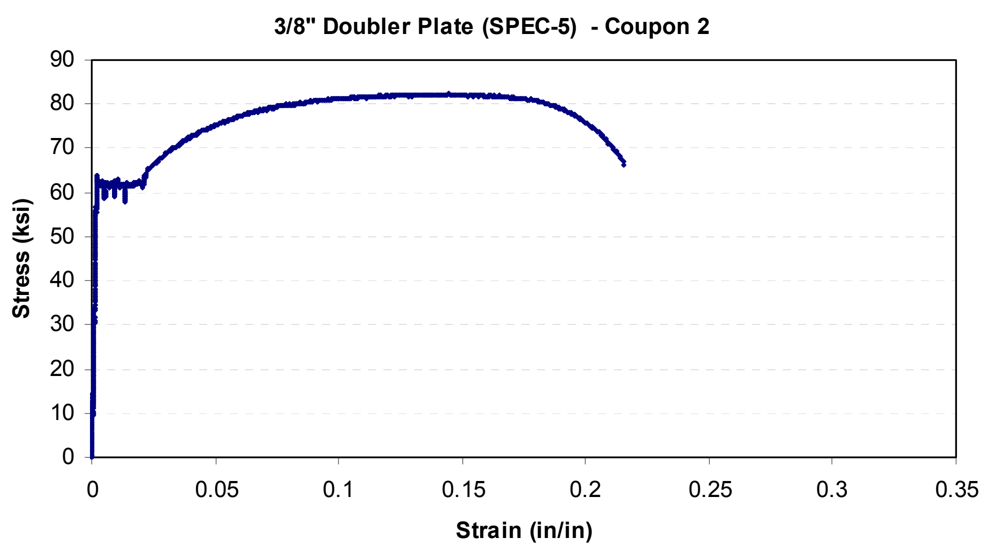
3/8" Doubler Plate (SPEC-5) - Coupon 2
Stress (ksi)
Strain (in/in)
0
10
20
30
40
50
60
70
80
90
0
0.05
0.1
0.15
0.2
0.25
0.3
0.35

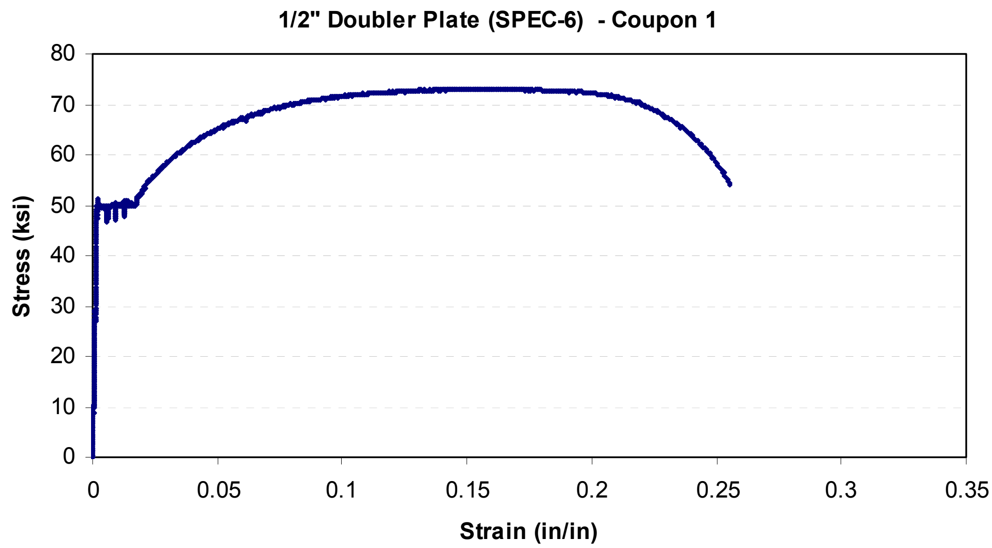
1/2" Doubler Plate (SPEC-6) - Coupon 1
Stress (ksi)
Strain (in/in)
0
10
20
30
40
50
60
70
80
0
0.05
0.1
0.15
0.2
0.25
0.3
0.35

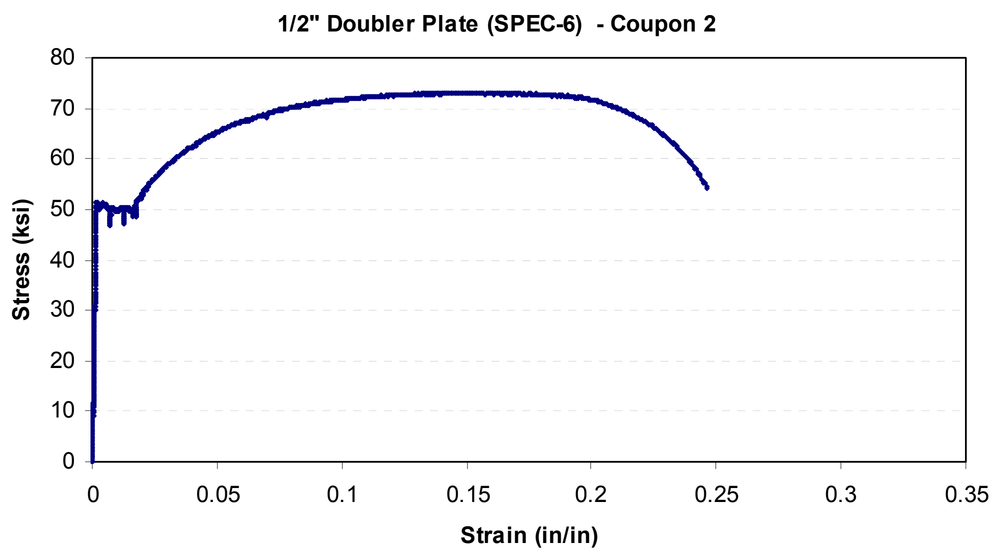
1/2" Doubler Plate (SPEC-6) - Coupon 2
Stress (ksi)
Strain (in/in)
0
10
20
30
40
50
60
70
80
0
0.05
0.1
0.15
0.2
0.25
0.3
0.35

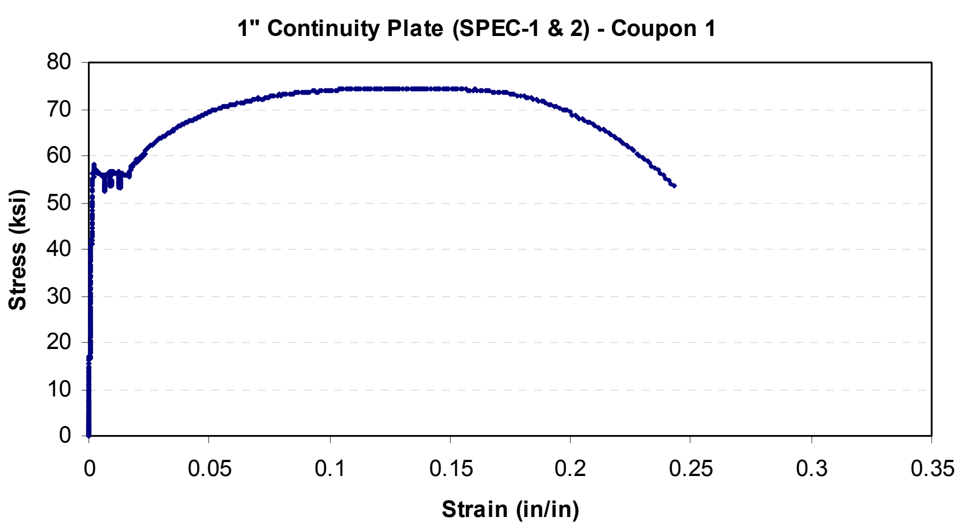
1" Continuity Plate (SPEC-1 & 2) - Coupon 1
Stress (ksi)
Strain (in/in)
0
10
20
30
40
50
60
70
80
0
0.05
0.1
0.15
0.2
0.25
0.3
0.35

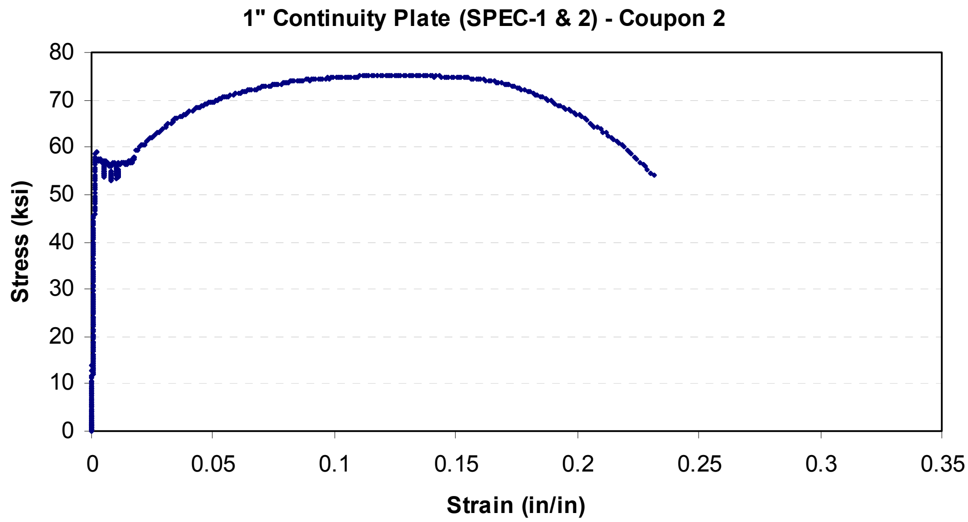
1" Continuity Plate (SPEC-1 & 2) - Coupon 2
Stress (ksi)
Strain (in/in)
0
10
20
30
40
50
60
70
80
0
0.05
0.1
0.15
0.2
0.25
0.3
0.35

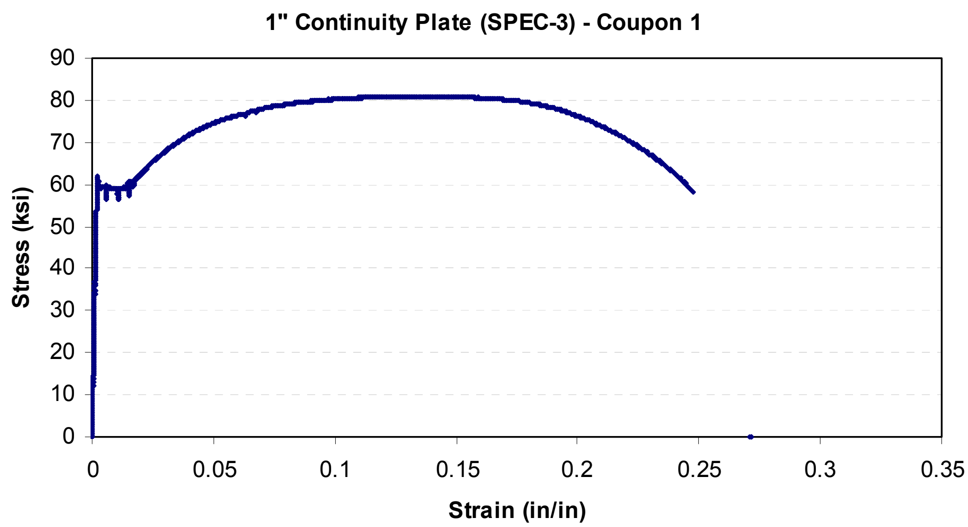
1" Continuity Plate (SPEC-3) - Coupon 1
Stress (ksi)
Strain (in/in)
0
10
20
30
40
50
60
70
80
90
0
0.05
0.1
0.15
0.2
0.25
0.3
0.35

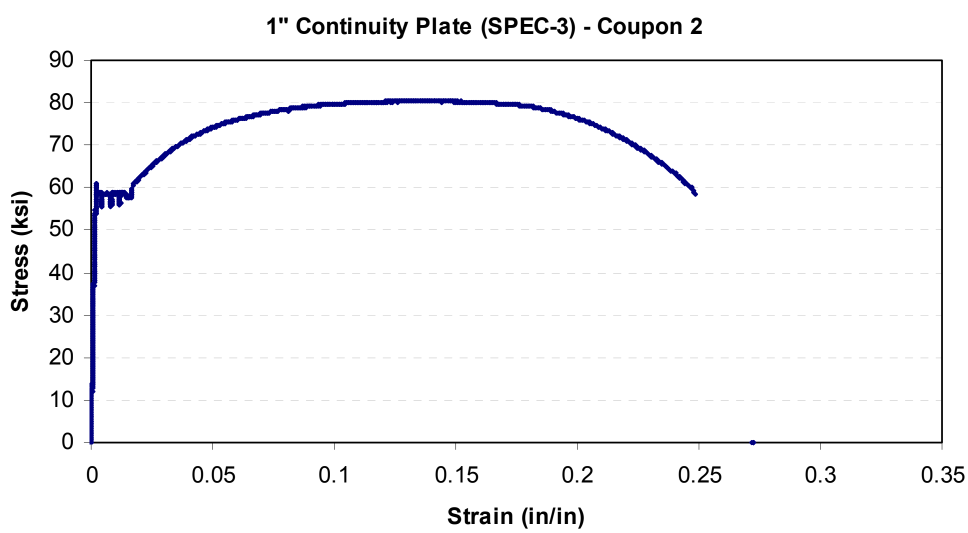
1" Continuity Plate (SPEC-3) - Coupon 2
Stress (ksi)
Strain (in/in)
0
10
20
30
40
50
60
70
80
90
0
0.05
0.1
0.15
0.2
0.25
0.3
0.35

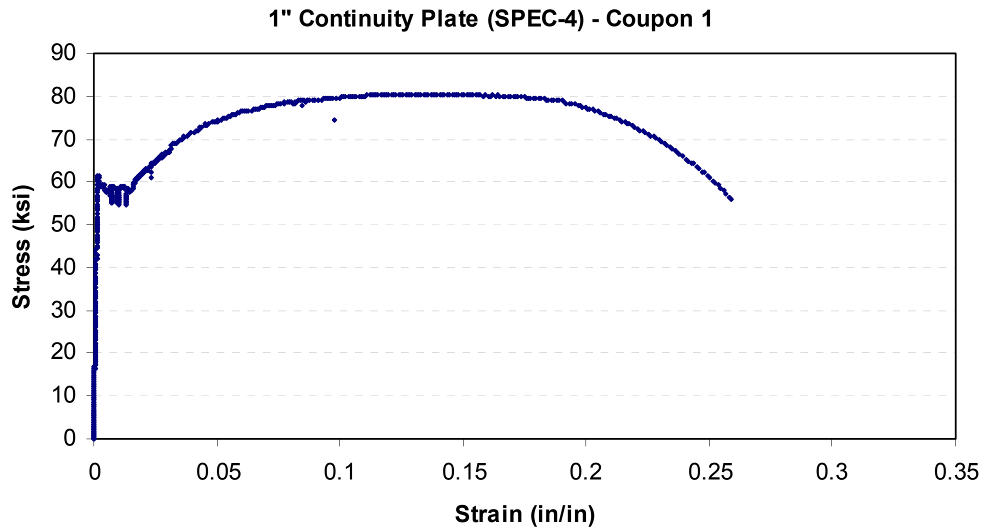
1" Continuity Plate (SPEC-4) - Coupon 1
Stress (ksi)
Strain (in/in)
0
10
20
30
40
50
60
70
80
90
0
0.05
0.1
0.15
0.2
0.25
0.3
0.35

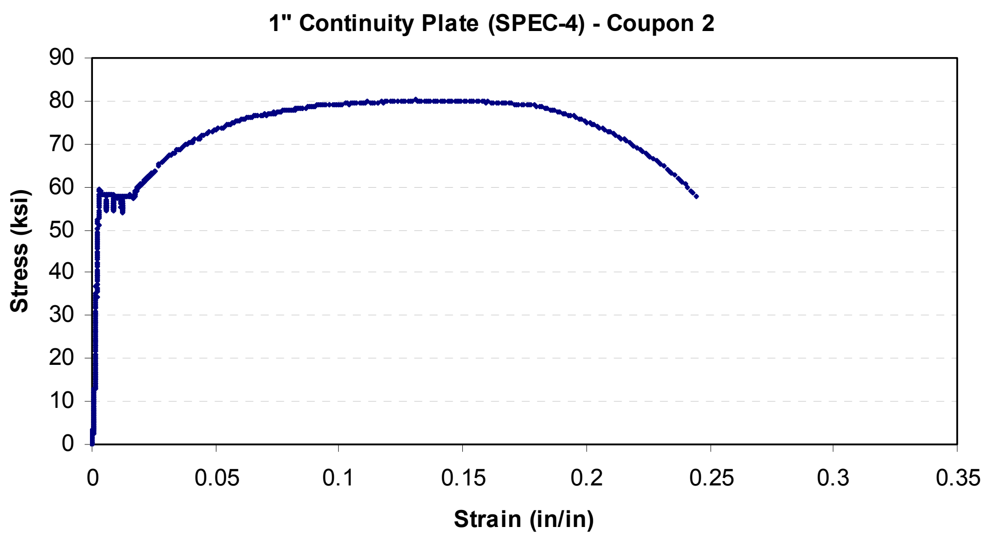
1" Continuity Plate (SPEC-4) - Coupon 2
Stress (ksi)
Strain (in/in)
0
10
20
30
40
50
60
70
80
90
0
0.05
0.1
0.15
0.2
0.25
0.3
0.35

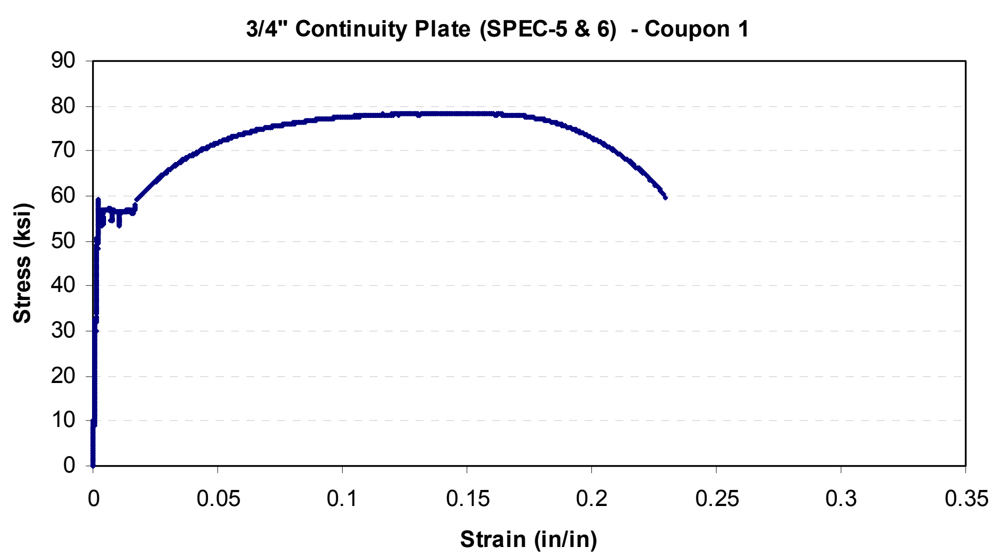
3/4" Continuity Plate (SPEC-5 & 6) - Coupon 1
Stress (ksi)
Strain (in/in)
0
10
20
30
40
50
60
70
80
90
0
0.05
0.1
0.15
0.2
0.25
0.3
0.35

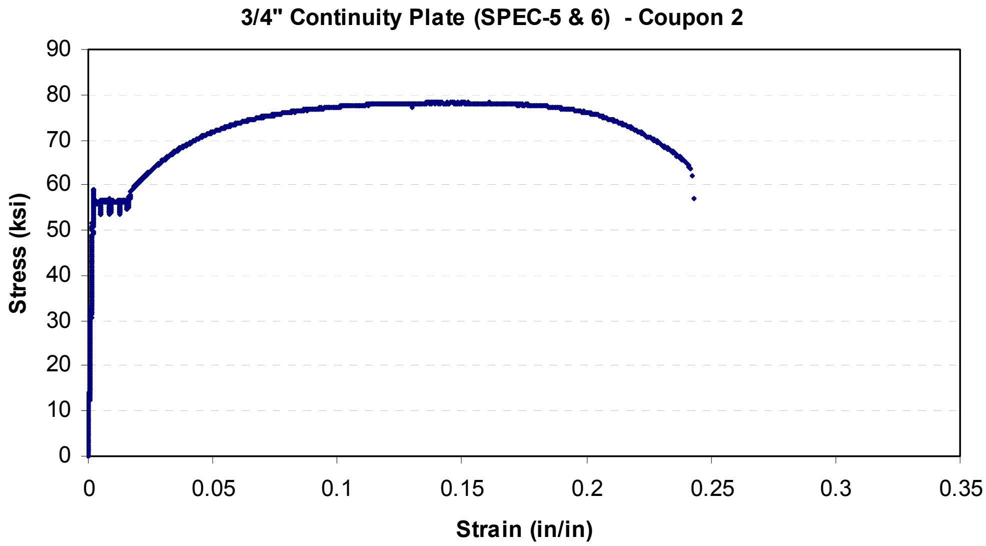
3/4" Continuity Plate (SPEC-5 & 6) - Coupon 2
Stress (ksi)
0
10
20
30
40
50
60
70
80
90
Strain (in/in)
0
0.05
0.1
0.15
0.2
0.25
0.3
0.35

Appendix E

Weld Metal Charpy V-Notch Toughness Test Report

(This page left blank)

Test Plate ID	Weld metal		Preheat Temp. (°F)	Interpass Temp. (°F)	Current Type (Polarity)	AMP	WFS (IPM)	Voltage (Volts)	Travel Speed (IPM)	Layer /Pass	Heat Input (KJ/in)	Comments
	Class	Diameter										
TP-1	E70T-6	3/32”	70	300±25	DCEP	440	240	24	13.5	4/10	46.9	CVN, tensile
TP-2	E70T-6	3/32”	70	200±50	DCEP	330	155	22	11	5/13	39.6	CVN, tensile
TP-3	E70T-6	3/32”	70	200±50	DCEP	340	156	22	11.5	5/13	39.0	CVN
TP-4	E70T-6	3/32”	300±25	500±50	DCEP	480	294	28	10.3	3/5	78.3	CVN, tensile
TP-5	E70T-6	3/32”	300±25	500±50	DCEP	480	294	28	10.3	3/5	78.3	CVN
TP-6	E71T-8	0.068”	70	300±25	DCEN	260	190	21	9	4/12	36.4	CVN
TP-7	E71T-8	0.068”	70	300±25	DCEN	260	190	21	9	4/12	36.4	CVN
TP-8	E70T-1	3/32”	70	300±25	DCEP	400	171	28	12.5	4/10	53.8	CVN
TP-9	E70T-1	3/32”	70	300±25	DCEP	400	171	28	12	4/10	56.0	CVN
TP-10	/E71T-8	3/32” /0.068”	70	300±25	DCEP / DCEN	400 /260	171 /168	28 /20	12 /8.5	5/14	56.0 /36.7	CVN
TP-11	E70T-6	3/32”	70	200±50	DCEP	430	210	24	12	5/10	51.6	CVN
TP-12	E70T-6	3/32”	70	200±50	DCEP	465	270	26	9.5	4/8	76.4	CVN
TP-13	E70T-6	3/32”	150	500±25	DCEP	460	246	26	9.5	7/15	75.5	Mockup Spec
TP-14	E70T-6	3/32”	70	300	DCEP	460	240	26	14.6	5/9	49.2	CVN
TP-15	E70T-6	3/32”	150	300±25	DCEP	460	240	26	15	7/13	47.8	Mockup Spec
TP-16	E70T-6	3/32”	70	300±25	DCEP	460	240	26	15	5/9	47.8	No CVN, tensile
TP-17	E70T-6	3/32”	70	300±25	DCEP	460	240	26	15	5/9	47.8	CVN and tensile
TP-18	E70T-6	3/32”	150	300±25	DCEP	460	240	26	15	7/15	47.87	Mockup Spec

The above table is the weld metal CVN test plates WPS Summary. TP13, TP15 and TP18 are connection mock-ups for Supplemental Welder Qualification according to FEMA-353 (Part I 3.3.1 and Appendix B).

Test Results

1. TP-1 to TP-10

Specimen Number	Electrodes	Test Temperature (°F)	Actual Temperature (°F)	Energy Absorbed (ft-lb)	Notes	Average After Dropping the Highest and Lowest
TP1-1	E70T-6 D=3/32"	0	0±1	14.5		16.2
TP1-2		0	0±1	19.0		
TP1-3		0	0±1	21.0		
TP1-4		0	0±1	15.0		
TP1-5		0	0±1	12.5		
TP2-1	E70T-6 D=3/32" Low HIL	70	73.4	44.0		38.8
TP2-2		70	73.4	37.0		
TP2-3		70	73.4	39.5		
TP2-4		70	73.4	40.0		
TP2-5		70	73.4	21.0		
TP3-1	E70T-6 D=3/32" Low HIL	70	73.6	43.0		34.0
TP3-2		70	73.6	39.0		
TP3-3		70	73.6	31.0		
TP3-4		70	73.6	29.0		
TP3-5		70	73.6	32.0		
TP4-1	E70T-6 D=3/32" High HIL	70	73.8	46.0		44.5
TP4-2		70	73.8	46.5		
TP4-3		70	73.8	39.5		
TP4-4		70	73.8	44.5		
TP4-5		70	73.8	43.0		
TP5-1	E70T-6 D=3/32" High HIL	70	73.8	48.5		51.2
TP5-2		70	73.8	54.0		
TP5-3		70	73.8	44.0		
TP5-4		70	73.8	51.5		
TP5-5		70	73.8	53.5		
TP6-1	E71T-8 D=.068"	0	0±1	53.0		55.5
TP6-2		0	0±1	45.0		
TP6-3		0	0±1	62.0		
TP6-4		0	0±1	53.5		
TP6-5		0	0±1	60.0		
TP7-1	E71T-8 D=.068"	70	73.8	89.5		89.2
TP7-2		70	73.8	88.5		

TP7-3		70	73.8	91.0		
TP7-4		70	73.8	89.5		
TP7-5		70	73.8	49.5		
TP8-1	E70T-1 D=3/32"	0	0±1	53.0		46.3
TP8-2		0	0±1	39.0		
TP8-3		0	0±1	41.0		
TP8-4		0	0±1	50.0		
TP8-5		0	0±1	48.0		
TP9-1	E70T-1 D=3/32"	70	73.6	114.0		111.5
TP9-2		70	73.6	111.0		
TP9-3		70	73.6	109.5		
TP9-4		70	73.6	101.0		
TP9-5		70	73.6	121.5		
TP10-1	E70T-1 & E71T-8 Mixed	70	73.6	100.5		94.3
TP10-2		70	73.6	88.5		
TP10-3		70	73.6	96.5		
TP10-4		70	73.6	98.0		
TP10-5		70	73.6	69.0		

2. TP-11 and TP-12

Specimen Number	Electrodes	Test Temperature (°F)	Actual Temperature (°F)	Energy Absorbed (ft-lb)	Notes	Average After Dropping the Highest and Lowest
TP11-1	E70T-6 D=3/32"	70	72.4	54.5		52.8
TP11-2		70	72.4	51.0		
TP11-3		70	72.4	52.0		
TP11-4		70	72.4	57.5		
TP11-5		70	72.4	52.0		
TP12-1	E70T-6 D=3/32"	0	0±1	11.0		10.7
TP12-2		0	0±1	24.0		
TP12-3		0	0±1	9.0		
TP12-4		0	0±1	10.5		
TP12-5		0	0±1	10.5		

3. TP-13

Specimen Number	Electrodes	Test Temperature (°F)	Actual Temperature (°F)	Energy Absorbed (ft-lb)	Notes	Average After Dropping the Highest and Lowest
TP13-1	E70T-6	0	0±1	7.0		8.3

TP13-2	D=3/32"	0	0±1	6.0		
TP13-3		0	0±1	10.0		
TP13-4		0	0±1	8.0		
TP13-5		0	0±1	13.0		
TP13-6		70	71.8	24.5		26.3
TP13-7		70	71.8	18.5		
TP13-8		70	71.8	27.5		
TP13-9		70	71.8	27.0		
TP13-10		70	71.8	28.0		
TP13-11		120	120±1	25.0	Average of Three	33.0
TP13-12		120	120±1	38.5		
TP13-13		120	120±1	35.5		
TP13-14		212	208	40.0	Average of Three	45.3
TP13-15		212	208	46.5		
TP13-16		212	208	49.5		

4. TP-14

Specimen Number	Electrodes	Test Temperature (°F)	Actual Temperature (°F)	Energy Absorbed (ft-lb)	Notes	Average After Dropping the Highest and Lowest
TP14-1	E70T-6 D=3/32"	0	0±1	31.0		34.3
TP14-2		0	0±1	35.0		
TP14-3		0	0±1	35.5		
TP14-4		0	0±1	34.0		
TP14-5		0	0±1	34.0		
TP14-6		70	73	61.5		61.5
TP14-7		70	73	63.5		
TP14-8		70	73	63.0		
TP14-9		70	73	50.0		
TP14-10		70	73	60.0		
TP14-11		-20	-20	27.0	Average of Three	28.7
TP14-12		-20	-20	27.5		
TP14-13		-20	-20	31.5		
TP14-14		40	40	49.0	Average of Three	46.3
TP14-15		40	40	44.5		
TP14-16		40	40	45.5		

5. TP-15

Specimen Number	Electrodes	Test Temperature (°F)	Actual Temperature (°F)	Energy Absorbed (ft-lb)	Average (ft-lb)
TP15-1	E70T-6	0	0±1	25.0	24.3
TP15-2		0	0±1	22	
TP15-3		0	0±1	26	
TP15-4		70	74.6	44.0	42.5
TP15-5		70	74.6	40.5	
TP15-6		70	74.6	43	

6. TP-17

Specimen Number	Electrodes	Test Temperature (°F)	Actual Temperature (°F)	Energy Absorbed (ft-lb)	Average (ft-lb)
TP17-1	E70T-6	0	0±1	29.5	30.7
TP17-2		0	0±1	29.0	
TP17-3		0	0±1	33.5	
TP17-4		70	75.4	49.0	50.8
TP17-5		70	75.4	52.5	
TP17-6		70	75.4	51.0	

7. TP-18

Specimen Number	Electrodes	Test Temperature (°F)	Actual Temperature (°F)	Energy Absorbed (ft-lb)	Average (ft-lb)
TP18-1	E70T-6	0	0±1	24.0	25.8
TP18-2		0	0±1	23.5	
TP18-3		0	0±1	25.5	
TP18-4		0	0±1	28.5	
TP18-5		0	0±1	27.5	
TP18-6		70	73.8	48.0	45.6
TP18-7		70	73.8	43.5	
TP18-8		70	73.8	48.5	
TP18-9		70	73.8	41.5	
TP18-10		70	73.8	44.0	
TP18-11		70	73.8	49.0	
TP18-12		70	73.8	49.0	
TP18-13		70	73.8	50.0	
TP18-14		70	73.8	51.0	

TP18-15		70	73.8	41.5	
TP18-16		70	73.8	42.5	
TP18-17		70	73.8	39.5	
TP18-18		70	73.8	44.5	

Appendix F

SPEC-1, SPEC-2, and SPEC-6 Fracture Surface SEM Pictures

(This page left blank)

1. SPEC-1

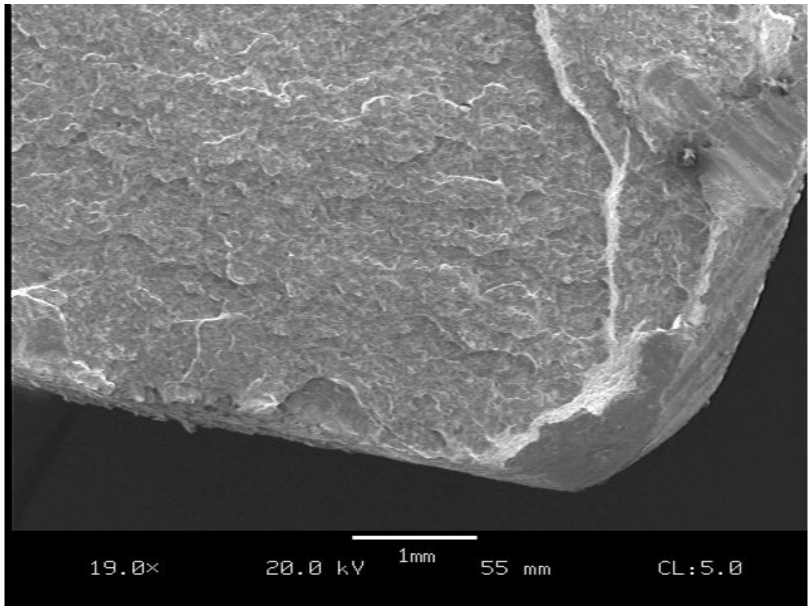

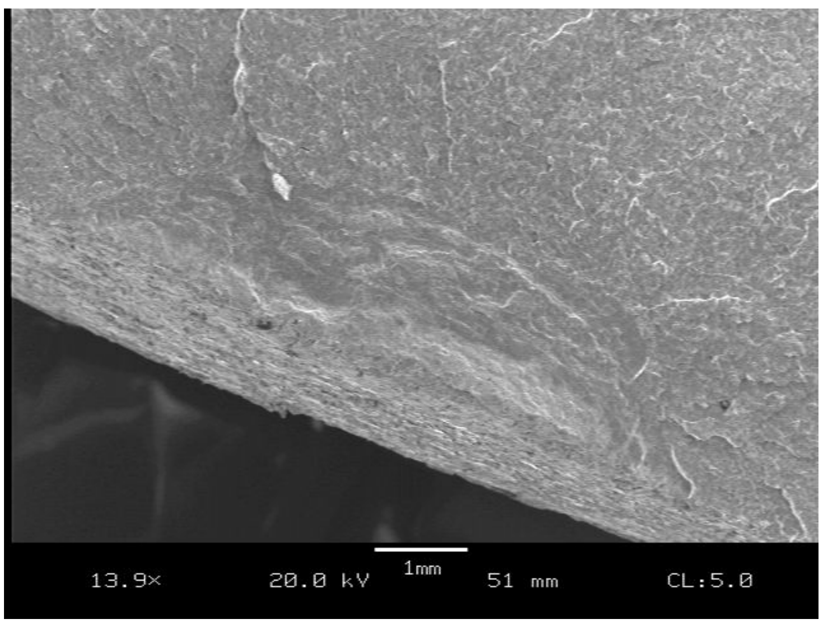

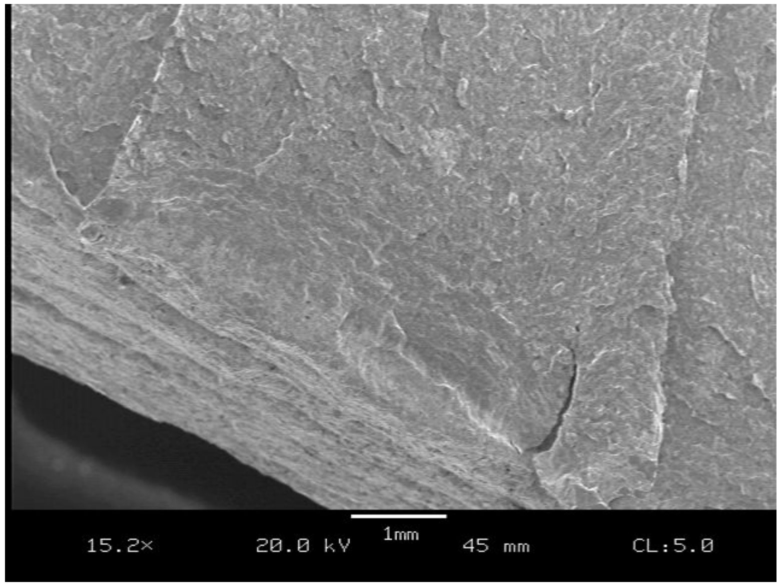
15.2×
20.0 kV
1mm
45 mm
CL:5.0

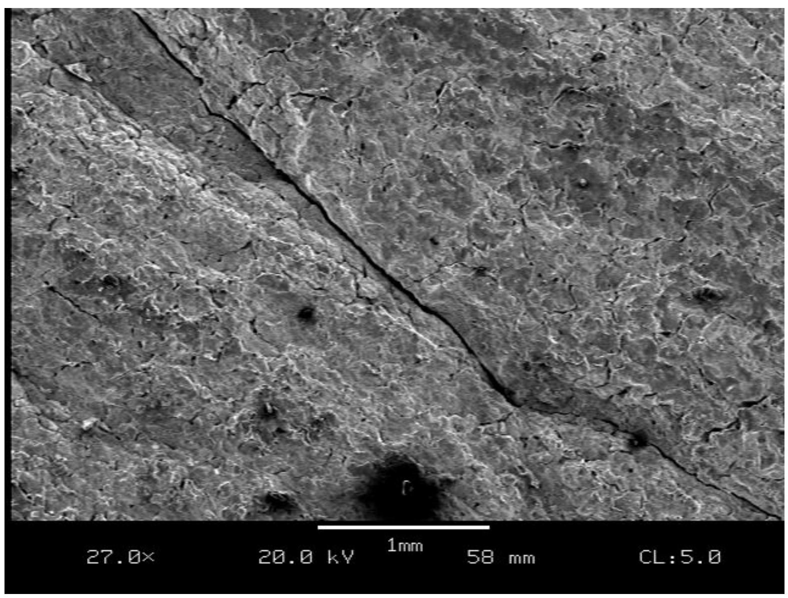
27.0×
20.0 kV
1mm
58 mm
CL:5.0

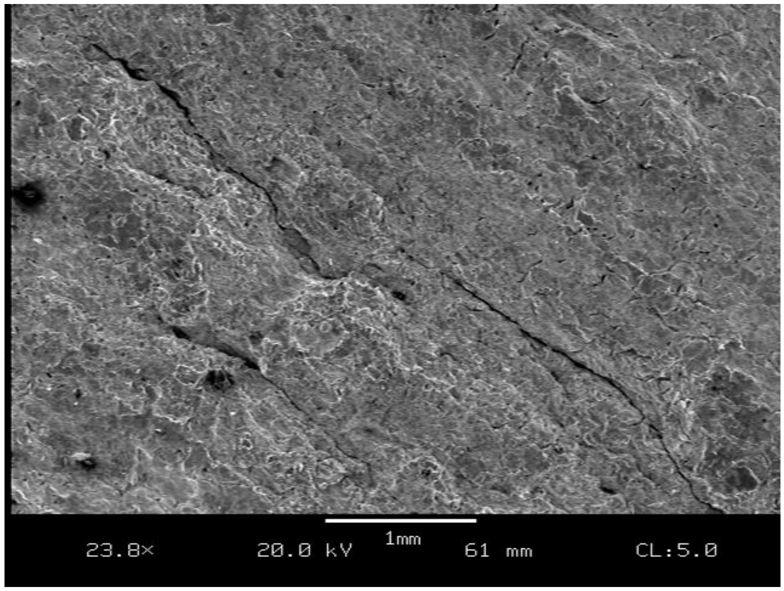
1mm
23.8×
20.0 kV
61 mm
CL:5.0

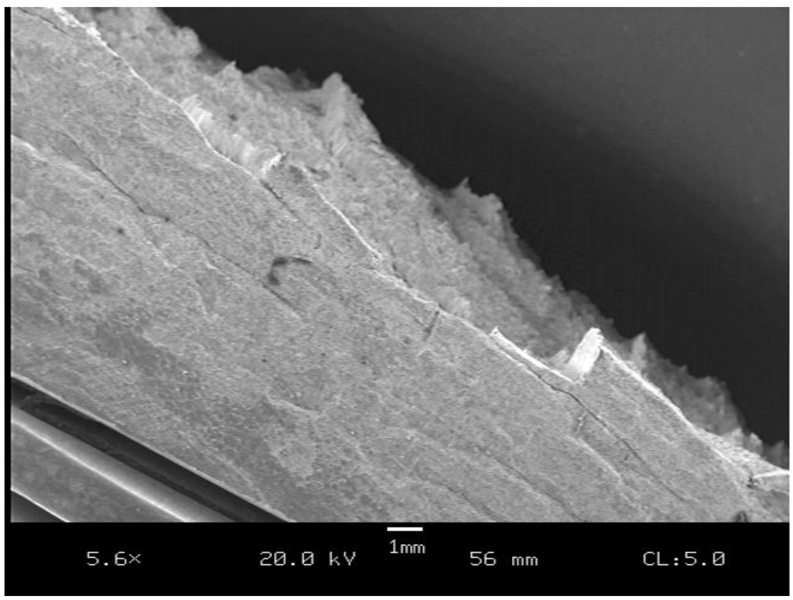
1mm
5.6×
20.0 kV
56 mm
CL:5.0

2. SPEC-2

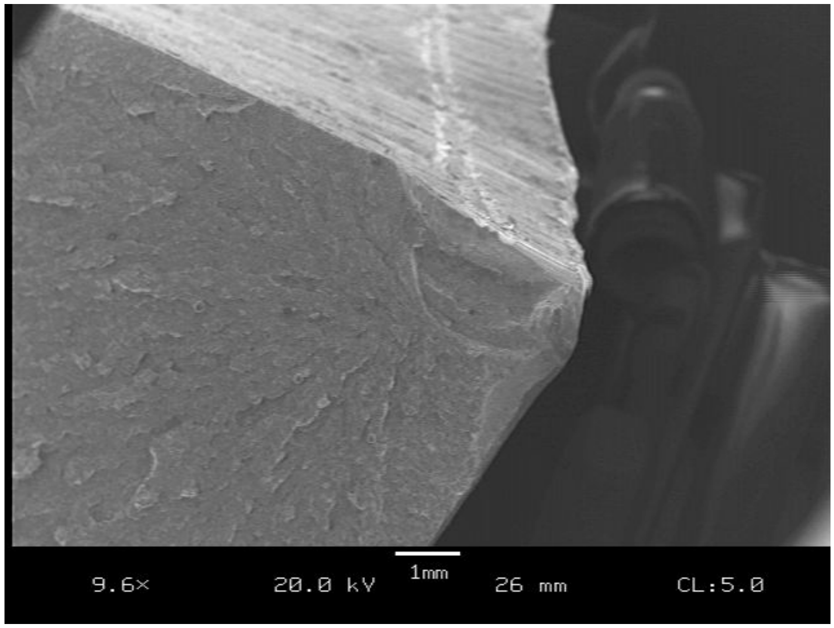

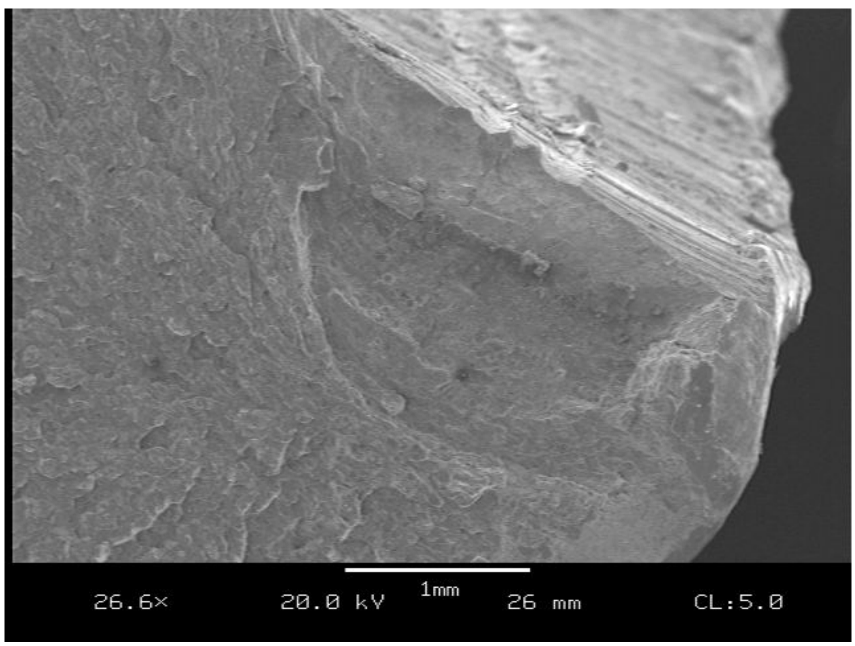

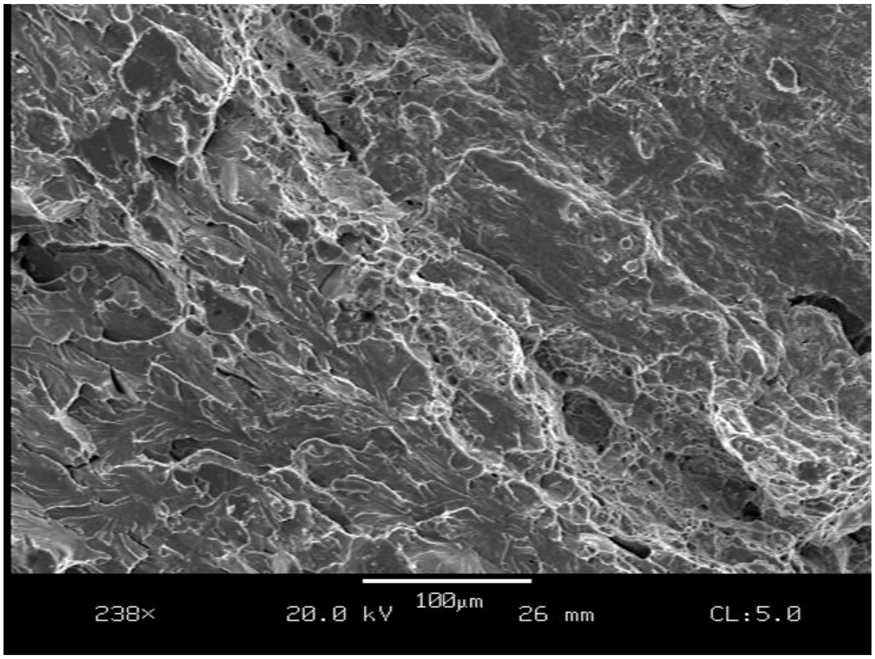
238×
20.0 kV
100µm
26 mm
CL:5.0

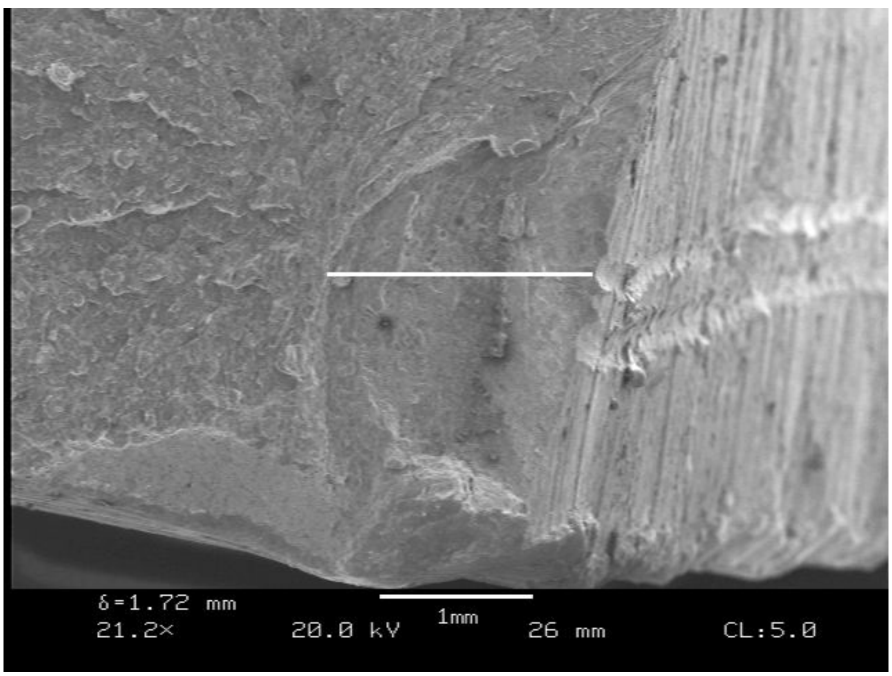
δ=1.72 mm
21.2×
20.0 kV
1mm
26 mm
CL:5.0

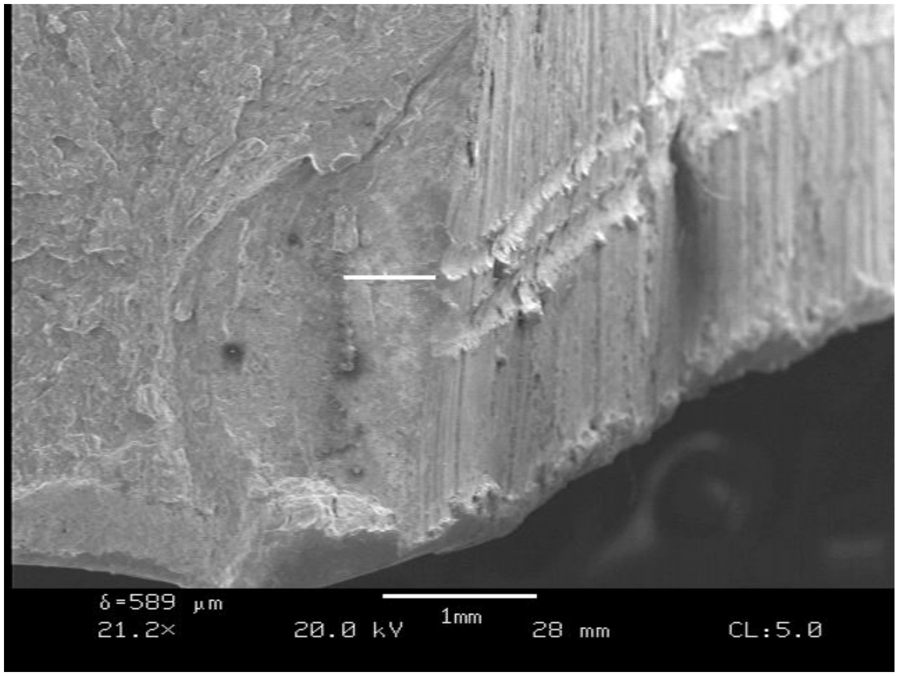
δ=589 μm
21.2×
20.0 kV
1mm
28 mm
CL:5.0

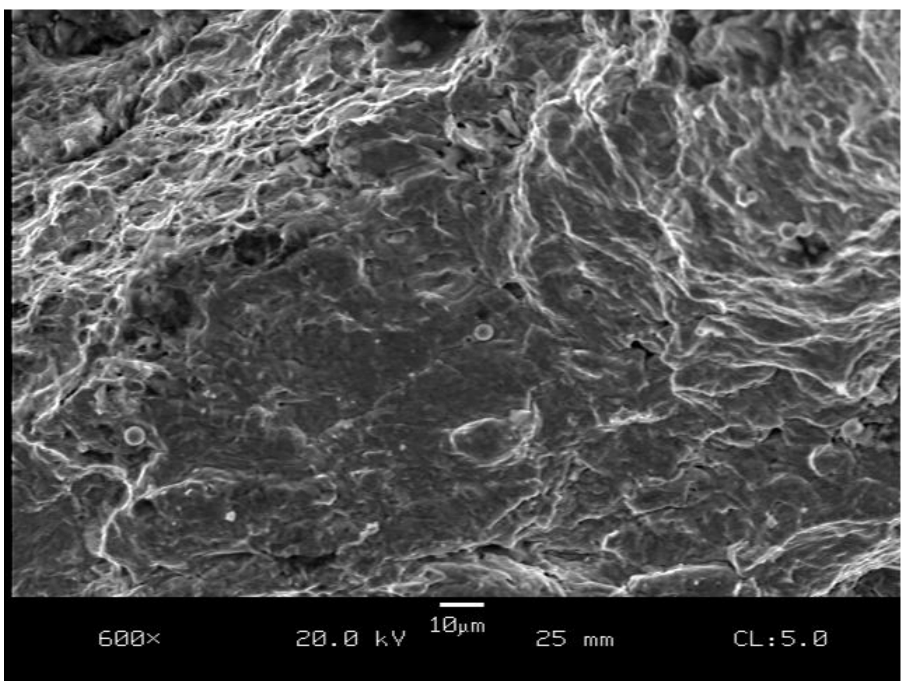
600×
20.0 kV
10μm
25 mm
CL:5.0

3. SPEC-6

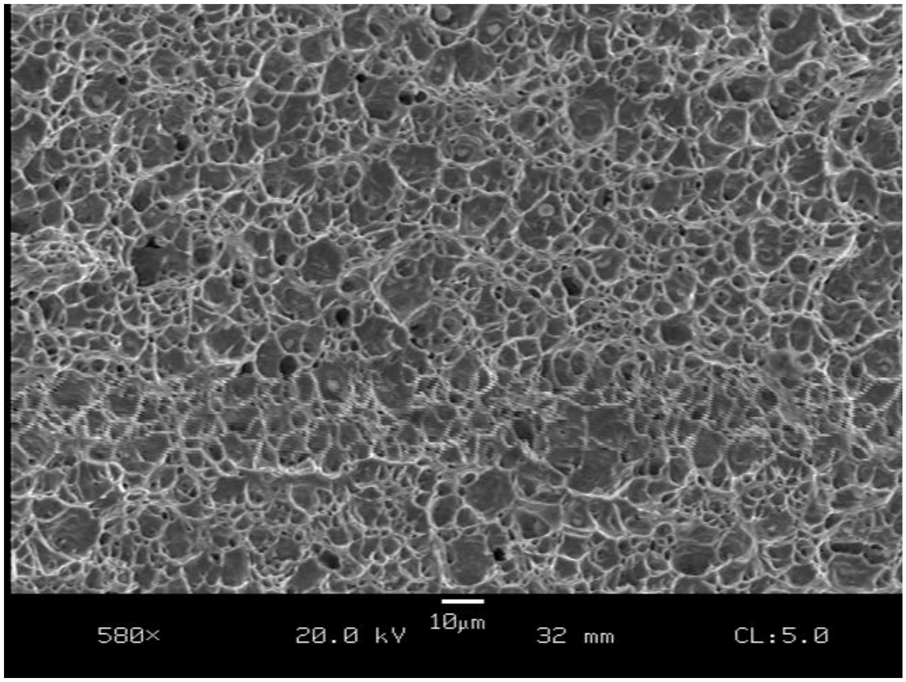

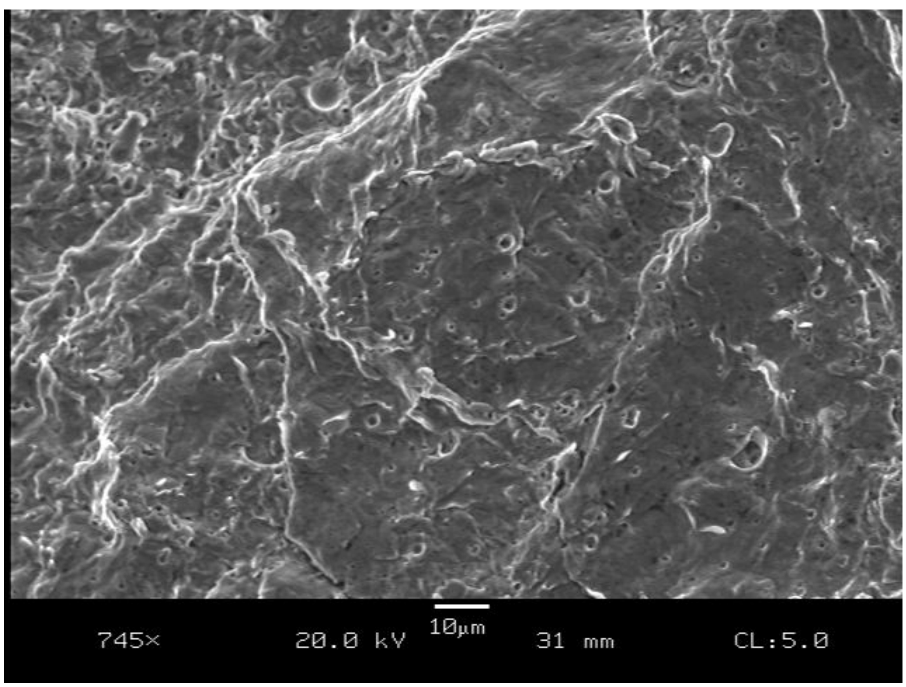

(This page left blank)

Appendix G

Warping Normal Stress Calculation – Solution for θ”

(This page left blank)

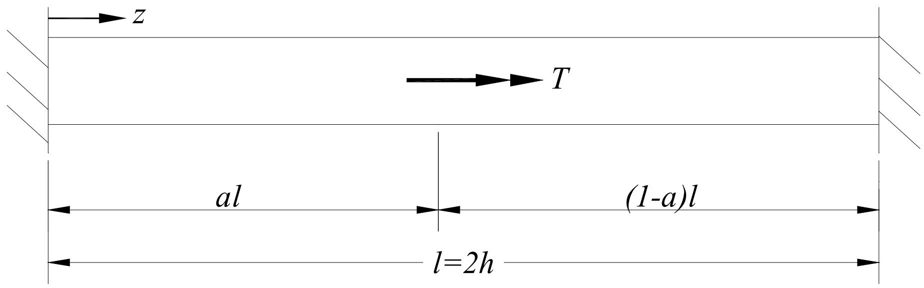

1. Method 1: Use the charts in Appendix B of *Torsional Analysis of Structural Steel Members*, AISC Steel Design Guide Series 9 (Seaburg and Carter, 1997), considering Case 6. Since α is between 0.3 and 0.5, the value for θ" can be interpolated between the charts with α = 0.3 and α = 0.5. The charts are given below.

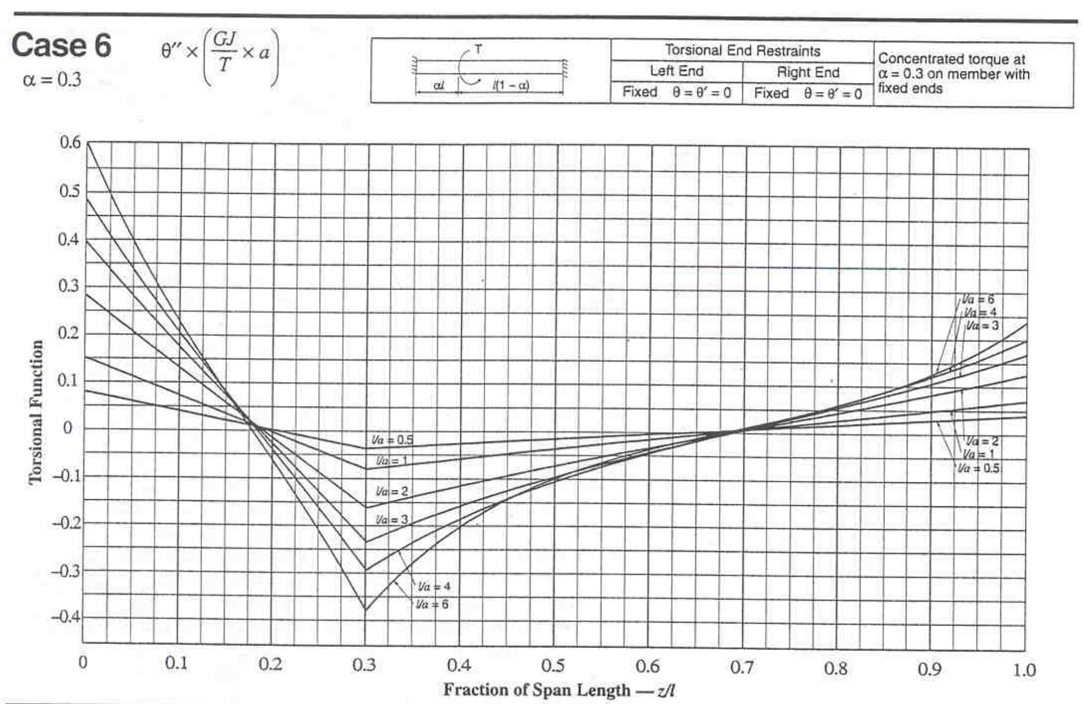

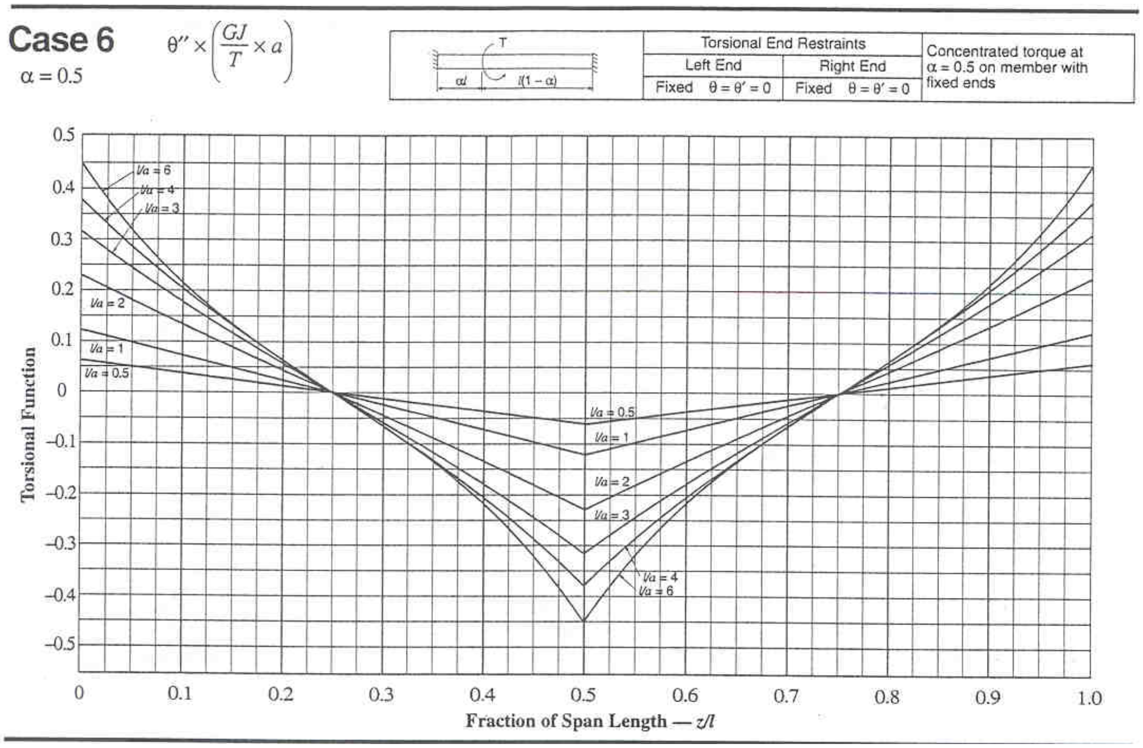

2. Method 2: Differentiate the solution from the differential equation for the column twist angle θ.
   The solution for Case 6 is as follows (see Appendix C of *Torsional Analysis of Structural Steel Members* (Seaburg and Carter, 1997)):

When $0 \le z \le \alpha l$

$$\theta = \frac{Ta}{(H+1)GJ}\left\{\left[H \times \left(\frac{1}{\sinh\frac{l}{a}} + \sinh\frac{\alpha l}{a} - \frac{\cosh\frac{\alpha l}{a}}{\tanh\frac{l}{a}}\right) + \left(\sinh\frac{\alpha l}{a} - \frac{\cosh\frac{\alpha l}{a}}{\tanh\frac{l}{a}} + \frac{1}{\tanh\frac{l}{a}}\right)\right] \times \left[\cosh\frac{z}{a} - 1.0\right] - \sinh\frac{z}{a} + \frac{z}{a}\right\};$$

when $\alpha l \le z \le l$

$$\theta = \frac{Ta}{\left(1+\frac{1}{H}\right)GJ}\left\{\left[\frac{\left(\cosh\frac{\alpha l}{a} - 1.0\right)}{H \times \sinh\frac{l}{a}} + \frac{\left(\cosh\frac{\alpha l}{a} - \cosh\frac{l}{a} + \frac{l}{a} \times \sinh\frac{l}{a}\right)}{\sinh\frac{l}{a}}\right] + \cosh\frac{z}{a}\left[\frac{\left(1.0 - \cosh\frac{\alpha l}{a}\right)}{H \times \tanh\frac{l}{a}} + \frac{\left(1.0 - \cosh\frac{\alpha l}{a} \times \cosh\frac{l}{a}\right)}{\sinh\frac{l}{a}}\right] + \sinh\frac{z}{a}\left[\frac{\left(\cosh\frac{\alpha l}{a} - 1.0\right)}{H} + \cosh\frac{\alpha l}{a}\right] - \frac{z}{a}\right\}$$

where, $$H=\frac{\left[\dfrac{\left(1.0-\cosh\dfrac{\alpha l}{a}\right)}{\tanh\dfrac{l}{a}}+\dfrac{\left(\cosh\dfrac{\alpha l}{a}-1.0\right)}{\sinh\dfrac{l}{a}}+\sinh\dfrac{\alpha l}{a}-\dfrac{\alpha l}{a}\right]}{\left[\dfrac{\left(\cosh\dfrac{l}{a}+\cosh\dfrac{\alpha l}{a}\times\cosh\dfrac{l}{a}-\cosh\dfrac{\alpha l}{a}-1.0\right)}{\sinh\dfrac{l}{a}}+\dfrac{l}{a}(\alpha-1.0)-\sinh\dfrac{\alpha l}{a}\right]}$$

Thus, the second derivative of the twist angle θ with respect to longitudinal distance z is

$$\theta''=\frac{T}{GJa(H+1)}\left\{\left[H\times\left(\frac{1}{\sinh\frac{l}{a}}+\sinh\frac{\alpha l}{a}-\frac{\cosh\frac{\alpha l}{a}}{\tanh\frac{l}{a}}\right)+\left(\sinh\frac{\alpha l}{a}-\frac{\cosh\frac{\alpha l}{a}}{\tanh\frac{l}{a}}+\frac{1}{\tanh\frac{l}{a}}\right)\right]\times\cosh\frac{z}{a}-\sinh\frac{z}{a}\right\},\ \text{for } 0\le z\le\alpha l$$

and when z = αl (i.e., at the location of the beam bottom flange, where the torque is applied, and hence the maximum warping normal stress is located), θ” becomes:

$$\theta''\big|_{z=\alpha l}=\frac{T}{GJa(H+1)}\left\{\left[H\times\left(\frac{1}{\sinh\frac{l}{a}}+\sinh\frac{\alpha l}{a}-\frac{\cosh\frac{\alpha l}{a}}{\tanh\frac{l}{a}}\right)+\left(\sinh\frac{\alpha l}{a}-\frac{\cosh\frac{\alpha l}{a}}{\tanh\frac{l}{a}}+\frac{1}{\tanh\frac{l}{a}}\right)\right]\times\cosh\frac{\alpha l}{a}-\sinh\frac{\alpha l}{a}\right\}$$

Note: $a=\sqrt{\dfrac{EC_w}{GJ}}$;

E = modulus of elasticity for the column steel;
G = shear modulus of elasticity for the column steel;
C_w = warping constant for the column cross-section;
J = torsional constant for the column cross-section;
T = torque applied by the beam compression (bottom) flange to column;
l = length of column between two fixed ends, where l = 2h, and h is the story height;
α = fraction of the total column length indicating the location of the applied torque (beam bottom flange);
z = longitudinal distance along the column.

(This page left blank)